

Two-Temperature Solution and Spectral Analysis of Flows Around Compact Objects

A

THESIS SUBMITTED

To

PT. RAVISHANKAR SHUKLA UNIVERSITY, RAIPUR

FOR

THE DEGREE OF DOCTOR OF PHILOSOPHY

IN

PHYSICS

UNDER THE FACULTY OF SCIENCE

2021

SUPERVISOR :

Dr. Indranil Chattopadhyay

(Scientist)

ARIES, Manora Peak

Nainital – 263 001

INVESTIGATOR :

Shilpa Sarkar

(Senior Research Fellow)

ARIES, Manora Peak

Nainital – 263 001

Research Centre

ARYABHATTA RESEARCH INSTITUTE OF OBSERVATIONAL
SCIENCES (ARIES)

MANORA PEAK, NAINITAL 263 001, INDIA

Declaration by Candidate

I declare that the thesis entitled *Two-Temperature Solution and Spectral Analysis of Flows Around Compact Objects* is my own work conducted under the supervision of *Dr. Indranil Chattopadhyay* at *Aryabhata Research Institute of observational sciencES (ARIES), Nainital, Uttarakhand, India*, approved by the Research Degree Committee. I have put in more than 300 days of attendance excluding course work with the supervisor at the center.

I further declare that to the best of my knowledge the thesis does not contain any part of any work, which has been submitted for the award of any degree either in this University or in any other University/Deemed university without proper citation.

Dr. Indranil Chattopadhyay

Signature of the Supervisor

SCIENTIST 'F'
ARIES NAINITAL

Shilpa Sarkar

Signature of the Candidate

Prof. Dipankar Banerjee

Signature of the Director, ARIES

Director
Aryabhata Research Institute Of
Observational Sciences (ARIES)
(Under Department of Science & Technology)

Signature of the Chairman, DRC

CHAIRMAN,
Deptt. Research Commission
Inst. in Physics & Astrophysics
University, RAIPUR, (CG)



Certificate by the Supervisor

This is to certify that the work entitled *Two-Temperature Solution and Spectral Analysis of Flows Around Compact Objects* is a piece of research work done by *Ms. Shilpa Sarkar* under my guidance and supervision for the degree of Doctor of Philosophy in *PHYSICS* of Pt. Ravishankar Shukla University, Raipur (Chhattisgarh), India. The candidate has put in an attendance of more than 300 days excluding course work with me.

To the best of my knowledge and belief this thesis

1. Embodies the work of the candidate himself.
2. Has duly been completed.
3. Fulfills the requirements of the Ordinance relating to the Ph.D. degree of the University;
and
4. Is up to the standard both in respect of contents and language for being referred to the examiner.



Dr. Indranil Chattopadhyay

Signature of the Supervisor

SCIENTIST 'F'
ARIES, NAINITAL

Forwarded,



Signature of the Chairman, DRC

CHAIRMAN,
Dept. Research Committee
Ph.D. in Physics & Astrophysics
Pt. Ravishankar Shukla University, RAIPUR, (CG)



Prof. Dipankar Banerjee

Signature of the Director, ARIES

Director
Aryabhata Research Institute Of
Observational Sciences (ARIES)
(Under Department of Science & Technology)

Declaration on Plagiarism

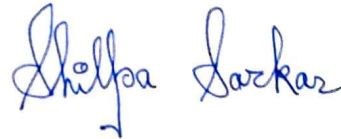
I declare that all materials in my thesis entitled ***“Two-Temperature Solution and Spectral Analysis of Flows Around Compact Objects”*** are my own work and do not involve plagiarism. I also certify that

a. No sentence, equation, diagram, table, paragraph or section has been copied verbatim from previous work unless it is placed under quotation marks and duly referenced.

b. The work presented is original and my own work. No ideas, processes, results or words of others have been presented as my own work.

c. Report on Plagiarism check is appended.

Raipur, Dated : 22.07.2021



SHILPA SARKAR

Name & Signature of the Candidate

Forwarded,



Signature of the Chairman, DRC



Prof. Dipankar Banerjee

Signature of the Director, ARIES

CHAIRMAN,
DRC Research Committee
SOS in Physics & Astrophysics
Pt. N.S. University, RAIPUR, (C.G.)

Director
Aryabhata Research Institute Of
Observational Science (ARIES)
(Under Department of Science & Technology)

Urkund Analysis Result

Analysed Document: Two-Temperature Solution and Spectral Analysis of Flows Around Compact Objects(Shilpa Sarkar).pdf (D110516197)
 Submitted: 7/16/2021 1:44:00 PM
 Submitted By: library_prsu@rediffmail.com
 Significance: 2 %

Sources included in the report:

indu-thesis.pdf (D58709283)
 indu-thesis.pdf (D58917086)
 Thesis_Kuldeep_Singh.pdf (D88887293)
 Work - Copy.pdf (D109015566)
 Work - Copy.pdf (D109015681)
 15830f.pdf (D52323168)
 PhD Thesis of Sandip Dutta 08-02-2021.pdf (D94893164)
 thesis.pdf (D28291449)
 thesis22.pdf (D30290039)
 SM-thesis-urkund.pdf (D109266861)
 Sagar Mondal PhD Thesis (2021)-Plagiarism Check.pdf (D109724257)
 75095be7-d09b-4eca-8d50-2cb3b1e82a6e
 27dd2d71-69c7-44a9-9c01-bdbbe5f092dd
 ad049d87-11ba-44a9-b184-e826f11cff57
<https://www.sfu.ca/~vjungic/Ramsey/RamseyNotes.pdf>
<https://www.aanda.org/articles/aa/pdf/2018/06/aa31830-17.pdf>
<https://arxiv.org/pdf/1802.05677>
<https://arxiv.org/pdf/1712.05534>
https://www.researchgate.net/publication/321873654_Properties_of_Two-Temperature_Dissipative_Accretion_Flow_Around_Black_Holes
<https://arxiv.org/pdf/2007.10861>
<https://academic.oup.com/mnras/article/402/2/961/1103036>
<https://arxiv.org/pdf/1605.03184>
<https://iopscience.iop.org/article/10.1086/308768/fulltext/40355.text.html>
<https://arxiv.org/pdf/1712.07588>
https://www.aanda.org/articles/aa/full_html/2018/06/aa31830-17/aa31830-17.html
<https://arxiv.org/pdf/2005.01276>

Instances where selected sources appear:

58


 University Librarian
 Pt. Ravishankar Shukla University
 Raipur (C.G.)

Copy Right Transfer Approval Form

APPENDIX - 5

Copy Right Transfer Approval Form (Clause 14e of the Ordinance - 45)

Name of the Candidate: Shilpa Sarkar
Department: School of Studies in Physics and Astrophysics
Degree : Doctor of Philosophy in Physics
University: Pt. Ravishankar Shukla University, Raipur
Supervisor: Dr. Indranil Chattopadhyay
Thesis Title: Two-Temperature Solution and Spectral Analysis
of Flows Around Compact Objects
Year of Award:

Agreement

1. I hereby declare that, if appropriate, I have obtained and attended hereto a written permission/statement from owner(s) of each third party copyrighted matter to be included in my thesis/dissertation, allowing distribution as specified below.
2. I hereby grant to the university and its agents the non-exclusive license to archive and make accessible, under the condition specified below, my thesis/dissertation, in whole or in part in all forms of media, now or hereafter known. I retain all other ownership rights to the copyright of the thesis/dissertation. I and my Supervisor, also retain the right to use in future works (such as articles or books) all or part of this thesis, dissertation, or project report.

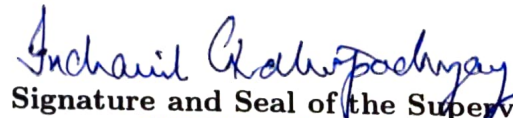
Condition:

1. Release the entire work for access worldwide


Signature of the Candidate

Place : RAIPUR

Date : 22.07.2021


Signature and Seal of the Supervisor

SCIENTIST F
ARIES NAINITAL



Signature and Seal of the Director

Director

Aryabhata Research Institute of
Observational Sciences (ARIES)
(Under Department of Science & Technology)

ARIES/AC/CC/2016/05

ARYABHATTA RESEARCH INSTITUTE OF OBSERVATIONAL SCIENCES

(An autonomous Institute under the Department of Science & Technology)

Manora Peak, Nainital

Pre Ph.D Course work - 2015-16

It is certified that **Ms. Shilpa Sarkar** attended and successfully completed the Pre-PhD course work conducted at ARIES during the session August 2015- July 2016.

Her performance in the course work was found satisfactory and she has obtained an aggregate of **72.1%**.



Wahab Uddin
(Acting Director)



Manish Naja
(Chairman, Academic Committee)

SCHOOL OF STUDIES IN PHYSICS AND ASTROPHYSICS
PT. RAVISHANKAR SHUKLA UNIVERSITY,
RAIPUR - 492010 CHHATTISGARH (INDIA)



Dr. D. P. Bisen
M. Phil, Ph. D.
Profess & Head

Phone : (M) 9406201131, 7987186589
(O) (0771) 2262864
Email : hodphysics98@gmail.com
: dpbisen@rediffmail.com

Ref. : ...1619/...Phy/2021

Raipur

Date : ...19/07/2021

CERTIFICATE

This is to certify that **Shilpa Sarkar** has given Pre-Ph.D. seminar on her thesis entitled “**Two-Temperature Solution and Spectral Analysis of Flows Around Compact Objects**” on **15.07.2021** at School of Studies in Physics & Astrophysics, Pt. Ravishankar Shukla University, Raipur (C. G.). **Shilpa Sarkar**'s presentation has been very satisfactory and DRC members have recommended for the submission of her Ph. D. Thesis.

D. P. Bisen
19/07/2021

Chairman

Departmental Research Committee
SoS in Physics & Astrophysics
Pt. Ravishankar Shukla University, Raipur (C. G.)

SCHOOL OF STUDIES IN PHYSICS AND ASTROPHYSICS
PT. RAVISHANKAR SHUKLA UNIVERSITY,
RAIPUR - 492010 CHHATTISGARH (INDIA)



Dr. D. P. Bisen
M. Phil, Ph. D.
Profess & Head

Phone : (M) 9406201131, 7987186589
(O) (0771) 2262864
Email : hodphysics98@gmail.com
: dpbisen@rediffmail.com

Ref. : 16.20/Phy/2021.

Raipur,

Date : 19/07/2021

PLAGIARISM VERIFICATION REPORT

This is to certify that plagiarism check of the Ph.D. thesis submitted by **Shilpa Sarkar** entitled “**Two-Temperature Solution and Spectral Analysis of Flows Around Compact Objects**” has been carried out by **Pt. Sunder Lal Sharma Library of Pt. Ravishankar Shukla University, Raipur (C.G.) India**. On the basis of this report it has been found that the percentage of similarity is 2%; within acceptable limit (less than 10%). Therefore almost no plagiarism was found.

Hence DRC recommends the thesis may be dispatched to the reviewers for further action.


19/07/2021
Chairman

Departmental Research Committee
SoS in Physics & Astrophysics
Pt. Ravishankar Shukla University, Raipur (C.G)

SCHOOL OF STUDIES IN PHYSICS AND ASTROPHYSICS
PT. RAVISHANKAR SHUKLA UNIVERSITY,
RAIPUR - 492010 CHHATTISGARH (INDIA)



Dr. D. P. Bisen
M. Phil, Ph. D.
Profess & Head

Phone : (M) 9406201131, 7987186589
(O) (0771) 2262864
Email : hodphysics98@gmail.com
: dpbisen@rediffmail.com

Ref. : 1621/Phy/2021

Raipur

Date : 19/07/21

CERTIFICATE OF PUBLICATION

This is to certify that **Shilpa Sarkar** has published her research work in various reputed international journals having **Science Citation Index (SCI) with IMPACT FACTOR** as listed in Thomson Reuters which are given below:

List of Publications

Publications In Refereed Journal:

1. Two temperature solutions and emergent spectra from relativistic accretion discs around black holes
Sarkar, S; Chattopadhyay, I; Laurent, P, 2020, Astronomy & Astrophysics (A&A), 642, A209. (Impact factor : 5.636)

2. General relativistic two-temperature accretion solutions for spherical flows around black holes
Sarkar, S; Chattopadhyay, I, 2019, International Journal of Modern Physics D (IJMPD), 28, 1950037 (Impact factor : 2.154)

3. Two temperature accretion through magnetic funnels onto neutron stars
Sarkar, S; Singh, K; Chattopadhyay, I; Laurent, P, 2021, Astronomy & Astrophysics (A&A), under review (Impact factor : 5.802)

4. Spectral signature of annihilation lines in advective accretion discs around black holes
Sarkar, S; Chattopadhyay, I; Laurent, P, 2021, The Astrophysical Journal (ApJ), to be submitted (Impact factor : 5.745)

5. Transverse oscillations in a coronal loop triggered by a jet
Sarkar, S; Pant, V; Srivastava, A. K.; Banerjee, D, 2016, Solar Physics, 291, 3269 (Impact factor : 3.272)

Conference Proceedings:

1. Pair production and annihilation in advective accretion disks around black holes
Sarkar, S; Chattopadhyay, I; 2020, J. Phys.: Conf. Ser, 1640, 012022 (Impact factor : 0.65)

2. Two-temperature advective transonic accretion flows around black holes
Sarkar, S; Chattopadhyay, I; 2019, J. Phys.: Conf. Ser, 1336, 012019 (Impact factor : 0.64)


19/07/2021

Chairman

Departmental Research Committee
SoS in Physics & Astrophysics
Pt. Ravishankar Shukla University, Raipur (C. G.)

“Physicists are made of atoms.

A physicist is an attempt by an atom to understand by itself.”

— Michio Kaku

“A black hole holds all the colors of the universe”

— Anthony T. Hincks: An author of life, Volume 1

ACKNOWLEDGEMENTS

It is indeed a great joy to come to the milestone of this beautiful journey, and to express my deep respect and gratitude towards all my well wisher who have always supported and encouraged me throughout this journey.

I first and foremost pay my gratitude and sincere thanks to my PhD supervisor Dr. Indranil Chattopadhyay for all his encouragement and guidance which he provided me. I deeply appreciate his valuable scientific discussions, remarks and comments. I am particularly influenced by his motivating attitude, and immense knowledge. I am also grateful to him for building-up my own skills and potential to carry out insightful scientific research work independently. Not only professional we also shared a personal attachment, which helped me build up into a more strong person.

I express my deep gratitude to current ARIES director Prof. Dipankar Banerjee for his kind support and encouragement towards my PhD and research works. Not only director of my institute, but he has been the helping hand since my M.Sc., under whom I did my dissertation in 2015 at IIA, Bengaluru. That was the first time I went out of my house to do my studies. He has been a constant source of encouragement and gave me a direction in my life. He was constantly present there and is even now, to guide me at every step. I also express my sincere and soulful thanks to former directors - Dr. Wahab Uddin and Late Dr. Anil Kumar Pandey for all the help they provided during my PhD tenure. I would like to thank Dr. Vaibhav Pant. Literally he is my first guide. Most part of my M.Sc dissertation and my first paper is contributed because of the hard work and the potential that he saw inside me, when I was just a college student. Although afraid of him till now, but I have a deep respect towards him and that is unmatched. Fortunate enough I could meet him when he joined ARIES as a faculty. Seeing him from a 3rd year PhD student to a faculty at ARIES, he is still the same. I learnt a lot from him, especially professionalism and helping others. I will always look upto him! I am also thankful to all other scientists, especially Dr. Kuntal, Dr. Jeewan, Dr. Ramakant, Dr. Manish and Dr. S. B. Pandey, and other staffs at ARIES (especially Prashant ji and Ramdayal ji) for always helping and supporting me and providing me a positive environment. Finally, I acknowledge the financial support provided by the Department of Science and Technology (DST), New Delhi, India.

My sincere thanks to Prof. S. K. Pandey, Prof. D. P. Bisen, Prof. Nameeta Brahme and Prof. N. Chakradhari and all other member of Physics department at Raipur University for their kind support in all the academic and administrative matters. I heartily

thank all students and colleagues at Raipur University for their help and support in various matters related to Raipur University.

I want to thank Prof. Philippe Laurent, with whom I worked for a month at CEA, Saclay, France. Apart from being a very nice person, he gave me an exposure to work in abroad, visit his institute and collaborate. He took care of everything possible and made my journey all the way more easy and exciting.

I express my utmost love and gratitude to (Dr.) Abhishek Paswan and his family as well as my family for supporting me in every situation of my life, through my ups and downs and also for staying beside me unconditionally and encouraging me to continue higher studies and research works. Abhishek's part in my life is inexpressible and unparallel. Thank you!

I am thankful to my all batch mates, specially to Gaurav (Bhaiya) and Bharti, for their help and providing several nice and joyful moments. Sad or happy, we were always together. From start of the PhD to last, we shared every tiny moment spent at ARIES together. I would always keep these memories with me. I would like to thank Kuldeep bhaiya for always being there when I needed him. A nice person at heart and always helpful. I would like to thank Raj! His help is uncountable. These two people have been there always, whether I had fever, my amazon parcels, my thesis, my paper, my visa etc. We also shared fruitful scientific discussions.

I also express my sincere thanks to all my juniors (especially Arpan for sharing his logical views always) and seniors (especially Subhash Da for the mentorship and long discussions and arguments and Mukesh Bhaiya) for their kind help in various matters and for making a enjoyable atmosphere during my PhD. I express my special thanks to - Aditya Jaiswal (the movies we saw together with Bhaiya, the gifts you gave, the parties we celebrated, playing ludo at Simz), Aditya Priyadarshi, Manju Da, Ritesh and Pankaj Bhaiya with whom I cherished every moment spent. I would also like to thank my roommate Bhavya for being ever sweet to me. Their company had been great throughout my stay at ARIES.

— Shilpa

ABSTRACT

Black holes (BHs) are one of the most exotic objects found in the Universe. They fall into a class of astrophysical objects termed as *compact objects*. Apart from BHs, neutron stars (NSs) and white dwarfs (WDs) also fall into this classification. Such a name ‘compact’ is derived because, all these objects have very high values of compactness ratio ($\mathcal{C}_{\mathcal{R}}$) which is defined as the ratio of the mass of the object to its radius. $\mathcal{C}_{\mathcal{R}}$ of compact objects are generally > 100 times than that of a normal Sun-like star. This high $\mathcal{C}_{\mathcal{R}}$ is responsible for their large surface gravitational potentials and hence, they exhibit a phenomena called *accretion*, which is the most efficient mechanism known till now, to convert the gravitational potential energy of the matter into radiation. The accretion flows around compact objects carry imprints of the nature of the central object. Hence, modelling of accretion flows is necessary. Based on this theme, we carried out our thesis work.

One of the processes that play a significant role in the accretion physics of a BH system as well as in shaping the spectrum is — *production of $e^+ - e^-$ pairs and their annihilation*. In this thesis, we aim to address and study the effect of pairs in accretion flows around BHs, in addition to computing the emitted spectrum. The pairs are mostly assumed to be produced from the interaction of photons present in radiation fields created due to different dissipative processes like bremsstrahlung, synchrotron and their respective inverse-Comptonizations. These pairs can annihilate giving rise to an additional radiation field. We found from the analysis done, that pairs are indeed responsible for shaping the observable spectrum. They play a significant role, especially in those systems which harbour large radiation fields. One of the interesting results of this work is the presence of a distinct annihilation bump near $\sim m_e c^2$ in the spectrum. This feature was found consistently in all the solutions, where ample of pairs were produced. Also, we found an increase in luminosity in the accreting system, due to the production of pairs.

The above work was done in one-temperature regime. One-temperature solutions are important to the extent that, it gives a general idea about the flow behaviour, its dynamics as well as energetics. It can extract the essential qualitative features of the flow without getting involved into the other complexities of an accreting system. But, to accurately extract the luminosity and spectra of an accretion flow, one needs to have information of electron temperature (T_e) inside the flow, which may or may not be comparable to proton temperature (T_p). Thus, we also investigated extensively two-temperature accretion flows in this thesis.

We identified one of the major problems present in two-temperature theory which is ‘degeneracy’. This degeneracy is caused because of the increase in number of flow variables, without any increase in the number of governing equations, *i.e.* now instead of a single temperature, we have two different temperatures, T_e and T_p . But, there is no known principle dictated by plasma physics which may constrain the relation between these two temperatures, at any point of the flow. This problem is not new and has been skirted out by many authors by parametrising T_e and T_p or assuming T_e (or T_p) value at any boundary or by some other arbitrary assumptions. This thesis work addressed and investigated this issue for the first time. Also, a novel methodology has been proposed to remove the degeneracy such that a given set of constants of motion harbour a unique solution. This is the main highlight of my thesis work. We validated the proposed methodology on different compact objects (BHs and NSs) as well as different types of accretion flows (spherical, rotating and accretion along magnetic funnels). The degeneracy is irrespective of the nature of central object. This is the first time, to the best of our knowledge, that such work has been done. After constraining degeneracy we studied and analysed the spectrum of the unique two-temperature accretion solutions around these objects.

Thus, in short, this thesis aims to study accretion flows around compact objects, specifically BHs and NSs, alongwith analysing their spectrum, for a broad range of parameter space.

LIST OF PUBLICATIONS

PUBLICATIONS IN REFEREED JOURNAL:

1. *Two temperature solutions and emergent spectra from relativistic accretion discs around black holes*
Sarkar, S; Chattopadhyay, I; Laurent, P, 2020, *Astronomy & Astrophysics (A&A)*, 642, A209, (Impact factor : 5.636)
2. *General relativistic two-temperature accretion solutions for spherical flows around black holes*
Sarkar, S; Chattopadhyay, I, 2019, *International Journal of Modern Physics D (IJMPD)*, 28, 1950037 (Impact factor : 2.154)
3. *Two temperature accretion through magnetic funnels onto neutron stars*
Sarkar, S; Singh, K; Chattopadhyay, I; Laurent, P, 2021, *Astronomy & Astrophysics (A&A)*, under review (Impact factor : 5.802)
4. *Spectral signature of annihilation lines in advective accretion discs around black holes*
Sarkar, S; Chattopadhyay, I; Laurent, P, 2021, *The Astrophysical Journal (ApJ)*, to be submitted (Impact factor : 5.745)
5. *Transverse oscillations in a coronal loop triggered by a jet* [†]
Sarkar, S; Pant, V; Srivastava, A. K.; Banerjee, D, 2016, *Solar Physics*, 291, 3269 (Impact factor : 3.272)

[†]This paper is not included in my thesis

CONFERENCE PROCEEDINGS

1. *Pair production and annihilation in advective accretion disks around black holes*

[Sarkar, S](#); Chattopadhyay, I; 2020, *J. Phys.: Conf. Ser.*, 1640, 012022 (**Impact factor : 0.65**)

2. *Two-temperature advective transonic accretion flows around black holes*

[Sarkar, S](#); Chattopadhyay, I; 2019, *J. Phys.: Conf. Ser.*, 1336, 012019 (**Impact factor : 0.64**)

NOTATIONS AND ABBREVIATIONS

The most commonly used notations and abbreviations in the thesis are given below. If a symbol has been used in a different connection than listed here, it has been explained at the appropriate place.

Notations

e or e^-	Electron
e^+	Positron
p	Proton
M	Mach number
M_*	Mass of a star
M_\odot	Mass of Sun
M_{BH}	Black hole mass
R_*	Radius of a star
R_\odot	Radius of Sun
$\mathcal{C}_{\mathcal{R}}$	Compactness ratio
T	Temperature
Θ	Dimensionless temperature
n	Number density (in units of cm^{-3})
n_l	Number density of leptons (in units of cm^{-3})
ξ	Composition parameter = n_p/n_{e^-}
χ	Ratio of mass of electron to mass of proton = m_e/m_p
ρ	Mass density (in units of g/cm^{-3})
e	Energy density
m	Mass
p	Isotropic gas pressure
h	Specific enthalpy
Γ	Adiabatic index
N	Polytropic index
r	Radial distance
r_s	Schwarzschild radius = $2GM_{\text{BH}}/c^2$
r_g	Unit of distance (radius), defined as GM_{BH}/c^2
r_{ci}	Inner sonic point
r_{cm}	Middle sonic point
r_{co}	Outer sonic point

r_{sh}	Shock location
r_{ps}	Primary shock location
r_{ss}	Secondary shock location
r_{corot}	Co-rotation radius
r_{d}	Disc radius
v	Velocity
u^μ	Components of four-velocity
$g^{\mu\nu}$	Metric tensor components
γ	Lorentz factor
a_{s}	Sound-speed
t	Timescales
H	Half-height
θ^c	Angle which the surface of the flow makes with the normal
θ^o	Angle within which photons will be captured by the BH
P	Period
B	Magnetic field
a_*	Black hole spin parameter
λ	Specific angular momentum
l or u_ϕ	Covariant azimuthal component of four-velocity
L	Luminosity
L_{Edd}	Eddington luminosity
L_{A}	Accretion luminosity
L_{b}	Local bulk angular momentum
L_0	Bulk angular momentum at the horizon
η_{r}	Radiative efficiency
η_{v}	Viscosity coefficient
ν	Frequency (in Hz)
ν_{v}	Kinematic viscosity
α	Spectral index
α_{v}	Shakura-Sunyaev viscosity parameter
α_{f}	Fine-structure constant
β	Ratio of magnetic pressure to gas pressure
β_{d}	Uncertainties in the heating due to magnetic energy dissipation
δ_{v}	Fraction of viscous energy dissipated which is transferred to protons
δ_{B}	Fraction of magnetic energy dissipated which is transferred to protons

\mathcal{E}	Canonical form of Bernoulli constant
E	Generalized Bernoulli constant
E_{NF}	Energy from nuclear fusion
E_{A}	Energy released due to accretion
Q^+	Heating rate
Q^-	Cooling rate
Q_{v}	Heating due to viscous dissipation
Q_{B}	Heating due to magnetic dissipation
δQ	Difference in heating and cooling rates ($Q^+ - Q^-$)
ζ	Enhancement factor relating to Comptonization
CR	Compression ratio
S	Shock strength
Φ_{g}	Gravitational potential energy
Φ_{PWP}	Paczyński and Witta potential
Φ_{centri}	Energy due to centrifugal force
Ψ	Magnetic flux function
\dot{M}	Accretion rate
\dot{M}_{Edd}	Eddington rate
$\dot{\mathcal{M}}$	Entropy accretion rate
in	Values near horizon
τ_{es}	Optical depth
G	Gravitational constant
c	Speed of light
k	Boltzmann constant
e_{c}	Charge of an electron
r_{e}	Electron radius
$\ln \Lambda$	Coulomb logarithm
σ_{T}	Thomson scattering cross-section

Abbreviations

ADAF	A dvection- D ominated A ccretion F low
AGN	A ctive G alactic N ucleus
ARIES	A ryabhata R esearch I nstitute of observational S cienc ES
BH	B lack H ole

CR EoS	Chattopadhyay & Ryu Equation of State
CV	Cataclysmic Variable
EHT	Event Horizon Telescope
EoM	Equations of Motion
EoS	Equation of State
Eq	Equation
Fig	Figure
GR	General-Relativistic
HD	Hydro-Dynamic
HMXB	High-Mass X-ray Binary
ISCO	Inner Stable Circular Orbit
LMXB	Low-Mass X-ray Binary
MCP	Multiple Critical Point
MHD	Magneto-Hydro-Dynamic
MVB	Multi-Valued Branch
NP	Newtonian Potential
NS	Neutron Star
PA	Peitz & Appl
PWP	Paczyński & Witt Potential
SB	Supersonic Branch
SC19a	Sarkar & Chattopadhyay, 2019a
SLE76	Shapiro, Lightman & Eardley, 1976
SS	Shakura & Sunyaev
SSD	Shakura & Sunyaev Disc
TS	Transonic Solution
WD	White Dwarf
XRB	X-Ray Binary
YSO	Young-Stellar Object

Contents

LIST OF FIGURES	xxxv
LIST OF TABLES	xxxvii
1 INTRODUCTION	1
1.1 OVERVIEW	1
1.2 COMPACT OBJECTS	1
1.3 OBSERVING COMPACT OBJECTS	2
1.4 THE THEORY OF ACCRETION	3
1.4.1 EDDINGTON LIMIT	4
1.4.2 FOUNDATIONS OF ACCRETION THEORY: ADVANCES IN MODELLING OF ACCRETION FLOWS	5
1.5 ONE-TEMPERATURE AND TWO-TEMPERATURE ACCRETION FLOWS	10
1.6 RELATIVISTIC EQUATION OF STATE	13
1.7 GENERAL-RELATIVITY AND PSEUDO-NEWTONIAN POTENTIAL	14
1.8 THE PRESENT WORK	15
1.8.1 MOTIVATION	15
1.8.2 THESIS LAYOUT	17
2 MATHEMATICAL FRAMEWORK	19
2.1 OVERVIEW	19
2.2 GENERAL-RELATIVISTIC HYDRODYNAMIC EQUATIONS	19
2.3 MAGNETOHYDRODYNAMIC EQUATIONS	23
2.4 EQUATION OF STATE	24
2.5 DISSIPATIVE PROCESSES	25
2.5.1 VISCOUS HEATING	25
2.5.2 HEATING DUE TO MAGNETIC DISSIPATION	25
2.5.3 COULOMB COUPLING	26

CONTENTS

2.5.4	INVERSE-BREMSSTRAHLUNG	26
2.5.5	BREMSSTRAHLUNG	26
2.5.6	SYNCHROTRON	27
2.5.7	INVERSE-COMPTONIZATION	27
2.5.7.1	COMPTONIZED BREMSSTRAHLUNG	27
2.5.7.2	COMPTONIZED SYNCHROTRON	28
2.5.8	COMPTON HEATING	28
2.5.9	ANNIHILATION	28
2.6	SPECTRAL ANALYSIS	29
2.7	CRITICAL POINT CONDITIONS	30
2.8	SHOCK CONDITIONS	31
2.9	A GENERAL APPROACH TO OBTAIN A GLOBAL TRANSONIC SOLUTION	32
3	ONE-TEMPERATURE ACCRETION FLOWS AROUND BLACK HOLES	33
3.1	INTRODUCTION	33
3.2	ASSUMPTIONS AND EQUATIONS USED	35
3.2.1	HEATING AND COOLING MECHANISMS	37
3.2.2	PAIR PRODUCTION AND ANNIHILATION RATES	38
3.3	METHODOLOGY TO OBTAIN SOLUTIONS	39
3.3.1	FINDING A GENERAL ONE-TEMPERATURE TRANSONIC SOLUTION – I : WITHOUT PAIRS	39
3.3.2	FINDING A GENERAL ONE-TEMPERATURE TRANSONIC SOLUTION – II : INCLUSION OF PAIR PROCESSES	43
3.4	RESULTS	44
3.4.1	ONE-TEMPERATURE ACCRETION SOLUTIONS – I : WITHOUT PAIRS	45
3.4.1.1	A TYPICAL ACCRETION SOLUTION	45
3.4.1.2	A TYPICAL SHOCKED SOLUTION	48
3.4.1.3	SOLUTIONS IN $E - L_0$ PARAMETER SPACE	50
3.4.1.4	VARIATION OF SOLUTIONS WITH CHANGE IN α_v	52
3.4.1.5	VARIATION OF SOLUTIONS WITH CHANGE IN \dot{M}	53
3.4.2	ONE-TEMPERATURE ACCRETION SOLUTIONS – II : INCLUSION OF PAIRS	54
3.4.2.1	BREMSSTRAHLUNG DOMINATED SOLUTIONS	55
3.4.2.1.1	A TYPICAL ACCRETION SOLUTION AND SPEC- TRUM	55

3.4.2.2	BREMSSTRAHLUNG AND SYNCHROTRON DOMINATED SOLUTIONS	57
3.4.2.2.1	A TYPICAL ACCRETION SOLUTION	57
3.4.2.2.2	EMISSIVITIES AND SPECTRUM	58
3.4.2.2.3	CONTRIBUTION OF DIFFERENT REGIONS OF A PAIR-PRODUCING ACCRETION DISC TO THE TOTAL SPECTRUM	60
3.4.2.2.4	VARIATION OF SOLUTIONS WITH CHANGE IN E	60
3.4.2.2.5	SOLUTIONS IN $\dot{M} - L_0$ PARAMETER SPACE	63
3.5	DISCUSSIONS AND CONCLUSIONS	67
4	DEGENERACY: A GENERIC PROBLEM IN TWO-TEMPERATURE SOLUTIONS; ENTROPY: THE TOOL TO REMOVE IT	71
4.1	OVERVIEW	71
4.2	HISTORY OF TWO-TEMPERATURE ACCRETION FLOWS	71
4.3	DEGENERACY: A GENERIC PROBLEM	73
4.4	ENTROPY: A TOOL TO REMOVE IT	74
4.4.1	ONE-TEMPERATURE ACCRETION FLOWS: ENTROPY ACCRETION RATE EXPRESSION	75
4.4.2	TWO-TEMPERATURE ACCRETION FLOWS: ENTROPY ACCRETION RATE EXPRESSION	76
4.4.3	APPLICATION OF ENTROPY ACCRETION RATE FORMULA	78
5	TWO-TEMPERATURE FLOWS AROUND BLACK HOLES – I: SPHERICAL ACCRETION	81
5.1	INTRODUCTION	81
5.2	ASSUMPTIONS AND EQUATIONS USED	83
5.3	SOLUTION PROCEDURE	84
5.3.1	METHOD TO FIND SONIC POINT: ONE-TEMPERATURE VERSUS TWO-TEMPERATURE	85
5.4	RESULTS	86
5.4.1	INVESTIGATING DEGENERACY IN TWO-TEMPERATURE FLOWS	86

CONTENTS

5.4.2	ENTROPY MEASURE AS A TOOL TO REMOVE DEGENERACY IN TWO-TEMPERATURE FLOWS	87
5.4.3	PROPERTIES OF UNIQUE TWO-TEMPERATURE TRANSONIC SOLUTIONS	88
5.4.3.1	CRITICAL POINT PROPERTIES:	88
5.4.3.2	FLOW VARIABLES AND EMISSIVITY	89
5.4.3.3	DEPENDENCE OF ACCRETION FLOW ON E AND \dot{M}	91
5.4.3.4	EFFECT OF THE MASS OF THE CENTRAL BH	92
5.4.3.5	LUMINOSITY AND EFFICIENCY OF THE SYSTEMS	95
5.4.3.6	EFFECT OF DISSIPATIVE PROTON HEATING	95
5.5	DISCUSSIONS AND CONCLUSIONS	97
6	TWO-TEMPERATURE FLOWS AROUND BLACK HOLES – II: ROTATING ACCRETION FLOWS	99
6.1	INTRODUCTION	99
6.2	ASSUMPTIONS AND EQUATIONS USED	100
6.2.1	CONICAL FLOWS	102
6.2.2	FLOWS IN HYDROSTATIC EQUILIBRIUM IN THE TRANSVERSE DIRECTION	103
6.3	SOLUTION PROCEDURE	104
6.3.1	METHOD TO OBTAIN SONIC POINTS IN TWO-TEMPERATURE ROTATING FLOWS	104
6.3.2	PRESENCE OF DEGENERACY IN TWO-TEMPERATURE TRANSONIC SOLUTIONS: METHOD TO REMOVE IT AND OBTAIN UNIQUE TRANSONIC SOLUTIONS, INVOKING THE SECOND LAW OF THERMODYNAMICS	107
6.3.2.1	CONICAL FLOWS	107
6.3.2.2	FLOWS IN HYDROSTATIC EQUILIBRIUM IN THE TRANSVERSE DIRECTION	109
6.3.3	STABILITY ANALYSIS OF THE HIGHEST ENTROPY TRANSONIC SOLUTION	111
6.4	RESULTS	112
6.4.1	CONICAL FLOWS	112
6.4.1.1	GENERAL TWO-TEMPERATURE SOLUTIONS	113
6.4.1.2	LUMINOSITY AND EFFICIENCY OF BONDI FLOWS AS COMPARED TO ROTATING FLOWS :	114

6.4.2	FLOWS IN HYDROSTATIC EQUILIBRIUM IN THE TRANSVERSE DIRECTION	115
6.4.2.1	GENERAL TWO-TEMPERATURE SOLUTIONS	115
6.4.2.2	CONTRIBUTION OF DIFFERENT REGIONS OF THE ACCRETION DISC TO THE OVERALL SPECTRUM :	118
6.4.2.3	DEPENDENCE OF ACCRETION SOLUTIONS AND CORRESPONDING SPECTRA WITH ENERGY AND ANGULAR MOMENTUM:	119
6.4.2.4	SHOCKED SOLUTION, SPECTRA AND THE PARAMETER SPACE:	122
6.4.2.5	DEPENDENCE OF SPECTRUM ON β :	124
6.4.2.6	DEPENDENCE OF SOLUTIONS AND SPECTRA ON β_d :	125
6.4.2.7	POSSIBILITY OF PAIR PRODUCTION AND PION PRODUCTION	126
6.4.2.8	DEPENDENCE ON \dot{M} AND M_{BH} :	127
6.4.2.9	LUMINOSITY, EFFICIENCY AND SPECTRAL INDEX OF TWO-TEMPERATURE FLOWS :	128
6.4.2.10	COMPARISON WITH OBSERVATIONS:	129
6.5	DISCUSSIONS AND CONCLUSIONS	131
7	TWO-TEMPERATURE ACCRETION FLOWS AROUND NEUTRON STARS	135
7.1	INTRODUCTION	135
7.2	GOVERNING EQUATIONS AND ASSUMPTIONS	136
7.2.1	STREAM FUNCTION AND THE STRONG MAGNETIC FIELD ASSUMPTION	137
7.2.2	FINAL FORM OF EQUATIONS	138
7.2.3	ENTROPY ACCRETION RATE EXPRESSION	140
7.2.4	SONIC POINT CONDITIONS AND SHOCK CONDITIONS	140
7.3	SOLUTION METHODOLOGY	141
7.3.1	TWO-TEMPERATURE ACCRETION FLOWS AROUND NS: DEGENERACY AND THE DIFFICULTY IN REMOVING IT	141
7.3.2	METHODOLOGY TO OBTAIN UNIQUE TWO-TEMPERATURE TRANSONIC SOLUTION AROUND AN NS	142
7.4	RESULTS	147
7.4.1	A TYPICAL TWO-TEMPERATURE ACCRETION SOLUTION AROUND AN NS	148

CONTENTS

7.4.2	CONTRIBUTION OF DIFFERENT REGIONS OF AN ACCRETION FLOW TO THE OBSERVABLE SPECTRUM	150
7.4.3	SHOCK ANALYSIS	152
7.4.3.1	PROPERTIES OF PRIMARY SHOCK	152
7.4.3.2	PROPERTIES OF SECONDARY SHOCK	154
7.4.4	EFFECT OF MAGNETIC FIELD AND SPIN PERIOD ON THE AC- CRETION SOLUTION	157
7.4.5	EFFECT OF BERNOULLI PARAMETER ON ACCRETION FLOWS . . .	158
7.4.6	EFFECT OF VARIATION OF ACCRETION RATE	161
7.5	DISCUSSIONS AND CONCLUSIONS	163
8	HIGHLIGHTS, CONCLUSIONS AND FUTURE PROSPECTS	165
8.1	SUMMARY OF THE THESIS	165
8.1.1	ONE-TEMPERATURE ACCRETION FLOWS AROUND BLACK HOLES .	165
8.1.2	TWO-TEMPERATURE ACCRETION FLOWS	166
8.1.2.1	TWO-TEMPERATURE FLOWS AROUND BLACK HOLES . .	167
8.1.2.2	TWO-TEMPERATURE FLOWS AROUND NEUTRON STARS .	168
8.2	SCOPE OF FUTURE RESEARCH WORK	168
8.2.1	TWO-TEMPERATURE MODELLING OF ACCRETION DISCS AROUND KERR BHs	168
8.2.2	MONTE-CARLO SIMULATIONS	169
8.2.3	STUDYING OF ACCRETION FLOWS AROUND WHITE DWARFS . . .	170
8.2.4	NUMERICAL SIMULATIONS	170
8.2.5	OBSERVATIONS AND DATA ANALYSIS	170
A	TWO-TEMPERATURE ACCRETION DISCS AROUND BHs: IN HYDROSTATIC EQUI- LIBRIUM IN THE TRANSVERSE DIRECTION	171
A.1	EFFECT OF VISCOSITY IN THE SYSTEM	171
A.2	ESTIMATION OF ELECTRON-POSITRON PAIR PRODUCTION IN ADVEC- TIVE TWO-TEMPERATURE ACCRETION DISC	173
A.3	ESTIMATION OF GAMMA-RAY EMISSION BY PION INTERACTION	174
B	TWO-TEMPERATURE ACCRETION FLOWS AROUND NSs	177
B.1	REGENERATING ONE-TEMPERATURE ACCRETION SOLUTION AROUND NS USING THE NEW METHODOLOGY PROPOSED	177
	REFERENCES	188

List of Figures

1.1	Accreting systems distinguished on the basis of flow structure, where (a) represents a spherical accretion flow or popularly known as Bondi flow, (b) general rotating flow or a flow with angular momentum and (c) magnetised accretion flow or funnel flow.	6
2.1	Photon capture by the strong gravity of BH is presented. Photons emitted at r (in units of r_g) and propagating within the black shaded cone is trapped by the central BH (inside the grey shaded region). Blue lines, represent the radiation which escapes. In this plot, $r = 2$ is the location of the event horizon.	30
3.1	A cartoon diagram representing an accretion disc around a BH. The disc is assumed to be axisymmetric, advective, transonic in nature and rotating with viscous stresses removing angular momentum outwards. At every radius of the flow, there are radiative processes which gives rise to photon fields, conducive enough for the production of pairs. These pairs can annihilate and produce an additional radiation field.	35
3.2	Flowchart representing the methodology to obtain a transonic solution. . .	42
3.3	Methodology to obtain a general transonic solution (TS) is presented using iteration technique on Θ_{in} . Panel (a) finds r_{ci} (marked using solid black circle) and the TS is represented using dashed red curve, (b) finds r_{co} (marked using black star) and the corresponding TS is plotted using solid red curve. Thus, for the present set of flow parameters used, we have MCP. The flow does not harbour a shock, hence the final global TS (solid red line) passes through r_{co} and is plotted in panel (c). Flow parameters used are, $E = 1.001$, $\lambda_{\text{in}} = 2.65$, $\alpha_v = 0.01$, $\beta = 0.5$, $\beta_d = 0.01$, $\dot{M} = 0.5\dot{M}_{\text{Edd}}$ and $M_{\text{BH}} = 10M_{\odot}$	43

LIST OF FIGURES

- 3.4 Finding of transonic solution with pairs, using feedback iterative technique. Iteration 1 is pair-free. From iteration 2 onwards, pair-production and annihilation processes are included. Iteration process continues until the solutions converge. The corresponding change in Mach number, $M = v/a$ (panel a) and composition of the flow, $\xi = n_p/n_{e^+}$ (panel b) with the change in iteration are plotted. Stars in panel (a) represent the sonic points. The flow parameters used are, $E = 1.001$, $\lambda_{\text{in}} = 2.5$, $\dot{M} = 0.6\dot{M}_{\text{Edd}}$, $\alpha_v = 0.05$ and $M_{\text{BH}} = 10M_{\odot}$ 43
- 3.5 (a) Global accretion solution, M (solid, red) and other flow variables like (b) v (solid, orange), (c) l (solid, magenta), (d) E (solid, brown), (e) T (solid, green) and (f) Γ (solid, blue) are plotted against r . The sonic point is represented using black star. The flow parameters used are, $E = 1.0005$, $\lambda_{\text{in}} = 2.639$, $\beta = 0.1$, $\beta_d = 0.01$, $\alpha_v = 0.01$, $\dot{M} = 0.2\dot{M}_{\text{Edd}}$ and $M_{\text{BH}} = 10M_{\odot}$. The corresponding L_0 is 2.850. 45
- 3.6 We plot against r in panel (a) n (solid, violet), (b) individual radiative mechanisms Q^- in units of $\text{ergs cm}^{-3} \text{ s}^{-1}$ (see label given inset), and total of all these processes (solid, black curve) and (c) total cooling (Q^- , dashed, dark-green), heating due to magnetic dissipation (Q_B , solid, light-green) and heating due to viscous dissipation (Q_v , dotted, blue) all in dimensionless units. The flow parameters used are same as in Fig. 3.5. 47
- 3.7 We plot in panel (a) T_e as a function of r . In panel (b) we plot the spectrum in solid, black line. Individual contributions are also plotted in this panel (see inset for label) The flow parameters used are same as in Fig. 3.5. . . . 48
- 3.8 Plotted are (a) M , (b) v , (c) l , (d) E , (e) T , (f) Γ , (g) n , (h) total cooling, Q^- (solid, black) in units of $\text{ergs cm}^{-3} \text{ s}^{-1}$ along with the contribution from individual components (see label inset), and (i) in dimensionless units, Q^- (dashed, dark-green), Q_B (solid, light-green) and Q_v (dotted, blue). There is a shock at $r_{\text{sh}} = 18.377$ (marked using arrows) and r_{co} and r_{ci} are represented using black star and solid black circle respectively. The flow parameters used are: $E = 1.002$, $\lambda_{\text{in}} = 2.730$, $\beta = 0.4$, $\beta_d = 0.01$, $\alpha_v = 0.01$, $\dot{M} = 0.3\dot{M}_{\text{Edd}}$ and $M_{\text{BH}} = 10M_{\odot}$ 49
- 3.9 We plot in panel (a) T_e as a function of r . In panel (b) we plot the spectrum in solid, black line along with the individual contributions. The flow parameters used are same as in Fig. 3.8. 50

3.10	Variation of solutions with change in E and L_0 of the flow. Rest of the flow parameters are, $\beta = 0.1$, $\beta_d = 0.01$, $\alpha_v = 0.01$, $\dot{M} = 0.1\dot{M}_{\text{Edd}}$ and $M_{\text{BH}} = 10M_{\odot}$	51
3.11	Variation of spectrum with change in E and L_0 of the flow. Rest of the flow parameters are same as in Fig. 3.10.	52
3.12	Effect of α_v on (a) M , (b) l and (c) spectrum. The different curves represent solutions with different values of α_v (see top label). The other flow parameters used are, $E = 1.0005$, $L_0 = 3.023$, $\beta = 0.5$, $\beta_d = 0.01$, $\dot{M} = 0.1\dot{M}_{\text{Edd}}$ and $M_{\text{BH}} = 10M_{\odot}$	53
3.13	Plotted are (a) M , (b) l , (c) T , (d), n , (e) Q_v in dimensionless units and (f) total cooling, Q^- also in dimensionless units. Each curve represent solutions with different \dot{M} values labelled in the plot. Other flow parameters are: $E = 1.001$, $L_0 = 3.185$, $\beta = 0.8$, $\beta_d = 0.01$, $\alpha_v = 0.01$ and $M_{\text{BH}} = 10M_{\odot}$	54
3.14	We plot (a) T_e and (b) corresponding spectrum for different \dot{M} values. Other flow parameters used are same as in Fig. 3.13.	55
3.15	(a) M , l and (b) ξ vs $\log r$ plotted for different accretion rates of the system. Their corresponding spectrum is plotted in panel (c). The accretion rates used are: $\dot{M} = 0.1\dot{M}_{\text{Edd}}$ (dotted, red), $\dot{M} = 0.4\dot{M}_{\text{Edd}}$ (dashed, green) and $\dot{M} = 0.8\dot{M}_{\text{Edd}}$ (solid, blue). Rest of the flow parameters are $E = 1.001$, $\lambda_{\text{in}} = 2.60$, $\alpha_v = 0.01$ and $M_{\text{BH}} = 10M_{\odot}$	56
3.16	General one-temperature accretion solution in the presence of pair production and annihilation process. We plot against r the solution and the corresponding flow variables: (a) M , (b) v , (c) ξ , (d) T , (e) Γ and (f) l . The flow parameters used are, $E = 1.002$, $L_0 = 2.880$, $\beta = 0.1$, $\beta_d = 0.01$, $\alpha_v = 0.01$, $\dot{M} = 0.98\dot{M}_{\text{Edd}}$ and $M_{\text{BH}} = 10M_{\odot}$	57
3.17	We plot against r in panel (a) B (solid, brown), (b) radiative mechanisms Q^- in units of $\text{ergs cm}^{-3} \text{ s}^{-1}$ (solid, black), (c) Q^- (solid, light-blue), Q_B (dotted, dark-blue) and Q_v (dashed, violet) all in dimensionless units, and (d) spectrum (solid, black). In panels (b) and (d), the individual components have also been plotted (see label inset). We see a distinct annihilation line (single-dot long-dashed, red) present in the spectrum (panel d). The flow parameters used are same as in Fig. 3.16.	58

LIST OF FIGURES

- 3.18 We plot in panel (A) variation of ξ against r . We have shaded different regions using different colours. The spectrum corresponding to the shaded region is plotted in panels (a1)–(a5) using the same colour coding in solid curves. Individual emission processes have also been plotted inset using different linestyles. The flow parameters used are same as in Fig. 3.16. We see the signature of distinct annihilation line (single-dot long-dashed line). 59
- 3.19 Variation in topology of the solution with change in E , values of which are written inset. Each solution is colour coded with a colour bar representing n_{e+} . The flow parameters for these solutions are, $L_0 = 3.081$, $\beta = 0.1$, $\beta_d = 0.01$, $\alpha_v = 0.01$, $\dot{M} = 0.7\dot{M}_{\text{Edd}}$ and $M_{\text{BH}} = 10M_{\odot}$ 61
- 3.20 Panels (b1)–(b8) plots the variation in ξ with r and panels (c1)–(c8) plots the corresponding observable spectrum (solid curve), where the annihilation spectrum is represented using single-dot long-dashed grey line. Higher the value of E more will be the production of pairs and a clear signature of annihilation is present in the spectrum. The flow parameters used are same as in Fig. 3.19. 62
- 3.21 Variation in solution topology with L_0 and \dot{M} of the flow (corresponding values written inside the figure). Rest of the flow parameters are, $E = 1.0008$, $\beta = 0.1$, $\beta_d = 0.01$, $\alpha_v = 0.01$ and $M_{\text{BH}} = 10M_{\odot}$ 63
- 3.22 Variation in T (a1, b1, c1), Γ (a2, b2, c2) and dimensionless cooling rate Q^- (a3, b3, c3). Each row is for different values of \dot{M} (values written at the right side), while each panel shows curves corresponding to different L_0 s. The flow parameters are same as in Fig. 3.21. 64
- 3.23 Variation of ξ with r . Higher \dot{M} solutions, show higher values of pair production and hence a large decrease in ξ . The flow parameters are same as in Fig. 3.21. 64
- 3.24 Observable spectrum (solid curves) for the solutions given in Fig. 3.21. Contribution from annihilation is represented using single-dot long-dashed grey line. A consistent annihilation line is visible in almost all solutions with $\dot{M} = 1.00\dot{M}_{\text{Edd}}$. Also, inside each panel we represent the spectrum of a pair-free solution using dashed, black curve. 65
- 5.1 Cartoon diagram representing spherical flow around a BH. The arrows represent the direction of accretion. 83

- 5.2 Accretion \dot{M} (solid, red) and wind \dot{M} (dotted, red) as a function of r are plotted. The different solutions in different panels are obtained by changing T_{pin} (values of which are written at the top of each panel) but are for the same set of constants of motion $\Rightarrow \dot{M} = 0.01\dot{M}_{\text{Edd}}$ and $E = 1.0001$. The solution is for a $10M_{\odot}$ BH. 86
- 5.3 Top left panel: Variation of $\dot{\mathcal{M}}_{\text{in}}$ as a function of T_{pin} for accretion flow with $\dot{M} = 0.1\dot{M}_{\text{Edd}}$ and $E = 1.001$ onto a $10M_{\odot}$ BH. Panels ‘a’ to ‘e’ presents M vs r (solid) corresponding to each of the points ‘a’—‘e’ on the $\dot{\mathcal{M}}_{\text{in}}-T_{\text{pin}}$ curve. The stars represent the location of the sonic points (r_c). At $T_{\text{pin}} = 5.0 \times 10^{11} K$ (marked ‘c’) entropy maximises, so panel ‘c’ is the correct solution for the given set of constants of motion: E and \dot{M} 87
- 5.4 Variation of sonic points and its properties with the accretion rate (\dot{M}) of the BH. Here we have assumed $M_{\text{BH}} = 10M_{\odot}$. We have used accretion rate values, $\dot{M} = 0.01\dot{M}_{\text{Edd}}$ (solid, yellow), $0.10\dot{M}_{\text{Edd}}$ (dotted, red), $0.50\dot{M}_{\text{Edd}}$ (dashed, magenta), $1.00\dot{M}_{\text{Edd}}$ (long-dashed, green) and $5.00\dot{M}_{\text{Edd}}$ (dot-dashed, blue). 89
- 5.5 Variation of (a) M ; (b) E ; (c) T_p (dotted, blue) and T_e (solid, magenta); (d) Γ_p (dotted, blue) and Γ_e (solid, magenta); (e) v ; and (f) Coulomb coupling (Q_{ep} , single-dot long-dashed, orange) and total electron cooling (Q_e^- , solid, black) alongwith the individual components: bremsstrahlung (Q_{br} , dotted, red), synchrotron (Q_{syn} , short-dashed, blue), inverse-Comptonization (Q_{ic} , long-dashed, magenta) and inverse-bremsstrahlung (Q_{ib} , single-dot short-dashed, green) are plotted as functions of r . The black star on the M distribution (panel a) represent the location of r_c . The accretion disc parameters are, $E = 1.00001$, $\dot{M} = 0.01\dot{M}_{\text{Edd}}$ and $M_{\text{BH}} = 10M_{\odot}$ 90
- 5.6 Variation of v (a_1, b_1, c_1); electron number density, n_{e^-} (a_2, b_2, c_2) and T_p & T_e in panels (a_3, b_3, c_3), as a function of r . The generalized Bernoulli parameter changes from the left panels $E = 1.0001$ (a_1, a_2, a_3), to the middle panels $E = 1.001$ (b_1, b_2, b_3) and then to the right panels $E = 1.01$ (c_1, c_2, c_3). Other parameters selected are $M_{\text{BH}} = 10M_{\odot}$ and $\dot{M} = 0.01\dot{M}_{\text{Edd}}$. 92

LIST OF FIGURES

- 5.7 Variation of v (a_1, b_1, c_1); electron number density, n_{e^-} (a_2, b_2, c_2), T_p & T_e in panels (a_3, b_3, c_3) and various emissivities ($Q_e^-, Q_{br}, Q_{syn}, Q_{ic}, Q_{ib}$ and Q_{ep}) (a_4, b_4, c_4) as a function of r . The accretion rate changes from the left panels $\dot{M} = 0.01$ (a_1, a_2, a_3, a_4), to the middle panels $\dot{M} = 0.2$ (b_1, b_2, b_3, b_4) and then to the right panels $\dot{M} = 0.5$ (c_1, c_2, c_3, c_4). Other parameters selected are, $M_{BH} = 10 M_\odot$ and $E = 1.0001$ 93
- 5.8 Variation of n_{e^-} (a_1, b_1, c_1); emissivities and Coulomb coupling (a_2, b_2, c_2) as function of r . Left column panels (a_1 and a_2) are for $M_{BH} = 10M_\odot$, the middle column are for $M_{BH} = 10^3M_\odot$ (b_1, b_2) and for right column $M_{BH} = 10^6M_\odot$ (c_1, c_2). Other parameters selected are $E = 1.0001$ and $\dot{M} = 0.5\dot{M}_{Edd}$ 94
- 5.9 (a) Luminosity, L , and (b) efficiency η_r as a function of \dot{M} . Each curve corresponds to $M_{BH} = 10^8M_\odot$ (solid, red) and $M_{BH} = 10M_\odot$ (dotted, blue). $E = 1.001$ for both these flows. 95
- 5.10 Three-velocity v (a_1, b_1), temperatures (a_2, b_2) and emissivities, heating and Coulomb coupling (a_3, b_3) as a function of r . The solutions are for $\dot{M} = 0.01\dot{M}_{Edd}$ (a_1 — a_3) and $\dot{M} = 0.5\dot{M}_{Edd}$ (b_1 — b_3). Other parameters are, $E = 1.001$ and $M_{BH} = 10M_\odot$ 96
- 6.1 Cartoon diagram representing conical flow around a BH. The half-height is a constant function of r and θ^c is the angle which the surface of the flow makes with the normal. 102
- 6.2 Cartoon diagram representing flows in hydrostatic equilibrium in the vertical direction. The half-height is a function of r, v, λ, Θ_e and Θ_p . In this cartoon diagram, a shocked solution is represented and therefore, the inner region is seen to expand suddenly at a given r . This is because the flow is in hydrostatic equilibrium and is allowed to expand freely (unlike conical flows). In shock-free solutions, sudden expansion of the disc does not occur. Rather, it is gradual, depending on the heating and cooling present in that region. 103

- 6.3 Method to find sonic points. Solutions are presented in terms of $M(=v/a)$ vs $\log r$ plot. $\Theta_{\text{pin}} = 7.162 \times 10^{-2}$ for all iterations. Panel (a) iterations to obtain r_{ci} (black circle) and panel (b) iterations to obtain r_{co} (black star). Various branches plotted are MB (dot dashed, green), TS (dashed, red) and SB (dot dashed, blue). Respective Θ_{ein} s are mentioned inside the panels. Panel (c) plots full set of TSs: global accretion solution (solid, red) through r_{co} and accretion solution through r_{ci} (dashed, red). Equatorial global wind (through r_{co}) and non global wind (through r_{ci}) are represented using dotted, red curve. The accretion disc flow parameters used are $\lambda = 2.5$, $E = 1.000045$, $\dot{M} = 0.001\dot{M}_{\text{Edd}}$ and $M_{\text{BH}} = 10M_{\odot}$ 105
- 6.4 Left: (a) $\dot{\mathcal{M}}_{\text{in}}$ vs T_{pin} plot for spherical flows. Single sonic point exist for every T_{pin} . Panels (a1-a4) M vs $\log r$ plot for various T'_{pin} s marked with solid coloured dots in panel (a). The values of T_{pin} are: (a1) $3.0 \times 10^{11}K$, (a2) $4.0 \times 10^{11}K$, (a3) $5.0 \times 10^{11}K$, (a4) $6.0 \times 10^{11}K$. Right: (b) Shows $\dot{\mathcal{M}}_{\text{in}}$ vs T_{pin} plot for rotating conical flows ($\lambda = 2.5$). Solid black curve is for the solutions passing through r_{co} , while dotted black curve is for solutions passing through r_{ci} . Panels (b1-b4): Shows solutions for various T'_{pin} s marked in panel (b), value of which are: (b1) $4.0 \times 10^{11}K$, (b2) $5.1 \times 10^{11}K$, (b3) $6.4 \times 10^{11}K$, (b4) $6.7 \times 10^{11}K$, (b5) $6.86 \times 10^{11}K$, (b6) $8.0 \times 10^{11}K$. Entropy maximises at a certain T_{pin} in both the cases (green star). Corresponding unique solutions are plotted in panels (a2) and (b2). Flow parameters used are $E = 1.002$, $\dot{M} = 0.05\dot{M}_{\text{Edd}}$, $M_{\text{BH}} = 10M_{\odot}$, $\theta^c = 60^\circ$ 108
- 6.5 Left: M vs $\log r$ plot for various values of T_{pin} : (a) $3.1 \times 10^{11}K$, (b) $5.605 \times 10^{11}K$, (c) $6.04 \times 10^{11}K$, (d) $6.460 \times 10^{11}K$, (e) $6.554 \times 10^{11}K$ and (f) $7.0 \times 10^{11}K$. Global solutions are represented by solid lines. In panel (g) $\dot{\mathcal{M}}_{\text{in}}$ vs T_{pin} is plotted. Solid black curve is for the solutions passing through r_{co} , while dotted black curve is for solutions passing through r_{ci} . Panels (a)–(f) are the solutions corresponding to the points marked in right panel (g). The disc flow parameters are $E = 1.0015$, $\lambda = 2.6$ and $\dot{M} = 0.02\dot{M}_{\text{Edd}}$. The space time is described by a BH of mass $10M_{\odot}$ and the system is in hydrostatic equilibrium in the vertical direction. 109

LIST OF FIGURES

- 6.6 Stability analysis of the unique transonic two-temperature solution with maximum entropy. The flow parameters used are same as Fig. 6.5. $\Delta = (d\dot{\mathcal{M}}_{\text{in}}/dT_{\text{pin}})$ is plotted against variation of T_{pin} . The arrows indicate that Δ converge at $T_{\text{pin}} = T_{\text{pin}|_{\text{max}}}$ (blue dot) and is the stable equilibrium solution. This T_{pin} is the solution with maximum entropy marked ‘c’ in Fig. 6.5g. 112
- 6.7 We plot (a) Mach number (M), (b) v (solid, cyan) and v_ϕ (dotted, blue), (c) T_p (solid, orange), T_e (dotted, red), (d) Γ_p (solid, orange), Γ_e (dotted, red), (e) $\log(n)$ (solid, magenta), (f) E (solid, brown), with respect to $\log r$. In panel (g) we plot the total spectrum (solid black) along with contributions coming from bremsstrahlung emission (dotted violet), synchrotron (dashed yellow) and inverse Comptonization (dotted-dashed grey). The set of flow parameters used are $E = 1.00001$, $\lambda = 3.0$, $\dot{M} = 0.001\dot{M}_{\text{edd}}$, $M_{\text{BH}} = 10M_\odot$ and $\theta^c = 60^\circ$ 113
- 6.8 Plot shows the variation of L (in ergs s^{-1}) with \dot{M} (normalised with respect to \dot{M}_{Edd}). The colour bar shows the change in efficiency, η_r (in logarithmic scale). The circled points are for spherical flows while diamond shaped points are for flows having angular momentum $\lambda = 2.4$. The other flow parameters used here are, $E = 1.001$, $M_{\text{BH}} = 10M_\odot$ and $\theta^c = 60^\circ$ 114
- 6.9 (a) $\dot{\mathcal{M}}_{\text{in}}$ is plotted against T_{pin} . The entropy for inner sonic point solutions (dotted, black) and outer sonic points (solid, black) are presented. T_{pin} marked with green triangle corresponds to maximum entropy solution. Flow variables plotted are (b) M (solid, green), (c) v (solid, cyan) and v_ϕ (dotted, blue), (d) $\log n$ (solid, magenta), (e) T_p (dotted, red), T_e (solid, orange), (f) Γ_p (dotted, red), Γ_e (solid, orange), (g) E (solid, brown) as functions of $\log r$. The flow parameters are $E = 1.000045$, $\lambda = 2.5$, $\dot{M} = 0.001\dot{M}_{\text{Edd}}$ and $M_{\text{BH}} = 10M_\odot$. In panel (b), the sonic point is marked with a black star. 116
- 6.10 Top three panels shows the emissivity vs $\log r$ plot for the flow presented in Fig. 6.9. Bottom panel (d) shows the spectrum of the accretion flow. . . 117

- 6.11 (a) M and (b) $\log T$ vs $\log r$ and (c) total spectrum (solid, black) and contribution from various length scales of the accretion disc, $2-3r_g$ (dotted, magenta), $3-5r_g$ (dashed, blue), $5-8r_g$ (single-dotted short-dashed, green), $8-10r_g$ (single-dotted long-dashed, brown), $10-100r_g$ (double-dotted short-dashed, orange) and $100-1000r_g$ (triple-dotted short-dashed, red). Flow parameters are $E = 1.0002$, $\lambda = 2.48$, $\dot{M} = 0.05\dot{M}_{\text{Edd}}$ and $M_{\text{BH}} = 10M_{\odot}$. . 118
- 6.12 Variation of solutions, M as a function of $\log r$ with variation of E and λ . From left to right specific energy increases as $E = 1.0005, 1.001, 1.003$ and 1.01 . From top to bottom the angular momentum increases as $\lambda = 2.40, 2.55, 2.70$ and 2.85 . Other parameters are $\dot{M} = 0.01\dot{M}_{\text{Edd}}$ and $M_{\text{BH}} = 10M_{\odot}$. 120
- 6.13 Variation of spectrum with E and λ . The set of values for E and λ and other parameters are same as that in Fig. 6.12. 121
- 6.14 (a) A typical shocked solution (a) with its corresponding number density (b), emissivities (c) and spectrum (d) is presented. The parameters taken are $E = 1.002$, $\lambda = 2.58$, $\dot{M} = 0.2\dot{M}_{\text{Edd}}$ and $M_{\text{BH}} = 10M_{\odot}$ 123
- 6.15 Shock parameter space for $\dot{M} = 0.01\dot{M}_{\text{Edd}}$ (solid, green), $0.10\dot{M}_{\text{Edd}}$ (dashed, blue) and $1.00\dot{M}_{\text{Edd}}$ (dotted, red) around a $10M_{\odot}$ BH. 124
- 6.16 Change in spectra with increase in $\beta = 0.002$ (solid, blue), 0.01 (dashed, green) and 0.02 (dotted, red). Other parameters used are $E = 1.003$, $\lambda = 2.54$ and $\dot{M} = 0.1\dot{M}_{\text{Edd}}$ in an accretion disc around $M_{\text{BH}} = 10M_{\odot}$. . . 124
- 6.17 Plotted are the accretion solutions (a1, b1) and their corresponding spectra (a2, b2) for a flow with $E = 1.001$, $\lambda = 2.61$ around $M_{\text{BH}} = 10M_{\odot}$. Various curves are for $\beta_d = 0.013$ (solid, blue), $\beta_d = 0.015$ (dashed, green) and $\beta_d = 0.017$ (dotted, red). The accretion rates and ratio of magnetic to gas pressure are chosen are $\dot{M} = 1.0\dot{M}_{\text{Edd}}$, $\beta = 0.2$ (a1, a2) and $\dot{M} = 1.5\dot{M}_{\text{Edd}}$, $\beta = 0.15$ (b1, b2). 125
- 6.18 Spectra from (a) $M_{\text{BH}} = 10M_{\odot}$ for different accretion rates $\dot{M} = 0.1\dot{M}_{\text{Edd}}$ (solid, blue), $\dot{M} = 0.6\dot{M}_{\text{Edd}}$ (dashed, green) and $\dot{M} = 1.2\dot{M}_{\text{Edd}}$ (dotted, red); (b) $\dot{M} = 0.1\dot{M}_{\text{Edd}}$ but around $M_{\text{BH}} = 10M_{\odot}$ (solid, blue), $M_{\text{BH}} = 10^3M_{\odot}$ (dashed, magenta) and $M_{\text{BH}} = 10^6M_{\odot}$ (dotted, brown). Other disc parameters are $E = 1.001$ and $\lambda = 2.4$ 128

LIST OF FIGURES

- 6.19 (a) Variation of bolometric luminosity (in ergs s^{-1}) and (b) efficiency (in %) as a function of \dot{M} (in units of Eddington rate, \dot{M}_{edd}). Colour bar indicates the spectral index (α). BHs of different masses : $10M_{\odot}$ (small circle), 10^3M_{\odot} (medium circle) and 10^6M_{\odot} (largest circle) are represented with increasing sizes of the circles. The parameters used here are $E = 1.001$ and $\lambda = 2.4$ 129
- 6.20 Model spectrum obtained from entropy maximisation formulation (solid, black) is fitted onto the observations of M87 spectrum (data points acquired from Mandal & Chakrabarti (2008) and references therein). 130
- 7.1 Representation of a magnetised accretion flow, with magnetic moment (μ) co-aligned with the rotation (Ω) axis of the star. Matter is accreted along magnetic flux tube, which connects the accretion disc to the surface of the NS. The sonic point is marked as r_c , primary shock is marked as r_{ps} and r_* is the radius of NS. 137
- 7.2 Panel (a) shows a cartoon diagram of an accretion flow geometry where matter is accreted till it reaches a radius, $r_{\text{in}} \sim r_g (< r_*)$. In panel (b), corresponding projected solution is plotted (solid red curve). In panel (c), a cartoon representing accretion geometry around a NS is given. Accretion flow on reaching the NS surface forms a primary shock at r_{ps} . The projected solution (plotted in panel b) on satisfying the NS boundary condition is plotted in panel (d), with the ‘ghost solution’ represented in dotted grey. The region between r_{in} and r_* is shaded with grey. Primary shock is at $r_{\text{ps}} = 3.301r_g$ (downward red arrow). The constants of motion of the flow are: $E = 0.9984$, $P = 1.1\text{s}$ and $\dot{M} = 10^{14}\text{g/s}$, while the NS properties are, $M_* = 1.4M_{\odot}$, $r_* = 10^6\text{cm}$ and $B_* = 10^{10}\text{G}$. T_{pin} at r_{in} is $1 \times 10^{11}\text{K}$ 144
- 7.13 Accretion flow variables (a) M , (b) $\log T_p$, (c) $\log T_e$, (d) $\log n$ are plotted w.r.t $\log r$. In panel (e) corresponding continuum spectra of the flow is presented. Each curve inside these panels correspond to different values of E (labelled inset). Flow parameters are, $P = 1.0\text{s}$, $\dot{M} = 10^{15}\text{g/s}$ and $B_* = 10^{10}\text{G}$ 160

- A.1 We present (a) distribution of specific angular momentum (λ) and (b) heating in the system as a function of radius ($\log r$), when viscosity assumed is relativistic (PA, solid, green) and Newtonian (SS, dotted, magenta). In panel (b) we also compare the heating due to magnetic dissipation, Q_B (blue, dashed), assuming $\beta_d = 0.02$. The flow parameters are $E = 1.0005$, $\alpha_v = 0.01$, $\lambda_{in} = 2.60$, $\dot{M} = 0.01\dot{M}_{Edd}$ and $M_{BH} = 10M_{\odot}$ 171
- A.2 (a1, b1) Comparison of number density of protons n_{p+} (solid, black), positron number densities n_{e+} (without annihilation, dotted, blue) and with both production and annihilation rates (dashed, green). (a2, b2) Comparison of emissivities of the total radiative cooling Q_{tot} (solid, brown) and emissivities due to annihilation of pairs Q_{ann} (dotted, red). We used two sets of accretion disc parameters, (a1, a2) $\dot{M} = 1.0$, $\beta = 0.2$ and (b) $\dot{M} = 1.5$, $\beta = 0.15$. The other parameters are $\beta_d = 0.013$, $E = 1.001$, $\lambda = 2.41$ and $M_{BH} = 10M_{\odot}$. 174
- A.3 Dependence of (1) $\log T_p$ as a function of $\log r$ and (2) $\log \nu L_{\nu}$ with $\log \nu$ for (a1, a2) different accretion rates: $\dot{M} = 0.01$ (dotted, red), 0.1 (dashed, green) and 1.0 (solid, blue) and (b1, b2) different BH masses: $M_{BH} = 10^2$ (solid, blue), 10^4 (dashed, green), 10^6 (dotted, red). The gamma ray emission is presented in grey in both the spectrums. 176

List of Tables

1.1	Properties of compact objects	2
3.1	Luminosity and efficiency of pair-producing and pair-free solutions for the flows represented in Fig. 3.21	66
6.1	Various flow properties of the solutions plotted in Figs. 6.5a–f. The disc parameters used are $E = 1.0015$, $\lambda = 2.6$, $\dot{M} = 0.02\dot{M}_{\text{Edd}}$ around $M_{\text{BH}} = 10M_{\odot}$	111
6.2	Spectral properties of the regions marked in Fig. 6.11	119
6.3	Various flow properties of the solutions plotted in Fig. 6.17.	126
6.4	Various properties of the spectra plotted in Fig. 6.18a (left table) and Fig. 6.18b (right table).	128
7.1	Spectral properties of the regions shaded in Fig. 7.6	152
7.2	The effect of variation of E on solutions plotted in Fig. 7.13	159

Chapter 1

INTRODUCTION

1.1 OVERVIEW

Black Holes (BHs) are one of the most exotic objects found in the Universe. They cannot be directly observed (hence, ‘black’), but it is possible to map their environment and guess their presence by studying the physics of matter around them. Using this concept, the Event Horizon Telescope (EHT) gave us the first-ever image of a BH or, more appropriately, its ‘*silhouette*’ on April 10, 2019, ruining all the criticisms prevailing on its existence ([Event Horizon Telescope Collaboration et al., 2019](#)). This major breakthrough in the history of science has opened up a new window to understand BH physics and test the general theory of relativity in an altogether new perspective and dimension. From science to technology, EHT has indeed enlarged the horizon of physics. This chapter briefly introduces BHs and other compact objects like neutron stars (NSs) and white dwarfs (WDs). The aforementioned objects also exhibit exotic phenomena around them, for example, accretion. This will be discussed, along with a brief history of the developments made to model and hence understand these objects. In the end, the motivation behind this thesis work will be presented.

1.2 COMPACT OBJECTS

BHs fall into a class of astrophysical objects known as Compact Objects. NSs and WDs also fall into this classification. These objects share some basic common features. Firstly, they represent the end products of stellar evolution, that is, when a star dies. Thus, these objects are unable to restrict the gravitational collapse by generating thermal or radiation pressure. While WDs are supported by the pressure exerted by degenerate electrons,

1. INTRODUCTION

NSs are supported by the pressure of degenerate neutrons. When these degeneracy pressures are insufficient to halt a gravitation collapse, BHs are formed. BHs are completely collapsed objects: collapsed to singularities, making them one of the most spectacular objects found in the Universe. The second reason, because of which these objects are grouped together, is their extremely small size, which is quantified using a ratio called the *compactness ratio* ($\mathcal{C}_{\mathcal{R}}$). This is defined as the ratio of the mass of the star (M_*) to the radius of the star (R_*). Thus, $\mathcal{C}_{\mathcal{R}} = M_*/R_*$, values of which, in the case of WDs, NSs and BHs are written below in Table 1.1, in decreasing order.

Table 1.1: Properties of compact objects

Object	Mass (M_*) [†]	Radius (R_*) [†]	$\mathcal{C}_{\mathcal{R}} = M_*/R_*$
Black hole	$\gtrsim 3 - 10^9 M_{\odot}$	$r_s \simeq 3(M_*/M_{\odot})$ km	1
Neutron star	$\sim 1 - 3M_{\odot}$	~ 10 km	0.3 – 0.9
White dwarf	$\sim 1M_{\odot}$	$\sim 7 \times 10^3$ km	4.2×10^{-4}
Sun-type star	$1M_{\odot}$	$\sim 7 \times 10^5$ km	4.2×10^{-6}

[†] The values quoted are, as per the current understanding, and the limits are still highly debatable (Shapiro & Teukolsky, 1983). Values of $\mathcal{C}_{\mathcal{R}}$ are in units of $2G/c^2$.

In this table, $r_s = 2GM_*/c^2$, is the Schwarzschild radius, where G is the Gravitational constant and c is the speed of light. M_{\odot} and R_{\odot} represents the solar mass ($M_{\odot} = 1.989 \times 10^{33}$ gm) and solar radius ($R_{\odot} = 6.960 \times 10^{10}$ cm) respectively. The BH values mentioned in the first row of Table 1.1, is for a Schwarzschild (non-rotating) BH. In the case of rotating BHs or Kerr BHs, $R_* = (1 + \sqrt{1 - a_*^2})r_s/2$, where a_* is the spin parameter that varies between 0, representing a Schwarzschild BH, to 1 which represents a maximally rotating Kerr BH. This suggests that R_* is further decreased with the increase in spin of the BH. This will increase the $\mathcal{C}_{\mathcal{R}}$ further. We can conclude that $\mathcal{C}_{\mathcal{R}}$ of compact objects are generally more than 100 times the $\mathcal{C}_{\mathcal{R}}$ of a Sun-like star. The exceedingly small size in compact objects is responsible for their large surface gravitational potentials, implying that general relativity plays an important role in these systems.

1.3 OBSERVING COMPACT OBJECTS

WDs have long cooling timescales, because of which it can essentially be observed in the optical wavelengths. NSs have strong magnetic fields, the magnetic moment of which, if misaligned with the star’s rotation axis, gives periodic pulses. These objects are known as pulsars and can be observed as a strong radio source in the sky. BHs, on the other hand, are completely ‘black’ (as the name suggests) and hence cannot be observed directly. The

gravity is so strong that no information can escape. However, it can be observed indirectly through the effect it exerts on its environment. The extreme \mathcal{C}_R enables them to exhibit a phenomenon called ‘*accretion*’. BHs can solely be detected from the enormous amount of energy they liberate through this process. In the Universe, BHs are found with mass ranging from stellar-mass to super-massive. Stellar-mass BHs accrete matter from their binary counterpart and are visible in the sky as X-ray binaries (XRBs). Super-massive ($\sim 10^6 - 10^9 M_\odot$) BHs, on the other hand, can feed on an entire galaxy. Centres of such active galaxies are famously known as the Active Galactic Nuclei (AGN) and are one of the brightest sources observed in the Universe. Some super-massive BHs could also be inactive, like Sgr A*, a $10^6 M_\odot$ BH located at the center of our own galaxy, the Milky Way. Not only BHs, NSs and WDs have also been found to be accreting matter from a companion star and are popularly known as accreting X-ray pulsars and Cataclysmic Variables (CVs), respectively.

1.4 THE THEORY OF ACCRETION

Before the 21st century, when stars and their assemblies were the sole observable objects in the sky, people believed that nuclear energy is the primary energy source in the Universe. But things got revolutionised after the discovery of quasars, which made it apparent that nuclear energy is insufficient to power these quasi-stellar objects. At this time, accretion onto compact objects was realised as a potential mechanism to explain the enormous amount of energies released. Presently, the observational evidence of accretion discs around young-stellar objects (YSOs), CVs, accreting X-ray pulsars, high-mass X-ray binaries (HMXB), low-mass X-ray binaries (LMXB) and AGNs, have placed us beyond doubt that accretion is a natural, efficient and powerful mechanism to explain high-energy emissions.

Accretion is defined as the accumulation of matter from the ambient medium, onto an object, due to its gravitational pull. During this process, the gravitational potential energy of the accreted matter is extracted, leading to the release of huge amount of energies. We compare below the efficiency of the energy sources mentioned before.

(a) **Nuclear energy:** Nuclear fusion involves the conversion of four hydrogen atoms to one helium atom. The energy released during this process is:

$$\Delta E_{\text{NF}} = 7 \times 10^{-3} mc^2, \quad (1.1)$$

suggesting that the efficiency of this reaction is $\eta_{\text{NF}} = 0.007$, which is adequate enough to

1. INTRODUCTION

power a star.

(b) **Gravitational energy:** If a mass ‘ m ’ falls from infinity onto a star of mass M_* and radius R_* , then the energy released due to accretion is:

$$\Delta E_A = \frac{GM_*m}{R_*}. \quad (1.2)$$

From the above formula, it is evident that the efficiency of accretion strongly depends on the M_*/R_* ratio or the compactness ratio (\mathcal{C}_R).

But it is important to note here that Eq. 1.2 refers to 100% efficient energy conversion (gravitational energy to radiation). In general, this energy conversion is limited by an efficiency factor, η_r . Thus, we have:

$$\Delta E_A = \eta_r \frac{GM_*m}{R_*}. \quad (1.3)$$

The inner boundary conditions, flow structure and other factors regulate the efficiency. This will be dealt with, in more details, in the later chapters.

If we express the radius of the star in terms of Schwarzschild radius ($r_s = 2GM_*/c^2$), that is $R_* = \mathbb{F}r_s$, then from Eq. 1.3, we have,

$$\Delta E_A = \eta_r \frac{mc^2}{2\mathbb{F}}. \quad (1.4)$$

Thus, the energy released due to accretion is of the order of rest-mass energy of the matter (mc^2) falling onto the object. Thus, for compact objects whose radius is small (value of \mathbb{F} is low), the amount of energy released is significant. For objects other than these, e.g. normal stars, the energy yield is small, and accretion is not a viable mechanism that can power them.

1.4.1 EDDINGTON LIMIT

Increasing the accretion efficiency of a system suggests that the luminosity obtained would also increase. But this increase in luminosity cannot go on forever and hence cannot be infinite. Eddington limit helps to set an upper limit on the maximum luminosity of an astronomical object. Let us consider a particle of mass ‘ m ’ being accreted by a central gravitating object. But the radiation pressure present inside this gas cloud would try to push the particle outwards. When this pressure is significant, the accretion process can be halted. This limiting value, when the gravitational attraction on a particle is balanced by the radiation pressure, is called the *Eddington limit*. The corresponding luminosity

and accretion rate is known as *Eddington luminosity* (L_{Edd}) and *Eddington rate* (\dot{M}_{Edd}) respectively. The expression for Eddington luminosity is:

$$L_{\text{Edd}} = \frac{4\pi GM_* m_p c}{\sigma_T} \simeq 1.26 \times 10^{38} \left(\frac{M_*}{M_\odot} \right) \text{ erg s}^{-1} \quad (1.5)$$

where, σ_T is the Thomson scattering cross-section. To derive the above expression, a spherically symmetric fully ionized gas cloud was considered, where the protons and electrons were assumed to be coupled strongly through Coulomb force. Thus, the above estimation is crude. Despite all the caveats, this limit gives us a proper qualitative picture of the system and is frequently used as a standard unit in many astrophysical cases.

We define here a relation between accretion luminosity and accretion rate of a system. The accretion luminosity obtained, when kinetic energy of the infalling matter, accreted at the rate of \dot{M} (g/s) is converted into radiation:

$$L_A = \eta_r \frac{GM_* \dot{M}}{R_*} = \eta_r \dot{M} c^2. \quad (1.6)$$

where, η_r has been defined in Eq. 1.3. Equating this equation with Eq. 1.5, we define the Eddington rate as:

$$\dot{M}_{\text{Edd}} = 1.44 \times 10^{17} \left(\frac{1}{\eta_r} \right) \left(\frac{M_*}{M_\odot} \right) \text{ g s}^{-1} \quad (1.7)$$

The above standard Eddington values discussed are of prime importance and will be frequently used throughout this thesis work, as and whenever required.

1.4.2 FOUNDATIONS OF ACCRETION THEORY: ADVANCES IN MODELLING OF ACCRETION FLOWS

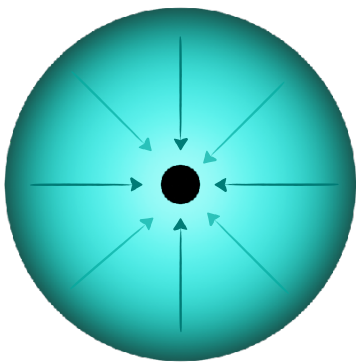
The theory of accretion began in 1939 with the seminal work by [Hoyle & Lyttleton](#). This paper introduced the concept of accretion and obtained for the first time, a formula for the accretion rate of an object. Thereafter, a lot of accretion models have been developed from time to time in order to match with the latest observations. In this section, we briefly introduce them, based on accretion flow structure.

Spherical flows or Bondi flows

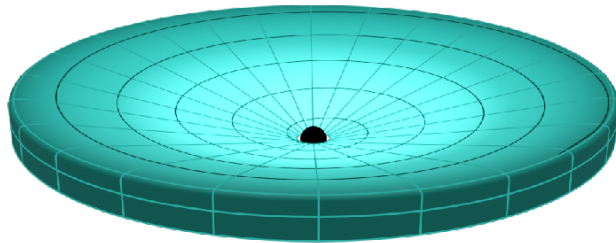
In 1952, [Bondi](#) gave the first full analytical solution for spherical accretion flows (also known as ‘*Bondi flows*’), around a static gravitating star. In this type of flow, the matter is assumed to be radially falling upon the gravitational attraction of the central object. Fig. 1.1a represents a spherically symmetric accreting system. This theory is also relevant

1. INTRODUCTION

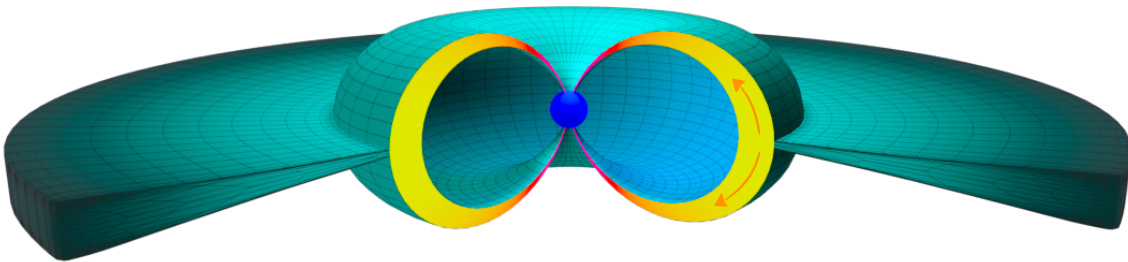
for the case of stellar winds (Blumenthal & Mathews, 1976; Holzer, 1977; Parker, 1962, 1965). But it took ten years, until the discovery of quasars and X-ray sources in 1960s, after which accretion phenomena gained popularity. Salpeter (1964) and Zel’dovich (1964) concluded that accretion onto “extremely massive objects of relatively small size” is the only plausible mechanism that could drive and power the luminous objects found in the Universe. But unfortunately, these authors could not explain the observed luminosities using the Bondi accretion model (known at that time). The matter being radially falling have short infall timescales compared to their cooling timescales, leading to low radiative efficiency of such flows (Michel, 1972).



(a) Spherical accretion



(b) Rotating flow



(c) Magnetised accretion flow

Figure 1.1: Accreting systems distinguished on the basis of flow structure, where (a) represents a spherical accretion flow or popularly known as Bondi flow, (b) general rotating flow or a flow with angular momentum and (c) magnetised accretion flow or funnel flow.

Rotating flows

The low radiative efficiency of Bondi flows led to the development of the famous *Shakura & Sunyaev disc model* (SSD) or the *Keplerian disc model* in 1973. In this model, mat-

ter is assumed to be rotating in Keplerian orbits with an anomalous viscosity removing angular momentum outwards, to accrete matter inwards. Fig. 1.1b represents a general rotating accretion flow. The assumption of a rotation-dominated disc, allowed the matter to radiate for longer durations, increasing the radiative efficiency. An SSD disc produces a *multicoloured blackbody spectrum*, owing to its optically thick nature. Hence, it could successfully regenerate the thermal component in the spectrum of compact objects, but could not explain the high energy non-thermal part present in those spectrums. In addition, the assumption of Keplerian angular velocity at each annulus implied that the disc is arbitrarily terminated at the inner stable circular orbit or ISCO. Soon, SSD was found to be thermally and secularly unstable (Lightman & Eardley, 1974; Pringle et al., 1973). Thorne & Price (1975) argued that this instability could expand the inner region of SSD into a gas-pressure dominated region, which is optically thin and geometrically thick. Shapiro et al. (1976) (hereafter, SLE76) assumed this puffed up region to be fully ionised and composed of protons and electrons, described by two different temperature distributions. This theory is popularly known as *two-temperature modelling*. Using this model, the non-thermal component of Cygnus X-1 spectrum (available at that time), spanning from 8 to 500 keV, was successfully explained. Unfortunately, this model was also found to be thermally unstable (Piran, 1978), but this paper served as one of the cornerstones in the two-temperature accretion theory. Thick-accretion disc models then came into existence, which could explain the observation of sources with high Eddington rates (Abramowicz et al., 1980; Paczynski & Abramowicz, 1982).

The models that have been discussed hitherto did not deal with the advection term properly. The heating and cooling rates inside a system need not be equal, and some part of the heat could be advected inwards, along with the bulk motion of the flow. In 1988, Abramowicz et al. extensively investigated advection in their ‘*slim*’ optically thick accretion disc model and found that the solutions obtained were thermally and viscously stable. The importance of advection in inducing stability in the system was further demonstrated, using self-similar solutions, by Abramowicz et al. (1995); Narayan & Yi (1994, 1995). These discs are today broadly classified as *advection-dominated accretion flows* or ADAFs (Bisnovatyi-Kogan & Lovelace, 1997, 2001; Ichimaru, 1977).

A conclusion can be drawn from the above discussions that an accretion flow need not be Keplerian everywhere but can also be sub-Keplerian or a combination of both (Chakrabarti & Titarchuk, 1995). Also, flows around compact objects are generally transonic in nature. Subsequently, there was a significant body of work done by several authors on advective, transonic flows where they did not focus on any particular accretion disc-type

1. INTRODUCTION

but obtained global class of accretion solutions (Chakrabarti, 1989, 1996; Chattopadhyay & Chakrabarti, 2011; Chattopadhyay & Kumar, 2016; Fukue, 1987; Kazanas et al., 1997; Kumar et al., 2013; Liang & Thompson, 1980).

High energy pair-production processes: It is interesting to note here that, the hot accretion flows around compact objects predict electron temperatures which are conducive for the production of $e^+ - e^-$ pairs. The production, as well as annihilation of pairs might play a significant role in accretion disc dynamics as well as in shaping the observable spectrum. Herterich (1974) concluded that this process could significantly change the composition of the flow as well as the radiative output of the system. In 1979, Liang proposed one of the first models of an optically thin accretion disc solution, including pair production. He found an order of magnitude reduction in electron temperature because of enhanced cooling by these pairs. Lightman & Zdziarski (1987) studied the importance of pairs in AGNs and concluded that luminosities could be significantly reduced in the presence of pair production. Kusunose & Takahara (1988, 1989, 1990) in a series of papers, extensively investigated the effect of pairs in two-temperature accretion flows around BHs, where they assumed pair equilibrium. These papers covered almost all photon generation processes leading to the production of pairs: bremsstrahlung, synchrotron, their inverse-Comptonizations and external soft photons. But they found that forbidden regions would be formed when accretion rates exceed a certain critical value, which is characteristic of the type of photon distribution present in the system. No steady-state solutions are possible in these regions. The reason for its formation was later found to be the enforcement of pair equilibrium, even in situations where pair production rate exceed the pair annihilation rate (White & Lightman, 1989).

Self-consistent two-temperature works, including pairs, were conducted by Park & Ostriker (1989) and Park (1990), where they assumed spherical flows and implemented proper radiation hydrodynamic equations. They found that pair production and its annihilation rates are generally unequal and hence, the system does not satisfy pair equilibrium. They concluded that pair production can make the system 10-100 times more luminous. After ADAFs became popular, Kusunose & Mineshige (1996) investigated the effect of pairs in these disc models (also see, Esin, 1999). They concluded that advection provides stability to the solutions, and pairs have negligible effect in these systems. Even after the host of works done till now, the importance of pairs in accretion flows around BHs is still highly debatable.

Flows around strongly magnetised stars

In 1970s, a large number of pulsating X-ray sources were discovered, like Centaurus X-3 and Hercules X-1 (Giacconi et al., 1971; Schreier et al., 1972; Tananbaum et al., 1972). These observations led to the realisation that the central object can be a rotating magnetised star, emanating huge luminosities due to the accretion of matter from a binary companion. The misalignment between the star's magnetic axis and rotation axis, gives rise to this peculiar pulsating behaviour. Qualitative features of accretion flow around magnetised rotating stars were first described in details by Lamb et al. (1973). The magnetic field of a compact star has negligible influence on the matter which is very far away. But, for matter near the star's surface, strong magnetic fields dictate the dynamics of the accretion flow (Davidson & Ostriker, 1973; Pringle & Rees, 1972). In such a case, accretion occurs in the form of a disc up to a certain radius, where gas pressure and matter energy density are comparable to the magnetic energy density, after which matter gets channelled along the magnetic field lines until it hits the poles of the star. This phenomenon is known as a *magnetised accretion flow* or *funnel flow*. For matter to channel from the disc and rise along the field lines, field penetration theories were proposed (Ghosh & Lamb, 1979). Study on magnetised rotating stars, where the central object could either be an NS, WD, YSO or a T Tauri star, with aligned dipole magnetic field in the magnetohydrodynamic (MHD) regime, has been carried out by Ghosh & Lamb (1979); Koldoba et al. (2002); Lovelace et al. (1986, 1995) etc. Although the axes were aligned, these works successfully brought out the essential features, allowing us to deeply understand magnetised funnel flows.

The compact stars discussed here, possess hard surface; thus, the study of surface boundary condition is necessary (Fukue, 1987). Most of the works discussed above did not deal with this properly or took recourse to simplifying assumptions (Karino et al., 2008; Koldoba et al., 2002). Li et al. (1996) suggested that, as the matter reaches the star's surface supersonically, it will form a shock there. This shock would enhance the dissipation processes, making the flow radiate away all its kinetic energy, such that the matter can slowly settle down onto the star's surface. Thus, it was conjectured that most of the emission would be contributed from the post-shock region. A lot of works hence, focused just on this post-shock accretion column, which enabled them to study in detail the emission processes leading to the observable spectrum (Arons et al., 1987; Becker, 1998; Becker et al., 2012; Becker & Wolff, 2005a,b, 2007; Davidson, 1973; Wolff et al., 2019). It was emphasised in these works that Comptonisation is a very important radia-

1. INTRODUCTION

tion mechanism in accretion-powered pulsars and contribute significantly to the observed spectrum.

To obtain a proper picture of accretion flow around magnetised compact stars, it is imperative to obtain the global accretion solution that connects the flow from the accretion disc to the NS surface via a surface shock. Also, proper treatment of radiative processes should be considered, which help in cooling and settling down the matter at the star's surface. This was done by [Singh & Chattopadhyay \(2018a,b\)](#) (hereafter, [KSC18a](#); [KSC18b](#), respectively). They obtained global accretion solutions for a wide range of parameter space. In addition, the transonicity of the flow and the surface boundary conditions were also taken care of.

1.5 ONE-TEMPERATURE AND TWO-TEMPERATURE ACCRETION FLOWS

The extreme gravity around compact objects makes the infalling matter very hot, such that it is fully ionised. Hydrogen being the most abundant element in the Universe, an ionised plasma consists of protons (p) and electrons (e^-). Each species, because of their different masses, exhibit different values of relaxation timescales. Apart from the intra-species interaction, they are bound together by a Coulomb coupling term, which serves to exchange energy between them.

The importance of the Coulomb force in astrophysical flows has been investigated by several authors, few important being by [Colpi et al. \(1984\)](#); [Gould \(1981\)](#); [Park \(1990\)](#); [Spitzer \(1962\)](#); [Stepney \(1983\)](#); [Yuan & Narayan \(2014\)](#); [Yuan et al. \(2003\)](#). They argued that, in accretion flows around compact objects like BHs, NSs and WDs, electrons and protons are thermally decoupled and possess different temperature distributions ($T_e \neq T_p$, where T_e is the electron temperature and T_p is the proton temperature). There are various reasons which support this conjecture. They have been elaborately discussed below.

(1) **Timescales:** The timescale of the Coulomb coupling interaction (t_{e-p}) is larger than the infall timescale (t_{inf}). Thus, before the electrons and protons interact and achieve a one-temperature distribution, they fall towards the central object. We investigate this in greater details below.

A system is said to be thermally relativistic when the thermal energy (kT , where k is the Boltzmann constant, T is the temperature of the matter flow) is greater than or equal to the rest-mass energy of the matter constituting the system (mc^2). For protons to be relativistic, $T_p > m_p c^2/k \simeq 1.01 \times 10^{13}$ K, value of which is too high to be viable

inside accretion flows around compact objects. On the other hand, because of the lower mass of electrons, they become relativistic even at lower temperatures. A temperature of $T_e > m_e c^2/k \gtrsim 6 \times 10^9$ K is sufficient for electrons to become relativistic. It is to be noted that subscripts e and p used before represent electrons and protons, respectively. In astrophysical scenarios, the temperatures present in accretion flows are such that, electrons are generally relativistic in nature while protons remain non-relativistic. Or, in other words, $\Theta_e = kT_e/(m_e c^2) \gg 1$ or relativistic and $\Theta_p = kT_p/(m_p c^2) \ll 1$ or non-relativistic. Under these circumstances, the relaxation timescales for e-p collisions (in units of second) can be simplified to (Gould, 1981; Stepney, 1983):

$$t_{e-p} = \frac{3ck}{4\pi e_c^4 \ln \Lambda} \frac{m_e m_p}{n} \left(\frac{T_e}{m_e} \right) \simeq 3.1 \times 10^7 \frac{1}{n \ln \Lambda} T_e. \quad (1.8)$$

Here, e_c is the charge of an electron, $\ln \Lambda$ is the Coulomb logarithm, and n is the number density in units of cm^{-3} . Assuming charge neutrality in the system, $n_{e-} = n_p = n$.

We define here another timescale, which is called the infall timescale (t_{inf}). This is the time taken by a fluid element at radius r (say, in units of r_s), with velocity v (in units of c), to get accreted by the compact object of mass M_* . The expression (in units of second) is given as,

$$t_{\text{inf}} = \frac{rr_s}{vc} \simeq 10^{-5} \left(\frac{r}{v} \right) \left(\frac{M_*}{M_\odot} \right). \quad (1.9)$$

To compare the infall timescale with the Coulomb coupling timescale, we assume a simplified model, where the infall velocity is equal to the free-fall velocity. This will give a relation, $v = \sqrt{1/r}$. The number density would then vary as, $n \propto r^{-3/2}$, assuming a spherical accreting system with constant mass-flux (\dot{M}). Thus, we can define $n(r)$ as (Colpi et al., 1984):

$$n(r) = \frac{\dot{M}}{4\pi(m_e + m_p)(rr_s)^2(vc)} \simeq 1.8 \times 10^{17} r^{-3/2} \dot{M}_{18} M_{10}^{-2}. \quad (1.10)$$

where, M_{10} is the mass of the compact object in terms of $10M_\odot$, and \dot{M}_{18} is the accretion rate in units of 10^{18} g/s. Simplifying Eqs. 1.8 and 1.9, using Eq. 1.10 we have:

$$t_{e-p} = 0.2 \ln \Lambda^{-1} r^{3/2} \dot{M}_{18}^{-1} M_{10}^2 \left(\frac{T_e}{10^9 \text{K}} \right), \quad (1.11)$$

$$\text{and } t_{\text{inf}} = 10^{-4} r^{3/2} M_{10}. \quad (1.12)$$

1. INTRODUCTION

Dividing t_{inf} by $t_{\text{e-p}}$ using the above expressions, we get:

$$\frac{t_{\text{inf}}}{t_{\text{e-p}}} \simeq 5 \times 10^{-3} \dot{M}_{18} M_{10}^{-1} \left(\frac{T_e}{10^9 \text{K}} \right)^{-1}, \quad (1.13)$$

where, we have assumed $\ln \Lambda = 10$. Thus, as mentioned before, the condition for a flow to be of two-temperatures is, $t_{\text{inf}} < t_{\text{e-p}}$, *i.e.*, the flow does not give enough time (shorter infall timescale) to the species to settle down into a single temperature distribution. We can see from Eq. 1.13 that for any temperature $T_e > 10^6$ K, $t_{\text{inf}}/t_{\text{e-p}} < 1$, for a $10M_{\odot}$ object with accretion rate, $\dot{M}_{18} = 1$. For $M_{10} > 1$, two-temperature condition is achieved, even for low temperatures. It is to be noted that the aforementioned values are reasonable for general astrophysical cases. Hence, we can conclude that the infall timescales are generally shorter than Coulomb coupling timescales, and a two-temperature accretion flow is a reasonable expectation.

(2) **Mass differences:** Protons are more than 1000 times heavier than electrons, because of which it remains non-relativistic even if the temperature of the flow is high. In comparison, electrons become relativistic even at lower temperatures, as have been discussed before. Thus, the adiabatic index (Γ) of electrons is $\sim 4/3$, while for protons, $\Gamma \sim 5/3$. Under adiabatic conditions, compressional heating (arising due to accretion of matter onto a compact star), would follow the relation for temperature as $T \propto \rho^{\Gamma-1}$. Thus, we have $T_e \propto \rho^{1/3}$, while $T_p \propto \rho^{2/3}$. Hence, protons and electrons are differently heated and a two-temperature distribution is plausible.

(3) **Electrons are the main radiators:** Electrons scatter and radiate much more efficiently than protons and can emit most of the energy. This ensures the electron temperature to be sufficiently different from the protons.

To conclude, an accretion flow has a natural tendency to relax into two different temperature distributions: one defining protons and the other electrons, thus the name, *two-temperature modelling*. These flows gained prominence after the work done by SLE76 explained the high energy power-law part of Cygnus X-1. Thereafter two-temperature modelling has been widely used in interpreting the spectra of Sagittarius A*, XTE J1118+480 etc. Some notable works done in this regime are Chakrabarti & Titarchuk (1995); Dhihngia et al. (2018, 2020); Mandal & Chakrabarti (2005); Nakamura et al. (1996); Narayan & Yi (1995); Rajesh & Mukhopadhyay (2010). Two-temperature works on magnetised stars were done by Langer & Rappaport (1982); Saxton et al. (2005) etc.

But it is important to note here that, there have been apprehensions of more efficient energy exchange processes, which might exist between protons and electrons, in addition to Coulomb coupling. In that case, the accretion flow may settle down into a single temperature distribution (Phinney, 1981). Begelman & Chiueh (1988) used plasma waves, and Sharma et al. (2007) used magneto-rotational instability to increase the energy exchange between the two species inside the flow. However, some authors have raised doubts about the effectiveness of these processes (Abramowicz & Fragile, 2013; Blaes, 2014). If we assume that in special cases, these processes or the Coulomb coupling is strong enough, then the flow would attain a *one-temperature distribution*. Although, in the present state, it is still highly debatable whether these processes are efficient enough, but because of the simplicity, numerous works have been done in this regime (Chattopadhyay & Chakrabarti, 2011; Chattopadhyay & Kumar, 2016; Fukue, 1987; Kumar & Chattopadhyay, 2014). Although simple, it can bring out the essential features of an accretion flow, without getting involved in the complexities, like that present in two-temperature theory (Liang & Thompson, 1980; Rajesh & Mukhopadhyay, 2010).

In the discussions made till now, we did not consider the presence of positrons (e^+). There could be external positrons present, or some can be produced during pair producing processes inside an accretion flow. If positrons are present, they would have a general tendency to possess the same temperature as electrons (T_e) because of their same mass (m_e). So, the above arguments would remain unchanged.

1.6 RELATIVISTIC EQUATION OF STATE

Flows around compact objects are generally trans-relativistic in nature, *i.e.*, very far away from the central object, matter is *thermally* as well as *kinetically* non-relativistic, and as it approaches the gravitating centre, it becomes kinetically relativistic and thermally sub-relativistic/relativistic. As have been mentioned before, matter is said to be thermally relativistic when $\Theta = kT/mc^2 \gtrsim 1$ and adiabatic index $\Gamma \sim 4/3$, and is non-relativistic if $\Theta < 1$ and $\Gamma \sim 5/3$. So, not only the temperature, but also the mass of the species decide the thermal nature of a flow. Especially in two-temperature flows, where we consider two species, with masses differing by $\gtrsim 1000$ times, an equation of state (EoS) with fixed adiabatic index is untenable. To incorporate the trans-relativistic nature of the different species, one needs to utilise a variable adiabatic index EoS.

Chandrasekhar (1939) obtained the exact, relativistically perfect EoS with variable adiabatic index. Thereafter, Cox & Giuli (1968); Sygne (1957) rederived it, giving their own EoS for single-species flow. But these EoSs are difficult to implement in numerical

1. INTRODUCTION

calculations because of the presence of modified Bessel functions. Also, they considered only single species. Inspired by these works, [Chattopadhyay \(2008\)](#); [Chattopadhyay & Ryu \(2009\)](#), proposed an approximate EoS for multispecies flow with variable adiabatic index (CR EoS, hereafter), which is analytical and computationally easy to handle. Although approximate, it matches perfectly well ([Vyas et al., 2015](#)) with that obtained by [Chandrasekhar \(1939\)](#).

1.7 GENERAL-RELATIVITY AND PSEUDO-NEWTONIAN POTENTIAL

The general theory of relativity plays an important role in determining the environment around compact objects. A general-relativistic (GR) treatment is necessary for modelling flows around these objects, especially in the inner regions where gravity is very strong. But extensive and tedious calculations along with computation are needed to correctly work in the GR regime. In 1980, [Paczyński & Wiita](#) proposed a pseudo-Newtonian potential, which can mimic the effects of strong gravity around a Schwarzschild black hole. This potential is famously known as the [Paczyński & Wiita](#) potential (PWP) and is expressed as:

$$\Phi_{\text{PWP}} = -\frac{GM_*}{R - r_s}, \quad \text{where, } R = rr_s \text{ and } r_s = \frac{2GM_*}{c^2} \quad (1.14)$$

The above potential has been widely used to model astrophysical flows around Schwarzschild black holes as well as other compact objects. The wide acceptance of PWP is because it can accurately reproduce the:

- (1) marginally stable circular orbit location ($r_{\text{ms}} = 3r_s$)
- (2) marginally bound orbit location ($r_{\text{mb}} = 2r_s$)
- (3) Keplerian angular momentum expression.

PWP led to the development of a wide variety of other pseudo-Newtonian potentials, trying to mimic other properties of a Schwarzschild BH ([Kluźniak & Lee, 2002](#); [Nowak & Wagoner, 1991](#)). Few also went ahead to define the space-time curvature around Kerr BHs ([Chakrabarti & Khanna, 1992](#); [Mukhopadhyay & Misra, 2003](#); [Semerák & Karas, 1999](#)). But, even after the various studies conducted, PWP is still found to be the most exact one, for application onto Schwarzschild space-times ([Artemova et al., 1996](#)).

1.8 THE PRESENT WORK

Based on the above mentioned theme, we briefly discuss below the motivation behind carrying out this thesis. The thesis layout has thereafter been given.

1.8.1 MOTIVATION

Modelling of accretion flows around compact objects is not new and has been rigorously carried out to match the latest observations. Mapping of their environment is necessary since the surrounding matter flow carry imprints of the nature of the central object.

One of the processes that play a significant role in the accretion physics of a BH system as well as in shaping the spectrum is — *production of $e^+ - e^-$ pairs and their annihilation*. [Yahel & Brinkmann \(1981\)](#) claimed that there would be a characteristic spectral signature, a bump like feature near $m_e c^2$, due to $e^+ - e^-$ pairs. This signature will always be detectable in the spectrum unless the number density of pairs in an accretion flow is very low. Few works suggested that $e^+ - e^-$ pairs could significantly change the observed luminosities. This is because the photons that escaped the accretion disc and contributed to the spectrum are now being used to create pairs. But it may be noted that cooling would also increase because of the creation of pairs, which might lead to an increase in luminosity, rather than a decrease. Also, annihilation of pairs is an additional component in the spectrum. The interplay between these processes will determine the observed luminosity. Many works have criticised the importance of pairs and concluded that they have negligible effect on the spectrum and luminosity. Different conclusions were drawn because of the inconsistency in modelling of these flows as well as the assumptions used. Most of the initial works dealing with pair production either assumed a static plasma flow or an enforced pair equilibrium or both ([Kusunose & Takahara, 1988, 1989, 1990](#); [Lightman et al., 1987](#); [Svensson, 1982a,b, 1984](#)). This led to the formation of forbidden regions or unstable solutions. Also, discrepancies arose because of the inclusion of different radiative processes, which provided different radiation field environment for the production of pairs. Thus, pair production was found to be significant in some cases while it was negligible in others. To obtain a complete picture of the effect of pairs in accretion disc dynamics, it is essential to study and consider all the radiation fields that could be present inside an accretion flow. Pair production and annihilation is a highly non-linear process too. As correctly quoted by [Lightman \(1982\)](#) – “pairs produce photons, and photons produce more pairs”. So, it is important to investigate its role in greater details. In this thesis, we aim to address and study the effect of pairs in accretion flows around BHs along with obtaining their spectrum.

1. INTRODUCTION

One-temperature works ($T_e = T_p$), although simplified and easy to work upon, yield temperatures around $\sim 10^{11} - 10^{12}\text{K}$, which are very high and not consistent with the observations. Along with this fact, it has been found that, in most of the astrophysical cases, the Coulomb coupling is weak, justification of which has been given in Section 1.5. This suggests that, before the leptons and protons interact and achieve a single temperature distribution, they fall towards the central object. Also, leptons are the main radiators. So it is important to study its temperature variation throughout an accretion flow to compute the spectrum. A two-temperature modelling is, therefore, necessary to get a proper picture of the system. BHs possess an event horizon, which ensures matter to achieve the speed of light. Accretion process around NSs, on the other hand, is entirely different due to the presence of strong magnetic fields and a hard surface, which dictates the dynamics of flow around them. Thus, there is a need to model these flows in order to have a knowledge of the underlying physics present in these systems.

The most striking feature of the earlier two-temperature works was the dependence of solution obtained, on the choice of inner or outer boundary conditions, unlike in the case of one-temperature hydrodynamics, where we know that transonic solutions are unique for a given set of constants of motion. The problem with two-temperature solutions is that, without any increase in the number of governing equations, the number of flow variables increases, *i.e.*, now instead of a single temperature, one has to consider two different temperatures for the two different species. In addition, there is no known principle dictated by plasma physics that may constrain the relation between these two-temperatures at any boundary. Previous works done were dependent on arbitrary choices, which did not ‘haunt’ one-temperature solutions. This gives rise to degeneracy of solutions, *i.e.* multiple transonic solutions for the same set of constants of motion. A wrong choice of solution would provide us with a wrong spectrum and hence an incorrect picture of the system. We attend and investigate this problem in greater details in this thesis. Our motivation is to propose a general methodology to find unique transonic two-temperature accretion solution around BHs as well as NSs, without taking recourse to any assumptions. This issue has yet not been addressed so far, to the best of our knowledge. Apart from that, we want to study the solutions and analyse the spectrum for two-temperature accretion flows around BHs and NSs.

It is to be noted that the temperature of protons and leptons in an accretion flow, vary by orders of magnitude from a large distance to the central object, so a non-relativistic EoS or EoS with fixed adiabatic indices, is untenable. Thus, for all the above mentioned

works, we use the CR EoS, which computes the adiabatic indices consistently throughout an accretion flow, depending on the temperature and mass of the species.

In short, the motivation of this thesis is to study accretion flows around BHs and NSs along with analysing their spectrum, for a broad range of parameter space.

1.8.2 THESIS LAYOUT

The layout of this thesis is discussed below:

- **Chapter 2: MATHEMATICAL FRAMEWORK** – We introduce the various equations required to model an accretion flow around BHs and NSs. The radiative processes, CR EoS, sonic point conditions and shock formation have been discussed.
- **Chapter 3: ONE-TEMPERATURE ACCRETION FLOWS AROUND BLACK HOLES** – We investigate viscous advective one-temperature accretion flows around Schwarzschild BHs, and study the effect of high-energy pair creation and annihilation processes. We also compute and analyse the accretion disc spectrum.
- **Chapter 4: DEGENERACY – A GENERIC PROBLEM IN TWO-TEMPERATURE SOLUTIONS; ENTROPY – A TOOL TO REMOVE IT** – We discuss the long outstanding problem of degeneracy present in two-temperature accretion flows and propose a general methodology to constrain it, such that a given set of constants of motion harbour a unique solution.
- **Chapter 5: TWO-TEMPERATURE FLOWS AROUND BLACK HOLES – I: SPHERICAL ACCRETION** – We successfully validate the methodology to obtain a unique transonic two-temperature accretion solution, first on spherical flows around Schwarzschild BHs. We also discuss the properties of these unique two-temperature solutions.
- **Chapter 6: TWO-TEMPERATURE FLOWS AROUND BLACK HOLES – II: ROTATING ACCRETION FLOWS** – We extend the methodology of constraining degeneracy in two-temperature theory to more realistic, rotating accretion flows around Schwarzschild BHs. Stability analysis of the unique solution was also performed. After removing degeneracy, self-consistent two-temperature accretion solutions were obtained and spectral analysis was also done.
- **Chapter 7: TWO-TEMPERATURE ACCRETION FLOWS AROUND NEUTRON STARS** – We further extend the work of studying unique two-temperature accretion flows to NSs. The methodology discussed in the previous chapters for removing degeneracy in

1. INTRODUCTION

BHs was extended, including the effect of a hard surface present in an NS. Again we successfully validated the proposed mechanism and obtained self-consistent accretion solutions along with analysing the spectrum around NSs.

- **Chapter 8: HIGHLIGHTS, CONCLUSIONS AND FUTURE PROSPECTS** – We summarise the work carried out in this thesis and highlight the major outcomes. We also discuss briefly the future plans relevant to the field.

Chapter 2

MATHEMATICAL FRAMEWORK

2.1 OVERVIEW

In this chapter, we introduce the mathematical structure and discuss the equations required to model an accretion flow. To capture the effects of strong gravity around BHs, we work in the pure general-relativistic (GR) regime. We assume stochastic magnetic fields in these accretion flows. Thus, a hydrodynamic (HD) approach suffice the problem. But this is untenable in the case of NSs where strong magnetic fields are present. Hence, we use MHD equations assuming [Paczynski & Wiita \(1980\)](#) potential (PWP) to study accretion flows around NSs.

2.2 GENERAL-RELATIVISTIC HYDRODYNAMIC EQUATIONS

In this section, we have employed a unit system where, $G = M_{\text{BH}} = c = 1$, such that the unit of length is $r_g = GM_{\text{BH}}/c^2$, velocity is in units of c and time is in units of $t_g = GM_{\text{BH}}/c^3$. Here, $M_{\text{BH}} =$ mass of the BH. The horizon is hence at $r_s = 2r_g$.

The space-time metric around a Schwarzschild BH is given by:

$$ds^2 = g_{tt}c^2dt^2 + g_{rr}dr^2 + g_{\theta\theta}d\theta^2 + g_{\phi\phi}d\phi^2, \quad (2.1)$$

where $g^{\mu\nu}$'s are the metric tensor components, with Greek indices μ and ν taking values $(0, 1, 2, 3)$, 0 representing the time-coordinate, and 1, 2, 3 are the usual spatial coordinates. The metric components are defined as, $g_{tt} = -(1 - 2/r)$, $g_{rr} = 1/(1 - 2/r)$, $g_{\theta\theta} = r^2$ and $g_{\phi\phi} = r^2\sin^2\theta$. Accretion flow is described about the equatorial plane, so we have $\theta = \pi/2$. The BH system modelled is in steady-state and is axis-symmetric, therefore $\partial/\partial t = \partial/\partial\phi = 0$. Moreover, at any point, we assume that only the radial gradient of any quantity is dominant; therefore, $\partial/\partial\theta = 0$.

2. MATHEMATICAL FRAMEWORK

The matter energy-momentum tensor for a viscous accretion flow is :

$$T^{\mu\nu} = (e + p)u^\mu u^\nu + pg^{\mu\nu} + t^{\mu\nu}, \quad (2.2)$$

where e and p are the internal energy density and isotropic gas pressure, respectively, measured in the local fluid frame and u^μ s are the components of four-velocity. $t^{\mu\nu}$ is defined as the viscous stress tensor and is given by $t^{\mu\nu} = -2\eta_v\sigma^{\mu\nu}$, assuming shear to be the only reason giving rise to viscosity inside the flow. Here, η_v is the viscosity coefficient, and $\sigma^{\mu\nu}$ is the relativistic shear tensor. Following the prescription of [Chattopadhyay & Kumar \(2016\)](#); [Peitz & Appl \(1997\)](#) and considering only the $r - \phi$ component of the shear tensor we have,

$$2\sigma_\phi^r = (g^{rr} + u^r u^r) \frac{du_\phi}{dr} - \frac{2u_\phi}{r} g^{rr}. \quad (2.3)$$

The equations governing a relativistic fluid are:

$$\text{Conservation of energy - momentum : } T_{;\nu}^{\mu\nu} = 0, \quad (2.4)$$

$$\text{Continuity equation : } (n_i u^\nu)_{;\nu} = (S_{\text{source}} - S_{\text{sink}})_i, \quad (2.5)$$

where, S_{source} , S_{sink} are the source and sink terms arising due to pair production and annihilation, respectively. i represent the species: protons (p), electrons (e^-) and positrons (e^+). We define the number density of electrons and positrons together as the number density of leptons, $n_l = n_{e^-} + n_{e^+}$. When particle production mechanisms or external positrons are absent, $n_{e^+} = 0$, then charge neutrality condition gives,

$$n_p = n_{e^-} = n. \quad (2.6)$$

But, when there are positrons present in the system, then the following condition needs to be satisfied:

$$n_{e^-} = n_p + n_{e^+}. \quad (2.7)$$

It is important to define here a composition parameter ([Chattopadhyay, 2008](#); [Chattopadhyay & Ryu, 2009](#)),

$$\xi = n_p/n_{e^-}, \quad (2.8)$$

where, $\xi = 0.0$ implies a flow with electron-positron pair plasma, $\xi = 1.0$ implies electron-proton plasma, while $0.0 < \xi < 1.0$ implies an electron-positron-proton plasma.

In the absence of particle creation and annihilation, Eq. 2.5 using Eq. 2.6 reduces to,

conservation of particle density flux, which is given as:

$$(nu^\nu)_{;\nu} = 0, \Rightarrow \frac{1}{\sqrt{-g}} \frac{\partial(\sqrt{-g}nu^\nu)}{\partial x^\nu} = 0, \quad (2.9)$$

where, g is the determinant of the metric tensor. Integrating Eq. 2.9, we get the accretion rate (\dot{M}) of the system, which is a constant of motion throughout the flow, given by,

$$\dot{M} = 4\pi\rho u^r r H, \quad (2.10)$$

where, ρ is the mass density and H is the half-height. For a conical or wedge flow, it is defined as, $H = r \cos \theta^c$, where, θ^c is the co-latitude of the surface of the conical flow. If the flow is in hydrostatic equilibrium in the transverse direction, then it is defined as (Chattopadhyay & Chakrabarti, 2011; Lasota, 1994):

$$H = \sqrt{\frac{pr^3}{\rho\gamma_\phi^2}}, \quad (2.11)$$

where, γ_ϕ is the Lorentz factor in the azimuthal direction.

Relativistic Navier-Stokes equation is obtained by projecting the four-divergence of $T^{\mu\nu}$ (Eq. 2.4) along the space direction and is given by:

$$[(e + p)u^\nu u^i_{;\nu} + (g^{i\nu} + u^i u^\nu)p_{;\nu}] + h^i_\mu t^{\mu\nu}_{;\nu} = 0. \quad (2.12)$$

Radial component of the above equation is:

$$u^r \frac{du^r}{dr} + \frac{1}{r^2} - (r - 3)u^\phi u^\phi + (g^{rr} + u^r u^r) \frac{1}{e + p} \frac{dp}{dr} = 0, \quad (2.13)$$

while the integrated form of the azimuthal component is:

$$\rho u^r (L_b - L_0) = t^r_\phi = -2\eta_\nu \sigma^r_\phi, \quad (2.14)$$

where, L_0 and $L_b = hu_\phi = hl$ are the bulk angular momentum defined at the horizon and local bulk angular momentum respectively. The specific angular momentum of a fluid is $\lambda = -u_\phi/u_t = -l/u_t$. $h = (e + p)/\rho$ is the specific enthalpy of the flow (Chattopadhyay & Kumar, 2016). We define, $\eta_\nu = \rho h \nu_\nu$, where, $\nu_\nu = \alpha_\nu a_s r f_c$ is the kinematic viscosity. Here, α_ν is the usual Shakura & Sunyaev α -viscosity parameter. $f_c = (1 - v^2)$ is defined following the prescription given in Peitz & Appl (1997) and this term ensures that $\sigma^r_\phi = 0$ at the horizon.

The first law of thermodynamics or the energy equation is, $u_\mu T^{\mu\nu}_{;\nu} = \Delta Q$, which can

2. MATHEMATICAL FRAMEWORK

be simplified to :

$$u^r \left[\left(\frac{e+p}{\rho} \right) \rho_{,r} - e_{,r} \right] = \Delta Q, \quad (2.15)$$

where, $\Delta Q = Q^+ - Q^-$ is the difference between the heating (Q^+) and cooling (Q^-) rates present in the system. These rates have been discussed in detail in Section 2.5. When the flow contains electrons and protons equilibrating at two different temperatures, we need to use the first law of thermodynamics separately for protons and electrons, unlike in the case of one-temperature flows where the Coulomb coupling being extremely strong allows protons and electrons to settle down to a single temperature and use of one first law of thermodynamics is sufficient (Chattopadhyay & Chakrabarti, 2011; Chattopadhyay & Kumar, 2016; Kumar & Chattopadhyay, 2017). The two energy equations in case of two-temperature flows are not completely independent and coupled by the Coulomb coupling term, which allows protons and electrons to exchange energy.

If we integrate Eq. 2.13 with the help of energy equation (Eq. 2.15), we obtain the *generalized Bernoulli constant* and is given by,

$$E = -h\gamma_v \sqrt{1 - \frac{2}{r} \exp(X_v + X_f)}, \quad (2.16)$$

where, X_f term mainly arises due to the heating and cooling processes present inside the system. X_v term arises because angular momentum is not constant in the presence of viscosity. In the inviscid case, $X_v = \ln \gamma_\phi$ and Eq. 2.16 reduces to:

$$E = -hu_t \exp(X_f). \quad (2.17)$$

The above expressions of generalized Bernoulli constant (in viscous case, Eq. 2.16 and inviscid case, Eq. 2.17) is conserved all throughout the flow, even in the presence of dissipation. In case of inviscid, adiabatic flows, with no dissipation, $X_v = X_f = 0$. Hence, we have:

$$E \rightarrow \mathcal{E} = -hu_t, \quad (2.18)$$

which is the *canonical form of relativistic Bernoulli constant* (Chattopadhyay & Chakrabarti, 2011; Chattopadhyay & Kumar, 2016).

We introduce few definitions here, which will be used throughout this thesis work. γ_v and γ_ϕ are the Lorentz factors in the radial and azimuthal directions respectively and are defined as $\gamma_v = \sqrt{1/(1-v^2)}$ and $\gamma_\phi = \sqrt{1/(1-v_\phi^2)}$ where $v_\phi = \sqrt{-u_\phi u^\phi / u_t u^t}$ and v is the velocity in the local co-rotating frame, which is defined as, $v^2 = \gamma_\phi^2 v_{\hat{r}}^2$, where, $v_{\hat{r}} = \sqrt{-u_r u^r / u_t u^t}$. The total Lorentz factor is therefore, $\gamma = \gamma_v \gamma_\phi$.

2.3 MAGNETOHYDRODYNAMIC EQUATIONS

For modelling accretion flows around NSs, we assume the flow to be steady, axisymmetric and inviscid (Chandrasekhar, 1956; Contopoulos, 1996; Lovelace et al., 1986; Ustyugova et al., 1999). The system of units used are same as that in the previous section except that the unit of length is in units of $r_s = 2GM_*/c^2$, where M_* is the mass of the NS. Axisymmetry suggests that flow velocity : $\mathbf{v} = \mathbf{v}_p + v_\phi \hat{\mathbf{e}}_\phi$ and magnetic field : $\mathbf{B} = \mathbf{B}_p + B_\phi \hat{\mathbf{e}}_\phi$. The subscripts p and ϕ represents the poloidal and toroidal component respectively, and $\hat{\mathbf{e}}$ is the unit vector. Using the above assumptions, the ideal MHD equations can be written as:

$$\text{Mass conservation equation : } \quad \nabla \cdot (\rho \mathbf{v}) = 0, \quad (2.19)$$

$$\text{Momentum conservation equation : } \quad (\rho \mathbf{v} \cdot \nabla) \mathbf{v} = -\nabla p + \frac{1}{c} (\mathbf{J} \times \mathbf{B}) - \rho \nabla \Phi_g, \quad (2.20)$$

$$\text{Faraday's law using ideal Ohm's law : } \quad \nabla \times (\mathbf{v} \times \mathbf{B}) = 0, \quad (2.21)$$

$$\text{Divergence constraint : } \quad \nabla \cdot \mathbf{B} = 0, \quad (2.22)$$

where, Φ_g is the gravitational potential of the NS and \mathbf{J} is the current density which is $= (\nabla \times \mathbf{B})c/4\pi$ from Ampere's law. In order to mimic the effects of strong gravity we use the Paczyński & Wiita potential, which has the form $\Phi_g = -GM_*/(r - r_s)$.

Apart from the above equations, we need the first law of thermodynamics to study the temperature variation inside the system in the presence of advection and dissipation, which is given by :

$$\frac{p}{\rho^2} \frac{d\rho}{dr} - \frac{d(\epsilon/\rho)}{dr} = \frac{Q^+ - Q^-}{\rho v_p} = \frac{\Delta Q}{\rho v_p}. \quad (2.23)$$

We introduce a flux function $\Psi(r, \theta)$ (Lovelace et al., 1986; Ustyugova et al., 1999), representing a specific magnetic field line. On integrating the equations presented from (2.19) to (2.22) along a given Ψ , we obtain quantities that remain conserved along each specific field line. They are: $\kappa(\Psi)$, $\Omega(\Psi)$, $L(\Psi)$ and $E(\Psi)$ arising due to the conservation of mass, angular velocity of field lines, total angular momentum and energy respectively. The derivation of these quantities are discussed below.

Integrating continuity equation 2.19, gives the equation for conservation of mass flux, which is given by,

$$\dot{M} = \rho v_p A_p = \text{constant}, \quad (2.24)$$

where, \dot{M} is known as the accretion rate of the system and A_p is the cross-sectional area perpendicular to the magnetic field B_p . This accretion rate obtained is similar to Eq. 2.10

2. MATHEMATICAL FRAMEWORK

obtained in GR HD regime. From Eq. 2.22, we obtain the magnetic flux conservation,

$$B_p A_p = \text{constant}. \quad (2.25)$$

Using Eqs. 2.24 and 2.25, we obtain a relation between v_p , ρ and B_p which is given by,

$$v_p = \frac{\kappa(\Psi)}{4\pi\rho} B_p, \quad (2.26)$$

where, $\kappa(\Psi) = \text{constant}$, is the ratio of mass flux to magnetic flux.

The Faraday equation 2.21 gives the conservation of helicity or the angular velocity $\Omega(\Psi)$ of the field lines,

$$\Omega(\Psi) = \omega - \frac{\kappa(\Psi)B_\phi}{4\pi\rho\tilde{r}} = \text{constant}, \quad (2.27)$$

where, $\tilde{r} = r\sin\theta$ and $\omega = v_\phi/\tilde{r}$ is the angular velocity of the matter.

From the azimuthal component of Euler equation 2.20, we get the conservation of total angular momentum $L(\Psi)$,

$$L(\Psi) = \omega\tilde{r}^2 - \frac{B_\phi\tilde{r}}{\kappa(\Psi)} = \text{constant}. \quad (2.28)$$

On integrating the poloidal component of the Euler equation 2.20 with the help of Eq. 2.23 and simplifying using Eqs. 2.27 and 2.28, we get the generalized Bernoulli constant or, in other words, the total energy E of the flow, which is given by,

$$E(\Psi) = \frac{1}{2}v_p^2 + \frac{1}{2}(\omega - \Omega)^2\tilde{r}^2 + h + \Phi_g - \frac{\Omega^2\tilde{r}^2}{2} + \int \frac{\Delta Q dr}{\rho v_p} = \text{constant}. \quad (2.29)$$

The last term arises due to the presence of dissipative processes in the system. E is a constant of motion even in the presence of dissipative processes. If dissipation is absent ($\Delta Q = 0$), the above equation reduces to what is called the canonical form of Bernoulli constant in MHD regime. This equation is similar to Eq. 2.16 obtained in case of GR HD regime.

2.4 EQUATION OF STATE

In order to solve the equations of motion discussed above, we need an EoS which relates the temperature, pressure and internal energy of the system. As stated before, we use the CR EoS throughout this thesis. The explicit form of CR EoS for multi-species flow is given by,

$$e = \sum_i e_i = \sum_i \left[n_i m_i c^2 + p_i \left(\frac{9p_i + 3n_i m_i c^2}{3p_i + 2n_i m_i c^2} \right) \right], \quad (2.30)$$

where, $i =$ proton (p), electron (e^-), positron (e^+). This can be reduced to a generic form:

$$e = n_{e^-} m_{e^-} c^2 f(\Theta, \xi), \quad (2.31)$$

where, ξ is the composition parameter, introduced in Eq. 2.8. $\Theta = \frac{kT}{m_e c^2}$ is the non-dimensional temperature which has been defined w.r.t the rest-mass energy of electron. f is a function of both Θ and ξ . For a two-temperature flow, instead of a single Θ , we need to consider two different temperatures: $\Theta_e (= kT_e/m_e c^2)$ and $\Theta_p (= kT_p/m_p c^2)$. Again, it is worthwhile to remember that positrons, because of their same mass as electrons, have the same temperature Θ_e .

The adiabatic index (Γ_i) and polytropic index (N_i) for each i^{th} species are given by,

$$\Gamma_i = 1 + \frac{1}{N_i}, \text{ and } N_i = \frac{df_i}{d\Theta_i}. \quad (2.32)$$

2.5 DISSIPATIVE PROCESSES

Here, we briefly discuss the dissipative processes leading to heating and cooling of the plasma in an accretion flow around BH and NS.

2.5.1 VISCOUS HEATING

Viscosity serves the basic purpose of removing angular momentum outwards, such that matter can get accreted inwards towards the central object. In addition to this mechanism, viscosity acting between differentially rotating annulus of an accretion flow around a BH, would heat up the matter. δ_v is the uncertainty parameter, which dictates the amount of this heat absorbed by protons, the rest $(1 - \delta_v)$ being shared by the leptons (Yuan & Narayan, 2014). We write the expression of viscous heating as (Chattopadhyay & Kumar, 2016):

$$Q_v = t^{r\phi} \sigma_{r\phi}. \quad (2.33)$$

2.5.2 HEATING DUE TO MAGNETIC DISSIPATION

Magnetic field is generally frozen into the highly conductive infalling plasma surrounding a BH. As the matter falls inwards, magnetic field strength increases by $\sim 1/r^2$, and hence magnetic energy density ($B^2/8\pi$) by $1/r^4$. In 1971, Shvartsman argued that before the magnetic energy density exceeds the thermal energy density, turbulence and hydromagnetic instabilities would lead to reconnection of magnetic field lines. In other words, it means that the magnetic energy density is limited by equipartition with thermal energy

2. MATHEMATICAL FRAMEWORK

density. This energy dissipated, would heat up the matter, either protons or electrons or both (fraction of heat transferred to each species is dictated by δ_B , similar to δ_v), ensuring relativistic temperatures even far away from the BH (Yuan et al., 2006). Apart from reconnection, dissipation of turbulent energy can also act as a heating term. Let us assume a parameter β_d which controls all these uncertainties in dissipative heating (Meszaros, 1975). The expression for dissipative heating rate as given by Ipser & Price (1982) is,

$$Q_B = \frac{3u^r c B^2}{2rr_s 8\pi} = \frac{3u^r c}{2rr_s} \beta_d p \quad \text{erg cm}^{-3} \text{s}^{-1}. \quad (2.34)$$

2.5.3 COULOMB COUPLING

Coulomb coupling (Q_{ep}) is an energy exchange term between the protons and leptons. It serves as a cooling term for protons and a heating term for leptons. Stepney (1983); Stepney & Guilbert (1983) did a detailed study of this interaction term and obtained a general expression, form of which is given below (in units of $\text{erg cm}^{-3} \text{s}^{-1}$),

$$Q_{ep} = \frac{3}{2} \frac{m_e}{m_p} n_l n_p \sigma_T c k \frac{T_p - T_e}{K_2(1/\Theta_e) K_2(1/\Theta_p)} \ln \Lambda \\ \times \left[\frac{2(\Theta_e + \Theta_p)^2 + 1}{\Theta_e + \Theta_p} K_1 \left(\frac{\Theta_e + \Theta_p}{\Theta_e \Theta_p} \right) + 2K_0 \left(\frac{\Theta_e + \Theta_p}{\Theta_e \Theta_p} \right) \right], \quad (2.35)$$

where, $K_n(x)$'s are the modified Bessel functions of second kind and n^{th} order.

2.5.4 INVERSE-BREMSSTRAHLUNG

Inverse-bremsstrahlung (Q_{ib}) is a radiative loss term for protons, expression of which is given below (Boldt & Serlemitsos, 1969):

$$Q_{ib} = 1.4 \times 10^{-27} n^2 \sqrt{\frac{m_e}{m_p} T_p} \quad \text{erg cm}^{-3} \text{s}^{-1}. \quad (2.36)$$

2.5.5 BREMSSTRAHLUNG

Emissivity due to bremsstrahlung (in $\text{erg cm}^{-3} \text{s}^{-1}$) is given by White & Lightman (1989),

$$Q_{br} = \frac{3}{8\pi} \alpha_f m_e c^3 n_p^2 \sigma_T F_{br}, \quad (2.37)$$

where, α_f is the fine-structure constant. F_{br} is the dimensionless radiation rate due to bremsstrahlung cooling, which has contributions from electron-proton and positron-proton ($e^\pm p$) collisions, electron-electron and positron-positron collisions ($e^\pm e^\pm$), and electron-positron collisions ($e^- e^+$). Thus, it can be represented as (Svensson, 1982a; White &

(Lightman, 1989) :

$$F_{\text{br}} = F_{\text{br } e^{\pm}p} + F_{\text{br } e^{\pm}e^{\pm}} + F_{\text{br } e^{-}e^{+}} \quad (2.38)$$

Each term in the above equation is determined using the expressions given in Svensson (1982a).

2.5.6 SYNCHROTRON

We have used thermal synchrotron radiation in our model, following the prescription of Wardziński & Zdziarski (2000). The emissivity is given by:

$$Q_{\text{syn}} = \frac{2\pi}{3} \frac{\nu_t^3}{rr_s} m_e \Theta_e \quad \text{erg cm}^{-3} \text{s}^{-1}, \quad (2.39)$$

where, ν_t is the turnover frequency above which the plasma is optically thin to synchrotron radiation and below which it is highly self-absorbed by the electrons itself (Narayan & Yi, 1995; Wardziński & Zdziarski, 2000).

2.5.7 INVERSE-COMPTONIZATION

The soft photons generated from bremsstrahlung and synchrotron processes can upscatter to higher energies on interacting with energetic electrons through a process called inverse-Comptonization (Q_{ic}). This radiative process leads to cooling of electrons. The average change in the photon energy upon scattering with electrons is quantified using an enhancement factor (ζ), which depends on the optical depth of the system. The expression for optical depth has been used from Turolla et al. (1986).

$$\tau_{\text{es}} = 0.4 \left[1 + (2.22T_e \times 10^{-9})^{0.86} \right]^{-1} \rho H r_s. \quad (2.40)$$

2.5.7.1 COMPTONIZED BREMSSTRAHLUNG

In case of Comptonized bremsstrahlung, we follow White & Lightman (1989). The Compton amplification factor is:

$$\zeta_{\text{br}} = f_{\text{br}} \frac{3}{4} \left[\ln \left(\frac{\Theta_e}{x_m} \right) \right]^2. \quad (2.41)$$

Here, f_{br} is the fraction of bremsstrahlung photons scattered into the Wien peak and $x_m = h\nu_m/(m_e c^2)$, is the dimensionless photon frequency above which photons are scattered into the Wien peak (Nakamura et al., 1996; Svensson, 1984).

The emissivity of bremsstrahlung Comptonization is obtained using Eq. 2.37 and is given as:

$$Q_{\text{cbr}} = \zeta_{\text{br}} Q_{\text{br}}. \quad (2.42)$$

2. MATHEMATICAL FRAMEWORK

2.5.7.2 COMPTONIZED SYNCHROTRON

The soft photons generated through thermal synchrotron process could be inverse-Comptonized by the electrons present in the plasma. The expression is given by (Wardziński & Zdziarski, 2000),

$$Q_{\text{csy}} = \zeta_{\text{syn}} Q_{\text{syn}}, \quad (2.43)$$

where, ζ_{syn} is expressed as,

$$\zeta_{\text{syn}} = 3\varphi \left(\frac{x_t}{\Theta_e} \right)^{\alpha_0 - 1} \left[\Gamma_{\text{inc}} \left(1 - \alpha_0, \frac{x_t}{\Theta_e} \right) + \frac{6\Gamma_{\text{inc}}(\alpha_0)P_{\text{sc}}}{\Gamma_{\text{inc}}(2\alpha_0 + 3)} \right]. \quad (2.44)$$

Here, Γ_{inc} is the incomplete gamma function, $x_t = \frac{h\nu_t}{m_e c^2}$ and $\varphi = \frac{[1+(2\Theta_e)^2]}{[1+10(2\Theta_e)^2]}$. α_0 is the slope of the power law photons generated due to inverse-Comptonization, at each radius.

It is defined as :

$$\alpha_0 = -\frac{\ln \mathcal{P}}{\ln \mathcal{A}}. \quad (2.45)$$

Here, \mathcal{P} is the probability that an escaping photon is scattered. It is defined as $\mathcal{P} = 1 - \exp(-\tau_{\text{es}})$. $\mathcal{A} = 1 + 4\Theta_e + 16\Theta_e^2$, is the average amplification factor in photon energy per scattering. The net spectral index (α) of the final inverse-Compton spectrum is obtained from the contribution of all the α_0 's.

2.5.8 COMPTON HEATING

Less energetic photons would cool the flow through the process of inverse-Comptonization. But in case, the temperature of the electrons is less than the temperature of the ambient photons, then the electrons will gain energy from the photons via Compton scattering. This will lead to Compton heating of the electrons. We assume that this has the same expression as that of inverse-Comptonization, but the sign changes (Esin, 1997). It causes heating rather than cooling. Therefore, $Q_e^+ = Q_{\text{comp}}$.

2.5.9 ANNIHILATION

In the presence of $e^+ - e^-$ pairs, annihilation can occur, which acts as an additional cooling mechanism, expression of which is given below (Svensson, 1982a,b):

$$Q_{\text{ann}} = n_{e^+} n_{e^-} r_e^2 m_e c^3 \frac{2\pi}{\frac{1}{1+6\Theta_e} + \frac{\Theta_e}{\ln(2\eta_E + 1) + \frac{1}{4}}}. \quad (2.46)$$

Here, $\eta_E \equiv \exp(-\gamma_E) = 0.5616$, where $\gamma_E = 0.5772$ is the Euler's constant and r_e is the classical electron radius.

2.6 SPECTRAL ANALYSIS

We included radiative processes like bremsstrahlung, synchrotron and their corresponding inverse-Comptonizations. These radiative processes lead to emissions that can be observed from radio to γ -rays. At each radius of the accretion flow, we have information of the total amount of radiation emitted by all these processes, as well as the amount of radiation emitted at each frequency (ν). For every frequency bin, we add up the contributions from all the regions of the flow to their respective values of frequency. This gives us the spectrum. If the emission from all regions of an accretion flow, for all the energies, are added up, we get the bolometric luminosity (L). The methodology to compute a spectrum has been adopted from [Shapiro \(1973\)](#).

A spectrum is mainly a function of v , T and ρ . Signatures of emission processes that dominate inside an accretion flow is imprinted in a spectrum. Also, there could be other features present, which can be functions of other flow parameters. To properly extract a spectrum, incorporation of all the general and special relativistic effects is necessary. Below, we explain the methodology to compute a spectrum.

Let us assume that the isotropic emissivity per frequency interval per unit solid angle in the fluid rest frame is j_ν . If we transform this emissivity, as seen by a static observer in the Schwarzschild frame, then by using special-relativistic transformations, this becomes :

$$j'_{\nu'} = j_\nu \frac{1 - v^2}{(1 - v \cos \theta^*)^2} \quad \text{and} \quad \nu' = \nu \frac{\sqrt{1 - v^2}}{(1 - v \cos \theta^*)}. \quad (2.47)$$

Here, θ^* is the angle which the velocity of the fluid element directed inwards makes with the line of sight.

It is to be noted that all the photons emerging from the disc need not reach the observer. If the central object is a BH, its extreme gravity will capture some of the photons and hence will be permanently lost. The amount of emission captured depends on the distance from the central BH. The expression to calculate this amount was given by [Shapiro \(1973\)](#); [Shapiro & Teukolsky \(1983\)](#); [Zeldovich & Novikov \(1971\)](#) :

$$|\cos \theta^o| = \sqrt{\frac{27}{4} \left(\frac{2}{r}\right)^2 \left(\frac{2}{r} - 1\right) + 1}, \quad (2.48)$$

where θ^o is the angle within which photons will be captured by the BH and hence lost. This has been represented in [Fig. 2.1](#), where photon capture angles are represented using black shaded cones.

2. MATHEMATICAL FRAMEWORK

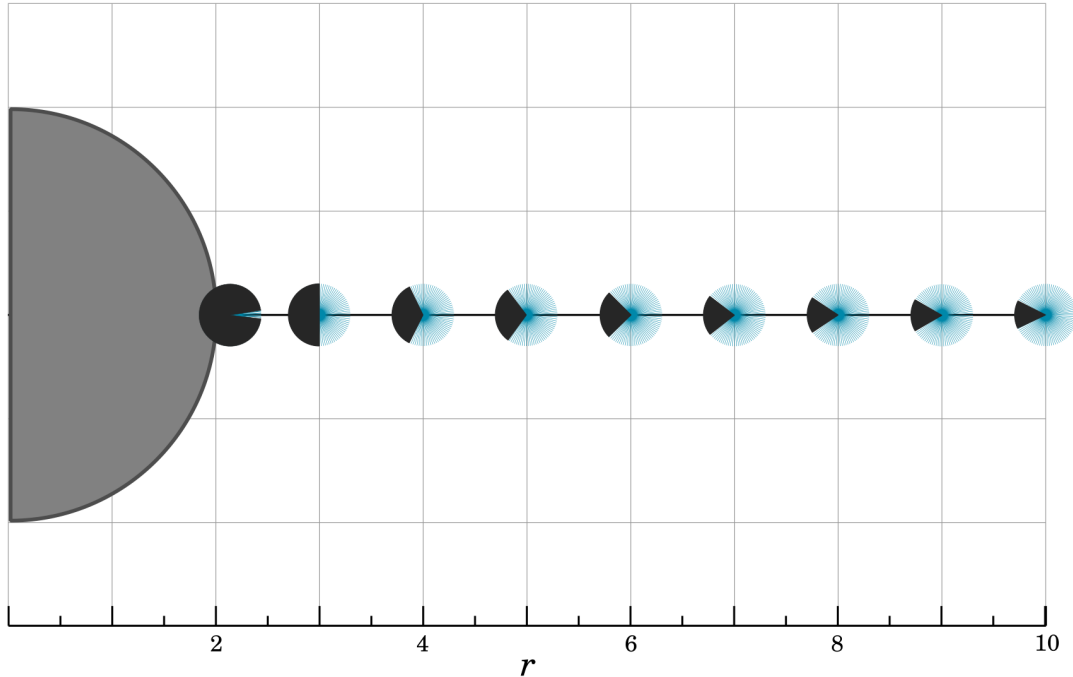


Figure 2.1: Photon capture by the strong gravity of BH is presented. Photons emitted at r (in units of r_g) and propagating within the black shaded cone is trapped by the central BH (inside the grey shaded region). Blue lines, represent the radiation which escapes. In this plot, $r = 2$ is the location of the event horizon.

On integrating the emission coefficient of any given emission process, over the whole volume of the disc, over all solid angles, taking into account θ^o : spectrum corresponding to that particular emission process will be obtained. Combining the spectrum of all emission processes gives the total observable spectrum. We have also accounted for the gravitational redshift, which introduces a factor of $\sqrt{1 - 2/r}$ in the observed frequency. Furthermore, to calculate the bolometric luminosity of the system, we integrate the frequency dependent emission coefficient over all the frequencies (see, [Shapiro, 1973](#)).

2.7 CRITICAL POINT CONDITIONS

Matter very far away from the central object is subsonic, *i.e.*, flow velocity (v) is less than the speed of sound in the medium (a_s), $v \ll a_s$. As matter gets accreted, the gravitational potential energy, $\Phi_g(r)$ increases, which in turn increases the kinetic energy of the matter. Thus, as a primary effect, v increases. But the matter is also compressed to smaller and smaller volumes, which increases the temperature and hence a_s . Thus, at certain point of the flow, say r_c , $v = a_s$. This point is called the *critical point* of the flow. After crossing

this point, matter is supersonic. Thus, an accretion flow has to pass through at least one critical point or has to be necessarily transonic in nature. Bondi showed that a transonic solution is the only plausible solution with maximum entropy. Similar to Bondi flows with single critical point, rotating flows possess multiple critical points (MCP). These are formed because a centrifugal force acts in the opposite direction to gravity. In the MCP regime, an accretion flow can also harbour shocks.

At the critical point, the differential equation for velocity has the form:

$$\frac{dv}{dr} = \frac{N}{D} = \frac{0}{0}. \quad (2.49)$$

The value of $(dv/dr)|_{r_c}$ is obtained using the L'Hospital's rule.

In the hydrodynamic case, critical points are also called *sonic points* because there is only one signal speed, which is the sound speed. In the MCP regime, an accretion flow could possess a maximum of three types of sonic points: inner (r_{ci}), middle (r_{cm}) and outer (r_{co}) (named according to its distance from the central object). Out of these three sonic points, r_{ci} and r_{co} are X-type sonic points (real velocity slope) and are physical, while r_{cm} is unphysical and matter cannot flow through it. r_{cm} is O-type (imaginary velocity slope) for inviscid, adiabatic flow, and spiral type (complex velocity slope) when dissipation is present.

In the MHD regime, a plasma has three signal speeds: Alfvén speed, slow and fast magneto-acoustic speeds. Thus, a magnetised accretion flow has multiple *kinds* of critical points, apart from the general multiple *types* of critical points. In a special case, when strong magnetic field assumption is satisfied, it does not allow for the formation or propagation of Alfvén and magneto-acoustic plasma waves. Hence, the corresponding critical points are absent. The only characteristic speed by which information can travel in such an accretion flow, is the sound speed. Thus, we reduce to a situation similar to a hydrodynamic accretion flow.

2.8 SHOCK CONDITIONS

The general expression of hydrodynamic shock conditions or the Rankine-Hugoniot conditions are (Chattopadhyay & Chakrabarti, 2011; Kumar & Chattopadhyay, 2014; Taub, 1948):

- Conservation of mass flux: $[\dot{M}] = 0$,
- Conservation of energy flux: $[\dot{E}] = 0$,

2. MATHEMATICAL FRAMEWORK

- Conservation of radial momentum flux: $[p_{\text{ram}} + p_{\text{thermal}}] = 0$,
- Conservation of azimuthal momentum flux: $[\dot{J}] = 0$.

The above equations are conservation of fluxes across the shock front (Chakrabarti, 1989). The square brackets denote the difference of the quantities across the shock. p_{ram} and p_{thermal} are the vertically averaged ram pressure and vertically averaged thermal pressure respectively. \dot{J} represents the angular momentum flux.

The MHD shock conditions (Kennel et al., 1989) have a form similar to Rankine-Hugoniot hydrodynamic shock conditions except that an additional magnetic pressure and magnetic energy appears in the momentum flux conservation and energy flux conservation equations respectively. Also, an electro-magnetic field flux conservation equation needs to be satisfied across the shock.

2.9 A GENERAL APPROACH TO OBTAIN A GLOBAL TRANSONIC SOLUTION

The general procedure to obtain a transonic solution for a given set of flow parameters (E , \dot{M} , λ , M_{BH} or M_{NS} etc.) is to first locate the critical points. In MCP regime, there will be many such locations. After the location has been identified, we integrate the continuity equations and differential equations of angular momentum, velocity and temperature(s), from the critical point inwards and outwards using 4th order Runge-Kutta method, in order to obtain self-consistent values of n_i , v , Θ (or Θ_e and Θ_p) respectively, throughout the flow. But in case of a dissipative flow, the location of critical point(s) are not known a priori, and finding these points is not trivial. The methodology to find such points differ in one-temperature and two-temperature flows, an elaborate discussion of which has been done in the coming chapters.

Chapter 3

ONE-TEMPERATURE ACCRETION FLOWS AROUND BLACK HOLES

3.1 INTRODUCTION

Modelling of hot accretion flows around BHs, gained popularity from 1980s, as it could model the thermal as well as non-thermal part of the spectrum obtained from observations (Rees et al., 1982; SLE76). After the inclusion of advection, these flows became thermally stable and have been since then, extensively used to explain the high energy emissions coming from AGNs, XRBs, microquasars etc. These flows predict electron temperature in accretion discs to be approximately equal to or greater than the electron rest mass energy $kT_e \gtrsim m_e c^2 = 511$ keV. It was soon realised that the production of $e^+ - e^-$ pairs and their annihilation is an important process, and might play a significant role in accretion disc dynamics as well as in shaping the emitted spectrum (Esin, 1999).

Shull (1979) and Wandel et al. (1984) obtained self-consistent solutions, including the effect of pairs, but details of the flow dynamics were ignored, and the radiative transfer part was not properly dealt with. They did not consider the effect of produced pairs back into the system. Yahel & Brinkmann (1981) and Yahel (1982) investigated pair production in the most self-consistent way. But their methodology to obtain solutions was too sensitive to the boundary conditions, which inhibited them from getting a larger picture of the

Some part of the results in this chapter are published in: Sarkar, Shilpa and Chattopadhyay, Indranil, 2020, *Journal of Physics Conference Series*, **1640**, 012022.

Rest are to be communicated: Sarkar, Shilpa; Chattopadhyay, Indranil and Laurent, Philippe, 2021.

3. ONE-TEMPERATURE ACCRETION FLOWS AROUND BLACK HOLES

parameter space. Following them, more realistic self-consistent two-temperature works, including pairs, were conducted by [Park & Ostriker \(1989\)](#) and [Park \(1990\)](#).

Pair processes can significantly change the radiative output of the system as well as composition of the flow ([Liang, 1979](#)). Different emission processes lead to the formation of different radiation fields in an accretion flow. Fraction of this radiation escapes and contributes to the observable spectrum, and the rest is advected inwards, with the bulk motion of the flow. However, this radiation field can also create pairs (depending on the photon energies and other parameters). Thereby, the observed luminosity can decrease because radiation is now used to create pairs. But we remember that, the new created electrons and positrons can radiate, increasing the luminosity of the system. Also, annihilation of pairs would take place, which is an additional emission process. At the same time, it serves as an additional radiation field that can give rise to pair creation. Thus, pair-production and annihilation is a highly non-linear process and [Lightman \(1982\)](#) correctly quoted, “pairs produce photons, and photons produce more pairs”.

There are three collisional processes which could lead to pair production: photon-photon, particle-particle and photon-particle interaction. The particle could either be an e^- , e^+ or p . Photon-particle interactions and particle-particle interactions are less important because their reaction cross-section decreases in the order of α_f ($= 1/137$) and α_f^2 , respectively. Hence, we can safely ignore them. Therefore, the most dominant process leading to the production of pairs in accretion flows is photon-photon interaction. [Herterich \(1974\)](#) showed that photon-photon pair production process has a threshold condition: $E_1 E_2 (1 - \cos \theta_{pp}) \geq 2(m_e c^2)^2$, where $E_1 = h\nu_1$ and $E_2 = h\nu_2$ are the energies of the interacting photons and θ_{pp} is the angle between them. Thus, photons of higher energies mainly contribute to the production of pairs.

To obtain a complete picture of the effect of pairs in accretion disc dynamics, it is essential to consider all the radiation fields. Also, the pairs which are not annihilated will be advected inwards with the flow, towards the central object (assuming negligible pair escape), and can radiate or annihilate there. Discrepancies in earlier works have arisen due to selective radiation processes being considered inside the flow. We investigate this matter in greater details in the GR regime, for one-temperature flows. One-temperature solutions are important because it gives a general idea about the flow behaviour, its dynamics, as well as energetics. Although simple, it brings out the essential qualitative features of the system without getting involved into the other complexities, like that present in two-temperature solutions, which is a matter of discussion in the upcoming chapters. Apart from that, one-temperature flows are valid in situations where Coulomb

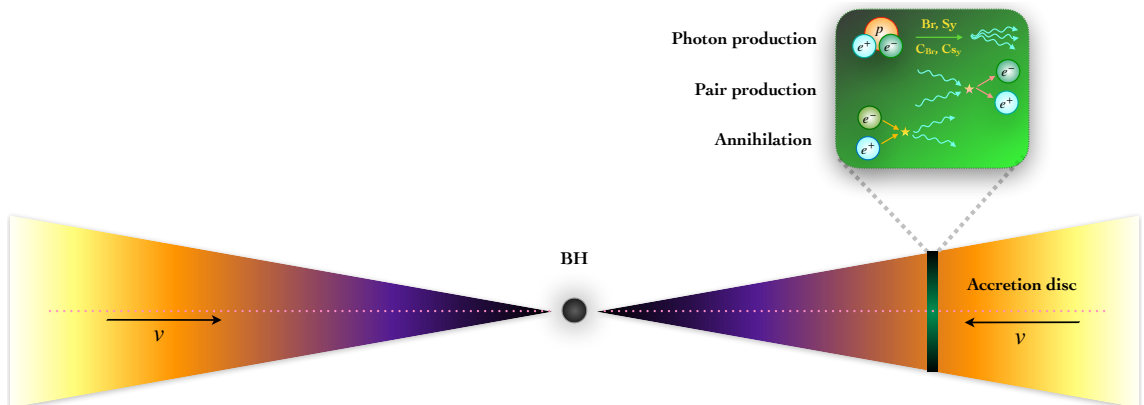


Figure 3.1: A cartoon diagram representing an accretion disc around a BH. The disc is assumed to be axisymmetric, advective, transonic in nature and rotating with viscous stresses removing angular momentum outwards. At every radius of the flow, there are radiative processes which gives rise to photon fields, conducive enough for the production of pairs. These pairs can annihilate and produce an additional radiation field.

coupling is strong or if there are any other collective effects present (Chattopadhyay & Chakrabarti, 2011; Chattopadhyay & Kumar, 2016; Kumar & Chattopadhyay, 2013, 2014, 2017; Kumar et al., 2013). Also, as have been discussed before, we used the CR EoS, which removed the constraint of specifying a fixed adiabatic index.

3.2 ASSUMPTIONS AND EQUATIONS USED

We assume an advective, viscous, transonic accretion disc around a Schwarzschild BH (see, Fig. 3.1). The treatment is in the pure GR regime, where the line element in spherical coordinate system is given by Eq. 2.1. We utilise the equations discussed in Section 2.2 to model the accretion flow. CR EoS for multi-species flow have been used throughout this work, general expression of which is given in Eq. 2.31. The function f present in the EoS, has the following form:

$$f = (2 - \xi) \left(1 + \Theta \frac{9\Theta + 3}{3\Theta + 2} \right) + \xi \left(\frac{1}{\chi} + \Theta \frac{9\Theta + 3/\chi}{3\Theta + 2/\chi} \right), \quad (3.1)$$

where, $\chi = m_e/m_p$.

Accretion flows are governed by the continuity equation Eq. 2.4, Navier-Stokes equation Eq. 2.5 and the first law of thermodynamics Eq. 2.15, collectively called the equations of motion (EoM), simplified forms of which in the one-temperature regime has been given below:

3. ONE-TEMPERATURE ACCRETION FLOWS AROUND BLACK HOLES

(1) **Continuity equation:** In the presence of pair production, particle four-flux is not conserved. So, we define the continuity equation separately for individual particles (p, e⁺ and e⁻).

- (a) Proton: In the presence of pair production, proton number density is not affected, and hence the continuity equation 2.5 can be integrated to obtain a form of conservation of proton mass flux or the proton-accretion rate of the system (\dot{M}_p). Thus, we have:

$$\dot{M}_p = 2\pi\rho_p u^r r H, \quad (3.2)$$

where, $\rho_p = n_p m_p$ is the proton mass density.

- (b) Positron: The continuity equation for obtaining positron number density can be written using Eq. 2.5 in the following form (Fukue, 1986; Yahel & Brinkmann, 1981):

$$\frac{dn_{e^+}}{dr} = \frac{(\dot{n}_C - \dot{n}_A)}{u^r} - \frac{n_{e^+}}{rHu^r} \frac{d(rHu^r)}{dr}, \quad (3.3)$$

where, \dot{n}_C and \dot{n}_A are the creation and annihilation rates per unit volume respectively, expressions of which will be discussed in Section 3.2.2.

- (c) Electron : Charge neutrality demands that the number of positive charges equals the number of negative charges. This gives us the electron number density (in units of cm⁻³):

$$n_{e^-} = n_{e^+} + n_p. \quad (3.4)$$

(2) **First law of thermodynamics:** Simplifying Eq. 2.15 using EoS (Eq. 2.31 combined with Eq. 3.1), we get the simplified form of first law of thermodynamics:

$$\frac{d\Theta}{dr} = -\frac{\Theta}{\Theta H_\Theta + N} \left(\mathcal{A} + \mathcal{B} \frac{dl}{dr} + \mathcal{C} \frac{dv}{dr} - \frac{\mathbb{Q} - \mathbb{P}}{2\Theta} \right), \quad (3.5)$$

where, $H_x = \frac{1}{H} \frac{\partial H}{\partial x}$, $\mathcal{A} = H_r + \frac{r-1}{r(r-2)}$, $\mathcal{B} = H_l$, $\mathcal{C} = H_v + \frac{1}{v(1-v^2)}$ and $\mathbb{Q} = \frac{\Delta Q(1+1/\chi)}{\rho u^r}$. The term \mathbb{P} has information on leptons internal energy consumed while creating pairs (Park, 1990). The expression is given by, $\mathbb{P} = \frac{2(1+1/\chi)}{\rho u^r} \frac{e_l + p_l}{n_l} (\dot{n}_C - \dot{n}_A)$, where, subscript l refers to the leptons.

(3) **Azimuthal component of Navier-Stokes equation:** Simplifying Eq. 2.14 using

Eq. 2.3, we have:

$$\frac{dl}{dr} = \left[-\frac{\rho u^r (L_b - L_0)}{\eta_v (1 - \frac{2}{r})} + \frac{2l}{r} \right] (1 - v^2), \quad (3.6)$$

where, $l = u_\phi = L_b/h$.

(4) **Radial component of Navier-Stokes equation:** On simplifying Eq. 2.13 using Eqs. 3.1-3.6, we obtain the differential equation for velocity:

$$\frac{dv}{dr} = \frac{\mathcal{N}}{\mathcal{D}}, \quad (3.7)$$

where, $\mathcal{N} = -\frac{1}{r(r-2)} + \frac{(r-3)l^2}{(r-2)r^3\gamma_v^2} + \frac{Na_s^2}{\Theta H_\Theta + \mathcal{N}} \left(\mathcal{A} + \mathcal{C} \frac{dl}{dr} + \frac{(1-\Theta H_\Theta)(\mathcal{Q}-\mathbb{P})}{h(1+1/\chi)Na_s^2} \right)$ and $\mathcal{D} = \frac{v}{1-v^2} - \frac{Na_s^2 \mathcal{B}}{\Theta H_\Theta + \mathcal{N}}$. The sound speed is defined as, $a_s = \sqrt{\frac{\Gamma p}{e+p}}$.

The generalized Bernoulli constant is a constant of motion even in the presence of dissipation. Its simplified form is obtained from Eq. 2.16, which gives:

$$E = -h\gamma_v \sqrt{1 - \frac{2}{r}} \exp(X_v + X_f), \quad (3.8)$$

where, $X_v = -\int \frac{(r-3)l^2(1-v^2)}{(r-2)r^3} dr$, $X_f = \int \left[\frac{\Delta Q}{\rho h u^r} - \frac{2}{\rho h u^r} \frac{e_l + p_l}{n_l} (\dot{n}_C - \dot{n}_A) \right] dr$.

3.2.1 HEATING AND COOLING MECHANISMS

- Cooling processes considered are: (1) bremsstrahlung (Q_{br} , see Eq. 2.37), (2) synchrotron (Q_{syn} , see Eq. 2.39), (3) inverse-Comptonization of bremsstrahlung photons (Q_{cbr} , see Eq. 2.42), (4) inverse-Comptonization of synchrotron photons (Q_{csy} , see Eq. 2.43) and (5) annihilation (Q_{ann} , see Eq. 2.46).
- Heating due to viscous (Q_v , see Eq. 2.33) and magnetic energy dissipation (Q_B , see Eq. 2.34) have been taken into account. Also, Compton heating (Q_{comp}) mechanism have been considered, see Section 2.5.8.
- The pairs produced would have an overall heating effect: $Q_{pair-heat} = \langle h\nu_1 + h\nu_2 \rangle \dot{n}_C$.

Thus to summarise : $Q^+ = Q_v + Q_B + Q_{comp} + Q_{pair-heat}$ and $Q^- = Q_{br} + Q_{syn} + Q_{cbr} + Q_{csy} + Q_{ann}$. In addition, we have implemented all the special and general relativistic transformations while computing the actual energy loss as well as while plotting the spectrum.

3. ONE-TEMPERATURE ACCRETION FLOWS AROUND BLACK HOLES

3.2.2 PAIR PRODUCTION AND ANNIHILATION RATES

Photons generated from the different radiation mechanisms interact with each other, leading to the production of $e^+ - e^-$ pairs. Hence, the details of photon generation and propagation are necessary. The optical depth of a system determines the effectiveness of interaction between the photons and leptons, and also the photon escape timescales, which is given by, $t_{\text{esc}} \approx (1 + \tau_{\text{es}})H/c$, where the expression of optical depth is given by Eq. 2.40.

The photon distribution function is necessary to define the interaction between them. Radiation field produced by bremsstrahlung photons, along with its inverse-Comptonization, follow a relatively flat spectrum with an exponential cut-off, and a Wien component (White & Lightman, 1989). Synchrotron photons follow Rayleigh-Jeans law (Narayan & Yi, 1995), and its inverse-Comptonized part can be approximated as a combination of cut-off power-law and a Wien peak (Wardziński & Zdziarski, 2000; Zdziarski, 1985). The spectrum for annihilation photons is given in Svensson (1982a,b). As have been previously argued, only the energetic (or hard) photons can meet the threshold criteria for pair production, thereby creating pairs. But most of the photons produced by synchrotron emission are too soft to satisfy the requirements. When inverse-Comptonized, these photons become hard, and consequently can contribute to the pair production process. Thus, we can safely neglect the contribution from synchrotron soft photons and only consider its Comptonized component, while estimating the number of pairs produced (Esin, 1999).

After we have information about the radiation fields present in the system, we identify all possible photon combinations that could lead to pair production. They can be collisions: (1) between Wien photons (\dot{n}_{WW}), (2) between Wien and flat unscattered bremsstrahlung photons (\dot{n}_{WF}), (3) between the photons belonging to the same unscattered flat part (\dot{n}_{FF}), (4) power law photons and Wien photons (\dot{n}_{PW}), (5) power-law photons and flat bremsstrahlung continuum photons (\dot{n}_{PF}), (6) between the same power law photons (\dot{n}_{PP}), (7) annihilation and Wien photons (\dot{n}_{AW}), (8) annihilation and flat bremsstrahlung photons (\dot{n}_{AF}), (9) annihilation and power-law photons (\dot{n}_{AP}) and (10) between annihilation photons themselves (\dot{n}_{AA}). Thus the creation rate can be written as:

$$\dot{n}_{\text{C}} = \dot{n}_{\text{WW}} + \dot{n}_{\text{WF}} + \dot{n}_{\text{FF}} + \dot{n}_{\text{PW}} + \dot{n}_{\text{PF}} + \dot{n}_{\text{PP}} + \dot{n}_{\text{AW}} + \dot{n}_{\text{AF}} + \dot{n}_{\text{AP}} + \dot{n}_{\text{AA}}. \quad (3.9)$$

All these ten combinations have been included in this work. The annihilation rate is given

by (Stepney & Guilbert, 1983; Svensson, 1982a,b):

$$\dot{n}_A = n_{e^+} n_{e^-} c r_e^2 \frac{\pi}{1 + \frac{2\Theta_e^2}{\ln(1.12\Theta_e + 1.3)}}. \quad (3.10)$$

3.3 METHODOLOGY TO OBTAIN SOLUTIONS

In Section 2.9, we briefly discussed the general methodology to obtain a transonic accretion solution. Here, we address it in more details. First, we enumerate the steps to obtain a one-temperature, viscous, radiative, transonic accretion flow around a BH, without any pair processes. Then, we proceed to obtain a transonic solution in the presence of pairs.

3.3.1 FINDING A GENERAL ONE-TEMPERATURE TRANSONIC SOLUTION – I : WITHOUT PAIRS

The system we are dealing with is dissipative in nature (viscous dissipation, as well as radiative processes, are included); hence information regarding the sonic point is not known a priori. For a given set of flow parameters (E , λ_{in} , α_v , \dot{M} , M_{BH} etc.), a solution may harbour one or more sonic points (see Section 2.7). Finding of sonic points is not trivial. The first step is to specify the boundary conditions. Horizon being a co-ordinate singularity, we select a point asymptotically close to the horizon, say $r_{\text{in}} = 2.001$ (in terms of r_g). It is to be noted that, in the sections to come, the subscript ‘in’ will be used to represent the values at r_{in} . The reason behind this choice of boundary is, near the horizon, values of many variables are known, $r \rightarrow 2r_g$ and $v \rightarrow c$. Also, $E \rightarrow \mathcal{E} = -hu_t$ (from Eq. 2.18), because asymptotically close to the horizon, gravity overpowers any process or interaction, preventing the matter from interacting with itself or its environment, making the region adiabatic in nature. We discuss below a step-by-step procedure for finding solutions. The methodology developed is inspired from the solution procedure given by Becker and his collaborators (Becker et al., 2008; Becker & Le, 2003; Gu & Lu, 2004).

1. Specify the flow parameters: E , α_v , β , β_d , \dot{M} and M_{BH} . These are constants of motion throughout the flow and, thereby, characterise a flow. β is defined as the ratio of the magnetic pressure to gas pressure and is important in the estimation of B and hence synchrotron radiation while β_d as defined in Section 2.5.2, is required in the estimation of magnetic energy dissipated in the system. δ_s are the fraction of viscous and magnetic energy transferred to protons, respectively (see Section 2.5.1 and 2.5.2 for more details).

3. ONE-TEMPERATURE ACCRETION FLOWS AROUND BLACK HOLES

2. Select $r_{\text{in}} = 2.001$ (in units of r_g) as the inner boundary and supply λ_{in} at r_{in} . Since there is viscosity present in the system, λ is not constant, and we need to self-consistently calculate its value at every point of the flow.
3. Compute the other inner boundary values (v_{in} , l_{in} and L_0): We first assume any arbitrary value of Θ_{in} . Also, adiabatic condition near the horizon reads, $E \simeq \mathcal{E} = -hu_t$.

- Evaluate the value of l_{in} from the definition of specific angular momentum, which is:

$$\lambda_{\text{in}} = -\frac{u_\phi}{u_t} = -\frac{l_{\text{in}}}{\frac{E}{h_{\text{in}}}},$$

where, h_{in} is a function of only Θ_{in} .

- Simplifying, $E = -h_{\text{in}}u_t = -h_{\text{in}}\sqrt{(1-2/r)}\gamma_v\gamma_\phi$ near the horizon, gives an analytical expression for velocity near the horizon (v_{in}). Supplying the values of E , $h_{\text{in}}(\Theta_{\text{in}})$ and l_{in} will provide the value of v_{in} .
 - $E \simeq \mathcal{E}$ implies, $\exp(X_v) = \gamma_\phi$ from Eq. 2.16. Calculating its derivative w.r.t r and then simplifying it would give a quadratic equation in $L_{\text{bin}} - L_0$ (where, $L_{\text{bin}} = L_{\text{b}|r \rightarrow r_{\text{in}}} = l_{\text{in}}h_{\text{in}}$). Solving this equation would allow us to estimate the value of L_0 , which is the bulk angular momentum at the horizon.
4. Finding sonic point (obtaining a correct value of Θ_{in}): After finding v_{in} , l_{in} and L_0 corresponding to a given arbitrary value of Θ_{in} , we integrate the EoM Eq. 3.3 and Eqs. 3.5-3.7, from r_{in} outwards (increasing r), using 4th order Runge-Kutta integration technique and obtain a solution. We check whether this solution, pass through a sonic point or not. If it does not, we change Θ_{in} and again find the values of v_{in} , l_{in} and L_0 (step 3) and integrate to find another solution. We iterate on Θ_{in} , until the sonic point conditions are satisfied (see Section 2.7, Eq. 7.19).
 5. Obtaining the transonic solution: As soon as we locate the sonic point (r_c), we find the derivative $dv/dr|_{r_c}$ using L' Hospital's rule and integrate further outwards, until we reach a point which is very far from the central object (say, around $r \rightarrow 10^4 r_g = r_{\text{out}}$) where, the velocity of the solution becomes negligible.
 6. Checking for other sonic points: Since angular momentum and relativistic effects induce the formation of multiple sonic points, we need to check whether any other sonic point exists for the same L_0 . For this, we change Θ_{in} by a considerable value and repeat steps described from 3-4. If there is another sonic point present, then we follow step 5 to obtain a transonic solution. It should be remembered that the

supplied combination of flow parameters (step 1 and 2) decide whether the flow harbours MCP or not.

7. Checking for shock transitions: When the flow possess MCP, we need to check whether the solutions passing through them satisfy shock conditions (see Section 2.8 for shock conditions). If satisfied, the global solution first passes through the outer sonic point (r_{co}) and becomes supersonic. Then, this matter encounters a centrifugal force driven shock transition (r_{sh}), after which it becomes subsonic. This matter then enters the horizon supersonically after passing through the inner sonic point (r_{ci}). At the shock location, although flow velocity becomes subsonic, the temperature and density jump to higher values.

These steps have been represented in the form of a flowchart given in Fig. 3.2. To explain this further, we obtain a transonic solution for flow parameters $E = 1.001$, $\lambda_{in} = 2.65$, $\alpha_v = 0.01$, $\beta = 0.5$, $\beta_d = 0.01$, $\dot{M} = 0.5\dot{M}_{Edd}$ and $M_{BH} = 10M_{\odot}$, and plot it in Fig. 3.3. The solution is represented using Mach number, defined as $M = v/a_s$, vs r plot. At $r = r_{in} = 2.001$, first we supply $\Theta_{in} = 0.2084 = \Theta_{in1}$ (see Fig. 3.3a) and follow steps 3–5 to get a solution. The solution obtained for this case is a completely supersonic branch (SB), dashed-dotted violet curve. This solution does not satisfy the outer boundary condition, which insists matter to be subsonic very far away from the central object. Thus, we can safely reject this branch of solution since it is unphysical. On changing the Θ_{in} to $0.2110 = \Theta_{in2}$, we obtain a multi-valued branch (MVB) solution, dashed-dotted orange curve. This solution is also unphysical since, at any given radius, a solution cannot have two values. We iterate on Θ_{in} (between the limits Θ_{in1} and Θ_{in2}) until $dv/dr = 0/0$ is satisfied at any r . This point is called the sonic point of the flow (r_c). For the current set of flow parameters used, at $\Theta_{in} = 0.2096 = \Theta_{in3}$ we obtain a transonic solution (TS) (dashed red curve) passing through $r_{ci} = 6.898$ (marked with solid black circle). This is represented in Fig. 3.3a. The given combination of flow parameters possess another sonic point r_{co} , apart from the r_{ci} . Keeping L_0 same at the horizon, we follow the procedure mentioned in step 6 and obtain another sonic point for $\Theta_{in} = 0.1547$. The corresponding TS (solid red line) now passes through $r_{co} = 203.809$ (marked with a black star), see Fig. 3.3b. We then checked for the shock conditions (step 7) and found that this solution does not harbour a shock. The global solution, therefore, passes through r_{co} only (solid red curve in Fig. 3.3c). Because of the absence of any shock jump, the TS passing through r_{ci} remains a non-global transonic solution (dashed red curve).

3. ONE-TEMPERATURE ACCRETION FLOWS AROUND BLACK HOLES

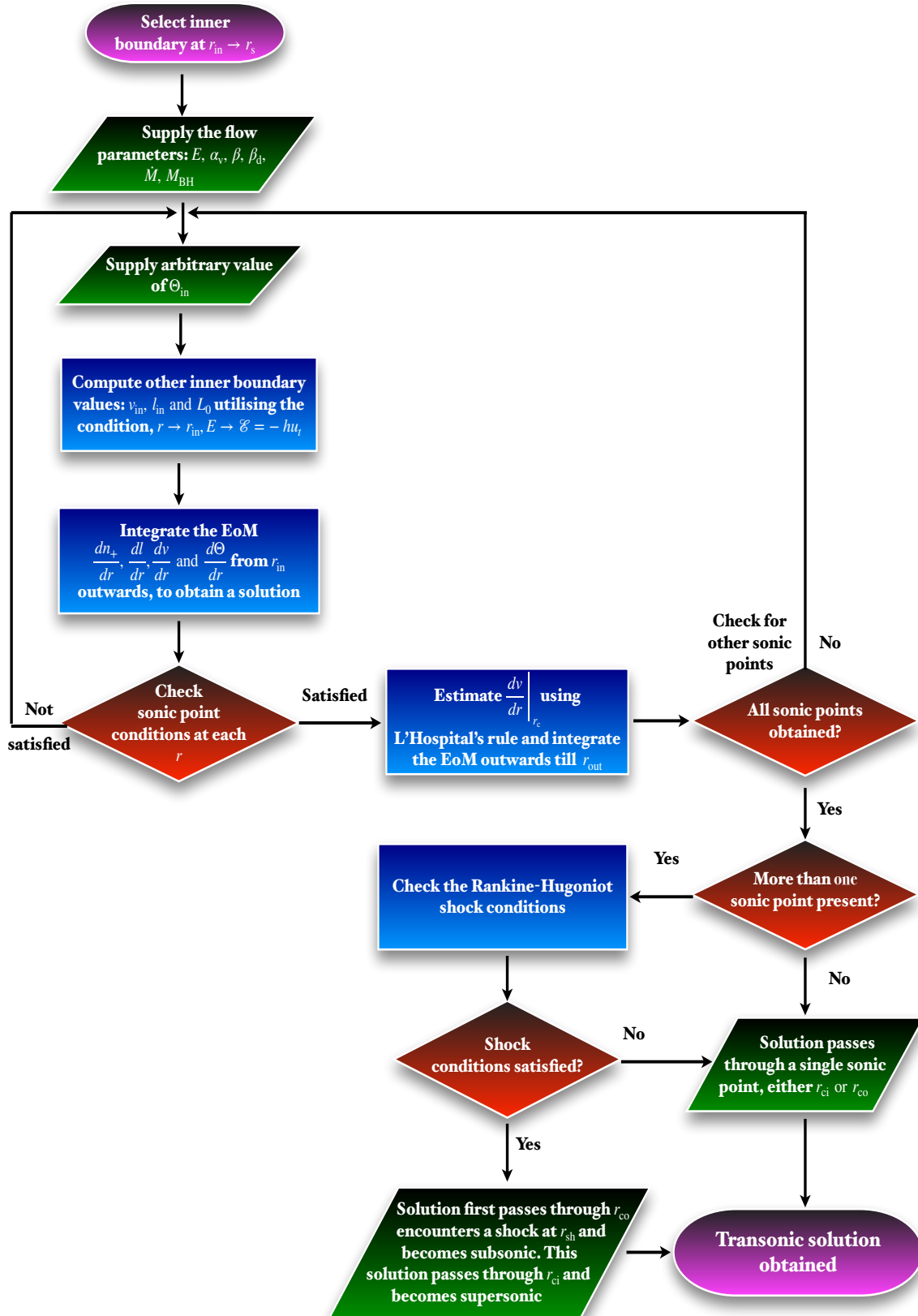


Figure 3.2: Flowchart representing the methodology to obtain a transonic solution.

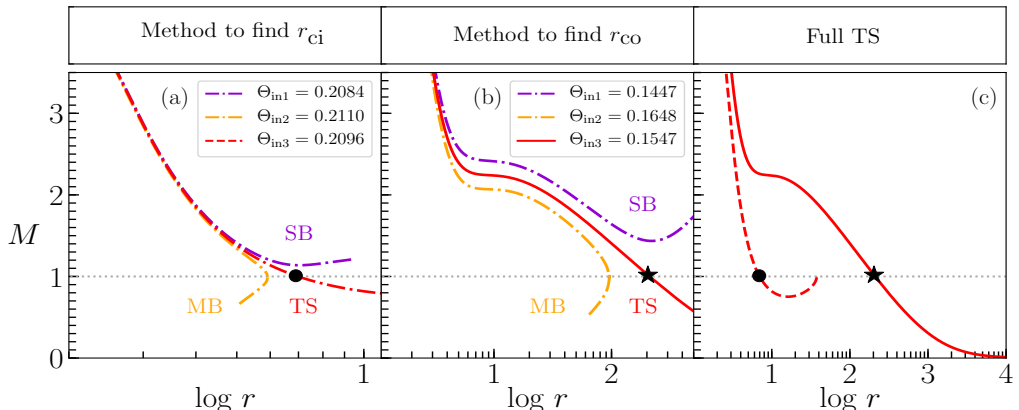


Figure 3.3: Methodology to obtain a general transonic solution (TS) is presented using iteration technique on Θ_{in} . Panel (a) finds r_{ci} (marked using solid black circle) and the TS is represented using dashed red curve, (b) finds r_{co} (marked using black star) and the corresponding TS is plotted using solid red curve. Thus, for the present set of flow parameters used, we have MCP. The flow does not harbour a shock, hence the final global TS (solid red line) passes through r_{co} and is plotted in panel (c). Flow parameters used are, $E = 1.001$, $\lambda_{\text{in}} = 2.65$, $\alpha_v = 0.01$, $\beta = 0.5$, $\beta_d = 0.01$, $\dot{M} = 0.5\dot{M}_{\text{Edd}}$ and $M_{\text{BH}} = 10M_{\odot}$

3.3.2 FINDING A GENERAL ONE-TEMPERATURE TRANSONIC SOLUTION – II : INCLUSION OF PAIR PROCESSES

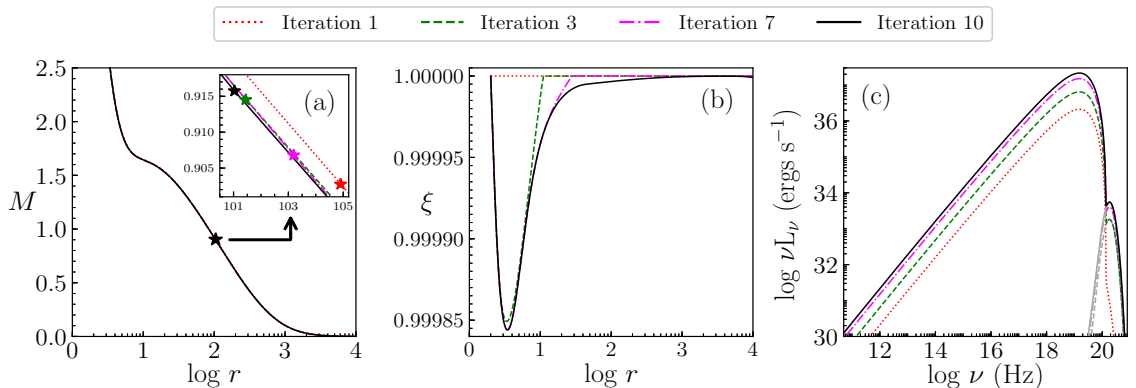


Figure 3.4: Finding of transonic solution with pairs, using feedback iterative technique. Iteration 1 is pair-free. From iteration 2 onwards, pair-production and annihilation processes are included. Iteration process continues until the solutions converge. The corresponding change in Mach number, $M = v/a$ (panel a) and composition of the flow, $\xi = n_p/n_{e+}$ (panel b) with the change in iteration are plotted. Stars in panel (a) represent the sonic points. The flow parameters used are, $E = 1.001$, $\lambda_{\text{in}} = 2.5$, $\dot{M} = 0.6\dot{M}_{\text{Edd}}$, $\alpha_v = 0.05$ and $M_{\text{BH}} = 10M_{\odot}$.

The methodology described above is for a pair-free model. As soon as we get a self-consistent, pair-free TS, we compute the maximum positron density, n_{e+} at each r , that

3. ONE-TEMPERATURE ACCRETION FLOWS AROUND BLACK HOLES

could be obtained if pair production had been present. We name it: iteration 1. In iteration 2, we repeat steps 3-7 meant to obtain a TS, but now include additional pair creation and annihilation processes, using n_{e^+} calculated from iteration 1. Now, we have a TS with pairs, and name it as iteration:2. Thereafter, we again compute the maximum n_{e^+} of this TS (as was done with TS obtained in iteration 1), and feed it back to the system. We continue this process of iterating, until the TSs converge.

To explain it further, we plot in Fig. 3.4, panel (a) global TSs and (b) corresponding composition of the flow, defined using $\xi = n_p/n_{e^-}$. We have for the time being, ignored the stochastic magnetic field in the system. Thus, synchrotron, its inverse-Comptonization and heating due to magnetic dissipation is absent. The flow parameters used are, $E = 1.001$, $\lambda_{\text{in}} = 2.5$, $\alpha_v = 0.05$, $\dot{M} = 0.6\dot{M}_{\text{Edd}}$ and $M_{\text{BH}} = 10M_{\odot}$. Iteration 1 is denoted using dotted red line. We can see that, the solution passes through a single r_{co} (marked with a red star in Fig. 3.4a, clearly visible in inset) and $\xi = 1$ for the first iteration (Fig. 3.4b), *i.e.* $n_{e^+} = 0$. As we perform iterations, there is an interplay between pair production, annihilation as well as change in radiative cooling due to increase in number density of e^- and e^+ . Coloured stars in Fig. 3.4a depict the sonic point, which shifts to different location with each iteration. After the iterations converge to a given solution, we select that to be the final pair producing TS. This is visible in Figs. 3.4a–b, where, we have performed 10 iterations and during the last iterations the solutions have almost converged (only intermediate iterations are plotted). The final transonic solution (Fig. 3.4a) and composition of the flow (Fig. 3.4b), in the presence of pair production and annihilation, for the given set of flow parameters, is shown in solid, black line. In Fig. 3.4c, we plot the change in spectrum with iterations. Grey curves depict the emission due to annihilation, corresponding to each iteration, while the rest of the spectral emission comes from bremsstrahlung and its inverse-Comptonization. We see that, in iteration 1, there is no emission from annihilation, because of the absence of positrons. While, as we increase the number of iterations, the spectral shape changes depending on the pair processes and annihilation, ultimately converging to the spectrum shown in solid, black line.

3.4 RESULTS

We divide the result section into two parts, where the first part discusses with typical one-temperature accretion solutions without the presence of any pairs. Thereafter we include pairs and discuss global transonic accretion solutions in the presence of pair-production and annihilation. In all these cases we also analyse their corresponding spectrum assuming relativistic effects.

3.4.1 ONE-TEMPERATURE ACCRETION SOLUTIONS – I : WITHOUT PAIRS

In this section, we discuss and analyse global one-temperature, viscous, advective, transonic accretion solutions, without the presence of any pairs using the methodology discussed in Section 3.3.1. The solutions are parametrised by E , λ_{in} , β , β_{d} , α_{v} , \dot{M} , M_{BH} . We note that the accretion rates are quoted in terms of the Eddington rate (\dot{M}_{Edd}), therefore, the information on M_{BH} also enters the solution. We also discuss the spectral properties of the obtained solutions.

3.4.1.1 A TYPICAL ACCRETION SOLUTION

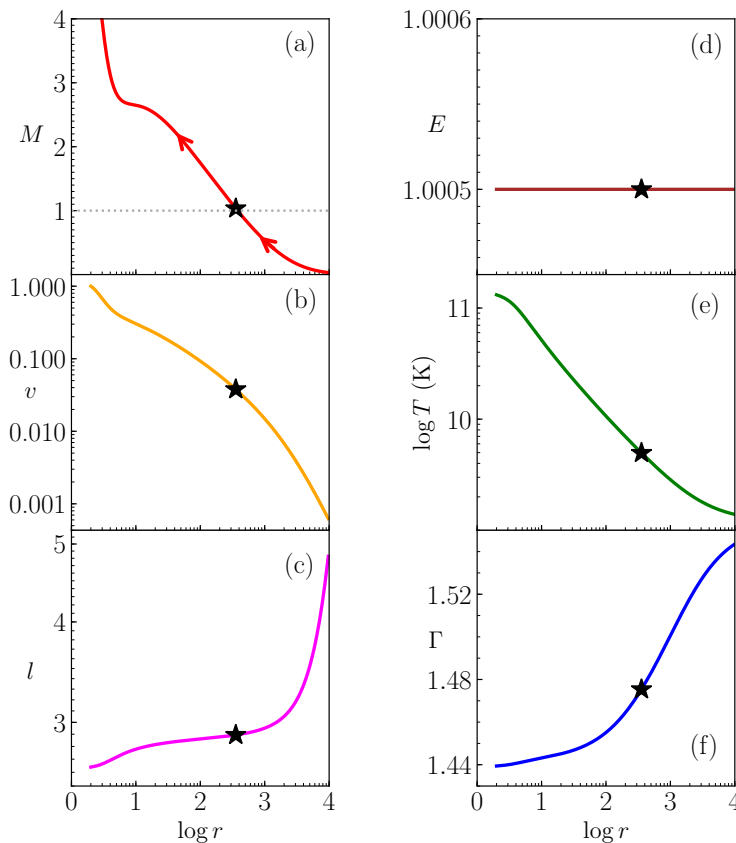


Figure 3.5: (a) Global accretion solution, M (solid, red) and other flow variables like (b) v (solid, orange), (c) l (solid, magenta), (d) E (solid, brown), (e) T (solid, green) and (f) Γ (solid, blue) are plotted against r . The sonic point is represented using black star. The flow parameters used are, $E = 1.0005$, $\lambda_{\text{in}} = 2.639$, $\beta = 0.1$, $\beta_{\text{d}} = 0.01$, $\alpha_{\text{v}} = 0.01$, $\dot{M} = 0.2\dot{M}_{\text{Edd}}$ and $M_{\text{BH}} = 10M_{\odot}$. The corresponding L_0 is 2.850.

In Figs. 3.5a-f, we present a global accretion solution along with its flow variables for parameters $E = 1.0005$, $\lambda_{\text{in}} = 2.639$, $\beta = 0.1$, $\beta_{\text{d}} = 0.01$, $\alpha_{\text{v}} = 0.01$, $\dot{M} = 0.2\dot{M}_{\text{Edd}}$ and

3. ONE-TEMPERATURE ACCRETION FLOWS AROUND BLACK HOLES

$M_{\text{BH}} = 10M_{\odot}$. The corresponding $L_0 = 2.850$. We represent the solution using $M = v/a_s$ vs r , and plot it in Fig. 3.5a using solid, red curve. The arrows represent the direction of flow. We see that this solution passes through a single outer sonic point, $r_{\text{co}} = 355.672$ (in terms of r_g) where $M = 1$, (dotted grey line) and is marked using a black star. Flows with $M > 1$ is said to be supersonic while for $M < 1$ it is called subsonic. In Fig. 3.5b, v is plotted using solid, orange line. It can be concluded that matter velocity is very low, when it is far away from the central object ($v \ll 0.001$, in terms of c). But as it gets accreted, the kinetic energy of the matter increases, which finally achieves the speed of light near the event horizon ($r \rightarrow 2r_g = 2GM_{\text{BH}}/c^2$), thus satisfying the BH boundary condition. In Fig. 3.5c we plot covariant azimuthal component of four-velocity $l(= L_b/h)$ or u_{ϕ} using solid magenta line. We see that it increases outward, which is mainly because of the viscous transport of angular momentum in the outward direction. Viscosity helps to reduce angular momentum, such that matter can get accreted inwards ultimately being captured by the BH. The generalised Bernoulli parameter E is a constant of motion, even in the presence of dissipative processes and can be seen in Fig. 3.5d (solid, brown curve). We plot the T (in units of K) in and Γ as a function radius in Figs. 3.5e and f using solid, green and solid, blue curves respectively. Use of CR EoS has helped to remove any constraint of using fixed adiabatic index and we can see that it varies with r (solid, blue curve).

DISSIPATIVE PROCESSES

Accretion flows are subjected to heating and cooling mechanisms. The processes which have been considered in this work has been discussed in Section 3.2.1. For the solution obtained above, we plot the corresponding number density n (in units of cm^{-3}) in Fig. 3.6a using solid, violet line. Since, the flow is converging n increases inwards. We plot the magnitude of cooling processes (Q^-) present in the system in Fig. 3.6b in dimensional units, which is $\text{ergs cm}^{-3} \text{ s}^{-1}$. We have considered here: bremsstrahlung (Br, dotted, red), Comptonized bremsstrahlung (CBr, dashed, orange), synchrotron (Syn, single dot-dashed, magenta) and Comptonized synchrotron (CSy, double dot-dashed, blue). The total of all these emission processes have been plotted using solid, black curve. We see that values of all the emission processes increase, as matter move inwards, which is mainly because of the increase in T and n . But, as the matter nears the BH event horizon the infall velocity of the matter sharply increases, such that the cooling timescales far exceed the infall timescales, leading to low emission in these regions. Or in other words, the matter does not get sufficient time to radiate and hence the radiation trying to escape,

get advected with the matter and finally gets captured by the BH. For the present set of flow parameters we see that bremsstrahlung is the most dominant emission mechanism throughout the flow. The total emission in dimensionless units are plotted using dashed, dark-green line in Fig. 3.6c. Also plotted in the same panel are dimensionless heating rates, one caused by viscous dissipation (dotted, blue) and another due to magnetic dissipation (solid, light-green). Most of the angular momentum near the horizon has been transported outwards and there is less removal of angular momentum due to viscous dissipation in these regions. Thus, low values of viscous heat dissipated are evident (dotted, blue). However, we see that the heating due to magnetic dissipation does not decrease near the horizon. This emission process is a function of B and v (see, Eq. 2.34) which are generously increased when matter approaches the BH, and thereby does not cause any decrease in the corresponding heating (solid, light-green).

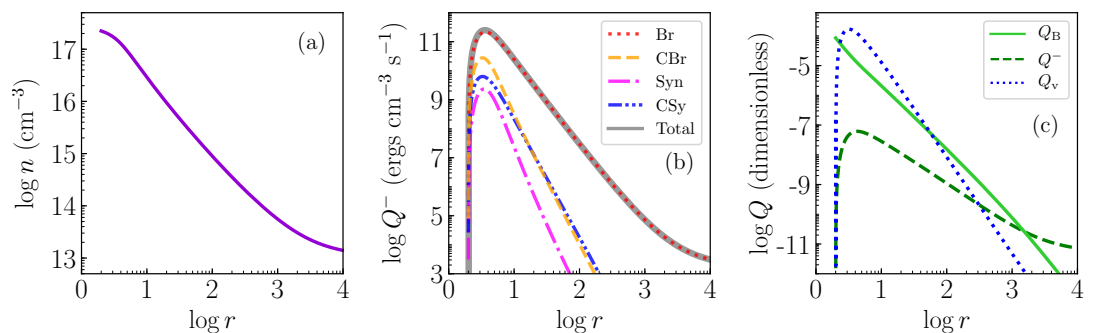


Figure 3.6: We plot against r in panel (a) n (solid, violet), (b) individual radiative mechanisms Q^- in units of $\text{ergs cm}^{-3} \text{s}^{-1}$ (see label given inset), and total of all these processes (solid, black curve) and (c) total cooling (Q^- , dashed, dark-green), heating due to magnetic dissipation (Q_B , solid, light-green) and heating due to viscous dissipation (Q_v , dotted, blue) all in dimensionless units. The flow parameters used are same as in Fig. 3.5.

SPECTRUM

In Fig. 3.7b, we plot the spectrum corresponding to the accretion solution given in Fig. 3.5. Since, electrons are the ones which radiate, a spectrum is predominantly formed because of the emission processes acting on electrons. Since, we are dealing in this work with one-temperature accretion flows, the information of T_e is lacking here. Thus, we adopt a methodology followed by Kumar & Chattopadhyay (2014); Singh & Chattopadhyay (2018a,b), where they obtained an approximate formula to compute T_e . The formula is

3. ONE-TEMPERATURE ACCRETION FLOWS AROUND BLACK HOLES

given as,

$$T_e = \left[-\frac{2}{3} + \frac{1}{3} \sqrt{4 - 2 \frac{(2N-3)}{(N-3)}} \right] \frac{m_e c^2}{k}. \quad (3.11)$$

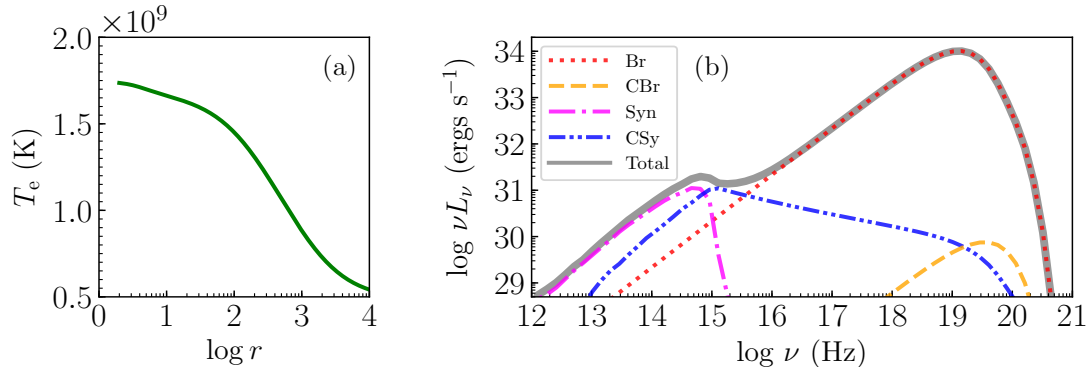


Figure 3.7: We plot in panel (a) T_e as a function of r . In panel (b) we plot the spectrum in solid, black line. Individual contributions are also plotted in this panel (see inset for label) The flow parameters used are same as in Fig. 3.5.

Using this T_e value, we compute the spectrum. Although approximate, this formula helps to qualitatively obtain and analyse the spectrum. This kind of factorisation has been extensively used in literature in multiple works to obtain the value of T_e . For the present case, the value of T_e is plotted in Fig. 3.7a using solid, green curve. The corresponding spectrum is plotted in Fig. 3.7b and represented by solid, black curve. In the same plot the individual contribution from different emission processes are also plotted: bremsstrahlung (Br, dotted, red), Comptonized bremsstrahlung (CBr, dashed, orange), synchrotron (Syn, single dot-dashed, magenta) and Comptonized synchrotron (CSy, double dot-dashed, blue). We have used the same colour and linestyle coding to represent the emission processes as we have used in Fig. 3.6b. We see that the higher frequencies are mainly dominated by the bremsstrahlung emission (dotted, red), while the low frequencies ($\nu < 10^{15}$ Hz) are dominated by synchrotron (single dot-dashed, magenta).

3.4.1.2 A TYPICAL SHOCKED SOLUTION

We discuss in this section a typical shocked solution and the corresponding variation in flow variables. For this purpose, we have used the following set of flow parameters, $E = 1.002$, $\lambda_{\text{in}} = 2.730$, $\beta = 0.4$, $\beta_d = 0.01$, $\alpha_v = 0.01$, $\dot{M} = 0.3\dot{M}_{\text{Edd}}$ and $M_{\text{BH}} = 10M_{\odot}$. The corresponding L_0 obtained is 3.03. In Fig. 3.8a, we plot M vs r in solid, red curve. The solution first passes through $r_{\text{co}} = 100.928$ (marked using black star) and then becomes supersonic ($M > 1$). Due to the combined effect of centrifugal and thermal gradient

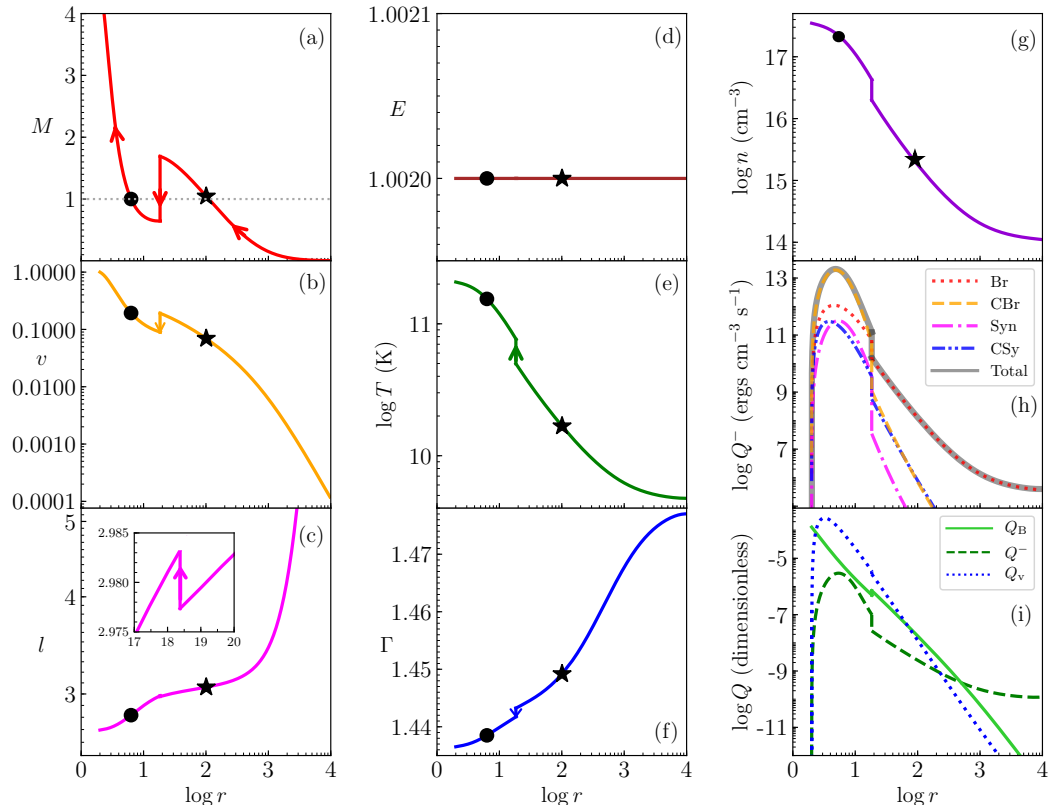


Figure 3.8: Plotted are (a) M , (b) v , (c) l , (d) E , (e) T , (f) Γ , (g) n , (h) total cooling, Q^- (solid, black) in units of $\text{ergs cm}^{-3} \text{s}^{-1}$ along with the contribution from individual components (see label inset), and (i) in dimensionless units, Q^- (dashed, dark-green), Q_B (solid, light-green) and Q_v (dotted, blue). There is a shock at $r_{\text{sh}} = 18.377$ (marked using arrows) and r_{co} and r_{ci} are represented using black star and solid black circle respectively. The flow parameters used are: $E = 1.002$, $\lambda_{\text{in}} = 2.730$, $\beta = 0.4$, $\beta_d = 0.01$, $\alpha_v = 0.01$, $\dot{M} = 0.3\dot{M}_{\text{Edd}}$ and $M_{\text{BH}} = 10M_{\odot}$.

forces acting against gravity, this solution encounters a shock at $r_{\text{sh}} = 18.377$ and becomes subsonic ($M < 1$). The shock transition is marked using red arrow. As the matter is accreted inwards, the flow again gains velocity and becomes supersonic after passing through $r_{\text{ci}} = 6.304$ (marked using solid black circle) and finally enters the horizon supersonically. It is to be remembered that shocks are formed for certain combination of flow parameters in the multiple critical point regime. Corresponding v (solid, orange), l (solid, magenta), E (solid, brown), T (solid, green), Γ (solid, blue) and n (solid, violet) are plotted in Figs. 3.8b, c, d, e, f and g respectively. We see that the velocity decreases at the shock front while l , T and n increases. A lower value of Γ is an indication of increased T or more relativistic, relative to a higher value of Γ . Thus a decrease

3. ONE-TEMPERATURE ACCRETION FLOWS AROUND BLACK HOLES

at shock front is observed in Γ (Fig. 3.8f), because of the corresponding increase in T (Fig. 3.8e). The generalised Bernoulli constant E , is a constant of motion throughout the flow (Fig. 3.8d). The total cooling, Q^- (solid, black) due to different radiative processes and their individual contributions have been plotted in Fig. 3.8h: bremsstrahlung (Br, dotted, red), Comptonized bremsstrahlung (CBr, dashed, orange), synchrotron (Syn, single dot-dashed, magenta) and Comptonized synchrotron (CSy, double dot-dashed, blue). All are in units of $\text{ergs cm}^{-3} \text{ s}^{-1}$. Similarly, we plot in dimensionless units Q^- (dashed, dark-green), Q_B (solid, light-green) and Q_v (dotted, blue) in Fig. 3.8i. We see that at the shock front, the radiative losses increase sharply. In the pre-shock region, emission is mainly dominated by bremsstrahlung, (dotted, red) but in the post-shock region the Comptonized bremsstrahlung component (dashed, orange) dominates. Q_B is found to decrease, which is mainly because of the decrease in v .

We plot the corresponding T_e (solid, green) and spectrum (solid, black) of the above solution in Figs. 3.9a–b respectively. We see an increase in T_e at the shock front. The obtained spectrum plotted in Fig. 3.9b is majorly dominated by bremsstrahlung in the higher frequency range and by synchrotron and its inverse-Comptonization in the lower frequency range.

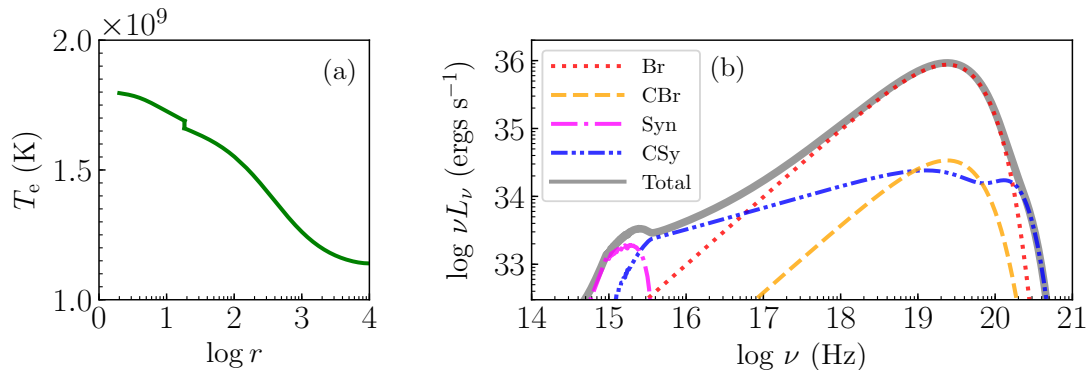


Figure 3.9: We plot in panel (a) T_e as a function of r . In panel (b) we plot the spectrum in solid, black line along with the individual contributions. The flow parameters used are same as in Fig. 3.8.

3.4.1.3 SOLUTIONS IN $E - L_0$ PARAMETER SPACE

In this section, we study the variation of solutions in Fig. 3.10 and their corresponding spectrums in Fig. 3.11, with change in E and L_0 of the flow. For this purpose we have kept fixed, rest of the parameters of the flow, whose values are $\beta = 0.1$, $\beta_d = 0.01$, $\alpha_v = 0.01$, $\dot{M} = 0.1\dot{M}_{\text{Edd}}$ and $M_{\text{BH}} = 10M_{\odot}$. We have increased L_0 from left to right, where

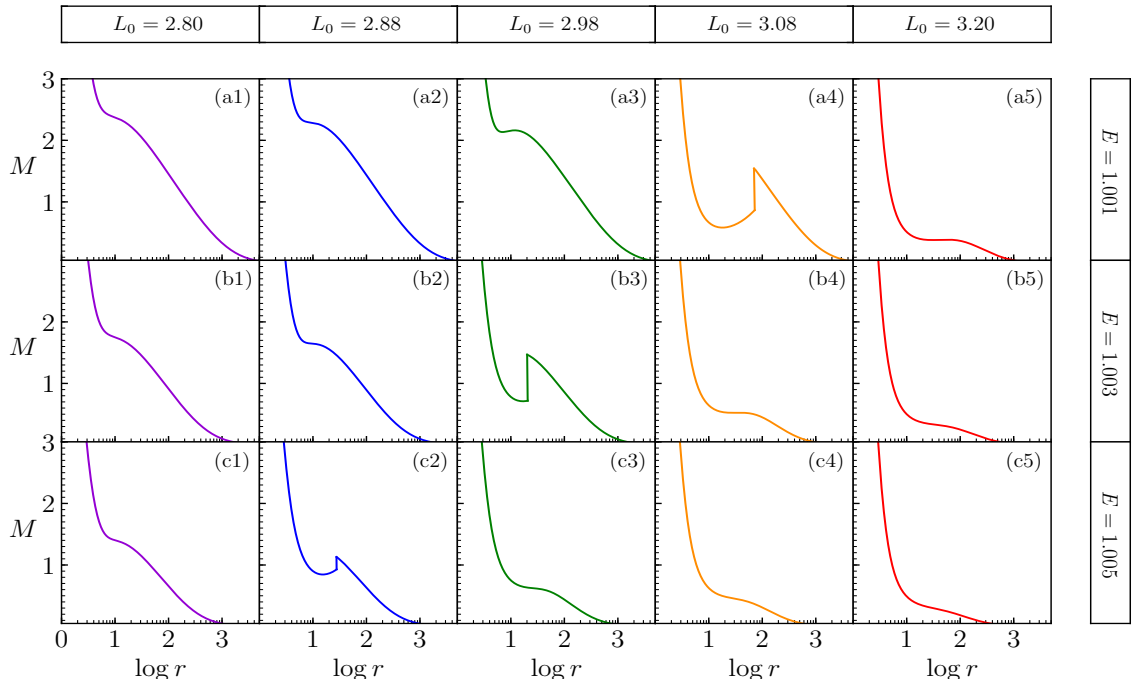


Figure 3.10: Variation of solutions with change in E and L_0 of the flow. Rest of the flow parameters are, $\beta = 0.1$, $\beta_d = 0.01$, $\alpha_v = 0.01$, $\dot{M} = 0.1\dot{M}_{\text{Edd}}$ and $M_{\text{BH}} = 10M_{\odot}$.

$L_0 = 2.80 \Rightarrow$ Figs. 3.10a1–c1 (solid, violet), $L_0 = 2.88 \Rightarrow$ Figs. 3.10a2–c2 (solid, blue), $L_0 = 2.98 \Rightarrow$ Figs. 3.10a3–c3 (solid, green), $L_0 = 3.08 \Rightarrow$ Figs. 3.10a4–c4 (solid, orange), $L_0 = 3.20 \Rightarrow$ Figs. 3.10a5–c5 (solid, red). From top to bottom, we increased E , where $E = 1.001 \Rightarrow$ Figs. 3.10a1–a5, $E = 1.003 \Rightarrow$ Figs. 3.10b1–b5 and $E = 1.005 \Rightarrow$ Figs. 3.10c1–c5. For low bulk angular momentum values (L_0), the solution passes through a single r_{ci} , similar to a spherical Bondi flow, irrespective of the value of E (see, Figs. 3.10a1–c1). But as L_0 is increased, the centrifugal force starts to dominate and a centrifugal force mediated shock transition occurs. This shock is formed even for lower values of L_0 when E value is large, because of the domination of a thermal pressure resisting the matter in addition to centrifugal force. Thus, at $E = 1.001$, a shock is formed for $L_0 = 3.08$ (Fig. 3.10a4) but when $E = 1.003$, a shock is formed for a low $L_0 = 2.98$ value (Fig. 3.10b3). For even higher energy $E = 1.005$, the formation of shock happens at $L_0 = 2.88$ (Fig. 3.10c2). When angular momentum of the flow is very high, azimuthal component of velocity v_{ϕ} is large and the radial component (which is v) is low. So, for flows to become supersonic, $v > a_s$, this condition will be satisfied only near the BH, where v will be larger. Thus, the sonic points shift towards the BH.

When E is higher, the solution is already sampling a higher temperature at infinity or

3. ONE-TEMPERATURE ACCRETION FLOWS AROUND BLACK HOLES

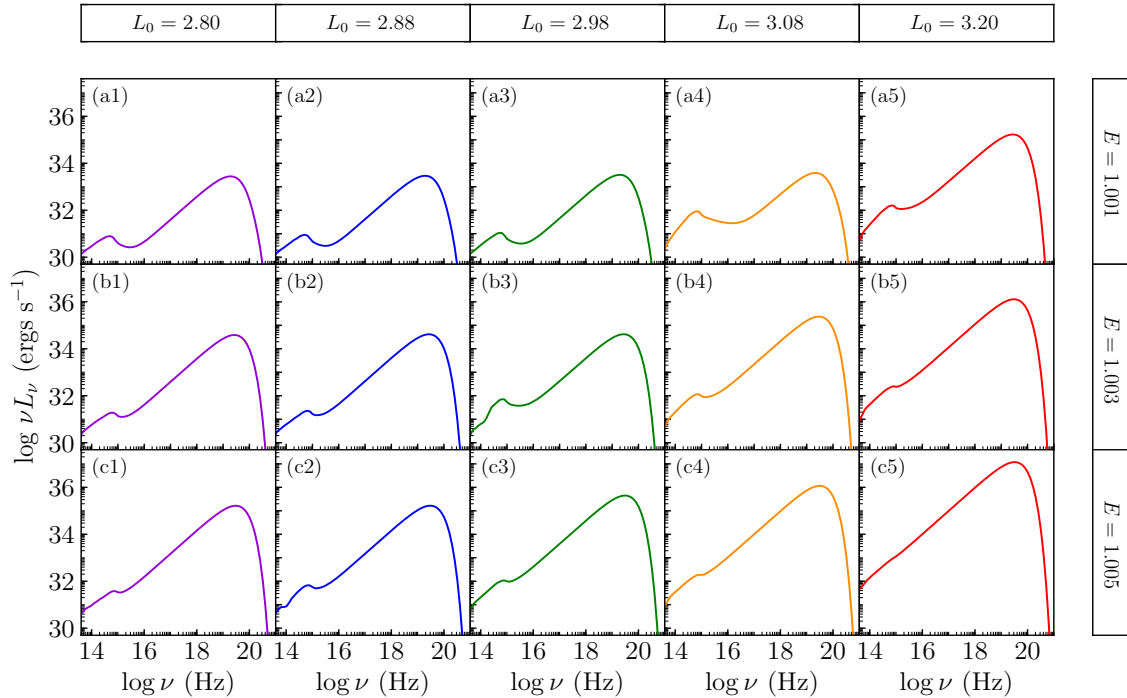


Figure 3.11: Variation of spectrum with change in E and L_0 of the flow. Rest of the flow parameters are same as in Fig. 3.10.

the a_s distribution of the flow is higher. This makes the sonic point to move further close to the horizon. Thus, inner sonic points are obtained even at low L_0 when E is higher (Figs. 3.10c3–c5). The corresponding spectrums are plotted in Fig. 3.11. We see that as L_0 is increased the luminosity increases gradually and is two orders of magnitude higher at $L_0 = 3.20$ from the luminosity at $L_0 = 2.80$, irrespective of the value of E . Increasing E , keeping L_0 constant, makes the system more luminous, which, as has been argued before is because the solution is hotter for higher E .

3.4.1.4 VARIATION OF SOLUTIONS WITH CHANGE IN α_v

In this section, we analyse the effect of α_v (usual Shakura & Sunyaev viscosity parameter), which controls viscosity inside accretion flows. In Fig. 3.12a, solutions are plotted, where each curve represent different values of α_v : 0.005 (solid, orange), 0.01 (dotted red), 0.015 (dashed, green), 0.02 (single dot-short dashed, blue), 0.03 (single dot-long dashed, violet), 0.04 (double dot-short dashed, magenta) and 0.05 (double dot-long dashed, black). The other flow parameters are, $E = 1.0005$, $L_0 = 3.023$, $\beta = 0.5$, $\beta_d = 0.01$, $\dot{M} = 0.1\dot{M}_{\text{Edd}}$ and $M_{\text{BH}} = 10M_\odot$. We see that, as α_v increases, l increases (see, Fig. 3.12b). This is because, a higher value of α_v will remove more angular momentum. Thus, at any given r ,

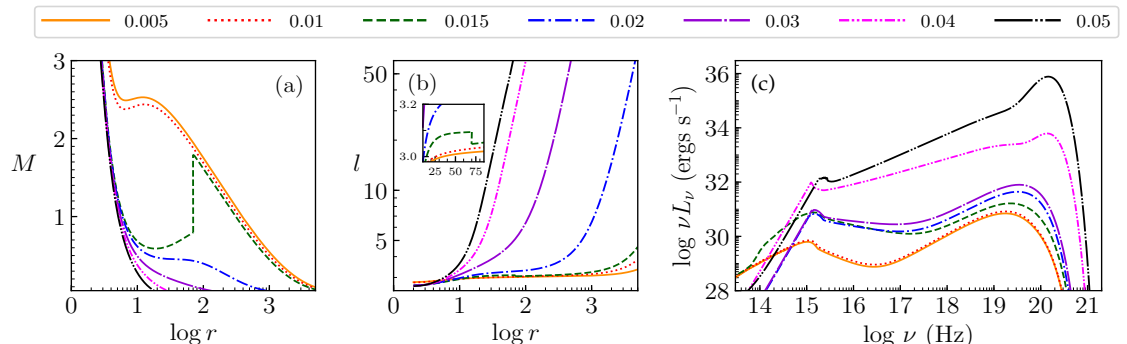


Figure 3.12: Effect of α_v on (a) M , (b) l and (c) spectrum. The different curves represent solutions with different values of α_v (see top label). The other flow parameters used are, $E = 1.0005$, $L_0 = 3.023$, $\beta = 0.5$, $\beta_d = 0.01$, $\dot{M} = 0.1\dot{M}_{\text{Edd}}$ and $M_{\text{BH}} = 10M_{\odot}$.

a higher value of α_v has a larger value of l . This increase in angular momentum would be accompanied by an increase in cooling processes and hence an increase in luminosity of the system is conjectured. This is clearly proved from Fig. 3.12c, where the corresponding spectrums are plotted. Although, viscous dissipation has a heating effect, the cooling due to large values of angular momentum surpass any kind of heating. The luminosity for $\alpha_v = 0.005$ is 2.281×10^{31} ergs s^{-1} , while for $\alpha_v = 0.05$ its value is 1.106×10^{36} ergs s^{-1} , which is five orders of magnitude higher. Thus, we can conclude that a system with higher viscosity would be more luminous and hence more efficient.

3.4.1.5 VARIATION OF SOLUTIONS WITH CHANGE IN \dot{M}

We study here, the effect of variation of accretion rate of the system on the global accretion solution. In Fig. 3.13a, solutions are plotted, which is represented using M vs r plot. Correspondingly we plot in panels (b) l , (c) T , (d), n , (e) Q_v in dimensionless units and (f) total cooling, Q^- also in dimensionless units. Each curve inside these panels represent different accretion rate values: $0.001\dot{M}_{\text{Edd}}$ (solid, yellow), $0.1\dot{M}_{\text{Edd}}$ (dashed, orange), $0.5\dot{M}_{\text{Edd}}$ (dotted, red), $0.6\dot{M}_{\text{Edd}}$ (single dot-short dashed, brown), $0.7\dot{M}_{\text{Edd}}$ (single dot-long dashed, magenta), $0.8\dot{M}_{\text{Edd}}$ (double dot-short dashed, violet), $0.9\dot{M}_{\text{Edd}}$ (double dot-long dashed, blue) and $1.0\dot{M}_{\text{Edd}}$ (triple dot-short dashed, black). The rest of the flow parameters used are: $E = 1.001$, $L_0 = 3.185$, $\beta = 0.8$, $\beta_d = 0.01$, $\alpha_v = 0.01$ and $M_{\text{BH}} = 10M_{\odot}$. An increase in accretion rate increases the amount of matter supplied to the system and n increases, which is clear from Fig. 3.13d. This increase in n increases the cooling processes, thereby allowing the system to accrete more hotter flows, see T plot

3. ONE-TEMPERATURE ACCRETION FLOWS AROUND BLACK HOLES

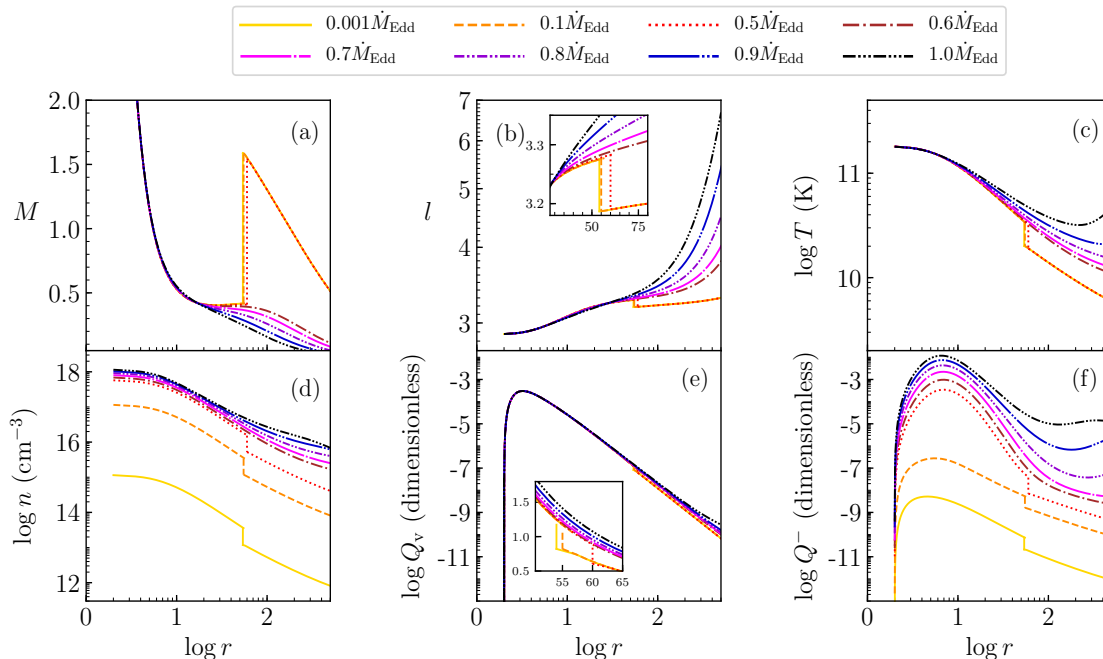


Figure 3.13: Plotted are (a) M , (b) l , (c) T , (d) n , (e) Q_v in dimensionless units and (f) total cooling, Q^- also in dimensionless units. Each curve represent solutions with different \dot{M} values labelled in the plot. Other flow parameters are: $E = 1.001$, $L_0 = 3.185$, $\beta = 0.8$, $\beta_d = 0.01$, $\alpha_v = 0.01$ and $M_{\text{BH}} = 10M_{\odot}$.

in Fig. 3.13c. This makes the system more luminous, Fig. 3.13f. However, since α_v is constant for all these solutions, l and Q_v does not vary much and is clear from Figs. 3.13b and e respectively. For solutions harbouring shocks, $\dot{M} = 0.001\dot{M}_{\text{Edd}}$, $0.1\dot{M}_{\text{Edd}}$ and $0.5\dot{M}_{\text{Edd}}$, the corresponding shock signatures are visible in all the flow variables. We plot in Fig. 3.14a, T_e and Fig. 3.14b the corresponding spectrum. We see that the increase in luminosity is significant with the increase in \dot{M} .

3.4.2 ONE-TEMPERATURE ACCRETION SOLUTIONS – II : INCLUSION OF PAIRS

In this section, we investigate pair-production and annihilation in viscous advective accretion discs, assuming radiation fields discussed in Section 3.2.1. We proceed step by step, and at first include bremsstrahlung and its inverse-Comptonization as the sole radiative process present in the system. Then we proceed to include all the radiative processes, that could be present inside an accretion flow around BH. We utilise the methodology discussed in Section 3.3.2 to obtain global accretion solutions. We also analyse the corresponding spectrum. The difference between the solutions presented in this section and the solutions presented in Section 3.4.1, is in the presence of e^+ . Here, pair equilibrium

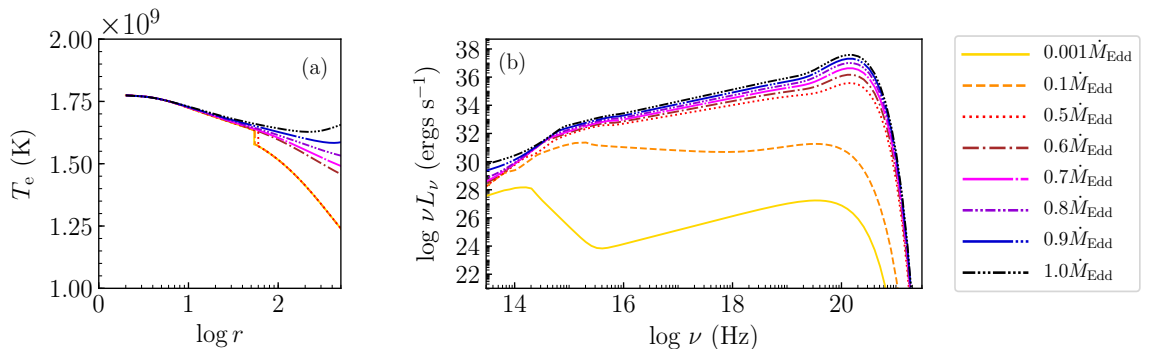


Figure 3.14: We plot (a) T_e and (b) corresponding spectrum for different \dot{M} values. Other flow parameters used are same as in Fig. 3.13.

demands Eq. 2.7 to be satisfied. The accretion rates quoted throughout this section is \dot{M}_p or the proton accretion rate (see, Eq. 3.2), which is a constant of motion in the presence of pair production. For the sake of simplicity we have represented them as \dot{M} .

3.4.2.1 BREMSSTRAHLUNG DOMINATED SOLUTIONS

In this part, we assume that there are no stochastic magnetic fields present inside the flow. Hence, synchrotron, its inverse-Comptonization and heating due to magnetic dissipation are absent. Only bremsstrahlung and Comptonized bremsstrahlung are the most dominant emission mechanisms. The pair creation rate (Eq. 3.9) now have six terms, the power-law photon field originating from inverse-Comptonization of synchrotron soft photons is absent. The results of this section have reported in Sarkar & Chattopadhyay (2020).

3.4.2.1.1 A TYPICAL ACCRETION SOLUTION AND SPECTRUM

In Fig. 3.15, we present a general transonic one-temperature solution, including pair processes. Fig. 3.15a plots a typical accretion solution M vs $\log r$ (left Y-axis) and l (right Y-axis), while the composition of the flow, $\xi = n_p/n_{e^-} = n_p/(n_p + n_{e^+})$ is plotted in Fig. 3.15b. The different curves in each panel, represent different accretion rates of the system: $\dot{M} = 0.1\dot{M}_{\text{Edd}}$ (dotted, red), $\dot{M} = 0.4\dot{M}_{\text{Edd}}$ (dashed, green) and $\dot{M} = 0.8\dot{M}_{\text{Edd}}$ (solid, blue). Other flow parameters are, $E = 1.001$, $\lambda_{\text{in}} = 2.60$, $\alpha_v = 0.01$ and $M_{\text{BH}} = 10M_\odot$. From the plot it is apparent that for these set of flow parameters only r_{co} exists. As we increase the \dot{M} of the system r_c shifts inwards, towards the BH (clearly visible for $\dot{M} = 0.8\dot{M}_{\text{Edd}}$ solution). This is mainly because of the increase in cooling of the system, with the increase in \dot{M} . We note that there is a minor decrease in the location of r_c for the solution with accretion rate $0.4\dot{M}_{\text{Edd}}$ as compared to $0.1\dot{M}_{\text{Edd}}$. The solutions, are hence,

3. ONE-TEMPERATURE ACCRETION FLOWS AROUND BLACK HOLES

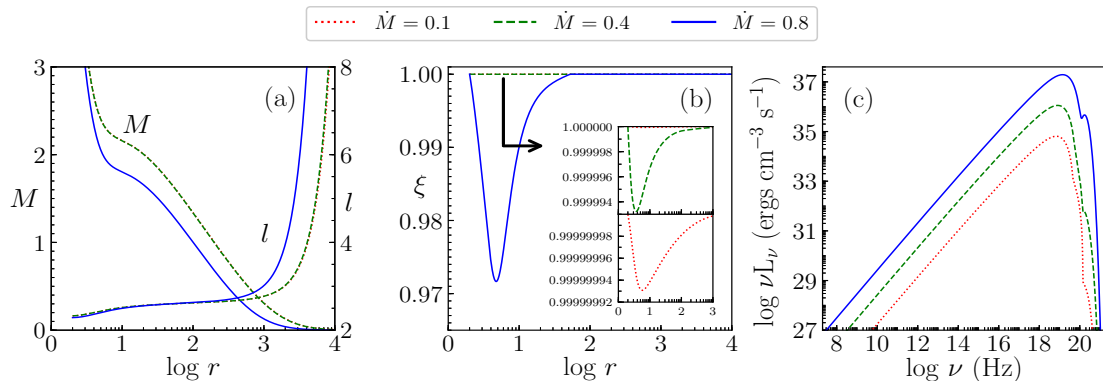


Figure 3.15: (a) M , l and (b) ξ vs $\log r$ plotted for different accretion rates of the system. Their corresponding spectrum is plotted in panel (c). The accretion rates used are: $\dot{M} = 0.1\dot{M}_{\text{Edd}}$ (dotted, red), $\dot{M} = 0.4\dot{M}_{\text{Edd}}$ (dashed, green) and $\dot{M} = 0.8\dot{M}_{\text{Edd}}$ (solid, blue). Rest of the flow parameters are $E = 1.001$, $\lambda_{\text{in}} = 2.60$, $\alpha_v = 0.01$ and $M_{\text{BH}} = 10M_\odot$.

seemed to be overlapped in Fig. 3.15a. Fig. 3.15b suggests the presence of e^+ in the flow. A decrease in ξ , means an increase in the number of e^+ . Very far away from the central object (or at infinity) and just near the horizon, $\xi \approx 1$, suggesting that n_{e^+} is negligible in these regions. At infinity, radiative mechanisms are less effective due to low temperatures and low number densities. Thus, the radiation field giving rise to pair production is weak, leading to negligible production of e^+ . While, near the horizon photon trapping effects of the BH dominate, thereby reducing the number density of photons and hence lowering of pair production rates occur (also, see Fig. 3.6b). However, there could be ample amount of advected e^+ and e^- in these regions, which can be responsible for higher number of pairs in these regions. But we find that the high annihilation rate in these regions are responsible for reducing n_{e^+} to ~ 0 or $\xi \approx 1$. Now, as we increase \dot{M} , matter supply becomes more, hence, there is more cooling in the system. This will, in turn, increase the amount of radiation field present in the system, thereby a higher pair production rate is achieved. This leads to the rise in n_{e^+} in the flow and a corresponding decrease in ξ , see Fig. 3.15b. In Fig. 3.15c, spectrums are plotted, where, with the increase in \dot{M} , the system becomes more luminous. There is a feature in all the spectrums near $\sim m_{e^-}c^2$, whose magnitude increases with the increase in \dot{M} of the system and is distinctly visible for $\dot{M} = 0.8\dot{M}_{\text{Edd}}$. This bump is a signature of annihilation photons. More the \dot{M} more would be the pairs produced and hence more will be the photons generated through pair annihilation.

3.4.2.2 BREMSSTRAHLUNG AND SYNCHROTRON DOMINATED SOLUTIONS

Magnetic fields are ubiquitous and present everywhere in the Universe, hence, they play an important role in accretion flows. Thus, inclusion of radiative processes like synchrotron and inverse-Comptonization is necessary to get a correct picture and to know the importance of pairs in accretion flows around BHs. Therefore, we investigate in this section, pair-production and annihilation, in the presence of all photon fields. The pair creation rate used is that given in Eq. 3.9.

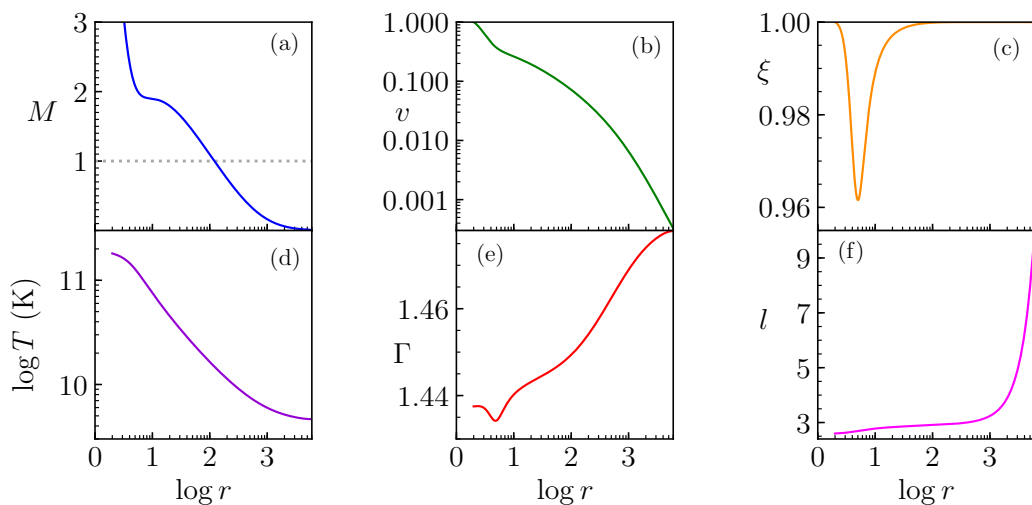


Figure 3.16: General one-temperature accretion solution in the presence of pair production and annihilation process. We plot against r the solution and the corresponding flow variables: (a) M , (b) v , (c) ξ , (d) T , (e) Γ and (f) l . The flow parameters used are, $E = 1.002$, $L_0 = 2.880$, $\beta = 0.1$, $\beta_d = 0.01$, $\alpha_v = 0.01$, $\dot{M} = 0.98\dot{M}_{\text{Edd}}$ and $M_{\text{BH}} = 10M_{\odot}$.

3.4.2.2.1 A TYPICAL ACCRETION SOLUTION

We present and discuss here a typical one-temperature accretion solution, in the presence of pair creation and annihilation process as well as other heating and cooling mechanisms. Bremsstrahlung, synchrotron and their respective inverse-Comptonizations have been taken into account for obtaining the solution. The flow parameters used for this purpose are, $E = 1.002$, $L_0 = 2.880$, $\beta = 0.1$, $\beta_d = 0.01$, $\alpha_v = 0.01$, $\dot{M} = 0.98\dot{M}_{\text{Edd}}$ and $M_{\text{BH}} = 10M_{\odot}$. In Fig. 3.16a, M vs r is plotted using solid, blue line. We see that the global accretion solution passes through $r_{\text{co}} = 119.937$. Flow variables (b) v (solid, green), (c) ξ (solid, orange), (d) T (solid, violet), (e) Γ (solid, red) and (f) l (solid, magenta) are also plotted against r . In Fig. 3.16c, the value of ξ decreases to a minimum of around 0.96 at $r \sim 5$, indicating that a large amount of positrons are formed near these regions.

3. ONE-TEMPERATURE ACCRETION FLOWS AROUND BLACK HOLES

There is a corresponding dip in Γ (see, Fig. 3.16e) in the same region. The relativistic nature of matter not only depends on the T but also on the mass of the species (see, Fig. C1 of Vyas et al., 2015). A change in the composition of the flow, should, in general, be reflected in the Γ index and CR EoS helps to smoothly adjust the Γ values inside the flow accordingly. For a given T if the mass of the species is less, matter is more relativistic ($kT/mc^2 > 1$) and Γ value is low. Since, there is ample amount of pair production in the region near the BH, masses of pairs being $m_{e^-} \ll m_p$, the Γ values decrease.

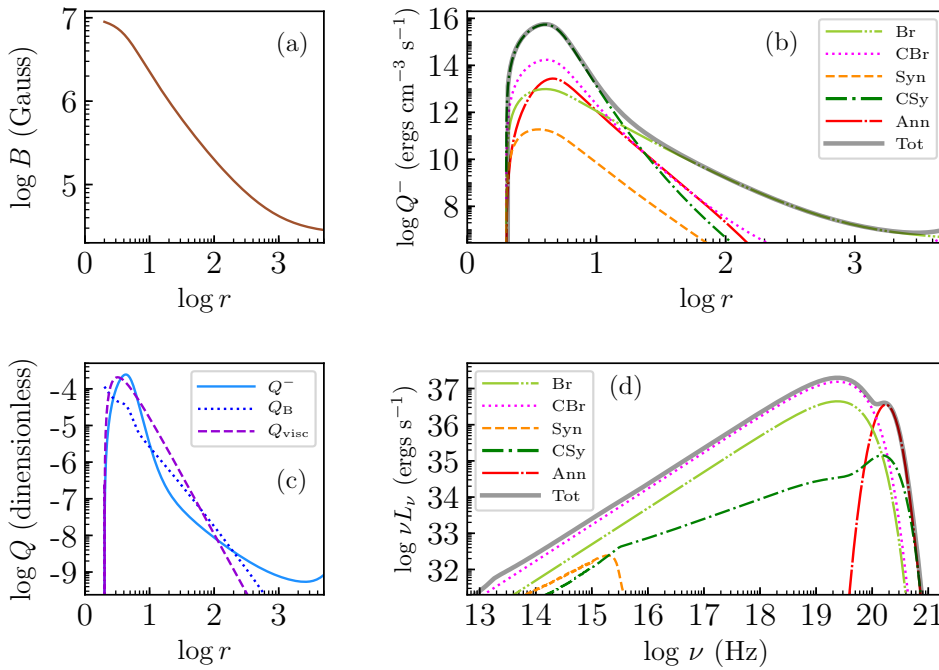


Figure 3.17: We plot against r in panel (a) B (solid, brown), (b) radiative mechanisms Q^- in units of $\text{ergs cm}^{-3} \text{s}^{-1}$ (solid, black), (c) Q^- (solid, light-blue), Q_B (dotted, dark-blue) and Q_v (dashed, violet) all in dimensionless units, and (d) spectrum (solid, black). In panels (b) and (d), the individual components have also been plotted (see label inset). We see a distinct annihilation line (single-dot long-dashed, red) present in the spectrum (panel d). The flow parameters used are same as in Fig. 3.16.

3.4.2.2.2 EMISSIVITIES AND SPECTRUM

To investigate further the reason for pair production, we plot in Fig. 3.17, (a) B (solid, brown), (b) Q^- (solid, black) along with the individual contributions from different radiative processes, all in dimensional units, $\text{ergs cm}^{-3} \text{s}^{-1}$, (c) Q^- (solid, light-blue), Q_B (dotted, dark-blue) and Q_v (dashed, violet) all in dimensionless units, and (d) spectrum (solid, black) with the contribution from each emission mechanism. The flow parameters

are same as in Fig. 3.16. In Figs. 3.17b–d both, the contributions from each radiative process are plotted using the same colour coding: bremsstrahlung (Br, double-dot long-dashed, light-green), Comptonized bremsstrahlung (CBr, dotted, magenta), synchrotron (Syn, dashed, orange), Comptonized synchrotron (CSy, single-dot short-dashed, dark-green) and annihilation (single-dot long-dashed, red). We see that the emission (see, Fig. 3.17b) maximises in regions very near the BH, $r < 20$, where it is mostly contributed from Comptonized synchrotron. Comptonized photons are majorly composed of higher frequency photons which are hard enough to meet the threshold criteria for pair production. Thus, we can see a corresponding increase in n_{e+} or a dip in the value of ξ (see, Fig. 3.16c) especially near these regions. At regions, $r \rightarrow 2r_g$, where the extreme gravity of BH traps all the photons, the emission decreases followed by a corresponding decrease in n_{e+} . A discussion on the same line has been already made in Section 3.4.2.1.1. In Fig. 3.17d, the observable spectrum is plotted (solid, black), where we can see that there is a bump at $\nu \approx 2 \times 10^{20}$ Hz, which is a signature of annihilation present in the system. This feature is similar to what was observed in Section 3.4.2.1, where we took only bremsstrahlung and its inverse-Comptonization to be the radiation field producing pairs (see, Fig. 3.15c).

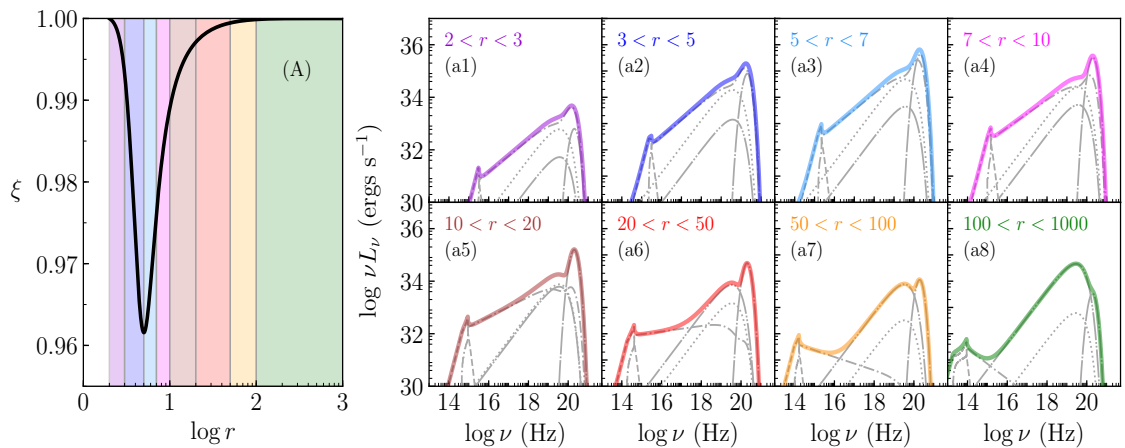


Figure 3.18: We plot in panel (A) variation of ξ against r . We have shaded different regions using different colours. The spectrum corresponding to the shaded region is plotted in panels (a1)–(a5) using the same colour coding in solid curves. Individual emission processes have also been plotted inset using different linestyles. The flow parameters used are same as in Fig. 3.16. We see the signature of distinct annihilation line (single-dot long-dashed line).

3. ONE-TEMPERATURE ACCRETION FLOWS AROUND BLACK HOLES

3.4.2.2.3 CONTRIBUTION OF DIFFERENT REGIONS OF A PAIR-PRODUCING ACCRETION DISC TO THE TOTAL SPECTRUM

In this section, we investigate the dominance of different emission processes in different regions of the accretion disc and their individual contribution to the total observable spectrum. For this purpose, we divide the accretion flow into small regions. In Fig. 3.18A we have plotted the variation in ξ with r and shaded inside this panel are different regions using different colours. The regions are: (1) $2 < r < 3$ (violet), (2) $3 < r < 5$ (dark-blue), (3) $5 < r < 7$ (light-blue), (4) $7 < r < 10$ (magenta), (5) $10 < r < 20$ (brown), (6) $20 < r < 50$ (red), (7) $50 < r < 100$ (orange) and (8) $100 < r < 1000$ (green). The spectrums corresponding to these regions have been plotted from Figs. 3.18a1–a5 respectively in solid curves. The different emission processes have been plotted in grey using different linestyles: bremsstrahlung using double-dot long-dashed linestyle, Comptonized bremsstrahlung using dotted line, synchrotron using dashed line, Comptonized synchrotron using single-dot short-dashed line and annihilation is represented using single-dot long-dashed line. As we move far away from the BH (regions $r > 7$), the luminosity decreases, because of the decrease in T and n accompanied by a decrease in the emission processes. However, very near the horizon, because of BH photon trapping effects the luminosity is also found to decrease. We see that different emission processes dominate in different regions of the accretion disc and contribute to the emission spectrum. In regions $r > 20$ (see, Figs. 3.18a5–a8), bremsstrahlung dominates and mostly contributes to the spectral shape, while below this (see, Figs. 3.18a1–a4), Comptonized synchrotron shapes the observable spectra. This is equivalent to the interpretation done for Fig. 3.17b, which discusses the magnitude of each emission process at every r . In Figs. 3.18a1–a5, we see that annihilation line is distinctly visible in all cases, but mostly its contribution comes from a region below < 50 and maximises in the range $5 < r < 7$ (Fig. 3.18a3, solid, light-blue). This is the region, where ξ is found to be minimum (see, Fig. 3.18A). The total bolometric luminosity of this system is $L = 6.696 \times 10^{37}$ ergs s^{-1} with an efficiency of $\eta_r = 4.704\%$, and the the annihilation luminosity is $L_{\text{ann}} = 1.344 \times 10^{37}$ ergs s^{-1} , which is $\sim 1/5^{\text{th}}$ of L .

3.4.2.2.4 VARIATION OF SOLUTIONS WITH CHANGE IN E

In this section, we analyse the variation of solutions with change in E . The flow parameters used are, $L_0 = 3.081$, $\beta = 0.1$, $\beta_d = 0.01$, $\alpha_v = 0.01$, $\dot{M} = 0.7\dot{M}_{\text{Edd}}$ and $M_{\text{BH}} = 10M_{\odot}$. In Fig. 3.19, we plot M vs r for different values of E : (a1) $E = 1.0001$, (a2) $E = 1.0005$, (a3) $E = 1.001$, (a4) $E = 1.002$, (a5) $E = 1.003$, (a6) $E = 1.004$, (a7) $E = 1.005$ and (a8) $E = 1.006$. The solutions are colour coded where the colour bar represent the values of

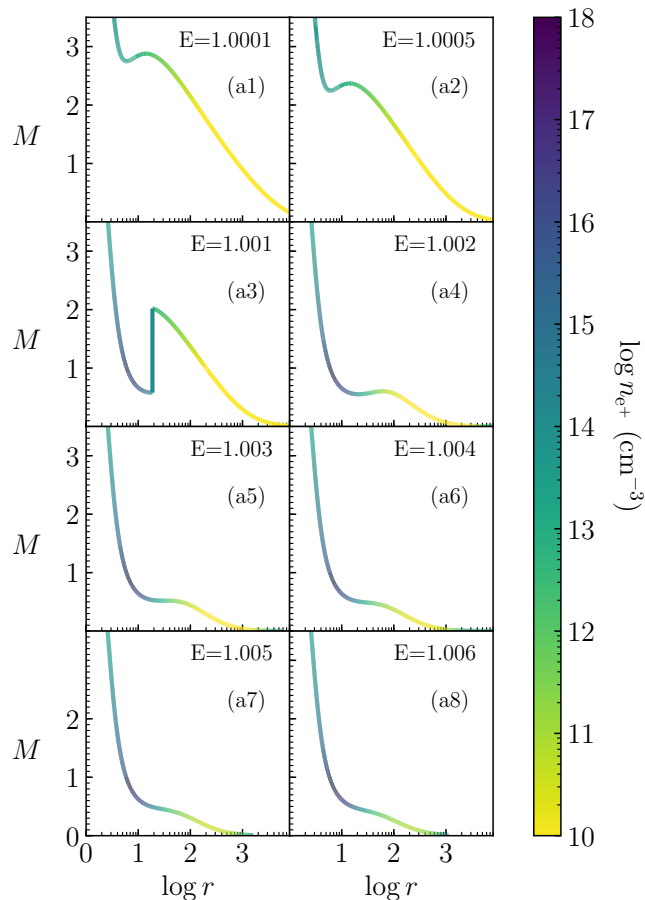


Figure 3.19: Variation in topology of the solution with change in E , values of which are written inset. Each solution is colour coded with a colour bar representing n_{e^+} . The flow parameters for these solutions are, $L_0 = 3.081$, $\beta = 0.1$, $\beta_d = 0.01$, $\alpha_v = 0.01$, $\dot{M} = 0.7\dot{M}_{\text{Edd}}$ and $M_{\text{BH}} = 10M_{\odot}$.

n_{e^+} . Darker the colour more is the number of e^+ . The change in topology of solutions with increase in E is similar to Fig. 3.10, which was for a pair-free model. As the thermal energy increase with the increase in E , the inflowing matter is restricted giving rise to shock transitions as can be seen for $E = 1.001$, Fig. 3.19a3. For further increase in E , the speed of sound increases because the flow will sample higher temperature at infinity. This will make the sonic point to move gradually inwards towards the central object. Hence, for $E \geq 1.002$ (see, Figs. 3.19a4–a8) we find solutions passing through only a single r_{ci} .

Given a value of E , from the colour bar plot it can be inferred that, e^+ s are formed in regions very close to the BH horizon (darker shades seen). As E is increased, keeping the value of r same, the n_{e^+} value increases and becomes highest for the highest E . This can also be concluded from Fig. 3.20b1–b8, where, the variation of ξ is presented. As, E is

3. ONE-TEMPERATURE ACCRETION FLOWS AROUND BLACK HOLES

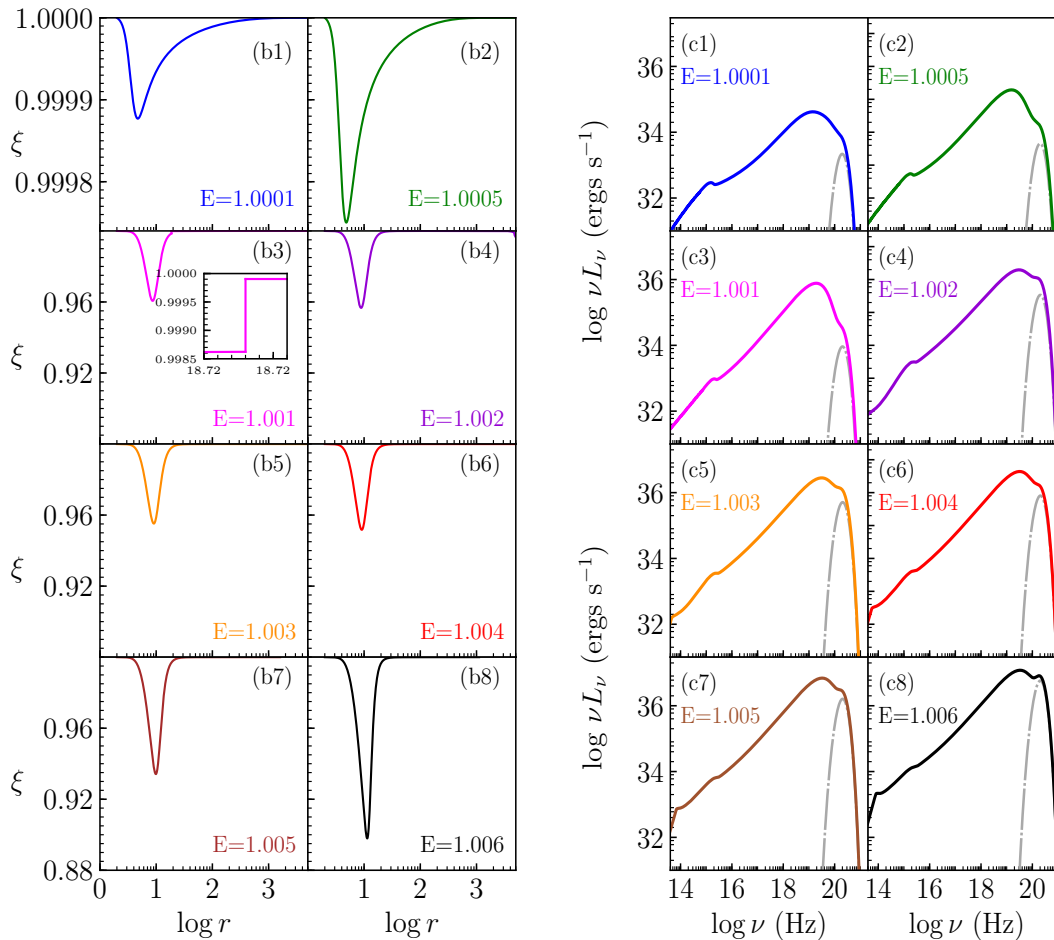


Figure 3.20: Panels (b1)–(b8) plots the variation in ξ with r and panels (c1)–(c8) plots the corresponding observable spectrum (solid curve), where the annihilation spectrum is represented using single-dot long-dashed grey line. Higher the value of E more will be the production of pairs and a clear signature of annihilation is present in the spectrum. The flow parameters used are same as in Fig. 3.19.

increased, ξ increases and reaches a minimum of ~ 0.89 for $E = 1.006$ (see, Fig. 3.20b8). In case the solution harbours a shock, an interesting feature of shock jump is also reflected in ξ . This is seen for $E = 1.001$ and Fig. 3.20b3. The sudden decrease in the value of ξ suggests that there is a corresponding increase in n_{e^+} at the shock front. We plot the respective spectra in Figs. 3.20c1–c8. The solid curves represent the total observable spectrum and the single-dot long-dashed grey line represents the annihilation spectrum. For lower values of E , although a bump is visible, but majority of the emission from the solution masks this feature. However, annihilation is clearly visible in energies 1.005 and 1.006 (see, Figs. 3.20c7–c8 respectively). We can conclude that the appearance of this feature is in direct relation with the amount of pairs formed inside the accretion flow.

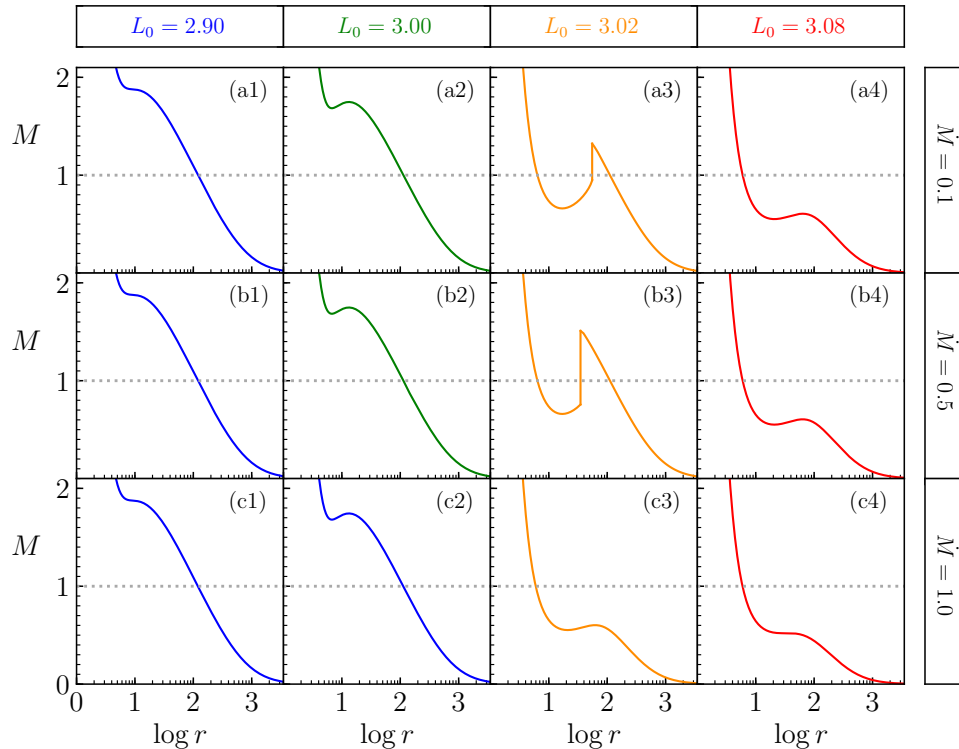


Figure 3.21: Variation in solution topology with L_0 and \dot{M} of the flow (corresponding values written inside the figure). Rest of the flow parameters are, $E = 1.0008$, $\beta = 0.1$, $\beta_d = 0.01$, $\alpha_v = 0.01$ and $M_{\text{BH}} = 10M_\odot$

3.4.2.2.5 SOLUTIONS IN $\dot{M} - L_0$ PARAMETER SPACE

In this section, we analyse, the variation of solutions with change in L_0 and \dot{M} for flow parameters, 1.0008 , $\beta = 0.1$, $\beta_d = 0.01$, $\alpha_v = 0.01$ and $M_{\text{BH}} = 10M_\odot$. We have increased L_0 from left to right, where $L_0 = 2.90 \Rightarrow$ Figs. 3.21a1–c1 (solid, blue), $L_0 = 3.00 \Rightarrow$ Figs. 3.21a2–c2 (solid, green), $L_0 = 3.02 \Rightarrow$ Figs. 3.21a3–c3 (solid, orange), $L_0 = 3.08 \Rightarrow$ Figs. 3.21a4–c4 (solid, red). From top to bottom, we have increased \dot{M} , where $\dot{M} = 0.1\dot{M}_{\text{Edd}} \Rightarrow$ Figs. 3.21a1–a4, $\dot{M} = 0.5\dot{M}_{\text{Edd}} \Rightarrow$ Figs. 3.21b1–b4 and $\dot{M} = 1.0\dot{M}_{\text{Edd}} \Rightarrow$ Figs. 3.21c1–c4.

The variation in solution topology with increase in value of L_0 and \dot{M} are similar and the reasonings are exactly the same as discussed in Sections 3.4.1.3 and 3.4.1.5 respectively for pair-free solution. However, because of the presence of pair producing processes, the exact values of flow parameters where global solution either passes through r_{co} or r_{ci} or harbours a shock, only differs. We plot flow variables like T (a1, b1, c1), Γ (a2, b2, c2) and dimensionless cooling rate, Q^- (a3, b3, c3) in Fig. 3.22. Each row corresponds to different accretion rate systems. Inside each panel, different curves represent solutions

3. ONE-TEMPERATURE ACCRETION FLOWS AROUND BLACK HOLES

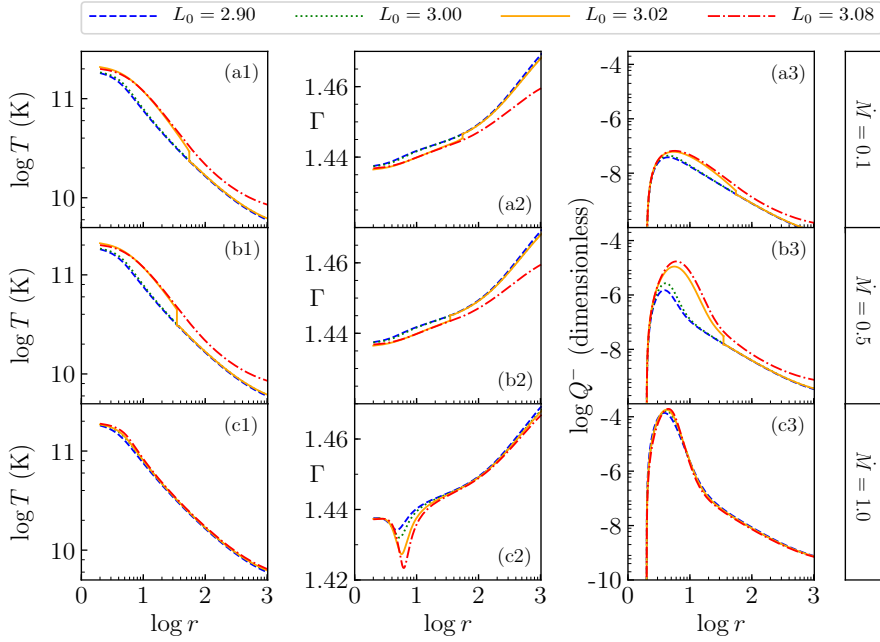


Figure 3.22: Variation in T (a1, b1, c1), Γ (a2, b2, c2) and dimensionless cooling rate Q^- (a3, b3, c3). Each row is for different values of \dot{M} (values written at the right side), while each panel shows curves corresponding to different L_0 s. The flow parameters are same as in Fig. 3.21.

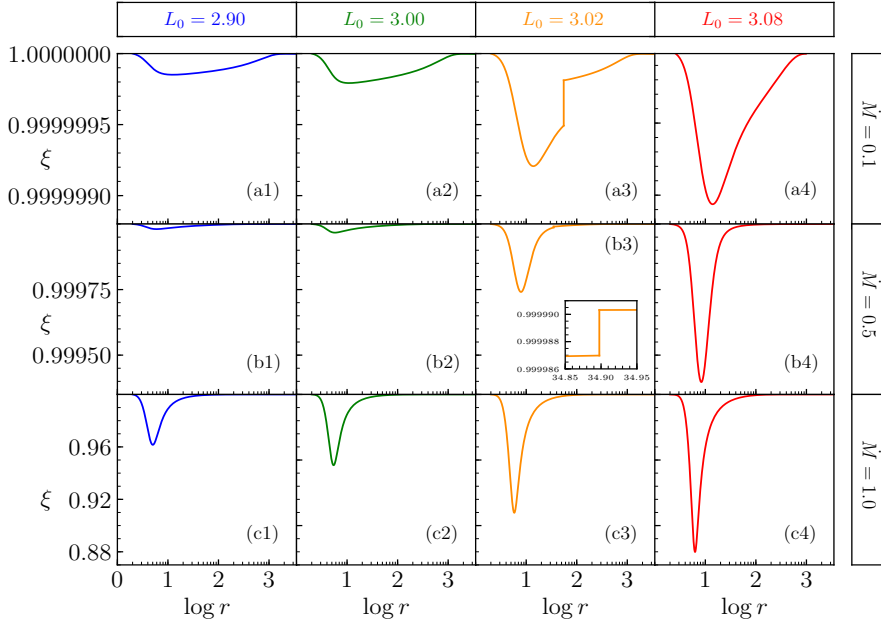


Figure 3.23: Variation of ξ with r . Higher \dot{M} solutions, show higher values of pair production and hence a large decrease in ξ . The flow parameters are same as in Fig. 3.21.

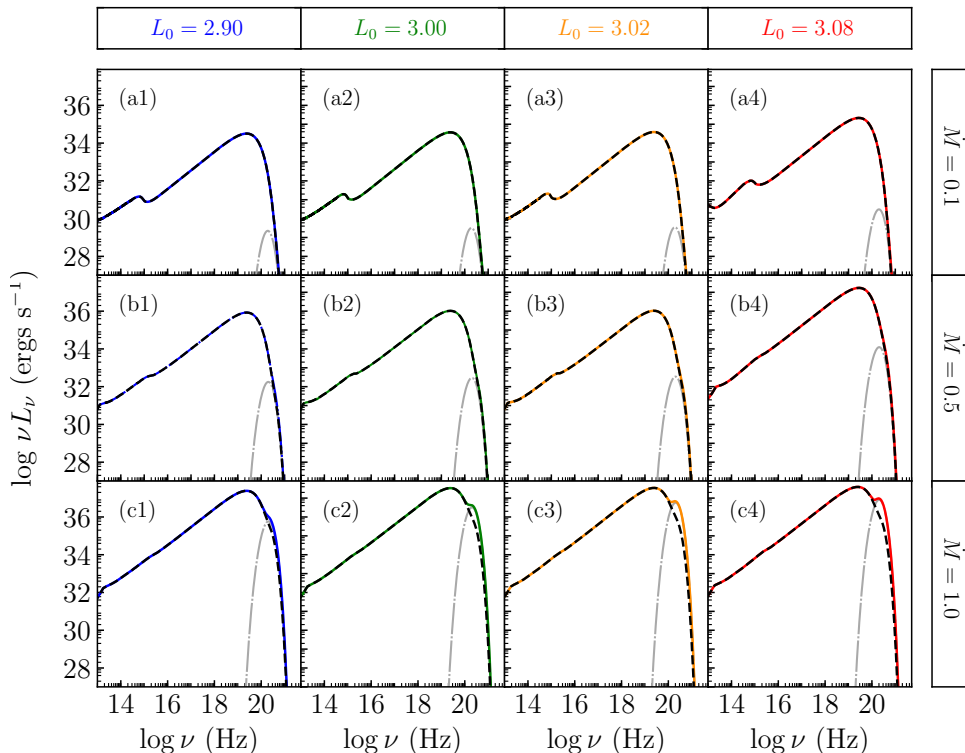


Figure 3.24: Observable spectrum (solid curves) for the solutions given in Fig. 3.21. Contribution from annihilation is represented using single-dot long-dashed grey line. A consistent annihilation line is visible in almost all solutions with $\dot{M} = 1.00\dot{M}_{\text{Edd}}$. Also, inside each panel we represent the spectrum of a pair-free solution using dashed, black curve.

with different L_0 values. A higher L_0 , for a given \dot{M} (a given row in Fig. 3.22) possess a higher temperature (see, Figs. 3.22a1–c1). The value of T becomes even higher with the increase in the value of \dot{M} . From Figs. 3.22a3–c3, we see that the cooling also increases, with increase in L_0 and \dot{M} . At the shock front, T jumps to higher values along with a corresponding enhancement in cooling (see, Figs. 3.22a1, b1, a3, b3, solid, orange curve which corresponds to $L_0 = 3.02$)

We plot the corresponding ξ variation in Fig. 3.23. A minimum value of ξ can be seen for $L_0 = 3.08$ and $\dot{M} = 1.00\dot{M}_{\text{Edd}}$ (Fig. 3.23c4). Here, the Γ is also very low (see, Fig. 3.22c2, dot dashed red). A higher angular momentum and \dot{M} is conducive of excessive cooling and hence large radiation fields would be formed. This leads to the production of pairs. For low \dot{M} s (see, Figs. 3.23a1–a4 and b1–b4), the amount of pairs produced is very low. We can conclude that a higher \dot{M} solution is likely to produce more pairs, thereby changing the solution and values of other flow variables. Shocked solutions, show jumps in ξ at r_{sh} (see, Figs. 3.23a3, b3).

3. ONE-TEMPERATURE ACCRETION FLOWS AROUND BLACK HOLES

Table 3.1: Luminosity and efficiency of pair-producing and pair-free solutions for the flows represented in Fig. 3.21

L_0	\dot{M} (\dot{M}_{Edd})	Pairs		Without Pairs		Fractional increase in L because of pairs (%) [†]
		L (ergs s ⁻¹)	η_r %	L (ergs s ⁻¹)	η_r %	
2.90	(a1) 0.1	9.16922×10^{34}	0.07085	9.16915×10^{34}	0.07084	7.42896×10^{-4}
	(b1) 0.5	2.42392×10^{36}	0.37458	2.42336×10^{36}	0.37449	0.02319
	(c1) 1.0	7.11621×10^{37}	5.49851	7.03525×10^{37}	5.43595	1.13766
3.00	(a2) 0.1	1.06587×10^{35}	0.08236	1.06586×10^{35}	0.08235	9.77838×10^{-4}
	(b2) 0.5	2.98827×10^{36}	0.46179	2.98728×10^{36}	0.46163	0.03308
	(c2) 1.0	1.02295×10^{38}	7.90411	9.85580×10^{37}	7.61532	3.65368
3.02	(a3) 0.1	1.11016×10^{35}	0.08577	1.11015×10^{35}	0.08577	1.05743×10^{-3}
	(b3) 0.5	3.01743×10^{36}	0.46629	3.01634×10^{36}	0.46613	0.03603
	(c3) 1.0	1.06810×10^{38}	8.37867	1.00773×10^{38}	7.90504	5.65282
3.08	(a4) 0.1	6.17449×10^{35}	0.47708	6.17317×10^{38}	0.47698	0.021399
	(b4) 0.5	5.96115×10^{37}	9.21205	5.93568×10^{37}	9.12734	0.433137
	(c4) 1.0	1.22283×10^{38}	10.61628	1.13833×10^{38}	9.88267	6.91019

[†] We used 5 places after decimal in order to show the lowest change available in L because of the presence of pairs, especially meant for low \dot{M} s, where there is negligible change in L even in the presence of pairs.

We plot the corresponding spectrum in Fig. 3.24 using solid curves and contribution from annihilation is represented using single-dot long-dashed grey line. The luminosity increases with L_0 (left to right across the figure), because matter gets sufficient time to radiate. Also, the luminosity increases with \dot{M} (top to bottom), because a large amount of matter is supplied, which will allow more radiative cooling. The annihilation line feature is only visible for solutions with $\dot{M} = 1.0$ (see, Figs. 3.24c1–c4) and maximally for $L_0 = 3.08$, which is the solution producing maximum pairs (see, Fig. 3.23c4).

In this figure, for all panels we represent using dashed black line, the spectrum of a pair-free solution, obtained using the respective flow parameters. If the accretion flow did not allow for any pair creation or annihilation, then the spectrum would look like to what has been plotted in dashed, black curve. For $\dot{M} = 0.1\dot{M}_{\text{Edd}}$ and $0.5\dot{M}_{\text{Edd}}$ (see, Figs. 3.24a1–a4, b1–b4), the spectrum remains almost unchanged. The same can be seen from Table 3.1, where, we have written the bolometric luminosity (L) and efficiency (η_r) for solutions with and without pairs. Also in the last column of this table, we compute the percentage of fractional increase in luminosity because of the presence of pairs in the accretion flow. We can see from the tabulated numbers, that for low \dot{M} values the fractional increase remains

$\leq 0.05\%$, which suggests that pair production in these solutions have negligible effect on the observable spectrum. But as we increase the accretion rate, for $\dot{M} = 1.0$ we can infer from the table as well as Figs. 3.24c1–c4, that there is visible change in L . In these solutions ample amount of pairs have been produced leading to a distinct annihilation signature in the spectrum. In their corresponding pair-free solution spectrum (dashed, black curve) we could not anymore see the annihilation line. The maximum increase in L happens for $L_0 = 3.08$, where, in the presence of pair production there is a 7% increase in luminosity. We can thereby conclude that pair production can make a system more luminous, only in cases where n_{e^+} produced is large.

3.5 DISCUSSIONS AND CONCLUSIONS

In this chapter, we present one-temperature advective, viscous, transonic accretion solutions, in the presence of cooling processes like bremsstrahlung, synchrotron, their respective inverse-Comptonizations as well as incorporating pair production and annihilation mechanisms. A full GR treatment has been considered, to capture the effects of strong gravity. Also, there was no fixed adiabatic index for the flow. CR EoS helped us in dealing with it. The use of a relativistic EoS like CR EoS in treating trans-relativistic flows is necessary and important to incorporate in the model. Pair production was assumed to be from the interactions between the photons generated through the above mentioned radiative processes. The regime where the work has been performed is one-temperature, which allowed us to bring out the qualitative features of an accretion flow, in the presence of pairs. It helped us to focus on the effect of pairs, without getting involved into the other complexities as present in two-temperature flows, which will be discussed in the chapters to follow.

In accretion flows around BHs, the temperatures are conducive for the production of pairs. These pairs can also annihilate creating an additional radiation field. This radiation field in addition to the other fields present inside the system can give rise to more pairs. Thus, there is an interplay between pair production and annihilation, which will determine the dynamics of the flow. Since, the solutions obtained are in steady state, we need to feedback the information of pair production \rightarrow its annihilation \rightarrow again pair production, into the system. For this, we use an iterative technique to find the number of pairs produced at each location of the accretion flow. This information is then fed back into the system to calculate the amount of annihilation possible. After that we again compute the number of pairs produced. These iterations were carried on, until the solutions converged.

3. ONE-TEMPERATURE ACCRETION FLOWS AROUND BLACK HOLES

Using this methodology, we obtained and thereafter analysed pair producing solutions and their spectrum.

As a preliminary step and to give an overview of typical one-temperature transonic solutions, we discussed first the pair-free solutions and analysed their spectrum. The importance of different flow parameters (like, E , L_0 , \dot{M} , α_v) on accretion solutions were investigated. It was seen that, depending on the combination of flow parameters, the global solution either passes through a single outer sonic point (r_{co}), or inner sonic point (r_{ci}) or both the sonic points via a shock transition (r_{sh}). We saw that with increase in E and L_0 , the system becomes more hotter and luminous. The topology of the solutions also changed. With increase in \dot{M} , amount of matter supplied to the system increases or in other words the number density increases. This in turn, increase the cooling rate which is reflected through the increase in luminosity. For example, we saw an increase of ~ 7 orders of magnitude in L when \dot{M} was increased from $0.1\dot{M}_{Edd}$ to $1\dot{M}_{Edd}$. We also investigated the variation of solutions with changed in viscosity in the system, which is tuned using α_v : [Shakura & Sunyaev](#) viscosity parameter. A larger transport of angular momentum was found for higher values of viscosity. This caused the angular momentum to increase, thereby allowing matter to cool for longer durations. Hence systems with large α_v s were more luminous.

Now, we extended the above work, to incorporate pair-production and annihilation. First, we included only bremsstrahlung and its inverse-Comptonization as the only radiative process present inside the flow, and ignored the presence of any stochastic magnetic fields. We assume that the radiation field inside an accreting system is mainly dominated by these two emission processes ([Sarkar & Chattopadhyay, 2020](#)). We find that the number of pairs produced by bremsstrahlung, inverse-Compton and annihilation photons are significant for only $\dot{M} = 0.8\dot{M}_{Edd}$, where minimum ξ is around ~ 0.97 . For accretion rates lower than this, n_{e^+} is so low, that we can safely neglect the presence of any pairs. Also, the maximum number of pairs are produced in a region $< 50r_g$. When the number density of pairs is not very low, like for accretion rates $> 0.8\dot{M}_{Edd}$, there is a bump near $m_e c^2$ in the spectrum. This is a spectral signature of the annihilated photons.

Thereafter, to be more conclusive about the importance of pairs and the annihilation line in accretion flows having pairs, we carried out detailed analysis of this work by incorporating all the radiative processes, starting from bremsstrahlung, synchrotron to including their respective inverse-Comptonization components. Since, there have been discrepancies in literature arising because of the selective radiative processes been taken into account, we tried to incorporate all of them in order to get a correct picture of the

importance of pairs. The effect of variation of flow parameters like E , L_0 , \dot{M} etc on pair-producing solutions were found to be on similar lines as for a pair-free solution. That is, with increase in their values, the solution becomes more hotter and more luminous. The only difference is in the production of e^+ . The solutions which were cooling efficient or where the radiation field was large, it was found that the production of pairs were significant. The value of ξ reached to a minimum of 0.88 in few cases. Interestingly, a distinct annihilation feature near $\sim m_e c^2$ in the spectrum was found consistently in all the solutions, where ample pairs were produced. [Yahel & Brinkmann \(1981\)](#) also found this line, in their model. This conclusion, is similar to what was obtained when we took only bremsstrahlung and its inverse-Comptonization, except that this time, the number pairs produced are more significant because of the presence of additional radiation fields. In all other low pair producing cases this annihilation line was masked by the emission from other radiative processes. We found that the origin of this line or the maximum contribution to this emission feature, comes from a region very close to the BH event horizon, especially from $5 - 10r_g$, where most of the radiation is produced.

When we compared a pair producing solution with a pair-free solution, we found that there was always an increase in luminosity in an accretion solution producing pairs, however low it might be. For very low \dot{M} , the change in L can be neglected, but for higher \dot{M} s where the number of pairs produced are higher, the fractional increase in luminosity is large and the maximum increase obtained was 7% for $\dot{M} = 1\dot{M}_{\text{Edd}}$ (where, L_0 was also higher, indicating a further increased cooling). For a pair-free solution, the annihilation line contribution was absent.

Thus, to conclude, we found that pairs play a major role in accretion systems, which harbour large radiation fields (solutions with higher \dot{M} , E etc.) and can essentially be responsible for shaping the observable spectrum.

Chapter 4

DEGENERACY: A GENERIC PROBLEM IN TWO-TEMPERATURE SOLUTIONS; ENTROPY: THE TOOL TO REMOVE IT

4.1 OVERVIEW

One-temperature solutions are important to the extent that, it gives a general idea about the flow behaviour, its dynamics as well as energetics (Becker & Le, 2003; Chattopadhyay & Chakrabarti, 2011; Kumar & Chattopadhyay, 2014; Le & Becker, 2005). To accurately extract the luminosity and spectra of an accreting flow, one needs to have information of the electron temperature (T_e) inside the flow, which may or may not be comparable to the proton temperature (T_p). In many astrophysical cases, Coulomb coupling is found to be weak. Also, electrons are more prone to radiative cooling, compared to protons. This can make the electron temperature deviate largely from the protons, especially in the inner regions of an accretion disc. Therefore, an accretion flow is likely to follow two different temperature distributions, one-temperature defining protons and the other electrons (see, Section 1.5 for more discussion).

4.2 HISTORY OF TWO-TEMPERATURE ACCRETION FLOWS

The theory of two-temperature accretion discs started way back in 1976, with the famous work done by Shapiro et al. (1976). They argued that the instability persisting at the inner region of SSD could swell into an optically thin gas pressure dominated region with

4. DEGENERACY: A GENERIC PROBLEM IN TWO-TEMPERATURE SOLUTIONS; ENTROPY: THE TOOL TO REMOVE IT

electrons and protons maintaining two separate temperature distributions, because of weak Coulomb coupling. Using this model, they successfully regenerated the hard X-ray, power-law part of Cygnus X-1 spectrum, available at that time. It was gradually concluded that although one-temperature works ($T_e = T_p$) are easy to work upon, unfortunately yield very high temperatures $\sim 10^{11} - 10^{12}$ K, which are not consistent with the observations. Thus, research on two-temperature accretion flow started to gain prominence and a host of works have been done in this regime, few being discussed below.

[Liang & Thompson \(1980\)](#) investigated the formation and nature of MCP in rotating accretion flows, assuming one-temperature regime, but they also discussed briefly, an important fact regarding two-temperature flows. They pointed out that, in the absence of any guiding principle coupling electrons and ions, the only way to obtain a transonic two-temperature solution, is to parametrise T_p/T_e to a constant value. Further works done in two-temperature regime by [Chakrabarti & Titarchuk \(1995\)](#); [Colpi et al. \(1984\)](#); [Laurent & Titarchuk \(1999\)](#); [Mandal & Chakrabarti \(2005\)](#), focussed on implementing accurate radiative processes and computing a spectrum, assuming freely falling matter around BHs, thereby bypassing the issue of transonicity. In 1995, [Narayan & Yi](#) extensively discussed the nature of two-temperature, optically thin advective accretion discs around compact objects. The equations of motion were solved under the self-similar assumption, which is plausible only at a very large distance from the central object and not near it. Additionally, a self-similar solution is not transonic. The authors also neglected the electron advection term and assumed that the heating and cooling rates of electrons to be equal, This extra assumption helped them to deal away with any kind of parametrisation, that was otherwise assumed by [Liang & Thompson \(1980\)](#) to obtain a consistent solution. [Nakamura et al. \(1997, 1996\)](#), was amongst the first, who self-consistently solved two-temperature transonic accretion solutions and properly dealt with the advection terms without any assumption. However at the outer boundary, the authors assumed ion temperature to be a fraction of the virial temperature and Coulomb coupling was equated with bremsstrahlung. This, unfortunately, allowed them to obtain a limited class of solutions. [Manmoto et al. \(1997\)](#) extended [Nakamura et al.](#)'s work and computed the spectrum. In addition, they slightly modified the outer boundary conditions, where the total gas temperature (and not the ion temperature) was assumed to be a fraction of the virial temperature and equated Coulomb coupling with the total cooling of electrons (bremsstrahlung, synchrotron and Comptonization).

[Rajesh & Mukhopadhyay \(2010\)](#) offered a more complete picture of two-temperature accretion flows around Schwarzschild as well as Kerr BHs. Recently, a more general

transonic advective two-temperature accretion solution was obtained by [Dihingia et al. \(2018\)](#), where they obtained global class of transonic two-temperature solutions including accretion-shocks. They extended this work on magnetized accretion discs around Kerr BHs as well ([Dihingia et al., 2020](#)).

Thus, two-temperature accretion flows have been popularly used to model the spectrum of BH accretion discs and other compact objects. They have been successful in explaining the observations of BH binaries and AGNs *e.g.* Cygnus-X1, Sagittarius A*, M87, XTE J1118+480 etc ([Mandal & Chakrabarti, 2005, 2008](#); [Yuan & Narayan, 2014](#); [Yuan et al., 2006](#)).

4.3 DEGENERACY: A GENERIC PROBLEM

The most striking feature of a transonic two-temperature flow is that, the solutions depend on the choice of inner or outer boundary conditions. But from one-temperature hydrodynamics we know that, a transonic solutions is *unique* for a given set of constants of motion. In Chapter 3, which was based on one-temperature accretion flows, no arbitrary assumptions were imposed, while obtaining a solution. Most of the works done in two-temperature regime either did not use the constants of motion of the flow (*e.g.*, generalized Bernoulli constant¹) or did not utilise the information of entropy close to the horizon, to obtain solutions. The hydrodynamics of one-temperature regime is more complete and systematic, while this approach is sadly lacking in two-temperature regime.

The number of equations describing a flow, in one-temperature and two-temperature regime, are exactly the same, but there is one more variable in case of two-temperature flows (*i.e.* the existence of different proton and electron temperature distribution). Or in other words, the problem with two-temperature solutions is that, without any increase in the number of governing equations, the number of flow variable increases, *i.e.* to say, now instead of a single temperature (T), one has to consider two different temperatures (T_e, T_p). In addition, there is no known principle dictated by plasma physics which may constrain the relation between these two temperatures, at any point of the flow.

Obtaining a self-consistent two-temperature flow would require solving the basic hydrodynamic equations, but since there is one more flow variable in the two-temperature regime, the system is *degenerate*. We obtain a large number of transonic solutions, each with a different sonic point than the rest, for the same set of constants of motion of the flow. Hint of this problem of degeneracy was reported briefly in [Liang & Thompson \(1980\)](#),

¹generalized Bernoulli parameter in steady state, is a constant of motion, even in presence of dissipation [Chattopadhyay & Kumar \(2016\)](#); [Kumar & Chattopadhyay \(2013, 2014\)](#), see Eq. 2.16 and 2.29

4. DEGENERACY: A GENERIC PROBLEM IN TWO-TEMPERATURE SOLUTIONS; ENTROPY: THE TOOL TO REMOVE IT

however, the problem was skirted out by parametrising the temperatures of proton and electron to some constant value. A similar methodology was adopted by some authors, where instead of parametrising, they specified either the electron or proton temperature in a chosen boundary and then iterated the other flow variables to obtain a transonic solution. However, a different combination of electron and proton temperature in that boundary, can give rise to another transonic solution, but for the same value of generalized Bernoulli parameter (E). This gives rise to degeneracy of solutions, *i.e.*, multiple transonic solutions for the same set of constants of motion. Some authors even assumed specific relations between electron heating and cooling, in order to obtain a solution. But all these choices are arbitrary and a solution obtained assuming them, cannot be considered a unique solution. Such arbitrary choices were not encountered in one-temperature works, since a transonic one-temperature solution is unique for a given set of constants of motion.

4.4 ENTROPY: A TOOL TO REMOVE IT

A two-temperature theory is degenerate, because of the reasons discussed above. We obtain multiple transonic solutions, for the same set of constants of motion. But nature would prefer only one solution but the question is which one. A global treatment of two-temperature theory would require, all the equations to be solved self-consistently, without taking recourse to any arbitrary assumption on temperature values, at any boundary of the flow.

Hydrodynamic equations of motion, even in the one-temperature regime, admit infinite number of solutions (multi-valued branch and supersonic branch, abbreviated as MVB and SB respectively, was discussed in Section 3.3, Fig. 3.3), but a transonic solution (TS) is physically most favoured by nature, because it has the highest entropy among all possible global solutions (Bondi, 1952). In addition, the location of sonic point corresponds to a unique boundary. Following the footsteps of Bondi (1952), we can look for highest entropy solution in two-temperature theory as well in order to remove degeneracy. But it is different this time, since all the solutions are already transonic and among them only one solution is correct (or, which nature should prefer). Not only Bondi, but Becker & Le (2003) and Becker et al. (2008) utilised in a similar fashion, the concept of entropy close to the horizon along with the information of generalized Bernoulli parameter, to find a sonic point and therefore a transonic solution, in the one-temperature limit. Based on this approach, many works were performed to model accretion flows around BHs, in the

one-temperature limit (Chattopadhyay & Kumar, 2016; Kumar & Chattopadhyay, 2013, 2014; Le et al., 2016; Lee & Becker, 2017).

However, the two-temperature energy equation, in adiabatic limit, is not integrable, unlike in one-temperature regime where an analytical expression of entropy can be obtained (Chattopadhyay & Kumar, 2016; Kumar & Chattopadhyay, 2013, 2014; Kumar et al., 2013). Below, we extensively discuss this issue.

4.4.1 ONE-TEMPERATURE ACCRETION FLOWS: ENTROPY ACCRETION RATE EXPRESSION

Here, we derive the entropy accretion rate formula for one-temperature flows. We use the energy equation, which is defined in the GR regime by Eq. 2.15 and present the methodology of obtain the entropy accretion rate measure of a TS.

For one-temperature flows, we have a single $\Theta (= kT/(m_e c^2))$, thus a single energy equation needs to be solved. In the adiabatic limit, this is reduced to:

$$\frac{e + p}{\rho} \frac{d\rho}{dr} - \frac{de}{dr} = 0, \quad (4.1)$$

$$\implies \frac{p}{\rho^2} \frac{d\rho}{dr} - \frac{d(e/\rho)}{dr} = 0. \quad (4.2)$$

When we consider PWP instead of GR, the first law of thermodynamics is given by Eq. 2.23. In the adiabatic limit, it is reduced to the same expression as above (Eq. 4.2). Integrating this equation using the CR EoS (Eq. 2.30) gives a relation between Θ and ρ , which is:

$$\rho = \kappa \exp\left(\frac{f - \tilde{\chi}}{2\Theta}\right) \Theta^{\frac{3}{2}} (3\Theta + 2)^{\frac{3(2-\xi)}{4}} \left(3\Theta + \frac{2}{\chi}\right)^{\frac{3\xi}{4}}, \quad (4.3)$$

where, $\tilde{\chi} = 2 - \xi(1 - 1/\chi)$, $\chi = m_e/m_p$, $\xi = n_p/n_e$ (composition parameter, defined many times in the previous chapters), and κ is an integration constant, which is a measure of entropy. We define the *entropy accretion rate* of a system as:

$$\dot{\mathcal{M}} = \frac{\dot{M}}{4\pi\kappa}. \quad (4.4)$$

Using the form of \dot{M} given in Eq. 2.10 for the case of a BH in GR regime, we get (Chattopadhyay & Kumar, 2016; Kumar & Chattopadhyay, 2017):

$$\dot{\mathcal{M}}_{\text{1T-BH}} = \exp\left(\frac{f - \tilde{\chi}}{2\Theta}\right) \Theta^{\frac{3}{2}} (3\Theta + 2)^{\frac{3(2-\xi)}{4}} \left(3\Theta + \frac{2}{\chi}\right)^{\frac{3\xi}{4}} (Hrur), \quad (4.5)$$

and using Eq. 2.24 as the expression of \dot{M} , for the case of a NS assuming PWP potential,

4. DEGENERACY: A GENERIC PROBLEM IN TWO-TEMPERATURE SOLUTIONS; ENTROPY: THE TOOL TO REMOVE IT

we get (Singh & Chattopadhyay, 2018a,b)

$$\dot{\mathcal{M}}_{1T-NS} = \exp\left(\frac{f - \tilde{\chi}}{2\Theta}\right) \Theta^{\frac{3}{2}} (3\Theta + 2)^{\frac{3(2-\xi)}{4}} \left(3\Theta + \frac{2}{\chi}\right)^{\frac{3\xi}{4}} (v_p A_p). \quad (4.6)$$

This equation has the same form as Eq. 4.5, except the last bracketed term. The last term is different, because of the different expressions of \dot{M} of a BH and NS, which is basically a function of r , v , and Θ . In the one-temperature regime, this entropy accretion rate formula is an extra equation, which helps in simplifying the methodology to obtain a transonic solution. This expression need not be necessarily used to obtain a solution. A unique TS could be found even without the use of this equation.

4.4.2 TWO-TEMPERATURE ACCRETION FLOWS: ENTROPY ACCRETION RATE EXPRESSION

Unfortunately, in the two-temperature regime, instead of one energy equation, we have two energy equations describing the temperature variation of the two species. But these equations are not completely independent and coupled by a Coulomb coupling term, which serves as an energy exchange term between protons and electrons. The integration of the energy equation in the two-temperature regime, is hence, spoiled by the presence of this Coulomb coupling term. We are thus prevented from obtaining an analytical expression for measure of entropy in the two-temperature regime, unlike what we obtained in the one-temperature regime (Eqs. 4.5–4.6).

But, we should remember that, near the horizon, gravity overpowers any other interactions or processes. Also matter just outside the horizon falls freely, where infall timescales are shorter than cooling or Coulomb coupling time scales. Thus, we can neglect the Coulomb coupling term. Henceforth, asymptotically close to the horizon, an analytical expression of entropy is admissible. We reported in Sarkar & Chattopadhyay (2019a), for the first time, a form of entropy measure, which could only be applied near the horizon. Using the formula obtained, we measured the entropies at the horizon, of the multiple transonic two-temperature solutions, obtained for a given set of constants of motion. We saw that the entropy maximised at a unique solution. From the second law of thermodynamics we select the solution with maximum entropy as the solution which nature would prefer. This solved the problem of degeneracy, present in two-temperature models. The stability analysis of these flows also confirmed that, the highest entropy solution is the most stable one.

For two-temperature regime, the energy equation in the adiabatic limit, using CR EoS is obtained by combining Eqs. 2.15 and 2.30, to get:

$$\begin{aligned}\frac{d\Theta_p}{dr} &= \frac{\Theta_p}{N_p} \frac{1}{n_p} \frac{dn_p}{dr} + Q_{ep} \tilde{\mathcal{E}}_p \\ \frac{d\Theta_e}{dr} &= \frac{\Theta_e}{N_e} \frac{1}{n_{e^-}} \frac{dn_{e^-}}{dr} - Q_{ep} \tilde{\mathcal{E}}_e.\end{aligned}\quad (4.7)$$

where, \mathcal{E}_i s are functions of v , ρ and Θ_i . Except \mathcal{E}_i , rest of the expressions are exactly the same, irrespective of whether the central object is a BH or an NS. Because of the presence of two-different species in the system, we have two-different energy equations. We see that even in the adiabatic limit, Q_{ep} is present, coupling both the equations. In one-temperature regime, when there was a single energy equation present, it was very easy to integrate the equation, to obtain a measure of entropy (Eqs. 4.5–4.6) But now, in two-temperature regime, due to the presence of Coulomb interaction term, Eqs. 4.7 is not integrable. However, in regions where Q_{ep} can be neglected, an analytical expression is admissible. Interestingly, such a region is available just outside the horizon, where gravity overwhelms any other interaction. Remembering this fact, that near the horizon Q_{ep} is negligible, Eqs. 4.7 can be integrated to obtain,

$$n_{\text{ein}} = \kappa_1 \exp\left(\frac{f_{\text{ein}}-1}{\Theta_{\text{ein}}}\right) \Theta_{\text{ein}}^{\frac{3}{2}} (3\Theta_{\text{ein}} + 2)^{\frac{3}{2}} \quad (4.8)$$

$$n_{\text{pin}} = \kappa_2 \exp\left(\frac{f_{\text{pin}}-1}{\Theta_{\text{pin}}}\right) \Theta_{\text{pin}}^{\frac{3}{2}} (3\Theta_{\text{pin}} + 2)^{\frac{3}{2}}. \quad (4.9)$$

Here, $f_i = 1 + \Theta_i \left(\frac{9\Theta_i+3}{3\Theta_i+2}\right)$, κ_1 and κ_2 are the integration constants which are measure of entropies and subscripts ‘in’ indicate quantities measured just outside the horizon ($r \rightarrow 2r_g = 2GM_*/c^2$).

Charge neutrality condition, then demands that, $n_{\text{ein}} = n_{\text{pin}} = n_{\text{in}}$ (assuming there is no pair-production or no external positrons present in the system). Therefore we can write,

$$\begin{aligned}n_{\text{in}}^2 &= n_{\text{ein}} n_{\text{pin}} \\ \Rightarrow n_{\text{in}} &= \sqrt{n_{\text{ein}} n_{\text{pin}}} \\ &= \kappa \sqrt{\exp\left(\frac{f_{\text{ein}}-1}{\Theta_{\text{ein}}}\right) \exp\left(\frac{f_{\text{pin}}-1}{\Theta_{\text{pin}}}\right) \Theta_{\text{ein}}^{\frac{3}{2}} \Theta_{\text{pin}}^{\frac{3}{2}} (3\Theta_{\text{ein}} + 2)^{\frac{3}{2}} (3\Theta_{\text{pin}} + 2)^{\frac{3}{2}}},\end{aligned}$$

where, $\kappa = \sqrt{\kappa_1 \kappa_2}$

4. DEGENERACY: A GENERIC PROBLEM IN TWO-TEMPERATURE SOLUTIONS; ENTROPY: THE TOOL TO REMOVE IT

Thus, an expression for entropy accretion rate can be obtained, substituting the above equation in Eq. 4.4:

$$\dot{\mathcal{M}}_{\text{in}} = \sqrt{\exp\left(\frac{f_{\text{ein}} - 1}{\Theta_{\text{ein}}}\right) \exp\left(\frac{f_{\text{pin}} - 1}{\Theta_{\text{pin}}}\right) \Theta_{\text{ein}}^{\frac{3}{2}} \Theta_{\text{pin}}^{\frac{3}{2}} (3\Theta_{\text{ein}} + 2)^{\frac{3}{2}} (3\Theta_{\text{pin}} + 2)^{\frac{3}{2}} (Hru^r)} \quad (4.10)$$

Thus, we get a measure of entropy, strictly valid near the horizon or in any region where the above discussed assumptions are valid. In case of a two-temperature flow around an NS, we have the same expression of entropy measure, except the last bracketed term, which will be $v_p A_p$, similar to what was obtained in entropy accretion rate form for one-temperature flows (see, Eq. 4.6).

This is the first time, an entropy measure form in two-temperature accretion theory is proposed.

4.4.3 APPLICATION OF ENTROPY ACCRETION RATE FORMULA

In a series of papers, namely [Sarkar & Chattopadhyay \(2019a,b\)](#); [Sarkar et al. \(2020\)](#), we attended the degeneracy problem and proposed a general methodology to remove degeneracy in two-temperature accretion flows around BHs. We utilised the concept of entropy, to find a unique transonic two-temperature accretion solution. Using the above entropy accretion rate formula (see, Eq. 4.10), entropies of all the degenerate solutions were measured. We found that the entropy maximised for a unique solution. Following the second law of thermodynamics, that nature would prefer a solution with maximum entropy, degeneracy was removed in two-temperature accretion flows. But the above equation is strictly valid near the horizon in case of a BH, where the free-fall condition of matter is valid.

We extended the work on two-temperature flows, to NSs as well ([Sarkar et.al., 2021, under review](#)). Unfortunately, an inner boundary condition similar to BH, is not present outside an NS surface. Strong gravity of NS can makes an accretion flow transonic, with matter approaching the NS surface supersonically, however, the poloidal velocity of the supersonic branch is not high enough to approach free-fall values. Moreover, the presence of a hard surface of NS intervenes the supersonic flow and drives a shock near the surface, after which matter slows down, finally settling down onto the NS surface. Thus, the presence of a hard surface in case of NS, do not allow matter to achieve free-fall velocities and the form of entropy measure proposed by us, is not valid for these flows. Even if it is assumed, that the supersonic matter directly hits the NS surface ([Koldoba et al., 2002](#)), without forming a shock, the matter would still not achieve velocities, high enough

($v \approx c$), to use the entropy expression and obtain an entropy measure close to the NS surface. In other words, neither the supersonic branch, nor the post shock flow achieves free-fall velocities. Therefore, one cannot obtain an entropy measure and the methodology followed in case of BHs, cannot be adopted directly, for flows around NSs. This has led to a serious problem of constraining the degeneracy in two-temperature flows around NSs. But we propose a novel methodology to remove degeneracy and obtain unique transonic two-temperature accretion solution around NSs, for a given set of constants of motion, utilising our entropy measure form (Eq. 4.10). We elaborately discuss it in Chapter 7 (Sarkar *et.al.*, 2021, under review).

After constraining degeneracy in both these compact objects, we proceed to obtain global accretion solution and perform spectral analysis of the flows. We study solutions for a large set of parameter space, to get a global picture of the BH as well as NS systems. Elaborate discussion on the methodology to obtain unique transonic two-temperature accretion solutions around BHs and NSs have been discussed individually, in their respective chapters.

Chapter 5

TWO-TEMPERATURE FLOWS AROUND BLACK HOLES – I: SPHERICAL ACCRETION

5.1 INTRODUCTION

One of the most spectacular objects found in the Universe are BHs. The properties of a BH are imprinted on the surrounding accretion flows, hence, modelling of these flows are important. This led to the development of innumerable models, which has been improvised from time to time to match with the latest observations. Matter accreted under the influence of strong gravity of BHs gets compressionally heated, such that the flow becomes fully ionised. Electrons being the main radiators, a system is more likely to settle down into two-different temperature distributions, one defining protons and the other electrons (see, Section 1.5 for a more detailed discussion). Two-temperature modelling is necessary because it helps in obtaining information of the electrons, which mainly contribute to the observable spectrum. But as discussed in the previous Chapter 4, *two-temperature theory is degenerate in nature*. For a given set of constants of motion, we have multiple transonic solutions, each with a distinct sonic point and property (no two solutions share the same property, or r_c). The degeneracy prevailing in two-temperature accretion flows is a long outstanding problem. In Chapter 4, we identified the problem of degeneracy and proposed that, ‘*entropy*’ is a tool, which can help constrain the degeneracy. Thereafter, we derived an entropy accretion rate formula, Eq. 4.10, for the first time in two-temperature accretion theory.

The results of this chapter are published in: **Sarkar, Shilpa and Chattopadhyay, Indranil**, 2019, *International Journal of Modern Physics D*, **28**, 1950037.

5. TWO-TEMPERATURE FLOWS AROUND BLACK HOLES – I: SPHERICAL ACCRETION

The theme of this chapter is to address the basic problem of *finding a ‘unique’ transonic two-temperature accretion solution around a Schwarzschild BH, and validate the novel methodology*. Since, this is the first time, a formula of entropy measure for two-temperature accretion flows has been derived, and a methodology to constrain degeneracy is proposed, it is necessary to remove all frills that might complicate and obscure the question at hand. Hence, as a first step, we consider radial accretion *i.e.*, rotation is neglected. Therefore, the flow geometry is spherical/conical with the presence of very little or negligible angular momentum. These flows are also known as Bondi flows. Spherical flows harbour a single sonic point due to the presence of gravity. The equations are hence simplified and is easy to implement. Assumption of a more complicated accretion model would have obscured the crux of the problem. Although spherical accretion might look very simple, however, it is not entirely implausible as an accretion model. [Chattopadhyay & Kumar \(2016\)](#); [Kumar & Chattopadhyay \(2014\)](#) have previously shown that the flow geometry in the inner region of an accretion disc around BH, is close to conical flow with low angular momentum. Therefore, radial accretion might be used to mimic the inner region of AGNs and microquasars. This is to be expected too, since the BH gravity would start to dominate over other interactions in the inner accretion region. As a result, a large number of papers do consider spherical flow to mimic the inner region of accretion flow ([Ipser & Price, 1982](#); [Kazanas et al., 1997](#); [Titarchuk et al., 1997](#)). In addition, standard accretion model onto isolated BH from inter-stellar medium is indeed spherical ([Beskin & Karpov, 2005](#); [Davies & Pringle, 1980](#)). We have worked in the pure GR regime, to capture the effects of strong gravity around BHs.

We propose in this work, a novel methodology to overcome the degeneracy problem, by laying down a prescription to obtain the correct solution. This is difficult since plasma physics do not impose any constraint on the relation between electron and proton temperatures at any distance from the BH horizon. Thus, we utilise the measure of entropy derived in Section 4.4.2, given by Eq. 4.10, which is strictly valid near the horizon, to constrain the degeneracy. Following second law of thermodynamics we select the maximum entropy solution to be the one preferred by nature. As far as we know, such an attempt has yet not been undertaken so far.

After removing degeneracy, we analyse and discuss general two-temperature accretion solutions for a wide range of parameter space. We use the two-temperature version of CR EoS to incorporate the trans-relativistic nature of accretion flows around BHs. Also different dissipative processes like bremsstrahlung, synchrotron and Comptonization have been taken into consideration in this work. Amount of energy exchanged between electrons and protons is computed using the relativistic version of Coulomb interaction term given by [Stepney \(1983\)](#). We note that, since radial flow has no angular momentum, viscous transport should be negligible. Absence of rotation reduces the shear stresses to negligible values. Assuming shear to be the only source of viscosity, viscous stresses can also be

ignored. Also, Coulomb coupling is not an efficient energy transfer process, therefore any viscous heating will anyway not find its way into heating up the electrons. Looking into all these factors, we ignored viscous dissipation and concentrated on two-temperature accretion flow by only considering cooling mechanisms in this work. However, at the end we consider dissipative proton heating (Ipser & Price, 1982) to mimic the effect of viscous heating, if any, present inside the system.

5.2 ASSUMPTIONS AND EQUATIONS USED

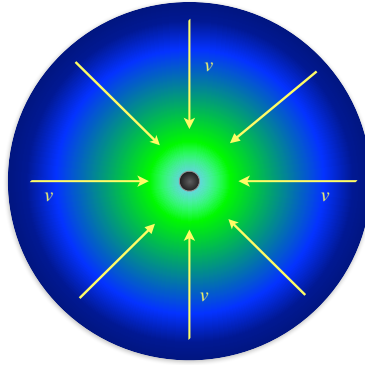


Figure 5.1: Cartoon diagram representing spherical flow around a BH. The arrows represent the direction of accretion.

We assume steady, advective, spherical accretion flows around Schwarzschild BH, a cartoon diagram of which is presented in Fig. 5.1. The background metric is given by Eq. 2.1. The flow is assumed to be fully ionised and composed of protons and electrons. We neglect in this work, the presence of any pairs and thereby any pair-producing mechanisms. Thus, $n_p = n_{e^-} = n$ and $\xi = 1$ (see, Eq. 2.6). We utilise the equations discussed in Section 2.2 for modelling these flows. CR EoS for multi-species flow has been used throughout this work, explicit form of which is given in Eq. 2.30. Unlike one-temperature flows, we now have two-different species in two-temperature flows. Thus, f present in the generic form of CR EoS (see, Eq. 2.31) is given by,

$$f = f_e + \frac{f_p}{\chi}, \quad (5.1)$$

where, $f_e = 1 + \Theta_e \left(\frac{9\Theta_e + 3}{3\Theta_e + 2} \right)$ and $f_p = 1 + \Theta_p \left(\frac{9\Theta_p + 3}{3\Theta_p + 2} \right)$.

As, there is no pair creation or annihilation present in the system, the continuity equation given by Eq. 2.5 can be written as Eq. 2.9. This can be integrated to obtain accretion rate of the flow, \dot{M} , expression of which is given by (also, see Eq. 2.10):

$$\dot{M} = 4\pi\rho u^r r^2 \cos\theta^c, \quad (5.2)$$

5. TWO-TEMPERATURE FLOWS AROUND BLACK HOLES – I: SPHERICAL ACCRETION

where, θ^c is assumed to be 60° throughout this chapter, unless mentioned otherwise.

The differential equation for proton and electron temperatures are obtained by simplifying Eq. 2.15 using CR EoS (Eq. 2.31 alongwith Eq. 5.1) and \dot{M} (Eq. 5.2), we get,

$$\frac{d\Theta_p}{dr} = -\frac{\Theta_p}{N_p} \left(\mathfrak{P} + \frac{1}{v(1-v^2)} \frac{dv}{dr} \right) - \frac{\mathbb{P}\chi\tilde{K}h}{N_p}, \quad (5.3)$$

$$\frac{d\Theta_e}{dr} = -\frac{\Theta_e}{N_e} \left(\mathfrak{P} + \frac{1}{v(1-v^2)} \frac{dv}{dr} \right) - \frac{\mathbb{E}\tilde{K}h}{N_e}, \quad (5.4)$$

respectively, where, $\tilde{K} = 1 + 1/\chi$, $\mathfrak{P} = \frac{2r-3}{r(r-2)}$; $\mathbb{E} = \frac{\Delta Q_e}{\rho hu^r}$; $\mathbb{P} = \frac{\Delta Q_p}{\rho hu^r}$. ΔQ in the proton energy equation can be written as, $\Delta Q_p = Q_p^+ - Q_p^-$ and in the electron energy equation it is, $\Delta Q_e = Q_e^+ - Q_e^-$. Since the flow contains electrons and protons equilibrating at two different temperatures, we need to use the first law of thermodynamics separately for protons and electrons. These two energy equations are coupled by a Coulomb coupling term (Q_{ep}) which allows protons and electrons to exchange energy within themselves. Thus, it acts as a heating term for electrons and cooling term for protons, $Q_p^- = Q_e^+ = Q_{ep}$. The cooling of electrons include contributions from three radiative cooling mechanisms namely bremsstrahlung (Q_{br}), synchrotron (Q_{syn}) and inverse-Comptonization (Q_{ic}). Therefore, $Q_e^- = Q_{br} + Q_{syn} + Q_{ic}$.

Simplifying Eq. 2.13, using Eqs. 2.30–2.32 and 5.1–5.4, we get the differential equation for velocity,

$$\frac{dv}{dr} = \frac{\mathcal{N}}{\mathcal{D}}, \quad (5.5)$$

where, $\mathcal{N} = -\frac{1}{r(r-2)} + a_s^2 \mathfrak{P} + (\Gamma_e - 1)\mathbb{E} + (\Gamma_p - 1)\mathbb{P}$ and $\mathcal{D} = \frac{v}{1-v^2} \left(1 - \frac{a_s^2}{v^2} \right)$.

Here, we have defined the sound speed as, $a_s^2 = \mathcal{G}/h\tilde{K}$, where $\mathcal{G} = \Gamma_e\Theta_e + \Gamma_p\Theta_p/\chi$.

GENERALIZED BERNOULLI CONSTANT

The expression for generalized Bernoulli constant is given in Eq. 2.17, where $X_f = \int \frac{\Delta Q_p + \Delta Q_e}{\rho hu^r} dr$. This is conserved throughout the flow even in the presence of dissipation. In case of non-dissipative/adiabatic flows, $E \rightarrow \mathcal{E} = -hu_t$, which is the canonical form of relativistic Bernoulli parameter (Chattopadhyay & Chakrabarti, 2011; Shapiro & Teukolsky, 1983).

5.3 SOLUTION PROCEDURE

Bondi (1952) has already proven that for a given set of flow parameters, entropy of the transonic global solution is maximum. Therefore, a TS is the solution which is most favoured by nature. The general procedure to obtain a TS in two-temperature is similar to the one in the single temperature regime, which is — for a given set of flow parameters, the

sonic point is located first and then the differential equations of velocity and temperatures are integrated, in order to obtain self-consistent values of flow variables (see, Section 3.3.1 for an extensive discussion, also see flowchart present in Fig. 3.2 for brief information regarding the methodology).

5.3.1 METHOD TO FIND SONIC POINT: ONE-TEMPERATURE VERSUS TWO-TEMPERATURE

A spherical flow harbours only a single sonic point. The first step in obtaining a general TS is to locate this r_c . Finding of r_c is not trivial in presence of heating and cooling. A general methodology to obtain r_c and hence a TS, in a dissipative system, has been elaborated in Section 3.3.1. But, the flow was assumed to be of one-temperature distribution. In short, it states the following.

\Rightarrow To find r_c we need to first choose a boundary: horizon or infinity. The advantage of choosing horizon as the boundary, is that atleast the inflow velocity at the horizon is known ($v_{in} = c$), while at the outer boundary value of v is arbitrary. Unfortunately, there is a coordinate singularity at the horizon, so one cannot start the integration starting from there. Therefore, we chose a location asymptotically close to the horizon, $r_{in} \rightarrow 2r_g$. Very close to the horizon gravity overwhelms all other interactions, therefore the flow becomes adiabatic, *i.e.*, as $r_{in} \rightarrow 2r_g$, $v \rightarrow c$ and $E \rightarrow \mathcal{E}$. At r_{in} , for one-temperature inviscid flow, there are two unknowns v_{in} and Θ_{in} (or T_{in}). So, for a given set of constants of motion, one can iterate Θ_{in} and obtain for each iteration a corresponding value of v_{in} (from the supplied value of E , see step 3 in Section 3.3.1). Taking these inner boundary values, we integrate the differential equations of v and Θ , to obtain a solution. It is not necessary that this solution would be transonic or pass through an r_c . So, we iterate Θ_{in} , until for a unique set of Θ_{in} and v_{in} , the solution would pass through a unique r_c (step 4 in Section 3.3.1). At the sonic point, $dv/dr|_{r_c} = 0/0$ form. The pictorial representation of this methodology is given in Fig. 3.3.

In the two-temperature regime, instead of two unknowns (v_{in} and Θ_{in}), we now have three unknowns: v_{in} , Θ_{ein} and Θ_{pin} at r_{in} . This is because of the presence of an extra temperature. But, unfortunately we do not have any additional equation, which can decide the relation between these variables. This makes the system degenerate. So now the methodology which needs to be followed, for a given set of constants of motion (E and \dot{M}) is, we fix Θ_{pin} to some arbitrary value and then follow the iteration technique used for finding one-temperature TSs (iterate on Θ_{ein} until the solution obtained satisfies, at any given r , the sonic point conditions). It is to be noted that, we can similarly fix Θ_{ein} and iterate on Θ_{pin} . Both of these methods would yield the same result. We get a TS, characterised by Θ_{pin} , v_{in} , Θ_{ein} at r_{in} . Since, the value of Θ_{pin} is arbitrary, it can be changed to another value, and the same methodology could be followed to obtain another TS. Interestingly, all are for the same set of constants of motion (same E and \dot{M}).

5. TWO-TEMPERATURE FLOWS AROUND BLACK HOLES – I: SPHERICAL ACCRETION

One has to remember that, now the system is under-determined, the consequence of which will be seen in the next section. It may be further noted that, while presenting results, we prefer to quote T_{pin} or T_{ein} , instead of Θ_{pin} or Θ_{ein} respectively. This will make it easier for the reader to relate to the problem.

5.4 RESULTS

We initially assume $Q_{\text{p}}^+ = 0$ to discuss various features of two-temperature solution. The effect of $Q_{\text{p}}^+ \neq 0$ will be discussed later in Section 5.4.3.6.

5.4.1 INVESTIGATING DEGENERACY IN TWO-TEMPERATURE FLOWS

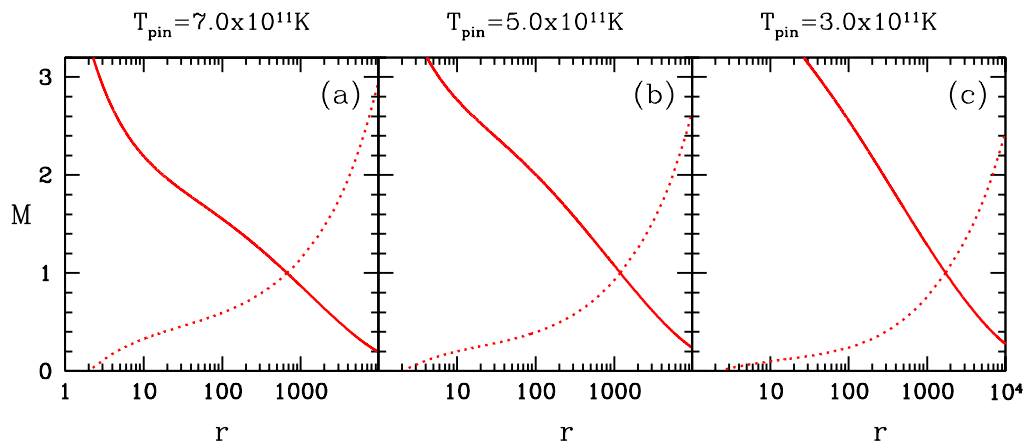


Figure 5.2: Accretion M (solid, red) and wind M (dotted, red) as a function of r are plotted. The different solutions in different panels are obtained by changing T_{pin} (values of which are written at the top of each panel) but are for the same set of constants of motion $\Rightarrow \dot{M} = 0.01\dot{M}_{\text{Edd}}$ and $E = 1.0001$. The solution is for a $10M_{\odot}$ BH.

In Figs. 5.2a–c, we present the accretion solutions of two-temperature Bondi flow for $M_{\text{BH}} = 10M_{\odot}$, $\dot{M} = 0.01\dot{M}_{\text{Edd}}$ and $E = 1.0001$. Each panel shows the accretion Mach number or $M = v/a_s$ (solid, red) and corresponding wind M (dotted, red) as a function of r . The crossing points are the location of sonic/critical points. The solid red line represents the global transonic accretion solution, because it satisfies the BH boundary conditions — subsonic very far away and reaching $v \rightarrow c$ near the BH horizon. The three solutions plotted in the figure are obtained by changing the proton temperature near the horizon, T_{pin} ($T_{\text{pin}} = T_{\text{p}}|_{r \rightarrow r_{\text{in}}}$), but for the same set of constants of motion for a given BH mass. This implies that different values of T_{pin} would yield different solutions, each with a unique sonic point position and sonic point properties. In Section 5.3.1, we pointed out that the two-temperature regime is under-determined, because we need to have information of an

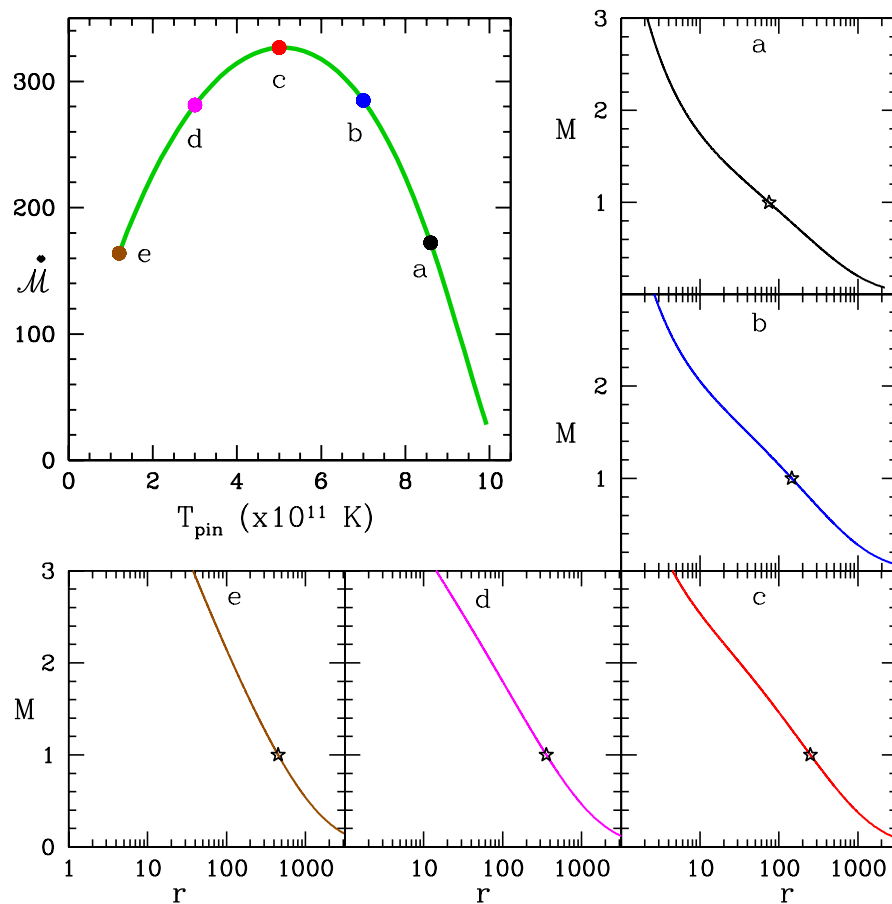


Figure 5.3: Top left panel: Variation of \dot{M}_{in} as a function of T_{pin} for accretion flow with $\dot{M} = 0.1\dot{M}_{Edd}$ and $E = 1.001$ onto a $10M_{\odot}$ BH. Panels ‘a’ to ‘e’ presents M vs r (solid) corresponding to each of the points ‘a’—‘e’ on the \dot{M}_{in} – T_{pin} curve. The stars represent the location of the sonic points (r_c). At $T_{pin} = 5.0 \times 10^{11} K$ (marked ‘c’) entropy maximises, so panel ‘c’ is the correct solution for the given set of constants of motion: E and \dot{M} .

extra unknown and the set of equations are incomplete. The degeneracy in solution is the direct fall out of such a scenario. All transonic two-temperature solutions, whether in exact GR or in pseudo-Newtonian regime, suffers from this deficiency. In the next section we will discuss, the physical principle to be followed in order to obtain a unique two-temperature transonic solution.

5.4.2 ENTROPY MEASURE AS A TOOL TO REMOVE DEGENERACY IN TWO-TEMPERATURE FLOWS

As has been shown in Figs. 5.2a—c, for a given set of constants of motion namely E and \dot{M} , there can be a plethora of TSSs, each differentiated by the T_{pin} at r_{in} . Now the only way this degeneracy can be removed is by invoking the second law of thermodynamics. It has been discussed in Section 4.4.2, that a general analytical expression of entropy measure

5. TWO-TEMPERATURE FLOWS AROUND BLACK HOLES – I: SPHERICAL ACCRETION

is not possible, however, the entropy of the accreting matter very close to the BH can be calculated using Eq. 4.10. So in Fig. 5.3, top left panel, we plot the measure of entropy $\dot{\mathcal{M}}_{\text{in}}$ at $r = r_{\text{in}}$ as a function of T_{pin} , for an accretion flow characterised by constants of motion $\dot{M} = 0.1\dot{M}_{\text{Edd}}$ and $E = 1.001$ onto a $10M_{\odot}$ BH. We have marked points ‘a’ to ‘e’ on the $\dot{\mathcal{M}}_{\text{in}}$ vs T_{pin} curve, and then have plotted the corresponding solutions (M vs r) in the adjacent panels also named as ‘a’ to ‘e’ (using same colour coding). It is easy to notice that the solutions with different T_{pin} s are completely different from each other, as the r_{c} s are found to vary by few $100r_{\text{g}}$ (for this particular set of E and \dot{M}). In particular, solution marked ‘a’ and that marked ‘e’, both, even share the same $\dot{\mathcal{M}}_{\text{in}}$ apart from sharing the same value of constants of motion. But, the sonic point of ‘a’ is at $r_{\text{c}} = 75.008$ and that of ‘e’ is at $r_{\text{c}} = 451.297$. Different proportions of T_{e} and T_{p} might give rise to the same $\dot{\mathcal{M}}_{\text{in}}$, all for the same set of E and \dot{M} ! This also implies a wrong choice of solution would lead us to wrong conclusions about the physical processes around BHs. *However, only one of them is correct.* It must be noticed that, of all the solutions, the entropy distribution has single well behaved maxima at $T_{\text{pin}} = 5 \times 10^{11}\text{K}$, and therefore, by the second law of thermodynamics, the accretion solution corresponding to this entropy at point ‘c’ on the curve is the correct one. In this way we constrain the degeneracy in two-temperature accretion flows.

5.4.3 PROPERTIES OF UNIQUE TWO-TEMPERATURE TRANSONIC SOLUTIONS

In the sections to follow, analysis of two-temperature flows were done using the maximum entropy solution, obtained by following the methodology discussed above.

5.4.3.1 CRITICAL POINT PROPERTIES:

For an adiabatic flow, given a value of E , location of sonic point is known a priori (Kumar et al., 2013). Since, in our case the flow is dissipative, sonic point can be located, only during obtaining of the solution. Two-temperature flows are under-determined, thus unique r_{c} can only be obtained after invoking the second law of thermodynamics. Taking all these factors into consideration, we plot E as a function of r_{c} (Fig. 5.4a); while v_{c} (Fig. 5.4b); Γ_{pc} , Γ_{ec} (Fig. 5.4c) and $\dot{\mathcal{M}}_{\text{in}}$ (Fig. 5.4d) are plotted as functions of E . Each panel has different curves representing accretion rates: $\dot{M} = 0.01\dot{M}_{\text{Edd}}$ (solid, yellow), $0.10\dot{M}_{\text{Edd}}$ (dotted, red), $0.50\dot{M}_{\text{Edd}}$ (dashed, magenta), $1.00\dot{M}_{\text{Edd}}$ (long-dashed, green) and $5.00\dot{M}_{\text{Edd}}$ (dot-dashed, blue). Here a BH of $10M_{\odot}$ has been considered. For low accretion rates ($\dot{M} \leq 0.1\dot{M}_{\text{Edd}}$), the range of r_{c} s can be anywhere between 3 to ∞ , while, for higher accretion rates, the r_{c} range decreases significantly (see, Fig. 5.4a). In presence of significant cooling (*i.e.*, higher \dot{M}), hot flows from larger distances can be accreted, which otherwise could not be accreted. Similarly, flows with higher E suggests higher thermal energies at infinity. As a result, v_{c} and the entropy ($\dot{\mathcal{M}}_{\text{in}}$) both are higher, for flows with

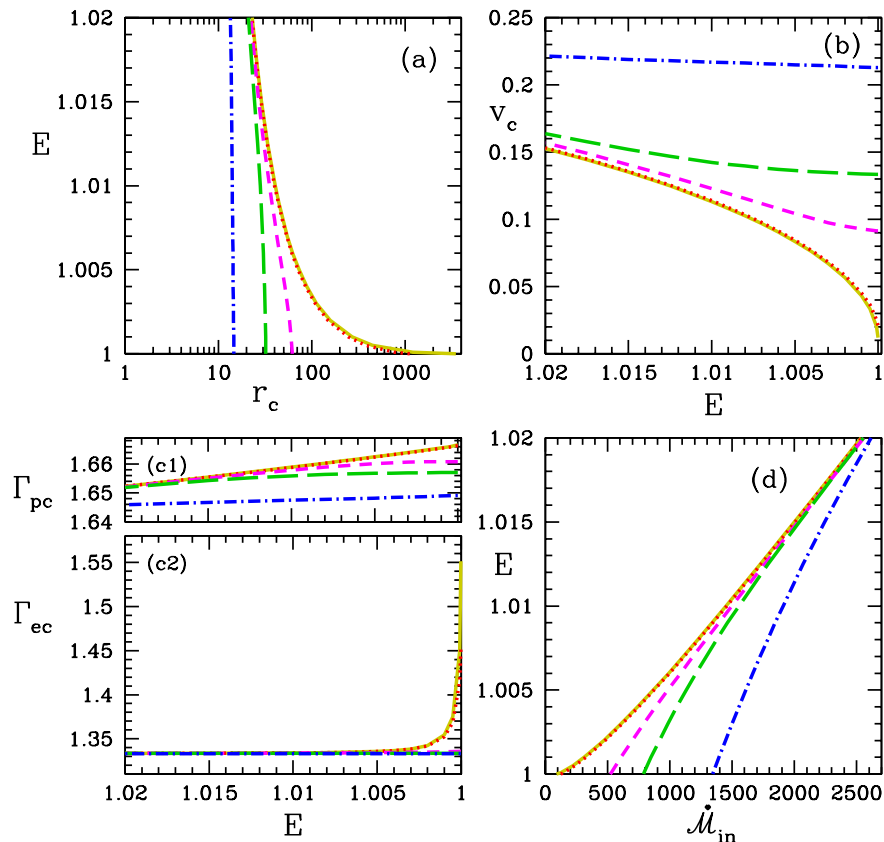


Figure 5.4: Variation of sonic points and its properties with the accretion rate (\dot{M}) of the BH. Here we have assumed $M_{\text{BH}} = 10M_{\odot}$. We have used accretion rate values, $\dot{M} = 0.01\dot{M}_{\text{Edd}}$ (solid, yellow), $0.10\dot{M}_{\text{Edd}}$ (dotted, red), $0.50\dot{M}_{\text{Edd}}$ (dashed, magenta), $1.00\dot{M}_{\text{Edd}}$ (long-dashed, green) and $5.00\dot{M}_{\text{Edd}}$ (dot-dashed, blue).

higher \dot{M} and E (see, Fig. 5.4b). The adiabatic indices plot present in Fig. 5.4c, concludes that electrons generally remain relativistic $\Gamma_{\text{ec}} \sim 4/3$, except when r_c is located very far away from the central BH where the temperatures are very low. While, $\Gamma_{\text{pc}} \sim 5/3$ suggests that protons are almost non-relativistic, irrespective of the location of r_c . This variation in Γ for different species, justifies our use of CR EoS. From all the plots it is clear that, for spherical accretion, there can be only one sonic point corresponding to a given E .

5.4.3.2 FLOW VARIABLES AND EMISSIVITY

In Figs. 5.5a–f, we present various flow variables corresponding to the unique Bondi accretion solution onto a BH of $10M_{\odot}$. The constants of motion are, $E = 1.00001$ and $\dot{M} = 0.01\dot{M}_{\text{Edd}}$. The flow variables plotted are (a) M , (b) E , (c) T_{p} (dotted, blue) & T_{e} (solid, magenta), (d) Γ_{p} (dotted, blue) & Γ_{e} (solid, magenta), (e) v and (f) Coulomb coupling (Q_{ep} , single-dot long-dashed, orange) and total electron cooling (Q_{e}^- , solid,

5. TWO-TEMPERATURE FLOWS AROUND BLACK HOLES – I: SPHERICAL ACCRETION

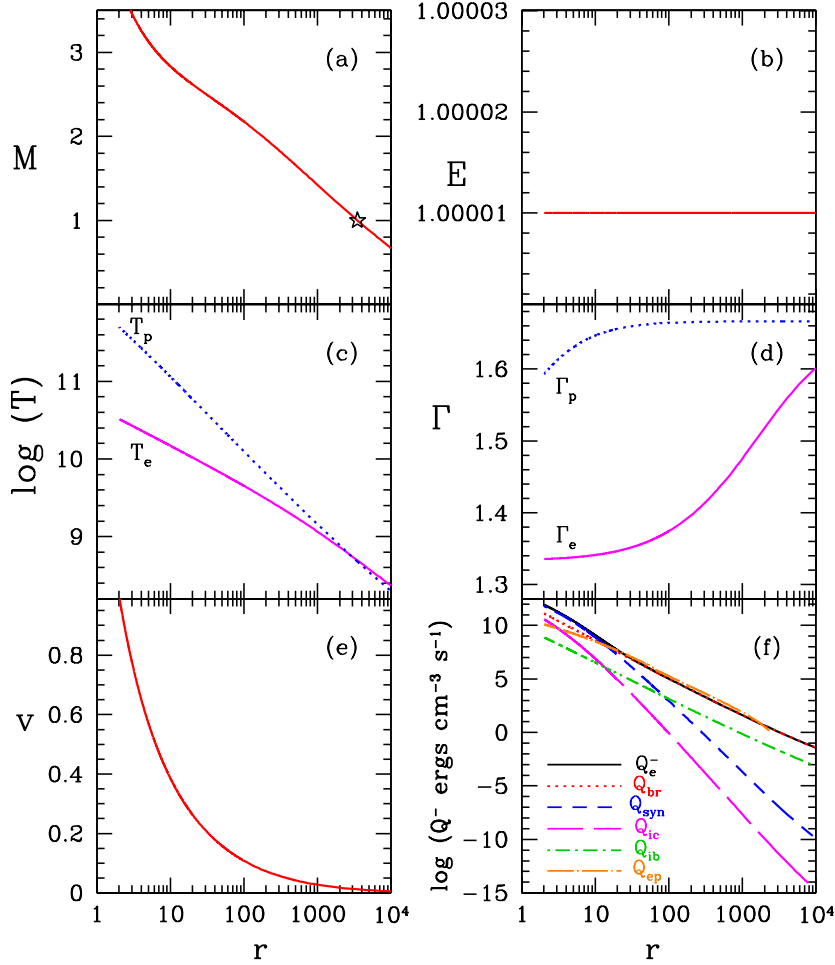


Figure 5.5: Variation of (a) M ; (b) E ; (c) T_p (dotted, blue) and T_e (solid, magenta); (d) Γ_p (dotted, blue) and Γ_e (solid, magenta); (e) v ; and (f) Coulomb coupling (Q_{ep} , single-dot long-dashed, orange) and total electron cooling (Q_e^- , solid, black) alongwith the individual components: bremsstrahlung (Q_{br} , dotted, red), synchrotron (Q_{syn} , short-dashed, blue), inverse-Comptonization (Q_{ic} , long-dashed, magenta) and inverse-bremsstrahlung (Q_{ib} , single-dot short-dashed, green) are plotted as functions of r . The black star on the M distribution (panel a) represent the location of r_c . The accretion disc parameters are, $E = 1.00001$, $\dot{M} = 0.01\dot{M}_{Edd}$ and $M_{BH} = 10M_{\odot}$.

black) alongwith the individual components: bremsstrahlung (Q_{br} , dotted, red), synchrotron (Q_{syn} , short-dashed, blue), inverse-Comptonization (Q_{ic} , long-dashed, magenta) and inverse-bremsstrahlung (Q_{ib} , single-dot short-dashed, green) emissivities. The black star in Fig. 5.5a indicates the location of r_c . The fact that E remains unchanged throughout the flow (see, Fig. 5.5b, solid red), confirms that, it is indeed a constant of motion even in the presence of dissipation. For matter present at very large r , $T_e \approx T_p$ while, $T_e < T_p$ for range $2 < r < 1000$ (Fig. 5.5c). Moreover, the electron fluid while travelling

a distance of about $10^4 r_g$ on the way to the BH, spans a temperature range of more than two orders of magnitude (Fig. 5.5c, solid, magenta) which means, $1.6 > \Gamma_e \sim 4/3$. The same is reflected in the Γ_e plot (see, Fig. 5.5d, solid, magenta) which do not have any constant value. On the other hand, the temperature of the proton fluid spans more than three orders of magnitude (Fig. 5.5c, dotted, blue), but due to its higher mass, Γ_p does not change much and remains around $\sim 5/3$, achieving a minimum value of ~ 1.6 just near the horizon, where T_p is maximum (Fig. 5.5d, dotted, blue). The distribution of Γ_e & Γ_p would change for a different set of constants of motion (E , \dot{M}). In other words, considering CR EoS is important. In Fig. 5.5f, we see that, Q_{br} dominates the radiative process for this particular set of E and \dot{M} , except near the horizon where the $Q_{\text{syn}} \gtrsim Q_{\text{br}}$. Q_{ic} is weak all throughout the flow, since the accretion rate of the system is low. Q_{ep} is comparable to Q_e^- , for a large range of r , except near the horizon, where, $Q_{\text{ep}} < Q_e^-$. This suggests that near the horizon electrons cool more, than its heated through Coulomb coupling. As a result, $T_e \ll T_p$, near the event horizon. So one can say, attainment of one-temperature distribution or, two-temperature distribution depends on the relative strength of Coulomb interaction and various radiative processes.

5.4.3.3 DEPENDENCE OF ACCRETION FLOW ON E AND \dot{M}

In Figs 5.6a₁—c₃, we show how global transonic two-temperature solutions depend on the value of E , a constant of motion. In the plot, we increased its value from left to right: $E = 1.0001$ (a₁, a₂, a₃), $E = 1.001$ (b₁, b₂, b₃) and $E = 1.01$ (c₁, c₂, c₃). The other flow parameters are $\dot{M} = 0.01\dot{M}_{\text{Edd}}$ and $M_{\text{BH}} = 10M_{\odot}$. We have plotted in Fig 5.6 top row: v (a₁, b₁, c₁) using solid red line; middle row: electron number density, n_{e^-} (a₂, b₂, c₂) using solid green line and bottom row: T_p & T_e (a₃, b₃, c₃) using dotted blue and solid magenta line respectively. The black star on the velocity curve shows the location of r_c . For higher E , r_c is formed closer to the horizon (also, see Fig. 5.4a). Increasing E , raises the temperature at the outer boundary and reduces v , thus n_{e^-} (in cm^{-3}) at the outer boundary is also higher for higher E .

Increasing \dot{M} has a similar effect on the accretion solutions. We study it using a similar plot as Fig. 5.6, but now with varying \dot{M} values, increasing from left to right and with fixed $E = 1.0001$ (see, Fig. 5.7). The values of \dot{M} are: $0.01\dot{M}_{\text{Edd}}$ (a₁ — a₄), $0.2\dot{M}_{\text{Edd}}$ (b₁ — b₄) and $0.5\dot{M}_{\text{Edd}}$ (c₁—c₄). We include an additional row at the end (4th row) which plots the different radiative emissivities present in the system as a function of r (Figs. 5.7a₄, b₄, c₄). Inset of each panel in the last row, is plotted, Q_e^- which is represented using solid, black curve, Q_{br} in dotted red, Q_{syn} in short-dashed blue, Q_{ic} in long-dashed magenta, Q_{ib} in single-dot short-dashed green and Q_{ep} using single-dot long-dashed orange curve.

Emission increases with the increase in \dot{M} and therefore a system can accrete hotter flow from large distances. As a result, r_c form closer to the horizon (also, see Fig. 5.4a). This is visible in Fig. 5.7 top row, where black star represents r_c . For low \dot{M} , we can

5. TWO-TEMPERATURE FLOWS AROUND BLACK HOLES – I: SPHERICAL ACCRETION

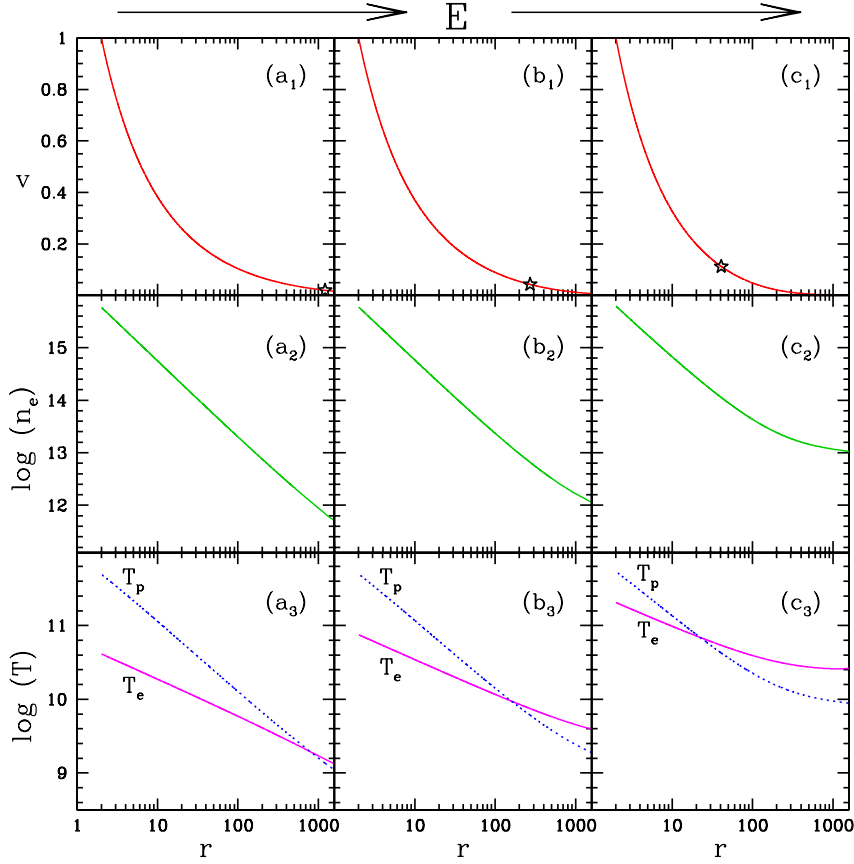


Figure 5.6: Variation of v (a_1, b_1, c_1); electron number density, n_{e^-} (a_2, b_2, c_2) and T_p & T_e in panels (a_3, b_3, c_3), as a function of r . The generalized Bernoulli parameter changes from the left panels $E = 1.0001$ (a_1, a_2, a_3), to the middle panels $E = 1.001$ (b_1, b_2, b_3) and then to the right panels $E = 1.01$ (c_1, c_2, c_3). Other parameters selected are $M_{\text{BH}} = 10M_{\odot}$ and $\dot{M} = 0.01\dot{M}_{\text{Edd}}$.

see from Fig. 5.7a₄ that, Q_{br} dominates (also see, Fig. 5.5f). Interestingly, for a distance $20 < r < 1000$, $Q_{\text{ep}} \approx Q_{e^-}$. Thus, $T_e \approx T_p$ in the same range. As the accretion rate increases, inverse-Compton cooling becomes more efficient and starts to dominate (Fig. 5.7b₄). The Q_{ep} term becomes less effective, as a result of which, the disagreement between T_e and T_p values increases. For even higher \dot{M} (Fig. 5.7c₄), inverse-Compton dominates the cooling throughout the accretion flow. The Coulomb term becomes even weaker and therefore T_e and T_p becomes significantly different from each other.

5.4.3.4 EFFECT OF THE MASS OF THE CENTRAL BH

To investigate the effect of change of BH mass, we plot in Fig. 5.8, n_{e^-} (a_1, b_1, c_1) and emissivities ($Q_{e^-}^-$, Q_{br} , Q_{syn} , Q_{ic} , Q_{ib} , Q_{ep}) (a_2, b_2, c_2) as a function of r in units of r_g . From left to right, BH mass increases with values: $M_{\text{BH}} = 10M_{\odot}$ (a_1, a_2), $M_{\text{BH}} = 10^3M_{\odot}$

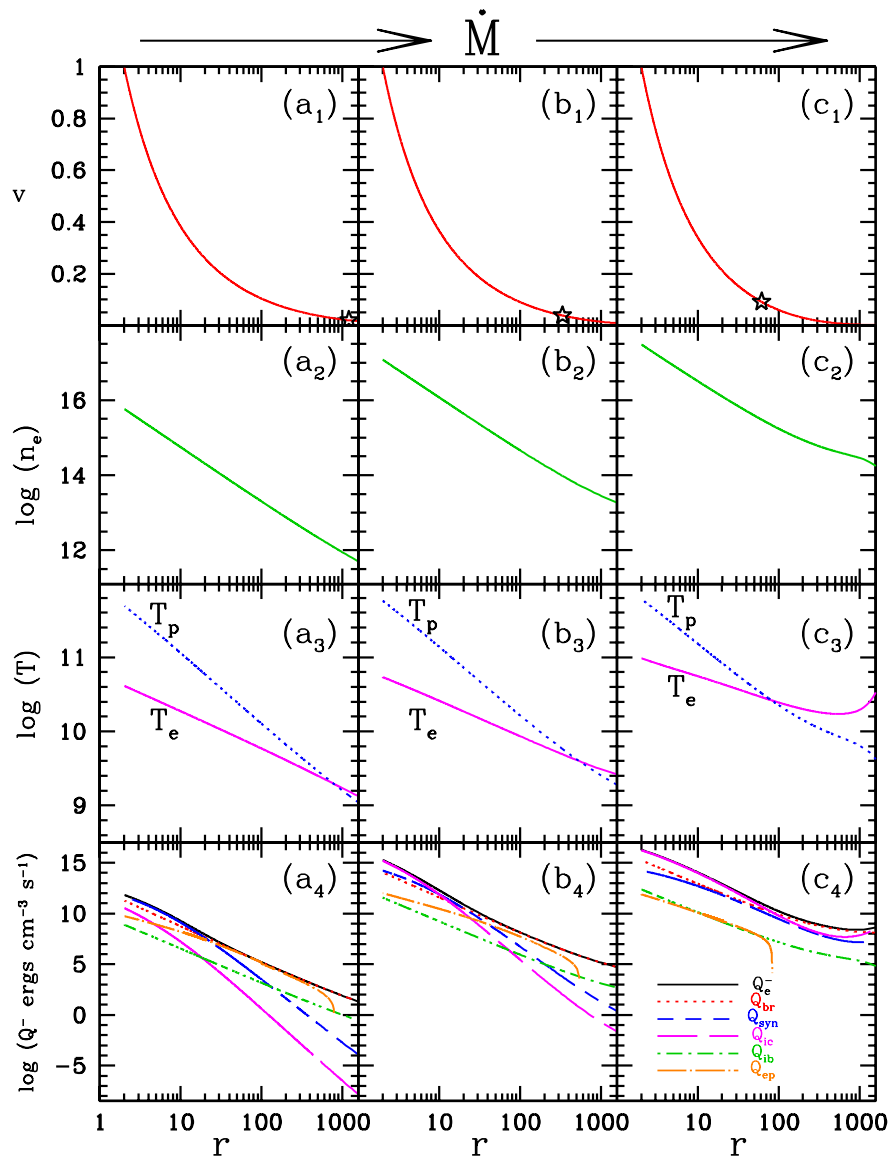


Figure 5.7: Variation of v (a₁, b₁, c₁); electron number density, n_{e^-} (a₂, b₂, c₂), T_p & T_e in panels (a₃, b₃, c₃) and various emissivities (Q_e^- , Q_{br} , Q_{syn} , Q_{ic} , Q_{ib} and Q_{ep}) (a₄, b₄, c₄) as a function of r . The accretion rate changes from the left panels $\dot{M} = 0.01$ (a₁, a₂, a₃, a₄), to the middle panels $\dot{M} = 0.2$ (b₁, b₂, b₃, b₄) and then to the right panels $\dot{M} = 0.5$ (c₁, c₂, c₃, c₄). Other parameters selected are, $M_{BH} = 10 M_\odot$ and $E = 1.0001$.

(b₁, b₂) and $M_{BH} = 10^6 M_\odot$ (c₁, c₂). Other flow parameters are, $E = 1.0001$ and $\dot{M} = 0.5 \dot{M}_{Edd}$. The accretion rate is described in units of Eddington rate, thus the information of BH mas is imprinted inside it (see, Eq. 1.7). So, for a given value of \dot{M} , the net amount of mass flux (in units of g/s) increases with the increase in central BH mass. Eventually, the length-scale increases. Thus, $1r_g$ is equivalent to $\sim 30\text{km}$ for a $10M_\odot$ BH, 3000km for 10^3M_\odot , $3 \times 10^6\text{km}$ for 10^6M_\odot BH and so on.

5. TWO-TEMPERATURE FLOWS AROUND BLACK HOLES – I: SPHERICAL ACCRETION

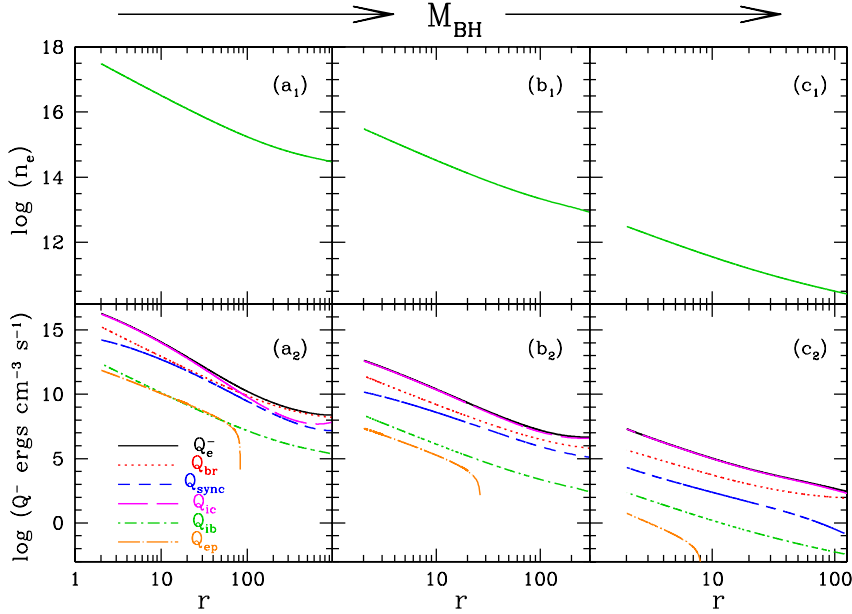


Figure 5.8: Variation of n_{e^-} (a₁, b₁, c₁); emissivities and Coulomb coupling (a₂, b₂, c₂) as function of r . Left column panels (a₁ and a₂) are for $M_{\text{BH}} = 10M_{\odot}$, the middle column are for $M_{\text{BH}} = 10^3M_{\odot}$ (b₁, b₂) and for right column $M_{\text{BH}} = 10^6M_{\odot}$ (c₁, c₂). Other parameters selected are $E = 1.0001$ and $\dot{M} = 0.5\dot{M}_{\text{Edd}}$.

Increase in BH mass suggests that n_{e^-} (in units of cm^{-3}) as well as local emissivity decreases, because it is proportional to the inverse of the mass of the BH. But the total cooling will increase since the volume would increase as M_{BH}^3 . As a result, net radiative cooling increases with M_{BH} . This allows hotter matter to flow onto a more massive BH, which pushes r_c closer to horizon even for matter starting with same E and \dot{M} (in units of \dot{M}_{Edd}). The sonic point for $M_{\text{BH}} = 10M_{\odot}$, 10^3M_{\odot} and 10^6M_{\odot} is at $r_c = 61.535$, 39.966 and 19.786 in units of r_g respectively. So it is clear that radial accretion onto larger BH, is hotter and more luminous than the smaller ones. As seen in Figs. 5.7a₄—c₄, for low \dot{M} where the number density is lower, Q_{ic} is generally lower than Q_{br} or Q_{sync} . But as we increase \dot{M} , Q_{ic} starts to dominate. Similarly, larger accreting BHs which increases the magnitude of mass flux, are more luminous and the total emissivity is dominated by Q_{ic} . This is plotted in Figs. 5.8a₂—c₂ (long-dashed, magenta). It also shows that for a lower mass BH and higher \dot{M} , Q_{sync} is similar to Q_{br} , however, for higher M_{BH} , Q_{br} is much stronger than Q_{sync} . Whatever may be the mass of the central BH or accretion rate, Q_{ib} is significantly lower than the net emissivity. The Coulomb coupling term Q_{ep} is negligible for high \dot{M} and decreases even more for flows around massive BHs, thus justifying the presence of two-temperature flows inside the system.

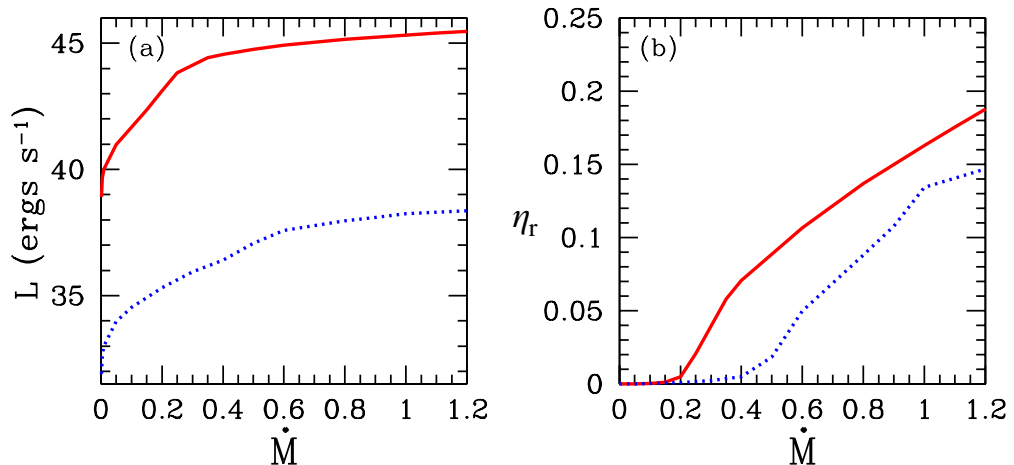


Figure 5.9: (a) Luminosity, L , and (b) efficiency η_r as a function of \dot{M} . Each curve corresponds to $M_{\text{BH}} = 10^8 M_{\odot}$ (solid, red) and $M_{\text{BH}} = 10 M_{\odot}$ (dotted, blue). $E = 1.001$ for both these flows.

5.4.3.5 LUMINOSITY AND EFFICIENCY OF THE SYSTEMS

Shapiro (1973) computed luminosity from Bondi flow only via bremsstrahlung process, and concluded that radial flow is not efficient enough. Also, the accretion model considered was not strictly of two-temperatures and all classes of solutions were not investigated. From Figs. 5.5 — 5.7 of this chapter, it is quite clear that different cooling processes starts to dominate at different \dot{M} . For lower \dot{M} , inverse-Compton is not a very dominant process, while this process is important for higher \dot{M} . Therefore, it can be safely assumed that both luminosity and efficiency of an accretion flow depends on \dot{M} .

In Fig. 5.9a, we plot the variation in luminosity (L) in units of ergs s^{-1} , with change in \dot{M} , for an accretion flow around $10 M_{\odot}$ (dotted, blue) and $10^8 M_{\odot}$ (solid, red) BH. In both cases, $E = 1.001$. The efficiency of a BH system can be written as, $\eta_r = L/(\dot{M}c^2)$, which is plotted in Fig. 5.9b, as a function of \dot{M} . For low $\dot{M} \lesssim 0.2\dot{M}_{\text{Edd}}$, the efficiency of conversion of accretion energy to radiation is really low, $\eta_r \lesssim 0.01$ for both kind of BHs. However, for $\dot{M} > 0.5\dot{M}_{\text{Edd}}$, the efficiency $\gtrsim 0.1$ for accretion onto a $10^8 M_{\odot}$ BH and comfortably produce $L \gtrsim 10^{44} \text{ergs s}^{-1}$. At super-Eddington accretion rates, super-massive BH produce luminosities above $10^{45} \text{erg s}^{-1}$, with efficiency $\eta_r \sim 0.2$.

5.4.3.6 EFFECT OF DISSIPATIVE PROTON HEATING

So far in this chapter, we have not assumed any explicit heating. In this section we consider dissipative magnetic heating, following the footsteps of Ipser & Price (1982). It mainly affects the protons, however, through Coulomb coupling the dissipated energy is also transmitted to the electrons. In Fig. 5.10, we plot in the top row (a₁–b₁): v (solid,

5. TWO-TEMPERATURE FLOWS AROUND BLACK HOLES – I: SPHERICAL ACCRETION

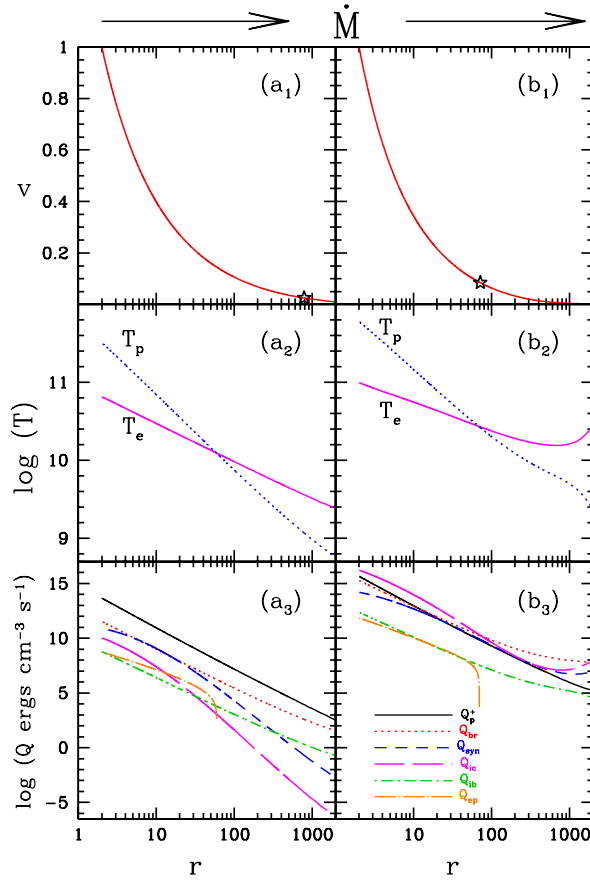


Figure 5.10: Three-velocity v (a₁, b₁), temperatures (a₂, b₂) and emissivities, heating and Coulomb coupling (a₃, b₃) as a function of r . The solutions are for $\dot{M} = 0.01\dot{M}_{\text{Edd}}$ (a₁–a₃) and $\dot{M} = 0.5\dot{M}_{\text{Edd}}$ (b₁–b₃). Other parameters are, $E = 1.001$ and $M_{\text{BH}} = 10M_{\odot}$.

red), middle row (a₂–b₂): temperatures, T_e (solid, magenta) & T_p (dotted, blue) and last row (a₃–b₃) various emissivities, heating rate (solid, black) and the Coulomb coupling term (all labelled inset). The two different columns are for $\dot{M} = 0.01\dot{M}_{\text{Edd}}$ (Figs. 5.10a₁–a₃) and $\dot{M} = 0.5\dot{M}_{\text{Edd}}$ (Figs. 5.10b₁–b₃). The flow parameters are, $E = 1.001$ and $M_{\text{BH}} = 10M_{\odot}$. Comparing Figs. 5.10a₁–a₃ with Figs. 5.6b₁–b₃, which are for the same accretion parameters but the latter is without heating, the effect of heating is clearly seen. The sonic point in the present case is pushed far away from the central BH. This concludes that the BH is accreting matter with lower temperatures at the outer boundary. Also, since \dot{M} is low, the heating term Q_p^+ dominates. For higher $\dot{M} = 0.5\dot{M}_{\text{Edd}}$ (see, Figs. 5.10b₁–b₃), Q_e^- dominates over Q_p^+ . The Coulomb coupling on either case is negligible. Heating processes quantitatively affect the solutions, if the dissipative heat only heats the protons. This is because, Coulomb coupling is not very effective in energy transfer from protons to electrons. This was also concluded by [Manmoto et al. \(1997\)](#).

5.5 DISCUSSIONS AND CONCLUSIONS

In this chapter, we focus on obtaining unique transonic two temperature accretion solution in steady state from all the degenerate solutions. First, we investigated the entropy accretion rate form and proposed a novel methodology by working in spherical flows. A correct two-temperature solution is very important, because a proper electron temperature distribution for a given boundary condition, produces the correct spectrum and luminosity. Moreover, analytical solutions obtained in this chapter is also important since, these solutions may act as tests, as well as, may be used as initial conditions for simulation codes.

Although there are few papers in the one-temperature regime, which used constants of motion to obtain the solutions, but as far as we know, probably there are none in the two-temperature domain which even addresses the issue of constants of motion while obtaining the solutions. Also, the use of a relativistic EoS (see, Eq. 2.30), has been few and far between even in the one-temperature theory. It may be remembered that, a fluid solution is not just characterised by its energy but also by its entropy and according to the second law of thermodynamics, any physical solution should correspond to the one with highest entropy. It was Bondi (1952) who used this principle in order to stress that a transonic solution is the correct accretion solution under the influence of gravity. Later Becker and his collaborators (Becker et al., 2008; Becker & Le, 2003; Le et al., 2016; Lee & Becker, 2017) used the information of energy as well as the entropy to obtain transonic accretion solutions around a BH in presence of dissipation. Since the set of equations in one-temperature flow is complete, so finding a transonic solution suffices the criteria for second law of thermodynamics (Bondi, 1952). However, as has been discussed extensively in this chapter, as well as the previous Chapter 4, the set of governing equations are less than the number of variables, second law of thermodynamics becomes essential even to find a proper solution. The novelty of this work is that we identified this long outstanding problem and laid down a prescription to overcome it, by actually following the footsteps of Bondi and Becker et al.

To focus on the problem of degenerate two-temperature solutions and its possible remedy, we considered a simple accretion model of radial flow onto a BH, since it possess a single sonic point. More complicated accretion models would have concealed the essence of the problem. Simple as it may be, but spherical accretion is preferred mode of accretion onto isolated BHs immersed in inter-stellar matter and this has been verified by many authors (Beskin & Karpov, 2005; Davies & Pringle, 1980). Moreover, the inner region of a BH accretion disc is also quasi-spherical and many researchers have considered radial inflow to mimic inner accretion disc (Kazanas et al., 1997; Titarchuk et al., 1997). Since radial flow has no angular momentum (quasi-spherical flow may have minuscule amount), viscous transport should be negligible for accretion onto isolated BH or in the inner region

5. TWO-TEMPERATURE FLOWS AROUND BLACK HOLES – I: SPHERICAL ACCRETION

of an accretion disc. Authors who have obtained transonic two-temperature solution before (Manmoto et al., 1997; Nakamura et al., 1996), are of the view that Coulomb coupling is not an efficient energy transfer process. Therefore any viscous heating will anyway not find its way into heating up the electrons. Looking into all these factors, we ignored viscous dissipation and concentrated on two-temperature accretion flows by only considering cooling mechanisms in this chapter. However, at the end we did consider the effect of dissipative proton heating, following the work of Ipser & Price (1982), to mimic the effects of viscous heat dissipation (if any, present inside the flow).

Using the methodology explained in Section 5.3, we obtained all possible transonic solutions for any given set of E and \dot{M} and found that the entropy maximised at a particular solution (see, Fig. 5.3). Following the second law of thermodynamics, we select the solution with maximum entropy as the solution which nature would prefer for the given set of constants of motion.

Thereafter, we studied and analysed the unique two-temperature spherical flows around BHs. We found that, for higher E and higher \dot{M} , sonic points were formed closer to the horizon, while for lower values of both the constants of motion, sonic points occurred at larger distances. We showed that for correct solutions the adiabatic index of electron and proton fluid varies from non-relativistic to relativistic values. We also showed that, different cooling processes become important at different values of \dot{M} . Therefore, radiative efficiency depends on \dot{M} . For $\dot{M} < 0.1\dot{M}_{\text{Edd}}$, whether it is a super-massive BH or a stellar one, the accretion flow is radiatively inefficient. But for a super-massive BH with $\dot{M} \gtrsim 0.6\dot{M}_{\text{Edd}}$, the accretion flow becomes radiatively efficient *i.e.*, more than 10%. On the other hand, for stellar-mass BHs, accretion becomes radiatively efficient when the accretion rate is close to the Eddington rate. We note here that special and general relativistic effects has not been considered in this work, while computing the luminosity and efficiency. Also photon trapping and photon bending effects were ignored. We take care of all these important factors in the next chapter, where we perform spectral analysis of more realistic accretion flows around BHs. Thus, the numbers quoted here for L and η_{r} can slightly reduce, but only near the horizon, where these effects are strong. The conclusions do not change qualitatively.

In this work it has been observed that, whenever inverse-Compton process dominates, the accretion flow becomes more luminous. This process becomes important for higher accretion rates. Therefore, it is not necessary that radial accretion will always be radiatively inefficient. It has been confirmed from the analysis done in this work is that, heating has a quantitative effect on the accretion solutions. Also, the Coulomb coupling is always found to be weak. Thus, an accretion flow should necessarily be of two-temperatures.

Chapter 6

TWO-TEMPERATURE FLOWS AROUND BLACK HOLES – II: ROTATING ACCRETION FLOWS

6.1 INTRODUCTION

In this chapter, we extend the work of finding unique two-temperature accretion flows, to more realistic accretion disc models. Matter accreted from the surrounding medium or a binary companion might possess angular momentum, which leads to the formation of accretion discs. These discs were introduced first by [Shakura & Sunyaev \(1973\)](#) and thus they are popularly known as SSDs. Rotating flows possess multiple critical points and can also harbour shocks ([Fukue, 1987](#); [Liang & Thompson, 1980](#)). Since, a two-temperature problem is degenerate, the presence of MCP complicates the scenario.

In Chapter 4, the problem of degeneracy was identified and we proposed a novel methodology to constrain this degeneracy. In Chapter 5, we successfully validated the methodology and obtained unique transonic two-temperature accretion solutions, for a given set of constants of motion, results of which were published in [Sarkar & Chattopadhyay \(2019a, hereafter, SC19a\)](#). But it was applied to flows having zero angular momentum. Such spherical flows have single sonic point which simplifies our problem, allowing us to focus only on the issue of degeneracy in two-temperature regime. In this chapter, we include angular momentum and analyse two types of accretion discs. First,

The results of this chapter are published in:

(1) [Sarkar, Shilpa; Chattopadhyay, Indranil and Laurent, Philippe](#); 2020, *Astronomy & Astrophysics*, **642**, A209.

(2) [Sarkar, Shilpa and Chattopadhyay, Indranil](#); 2019, *Journal of Physics Conference Series*, **1336**, 012019.

6. TWO-TEMPERATURE FLOWS AROUND BLACK HOLES – II: ROTATING ACCRETION FLOWS

we investigate *rotating conical accretion solutions* around BH. We discuss how SC19a is modified to obtain unique solution in the presence of MCP and shocks. Then, we move on to investigate *accretion flows in hydrostatic equilibrium* along the transverse direction. To handle the trans-relativistic nature of these flows, we use the CR EoS which freed us from specifying the adiabatic indices of each species.

Our motivation is to present a novel methodology to find unique transonic two-temperature accretion solutions for advective accretion discs around BHs. Radiative processes with proper special and general relativistic corrections have been incorporated, to compute the spectrum. In this chapter, we would like to analyse how the correct unique accretion solution depends on the constants of motion of the flow, along with the mass of the BH and discuss how these properties play an active role in shaping the spectrum. Furthermore, we intend to study the relative contribution of various radiative processes on the emitted spectrum and also investigate which part of the disc is likely to contribute the most in the emitted spectrum. In addition, we want to check whether an accretion shock imparts any special spectral signature. Apart from these, we would like to study the dependence of radiative efficiency and spectral index on the accretion rate and mass of the BH and also with the presence of different radiative processes.

6.2 ASSUMPTIONS AND EQUATIONS USED

In this chapter, we have worked in the pure GR regime to study two-temperature accretion flows around BHs. Also, we considered advection and radiative processes inside the system. Therefore, the equations of motion and approach used to model an accretion flow is similar to that used in Chapter 5 for spherical flows. But the difference is in the presence of angular momentum inside these flows. The exact expressions for differential equation of temperature and velocity, hence differ slightly, and have been discussed in this section. Angular momentum plays a very important role in accretion disc physics, because it can significantly modify the infall time scale. Also, a rotating flow can possess a maximum of three critical points: r_{ci} , r_{cm} and r_{co} , unlike in case of spherical flows where a single sonic point is present. In the MCP regime, shocks can also be present.

The dissipative processes assumed in this work are summarised below. For heating and cooling of protons :

$$Q_p^+ = \delta_B Q_B \quad \text{and} \quad Q_p^- = Q_{ep} + Q_{ib}, \quad (6.1)$$

respectively. And for heating and cooling of electrons :

$$Q_e^+ = (1 - \delta_B) Q_B + Q_{ep} + Q_{comp} \quad \text{and} \quad Q_e^- = Q_{br} + Q_{syn} + Q_{ic} \quad (6.2)$$

respectively. Therefore, $\Delta Q_p = \delta_B Q_B - Q_{ep} - Q_{ib}$ and $\Delta Q_e = (1 - \delta_B) Q_B + Q_{ep} + Q_{comp} -$

$Q_{\text{br}} - Q_{\text{syn}} - Q_{\text{ic}}$. More details regarding each term have been discussed in Section 2.5.

In our present study, we have investigated inviscid flows, since proper handling of GR form of viscosity in transonic flows is not trivial. The shear tensor in GR contains derivative of u_ϕ , v and other terms (Peitz & Appl, 1997). It is impossible to obtain a solution if all the terms of the shear tensor is considered. Peitz & Appl (1997) proposed an approximate form of shear tensor by neglecting all derivatives of v and then presented a limited class of solutions. Chattopadhyay & Kumar (2016) used the same form of viscosity but obtained the full range of solutions. Also they computed mass-loss from such advective accretion solutions. We envisage that the method to obtain viscous solution is not easy, since the Bernoulli parameter of viscous flow has no analytical form (see, Eq. 2.16). In addition, the sonic point is not known a priori and needs to be obtained as a part of eigenvalue of the solution. Moreover, the angular momentum on the horizon needs to be computed. And yet the solutions obtained are limited, because the viscosity is still phenomenological and various terms of the relativistic version of the shear tensor has to be neglected in order to obtain a solution. Two-temperature regime further complicates the problem, as has been pointed out above. Most of the works done in literature assumed Newtonian form of viscosity or the Shakura & Sunyaev α -viscosity prescription (hereafter SS), use of which, in our GR model would be inappropriate. So we avoided the use of any form of viscosity since the prime focus of this work, is to present a novel methodology to obtain unique transonic two-temperature solutions for accretion discs around BHs. In addition, it has been extensively shown in Figs. 2h-2i; 3h-3i of Chattopadhyay & Kumar (2016) that the specific angular momentum ($\lambda = -u_\phi/u_t$) and bulk angular momentum ($L = hu_\phi$) in few $100r_g$, is almost constant and sub-Keplerian. This is to be expected, as gravity supersedes all other interactions near the BH horizon. In order to exhibit the qualitative effect of viscosity, as a representative case, one-temperature, viscous accretion disc solutions are presented in Appendix A.1, by following the methodology of Chattopadhyay & Kumar (2016). We have used two forms of viscosity, where the viscous stress tensor is given by (i) $t_{r\phi} = -2\eta_v\sigma_{r\phi}$, (abbreviated as PA, see Eq. 2.14) and (ii) $t_{r\phi} = -\alpha_v p$ (SS form of viscosity). The form of $\sigma_{r\phi}$ of PA is adopted from Chattopadhyay & Kumar (2016); Peitz & Appl (1997) (also, see Chapter 3, where we used this viscous prescription). In Fig. A.1a, we show that for both the form of viscosities (PA and SS), $\lambda \approx \text{constant}$ for $r \lesssim 1000r_g$. Viscous dissipation can also heat up the matter. Thus, we compare the heating due to viscosity with the magnetic heat dissipated (also see, Section 2.5.2 and 5.4.3.6). In Fig. A.1b, we plot the heat dissipated by these processes. We see that, PA form of viscosity is stronger than the SS type of viscosity while it is in general much weaker than Q_B . It is comparable to Q_B only in a very narrow region. Thus, it is safe to conclude that the qualitative features of the flow are not hampered while neglecting viscosity.

In this chapter, we have ignored pion production and its contribution to the observed spectra, as well as ignored pair production arising from the interactions of high energy

6. TWO-TEMPERATURE FLOWS AROUND BLACK HOLES – II: ROTATING ACCRETION FLOWS

photons present inside the disc. Later in Appendix A.2 we will show from posteriori calculations regarding the contribution of both the processes.

The generalised Bernoulli parameter has the same form as in the previous Chapter (see, Section 5.2). The expression is given by Eq. 2.17. This is conserved throughout the flow.

6.2.1 CONICAL FLOWS

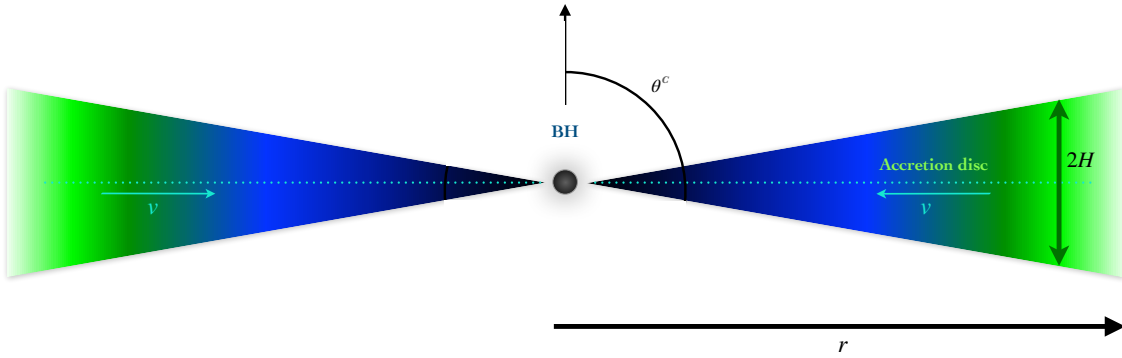


Figure 6.1: Cartoon diagram representing conical flow around a BH. The half-height is a constant function of r and θ^c is the angle which the surface of the flow makes with the normal.

In conical/wedge flows, $H = r \cos \theta^c$ (see, Fig. 6.2). Thus, \dot{M} has the same expression as Eq. 5.2. The energy equation can be simplified to obtain two differential equations for temperature, one for proton and another for electron. They are as follows:

$$\begin{aligned} \left. \frac{d\Theta_p}{dr} \right|_{\text{con}} &= -\frac{\Theta_p}{N_p} \left(\mathcal{A} + \frac{1}{v(1-v^2)} \frac{dv}{dr} \right) - \chi \mathbb{P}_{\text{con}} \\ \text{and } \left. \frac{d\Theta_e}{dr} \right|_{\text{con}} &= -\frac{\Theta_e}{N_e} \left(\mathcal{A} + \frac{1}{v(1-v^2)} \frac{dv}{dr} \right) - \mathbb{E}_{\text{con}}, \end{aligned} \quad (6.3)$$

where, $\mathcal{A} = -\frac{2r-3}{r(r-2)}$, $\mathbb{P}_{\text{con}} = \frac{\Delta Q_p \tilde{K}}{\rho u^r N_p}$ and $\mathbb{E}_{\text{con}} = \frac{\Delta Q_e \tilde{K}}{\rho u^r N_e}$. The subscript ‘con’ represents the conical flow. The differential equation for velocity is obtained by simplifying Eq. 2.13, using Eqs. 5.2, 6.3 and the CR EoS (see, Eqs. 2.31, 5.1), to get:

$$\left. \frac{dv}{dr} \right|_{\text{con}} = \frac{\mathcal{N}_{\text{con}}}{\mathcal{D}_{\text{con}}}, \quad (6.4)$$

where, $\mathcal{N}_{\text{con}} = -\frac{1}{r(r-2)} + \frac{\lambda^2 \gamma_\phi^2 (r-3)}{r^4} + a_s^2 \mathcal{A} + \frac{\Gamma_p N_p \mathbb{P}_{\text{con}} + \Gamma_e N_e \mathbb{E}_{\text{con}}}{h \tilde{K}} - \frac{\Delta Q}{\rho h u^r}$ and $\mathcal{D}_{\text{con}} =$

$$\frac{v}{1-v^2} \left(1 - \frac{a_s^2}{v^2}\right).$$

6.2.2 FLOWS IN HYDROSTATIC EQUILIBRIUM IN THE TRANSVERSE DIRECTION

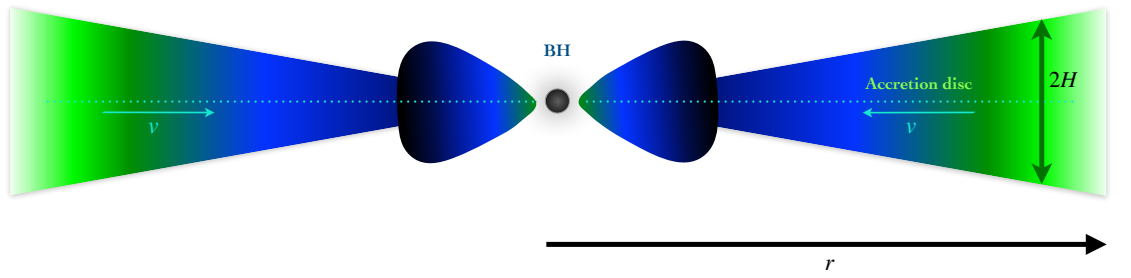


Figure 6.2: Cartoon diagram representing flows in hydrostatic equilibrium in the vertical direction. The half-height is a function of r, v, λ, Θ_e and Θ_p . In this cartoon diagram, a shocked solution is represented and therefore, the inner region is seen to expand suddenly at a given r . This is because the flow is in hydrostatic equilibrium and is allowed to expand freely (unlike conical flows). In shock-free solutions, sudden expansion of the disc does not occur. Rather, it is gradual, depending on the heating and cooling present in that region.

For flows in hydrostatic equilibrium in the vertical direction, the equation for half-height is given by Eq. 2.11. This can be simplified to:

$$H = \sqrt{\frac{[r^3 - \lambda^2(r-2)]}{\tilde{K}}} \left(\Theta_e + \frac{\Theta_p}{\chi} \right) \quad (6.5)$$

The differential equation for temperatures are:

$$\begin{aligned} \left. \frac{d\Theta_p}{dr} \right|_{\text{HE}} &= -\frac{2\Theta_p}{2N_p + 1} \left(\mathcal{B} + \frac{1}{v(1-v^2)} \frac{dv}{dr} \right) - \chi \mathbb{P}_{\text{HE}}, \\ \left. \frac{d\Theta_e}{dr} \right|_{\text{HE}} &= -\frac{2\Theta_e}{2N_e + 1} \left(\mathcal{B} + \frac{1}{v(1-v^2)} \frac{dv}{dr} \right) - \mathbb{E}_{\text{HE}}, \end{aligned} \quad (6.6)$$

where,

$$\mathcal{B} = -\frac{r}{r(r-2)} - \frac{3r^2 - \lambda^2}{2[r^3 - \lambda^2(r-2)]}, \quad \mathbb{P}_{\text{HE}} = \frac{2\Delta Q_p \tilde{K}}{\rho u^r (2N_p + 1)}, \quad \text{and} \quad \mathbb{E}_{\text{HE}} = \frac{2\Delta Q_e \tilde{K}}{\rho u^r (2N_e + 1)}.$$

The subscript ‘HE’ signifies flows in hydrostatic equilibrium. The expression of gradient

6. TWO-TEMPERATURE FLOWS AROUND BLACK HOLES – II: ROTATING ACCRETION FLOWS

of three-velocity has the form :

$$\left. \frac{dv}{dr} \right|_{\text{HE}} = \frac{\mathcal{N}_{\text{HE}}}{\mathcal{D}_{\text{HE}}}, \quad (6.7)$$

where, $\mathcal{N}_{\text{HE}} = -\frac{1}{r(r-2)} + \frac{\lambda^2 \gamma_\phi^2 (r-3)}{r^4} + a_s^2 \mathcal{B} + \frac{\Gamma_p N_p \mathbb{P} + \Gamma_e N_e \mathbb{E}}{h \tilde{K}} - \frac{\Delta Q}{\rho h w^r}$ and $\mathcal{D}_{\text{HE}} = \frac{v}{1-v^2} \left(1 - \frac{a_s^2}{v^2} \right)$.

6.3 SOLUTION PROCEDURE

Accretion disc around BHs are transonic in nature and may possess multiple critical/sonic points (Chakrabarti, 1989; Fukue, 1987; Liang & Thompson, 1980). We have seen this in Chapter 3, which discuss rotating one-temperature accretion flows around BHs (also, see, 2.7). The combined effect of the flow parameters like E , λ , & \dot{M} , determines the number of sonic points formed inside an accretion flow as well as topology of the solution.

Below in Section 6.3.1, we describe the method to find sonic points in rotating two-temperature accretion flows and in Section 6.3.2, we show that the transonic solutions are degenerate and discuss extensively how to remove the degeneracy. The discussion done below is irrespective of whether the flow is in hydrostatic equilibrium or is conical. Only the expression of half-height changes which induces only quantitative change in the system.

6.3.1 METHOD TO OBTAIN SONIC POINTS IN TWO-TEMPERATURE ROTATING FLOWS

In one-temperature regime, location of sonic point and its property is unique for a given set of constants of motion. In dissipative systems, sonic points are not known a priori and is obtained self-consistently by integrating the equations of motion. So, presently in the two-temperature regime for rotating flows, we follow exactly the same procedure to solve the equations, as was adopted in the spherical flows, see Section 5.3.1, except that for rotating flows MCP exist. We list down the procedure to obtain a transonic solution for rotating accretion flows below,

1. For a given set of values of E , λ & \dot{M} , we start integration from a point asymptotically close to the horizon at $r_{\text{in}} = 2.001$ (in units of r_g).
2. As $r_{\text{in}} \rightarrow 2$, $E \rightarrow \mathcal{E} = -h_{\text{in}} u_t = h_{\text{in}} (1 - 2/r_{\text{in}})^{1/2} \gamma_v \gamma_\phi$. Here $h_{\text{in}} = h_{\text{in}}(\Theta_{\text{pin}}, \Theta_{\text{ein}})$ is the specific enthalpy at r_{in} .
3. We supply Θ_{pin} .

4. We also supply a Θ_{ein} . Then, v_{in} is obtained as a function of the flow parameters and can be expressed as,

$$v_{\text{in}} = \left[1 - \frac{(1 - 2/r_{\text{in}})}{\mathcal{E}^2} \frac{r_{\text{in}}^3}{\{r_{\text{in}}^3 - \lambda^2(r_{\text{in}} - 2)\}} h_{\text{in}}^2 \right]^{1/2}$$

5. Using the values of Θ_{pin} , Θ_{ein} and v_{in} we integrate dv/dr , $d\Theta_p/dr$ and $d\Theta_e/dr$, from $r = r_{\text{in}}$ to outwards. As we integrate, we simultaneously check the sonic point conditions ($dv/dr = \mathcal{N}/\mathcal{D} = 0/0$).
6. If sonic point is not found, we supply another value of Θ_{ein} and repeat steps 4 and 5, until the sonic point conditions are satisfied.
7. Once a sonic point is found, we integrate the equations of motion from sonic point to larger distances and obtain the full, global, transonic two-temperature accretion solution.
8. After we locate one sonic point, we change Θ_{ein} again and repeat steps 4-7, in order to check if any other sonic point exists. If found, we obtain its corresponding transonic solution.

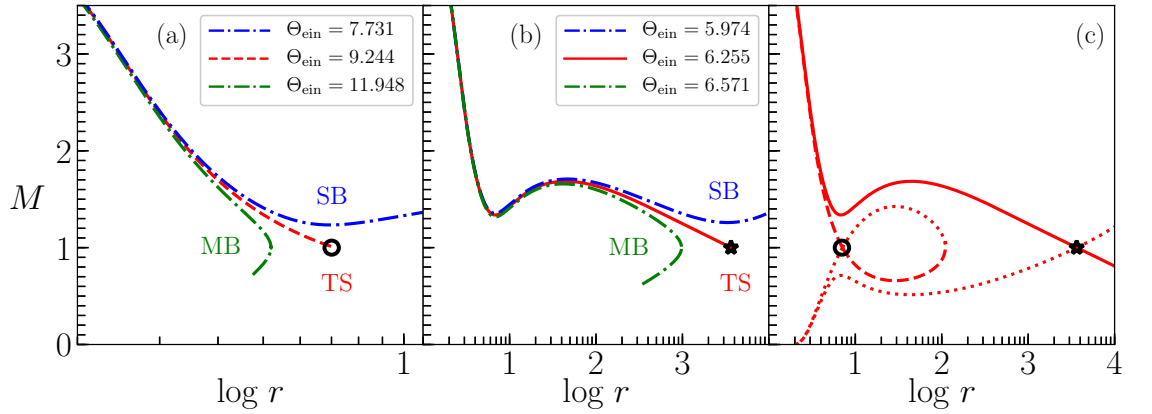


Figure 6.3: Method to find sonic points. Solutions are presented in terms of $M(=v/a)$ vs $\log r$ plot. $\Theta_{\text{pin}} = 7.162 \times 10^{-2}$ for all iterations. Panel (a) iterations to obtain r_{ci} (black circle) and panel (b) iterations to obtain r_{co} (black star). Various branches plotted are MB (dot dashed, green), TS (dashed, red) and SB (dot dashed, blue). Respective Θ_{ein} s are mentioned inside the panels. Panel (c) plots full set of TSs: global accretion solution (solid, red) through r_{co} and accretion solution through r_{ci} (dashed, red). Equatorial global wind (through r_{co}) and non global wind (through r_{ci}) are represented using dotted, red curve. The accretion disc flow parameters used are $\lambda = 2.5$, $E = 1.000045$, $M = 0.001\dot{M}_{\text{Edd}}$ and $M_{\text{BH}} = 10M_{\odot}$.

6. TWO-TEMPERATURE FLOWS AROUND BLACK HOLES – II: ROTATING ACCRETION FLOWS

This is basically the modified version of the methodology adopted by us in Chapter 3, see flowchart present in Fig. 3.2, where we obtained accretion solutions for a dissipative flow in the one-temperature regime (Le & Becker, 2005). We followed steps 1-7, while obtaining a general global transonic solution in case of two-temperature spherical flows (see Section 5.3.1). An additional step 8 is listed here, because rotating flows have multiple sonic points unlike spherical flows which possess only one sonic point.

We illustrate the procedure to find transonic solutions, enlisted above, in Figs. 6.3a—c. All three panels in this figure plots $M = v/a_s$ vs $\log r$. The accretion disc parameters are, $\lambda = 2.5$, $E = 1.000045$ and $\dot{M} = 0.001\dot{M}_{\text{Edd}}$ around a BH of $10M_\odot$. We would like to point out, that all these accretion disc parameters and the BH mass chosen are for representative purpose only. These have been varied and their effect on the solution have been studied later. In Fig. 6.3a, we present the method to obtain r_{ci} and the transonic solution through it. Following step 1, 2 and 3, we supply $\Theta_{\text{pin}} = 7.162 \times 10^{-2}$ for the aforementioned values of E , λ and \dot{M} . Following step 4, we start by supplying a high value of Θ_{ein} and obtain v_{in} . Then we integrate the equations of motion (step 5). For higher values of Θ_{ein} , we obtain multivalued branch (MB) of solutions. We plot one such MB solution (dot dashed, green) corresponding to $\Theta_{\text{ein}} = 11.948$. Clearly, MB solutions are not correct. We reduce the value of Θ_{ein} and repeat steps 4 and 5 (as mentioned in step 6). We observe that as we reduce Θ_{ein} , the MB solutions will approach the transonic solution, i.e., will shift rightward, but in all probability we would over shoot the transonic solution and end up with a purely supersonic branch (SB) solution (*i.e.* when $v > a_s$ or $M > 1$ at all r). We plot a representative case of a purely SB solution (dot dashed, blue) corresponding to $\Theta_{\text{ein}} = 7.731$. When the solutions corresponding to various Θ_{ein} suddenly shifts from a MB solution to a SB, then we know that the Θ_{ein} corresponding to a transonic solution (TS), lies in between these two values of Θ_{ein} . We iterate on the electron temperature at r_{in} within the range $7.731 < \Theta_{\text{ein}} < 11.948$ and obtain the transonic solution (TS) (dashed, red) and the sonic point is at $r_{\text{ci}} = 5.186$ (black circle). Then, by following step 7 we obtain the complete transonic solution from r_{in} to a large distance (say, r_{out}) through r_{ci} . In Fig. 6.3b, we present the procedure to find the existence of the outer sonic point for the same set of flow parameters. Following step 8 we reduce Θ_{ein} by a comparatively large value, such that we start obtaining MB type solutions similar to the ones we obtained before, while trying to locate r_{ci} . In panel (b) we present an example of MB solution (dot dashed, green) for $\Theta_{\text{ein}} = 6.571$. We repeat steps 4-6 and check when the solution jumps from MB to SB. This time it corresponds to $\Theta_{\text{ein}} = 7.106$ (dot dashed, blue). We iterate on Θ_{ein} between the two limits $6.571 < \Theta_{\text{ein}} < 7.106$, until we obtain a TS (solid, red) through $r_{\text{co}} = 3644.9$ (black star). No other physical sonic point exists for these flow parameters (E , λ , \dot{M}). In Fig. 6.3c, we plot the complete set of transonic solutions, accretion (dashed, red and solid, red) as well as equatorial wind solutions (dotted, red) for the disc parameters mentioned before.

The global accretion solution connecting infinity to the horizon is represented by solid, red line while dashed, red line represents accretion solution which is not global. We should remember that, not all set of disc parameters produce multiple sonic points and this point will be discussed in details in the later sections. Also, we note that if our supplied guess value of Θ_{pin} is unphysical, then even by iterating with all possible values of Θ_{ein} , sonic point conditions can never be satisfied.

6.3.2 PRESENCE OF DEGENERACY IN TWO-TEMPERATURE TRANSONIC SOLUTIONS: METHOD TO REMOVE IT AND OBTAIN UNIQUE TRANSONIC SOLUTIONS, INVOKING THE SECOND LAW OF THERMODYNAMICS

In the last section, we laid down the procedure to obtain TS, by supplying a guess value of Θ_{pin} and iterating with various values of Θ_{ein} , until we get the sonic point(s). This has been elaborately discussed in steps 1–8 of Section 6.3.1. Now, if we choose a different value of Θ_{pin} and again follow the same steps 1–8, for the same set of disc parameters (E , λ & \dot{M}), we will obtain a different transonic solution with distinctly different sonic point properties. This means, for a given set of constants of motion, two-temperature EoMs admit multiple transonic solutions. Since the number of EoMs are less than the number of flow variables, therefore even the transonic solutions become degenerate. From the second law of thermodynamics it is clear that out of all the possible solutions, only the solution with the highest entropy ($\dot{\mathcal{M}}$) should be favoured by nature (see, Chapter 4). In dissipative systems entropy is not conserved, so we measure entropy in the region near the event horizon (see, Eq. 4.10 of Section 4.4). For each transonic solution corresponding to a given Θ_{pin} , we compute $\dot{\mathcal{M}}_{\text{in}}$. If the computed $\dot{\mathcal{M}}_{\text{in}}$ is plotted with respect to Θ_{pin} then there is a clear maxima in $\dot{\mathcal{M}}_{\text{in}}$. Following the second law of thermodynamics, the solution (corresponding to a Θ_{pin}) with maximum entropy ($\dot{\mathcal{M}}_{\text{in}}$) is the physically plausible solution. Hence, we are able to constrain the degeneracy and obtain a unique transonic two-temperature solution for a given set of constants of motion.

6.3.2.1 CONICAL FLOWS

In this section, we illustrate the methodology to remove degeneracy and obtain unique two-temperature transonic solutions for conical flows around BHs. We present a similar analysis for flows in hydrostatic equilibrium in the transverse direction in the next section. Figs. 6.4a1–a4, shows the solutions for ‘spherical’ flows ($\lambda = 0$) and in Figs. 6.4b1–b6, solutions are for ‘rotating’ conical flows ($\lambda = 2.5$) around BH. Parameters used are $E = 1.002$, $\dot{M} = 0.05\dot{M}_{\text{edd}}$, $M_{\text{BH}} = 10M_{\odot}$, $\theta^c = 60^\circ$. Thus, the constants of motion are same in all the cases, but T_{pin} is varied to get different solutions. We can see that in case of spherical flows, the global solution always passes through a single sonic point (panels a1–a4), while in case of rotating flows, the flow might pass through one or more sonic

6. TWO-TEMPERATURE FLOWS AROUND BLACK HOLES – II: ROTATING ACCRETION FLOWS

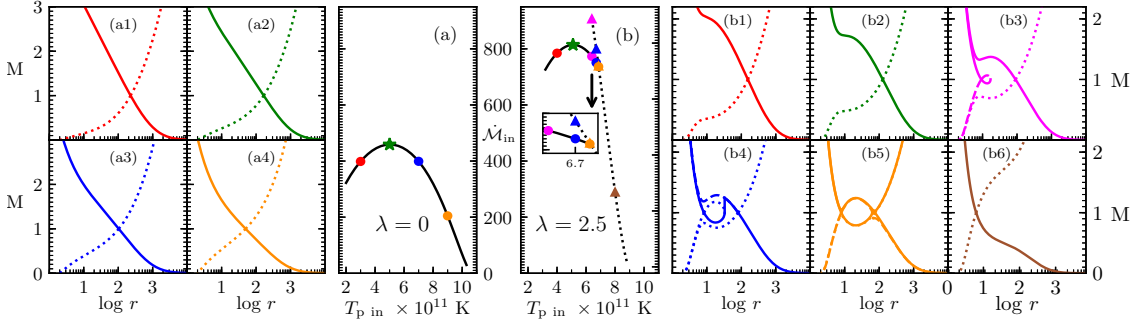


Figure 6.4: Left: (a) \dot{M}_{in} vs T_{pin} plot for spherical flows. Single sonic point exist for every T_{pin} . Panels (a1-a4) M vs $\log r$ plot for various T'_{pin} s marked with solid coloured dots in panel (a). The values of T_{pin} are: (a1) $3.0 \times 10^{11} K$, (a2) $4.0 \times 10^{11} K$, (a3) $5.0 \times 10^{11} K$, (a4) $6.0 \times 10^{11} K$. Right: (b) Shows \dot{M}_{in} vs T_{pin} plot for rotating conical flows ($\lambda = 2.5$). Solid black curve is for the solutions passing through r_{co} , while dotted black curve is for solutions passing through r_{ci} . Panels (b1-b4): Shows solutions for various T'_{pin} s marked in panel (b), value of which are: (b1) $4.0 \times 10^{11} K$, (b2) $5.1 \times 10^{11} K$, (b3) $6.4 \times 10^{11} K$, (b4) $6.7 \times 10^{11} K$, (b5) $6.86 \times 10^{11} K$, (b6) $8.0 \times 10^{11} K$. Entropy maximises at a certain T_{pin} in both the cases (green star). Corresponding unique solutions are plotted in panels (a2) and (b2). Flow parameters used are $E = 1.002$, $\dot{M} = 0.05\dot{M}_{edd}$, $M_{BH} = 10M_{\odot}$, $\theta^c = 60^\circ$.

points (panels b1–b6). In Figs. 6.4b1–b2, global solution passes through r_{co} only, while in Fig. 6.4b6 it passes through r_{ci} . In both the cases only one physical sonic point is present. In Figs. 6.4b3–b6, solution possess MCP, out of which in Fig. 6.4b4, we see that the flow harbours shock. So the global solution first passes through r_{co} , becomes supersonic and then after going through a shock transition, jumps to the subsonic branch and enter the BH supersonically after passing through r_{ci} .

A solution should be unique for a given set of constants of motion, but in Figs. 6.4a1–a4 and b1–b6, it was noticed that a change in T_{pin} gave solutions with completely new topology and sonic point properties. In Fig. 6.4, we plotted the case of spherical flows, in order to contrast for the complexity that arises due to the presence of angular momentum. Any wrong choice of solution would give us a completely different information of the system, and hence a wrong spectrum. So it is necessary to select the correct solution. The only way to deal with this degeneracy is to have a measure of entropy of the system. This measure of entropy is plotted in Fig. 6.4a (for spherical flows) and b (for rotating conical flows) against the corresponding T_{pin} s, using the entropy form given by Eq. 4.10.

In case of spherical flows, which possess single sonic points, there is a clear entropy maxima at $T_{pin|max} = 5 \times 10^{11} K$ (green star). By employing the second law of thermodynamics, we select this solution, present in Fig. 6.4a2. Thus, we are able to obtain a unique transonic two-temperature solution for the given set of constants of motion.

In case of general rotating flows, global solutions may pass through one or more sonic points. So the system is complicated unlike spherical flows. Dotted black curve in Fig. 6.4b

is for solutions passing through inner sonic points while solid black curve is for solutions passing through outer sonic points. In a certain range of T_{pin} both inner and outer sonic points exist (Figs. 6.4b3–b5). We can see that the entropy maximises in the outer sonic point branch of solutions (green star). Since flow starts from infinity, it would select the maximum entropy solution. Then, it could pass through an inner sonic point only if the shock conditions are satisfied (see Section 2.8). For the present case, $T_{\text{pin}} = 5.1 \times 10^{11} K$ possess maximum entropy and the global solution passes through outer sonic point (Fig. 6.4b2). In the sections to follow, we use this method of maximising entropy to obtain global advective transonic two-temperature accretion solutions.

6.3.2.2 FLOWS IN HYDROSTATIC EQUILIBRIUM IN THE TRANSVERSE DIRECTION

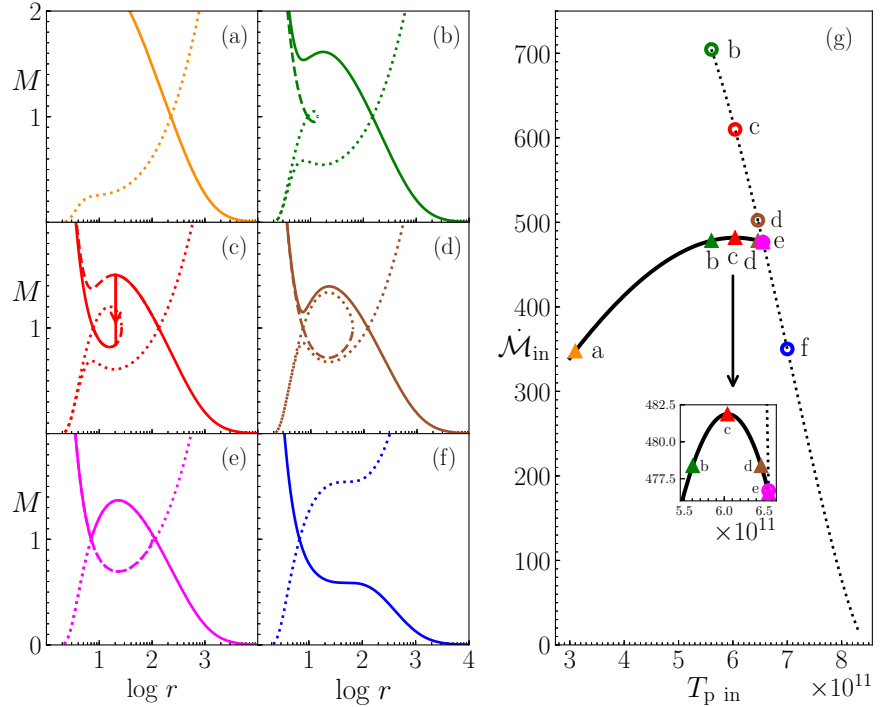


Figure 6.5: Left: M vs $\log r$ plot for various values of T_{pin} : (a) $3.1 \times 10^{11} K$, (b) $5.605 \times 10^{11} K$, (c) $6.04 \times 10^{11} K$, (d) $6.460 \times 10^{11} K$, (e) $6.554 \times 10^{11} K$ and (f) $7.0 \times 10^{11} K$. Global solutions are represented by solid lines. In panel (g) \mathcal{M}_{in} vs T_{pin} is plotted. Solid black curve is for the solutions passing through r_{co} , while dotted black curve is for solutions passing through r_{ci} . Panels (a)–(f) are the solutions corresponding to the points marked in right panel (g). The disc flow parameters are $E = 1.0015$, $\lambda = 2.6$ and $\dot{M} = 0.02\dot{M}_{\text{Edd}}$. The space time is described by a BH of mass $10M_{\odot}$ and the system is in hydrostatic equilibrium in the vertical direction.

We use exactly the same methodology as followed in the previous section to obtain unique two-temperature transonic solution for flows in hydrostatic equilibrium in the vertical direction. In Figs. 6.5a–g, we illustrate it. We choose the accretion disc flow

6. TWO-TEMPERATURE FLOWS AROUND BLACK HOLES – II: ROTATING ACCRETION FLOWS

parameters: $E = 1.0015$, $\lambda = 2.6$, $\dot{M} = 0.02\dot{M}_{\text{Edd}}$ and $M_{\text{BH}} = 10M_{\odot}$. As described above, we supply a Θ_{pin} or equivalently T_{pin} and then we iterate on Θ_{ein} (or T_{ein}) to obtain a transonic solution. The entropy accretion rate $\dot{\mathcal{M}}_{\text{in}}$ corresponding to the transonic solution for the particular T_{pin} is plotted in Fig. 6.5g. The solid, black line is for those T_{pin} whose solution passes through outer sonic point (r_{co}) and dotted, black line is for those passing through inner sonic point (r_{ci}). From this figure, we select few T_{pin} s (points marked ‘a’–‘f’) which are (a) $3.1 \times 10^{11}\text{K}$, (b) $5.605 \times 10^{11}\text{K}$, (c) $6.04 \times 10^{11}\text{K}$, (d) $6.460 \times 10^{11}\text{K}$, (e) $6.554 \times 10^{11}\text{K}$ and (f) $7.0 \times 10^{11}\text{K}$ and plot their solutions in terms of M vs $\log r$, presented in Figs. 6.5a–f respectively. The global accretion solutions are represented by solid curves, dotted are wind types, while the dashed curves are accretion solutions which are not global. There is a range of T_{pin} where both inner and outer sonic points are present and is the multiple sonic point regime. For example, ‘b’, ‘c’ and ‘d’ has both inner (marked circle) and outer sonic points (marked triangle). For point ‘e’, the solutions passing through inner and outer sonic points (magenta triangle and magenta circle), have almost the same value of $\dot{\mathcal{M}}_{\text{in}}$ (see inset). Corresponding solution is plotted in Fig. 6.5e, which shows that the global solution (connecting horizon to large distances) passes through r_{co} . Now, corresponding to point ‘a’ (orange triangle, in panel g), the solution passes only through r_{co} (Fig. 6.5a), while for point ‘f’ (blue circle), the solution passes through r_{ci} (Fig. 6.5f). However, the entropy is exactly same for both these points. This means, the solution character can be completely different even if $\dot{\mathcal{M}}_{\text{in}}$ has the same value. Similarly another pair ‘b’ and ‘d’ also has the same entropy but different T_{pin} . Also, their corresponding solutions are significantly different, although both solutions lie in the multiple sonic point regime. This shows that, not only all solutions presented in the figure have same E , \dot{M} , λ , but may have even same $\dot{\mathcal{M}}_{\text{in}}$ and yet the solutions are completely different. In order to drive home the point even further, we present T_{pin} , $\dot{\mathcal{M}}_{\text{in}}$, r_{c} , v_{c} , & L (luminosity) of all degenerate solutions in Table 6.1. Some solutions can be about four times more luminous than other solutions. It is evident from figure and table, that degeneracy in two-temperature model is a serious problem. Observational parameter like L is quite different for different degenerate solutions. Any random choice from the pool of degenerate solutions would provide us with a completely wrong information of the system and also a wrong spectrum. Removal of degeneracy is hence important. Although, all the solutions presented above have the same E , \dot{M} , λ , only one of them possess the highest entropy (highest $\dot{\mathcal{M}}_{\text{in}}$). In this particular case, the highest entropy solution is the one corresponding to point ‘c’ (red triangle) in $\dot{\mathcal{M}}_{\text{in}}-T_{\text{pin}}$ curve (Fig. 6.5g), and the correct, unique two-temperature accretion solution is represented in Fig. 6.5c (solid, red).

Thus, we successfully validate the entropy maximisation formulation to constrain degeneracy in rotating two-temperature accretions flows around BHs. In the last Chapter 5, we validated it for spherical flows as well. The beauty of the entropy expression (see, Eq. 4.10) proposed by us lies in the fact that, the entropy is always found to maximise at

a given distinct transonic solution for a given set of flow parameters, thereby allowing us to select only one solution out of all the degenerate solutions.

Table 6.1: Various flow properties of the solutions plotted in Figs. 6.5a–f. The disc parameters used are $E = 1.0015$, $\lambda = 2.6$, $\dot{M} = 0.02\dot{M}_{\text{Edd}}$ around $M_{\text{BH}} = 10M_{\odot}$.

	T_{pin} ($\times 10^{11} K$)	$\dot{\mathcal{M}}_{\text{in}}$		r_c		v_c		L ($\times 10^{33} \text{ ergs s}^{-1}$)
		Inner	Outer	Inner	Outer	Inner	Outer	
a	3.100	–	350.132	–	227.514	–	0.041	1.092
b	5.605	704.505	478.373	8.826	149.380	0.177	0.051	1.763
c	6.040	609.971	481.873	7.651	134.135	0.191	0.054	4.467
d	6.460	502.357	478.377	7.118	118.565	0.199	0.057	2.457
e	6.554	476.702	476.552	7.027	11.946	0.200	0.058	2.722
f	7.000	350.168	–	6.672	–	0.207	–	3.020

6.3.3 STABILITY ANALYSIS OF THE HIGHEST ENTROPY TRANSONIC SOLUTION

In this section, we investigate the stability of the unique transonic two-temperature solution selected from the available set of degenerate solutions. We note that the proposed unique solution is of highest entropy and by second law of thermodynamics, nature should prefer it. Therefore, the solution should be stable. However, because there is a degeneracy of solutions, we need to study the stability of the proposed unique solution too. We provide a qualitative analysis for stability of the unique two-temperature solution.

Let us assign $\dot{\mathcal{M}}_{\text{in}|_{\text{max}}} = \max(\dot{\mathcal{M}}_{\text{in}})$ and $T_{\text{pin}|_{\text{max}}} = T_{\text{pin}}$ for which $\dot{\mathcal{M}}_{\text{in}}$ is maximum. Let us further define δT_{pin} which is the difference between adjacent higher and lower T_{pin} and $\Delta = \left(d\dot{\mathcal{M}}_{\text{in}}/dT_{\text{pin}} \right)$ as the gradient of $\dot{\mathcal{M}}_{\text{in}}$. Now the change in $\dot{\mathcal{M}}_{\text{in}}$ is given by,

$$\delta \dot{\mathcal{M}}_{\text{in}} = \left(\frac{d\dot{\mathcal{M}}_{\text{in}}}{dT_{\text{pin}}} \right) \delta T_{\text{pin}} = \Delta \delta T_{\text{pin}} \quad (6.8)$$

It is clear that $\Delta = 0$ for any extrema of $\dot{\mathcal{M}}_{\text{in}} - T_{\text{pin}}$ curve, but the solution is said to be stable if T_{pin} moves away from the value $T_{\text{pin}|_{\text{max}}}$ and the system adjusts automatically, to regain its old value. We prefer the graphical method to investigate the stability and the technique is similar to the first derivative test for obtaining local extrema (Hernández Melo, 2014). We plot Δ vs T_{pin} in Fig. 6.6. At $T_{\text{pin}} < T_{\text{pin}|_{\text{max}}}$, the figure shows that $\Delta > 0$. Then from Eq. 6.8, $\delta \dot{\mathcal{M}}_{\text{in}} > 0$. So the system tends to go to higher $\dot{\mathcal{M}}_{\text{in}}$, which we denote using a rightward arrow. Similarly, for $T_{\text{pin}} > T_{\text{pin}|_{\text{max}}}$, $\Delta < 0$ which implies $\delta \dot{\mathcal{M}}_{\text{in}} < 0$. Since, by second law of thermodynamics, physical system would not like to decrease its entropy therefore for $T_{\text{pin}} > T_{\text{pin}|_{\text{max}}}$, the system would tend to come back to $T_{\text{pin}|_{\text{max}}}$.

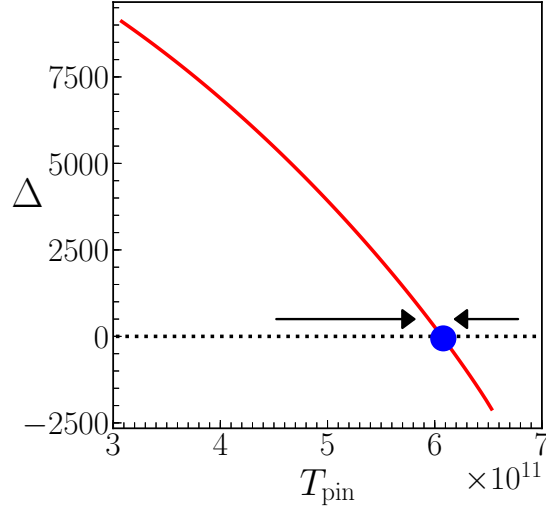


Figure 6.6: Stability analysis of the unique transonic two-temperature solution with maximum entropy. The flow parameters used are same as Fig. 6.5. $\Delta = \left(d\dot{\mathcal{M}}_{\text{in}}/dT_{\text{pin}}\right)$ is plotted against variation of T_{pin} . The arrows indicate that Δ converge at $T_{\text{pin}} = T_{\text{pin}|\text{max}}$ (blue dot) and is the stable equilibrium solution. This T_{pin} is the solution with maximum entropy marked ‘c’ in Fig. 6.5g.

We represent this in the figure by using a leftward arrow. In other words, entropy can only increase ($\delta\dot{\mathcal{M}}_{\text{in}} > 0$), if $T_{\text{pin}} \rightarrow T_{\text{pin}|\text{max}}$ from either side of $T_{\text{pin}|\text{max}}$. Hence, solution corresponding to $T_{\text{pin}} = T_{\text{pin}|\text{max}}$ is stable. Therefore, in addition to the fact that $T_{\text{pin}|\text{max}}$ corresponds to a solution with maximum entropy, we can conclude that the solution is also stable.

6.4 RESULTS

Two-temperature accretion solutions are parametrised by E , λ , \dot{M} . In addition, β_{d} and β controls heating and cooling. We have only analysed solutions with maximum entropy, selected from the available degenerate group of solutions using the methodology discussed in Section 6.3. First we present few solutions assuming rotating conical flows and then move on to discuss extensively flows in hydrostatic equilibrium.

6.4.1 CONICAL FLOWS

In this section we discuss results regarding rotating conical flows (Sarkar & Chattopadhyay, 2019b). Since, the geometry of the flow is fixed and is not allowed to expand or contract depending on the dissipation present in the system, these flows are generally much hotter than flows in hydrostatic equilibrium in the vertical direction, which is discussed

in the next section.

6.4.1.1 GENERAL TWO-TEMPERATURE SOLUTIONS

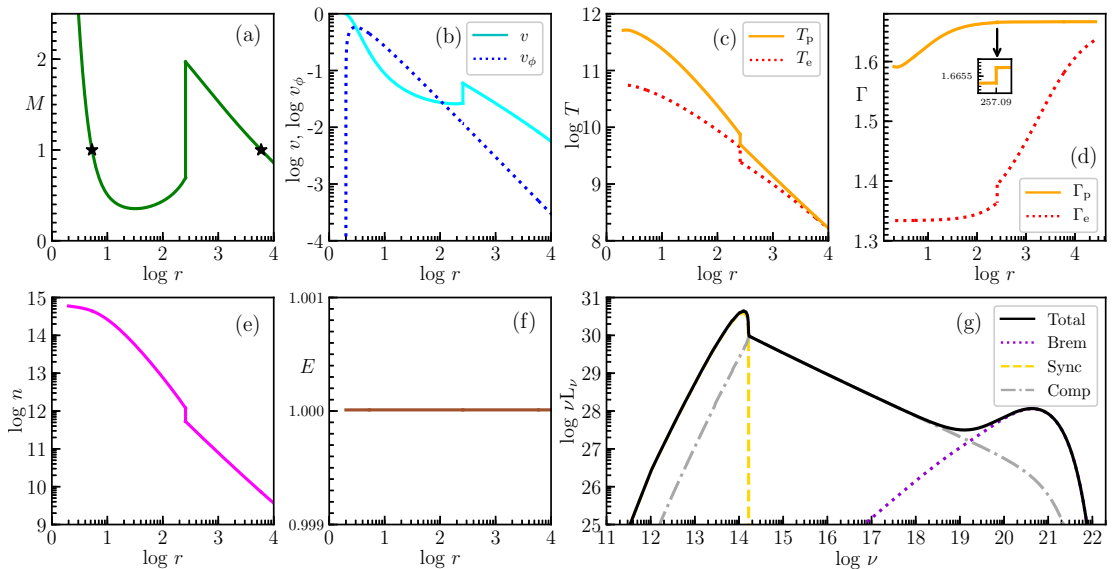


Figure 6.7: We plot (a) Mach number (M), (b) v (solid, cyan) and v_ϕ (dotted, blue), (c) T_p (solid, orange), T_e (dotted, red), (d) Γ_p (solid, orange), Γ_e (dotted, red), (e) $\log(n)$ (solid, magenta), (f) E (solid, brown), with respect to $\log r$. In panel (g) we plot the total spectrum (solid black) along with contributions coming from bremsstrahlung emission (dotted violet), synchrotron (dashed yellow) and inverse Comptonization (dotted-dashed grey). The set of flow parameters used are $E = 1.00001$, $\lambda = 3.0$, $\dot{M} = 0.001\dot{M}_{\text{edd}}$, $M_{\text{BH}} = 10M_\odot$ and $\theta^c = 60^\circ$

In Fig. 6.7, we plot a typical two-temperature transonic advective accretion disk solution with its corresponding flow variables. The parameters used are, $E = 1.00001$, $\lambda = 3.0$, $\dot{M} = 0.001\dot{M}_{\text{edd}}$, $M_{\text{BH}} = 10M_\odot$ and $\theta^c = 60^\circ$. In Fig. 6.7a we plot the global solution, which passes through multiple sonic points (solid, green line). First, the solution passes through an $r_{\text{co}} = 5935.59$ and then through $r_{\text{ci}} = 6.29$ (denoted by black stars) via a shock transition at $r_{\text{sh}} = 257.09$. After the shock, matter becomes subsonic but it ultimately falls into the BH supersonically after passing through the inner sonic point. The radial three-velocity (v) in co-rotating frame and flow velocity in the azimuthal direction (v_ϕ) is plotted in Fig. 6.7b (solid cyan and dotted blue respectively). The fate of v and v_ϕ near the horizon is quite different, one approaching c while the other going to 0, since near the BH, gravity is so strong that matter only has a radial velocity component and negligible azimuthal component. T_p (solid, orange) and T_e (dotted, red) as a function of r is plotted in Fig. 6.7c. At very large r , $T_p \simeq T_e$. But as the matter flows inwards, cooling processes in electrons starts to dominate. Thus, protons and electrons settle down

6. TWO-TEMPERATURE FLOWS AROUND BLACK HOLES – II: ROTATING ACCRETION FLOWS

into two-different temperatures. They are however coupled by a Coulomb coupling term which acts as an energy exchange term between the protons and electrons. But the term is weak, unlike in one-temperature case, where it is infinite. Fig. 6.7d shows that Γ of both protons (solid, orange) and electrons (dotted, red) varies with the flow. This justifies our use of CR EoS. Γ_p and $\Gamma_e \sim 1.66$ at very large distances, suggesting that both of them are thermally non-relativistic. When the flow nears the BH, Γ_e becomes mildly-relativistic and then relativistic with $\Gamma_e \sim 1.33$ near the horizon, though Γ_p never becomes truly relativistic. In Fig. 6.7e, we have plotted number density, n (in units of cm^{-3}) vs $\log r$. Since accretion is an example of convergent flow, the number density increases with decrease in radius. In Fig. 6.7f, we prove that the generalised Bernoulli constant is a constant of motion throughout the flow, even in the presence of dissipation. In Fig. 6.7g, we plot the spectrum for the accretion flow. It is plotted by summing up all the emissions coming from each radius. Spectrum of each emission process is also plotted separately. Bremsstrahlung is shown in dotted violet line, synchrotron by dashed yellow line and inverse-Comptonization by dotted-dashed grey line.

6.4.1.2 LUMINOSITY AND EFFICIENCY OF BONDI FLOWS AS COMPARED TO ROTATING FLOWS :

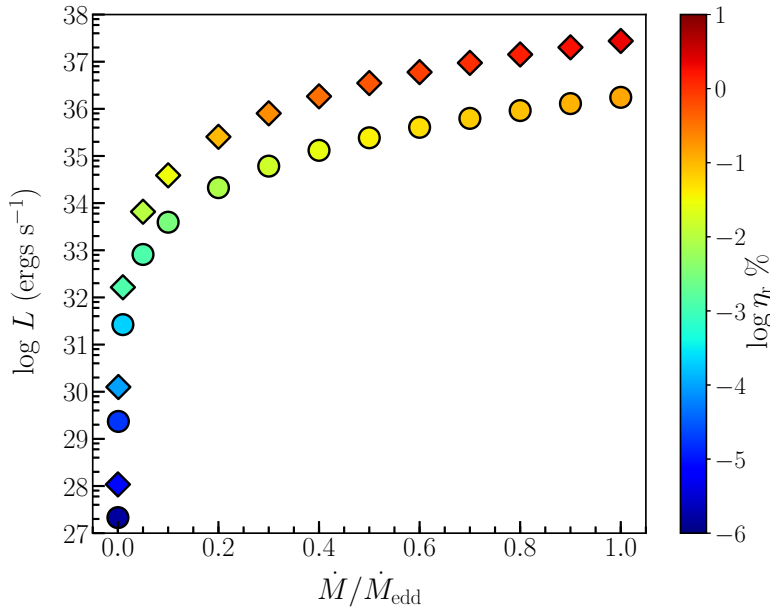


Figure 6.8: Plot shows the variation of L (in ergs s^{-1}) with \dot{M} (normalised with respect to \dot{M}_{Edd}). The colour bar shows the change in efficiency, η_r (in logarithmic scale). The circled points are for spherical flows while diamond shaped points are for flows having angular momentum $\lambda = 2.4$. The other flow parameters used here are, $E = 1.001$, $M_{\text{BH}} = 10M_{\odot}$ and $\theta^c = 60^\circ$

In Fig. 6.8, we have compared the change in luminosity with increase in accretion rate (\dot{M}),

which is in terms of Eddington rate (\dot{M}_{edd}). Circled points are for spherically symmetric flows, whereas diamond shaped points are for flows having angular momentum $\lambda = 2.4$. For both the flows parameters used are $E = 1.001$, $M_{\text{BH}} = 10M_{\odot}$ and $\theta^c = 60^\circ$. We can see that as the supplied matter is increased the luminosity increases, irrespective of the type of flow. It is apparent from the plot that Bondi flows are less luminous flows, about an order of magnitude lower than rotating flows. The presence of angular momentum slows down the matter giving it more time to radiate. The colour bar plots the efficiency of the system, which is given by the formula, $\eta_r = L/(\dot{M}c^2)$. The efficiency also has a similar trend, with the increase in accretion rate, efficiency increases but flows with angular momentum have a higher efficiency than spherical flows, at any given accretion rate.

While computing L and hence η_r of these systems, we took care of all general and special relativistic effects as well as photon capture and bending effects. Fig. 2.1 shows, that not all photons emitted by the accretion disc will reach the observer, see Section 2.6 for more details. This limits the efficiency of spherical flows to $< 10\%$ unlike what we obtained in Fig. 5.9 where these effects were not considered. But it is important to note that the qualitative nature of the flow is undisturbed by these effects, only the values differ. Hence, we took appropriate care of these effects in the sections and discussions to follow, in the rest of the chapter as well as thesis.

6.4.2 FLOWS IN HYDROSTATIC EQUILIBRIUM IN THE TRANSVERSE DIRECTION

In this section, we extensively discuss flows in hydrostatic equilibrium in the vertical direction (Sarkar et al., 2020). We have also analysed the spectrum. Throughout this section, we have used $\beta_d = 0.001$ and $\beta = 0.01$, unless stated otherwise. We have varied these parameters in Section 6.4.2.6 and 6.4.2.5 respectively, and have discussed their effect on accretion solution and observable spectrum.

6.4.2.1 GENERAL TWO-TEMPERATURE SOLUTIONS

In Fig. 6.9, we study a typical two-temperature transonic advective accretion disc solution. The parameters used are, $E = 1.000045$, $\lambda = 2.5$, $\dot{M} = 0.001\dot{M}_{\text{Edd}}$ and $M_{\text{BH}} = 10M_{\odot}$. In Fig. 6.9a we plot \mathcal{M}_{in} vs T_{pin} . The solution with $T_{\text{pin}} = 6.0 \times 10^{11} K$ has the maximum entropy (marked with green triangle) and the corresponding M vs $\log r$ (solid, green line) is plotted in Fig. 6.9b. The global solution passes through an outer sonic point whose position is $r_{\text{co}} = 3040.182$ (black star). The radial three-velocity (v ; cyan solid) in co-rotating frame and flow velocity in the azimuthal direction (v_ϕ ; dotted, blue) is plotted in Fig. 6.9c. Matter far away from the horizon has negligible velocity in radial as well as in azimuthal directions. But as it approaches the BH ($r \rightarrow r_g$), $v \rightarrow c$, thus satisfying

6. TWO-TEMPERATURE FLOWS AROUND BLACK HOLES – II: ROTATING ACCRETION FLOWS

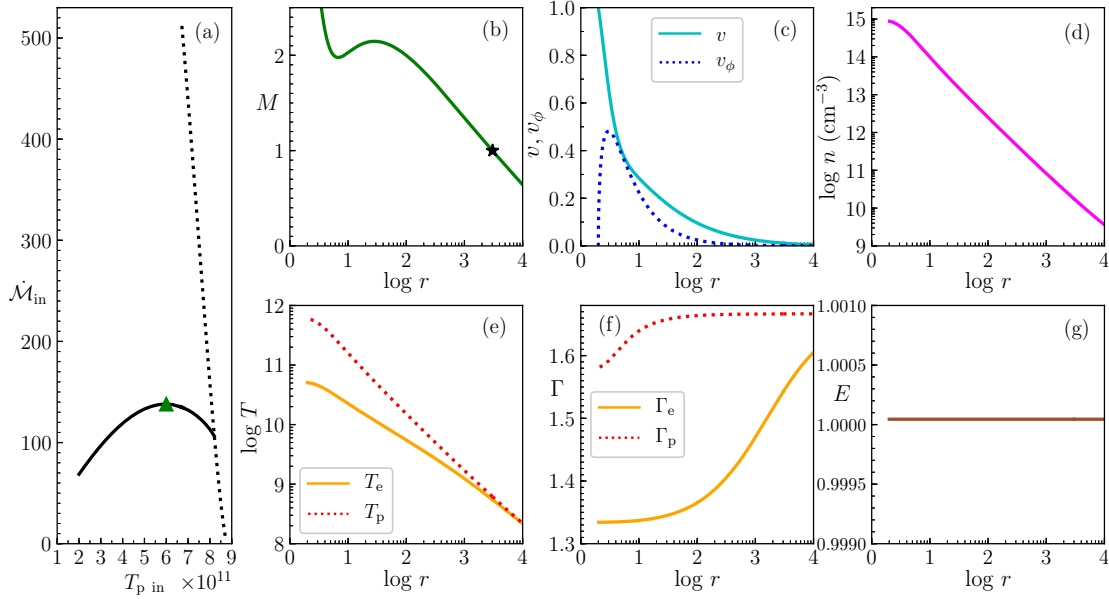


Figure 6.9: (a) \dot{M}_{in} is plotted against T_{pin} . The entropy for inner sonic point solutions (dotted, black) and outer sonic points (solid, black) are presented. T_{pin} marked with green triangle corresponds to maximum entropy solution. Flow variables plotted are (b) M (solid, green), (c) v (solid, cyan) and v_ϕ (dotted, blue), (d) $\log n$ (solid, magenta), (e) T_p (dotted, red), T_e (solid, orange), (f) Γ_p (dotted, red), Γ_e (solid, orange), (g) E (solid, brown) as functions of $\log r$. The flow parameters are $E = 1.000045$, $\lambda = 2.5$, $\dot{M} = 0.001\dot{M}_{\text{Edd}}$ and $M_{\text{BH}} = 10M_\odot$. In panel (b), the sonic point is marked with a black star.

the BH boundary condition. On the other hand, v_ϕ increases with the decrease of r , but maximises at $r = 3r_g$ and finally goes to zero on the horizon. This is mainly because near the horizon infall timescale is much shorter than any other timescales. The strong gravity does not allow the matter enough time to rotate in the azimuthal direction. In Fig. 6.9d we have plotted number density (in units of cm^{-3}) as a function of radius. The number density increases with the decrease in radius, as it should be for a convergent flow. T_p (dotted, red) and T_e (solid, orange) are plotted in Fig. 6.9e. The cooling processes are dominated by electrons compared to protons. They are however coupled by a Coulomb coupling term which acts as an energy exchange term between the protons and electrons, as have been discussed before. This term is weak, which allows protons and electrons to equilibrate into two different temperatures (T_p and T_e), unlike in the case of single-temperature flows where Coulomb coupling term is assumed to be very efficient which allows, protons and electrons to attain a single temperature. Panel Fig. 6.9f shows that adiabatic indices of both protons (dotted, red) and electrons (solid, orange), varies with the flow. This justifies our use of CR EoS. $\Gamma_p \sim 1.66$ and $\Gamma_e \sim 1.60$ at large distances away from the BH, hence both the species are thermally non-relativistic. When the flow

approaches the BH, Γ_e becomes relativistic *i.e.*, $\Gamma_e \sim 1.33$ near the horizon. We can see that Γ_p does not vary much but becomes mildly-relativistic near the horizon, owing to the higher mass of protons. In Fig. 6.9g, we prove that the generalized Bernoulli constant is a constant of motion throughout the flow, even in the presence of dissipation.

EMISSIVITIES AND SPECTRAL PROPERTIES :

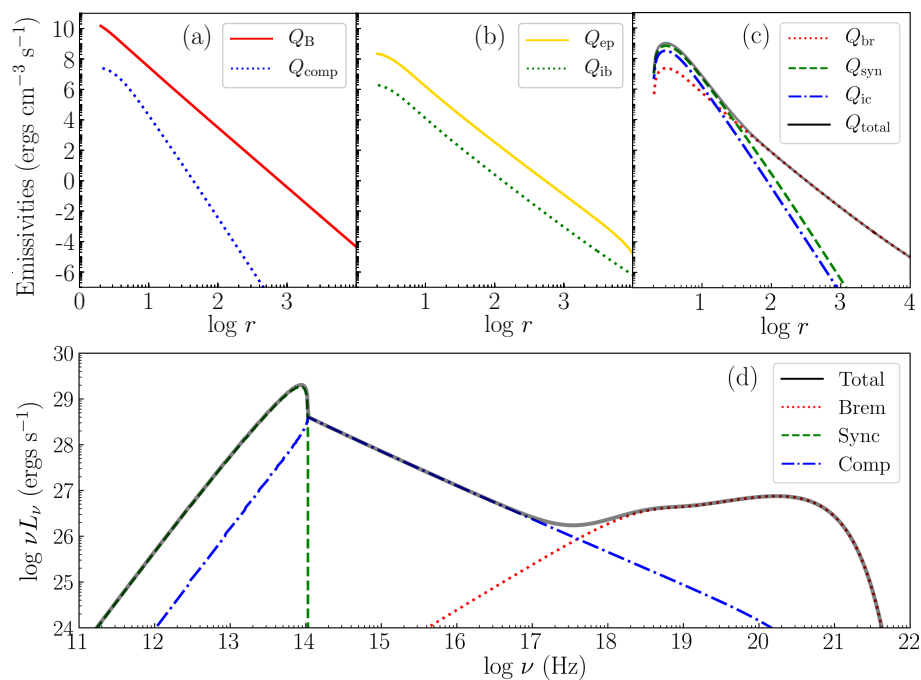


Figure 6.10: Top three panels shows the emissivity vs $\log r$ plot for the flow presented in Fig. 6.9. Bottom panel (d) shows the spectrum of the accretion flow.

In Fig. 6.10, we present the heating and cooling rates for the solution plotted in Fig. 6.9. In Fig. 6.10a, we plot the heating terms. Solid, red line represents the heating due to magnetic dissipation (Q_B). This amount of heat is assumed to be equally distributed among protons and electrons ($\delta_B = 0.5$, see Section 2.5.2). Dotted, blue line represents Compton heating of electrons (Q_{comp}). It is mainly the hard bremsstrahlung photons present inside the flow which leads to heating up of the electrons, owing to their higher energy than electrons. In Fig. 6.10b, we plot Coulomb Coupling term, Q_{ep} (solid, yellow line) and inverse bremsstrahlung (dotted, green line). We see that, Q_B is the strongest heating term.

In Fig. 6.10c we plot the emissivities of all the cooling processes for electrons : Q_{br} (dotted, red line), Q_{syn} (dashed, green line) and Q_{ic} (dot dashed, blue line). For the present set of disc parameters, at the outer boundary of the disc, the temperatures are non-relativistic and therefore, bremsstrahlung emission dominates over all other processes. In the inner regions of the accretion disc *i.e.*, close to the BH horizon, synchrotron

6. TWO-TEMPERATURE FLOWS AROUND BLACK HOLES – II: ROTATING ACCRETION FLOWS

and inverse-Comptonization becomes important and exceeds bremsstrahlung. However, inverse-Comptonization is less than synchrotron emission, mainly due to the low accretion rate of the flow. The total cooling of electrons is represented by a solid, black line. In panel Fig. 6.10d, we plot the spectrum for the accretion flow (solid, black line). It is plotted by summing up the contributions of all emission processes at each radius. General and special relativistic frame transformations from fluid rest frame to the observer frame has been taken into account while computing the spectra, including photon capture and photon bending effect due to the presence of strong gravity. This has been elaborately discussed in Section 2.6. Spectrum of each emission process is also plotted. Bremsstrahlung is shown in dotted, red line, synchrotron by dashed, green line and inverse-Comptonization by dot dashed, blue line. The overall luminosity of the system is low, $L = 2.536 \times 10^{29}$ ergs s^{-1} , with a radiative efficiency of $\eta_r = 1.957 \times 10^{-5}$. It may be noted that, efficiency is defined as $\eta_r = L/(\dot{M}c^2)$. The spectral index is $\alpha = 1.744$. To remember, α is the slope of the power-law photons that are generated due to inverse-Comptonization at each radius. Therefore, the net spectral index (α) of the final inverse-Compton spectrum is obtained from the contributions of all the values of α_0 at each radius of the disc (see, Eq. 2.45).

6.4.2.2 CONTRIBUTION OF DIFFERENT REGIONS OF THE ACCRETION DISC TO THE OVERALL SPECTRUM :

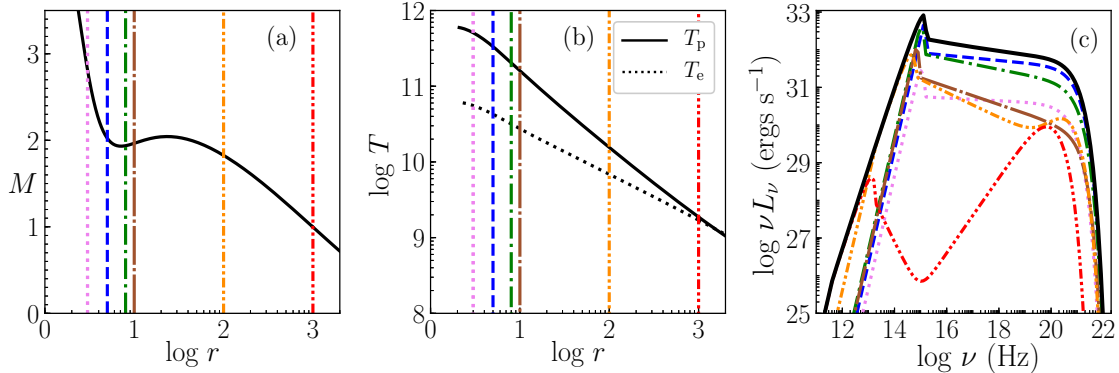


Figure 6.11: (a) M and (b) $\log T$ vs $\log r$ and (c) total spectrum (solid, black) and contribution from various length scales of the accretion disc, $2 - 3r_g$ (dotted, magenta), $3 - 5r_g$ (dashed, blue), $5 - 8r_g$ (single-dotted short-dashed, green), $8 - 10r_g$ (single-dotted long-dashed, brown), $10 - 100r_g$ (double-dotted short-dashed, orange) and $100 - 1000r_g$ (triple-dotted short-dashed, red). Flow parameters are $E = 1.0002$, $\lambda = 2.48$, $\dot{M} = 0.05\dot{M}_{\text{Edd}}$ and $M_{\text{BH}} = 10M_\odot$.

In Fig. 6.10d, we presented the contribution of all the emission processes in the total broad-band continuum spectrum. However, in this section, we would like to investigate

Table 6.2: Spectral properties of the regions marked in Fig. 6.11

Colour	Region (in r_g)	% of L_{tot}	α
Magenta	2-3	3.597	1.044
Blue	3-5	45.810	1.072
Green	5-8	35.250	1.141
Brown	8-10	6.965	1.236
Orange	10-100	7.845	1.323
Red	100-1000	0.286	2.392
–	1000-10000	0.247	2.233×10^{-5}

the contribution of various regions of an accretion disc to the overall spectrum. We chose a set of flow parameters $E = 1.0002$, $\lambda = 2.48$, $\dot{M} = 0.05\dot{M}_{\text{Edd}}$ and $M_{\text{BH}} = 10M_{\odot}$. In Fig. 6.11a, we plot the Mach number M of the accretion flow and in Fig. 6.11b, we plot T_p (solid, black) and T_e (dotted, black) as a function of $\log r$. In panels (a) and (b), we indicate various regions with vertical lines, which represents accretion disc section from $2 - 3r_g$ (dotted, magenta), $3 - 5r_g$ (dashed, blue), $5 - 8r_g$ (single-dotted short-dashed, green), $8 - 10r_g$ (single-dotted long-dashed, brown), $10 - 100r_g$ (double-dotted short-dashed, orange) and $100 - 1000r_g$ (triple-dotted short-dashed, red). The spectra from all these regions are separately over plotted in Fig. 6.11c, the colour coding of the spectra matches the region from which they are computed. The black curve represent the overall spectrum for the disc parameters stated above. The contribution from the region $r = 10^3 - 10^4 r_g$ is too low in the overall spectrum and therefore is not plotted, in order to avoid cluttering the figure. The spectrum computed from the region $2 - 3r_g$ is low inspite of high values of n and T_e , since significant number of photons emitted from that region, are captured by the BH. Most of the high energy emission is contributed by accreting matter from the region between $3 - 5r_g$ and $5 - 8r_g$, and the low-energy end of the spectra from this region is always around and above 10^{12}Hz . We have tabulated these details and other spectral properties in Table 6.2. We can conclude from the table that $\sim 90\%$ of the emission comes from a region $< 10r_g$ of the accretion disc. The lower energy part of the spectrum is mostly contributed by the outer part of the disc. Since we have only considered advective disc, the spectrum is hard and the radiative efficiency for this particular set of disc parameters is less than 1%.

6.4.2.3 DEPENDENCE OF ACCRETION SOLUTIONS AND CORRESPONDING SPECTRA WITH ENERGY AND ANGULAR MOMENTUM:

In Figs. 6.12 and 6.13, we investigate the dependence of accretion solutions and the corresponding spectra respectively, on E and λ for a $10M_{\odot}$ BH with $\dot{M} = 0.01\dot{M}_{\text{Edd}}$. In the figures, E increases from left to right and the values are $E = 1.0005, 1.001, 1.003$

6. TWO-TEMPERATURE FLOWS AROUND BLACK HOLES – II: ROTATING ACCRETION FLOWS

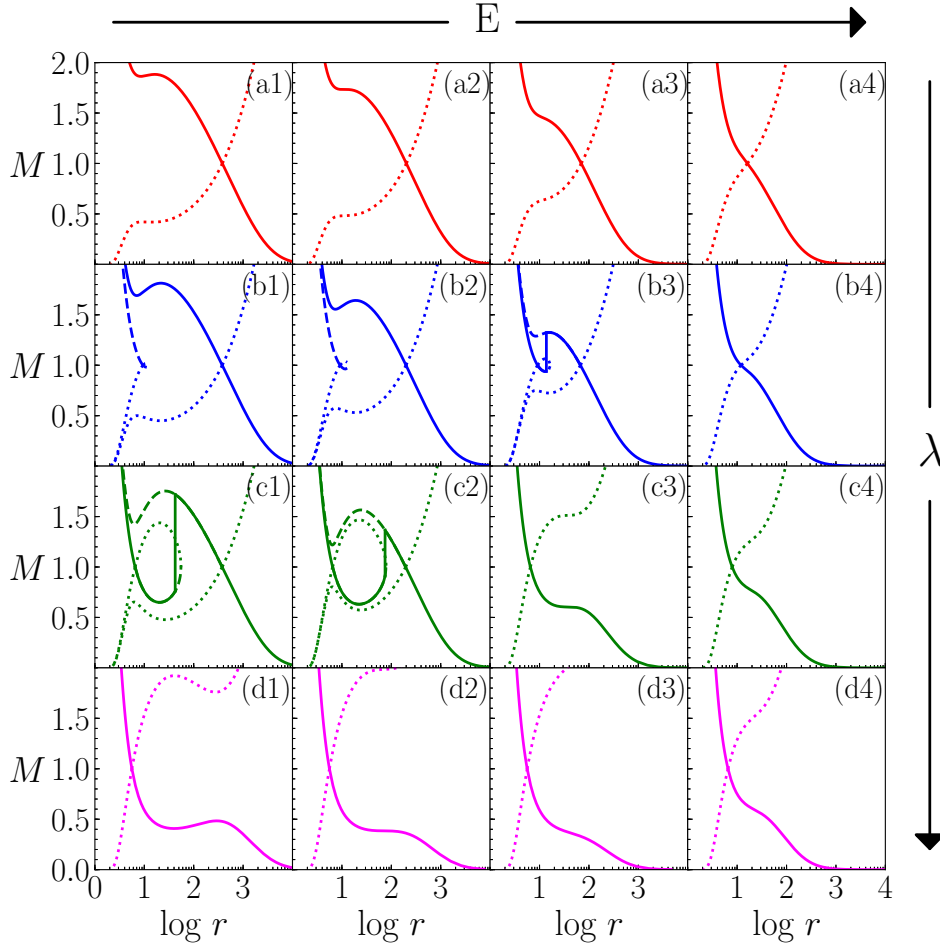


Figure 6.12: Variation of solutions, M as a function of $\log r$ with variation of E and λ . From left to right specific energy increases as $E = 1.0005, 1.001, 1.003$ and 1.01 . From top to bottom the angular momentum increases as $\lambda = 2.40, 2.55, 2.70$ and 2.85 . Other parameters are $\dot{M} = 0.01\dot{M}_{\text{Edd}}$ and $M_{\text{BH}} = 10M_{\odot}$.

and 1.01 . While, as we go from top to bottom, λ increases as $\lambda = 2.40, 2.55, 2.70$ and 2.85 . In short, E changes along the row while λ changes along the column. Low angular momentum flows ($\lambda = 2.40$) behave as Bondi flows, possessing single sonic point, through which the global solution passes (see Figs. 6.12a1-a4), irrespective of the value of E . As angular momentum increases, rotation head of the specific energy (E) of the flow play a significant role inside the system and multiple sonic points form in an appreciable section of the parameter space. For $\lambda = 2.55$ (Figs. 6.12b1-b3), multiple sonic point exists in a large range of E . In Figs. 6.12b1-b2, the global solution (solid, blue) passes through the outer sonic point whereas in panel Fig. 6.12b3, the solution (solid, blue) harbours a shock and passes through both inner and outer sonic points. In Fig. 6.12b4, only a single sonic point exist. This is mainly due to the fact, that for flows with higher energy,

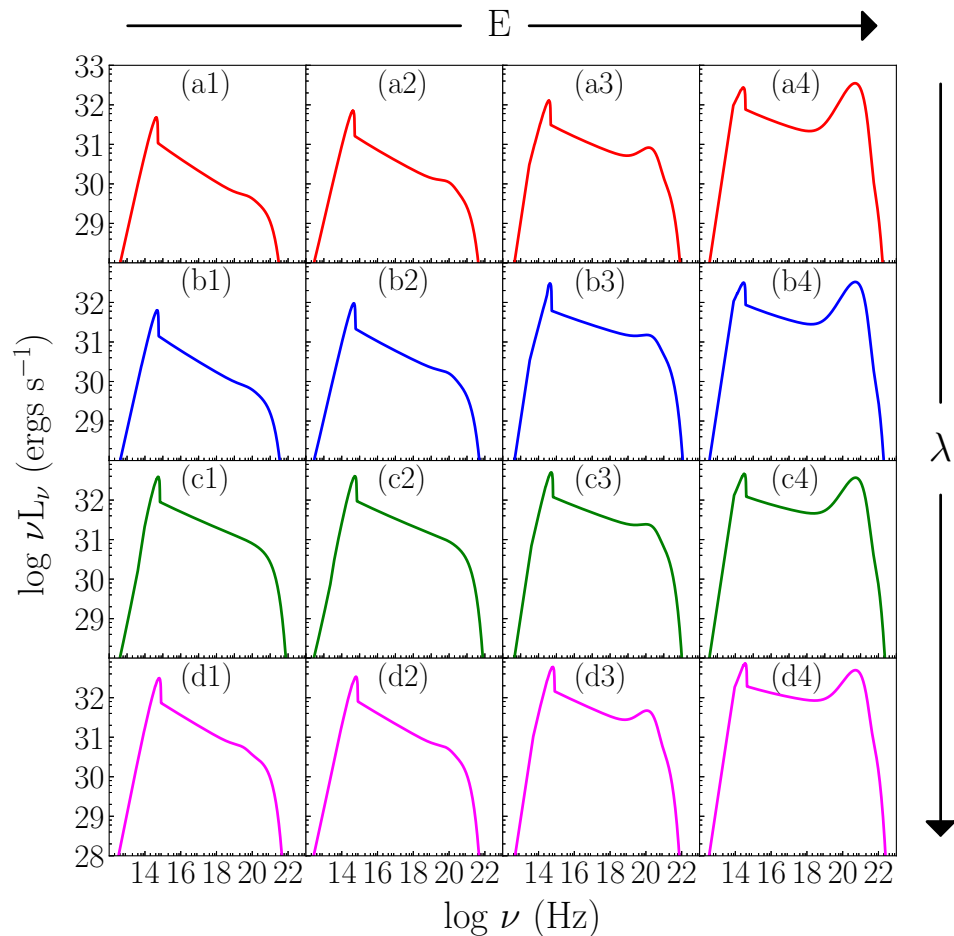


Figure 6.13: Variation of spectrum with E and λ . The set of values for E and λ and other parameters are same as that in Fig. 6.12.

the distribution of sound speed a_s is generally higher compared to flows with lower E . Therefore, the flow can only become transonic, when v increases significantly, which can happen only very close to the BH. For low values of E , the sound speed distribution $a_s(r)$ is comparatively low. Because the flow becomes transonic whenever the infall velocity $v(r)$ attains moderately high values, therefore the sonic points form further out. Angular momentum has different effect on the flow structure. If we increase λ , then the distribution of $v_\phi(r)$ increases. Higher values of v_ϕ restrict the increase of v to moderate values, except near the horizon. So, for flows with higher λ , the sonic points shift towards the BH. For even higher $\lambda \geq 2.85$, only inner sonic point exists irrespective of the value of E (see, Figs. 6.12d1–d4). In Figs. 6.12c1–c2 which are for $\lambda = 2.70$, shocks form even at lower energies.

Fig. 6.13, shows the corresponding spectra which spans from $10^{12} - 10^{22}$ Hz. As a general trend, with the increase in λ of the system, luminosity increases, since matter

6. TWO-TEMPERATURE FLOWS AROUND BLACK HOLES – II: ROTATING ACCRETION FLOWS

gets enough time to radiate. But the spectral shape and slope (arising because of inverse-Comptonization) remains roughly the same, except for the solutions which harbour shock. The spectral slope is flatter in case of shocked solutions. With the increase in E , thermal energy of the system increases, emission is hence higher. The spectral shape and slope is visibly changed. Bremsstrahlung emission, the broad peak in the higher frequency range, is increased with the increase in E (left to right), while angular momentum seems to have little effect on this particular radiative process. Since in this case we are dealing with a flow with low accretion rate, spectrum is relatively soft as inverse-Comptonization is not important.

6.4.2.4 SHOCKED SOLUTION, SPECTRA AND THE PARAMETER SPACE:

In Figs. 6.12b3, c1, c2, the accretion solutions admit stable shocks. As discussed before, for low λ , a flow admits only one sonic point (Figs. 6.12a1-a4). But as λ increases, the flow possess multiple sonic points. A flow can pass through both the sonic points only when the shock conditions are satisfied (see, Section 2.8). With the increase in λ , the centrifugal term increases, and the twin effect of the centrifugal and the thermal term can restrict the infalling matter, leading to a centrifugal pressure mediated shock transition. In the following section, we will analyse shocks present in two-temperature accretion flows.

In Fig. 6.14a, we present a typical shock solution for the parameters $E = 1.002$, $\lambda = 2.58$, $\dot{M} = 0.2\dot{M}_{\text{Edd}}$ and $M_{\text{BH}} = 10M_{\odot}$. For these parameters, the flow possess multiple sonic points. Dashed, blue line is for the accretion solution passing through r_{co} . When this solution becomes supersonic it encounters a shock at $r_{\text{sh}} = 20.952$. Then it jumps to the subsonic branch and enters the BH supersonically after crossing through r_{ci} . The global solution is represented with a solid, red line. The compression ratio ($R = u_-^r/u_+^r$, \pm implies post and pre-shock quantities, respectively) is 1.459 in this case. In Fig. 6.14b, we plot the number density as a function of r . At the shock there is an increase in number density of both protons and electrons equally. This leads to increased cooling in the system which is evident from Fig. 6.14c, where we plot emissivities of various cooling processes related to electrons. The corresponding spectrum is plotted in Fig. 6.14d. In Figs. 6.14c-d, bremsstrahlung is represented using dotted green line, synchrotron in dashed yellow and inverse-Comptonization in dashed-dotted magenta, while the total cooling is represented by solid black line. The accretion rate of the system is high, so the spectrum is mainly dominated by inverse-Comptonization, especially in the post-shock region. In Fig. 6.14d, the total spectrum of the system is plotted in black, while super imposed on it is the spectrum (solid blue) of the shock-free solution (dashed blue of panel a). The luminosity of the system is 2.831×10^{36} ergs s^{-1} , which corresponds to an efficiency (η_r) of 1.09%. If the solution would not have harboured any shock (dashed blue of panel a) then the luminosity of this shock-free solution (solid blue) is 1.293×10^{36} ergs s^{-1} and $\eta_r = 0.50\%$. Because of the shock, the luminosity and hence the efficiency of the system is

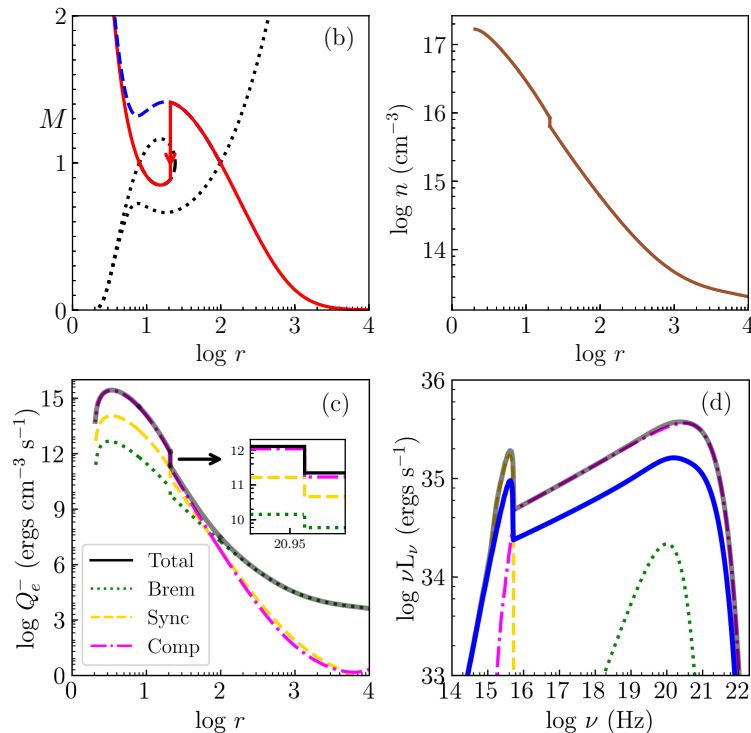


Figure 6.14: (a) A typical shocked solution (a) with its corresponding number density (b), emissivities (c) and spectrum (d) is presented. The parameters taken are $E = 1.002$, $\lambda = 2.58$, $\dot{M} = 0.2\dot{M}_{\text{Edd}}$ and $M_{\text{BH}} = 10M_{\odot}$.

doubled. However, it seems that there is no special spectral signature of shock in accretion flow, except that the luminosity of the power-law part of the spectrum increases. This is also evident from Figs. 6.13b3, c1 and c2.

The bounded region in E - λ space in Fig. 6.15, represents the shock parameter space, *i.e.*, a flow with E , λ values from the bounded region for the given \dot{M} , will under go a stable shock transition. Each bounded region or shock-parameter space is characterised by different accretion rate: $\dot{M} = 0.01$ (solid, green), $\dot{M} = 0.1$ (dashed, blue) and $\dot{M} = 1.0$ (dotted, red) around a $10M_{\odot}$ BH. We can see that as \dot{M} increases, the parameter space decreases and shifts to the lower angular momentum side. Higher value of \dot{M} implies higher rate of cooling and therefore, much hotter flow at the outer boundary can accrete and form the disc. And hence even for lower λ , the centrifugal term in conjunction with the thermal term can resist the infall to produce an accretion shock. That is why for higher \dot{M} , the shock parameter space shifts to the lower λ values. For low \dot{M} , the shock parameter space is almost similar. The parameter space significantly changes only in the presence of high accretion rates. More interestingly, it is clear that an accretion flow with high accretion rate may also harbour accretion shocks.

6. TWO-TEMPERATURE FLOWS AROUND BLACK HOLES – II: ROTATING ACCRETION FLOWS

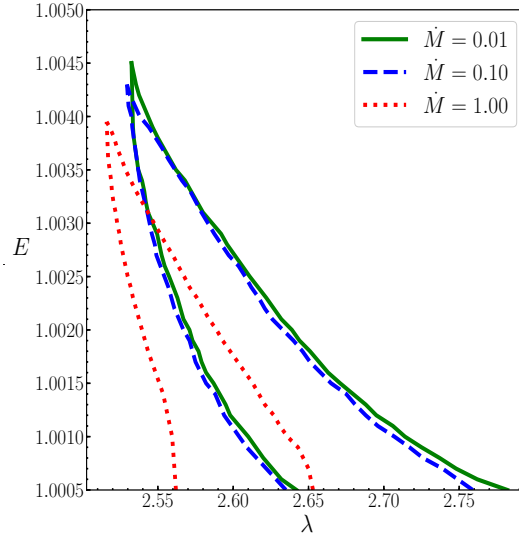


Figure 6.15: Shock parameter space for $\dot{M} = 0.01\dot{M}_{\text{Edd}}$ (solid, green), $0.10\dot{M}_{\text{Edd}}$ (dashed, blue) and $1.00\dot{M}_{\text{Edd}}$ (dotted, red) around a $10M_{\odot}$ BH.

6.4.2.5 DEPENDENCE OF SPECTRUM ON β :

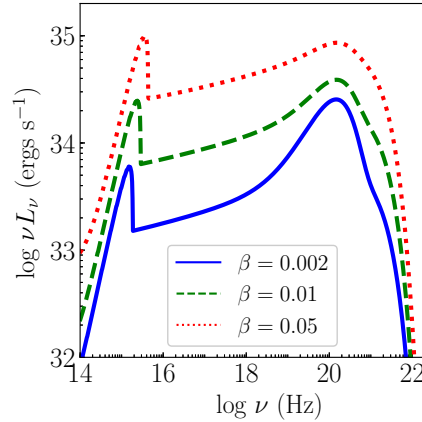


Figure 6.16: Change in spectra with increase in $\beta = 0.002$ (solid, blue), 0.01 (dashed, green) and 0.02 (dotted, red). Other parameters used are $E = 1.003$, $\lambda = 2.54$ and $\dot{M} = 0.1\dot{M}_{\text{Edd}}$ in an accretion disc around $M_{\text{BH}} = 10M_{\odot}$.

β controls the magnitude of stochastic magnetic field inside the flow. Any change in it would lead to the change in synchrotron emission from electrons and eventually change the radiation due to inverse-Comptonization. Hence, the spectra that an observer would see, significantly depends on the value of β . In Fig. 6.16, we plot the change in spectra with change in β for the flow parameters $E = 1.003$, $\lambda = 2.54$, $\dot{M} = 0.1\dot{M}_{\text{Edd}}$ and $M_{\text{BH}} = 10M_{\odot}$. We have varied β : 0.002 (solid, blue), 0.01 (dashed, green) and 0.02 (dotted, red). The present flow has high accretion rate where cooling is more pronounced. Even for low

β , the power law signature in the spectrum arising due to inverse-Comptonization is prominent, or in other words, the spectrum is hard. However, dominant emission comes from bremsstrahlung as can be inferred from its bump present at higher frequency regime. As we increase β , the bump feature vanishes. This is mainly due to the fact that with the increase in β , synchrotron emission and hence inverse-Comptonization increases more as compared to bremsstrahlung (which is independent of the magnitude of the magnetic field in the flow and hence, β), thereby masking the bump feature. The synchrotron turnover frequency also shifts to higher frequencies with the increase in β .

6.4.2.6 DEPENDENCE OF SOLUTIONS AND SPECTRA ON β_d :

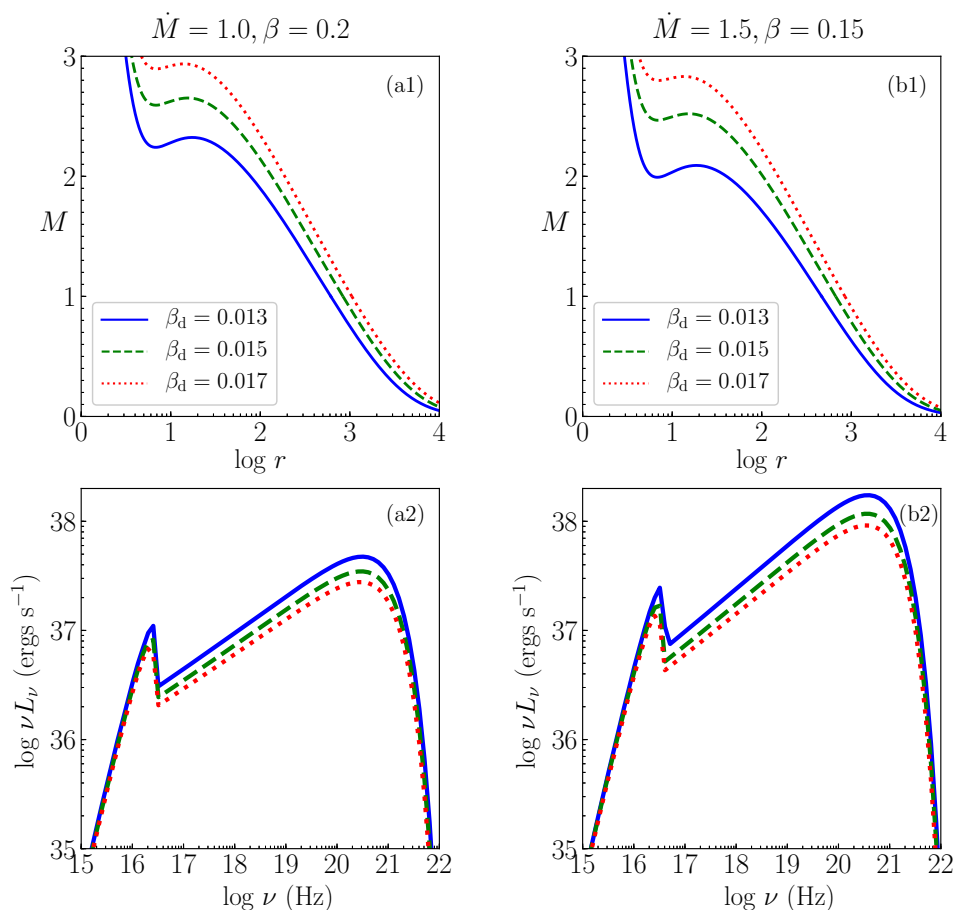


Figure 6.17: Plotted are the accretion solutions (a1, b1) and their corresponding spectra (a2, b2) for a flow with $E = 1.001$, $\lambda = 2.61$ around $M_{\text{BH}} = 10M_\odot$. Various curves are for $\beta_d = 0.013$ (solid, blue), $\beta_d = 0.015$ (dashed, green) and $\beta_d = 0.017$ (dotted, red). The accretion rates and ratio of magnetic to gas pressure are chosen are $\dot{M} = 1.0\dot{M}_{\text{Edd}}$, $\beta = 0.2$ (a1, a2) and $\dot{M} = 1.5\dot{M}_{\text{Edd}}$, $\beta = 0.15$ (b1, b2).

Fig. 6.10a showed that, magnetic dissipation (solid, red) is a more efficient heating mechanism compared to Compton heating (dotted, blue) as well as Coulomb heating of

6. TWO-TEMPERATURE FLOWS AROUND BLACK HOLES – II: ROTATING ACCRETION FLOWS

electrons (Fig. 6.10b, solid, yellow). In Figs. 6.17a1, a2–b1, b2, we vary β_d which controls magnetic dissipation. We compared the solutions and resultant spectra for $\beta_d = 0.013$ (solid, blue), 0.015 (dashed, green) and 0.017 (dotted, red). For Figs. 6.17a1–a2, we chose higher ratio between magnetic and gas pressure, $\beta = 0.2$ and accretion rate $\dot{M} = 1.0\dot{M}_{\text{Edd}}$. For Figs. 6.17b1–b2, we select $\dot{M} = 1.5\dot{M}_{\text{Edd}}$ and $\beta = 0.15$. For both the cases, we have $E = 1.001$, $\lambda = 2.61$ and $M_{\text{BH}} = 10M_{\odot}$. The sonic point, luminosities and spectral index of the accretion flows are given in Table 6.3. Evidently, luminosity and hence efficiency, decreases with increasing β_d but increases with increasing \dot{M} . If the dissipative heating is higher (i.e., higher β_d), then matter with lower temperature at large r may achieve the same E . Therefore, the accretion flow would have an overall lower temperature and would emit less. That is exactly what is observed in Figs. 6.17a2–b2, where the luminosity goes down with the increase in β_d . The spectrum is decisively hard for super-Eddington accretion rates. It means that no single flow parameter can dictate whether the spectrum will be hard or soft, instead all the flow parameters together contribute for the final outcome. However, it is clear that β_d do influence the emitted spectra and luminosity significantly.

Table 6.3: Various flow properties of the solutions plotted in Fig. 6.17.

Parameters	β_d	r_c	L $\times 10^{38}$ (ergs s $^{-1}$)	α
$\dot{M} = 1.0\dot{M}_{\text{Edd}}$ and $\beta = 0.20$	0.013	613.365	2.523	0.672
	0.015	838.022	1.877	0.680
	0.017	1053.310	1.514	0.683
$\dot{M} = 1.5\dot{M}_{\text{Edd}}$ and $\beta = 0.15$	0.013	466.718	8.31	0.606
	0.015	669.746	5.726	0.619
	0.017	849.084	4.518	0.625

6.4.2.7 POSSIBILITY OF PAIR PRODUCTION AND PION PRODUCTION

Till now, we have investigated how various factors and flow parameters affect the two-temperature accretion solutions and the resulting spectra. However, it may be noted that, we have ignored pair production from particle-particle interactions in the accretion disc or from accretion disc radiation. We have also ignored the production of gamma-rays due to high energy interactions like pion decay. We assumed that these processes will not significantly affect the solutions. In Appendix A.2, we investigate pair production process a posteriori. We compare the number densities of protons n_{p+} with positrons n_{e+} (Figs. A.2a1–b1) generated through photon interactions produced in accretion discs as well as compare the total emissivity Q_{total} with pair annihilation emissivity Q_{ann} (Figs. A.2a2–b2). We consider two sets of accretion disc parameters (1) $\dot{M} = 1.0$, $\beta = 0.2$ (Figs. A.2a1–

a2) and (2) $\dot{M} = 1.5$, $\beta = 0.15$ (Figs. A.2b1–b2). Rest of the parameters common in both the cases are, $\beta_d = 0.013$, $E = 1.001$ and $\lambda = 2.41$. These two accretion disc cases are described around a BH of $10M_\odot$. After the posteriori calculations, elaborately discussed in Appendix A.2, we can conclude that, $n_{e^+} \ll n_{p^+}$ and $Q_{\text{ann}} \ll Q_{\text{total}}$.

We note that, a similar analysis was done in Chapter 3, Section 3.4.2, where we investigated the importance of pairs in one-temperature accretion flows around BHs. From the analysis conducted there, we concluded that pair-production and hence annihilation is dominant in certain range of parameter space, where there is ample amount of radiation field present. We find that in the current posteriori calculation, the angular momentum value is low, which lowers the amount of cooling in the system, because matter would have higher infall velocities and lesser time to radiate. Thus, the conclusion is consistent with the results and discussions made in Section 3.4.2 of Chapter 3. To be more conclusive regarding the effect of pairs in two-temperature accretion flows, we need to self-consistently compute the number of pairs produced at each radius of the accretion disc, similar to the iterative feedback methodology used in Section 3.3.2, which was for one-temperature flows. Also, we need to study using different combination of flow parameters. In two-temperature flows, the degeneracy present in the system would further complicate the methodology used before to find pairs. Thus, we intend to study this in details in some future work.

In Appendix A.3 we compute the production of pions (π^0) a posteriori and the gamma rays emitted due to its decay. We plot $\log T_p$ vs $\log r$ in Figs. A.3a1–b1 and the corresponding spectra in Figs. A.3a2–b2. We study the generation of pions and gamma ray photons for two cases (1) by varying accretion rate ($\dot{M} = 0.01$: dotted, red, 0.1 : dashed, green and 1.0 : solid, blue) around a BH of $M_{\text{BH}} = 10M_\odot$ (Figs. A.3a1–a2) and (2) by varying mass of the BH ($M_{\text{BH}} = 10^2$: solid, blue, 10^4 : dashed, green and 10^6 : dotted, red), keeping accretion rate $\dot{M} = 0.1$ constant (Figs. A.3b1–b2). The other disc parameters are $E = 1.0007$, $\lambda = 2.61$, $\beta = 0.01$, & $\beta_d = 0.001$. Luminosity for higher \dot{M} is higher and so is the gamma-ray produced by decay of pions. Same trend is observed when we increase the BH mass. However, the gamma ray luminosity is always $< 10^{-5}$ times that of the total luminosity. Elaborate discussion on these two cases have been made in Appendix A.3.

6.4.2.8 DEPENDENCE ON \dot{M} AND M_{BH} :

In Fig. 6.18a, we plot the continuum spectra for $\dot{M} = 0.1\dot{M}_{\text{Edd}}$ (solid, blue), $\dot{M} = 0.6\dot{M}_{\text{Edd}}$ (dashed, green) and $\dot{M} = 1.2\dot{M}_{\text{Edd}}$ (dotted, red) from a disc around a BH of $10M_\odot$. The disc becomes brighter as \dot{M} increases, even the efficiency also increases. The spectra also becomes harder (α lower, $F_\nu \propto \nu^{-\alpha}$), mainly because the inverse-Compton output increases with the increase in number density of hot electrons inside the flow. However, the range of frequency ν on which the spectrum is distributed do not increase appreciably

6. TWO-TEMPERATURE FLOWS AROUND BLACK HOLES – II: ROTATING ACCRETION FLOWS

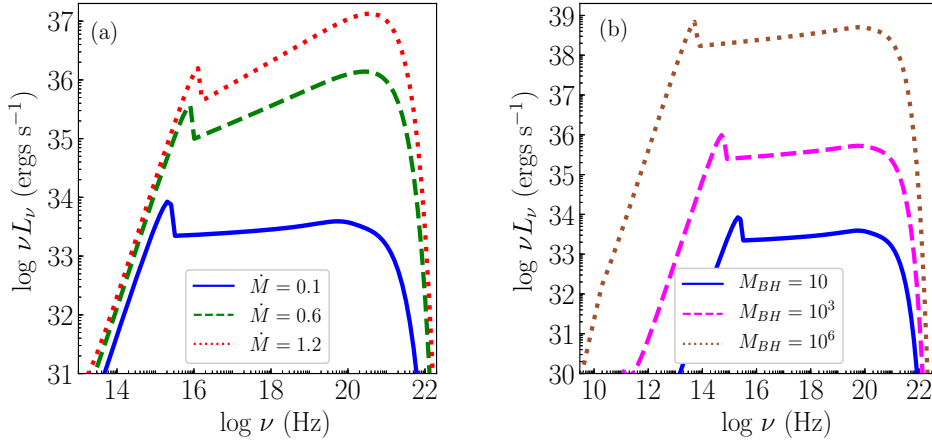


Figure 6.18: Spectra from (a) $M_{BH} = 10 M_\odot$ for different accretion rates $\dot{M} = 0.1 \dot{M}_{Edd}$ (solid, blue), $\dot{M} = 0.6 \dot{M}_{Edd}$ (dashed, green) and $\dot{M} = 1.2 \dot{M}_{Edd}$ (dotted, red); (b) $\dot{M} = 0.1 \dot{M}_{Edd}$ but around $M_{BH} = 10 M_\odot$ (solid, blue), $M_{BH} = 10^3 M_\odot$ (dashed, magenta) and $M_{BH} = 10^6 M_\odot$ (dotted, brown). Other disc parameters are $E = 1.001$ and $\lambda = 2.4$.

with the increase in accretion rate. Corresponding spectral properties are presented in Table 6.4 (left table):

Table 6.4: Various properties of the spectra plotted in Fig. 6.18a (left table) and Fig. 6.18b (right table).

\dot{M} (\dot{M}_{Edd})	L (ergs s ⁻¹)	η_r (%)	α
0.1	4.731×10^{34}	0.037	0.939
0.6	8.301×10^{36}	1.068	0.720
1.2	6.684×10^{37}	4.298	0.627

M_{BH} (M_\odot)	L (ergs s ⁻¹)	η_r (%)	α
10	4.731×10^{34}	0.037	0.939
10^3	6.426×10^{36}	0.049	0.936
10^6	6.106×10^{39}	0.047	0.915

In Fig. 6.18b, we plot spectra from discs with the same accretion rate $\dot{M} = 0.1 \dot{M}_{Edd}$, but around different M_{BH} which are $10 M_\odot$ (solid, blue), $10^3 M_\odot$ (dashed, magenta) and $10^6 M_\odot$ (dotted, brown). The more massive the black hole, the disc is brighter since absolute accretion rate increases. In addition the spectrum spans over a larger range of ν , with significant emission from radio to γ rays. It may be noted, higher M_{BH} results in a more broadband spectra, the disc becomes more luminous but the spectral index do not change much. The spectral properties are presented in Table 6.4 (right table).

6.4.2.9 LUMINOSITY, EFFICIENCY AND SPECTRAL INDEX OF TWO-TEMPERATURE FLOWS :

In Fig. 6.19a, we have calculated the luminosities and in Fig. 6.19b we plotted the efficiency of the accretion of matter onto BHs of different masses ($10 M_\odot$, $10^3 M_\odot$ and $10^6 M_\odot$) as

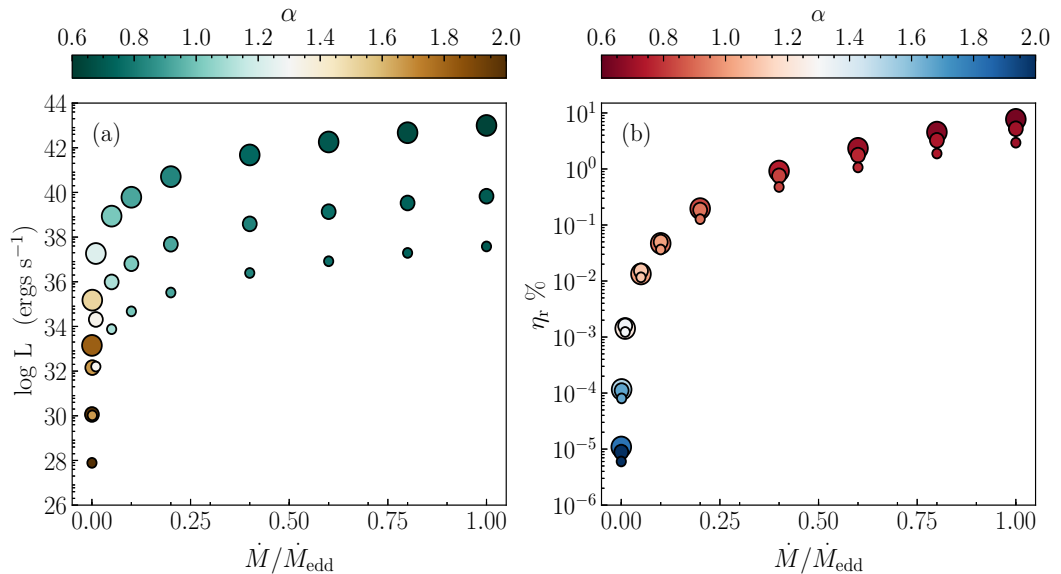


Figure 6.19: (a) Variation of bolometric luminosity (in ergs s^{-1}) and (b) efficiency (in %) as a function of \dot{M} (in units of Eddington rate, \dot{M}_{edd}). Colour bar indicates the spectral index (α). BHs of different masses : $10M_\odot$ (small circle), 10^3M_\odot (medium circle) and 10^6M_\odot (largest circle) are represented with increasing sizes of the circles. The parameters used here are $E = 1.001$ and $\lambda = 2.4$.

a function of accretion rate (\dot{M}). Size of the circles are in order of increasing value of BH mass. Parameters used are $E = 1.001$ and $\lambda = 2.4$. It may be noted that luminosity rises steeply with the increase in accretion rate of the system, for all BH masses. More the supply of matter, more would be the conversion of it into energy. However, at higher accretions rates, luminosities approach asymptotic values. Radiation emitted by accretion disc, is the effect of conversion of gravitational energy released in the act of accretion, into electro-magnetic radiation. So as \dot{M} increases, emission increases due to increased supply of matter. However, it cannot emit more than the energy obtained from the accretion process and therefore, it reaches a ceiling around $\eta \sim 10\%$. It is apparent from Fig. 6.19b, that efficiency is slightly affected by the BH mass. The spectral index (α) is represented as colour bar over both Figs. 6.19a, b. It changes visibly with the increase in accretion rate of the system (also, see Fig. 6.18a and Table 6.4 left table) but do not change much with the change in BH mass (also, see Fig. 6.18b and Table 6.4 right table).

6.4.2.10 COMPARISON WITH OBSERVATIONS:

The first BH to be imaged in the history is M87 (Event Horizon Telescope Collaboration et al., 2019), thereby confirming the existence of these exotic objects in the Universe. M87 has been modelled by different authors using different models (Chakrabarti, 1995; Di Matteo et al., 2003; Feng et al., 2016; Junor et al., 1999; Macchetto et al., 1997; Mandal

6. TWO-TEMPERATURE FLOWS AROUND BLACK HOLES – II: ROTATING ACCRETION FLOWS

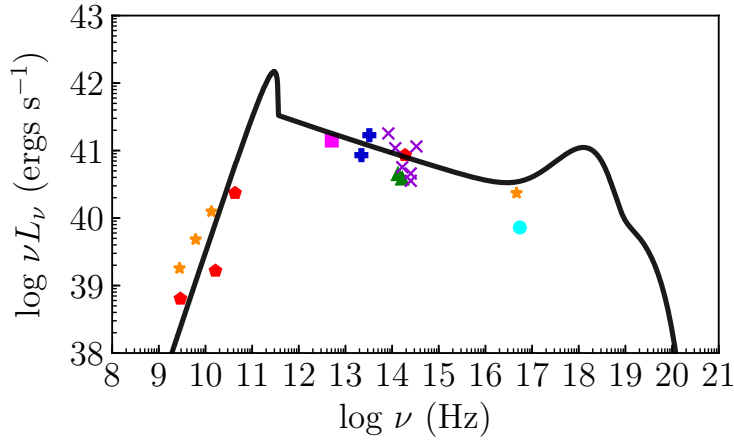


Figure 6.20: Model spectrum obtained from entropy maximisation formulation (solid, black) is fitted onto the observations of M87 spectrum (data points acquired from [Mandal & Chakrabarti \(2008\)](#) and references therein).

& Chakrabarti, 2008; Reynolds et al., 1996; Spencer & Junor, 1986; Vincent et al., 2021; Wielgus et al., 2020). In this section we investigate the spectrum of this $6.5 \times 10^9 M_{\odot}$ BH using the two-temperature accretion model proposed by us. It is well established that M87 is a low luminous AGN with $L \sim 10^{42}$ ergs s^{-1} located at a distance of ≈ 16 Mpc ([Biretta et al., 1991](#)). Also, the Bondi accretion rate quoted in literature is around $\sim 0.1 M_{\odot} \text{yr}^{-1}$ ([Di Matteo et al., 2003](#)). We use these values to fit the observed spectrum. Apart from these parameters, there are other free parameters like λ , E , β , β_d , δ_B etc, which needs to be played around to obtain the best fit.

We use the data provided in [Mandal & Chakrabarti \(2008\)](#) and references therein to get the observed data points. In Fig. 6.20, we plot different observed data points (mean values). They are: [Biretta et al. \(1991\)](#) (orange stars), [Ho \(1999\)](#) (red pentagons), [Sparks et al. \(1996\)](#) (violet cross), [Stiavelli et al. \(1997\)](#) (blue plus), [Perlman et al. \(2001\)](#) (magenta square), [Perlman & Wilson \(2005\)](#) (cyan dot) and [Maoz et al. \(2005\)](#) (green triangles). In solid black we plot the spectrum obtained by assuming $\lambda = 2.38$, $E = 1.000038$, $\beta = 0.05$ and $\beta_d = 0.015$. We select and use the maximum entropy solution, to extract the spectrum. We see that, the total luminosity obtained from our model is around 2×10^{42} ergs s^{-1} which is in close agreement with the observations. Also, the data points pass fairly well through the modelled spectrum, thereby validating the model proposed by us. This suggests that the use of the entropy maximisation formulation for selecting the solution and spectrum would be helpful in explaining observations. But, it is to be noted here that, that we have ignored the error bars. Although very low errors are present in the data points, these are important from the observational view point. Also, there are innumerable details which needs to be taken care of, while fitting an observed spectrum. We want to include all of

them in the best possible way in some future work.

6.5 DISCUSSIONS AND CONCLUSIONS

In this chapter we present our results in case of two-temperature rotating flows, that is flows having angular momentum. Pure GR treatment was made, which helped us model the strong gravity of BHs. In these flows, Coulomb coupling was never found to be too strong to make the flow attain a single temperature. We have also presented results of spherical flows in few cases, in order to contrast the differences of these flows with flows having angular momentum.

Our focus in this chapter is to obtain unique transonic solutions in two-temperature model. We, in Chapter 4, have reported that two-temperature solutions are degenerate in nature. Infinite transonic solutions exist for the same constants of motion. We solved the problem with the help of the entropy measure (Eq. 4.10) which was obtained from the first principles. We successfully validated in case of spherical flows in Chapter 5 and here in this chapter, we extended it to the case of rotating flows as well. But these systems are complex since they possess multiple sonic points, unlike single sonic points in spherical flows. For the given set of disc parameters, like generalized Bernoulli parameter (E), accretion rate (\dot{M}) and angular momentum (λ), a choice of proton temperature may produce a transonic solution through outer sonic point, some other choice of the temperature will produce a solution through inner sonic point, while some other will produce solutions which undergoes shock transition. The resulting radiation also vary accordingly. Infact some solutions may be four times more luminous compared to some other solutions (see Fig. 6.5 and Table 6.1). Therefore, this degeneracy issue is serious and needs urgent attention. We lay down the methodology to obtain a unique two-temperature solution using the principles of second law of thermodynamics. We stated that the solution with the highest entropy near the horizon is the correct solution. Since the proposed correct transonic solution is the one with the highest entropy, therefore it is warranted that these solutions should be stable for the relevant boundary conditions. Infact, the collective wisdom of the community on accretion solutions expect, that close to the horizon accretion should be transonic. However, for a given set of accretion disc parameters like \dot{M} , E and λ , we do have a large number of transonic two-temperature solutions, and the question of stability of the solutions arise. In Section 6.3.3, we showed that the gradient of entropy of the flow with the proton temperature *i.e.*, $d\dot{\mathcal{M}}_{\text{in}}/dT_{\text{pin}}$, is such that, it tends to push the solution towards the temperature corresponding to the highest entropy solution. In other words, if our proposed solution is perturbed, then $d\dot{\mathcal{M}}_{\text{in}}/dT_{\text{pin}}$ would automatically try to restore the solution to the one corresponding to the highest entropy. This is the first time, to the best of our knowledge, that such work has been done. This methodology to remove the degeneracy in two-temperature flows is

6. TWO-TEMPERATURE FLOWS AROUND BLACK HOLES – II: ROTATING ACCRETION FLOWS

required, since any wrong choice of solution would give us a wrong solution and hence an overall wrong information of the system.

In this chapter, we investigated different rotating accretion solutions (conical as well as flows in hydrostatic equilibrium) corresponding to different flow parameters and have also computed the spectrum. We considered the relativistic effects while generating the spectrum. Flows in hydrostatic equilibrium, as the name suggests, allows the accretion disc to puff up and shrink down, depending on the temperature present in the region. Heating processes will lead to increasing of the half-height of the accretion disc while excessive cooling will reduce the height. Such mechanism is not allowed in case of conical flows, where the height is a constant function of r . Thus, conical flows are found to be more hotter than flows in hydrostatic equilibrium. But the equations are simple in conical flows as $H \equiv f(r)$, which allowed us to focus more on the methodology of removing degeneracy in the MCP regime. After the methodology was validated, we worked on more realistic discs in hydrostatic equilibrium in the transverse direction. We analysed and focussed more on these solutions.

It is important to note that, in this chapter, we studied solutions of two-temperature accretion discs around non-rotating BHs. The spin of the BH may play an important role in jet generation via a process called Blandford-Znajek mechanism (Blandford & Znajek, 1977), however, accretion is still the primary mechanism to explain the observed luminosities. And a proper two-temperature accretion solution is the best way to obtain the spectra from such systems.

In this chapter, we obtained all possible solutions depending on E and λ for a given \dot{M} and M_{BH} (Fig. 6.12) and in addition we also plot the emitted spectrum (Fig. 6.13). This also shows that, \dot{M} or M_{BH} do not alone determine the emitted spectrum or even the luminosity. Depending on E and λ , the solution changes and so does the spectrum and luminosity. The constants of motion are uniquely linked to the obtained spectrum. There are indeed shocked accretion solutions even in the two-temperature regime. The shocked solutions are more luminous, because in the post-shock region inverse-Comptonization becomes effective, the intensity of the power-law photons increases, compared to a shock-free solution (Fig. 6.14). We also showed that accretion flow can harbour steady shocks in a small but significant patch of the energy angular momentum parameter space (see, Fig. 6.15). However, in general, the shock strength in two-temperature flow is lesser than that in a one-temperature flow. Moreover, we did not find any particular spectral signature of the presence of shock, only that the shocked solution is more luminous than shock-free ones. But, it has been found in cases of low accretion rate flows, where weak bremsstrahlung feature is visible (in the high frequency end of the spectrum) in a shock-free solution, this feature disappears in a shocked solution (see Figs. 6.13c1, c2).

Radiative properties of a BH system, depends on β and β_{d} along with E , λ , \dot{M} and M_{BH} . For low values of β and β_{d} , the radiative efficiency was around few percent, but for

higher values, the efficiency easily crossed ten percent, even for the same accretion rate and mass of the BH. We also showed that the spectra becomes broadband if the mass of the central BH considered is higher, it also becomes more luminous but the spectral index remains roughly the same. While, with the increase in accretion rate of the BH, the bandwidth of spectra remains the same, while the luminosity and the spectral index changes significantly.

We did not consider pair production from the radiation of the accretion disc. Neither did we consider particle production due to high energy interaction of the protons. To have a knowledge regarding the importance of these processes in two-temperature accretion discs, we used background solutions and computed a posteriori, the amount of pair production, annihilation and pion production in the system. The selected solutions showed that pair production is negligible, and therefore the contribution of the pair annihilation emission in the total spectrum of the disc is also negligible. Similarly, we showed, with the help of a posteriori estimate that the gamma-ray production from pion decay is also negligible. But to be more conclusive, we need to solve self-consistently the EoM in the presence of these processes (also, see Chapter 3). This is a scope of future work.

In this chapter, we did not consider viscosity of the flow, but invoking our results from our previous Chapter 3, on viscous accretion solutions in the one-temperature regime (see, Appendix A.1), we argued that since the angular momentum is almost constant in the inner part of the disc, and that the viscous heating is much weaker than the magnetic dissipation, we can safely neglect viscosity to ease our computation. Considering the single temperature viscous flow as the representative case, we may conclude that, there will not be any qualitative change by considering viscosity, although quantitative effect cannot be ruled out. Infact, since we showed magnetic dissipation to be a very efficient heating process, we could incorporate most heating processes by tuning the parameter β_d .

We also modelled the spectrum of M87 using the data from different sources (see, Mandal & Chakrabarti (2008) and references therein). The bolometric luminosity obtained was found to be close to that of the observed luminosity and the model closely fitted the observed data points (see, Fig. 6.20). This suggests that the use of the entropy maximisation formulation for selecting the solution and spectrum would be helpful in explaining observations. We intend to extensively carry out the work of explaining observations for different BH candidates with our proposed model in future.

To conclude, it is absolutely necessary to obtain unique transonic two-temperature solution. To interpret observations, it is compulsory that the hydrodynamics of the system is properly handled. Selecting any arbitrary solution would mislead us. We allowed the second law of thermodynamics to dictate and select the solution, without taking recourse to any assumptions, such that consistency is maintained. In addition to spherical flow (Chapter 5), unique accretion disc solutions also correspond to the highest entropy solution.

Chapter 7

TWO-TEMPERATURE ACCRETION FLOWS AROUND NEUTRON STARS

7.1 INTRODUCTION

Neutron stars (NSs) are one of the densest objects known in the Universe, with core densities surpassing nuclear densities. They can harbour magnetic fields upto 10^{15}G , everything packed within a size of $\lesssim 10$ km. Accreting NSs with strong magnetic fields were confirmed in 1970's, with the observations of Cen X-3 and Her X-1 (Giacconi et al., 1971). Thereafter, X-ray binary pulsars were discovered, whose magnetic axis was found to be misaligned with the rotation axes. Works by Ghosh & Lamb (1978); Ghosh et al. (1977); Lamb et al. (1973) etc., concluded that strong magnetic field of NS can control the dynamics of matter flow around it, compelling the accretion to occur in the form of a disc upto a certain radius and then via field lines (Davidson & Ostriker, 1973; Pringle & Rees, 1972).

It is important to obtain self-consistent transonic solutions, that connect the flow from the accretion disc to the NS surface (Karino et al., 2008; Koldoba et al., 2002) via a surface shock. It was suggested Li et al. (1996) that, as the matter reaches the star's surface supersonically it will form a shock there. This shock would enhance the dissipation processes, making the flow radiate away all its kinetic energy, such that the matter can slowly settle down onto the surface. These radiative process also determine the observable spectrum. Singh & Chattopadhyay (2018b) studied such magnetised accretion flows onto NS, assuming strong, dipole magnetic fields, axis of which was co-aligned with the rotation axis of the star (Ghosh & Lamb, 1979; Koldoba et al., 2002; Lovelace et al., 1995). Although the

The results of this chapter are under review: **Sarkar, Shilpa**; Singh, Kuldeep; Chattopadhyay, Indranil and Laurent, Philippe; 2021, *Astronomy & Astrophysics*.

7. TWO-TEMPERATURE ACCRETION FLOWS AROUND NEUTRON STARS

axes were co-aligned, this work was successful in bringing out the essential features, allowing us to deeply understand magnetised funnel flows. They obtained a complete picture of the system for a wide range of parameter space. They took care of the MHD integrals, conserved along the magnetic field lines along with the transonicity of the flow. Also, for certain combination of constants of motion, secondary shocks were also obtained (r_{ss}), apart from the primary/surface shock (r_{ps}). But, the spectral analysis of these flows were not done and radiative processes like blackbody emission and Comptonization of the seed soft photons, were not considered. Moreover, the electron temperature was not explicitly computed and was only estimated, since the analysis was done in the one-temperature regime. Because of the arguments discussed all along the previous chapters (see, Section 1.5, and Chapters 4, 5 and 6), there is a distinct possibility for an accretion flow to maintain two-temperatures, one temperature defining protons and the other electrons. In 1982, [Langer & Rappaport](#) studied funnel flows in two-temperature regime, but considered only the post-shock region, while obtaining solutions and computing the spectrum.

In this chapter, we investigate two-temperature accretion flows around NSs, extending the work of [Singh & Chattopadhyay \(2018a,b\)](#), which was done in one-temperature regime. As discussed in Chapter 4, two-temperature accretion flows are degenerate in nature. Because of the paucity of requisite number of equations, infinite number of solutions are possible, for a given set of constants of motion. It is important to note that, because of the presence of a hard surface in case of NS, matter do not achieve free-fall velocities and the form of entropy measure proposed in the previous chapter, is not valid for these flows. This has led to a serious problem of constraining the degeneracy in two-temperature flows around NSs (see, Section 4.4.3). Therefore, in this work, we propose a novel methodology to remove degeneracy and obtain unique transonic two-temperature solutions around NS, for a given set of constants of motion. We elaborately discuss it in the methodology section. Thereafter we proceed to obtain global accretion solution and perform spectral analysis. We obtain the spectrum, assuming dissipative processes like bremsstrahlung, synchrotron, blackbody emission, Comptonized bremsstrahlung, Comptonized synchrotron and Comptonized blackbody. We studied solutions for a large set of parameter space using CR EoS, to get a global picture of the NS system. In this work, we have used the [Paczyński & Wiita \(1980\)](#) potential to mimic the strong gravity around NS. Also, CR EoS has been used, since the flows we are going to deal with, are thermally trans-relativistic in nature as well as there are two-different species present in the system with masses differing by 1000 of times.

7.2 GOVERNING EQUATIONS AND ASSUMPTIONS

The work is done in the ideal MHD regime assuming steady, axisymmetric and inviscid flow ([Chandrasekhar, 1956](#); [Heinemann & Olbert, 1978](#); [Lovelace et al., 1986](#)) in spherical

coordinate system (r, θ, ϕ) . The ideal MHD equations have been given in Eqs. 2.19–2.22. These equations can be integrated to obtain a number of integrals which remain conserved along magnetic field lines (Ghosh et al., 1977; Koldoba et al., 2002; Mestel, 1968; Ustyugova et al., 1999; Weber & Davis, 1967), discussion of which is given in Section 2.3 (see, Eqs. 2.24–2.29).

7.2.1 STREAM FUNCTION AND THE STRONG MAGNETIC FIELD ASSUMPTION

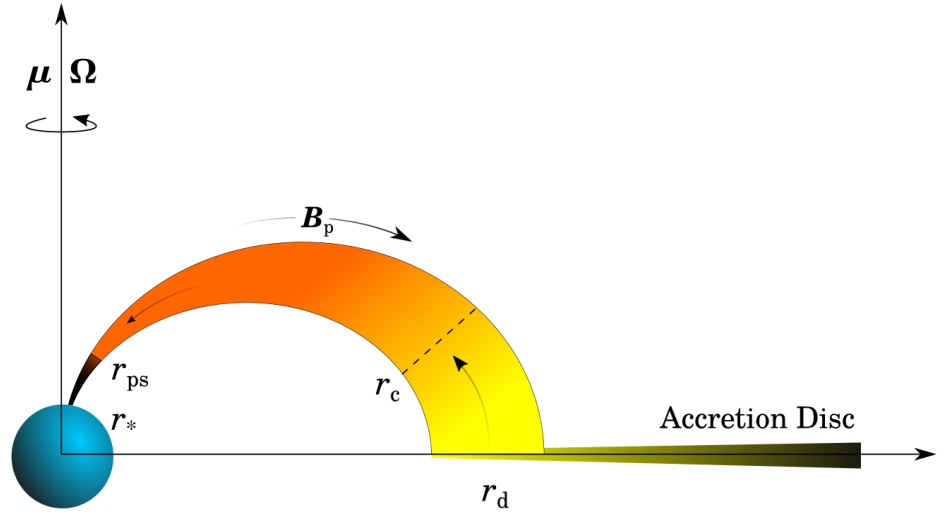


Figure 7.1: Representation of a magnetised accretion flow, with magnetic moment (μ) co-aligned with the rotation (Ω) axis of the star. Matter is accreted along magnetic flux tube, which connects the accretion disc to the surface of the NS. The sonic point is marked as r_c , primary shock is marked as r_{ps} and r_* is the radius of NS.

We assume the NS to have strong dipole-like magnetic field. The magnetic flux function for this field in spherical coordinates is,

$$\Psi = \frac{\mu}{r} \sin^2 \theta, \quad (7.1)$$

and the geometry of the dipole field lines is given by,

$$r = r_d(\Psi) \sin^2 \theta, \quad (7.2)$$

where, $r_d = \mu/\Psi$ is the radius from the center of the NS where the field line (Ψ) crosses the equatorial plane of the disc. In our work this is also the radius from where the matter starts channelling through the magnetic field lines, from the accretion disc as shown in Fig. 7.1. The poloidal magnetic field strength (B_p) is obtained using Eqs. 7.1 and 7.2, to

7. TWO-TEMPERATURE ACCRETION FLOWS AROUND NEUTRON STARS

get,

$$B_p(r) = \frac{\mu}{r^3} \sqrt{4 - \frac{3r}{r_d}}. \quad (7.3)$$

We assume the NS rotation axis to be co-aligned with the magnetic moment (μ) $\Rightarrow \Omega \parallel \mu$ (see, Fig. 7.1). Apart from this, we also assume that NS has strong magnetic field, such that matter flow does not affect the magnetic field geometry. This is valid when the magnetic energy density is much larger than the gas pressure and ram pressure (Koldoba et al., 2002) and can be expressed as,

$$B_p^2/8\pi \gg (p, \rho v_p^2) \quad (7.4)$$

Now, we define: $\rho_A = \kappa^2/(4\pi)$, which is the mass density at the Alfvén radius. Then, from Eq. 2.26, we have, $4\pi\rho v_p^2/B_p^2 = \rho_A/\rho = v_p^2/v_{Ap}^2 = M_A^2$, where is $v_{Ap}^2 = B_p^2/(4\pi\rho)$ is the Alfvén speed and M_A is the poloidal Alfvénic Mach number. Condition 7.4 then implies: $\rho_A/\rho \ll 1$ or $M_A^2 \ll 1$, or in other words, the flow is sub-Alfvénic. Solving for ω and B_ϕ using Eqs. 2.26 to 2.28, we get,

$$\omega = \Omega \left(1 - \frac{\rho_A}{\rho} \frac{r_A^2}{\tilde{r}^2}\right) \left(1 - \frac{\rho_A}{\rho}\right)^{-1} \quad \text{and} \quad B_\phi = \tilde{r}\Omega\sqrt{4\pi\rho_A} \left(1 - \frac{r_A^2}{\tilde{r}^2}\right) \left(1 - \frac{\rho_A}{\rho}\right)^{-1}. \quad (7.5)$$

where, $r_A^2 = \Lambda(\Psi)/\Omega(\Psi)$ is the Alfvén radius. Again, using the condition $\rho_A/\rho \ll 1$, the above expressions reduce to,

$$\frac{\omega - \Omega}{\Omega} = \frac{\rho_A}{\rho} \left(1 - \frac{r_A^2}{\tilde{r}^2}\right) \quad \text{and} \quad \frac{B_\phi}{B_p} = \frac{\tilde{r}\Omega}{v_p} \frac{\rho_A}{\rho} \left(1 - \frac{r_A^2}{\tilde{r}^2}\right). \quad (7.6)$$

Assuming further, that $(\rho_A/\rho)|1 - r_A/\tilde{r}^2| \ll 1$, we obtain,

$$|\omega - \Omega| \ll \Omega \quad \text{and} \quad \frac{B_\phi}{B_p} \ll 1. \quad (7.7)$$

The first relation of the above equation implies that matter moves with the same angular velocity as the field lines because of the strong magnetic field assumption. Now, as these field lines are strongly anchored to the surface of the NS, they rotate with the same angular velocity as that of the star, or $\Omega_{\text{matter}} = \Omega(\Psi) = \Omega_{\text{star}} = \Omega$. This also implies that r_d is very close to the co-rotation radius (r_{corot}) or $r_d \simeq r_{\text{corot}}$. The second relation implies that the toroidal component of the magnetic field is negligibly small, compared to its poloidal component.

7.2.2 FINAL FORM OF EQUATIONS

The effective potential of an accretion flow along a given field line $\Psi(r, \theta) = \text{constant}$, in a reference frame co-rotating with the star, that is rotating with an angular velocity Ω can

be represented as the sum of the gravitational and centrifugal forces,

$$\Phi(r) = \Phi_g + \Phi_{\text{centri}} = -\frac{GM_*}{r - r_g} - \frac{\Omega^2 r^2 \sin^2 \theta}{2}. \quad (7.8)$$

On simplifying the above equation, using the definition of r_d from Eq. 7.2 and the relations $r_{\text{corot}} \equiv (GM_*/\Omega^2)^{1/3}$ and $\alpha_n \equiv r_{\text{corot}}/r_d$, we get,

$$\Phi(r) = -\Omega^2 r_{\text{corot}}^2 \left[\frac{\alpha_n r_d}{r - r_g} + \frac{(r/r_d)^3}{2\alpha_n^2} \right]. \quad (7.9)$$

From the discussions made in Section 7.2.1 (see, Eq. 7.7), we assume $\alpha_n = 1$ throughout our work. Following the same conditions and using Eq. 7.9, we simplify generalised Bernoulli constant defined along a specific stream line $\Psi(r, \theta) = \text{constant}$, given in Eq. 2.29 to,

$$E(\Psi) = \frac{1}{2}v_p^2 + h + \Phi(r) + \int \frac{\Delta Q dr}{\rho v_p}. \quad (7.10)$$

This is a constant of motion in the presence of any dissipation processes present in the flow. If dissipation is absent ($\Delta Q = 0$), the above equation reduces to what is called the canonical form of Bernoulli constant and is given by,

$$\mathcal{E} = \frac{1}{2}v_p^2 + h + \Phi(r). \quad (7.11)$$

From Eqs. 2.26 and 7.3, we get the poloidal velocity relation,

$$v_p = \frac{\mu\kappa(\Psi)}{4\pi\rho r^3} \sqrt{4 - 3\frac{r}{r_d}}. \quad (7.12)$$

This equation suggests that the information of magnetic field is imprinted inside the velocity field.

In the equations to follow, we drop all the subscripts ‘p’ which implies the poloidal components and replace the variables v_p with v , B_p with B , A_p with A etc.

The differential equations for electron and proton temperatures are obtained from the first law of thermodynamics given by Eq. 2.23 and using Eqs. 2.30–2.32 and 7.12, to get,

$$\frac{d\Theta_e}{dr} = -\frac{\Theta_e}{N_e} \left[\frac{1}{v} \frac{dv}{dr} + \frac{3}{2r} \left(\frac{8 - 5r/r_d}{4 - 3r/r_d} \right) \right] - \mathbb{E}, \quad (7.13)$$

$$\frac{d\Theta_p}{dr} = -\frac{\Theta_p}{N_p} \left[\frac{1}{v} \frac{dv}{dr} + \frac{3}{2r} \left(\frac{8 - 5r/r_d}{4 - 3r/r_d} \right) \right] - \eta\mathbb{P}, \quad (7.14)$$

where, $\mathbb{E} = \Delta Q_e \tilde{K}/(\rho v N_e)$ and $\mathbb{P} = \Delta Q_p \tilde{K}/(\rho v N_p)$. Definition of ΔQ_e and ΔQ_p have been discussed in detail, in Section 2.5. We note that, apart from bremsstrahlung, synchrotron and their respective inverse-Comptonizations, we have also considered blackbody

7. TWO-TEMPERATURE ACCRETION FLOWS AROUND NEUTRON STARS

radiation from the thermal mound at the NS surface (formed due to accreted matter being settled down onto the hard surface of NS) and the inverse-Comptonization of these soft photons in the post-shock accretion column. The formula used to calculate the height and temperature of the thermal mound is from [Becker & Wolff \(2007\)](#). We follow their prescription to obtain the corresponding emissivity and spectrum.

Simplifying Euler equation (Eq. 2.20) or similarly, taking the derivative of the Bernoulli constant (Eq. 7.10), we obtain the differential equation for poloidal velocity,

$$\frac{dv}{dr} = \frac{\mathcal{N}(r, v, \Theta_e, \Theta_p)}{\mathcal{D}(r, v, \Theta_e, \Theta_p)}, \quad (7.15)$$

where,

$$\mathcal{N} = \frac{3a_s^2}{2r} \left(\frac{8 - 5r/r_d}{4 - 3r/r_d} \right) + \frac{\mathbb{E} + \mathbb{P}}{\tilde{K}} - \Phi' \quad \text{and} \quad \mathcal{D} = v^2 \left(1 - \frac{a_s^2}{v^2} \right). \quad (7.16)$$

We have defined the speed of sound in two-temperature magnetised flow as, $a_s^2 = (\Gamma_e \Theta_e + \Gamma_p \Theta_p / \eta) / \tilde{K}$.

7.2.3 ENTROPY ACCRETION RATE EXPRESSION

The expression for entropy accretion rate, using Eqs. 2.24, 4.4 and 4.10, can be written as,

$$\dot{\mathcal{M}}_{\text{in}} = \sqrt{\exp\left(\frac{f_{\text{ein}} - 1}{\Theta_{\text{ein}}}\right) \exp\left(\frac{f_{\text{pin}} - 1}{\Theta_{\text{pin}}}\right) \Theta_{\text{ein}}^{\frac{3}{2}} \Theta_{\text{pin}}^{\frac{3}{2}} (3\Theta_{\text{ein}} + 2)^{\frac{3}{2}} (3\Theta_{\text{pin}} + 2)^{\frac{3}{2}} (v_{\text{in}} A_{\text{in}})}. \quad (7.17)$$

This formula is similar to what was obtained for BH accretion flows (except the bracketed term, see Section 4.4.2). The importance of this formula in two-temperature theory have been discussed briefly in sections to follow.

7.2.4 SONIC POINT CONDITIONS AND SHOCK CONDITIONS

The critical point conditions are obtained from Eq. 7.15, by using the fact that at r_c , $dv/dr = \mathcal{N}/\mathcal{D} = 0/0$,

$$\mathcal{N} = 0 \quad \Rightarrow \quad \frac{3a_{\text{sc}}^2}{2r_c} \left(\frac{8 - 5r_c/r_{\text{dc}}}{4 - 3r_c/r_{\text{dc}}} \right) + \frac{\mathbb{E}_c + \mathbb{P}_c}{\tilde{K}} - \Phi'_c = 0 \quad (7.18)$$

$$\text{and} \quad \mathcal{D} = 0 \quad \Rightarrow \quad v_c = a_{\text{sc}}, \quad (7.19)$$

where, the subscript ‘c’ implies quantities at the sonic point. The value of $(dv/dr)|_{r_c}$ is obtained using the L’Hospital’s rule.

In the strong field regime, the MHD shock conditions ([Kennel et al., 1989](#)) reduces to

hydrodynamic shock conditions and they are given by,

$$\text{Conservation of mass flux : } [\rho v] = 0, \quad (7.20)$$

$$\text{Conservation of momentum flux : } [\rho v^2 + p] = 0, \quad (7.21)$$

$$\text{Conservation of energy flux : } \left[\rho v \left\{ \frac{1}{2} v^2 + h + \int \frac{\Delta Q dr}{\rho v} \right\} \right] = 0. \quad (7.22)$$

where, the square brackets imply the difference between the pre-shock and post shock flow variables (also, see Section 2.8).

7.3 SOLUTION METHODOLOGY

Accretion flow around NSs are transonic in nature, similar to BHs (Karino et al., 2008; Koldoba et al., 2002; Singh & Chattopadhyay, 2018b). They can harbour one or more critical (sonic) points, r_c 's. Apart from strong, ordered magnetic field of an NS, the presence of a hard surface is an additional major difference, that distinguishes it from a BH. The accretion flow onto an NS although accelerated to achieve transonicity by its strong gravity, has to settle down onto the NS surface. This will drive a terminating shock, also known as primary shock (r_{ps}). Additionally, there is possibility of formation of a secondary stable shock (r_{ss}), for certain combination of flow parameters, driven by the centrifugal and pressure gradient forces. It is formed between the primary shock and the co-rotation radius (i.e., $r_{ps} < r_{ss} < r_{corot}$). In other words, the topology of solutions depend on the combination of flow parameters used (e.g., E , P and \dot{M} ; B dictates the flow geometry) and have been reported recently in the single temperature regime by Singh & Chattopadhyay (2018a,b).

7.3.1 TWO-TEMPERATURE ACCRETION FLOWS AROUND NS: DEGENERACY AND THE DIFFICULTY IN REMOVING IT

Given a set of constants of motion, the set of equations are incomplete. Therefore, it is not possible to find a unique transonic solution for a given set of constants of motion around an NS. Similar problem was encountered in two-temperature accretion flows around BHs (see, Chapters 4, 5 and 6). This was not the case in one-temperature regime (see, Chapter 3), where one obtains a unique solution corresponding to a given set of constants of motion, for both BH or NS as central object. The presence of an extra temperature variable is responsible for this degeneracy. In the absence of any physical principle constraining the relation between these species, we utilised the concept of entropy to obtain a unique transonic two-temperature accretion solution. However, because of the presence of electron – proton energy exchange term or the Coulomb coupling term in the first law of thermodynamics, one cannot obtain an analytical expression for entropy measure. But it is known that near the BH horizon, strong gravity overwhelms any other interactions.

7. TWO-TEMPERATURE ACCRETION FLOWS AROUND NEUTRON STARS

Matter just outside the horizon falls freely and the infall timescales are shorter than cooling or Coulomb coupling time scales. Therefore, asymptotically close to the horizon, an analytical expression of entropy is admissible. Using this formula for entropy, strictly valid near the horizon, entropies of all the degenerate solutions were measured for flows around BHs (see Chapter 5 and 6). It was found that the entropy maximised for a certain solution. Following the second law of thermodynamics, that nature would prefer a solution with maximum entropy, degeneracy was removed in two-temperature accretion flows around BHs. Additionally, it was shown that the maximum entropy solution was the most stable one (Section 6.3.3).

7.3.2 METHODOLOGY TO OBTAIN UNIQUE TWO-TEMPERATURE TRANSONIC SOLUTION AROUND AN NS

We conclude from the above discussion that, accreting matter just outside the NS surface do not achieve free-fall velocities. Hence, maximising entropy method cannot be directly used to break the degeneracy of the solutions, unlike what was done for two-temperature flows around BHs. However, we can use a particular property of gravity to break the degeneracy. The gravitational pull on any particle of unit mass by an object of mass M_* , depends on the value of M_* and also on the distance between the centre of gravities of these two masses. Utilising this property we can conclude that, if a star of mass M_* and radius r_* , is confined in a radius r_{in} ($< r_*$), then the gravitational force experienced at a point r (where, $r > r_* > r_{\text{in}}$) would be exactly same, irrespective of whether the radius of the star is r_* or r_{in} .

Employing this property, the supersonic branch of the NS solution can be continued further to $< r_*$ ('ghost solution' or the projected transonic branch) until it reaches a point r_{in} . It is at this point, $r_{\text{in}} \sim r_g$ (r_g , being the Schwarzschild radius of the star), that $v \rightarrow$ free-fall is satisfied. In principle, it is now possible to obtain the entropy measure \mathcal{M}_{in} (using Eq. 7.17). Following the second law of thermodynamics, we identify the unique, maximum entropy solution out of the infinite solutions, all corresponding to the same set of constants of motion.

Before using this particular method to obtain unique two-temperature accretion solution around NSs, we have used this method first on regenerating solutions in the one-temperature regime, which is well understood, simple and does not exhibit degeneracy. Solution thus obtained using the proposed method in this work, perfectly matched with the solution obtained using the methodology adopted by Singh & Chattopadhyay (2018b). The validation is presented in Appendix B.1. Step by step method to obtain a unique two-temperature accretion solution around an NS is given below.

OBTAINING PROJECTED TRANSONIC SOLUTION ALONG WITH SATISFYING NS INNER BOUNDARY CONDITION

1. Supply the constants of motion (E, P, \dot{M}). Also, we need to supply surface magnetic field B_* of an NS of mass M_* and radius r_* . Magnetic field determines the flow geometry and is a known function of r .
2. We consider a point $r_{\text{in}} \sim r_g < r_*$. The solution between r_* and r_{in} is the projected accretion solution, had the star surface been at r_{in} rather than r_* . We call this solution the ‘ghost solution’. Since $r_{\text{in}} \sim r_g$, therefore v_{in} which is the poloidal velocity at r_{in} , approach free-fall velocity.
3. We supply Θ_{pin} and an initial guess value of Θ_{ein} at r_{in} .
4. We obtain the exact value of v_{in} , from the expression obtained by equating of $E \equiv \mathcal{E}(v_{\text{in}}, \Theta_{\text{pin}}, \Theta_{\text{ein}})$ (Eq. 7.11). $E \equiv \mathcal{E}$, because of the adiabatic conditions at r_{in} .
5. With the initial values of $v_{\text{in}}, \Theta_{\text{pin}}, \Theta_{\text{ein}}$ at r_{in} , we evaluate $dv/dr, d\Theta_p/dr$ and $d\Theta_e/dr$ (Eqs. 7.13-7.15) and then integrate these equations from $r = r_{\text{in}}$ outwards, with increasing r .
6. There is a high probability that the guess value of Θ_{ein} might lead to a completely supersonic branch (SB) solution or a multi-valued branch (MVB) solution (similar to dotted blue curve or dashed dotted green of Fig. B.1b in one-temperature case). So we iterate Θ_{ein} until the sonic point conditions are satisfied or $dv/dr \rightarrow 0/0$ form. Once the sonic point is found, we obtain the velocity gradient at the sonic point $dv/dr|_{r_c}$ by employing L’Hospital’s rule. As discussed before, there will be two values of velocity gradient at this point. We select the $dv/dr|_{r_c} < 0$ value and integrate outwards till the co-rotation radius is reached. In this way, we obtain the full global transonic solution.
7. It may be noted that there might be multiple sonic points for the same set of constants of motion and Θ_{pin} . For a given Θ_{pin} , which has produced a transonic solution, we continue to search for other sonic points by changing the guess value of Θ_{ein} by a large factor and then repeating steps 4-6. This second critical point may or may not exist depending upon the combination of the constants of motion supplied.
8. Once we obtain the complete transonic solution, we note down the entropy measure ($\dot{\mathcal{M}}_{\text{in}}$) at r_{in} using Eq. 7.17. Let us identify this solution with the value of Θ_{pin} .
9. This projected transonic solution needs to satisfy the NS surface boundary conditions. We trace this solution until the actual surface of the star, r_* is reached. Thereafter, we check for the shock conditions near the star surface (Eqs. 7.20–7.22). We select the primary shock location (r_{ps}) for which the subsonic branch satisfy the

7. TWO-TEMPERATURE ACCRETION FLOWS AROUND NEUTRON STARS

NS boundary condition, i.e. $v \rightarrow 0$ as $r \rightarrow r_*$. In this way, we obtain the global accretion solution satisfying NS boundary conditions.

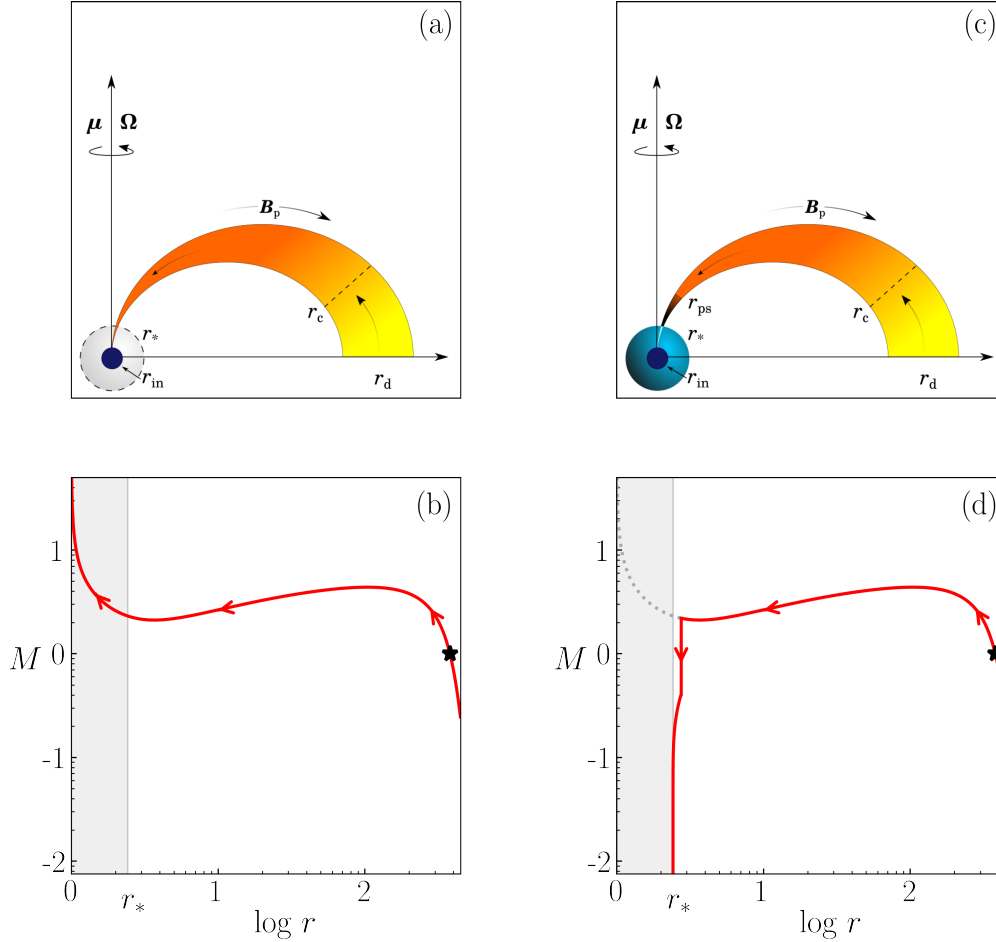


Figure 7.2: Panel (a) shows a cartoon diagram of an accretion flow geometry where matter is accreted till it reaches a radius, $r_{\text{in}} \sim r_{\text{g}} (< r_*)$. In panel (b), corresponding projected solution is plotted (solid red curve). In panel (c), a cartoon representing accretion geometry around a NS is given. Accretion flow on reaching the NS surface forms a primary shock at r_{ps} . The projected solution (plotted in panel b) on satisfying the NS boundary condition is plotted in panel (d), with the ‘ghost solution’ represented in dotted grey. The region between r_{in} and r_* is shaded with grey. Primary shock is at $r_{\text{ps}} = 3.301r_{\text{g}}$ (downward red arrow). The constants of motion of the flow are: $E = 0.9984$, $P = 1.1\text{s}$ and $\dot{M} = 10^{14}\text{g/s}$, while the NS properties are, $M_* = 1.4M_{\odot}$, $r_* = 10^6\text{cm}$ and $B_* = 10^{10}\text{G}$. T_{pin} at r_{in} is $1 \times 10^{11}\text{K}$.

The above methodology is illustrated more elaborately in Figs. 7.2a–d. In Figs. 7.2a and c, schematic diagram of an accretion flow around an NS whose magnetic moment and rotational axis are co-aligned is presented. The orange–yellow shade is the magnetic funnel through which matter gets accreted from the disc (r_{d}) to the NS surface. The flow becomes supersonic after r_{c} . In Fig. 7.2a, the methodology to find the projected solution

is illustrated. The star surface r_* is presented in dashed circle and r_{in} is the supposed radius which contains the same mass $= M_*$ of the NS but in a smaller radius. We consider $r_{\text{in}} \sim r_g$, so that $v \rightarrow$ free-fall, as $r \rightarrow r_{\text{in}}$. The gravitational pull on any particle at $r > r_*$, by an object of mass M_* is same, whether the object radius is r_* or r_{in} (as long as M_* is the same). This is a general property of gravity. Thus, once we consider the surface at r_{in} , or in other words, had the star been more compact, we can trace the supposed accretion solution. Fig. 7.2b plots this projected solution. Steps 1–8 has been followed for this purpose, which in brief reads: given a set of constants of motion: E , P and \dot{M} , we supply Θ_{pin} , a guess value of Θ_{ein} and obtain the value of v_{in} (steps 3–4). Iterating on the value of Θ_{ein} , we obtain the sonic point location(s) (steps 5–7). It is to be noted that Θ_{pin} is fixed throughout the iteration process. The constants of motion (or flow parameters) used for obtaining the solution are, $E = 0.9985$, $P = 1.16\text{s}$, $\dot{M} = 10^{15}\text{g/s}$, $B_* = 10^{10}\text{G}$, $M_* = 1.4M_\odot$ and $r_* = 10^6\text{cm}$. The guess value of proton temperature for this solution at r_{in} is $T_{\text{pin}} = 1 \times 10^{11}\text{K}$ ($= \Theta_{\text{pin}} m_p c^2 / k$). Θ_{ein} has been iterated to obtain the transonic solution (solid red curve, Mach number M vs $\log r$), where r_c is represented by a black star. The portion of the accretion solution inside the grey shaded region, i.e., between r_* and r_{in} , is the ‘ghost solution’. For the given set of flow parameters, multiple sonic points do not exist (see, step 7). This figure shows that the ghost solution is indeed a part of the actual accretion solution, as the solution within the shaded region, joins the physical solution smoothly at $r = r_*$ (see Appendix B.1, for a similar conclusion in one-temperature case). Once the complete transonic accretion solution is obtained, one may also find the location of the primary shock (r_{ps}), which is generally formed close to the r_* . We represent the situation via a cartoon diagram in Fig.7.2c, where after obtaining the full transonic solution, the shock condition due to the star surface (r_*) is satisfied at r_{ps} (dark shadow being the post-shock flow between r_* — r_{ps}). Following step 9, we obtain the location of r_{ps} and the accretion solution now satisfies the surface boundary condition of an NS (see Fig. 7.2d). The matter which is accreted and channelled via the magnetic field lines on reaching near the hard surface of the NS, experience a primary shock at r_{ps} (red downward arrow), after which the flow steadily settles down onto the surface of the star. However, as has been mentioned before, the equations of motion in the two temperature regime are incomplete and hence this solution is not unique.

To remember, the above steps are similar to finding a TS in case of two-temperature flows around BHs, except step 9 (see, Section 6.3.1). The last step comes because the NS has a hard surface which is responsible for slowing down of the supersonic accretion flow via a surface shock. BH does not possess such a hard surface and the accreted matter crosses the horizon supersonically. Also, the reason for presence of degeneracy in two-temperature solutions, is irrespective of the nature of central object.

7. TWO-TEMPERATURE ACCRETION FLOWS AROUND NEUTRON STARS

CONSTRAINING THE DEGENERACY: OBTAINING A UNIQUE SOLUTION

The following steps need to be implemented to constrain the degeneracy present in two-temperature accretion solutions around NSs (also, see Section 6.3.2 for a similar discussion but in case of BHs). The steps enumerated below are followed after a general transonic solution, satisfying NS inner boundary conditions have been obtained beforehand (using steps 1–9 discussed above).

10. For the same set of constants of motion, we change Θ_{pin} and repeat steps 3–8. We obtain another transonic solution and compute the corresponding $\dot{\mathcal{M}}_{\text{in}}$. We carry out this process for different Θ_{pin} s. At the end, we will have a range of Θ_{pin} s and their corresponding $\dot{\mathcal{M}}_{\text{in}}$ s, all for the same set of constants of motion.
11. Following the second law of thermodynamics, a unique accretion solution is the one with the maximum entropy.

In Figs. 7.3a1–f1, we plot the projected transonic accretion solution (solid curves) for different Θ_{pin} s (step 10). The flow parameters used are same as in Fig. 7.2. It is interesting to note that all these solutions are for the same set of constants of motion and hence we identify each solution using the value of Θ_{pin} . Their corresponding solutions which satisfy the NS boundary condition, are plotted in Figs. 7.3a2–f2. The dotted grey curve in each of these plots represent the ghost solution. Values of T_{pin} used to obtain the different transonic solutions are, $1 \times 10^{11}\text{K}$ (Figs. 7.3a1, a2, red), $4.2 \times 10^{11}\text{K}$ (Figs. 7.3b1, b2, orange), $5.0 \times 10^{11}\text{K}$ (Figs. 7.3c1, c2, magenta), $6.0 \times 10^{11}\text{K}$ (Figs. 7.3d1, d2, blue), $7.0 \times 10^{11}\text{K}$ (Figs. 7.3e1, e2, green), and $7.2 \times 10^{11}\text{K}$ (Figs. 7.3f1, f2, brown). Solid curves represent the accretion solution, dotted lines represent the excretion solution which is obtained because of the presence of two roots at $dv/dr|_{r_c}$ (step 6) and dashed curves represent accretion solutions which are not global. Accretion solutions presented in Figs. 7.3a1, a2 and f1, f2, possess single sonic point, where it is outer type for the former (r_{co} marked with black star) and inner type for the later (r_{ci} marked with black circle). Rest of the solutions presented in Figs. 7.3b1, b2–e1, e2, have multiple sonic points (black stars and circles). There is also a centrifugal force driven shock transition in Figs. 7.3d1, d2, which is called a secondary shock (r_{ss}). It is interesting to note that all these different topology of solutions are obtained for the same set of constants of motion. We plot the entropy measure $\dot{\mathcal{M}}_{\text{in}}$ at r_{in} vs T_{pin} in Fig. 7.3g (step 10). The solid black curve represent entropies of solutions having outer sonic points and dashed is for solutions with inner sonic points. The coloured stars and circles correspond to $\dot{\mathcal{M}}_{\text{in}}$ s of transonic solutions plotted in Figs. 7.3a1, a2–f1, f2 (colour coding has been kept the same). $\dot{\mathcal{M}}_{\text{in}}$ is found to maximise for $T_{\text{pin}} = 4.2 \times 10^{11}\text{K} = T_{\text{pin}|\text{max}}$. The projected transonic solution corresponding to $T_{\text{pin}|\text{max}}$ is plotted in Fig. 7.3b1 and after satisfying the NS surface boundary condition, which is the final global accretion solution, is plotted in Fig. 7.3b2. Although this solution,

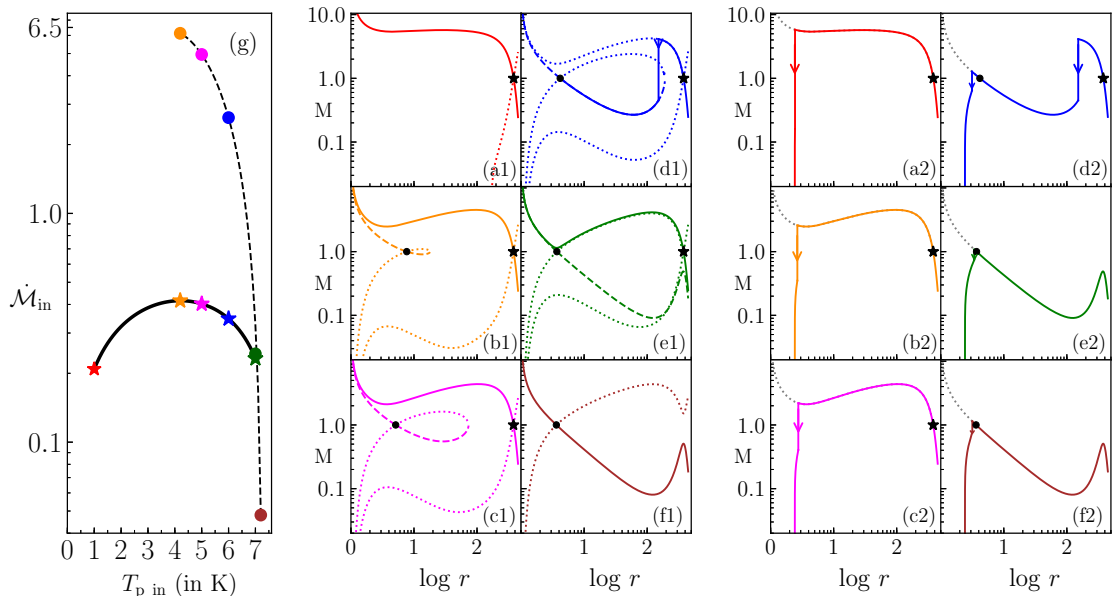


Figure 7.3: Methodology to remove degeneracy present in two-temperature accretion flows around NS. Panels (a1–f1) plots the projected accretion solutions (M vs $\log r$) obtained using $r_{\text{in}} \sim r_{\text{g}}$ as inner boundary. Panels (a2–f2) plots the same transonic solutions, after satisfying the NS surface boundary condition at $r = r_*$. All the solutions presented are for the same set of constants of motion but corresponds to different T_{pin} s (see text). The primary shock location (downward arrow), global (solid), excretion (dotted), non-global (dashed) and the ghost solutions (dotted grey), respectively are indicated accordingly. Outer sonic points (r_{co} , black star) and inner sonic points (r_{ci} , black circles) are marked over the solutions. Panel (g) plots the entropy accretion rate values $\dot{\mathcal{M}}_{\text{in}}$ for all the values of T_{pin} possible: solid black curve represents solutions passing through r_{co} and dashed black is for solutions passing through r_{ci} . Entropy is maximised at $T_{\text{pin}} = T_{\text{pin|max}} = 4.2 \times 10^{11} \text{K}$. Constants of motion are same as in Fig. 7.2.

possess multiple sonic point (orange star and orange circle), but due to the absence of a secondary shock transition, the global accretion solution passes through the outer sonic point (solid, orange). Thus, we conclude that the maximum entropy solution is the one which nature would prefer. Following the second law of thermodynamics, we constrained the degeneracy (step 11). As have been shown by us, in Chapters 5 and 6 (but for the case of BH), among all the degenerate solutions the one with maximum entropy is the unique accretion solution.

7.4 RESULTS

In this section we analyse in detail two temperature accretion flows around NS in the presence of dissipative processes. We also perform spectral analysis. The mass and radius of

7. TWO-TEMPERATURE ACCRETION FLOWS AROUND NEUTRON STARS

the NS is assumed to be $M_* = 1.4M_\odot$ and $r_* = 10^6\text{cm} = 2.418r_g$, respectively, throughout the chapter, until otherwise mentioned. We remember that all the solutions presented in this section possess the highest entropy and have been obtained utilising the methodology discussed in the previous section.

7.4.1 A TYPICAL TWO-TEMPERATURE ACCRETION SOLUTION AROUND AN NS

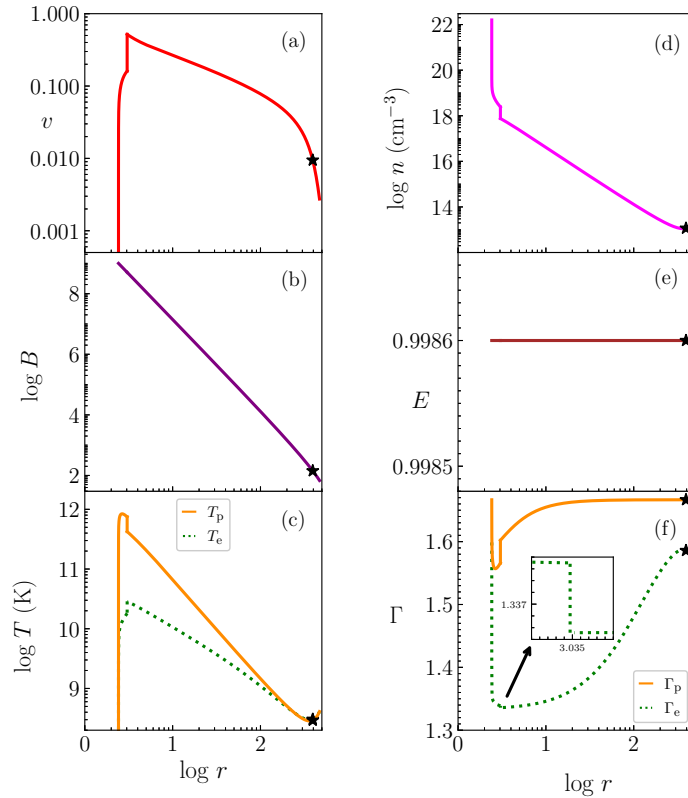


Figure 7.4: Flow variables corresponding to a typical two-temperature accretion solution around an NS are plotted. They are (a) v ; (b) $\log B$; (c) $\log T_p$ (solid, orange) and $\log T_e$ (dotted, green); (d) $\log n$; (e) E and (f) Γ_p (solid, orange) and Γ_e (dotted, green). The flow parameters are, $E = 0.9986$, $P = 1.25\text{s}$, $\dot{M} = 10^{14}\text{g/s}$ and $B_* = 10^9\text{G}$. For these parameters there is only one sonic point (r_{co}) marked with a black star.

We present a general two-temperature accretion solution around an NS in Fig. 7.4. The parameters used are, $E = 0.9986$, $P = 1.25\text{s}$, $\dot{M} = 10^{14}\text{g/s}$ and $B_* = 10^9\text{G}$. We plot flow variables in different panels which are: v (Fig. 7.4a), $\log B$ (Fig. 7.4b), $\log T_p$ and $\log T_e$ (Fig. 7.4c), $\log n$ (Fig. 7.4d), E (Fig. 7.4e) and Γ_p and Γ_e (Fig. 7.4f), all plotted as function of $\log r$. The location of sonic point, $r_{\text{co}} = 393.541r_g$ is marked with a black star and the location of the primary shock is at $r_{\text{ps}} = 3.035r_g$. In the post-shock region, enhanced density increases the cooling processes, which decreases the temperature as

well as the velocity drastically. Moreover, the flow geometry (dictated by B , Eq. 7.3) decreases faster than r^2 , which causes the n to increase sharply near the surface (Fig. 7.4d). The temperature of the species exhibits an interesting behaviour. T_p increases at the primary shock location due to shock heating, while, since the electrons primarily radiate, the enhanced density at the shock front causes T_e to dip at the primary shock location (Fig. 7.4c). The respective adiabatic indices follows the behaviour of the temperature distribution (Fig. 7.4f). The generalized Bernoulli parameter E , which is a constant of motion even in presence of dissipation is indeed found to be a constant (Fig. 7.4e).

EMISSIVITIES AND THE SPECTRUM

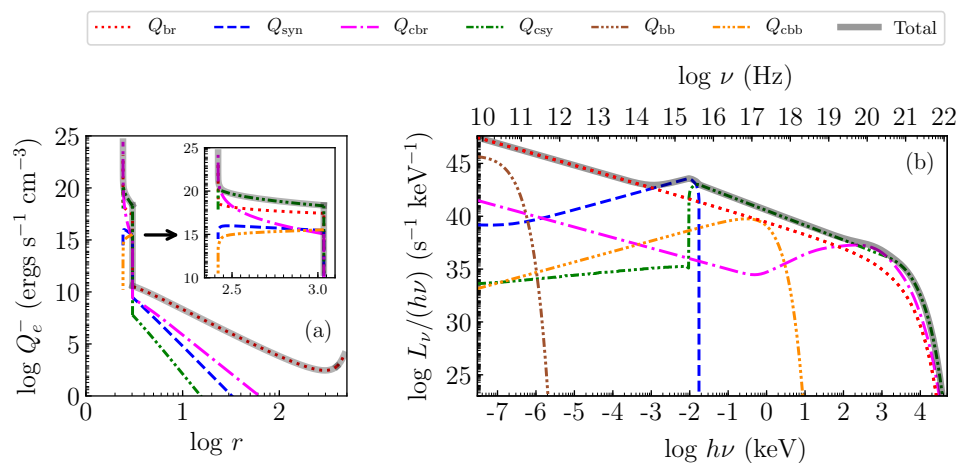


Figure 7.5: (a) Emissivities (Q_e^-) and (b) corresponding spectrum ($L_\nu/(h\nu)$ vs $h\nu$) are plotted. Various curves represent Q_{br} (dotted, red), Q_{syn} (dashed, blue), Q_{cbr} (dashed single-dotted, magenta), Q_{csy} (dashed double-dotted, green), blackbody emission Q_{bb} (dashed four-dotted, brown), Comptonized blackbody Q_{cbb} (dashed triple-dotted, orange) and the total contribution from all these processes is represented using solid black line. Parameters used are same as in Fig. 7.4.

In Figs. 7.5a and b, we plot the emissivities and spectrum respectively, for different cooling mechanisms which are: bremsstrahlung Q_{br} (dotted, red), synchrotron Q_{syn} (dashed, blue), Comptonized bremsstrahlung Q_{cbr} (dashed single-dotted, magenta) and Comptonized synchrotron Q_{csy} (dashed double-dotted, green). Matter accreted through magnetic flux tubes on settling down to the poles of NS may form a thermal mound. This thermal mound is a source of black-body photons of emissivity Q_{bb} (dashed four-dotted, brown), which on encountering with hot electrons can get Comptonized, whose emissivity is represented by Q_{cbb} (dashed triple-dotted, orange). The total emission from all these processes combined, is shown by solid black line. The flow parameters are same as that in Fig. 7.4. We find that Q_{br} dominates in the pre-shock region. As soon as the flow encounters primary shock, emission from all the processes increase due to the increase in

7. TWO-TEMPERATURE ACCRETION FLOWS AROUND NEUTRON STARS

number density of the system (see, Fig. 7.4d). After the primary shock, Q_{csy} dominates over all other emission processes. But very near the surface, Q_{br} and Q_{cbr} dominate because of the rapid increase in n . Also in this region, there is reduction in synchrotron and its Comptonized emission because of the decrease in T_e due to the increased cooling. The total luminosity of this system is $L = 2.759 \times 10^{34} \text{erg s}^{-1}$ with an efficiency of $\eta_r = L/(\dot{M}c^2) = 30.704\%$. Contribution of individual emission processes to the total luminosity are: bremsstrahlung= $6.909 \times 10^{32} \text{erg s}^{-1}$, synchrotron= $5.567 \times 10^{30} \text{erg s}^{-1}$, Comptonized synchrotron= $1.589 \times 10^{34} \text{erg s}^{-1}$, Comptonized bremsstrahlung= $1.100 \times 10^{34} \text{erg s}^{-1}$ and Comptonized blackbody= $2.052 \times 10^{30} \text{erg s}^{-1}$.

In Fig. 7.5b, we represent the spectrum in terms of $L_\nu/(h\nu)$ (in units of $\text{s}^{-1} \text{keV}^{-1}$) vs $h\nu$ (in keV). It is apparent from the figure, that bremsstrahlung emission contributes from radio to gamma rays: covering the whole electromagnetic spectrum. But it mainly dominates upto near-infrared frequencies. A hump in optical and near ultra-violet regime is contributed by synchrotron emission. A power law of spectral index $\alpha = 0.365$, covering from ultraviolet to X-rays is because of Comptonized synchrotron. A second hump is formed in the gamma ray region which is contributed by Comptonized bremsstrahlung. Blackbody emission from the thermal mound at the NS surface is represented by dashed four-dotted brown line and contributes mainly in the low energy part, while its Comptonized component represented by dashed triple-dotted orange line, contributes in the UV and soft X-rays.

7.4.2 CONTRIBUTION OF DIFFERENT REGIONS OF AN ACCRETION FLOW TO THE OBSERVABLE SPECTRUM

In Fig. 7.6 we examine the contribution of different regions of an NS accretion flow to the observed spectrum. The constants of motion of the flow are $E = 0.9985$, $P = 1.15\text{s}$ and $\dot{M} = 10^{15} \text{g/s}$, with surface magnetic field, $B_* = 5 \times 10^9 \text{G}$. In Fig. 7.6a, we plot M vs $\log r$. The global solution passes through $r_{\text{co}} = 375.720r_g$ (black star), which encounters a primary shock at $r_{\text{ps}} = 2.829r_g$ (downward black arrow) which is of strength $S = M_-/M_+ = 6.082$ and compression ratio $\text{CR}_{\text{ps}} = n_+/n_- = 4.571$. Profile of T_e (solid, orange) and T_p (dotted, magenta) are plotted in Fig. 7.6b left Y-axis and n (dashed, dark-blue) is plotted in right Y-axis. In Fig. 7.6a, we have divided the solution into six different regions (shaded with different colours). The regions are as follows: $2.418r_g (= r_*) - 2.829r_g$ (brown), $2.829r_g - 5r_g$ (violet), $5r_g - 7r_g$ (blue), $7r_g - 10r_g$ (green), $10r_g - 100r_g$ (yellow) and $100r_g - 444.810r_g$ (red). The spectrum from these regions are plotted respectively in Figs. 7.6c1–c6 following the same colour coding, in solid curves. In each of these panels, spectral contribution from different radiative processes are plotted in grey: Q_{br} (dotted), Q_{syn} (dashed), Q_{cbr} (dashed single-dotted), Q_{csy} (dashed double-dotted), Q_{bb} (dashed four-dotted) and Q_{cbb} (dashed triple-dotted). The total bolometric luminosity of the system is $L = 2.376 \times 10^{35} \text{erg s}^{-1}$ with an efficiency of $\eta_r = 26.442\%$. We have tabulated

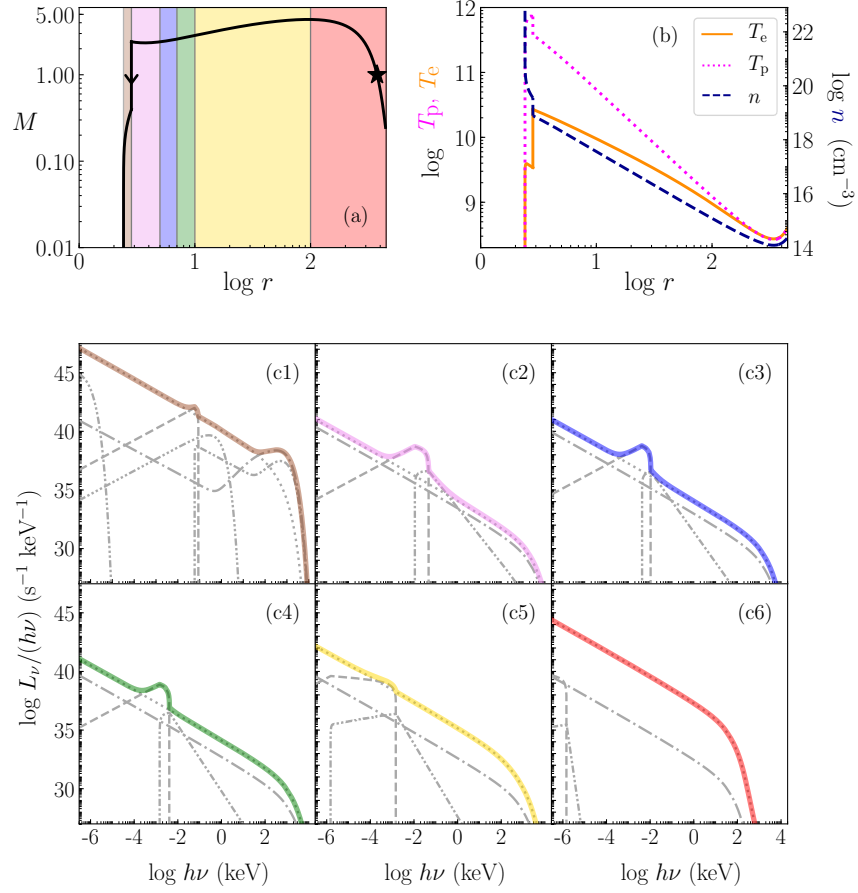


Figure 7.6: (a) Accretion solution M vs $\log r$ (solid, black) is plotted. Different regions have been marked, which are: $2.418r_g - 2.829r_g$ (brown), $2.829r_g - 5r_g$ (violet), $5r_g - 7r_g$ (blue), $7r_g - 10r_g$ (green), $10r_g - 100r_g$ (yellow) and $100r_g - 444.810r_g$ (red). (b) Variation of T_e (solid, orange), T_p (dotted, magenta) and n (dashed, dark-blue) are plotted. Spectral contribution of different regions marked in panel (a) have been correspondingly plotted in solid curves in panels (c1–c6), using the same colour coding. In each of these panels, contribution from individual emission processes are represented in grey (see text). The flow parameters used are, $E = 0.9985$, $P = 1.15s$, $\dot{M} = 10^{15}g/s$ and $B_* = 5 \times 10^9G$.

the contributions of each region in Table 7.1.

The existence of an NS hard surface causes the flow to come to a stop at r_* . This, combined with the effect of number density jump at r_{ps} , increases the cooling processes to such an extent, that most of the radiation comes from the post-shock region (Fig. 7.6c1). At r_{ps} , temperatures should generally increase due to compression of matter at the shock front, but the excessive radiative cooling causes T_e to drop to a lower value. Unlike electrons, protons cannot radiate efficiently. Thus, T_p follows the general trend as expected in a shock transition and jumps to a higher value. Conforming to the above arguments, we find that the post-shock region is very bright, with 99.99985% of the total luminosity (L_{tot}) contributed from this region. Contribution from Comptonized components decrease

7. TWO-TEMPERATURE ACCRETION FLOWS AROUND NEUTRON STARS

and becomes negligible for regions $> 10r_g$. Similarly, the hump which is a signature of synchrotron emission, decrease and vanish for $r > 100r_g$. This is due to the decrease in B with increase in radius (Eq. 7.3). Also, synchrotron self-absorption peak frequency (ν_t), decrease to lower energies, shifting from EUV in panel (c1) to optical in panel (c4). In regions $> 10r_g$, the total emission is mainly contributed from bremsstrahlung. It may be noted that, since we are adding up large sections of accretion flow in the last two panels c5: $10r_g - 100r_g$ and c6: $100r_g - 444.810r_g$, the amount of emission is higher compared to regions presented in panels c3 and c4.

Table 7.1: Spectral properties of the regions shaded in Fig. 7.6

Panel No.	Colour	Region (in r_g)	L (erg s^{-1})	% of L_{tot}
c1	Brown	2.418 – 2.829	2.376×10^{35}	99.99985
c2	Violet	2.829 – 5.0	1.158×10^{28}	4.875×10^{-6}
c3	Blue	5.0 – 7.0	5.567×10^{27}	2.343×10^{-6}
c4	Green	7.0 – 10.0	4.796×10^{27}	2.018×10^{-6}
c5	Yellow	10.0 – 100.0	1.586×10^{28}	6.676×10^{-6}
c6	Red	100.0 – 444.810	3.221×10^{29}	1.355×10^{-4}

7.4.3 SHOCK ANALYSIS

In this section, we examine the properties of primary as well as secondary shocks and their spectral signatures.

7.4.3.1 PROPERTIES OF PRIMARY SHOCK

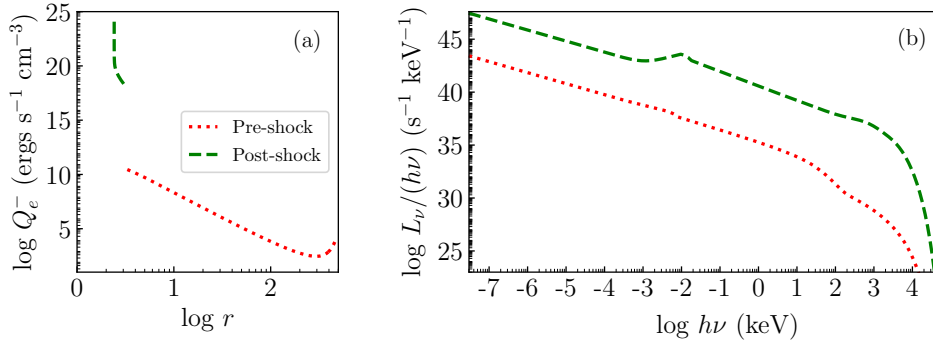


Figure 7.7: Plotted are (a) emissivity and (b) spectrum of post shock (dashed, green) and pre-shock (dotted, red) regions of an accretion flow. The set of parameters used are $E = 0.9986$, $P = 1.25s$, $\dot{M} = 10^{14}g/s$ and $B_* = 10^9G$.

A primary shock is necessary to slow down the matter such that the NS boundary condition can be satisfied. This slowing down happens because of dissipative or cooling processes,

which in turn is responsible for most of the emission coming from an NS. In the last section, we concluded that majority of the emission comes from the post-shock region. So, we compare the emission from pre-shock (dotted, red) and post-shock (dashed, green) regions separately, along with their contribution to the total spectrum, in Figs. 7.7a and b respectively. The flow parameters used are, $E = 0.9986$, $P = 1.25\text{s}$, $\dot{M} = 10^{14}\text{g/s}$ and $B_* = 10^9\text{G}$. The transonic accretion solution in this case possess a single sonic point. It is clear from Fig. 7.7a that, after the primary shock amount of emission increases by 8 – 9 orders of magnitude. This is also imprinted in the spectrum plotted in Fig. 7.7b, where the post-shock region emission dominates all throughout the electromagnetic spectrum and is the main contributor to the total luminosity and spectral shape. The fractional difference between L_{tot} and the luminosity from post-region is $\leq 2 \times 10^{-7}$, indicating that most of the luminosity indeed comes from the post-shock region.

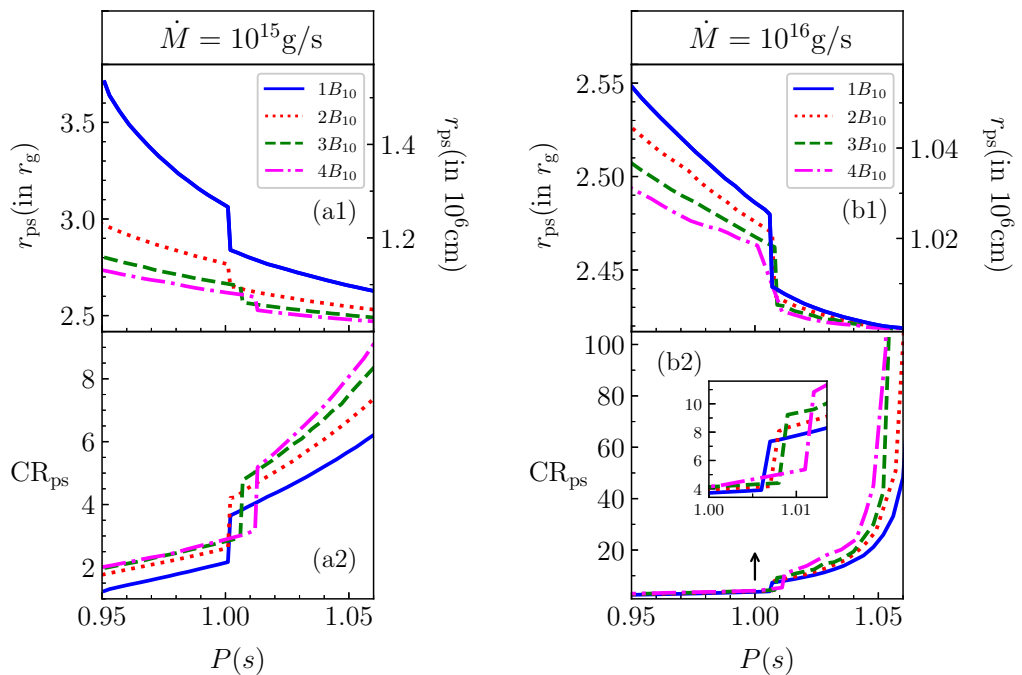


Figure 7.8: Primary shock location r_{ps} (a1, b1) and compression ratio CR_{ps} (a2, b2) as function of period P are plotted for two different accretion rates 10^{15}g/s (a1, a2) and 10^{16}g/s (b1, b2). In each panel there are four curves, representing four B_* values: B_{10} (solid, blue), $2B_{10}$ (dotted, red), $3B_{10}$ (dashed, green) and $4B_{10}$ (dashed dotted, magenta), where B_{10} represents magnetic field in units of 10^{10}G . The generalised Bernoulli parameter has been fixed to $E = 0.9984$ for all cases.

We now investigate the variation in primary shock location (r_{ps}) (Figs. 7.8a1, b1) and compression ratio (CR_{ps}) (Figs. 7.8a2, b2) as a function of rotation period (P) of the NS. This analysis has been done for four values of surface magnetic field (B_*): B_{10} (solid, blue), $2B_{10}$ (dotted, red), $3B_{10}$ (dashed, green) and $4B_{10}$ (dashed dotted, magenta), where B_{10} represents magnetic field in units of 10^{10}G . We also use two different values of accretion

7. TWO-TEMPERATURE ACCRETION FLOWS AROUND NEUTRON STARS

rate for this purpose, $\dot{M} = 10^{15}$ g/s (Figs. 7.8a1, a2) and $\dot{M} = 10^{16}$ g/s (Figs. 7.8b1, b2). The specific energy has been fixed to 0.9984 for all cases.

Shorter P implies faster spin, so the rotational energy enhances the resistance to the inflowing supersonic matter. As a result r_{ps} form at larger distances. This trend is irrespective of the magnitude of B_* and \dot{M} , and is apparent from Figs. 7.8a1, b1. In these plots, the left Y-axis represents the shock location in terms of r_g and the right Y-axis represents it in terms of $r_* = 10^6$ cm, which is the NS radius. At larger distance from the NS surface, the thermal energy and therefore the pressure is lower. As a result, CR_{ps} is lower too (see, Figs. 7.8a2, b2). It may be noted that with the increase in B_* , synchrotron and its Comptonization increases which in turn reduces the thermal energy. As a result, for a given P , increase in B_* decrease r_{ps} and increase CR_{ps} . Because of the same reason, r_{ps} is formed nearer to the NS surface for solutions with higher accretion rate (see Fig. 7.8b1) as compared to the corresponding lower accretion rate solutions (see Fig. 7.8a1). Since these primary shocks are formed near to the surface, the CR_{ps} s have very high values, especially when the rotation period is higher along with B_* value. This is seen in Fig. 7.8b2.

In Figs. 7.8a1, b1, a2, b2, as the rotation period is increased, a sudden drop appears near $P \sim 1.0$ s. This is due to the change in topology of global accretion solutions as we change the rotation period. For lower rotation periods (fast spin), matter becomes supersonic on passing through r_{ci} , while for higher rotation periods, matter crosses r_{co} and become supersonic. The P where this transition of accretion flow occurs from r_{ci} to r_{co} , r_{ps} is found to drop to a lower value. The location of this drop depends on the combination of flow parameters used.

7.4.3.2 PROPERTIES OF SECONDARY SHOCK

Now we study the importance of secondary shock in accretion flows around NS and discuss the necessity to obtain a global transonic solution which connects the matter from the accretion disc to NS poles. We present in Fig. 7.9a: an accretion solution and plot M along with its other flow variables in Fig. 7.9b (T_e and T_p) and Fig. 7.9c (n). We also plot the spectrum in Fig. 7.9d. The flow parameters are, $E = 0.9984$, $P = 0.98$ s, $\dot{M} = 10^{15}$ g/s and $B_* = 10^{10}$ G. The solution passes through r_{co} (marked using a black star) and becomes supersonic, which is shown in Fig. 7.9a. Centrifugal and pressure gradient forces oppose this supersonic matter which drives a shock at $r_{\text{ss}} = 124.074r_g$. This is termed as a secondary shock (SS). The post-shock subsonic flow then picks up speed due to the gravity of NS and again becomes supersonic at r_{ci} (black circle). This supersonic flow finally encounters the hard surface of the NS and as a result settles on it after passing through a primary shock at $r_{\text{ps}} = 3.247r_g$. Accretion solution which passes through these two shock locations: r_{ps} and r_{ss} , is presented using a solid, green curve in Fig. 7.9a. Suppose, we do not check for the Rankine-Hugoniot shock conditions

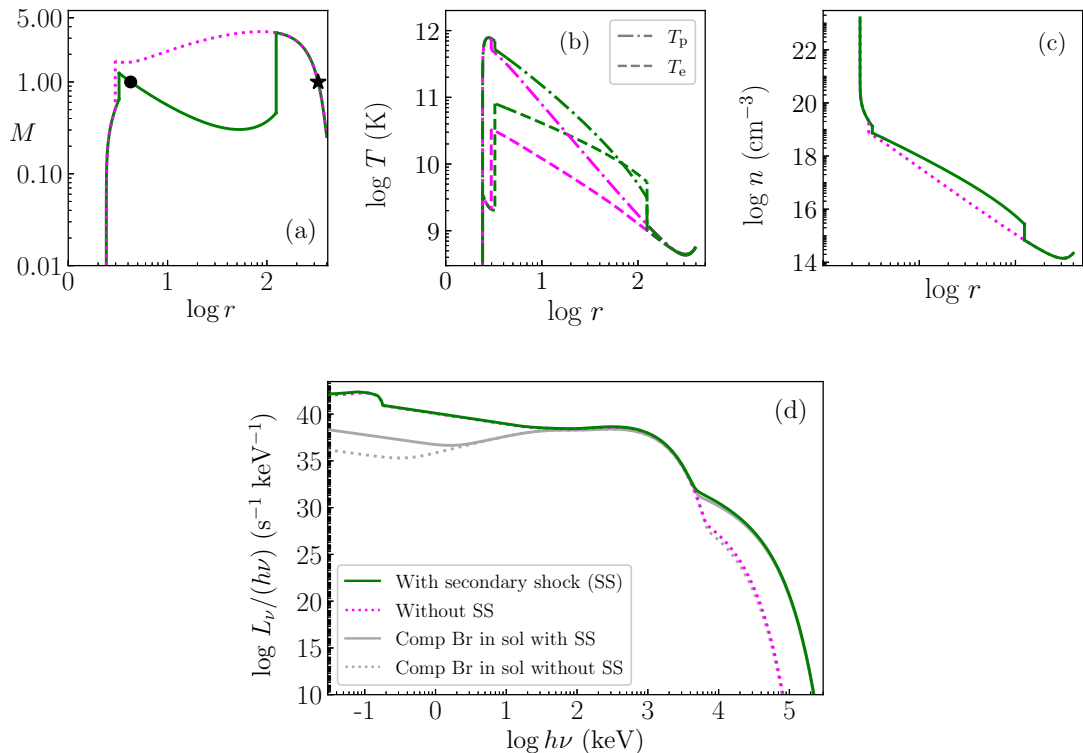


Figure 7.9: Comparison of accretion solutions, with (solid, green) and without secondary shock (dotted, magenta) transition. Plotted in panel (a) M vs $\log r$, where solid black circle and black star represents r_{ci} and r_{co} respectively; (b) T_p (dashed dotted) and T_e (dashed) (green is for solution with two shocks, magenta is for solution harbouring only a primary shock); (c) $\log n$; (d) comparison of continuum spectra along with the Comptonized bremsstrahlung components plotted in grey, with the same linestyle as the solutions. The flow parameters are, $E = 0.9984$, $P = 0.98\text{s}$, $\dot{M} = 10^{15}\text{g/s}$ and $B_* = 10^{10}\text{G}$.

(Eqs. 7.20–7.22) for regions $r < r_{co}$, then the flow will remain supersonic until it reaches near the NS surface, where it will encounter only a primary shock at $r_{ps} = 2.976r_g$. This flow is represented using dotted, magenta line. It is clear that the two solutions are quite different. In Fig. 7.9b, we compare the corresponding temperature distributions of both the electron population T_e (dashed) and the proton population T_p (dashed dotted) of the accretion solution with two shocks (green) and with only a single primary shock (magenta). Solution which does not harbour the secondary shock (dotted, magenta) is found to be much colder. Hence, r_{ps} for this solution is formed closer to the NS surface, where the thermal pressure is large. T_e at r_{ps} for both the solutions decreases, while at r_{ss} , it increases. This is because, in the post-shock flow of r_{ss} , the velocity start to increase just after the initial downward jump at the shock front. This reduces the infall time scales, thereby prohibiting the post-shock flow to loose enough energy through cooling. In case of primary shock, the velocity decrease at the shock front similar to r_{ss} , but it also steadily

7. TWO-TEMPERATURE ACCRETION FLOWS AROUND NEUTRON STARS

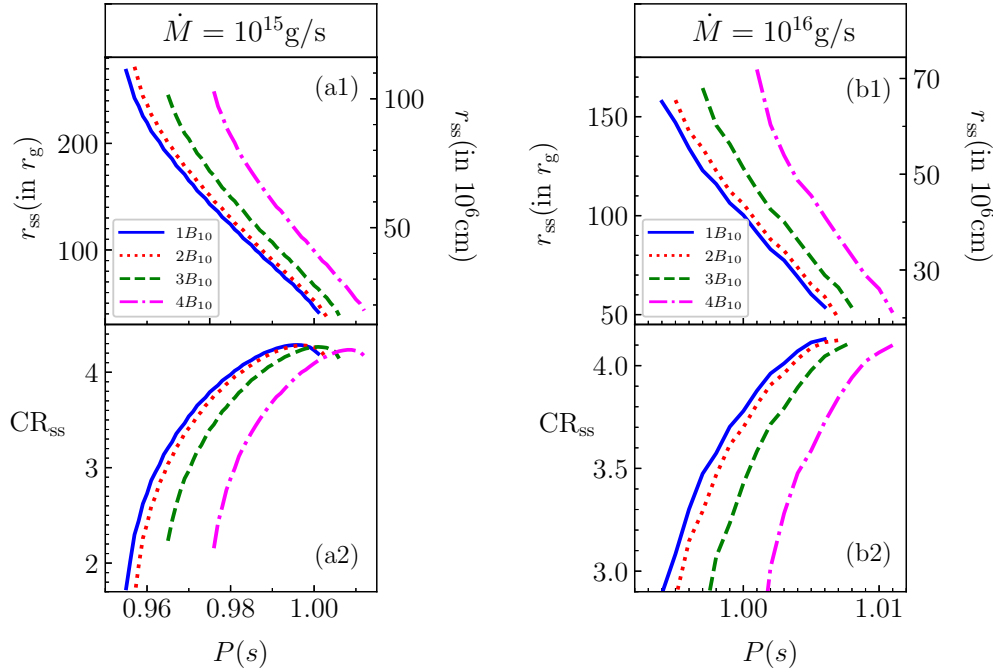


Figure 7.10: Secondary shock location r_{ss} (a1, b1) and compression ratio CR_{ss} (a2, b2) as function of period P are plotted for two different accretion rates 10^{15} g/s (a1, a2) and 10^{16} g/s (b1, b2). In each panel there are four curves, representing four B_* values: B_{10} (solid, blue), $2B_{10}$ (dotted, red), $3B_{10}$ (dashed, green) and $4B_{10}$ (dashed dotted, magenta), where B_{10} represents magnetic field in units of 10^{10} G. The generalised Bernoulli parameter has been fixed to $E = 0.9984$ for all cases.

decrease afterwards until it reaches the NS surface, where it finally settles down. Infall timescales in these cases become larger, allowing matter to radiate more. Therefore after r_{ps} , T_e gradually decreases. Since the radiative processes are not significant for the proton gas, its temperature increases in the post-shock region, irrespective of whether it is a primary or secondary shock. From the number density distribution in Fig. 7.9c, it is clear that the solution with two shocks (solid, green) is denser compared to the solution with only a primary shock (dotted, magenta). In Fig. 7.9d, we compare the continuum spectra of accretion flows with two-shocks (solid, green) and the solution with only primary shock (dotted, magenta). We plot here, in grey, the corresponding Comptonized bremsstrahlung components, keeping the same linestyle. The solution which harbours secondary shock as argued before, is much hotter and denser. Apart from that, the secondary shock is also quite strong. Because of all these reasons, the high energy tail of the spectrum extends beyond 5MeV, most of the emission being contributed from the enhanced Comptonized bremsstrahlung at r_{ss} . This extra high energy component obtained in gamma rays is a signature that a secondary shock exist.

In Figs. 7.10a1, b1 we plot the variation in r_{ss} and in Figs. 7.10a2, b2: their corresponding CR_{ss} , for different accretion rates, $\dot{M} = 10^{15}$ g/s (Figs. 7.10a1, a2) and $\dot{M} = 10^{16}$ g/s

(Figs. 7.10b1, b2). In each panel there are four curves, corresponding to four different B_* : B_{10} (solid, blue), $2B_{10}$ (dotted, red), $3B_{10}$ (dashed, green) and $4B_{10}$ (dashed dotted, magenta), where $B_{10} = 10^{10}\text{G}$. The generalised Bernoulli parameter is $E = 0.9984$ for all cases. This plot is similar to Fig. 7.8, except that the analysis is now done for secondary shocks, earlier it was for primary shocks. Unlike primary shocks, secondary shocks are formed for a certain combination of flow parameters and are located generally far away from the NS surface, as is apparent from the values presented in Figs. 7.10a1, b1. For any given B_* , the shock location decreases with increasing P (low spinning NS) and therefore the compression ratio CR_{ss} increases. This is similar to what was observed in case of primary shocks (see, Fig. 7.8a1, b1). The centrifugal force decreases, which causes the shock to move towards the NS surface. For a given value of P , r_{ss} increase with B_* , thereby decreasing CR_{ss} . Similar effect occurs when the accretion rate is increased. It may be noted that even though compression ratio of the secondary shock is less than the primary shock, but the secondary shock by itself is quite strong.

7.4.4 EFFECT OF MAGNETIC FIELD AND SPIN PERIOD ON THE ACCRETION SOLUTION

In this section, we study the change in solution topology and the observable spectra in Figs. 7.11 and 7.12 respectively for varying surface magnetic field values (B_*) and rotation periods (P) of the NS system. In both the figures, P decrease from left to right with values 2.22s, 2.16s, 2.10s and 2.08s, labelled as 1–4, while B_* increase on going from top to the bottom, with values: $0.5 \times 10^{10}\text{G}$, $1.0 \times 10^{10}\text{G}$ and $5.0 \times 10^{10}\text{G}$ and labelled as a–c. Rest of the parameters are $E = 0.999$ and $\dot{M} = 10^{15}\text{g/s}$.

For high spin period or slowly rotating NS, e.g. $P = 2.22\text{s}$ (Figs. 7.11a1, b1, c1), rotational energy is low, therefore the accretion solution possess only one outer type sonic point or r_{co} . However, for fast rotating NS or spin period like $P = 2.08\text{s}$ (Figs. 7.11a4, b4, c4), the rotational energy is quite high, such that the accretion flow can become supersonic ($M > 1$) only very close to the NS surface, i.e., possess only r_{ci} . For intermediate values of P , solutions would harbour secondary shock (Figs. 7.11a3, b3, c2).

Coming to the variation in B_* for fixed P , we see that for low values of B_* like $0.5 \times 10^{10}\text{G}$ and $1.0 \times 10^{10}\text{G}$, secondary shock can be formed for fast rotating NS, $P = 2.10\text{s}$, where centrifugal force is large (see Figs. 7.11a3, b3). However for higher magnetic fields $B_* = 5 \times 10^{10}\text{G}$, they can be found even for slow rotating NS, $P = 2.16\text{s}$ (Fig. 7.11c2). This is because, B determines the flow geometry or in other words, the flux tube thickness. This affects n , which in turn influence v and T_e . Also, the synchrotron cooling and its Comptonization depends on the value of B . Redistribution of the flow variables trigger shock transition.

The corresponding continuum spectra for the flows presented in Fig. 7.11 are given in Fig. 7.12. Bolometric luminosity (L) increases with decrease in P . A fast spinning

7. TWO-TEMPERATURE ACCRETION FLOWS AROUND NEUTRON STARS

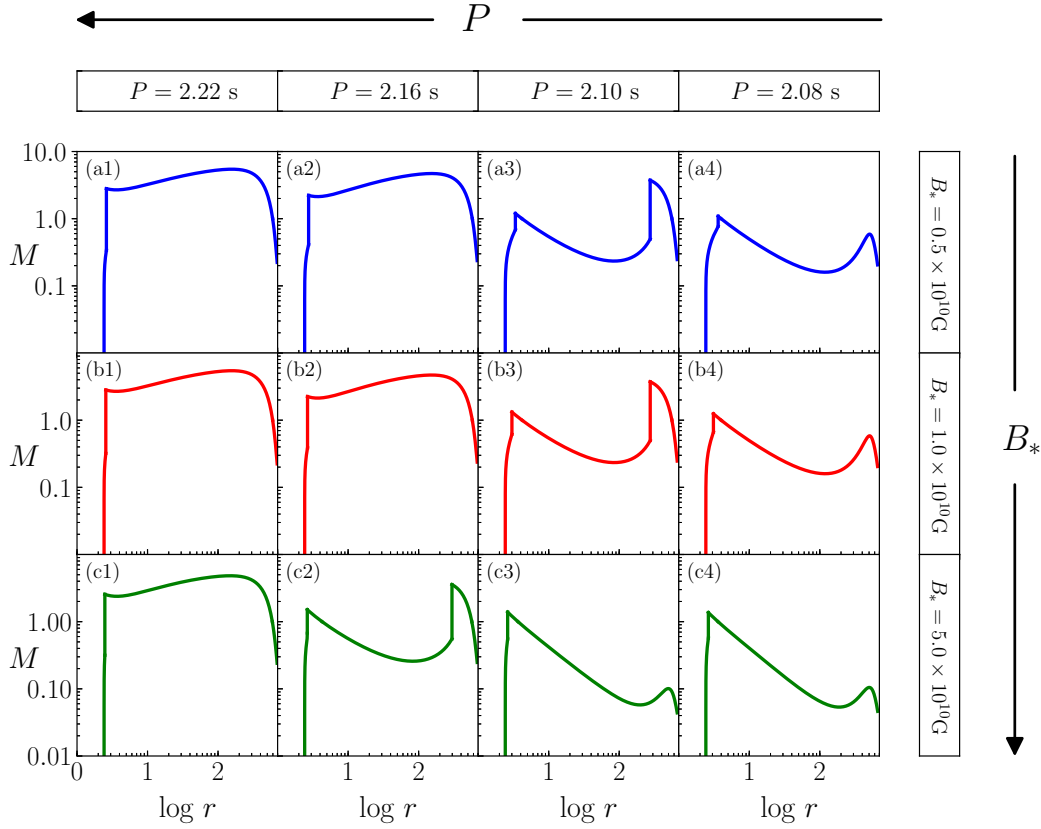


Figure 7.11: Plot showing the variation of solutions (M vs $\log r$) with change in surface magnetic field (B_*) and rotation period (P) of the NS. From left to right (1–4) we have decreased the period of NS (or increased the NS spin) and from top to bottom (a–c) B_* is increased (values written inset). Parameters used are $E = 0.999$ and $\dot{M} = 10^{15}$ g/s.

NS would restrict the infalling matter, allowing it to radiate for a longer duration. But with increase in B_* for a given P , L decreases. It may be remembered that $> 99\%$ of total luminosity comes from the region between r_* and r_{ps} and for higher B_* , post-shock T_e is smaller. Therefore, the total luminosity is less for flows with higher B_* . Moreover, flows with higher B_* produce a prominent synchrotron self-absorption peak, which shift to higher energies with increase in B_* . Interestingly, the combinations of P and B_* which admits secondary shocks (Figs. 7.11a3, b3, c2; and 7.12a3, b3, c2), exhibits extended high energy tail and high energy cut-offs ($> 5\text{MeV}$) similar to Fig. 7.9d. Extensive discussion about this feature has been done in Section 7.4.3.2.

7.4.5 EFFECT OF BERNOULLI PARAMETER ON ACCRETION FLOWS

In Fig. 7.13, we analyse the effect of change of Bernoulli parameter on accretion flows around NS. We plot in panel (a) M , (b) $\log T_p$, (c) $\log T_e$, (d) $\log n$ and (e) continuum spectra. Each curve inside these panels, correspond to different values of Bernoulli paramete-

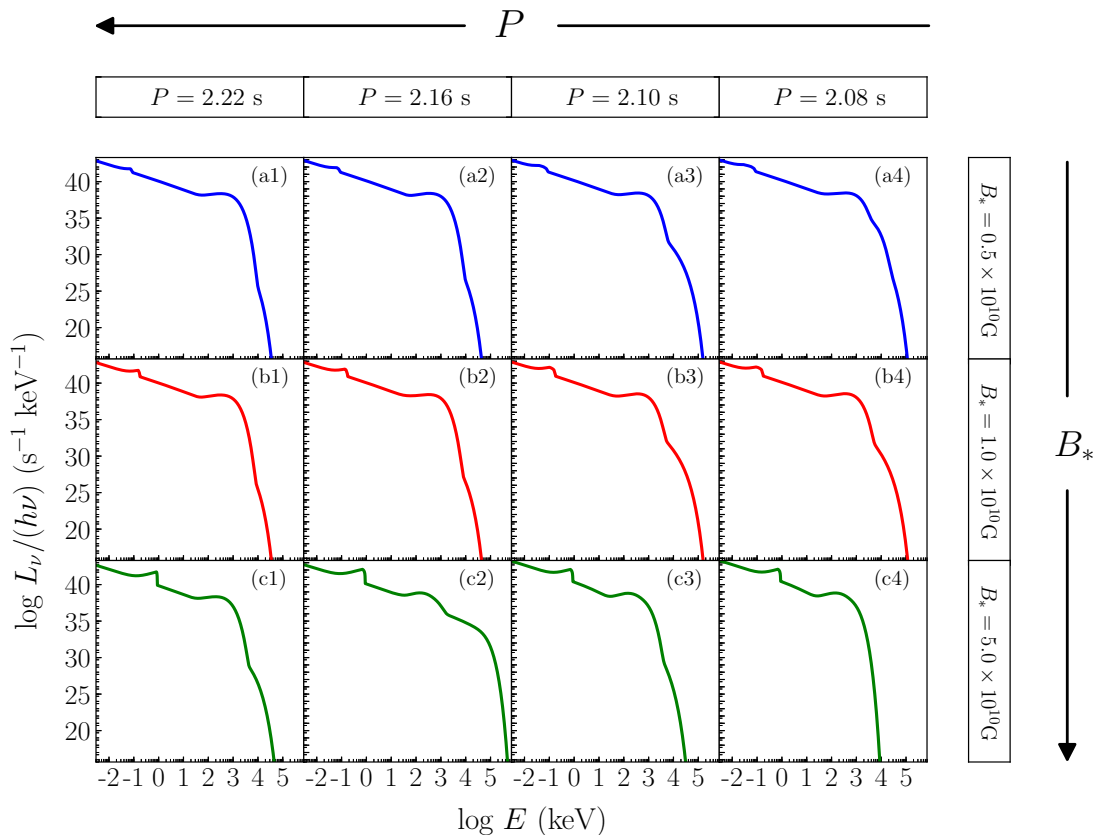


Figure 7.12: Plot showing the corresponding change in observable spectra with change in surface magnetic field (B_*) and rotation period (P) of the NS. Parameters used are same as in Fig. 7.11.

Table 7.2: The effect of variation of E on solutions plotted in Fig. 7.13

E	Primary shock		Secondary shock		L (ergs s $^{-1}$) $\times 10^{35}$
	r_{ps}	CR_{ps}	r_{ss}	CR_{ss}	
0.99820	2.419	229.896	–	–	0.068
0.99825	2.461	16.628	–	–	0.922
0.99830	2.548	8.736	–	–	1.595
0.99840	3.079	2.128	47.888	4.244	2.769
0.99842	3.260	1.748	129.522	3.950	2.915
0.99845	3.732	1.207	–	–	3.114

ter: 0.99820 (solid, red), 0.99825 (dotted, orange), 0.99830 (dashed, green), 0.9984 (dashed single-dotted, magenta), 0.99842 (dashed double-dotted, blue) and 0.99845 (dashed triple-dotted, brown). Other flow parameters are, $P = 1.0$ s, $\dot{M} = 10^{15}$ g/s and $B_* = 10^{10}$ G. Higher Bernoulli parameter implies higher temperature distribution (i.e., higher a_s). Therefore, matter becomes supersonic ($v > a_s$) after it is accelerated to a much higher infall

7. TWO-TEMPERATURE ACCRETION FLOWS AROUND NEUTRON STARS

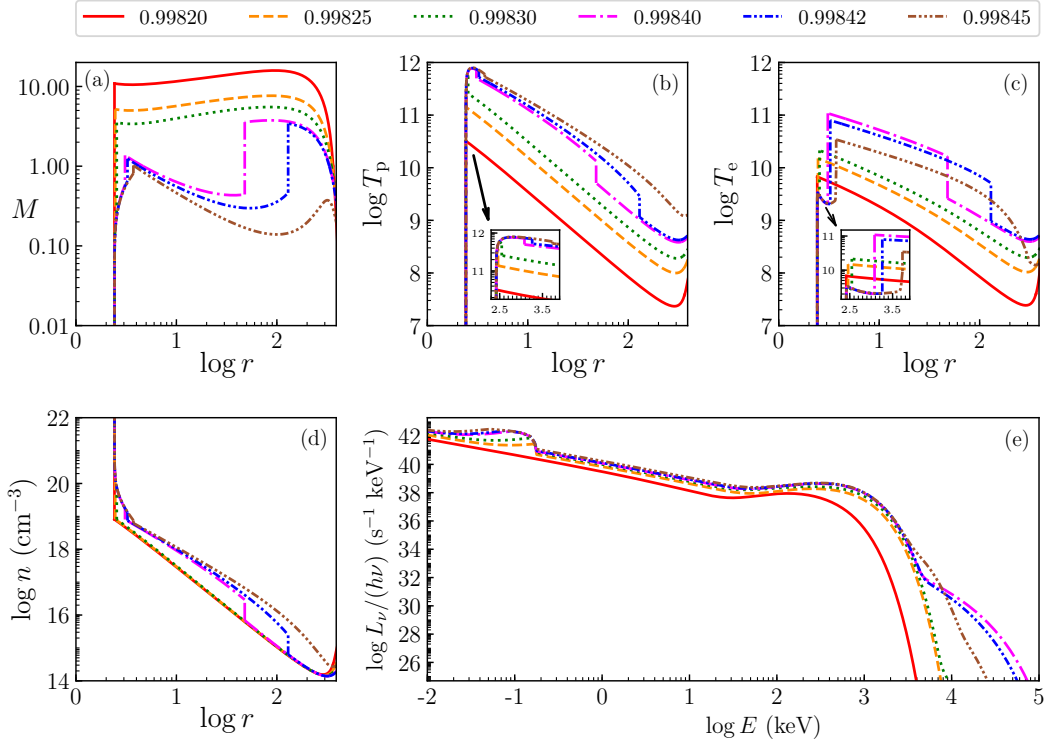


Figure 7.13: Accretion flow variables (a) M , (b) $\log T_p$, (c) $\log T_e$, (d) $\log n$ are plotted w.r.t $\log r$. In panel (e) corresponding continuum spectra of the flow is presented. Each curve inside these panels correspond to different values of E (labelled inset). Flow parameters are, $P = 1.0\text{s}$, $\dot{M} = 10^{15}\text{g/s}$ and $B_* = 10^{10}\text{G}$.

velocity by gravity, i.e., the sonic point moves inward. For low E , the accretion flow has one r_{co} . This is found for $E = 0.99820$ (solid, red), 0.99825 (dotted, orange) and 0.99830 (dashed, green). While, for higher $E = 0.99845$ (dashed triple-dotted, brown), the accretion flow has a single r_{ci} . For intermediate values of E , multiple sonic points may exist, which allows for the formation of secondary shock ($E = 0.9984$, dashed single-dotted, magenta and $E = 0.99842$, dashed double-dotted, blue). When E is large, the secondary shock will be formed at larger distance, because of higher thermal energy. Generally T_p is higher for higher E (Fig. 7.13b), while T_e is highest for energies which harbour secondary shocks (Fig. 7.13c). In Fig. 7.13d, variation in n is presented which shows that it increases with increase in E . When an accretion flow harbour secondary shock, there is a distinct density jump seen at the shock front. This leads to enhanced cooling, which is responsible for the appearance of a prominent high energy tail (dashed single-dotted, magenta and dashed double-dotted, blue curves in Fig. 7.13e). But this does not increase the bolometric luminosity substantially since secondary shock is formed in regions $> r_{\text{ps}}$ and we have already discussed that most of the luminosity is contributed from $r < r_{\text{ps}}$. However, the luminosity increase with increase in E . In Table 7.2, we summarise the

effect of variation of E on accretion flows onto NS. We list the values for which there are primary shock or both primary and secondary shocks, their shock locations, compression ratios and the corresponding luminosities. It is interesting to note that, secondary shock can also be stronger than a primary shock.

7.4.6 EFFECT OF VARIATION OF ACCRETION RATE

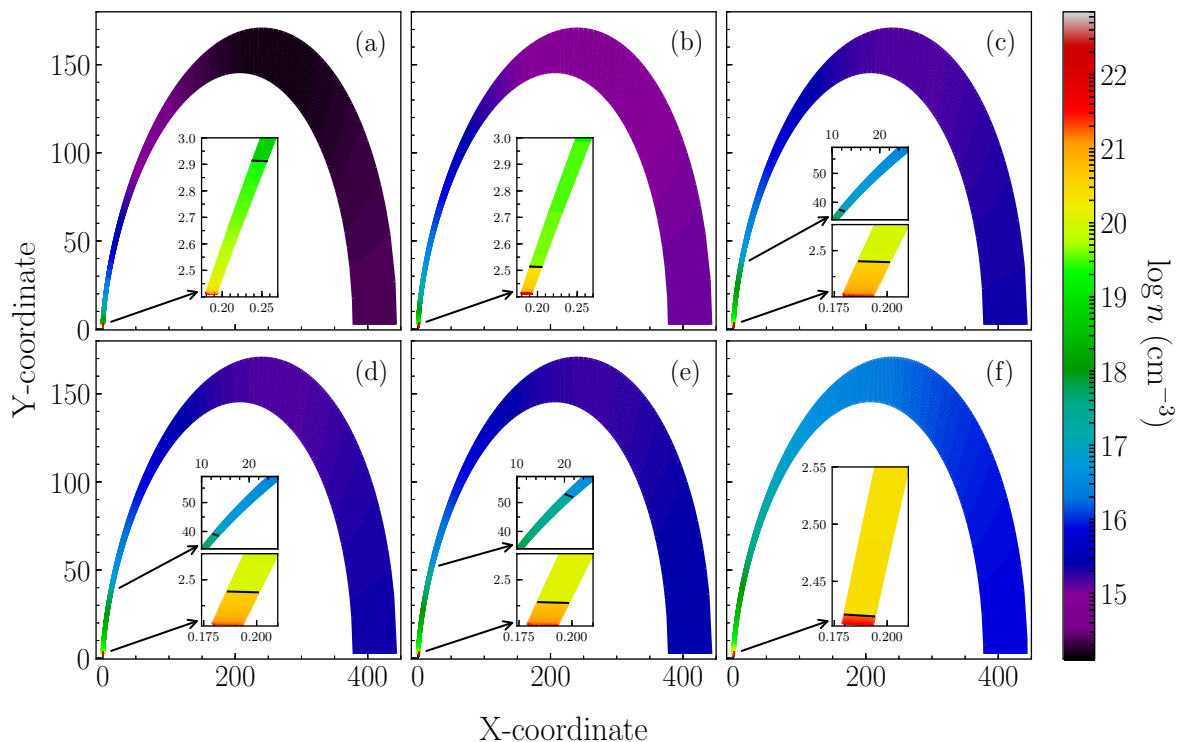


Figure 7.14: The variation of number density, n (represented using a colour bar) inside a flux tube plotted in two spatial dimension. The different panels correspond to systems with different \dot{M} : (a) 1.0×10^{15} g/s, (b) 5×10^{15} g/s, (c) 9.8×10^{15} g/s, (d) 1.0×10^{16} g/s, (e) 1.2×10^{16} g/s and (f) 2.5×10^{16} g/s. Other parameters are $E = 0.9983$, $P = 0.91$ s and $B_* = 8 \times 10^9$ G.

In Fig. 7.14 each panel, we plot the variation in number density (n) along a flux tube represented in two dimensional X-Y plane. The number density values, in units of cm^{-3} , are presented using a colour bar. The different panels show system with different \dot{M} : (a) 1.0×10^{15} g/s, (b) 5×10^{15} g/s, (c) 9.8×10^{15} g/s, (d) 1.0×10^{16} g/s, (e) 1.2×10^{16} g/s and (f) 2.5×10^{16} g/s. The other flow parameters are, $E = 0.9983$, $P = 0.91$ s and $B_* = 8 \times 10^9$ G. Due to strong magnetic field assumption, the flux tube width is independent of the \dot{M} value, which is apparent from the figure. However, n increases with increase in \dot{M} . In Figs. 7.14a, b, the flow passes through one r_{co} . With increase in \dot{M} ,

7. TWO-TEMPERATURE ACCRETION FLOWS AROUND NEUTRON STARS

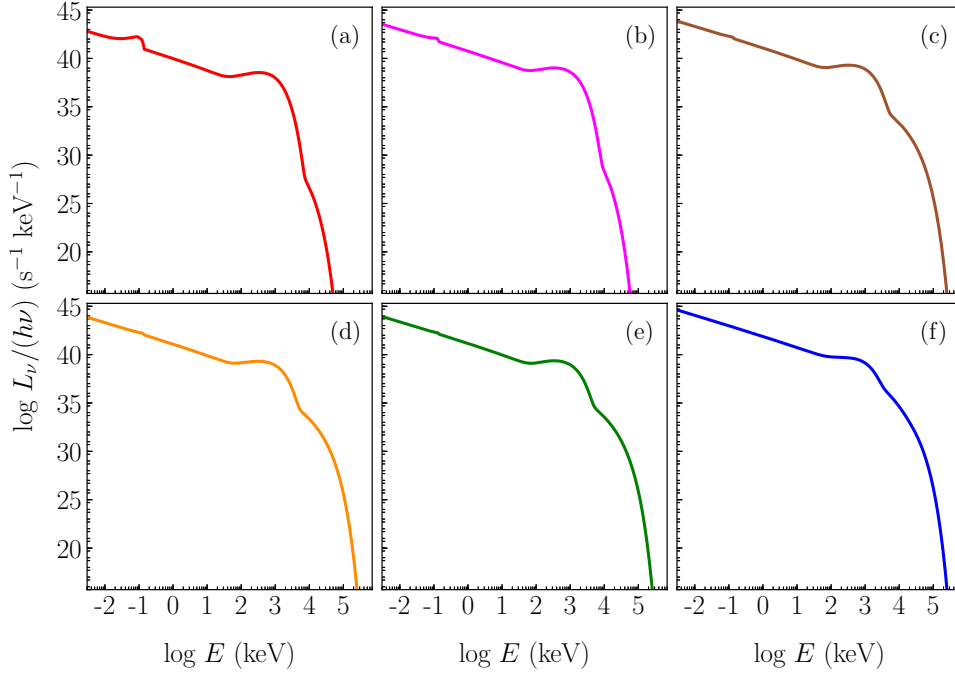


Figure 7.15: Spectra corresponding to the flows presented in Fig. 7.14.

accreting matter becomes hotter, increasing thermal pressure and as a result secondary shock appear, which is seen in Figs. 7.14c–e. In the inset of each panel, we zoomed the region around primary and secondary shocks. The location of secondary shock (r_{ps}) for panels c–e are, $38.131r_g$, $40.848r_g$ and $56.426r_g$, respectively, while r_{ps} values for panels a–f are, $2.928r_g$, $2.526r_g$, $2.493r_g$, $2.491r_g$, $2.470r_g$ and $2.428r_g$, respectively. If we further increase the accretion rate of the system, then the flow passes through a single inner sonic point (r_{ci}), which is formed very close to the NS surface. This is seen for accretion rate $2.5 \times 10^{16}\text{g/s}$ (Fig. 7.14f). All these solutions harbour primary shock irrespective of the presence of any secondary shock.

Spectra corresponding to Fig. 7.14 is plotted in corresponding panels of Fig. 7.15. The luminosity increases with increase in accretion rate of the system. A prominent synchrotron turnover frequency is observed around 0.1keV for $\dot{M} = 1.0 \times 10^{15}\text{g/s}$ (see, Fig. 7.15a). Its magnitude and location remains almost the same irrespective of \dot{M} , because, ν_t depends strongly on the value of B . But this signature subsides with increasing \dot{M} of the system. It is mildly visible for $5 \times 10^{15}\text{g/s}$ (see, Fig. 7.15b). For a given magnetic field structure, increasing \dot{M} , increases n and thereby bremsstrahlung emission and its Comptonization. Therefore, for higher \dot{M} systems, the synchrotron turn over frequency is masked from the dominance of bremsstrahlung emission. For solutions harbouring secondary shock, there is an extended power law, with the cut-off going to higher energies similar to spectra discussed in sections before.

7.5 DISCUSSIONS AND CONCLUSIONS

In this chapter we investigated two-temperature accretion flows around NSs. The major impediment for obtaining self-consistent two-temperature solution is that, the transonic solution is not unique. The total number of governing equations are less than the total number of flow variables to be computed. This problem is same as that observed for two-temperature flows around BHs. To conclude, the degeneracy in two-temperature regime is generic in nature and is irrespective of the type of central object. For a given set of constants of motion, infinite transonic solutions are admissible. We have solved the problem of degeneracy around BH, by computing the entropy of the flow very close to the BH horizon and then choosing the solution with the maximum entropy. It may be noted that, for two-temperature flows there is no analytical expression for entropy. But an entropy measure form can be derived only very close to the BH horizon, where the accreting matter approach free-fall velocity. However, the conditions outside an NS do not fulfil the above condition. Therefore, in this chapter we proposed a novel method to obtain a unique transonic two-temperature accretion solution around an NS. We traced the projected transition solution, assuming the NS to be more compact, such that the infall speed at this radius approach free-fall values. Obtaining all possible solutions for a given set of constants of motion, we choose the highest entropy solution following the second law of thermodynamics. This is the unique solution for the given set of constants of motion.

After proposing a general methodology to constrain degeneracy, we investigated two-temperature accretion solutions around NS for a wide range of parameter space. There are accretion solutions which become supersonic after passing through an outer sonic point, while others become supersonic after passing through the inner sonic point. There are even solutions which passes through outer sonic point and suffers a secondary shock, after which it becomes subsonic. Thereafter, this solution becomes supersonic after passing through the inner sonic point. All these solutions have one thing in common i. e., all these solutions ends up with a terminating shock on the NS surface. This shock ensures that the NS boundary conditions are satisfied. We found that almost the entire radiation is emitted from this post-shock flow. The secondary shock, thus, do not significantly influence the total luminosity, however it is responsible for an additional high energy tail or an extended high energy cut-off. So, there is a need to study the accretions solutions connecting the accretion disc to the NS poles, and not just investigate the radiative property of a freely falling accretion column onto an NS.

The compression ratio across the primary shocks are very high and depend on the combination of flow parameters used. Secondary shocks, on the other hand, have compression ratios less than that of primary shocks, but strength of these shocks are not very low. Apart from adding high energy tail via inverse-Comptonization of soft photons, such

7. TWO-TEMPERATURE ACCRETION FLOWS AROUND NEUTRON STARS

shocks can also aid in particle acceleration. Presence of high density and very low speed, makes the electron temperature distribution decrease at the primary shock location, due to enhanced cooling, contrary to what is expected at a shock front.

The combination of flow parameters present in an NS is important in determining the flow topology and the observable spectrum. Apart from the thermal Comptonization mechanisms considered in this chapter, there could be bulk motion Comptonization present in the system as well ([Becker & Wolff, 2005a, 2007](#)). An order of magnitude estimate of this emission process has been conducted. And we arrived at the conclusion that the accretion rates we have considered, radiation from the mound would not exert any significant resistance and would not change the qualitative nature of the solutions presented. A detailed discussion on this process is beyond the scope of this work and will be dealt with properly in our future works.

Chapter 8

HIGHLIGHTS, CONCLUSIONS AND FUTURE PROSPECTS

8.1 SUMMARY OF THE THESIS

Modelling of accretion flows is necessary for a better understanding of the underlying physics present around compact objects. This thesis is hence aimed, to study such accretion flows around BHs and NSs alongwith analysing their spectrum. Below, I discuss the highlights of the work carried out in this thesis.

8.1.1 ONE-TEMPERATURE ACCRETION FLOWS AROUND BLACK HOLES

We have worked on one-temperature accretion flows around BHs in the presence of cooling processes like bremsstrahlung, synchrotron, their respective inverse-Comptonizations as well as incorporating pair production and annihilation mechanisms. Such work was carried out in order to understand the importance of pairs in accretion disc dynamics and shaping the spectrum.

We found from the analysis done, that pairs indeed play a significant role in accretion disc dynamics, especially those systems which harbour large radiation fields (solutions with higher \dot{M} , E , L_0 etc.). Pairs have also been found to be essentially responsible for shaping the observable spectrum. Also, we proposed here, a feedback iterative method to obtain solutions, in order to include the information of interplay between pair production and annihilation inside the system. This is important, because pairs produce photons and vice-versa. We have analysed typical pair-free solutions and its spectrum apart from pair-producing solutions. The importance of different flow parameters (like, E , L_0 , \dot{M} , α_v) on accretion solutions were investigated in all the cases. The effect of variation of these flow parameters on pair-producing solutions were found to be on similar lines as for a pair-free solution. That is, with increase in their values, the solution became more hotter and more luminous. The only difference was in the production of e^+ . The solutions which were

8. HIGHLIGHTS, CONCLUSIONS AND FUTURE PROSPECTS

cooling efficient or where the radiation field was large, it was found that the production of pairs were significant (Sarkar & Chattopadhyay (2020), Sarkar, Chattopadhyay & Laurent (2021), to be submitted).

One of the interesting results of this work is the presence of a distinct annihilation bump near $\sim m_e c^2$ in the spectrum. This feature was found consistently in all the solutions, where ample of pairs were produced (similar to the work done by Yahel & Brinkmann (1981)). We found this line to originate from a region very close to the BH event horizon, $\sim 5 - 10r_g$, where most of the radiation is generated. This is in direct correlation with the amount of pair-production by radiation fields. Also, we compared the change in luminosity of a pair producing solution with a pair-free one, and found that there was always an increase in luminosity in an accretion solution producing pairs, however low it may be. For very low \dot{M} , the change in L can be neglected, but for higher \dot{M} s where the number of pairs produced are higher, the fractional increase in luminosity is large and the maximum increase obtained was 7% for $\dot{M} = 1\dot{M}_{\text{Edd}}$. Also, for a pair-free solution, the annihilation line contribution was totally absent from the spectrum.

8.1.2 TWO-TEMPERATURE ACCRETION FLOWS

One-temperature solutions are important to the extent that, it gives a general idea about the flow behaviour, its dynamics as well as energetics. To accurately extract the luminosity and spectra of an accreting flow, one needs to have information of T_e inside the flow, which may or may not be comparable to T_p . So, we investigated these flows in greater details in this thesis.

We identified one of the major problems present in two-temperature theory which is ‘degeneracy’. This degeneracy is caused because of the increase in number of flow variables, without any increase in the number of governing equations, *i.e.* now instead of a single T , we have two different temperatures, T_e and T_p . Unfortunately, there is no known principle dictated by plasma physics which may constrain the relation between these two temperatures, at any point of the flow. This problem is not new and has been skirted out by many authors by parametrising T_e and T_p or assuming T_e (or T_p) value at any boundary or by some other arbitrary assumptions. This thesis work addressed and investigated this issue for the first time. Also, a novel methodology has been proposed to remove it such that a given set of constants of motion harbour a unique solution. This is the main highlight of my thesis work.

OBTAINING A UNIQUE SOLUTION: ENTROPY A TOOL TO REMOVE DEGENERACY

It may be remembered that, a fluid solution is not just characterised by its energy but also by its entropy and according to the second law of thermodynamics, any physical solution should correspond to the one with highest entropy. Following this, we derived an

entropy measure form, valid just near the horizon or in any other region where gravity is strong enough suggesting infall timescales to be very much shorter than any other timescales. *This is the first time, an entropy measure form in two-temperature accretion theory has been proposed.* Thereafter, following the second law of thermodynamics, that nature prefers a solution with maximum entropy, we select the solution with the highest entropy. In this way, degeneracy was removed in two-temperature accretion flows. The novelty of the work done in this thesis, is that we identified this long outstanding problem and laid down a prescription to overcome it.

8.1.2.1 TWO-TEMPERATURE FLOWS AROUND BLACK HOLES

We successfully validated the entropy maximisation methodology proposed by us (to obtain a unique solution corresponding to a given set of constants of motion) on all types of accretion flows around BHs: spherical flows, rotating conical discs and rotating accretion discs in hydrostatic equilibrium. We found the entropy to maximise only for a certain unique solution, for a given set of constants of motion. A correct two-temperature solution is very important, because a correct T_e distribution is necessary to obtain the correct spectrum and luminosity. A wrong choice of solution would provide us with a wrong spectrum and hence an incorrect picture of the system.

After obtaining unique solutions, we studied and analysed them and their corresponding spectrums. In the work for spherical flows, we observed that, whenever E and \dot{M} increases or in other words the radiation processes become effective, the accretion flow becomes more luminous. Thus, it is not necessary that radial accretion will always be radiatively inefficient. Also, the Coulomb coupling was always been found to be weak, justifying that, an accretion flow should necessarily be of two-temperatures.

For rotating flows, we found that the global accretion solution passes through different types of sonic points: inner X-type or outer X-type. For few combination of flow parameters, shocks were also formed, where the global solution passes through both the inner and outer sonic points via a shock transition. A shocked solution was always found to be more luminous, because of the increase in inverse-Comptonization process, in the post-shock region. We concluded that, \dot{M} or M_{BH} do not alone determine the emitted spectrum or even the luminosity and E and λ are equally responsible in shaping the spectrum. Luminosity, efficiency and hardness of the spectra (low α) all increases with \dot{M} . Radiative properties of a BH system, also depends on β and β_d along with E , λ , \dot{M} and M_{BH} . For low values of β and β_d , the radiative efficiency was around few percent, but for higher values, the efficiency easily crossed ten percent, even for the same accretion rate and mass of the BH. We also showed that the spectra becomes broadband if the mass of the central BH considered is higher, it also becomes more luminous but the spectral index remains roughly the same. While, with the increase in accretion rate of the BH, the bandwidth of spectra remains the same, but the luminosity and the spectral index changes significantly.

8. HIGHLIGHTS, CONCLUSIONS AND FUTURE PROSPECTS

Apart from that, we also modelled the spectrum of M87 using the data from different sources (Mandal & Chakrabarti, 2008, and references therein). The bolometric luminosity obtained was found to be in close agreement to that of the observed luminosity and the model closely fitted the observed data points. This suggests that the use of the entropy maximisation formulation for selecting the solution and spectrum would be helpful in explaining observations. We intend to extensively carry out the work of explaining observations for different BH candidates with our proposed model in future.

8.1.2.2 TWO-TEMPERATURE FLOWS AROUND NEUTRON STARS

We further extend the work of obtaining and studying unique two-temperature accretion flows to NSs. The methodology discussed previously for removing degeneracy in BHs was extended, including the effect of a hard surface present in an NS. Using the property of gravity we utilised the entropy accretion rate form proposed by us, to the case of NSs as well. After removing degeneracy, we investigated the unique two-temperature accretion solutions around NSs and also analysed their spectrum. All the solutions had one thing in common *i.e.*, they end up with a terminating shock on the NS surface. This shock ensures that the NS boundary conditions are satisfied. We found that almost the entire radiation ($> 99.99\%$) is emitted from this post-shock flow. Apart from the primary/surface shock, secondary shocks can also be formed for a given combination of flow parameters. Although it does not significantly influence the total luminosity, however it is responsible for an additional high energy tail or an extended high energy cut-off. So, there is a need to study the accretions solutions connecting the accretion disc to the NS poles.

To conclude, it is absolutely necessary to obtain unique transonic two-temperature solution. To interpret observations, it is compulsory that the hydrodynamics of the system is properly handled. Selecting any arbitrary solution would mislead us. We allowed the second law of thermodynamics to dictate and select the solution, without taking recourse to any assumptions, such that consistency is maintained. This entropy maximisation formulation proposed by us, is a novel approach which has helped in selecting a unique solution from the infinite degenerate solutions obtained for a given set of constants of motion. The degeneracy is irrespective of the nature of central object. This is the first time, to the best of our knowledge, that such work has been done.

8.2 SCOPE OF FUTURE RESEARCH WORK

8.2.1 TWO-TEMPERATURE MODELLING OF ACCRETION DISCS AROUND KERR BHs

Kerr (spinning) BHs are one of the interesting objects found in the Universe. Because of the spin, the event horizon is less than r_s , increasing the efficiency of accretion process.

There is a consensus of the existence of a high-spin black hole at the Galactic center. Kerr BHs produce solutions with very high temperatures, especially near its horizon (Kumar & Chattopadhyay, 2017).

- Many works suggest that the observed spectrum is largely modified by black hole spin. We want to study the effect of spin on the observed spectrum.
- High temperatures suggest high emission processes and hence higher pair production than Schwarzschild BHs. It would be great to study the effect of these processes on the signature of annihilation line previously obtained around $m_e c^2$. The effect of spin on the magnitude and location of the annihilation line is a topic of further study.
- Pion production and hence gamma ray production can increase with increase in proton temperatures. When this process was taken into account while modelling two-temperature accretion discs, we found that the fractional change in bolometric luminosity of the disc was $< 10^{-5}$, suggesting that, it is not an efficient cooling mechanism. But in the spectral analysis, we found a hump near 10^{22} Hz, a distinct spectral signature arising due to the existence of pions (see, A.3). Also, some of the γ -rays can produce secondary $e^+ - e^-$ pairs through interactions with the radiation field present in the disc. It is interesting to study these phenomena for Kerr BHs.

8.2.2 MONTE-CARLO SIMULATIONS

The radiation processes incorporated so far have been computed locally. We assume the photons generated by bremsstrahlung and synchrotron to completely leave the system within the photon escape timescales and contribute to the observed spectrum. Rest are trapped within the flow and are directly eaten by the BH or are completely lost. Few of these photons upscatter to higher energies depending on the optical depth or number density of electrons present in that particular vertical column of the disc. Thus the radiation processes are measured in-situ. It is impossible to track each photon and compute its change in trajectory and energy each time it encounters an electron or another photon. Also, a photon from outer disc can interact with an electron in the inner disc and contribute to the spectrum. Thus, we should remember that photon propagation, in general, is of non-local nature. This calls for the need to work on Monte-Carlo simulations, which computes the exact trajectory of photons. We plan to club our two-temperature accretion disc models around BHs and NSs with the Monte-Carlo simulations and obtain self-consistent solutions and their corresponding spectra.

8. HIGHLIGHTS, CONCLUSIONS AND FUTURE PROSPECTS

8.2.3 STUDYING OF ACCRETION FLOWS AROUND WHITE DWARFS

WDs share a similar nature with other compact objects. Magnetic Cataclysmic variables exhibit an accretion process same as that of a NS. Unlike NSs they have weak magnetic fields of the order of $\sim 10^7\text{G}$, but still the flow can be strictly channelled in the form of accretion curtains along magnetic field lines. Our two-temperature model can be extended to study accretion flows around WDs and in determining the observed spectrum from these objects.

8.2.4 NUMERICAL SIMULATIONS

It is always interesting to study the steady state solutions obtained previously in the time domain. That is where numerical simulations comes into picture. Time-dependent shocks in accretion discs are believed to drive quasi-periodic oscillations and jets which can significantly change our observed spectrum. We can check these aspects only after doing simulations.

8.2.5 OBSERVATIONS AND DATA ANALYSIS

With the help of the models developed so far, one may be able to predict the physics around these compact objects along with its physical parameters like mass and accretion rates. Or inversely, all the theories developed in the above sections needs to be validated with the help of observations. So, we intend to match our models with the observations available for BH candidates and NSs in future.

Appendix A

TWO-TEMPERATURE ACCRETION DISCS AROUND BHs: IN HYDROSTATIC EQUILIBRIUM IN THE TRANSVERSE DIRECTION

A.1 EFFECT OF VISCOSITY IN THE SYSTEM

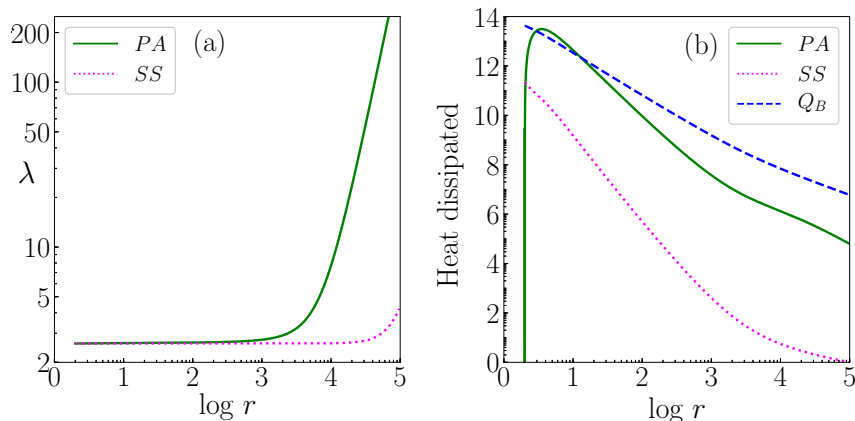


Figure A.1: We present (a) distribution of specific angular momentum (λ) and (b) heating in the system as a function of radius ($\log r$), when viscosity assumed is relativistic (PA, solid, green) and Newtonian (SS, dotted, magenta). In panel (b) we also compare the heating due to magnetic dissipation, Q_B (blue, dashed), assuming $\beta_d = 0.02$. The flow parameters are $E = 1.0005$, $\alpha_v = 0.01$, $\lambda_{\text{in}} = 2.60$, $\dot{M} = 0.01\dot{M}_{\text{Edd}}$ and $M_{\text{BH}} = 10M_{\odot}$.

In this appendix we discuss the effect of viscosity as (1) a mechanism to remove angular

A. TWO-TEMPERATURE ACCRETION DISCS AROUND BHS: IN HYDROSTATIC EQUILIBRIUM IN THE TRANSVERSE DIRECTION

momentum outwards and (2) a source of heating in the system. Handling of viscosity is not trivial and applying it to two-temperature flows might further complicate the scenario and divert us from the question at hand, which is to find the unique transonic two-temperature accretion solutions for rotating flows. Presently, we recall the physics of viscosity in a relativistic but a single-temperature disc like [Chattopadhyay & Kumar \(2016\)](#) and show that near the horizon viscosity would have marginal effect. In the outer region, it can have a more significant effect, but since that region contributes less in the spectrum, so for our purpose, we can neglect it without compromising on the qualitative aspect of the present work. We abbreviate [Chattopadhyay & Kumar \(2016\)](#); [Peitz & Appl \(1997\)](#) form of viscosity as PA. This viscosity prescription was used by us in Chapter 3 to obtain solutions. Using the same procedure, we find solutions for $E = 1.0005$, $\alpha_v = 0.01$, $\lambda_{\text{in}} = 2.60$, $\dot{M} = 0.01\dot{M}_{\text{Edd}}$ and $M_{\text{BH}} = 10M_{\odot}$. Also, we investigate another case of one-temperature flows using the same set of flow parameters but assuming a form of viscosity which is generally followed in non-relativistic accretion disc equations and is given by $t_{r\phi} = -\alpha_v P$. We abbreviate it as SS form of viscosity. We plot in Fig. A.1a, the angular momentum distribution of the system as a function of radius where solid, green curve represent PA form of viscosity, and dotted, magenta represent SS viscosity. It is evident from the figure that angular momentum has been transported outwards (for both the cases) due to the presence of viscosity. But within $\sim 1000r_g$, angular momentum is almost constant, similar to the case of inviscid flows. The SS form of viscosity is weaker so it is less efficient in removing angular momentum and hence angular momentum remains almost constant $\lesssim 3 \times 10^4 r_g$. So, neglecting viscosity within these regions does not affect the system qualitatively. Viscosity in addition to removing angular momentum, also heats up the system. We plot in Fig. A.1b the heat dissipated due to presence of PA form of viscosity (solid, green) and SS form of viscosity (dotted, magenta). We see that using SS viscosity is inefficient in heating up the system and is always 3 orders of magnitude less than PA viscosity. Very far away from the BH, it is 9 orders of magnitude less than the latter. We also compare the heating due to magnetic dissipation (Q_B , dashed, blue), which is the source of heating in this work of two-temperature inviscid flows. In Fig. A.1b, Q_B has been calculated using the velocity, temperature and pressure of the corresponding one-temperature flow and using $\beta_d = 0.02$. We see that Q_B is an efficient source of heating in the system. It always supersedes the heating due to presence of GR viscosity except in a very small region near the BH, where it becomes comparable. Thus, our assumption of taking Q_B as a source of heating in the absence of viscosity, suffice our problem. If viscosity would have been present then the total heating would not have changed much except in a very narrow region.

A.2 ESTIMATION OF ELECTRON-POSITRON PAIR PRODUCTION IN ADVECTIVE TWO-TEMPERATURE ACCRETION DISC

In this section we would estimate how much pair can be produced using a two-temperature accretion solution as the background solution. This analysis was performed in order to have a general idea of the importance of pair-production in two-temperature accretion flows. A detailed analysis, like that performed for one-temperature accretions flows in Chapter 3 is intended to be carried out in future. The advective two-temperature accretion disc solution take into account synchrotron emission which can produce ample amount of soft photons. These photons are too soft to satisfy the criterion for pair production (Esin, 1999). But these photons after interacting with high energy electrons can get upscattered to high energies, contributing to pair production. Also, the bremsstrahlung emission process produce ample amount of hard photons. Thus at any particular radius we can assume the radiation field to be made of a flat bremsstrahlung spectrum which is flat with a high energy cut-off and a Comptonization spectrum which is the sum of cut-off power law and the Wien tail (Esin, 1999; Gould & Schröder, 1967; Zdziarski, 1985). We use the formula given by Svensson (1984, see Eq. B1 of the paper) to compute the rate of photon photon pair production. These formulas are same as have been used in Chapter 3. But the pair density is estimated a posteriori, by using the temperature profile and velocity profile of the two-temperature solution of this work. The positron number density is computed from

$$n_{e^+} = \frac{1}{rH} \int (S^+ - S^-) r H dr. \quad (\text{A.1})$$

Here, n_{e^+} is the positron number density, S^\pm are the source and the sink terms or pair production and annihilation rate, respectively. S^\pm rates are adopted from Svensson (1982a, 1984). Since the accretion disc studied in this Chapter is composed of $e^- - p^+$ fluid, so we first integrate Eq. A.1 with only S^+ term to compute the maximum possible n_{e^+} produced. With this distribution of n_{e^+} , we compute annihilation rate. We iterate few times till the solutions converge. We compute pair production for the case of $\beta_d = 0.013$, $E = 1.001$, $\lambda = 2.41$ and $M_{\text{BH}} = 10M_\odot$. The rest of the parameters are: Figs. A.2a1–a2: $\dot{M} = 1.0$, $\beta = 0.2$ and Figs. A.2b1–b2: $\dot{M} = 1.5$, $\beta = 0.15$. In the upper panels (a1, b1), we compare the proton number density n_{p^+} (solid, black), estimated positron number density n_{e^+} when annihilation rate is ignored (dotted, blue) and the ones where both production and annihilation rates are considered (dashed, green). The blue curve is the maximum possible positrons that can be produced in the disc and $n_{e^+} \ll n_{p^+}$. In the bottom panels (a2, b2), we plot the corresponding emissivity Q_{ann} obtained due to the annihilation of pairs (dotted, red) and compare that with the total emissivity Q_{tot} (solid, brown). The estimated number density of positrons is negligible and the contribution to the total emissivity is negligibly small compared to the total emissivity obtained from

A. TWO-TEMPERATURE ACCRETION DISCS AROUND BHS: IN HYDROSTATIC EQUILIBRIUM IN THE TRANSVERSE DIRECTION

radiative processes like, synchrotron, bremsstrahlung and Comptonization.

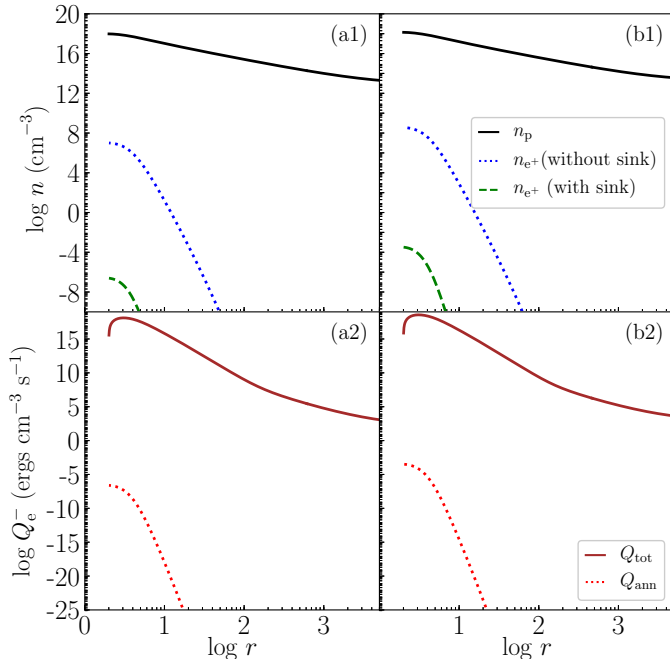
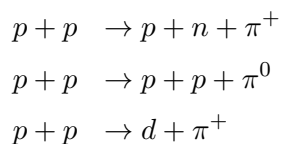


Figure A.2: (a1, b1) Comparison of number density of protons n_{p+} (solid, black), positron number densities n_{e+} (without annihilation, dotted, blue) and with both production and annihilation rates (dashed, green). (a2, b2) Comparison of emissivities of the total radiative cooling Q_{tot} (solid, brown) and emissivities due to annihilation of pairs Q_{ann} (dotted, red). We used two sets of accretion disc parameters, (a1, a2) $\dot{M} = 1.0$, $\beta = 0.2$ and (b) $\dot{M} = 1.5$, $\beta = 0.15$. The other parameters are $\beta_{\text{d}} = 0.013$, $E = 1.001$, $\lambda = 2.41$ and $M_{\text{BH}} = 10M_{\odot}$.

A.3 ESTIMATION OF GAMMA-RAY EMISSION BY PION INTERACTION

In this section, we discuss whether pion production lead to viable amount of cooling in the disc and have any observational signature. The reactions leading to pion (π^{\pm} , π^0) production by proton-proton interactions are as given below (Eilek, 1980):



The threshold temperature for these reactions is 290 MeV. For negative pions, temperatures of > 2 GeV are required. Thus, it is can be assumed that negligible π^- will be

present in the disc. The π^0 further decay into gamma-ray photons (Kolykhalov & Syunyaev, 1979):

$$\pi^0 \rightarrow 2\gamma_{\text{ph}} \quad (\text{A.2})$$

and, π^+ decays into muon and muon neutrinos, which further decays into electron neutrinos, muon anti-neutrinos and positrons, respectively.

$$\begin{aligned} \pi^+ &\rightarrow \mu^+ + \nu_\mu \\ \mu^+ &\rightarrow \nu_e + e^+ + \bar{\nu}_\mu \end{aligned} \quad (\text{A.3})$$

We restrict our study to neutral pions π^0 since we are interested to study the gamma ray emissivities obtained from an accreting Schwarzschild BH. The rate of π^0 production is given by (in units of $\text{cm}^{-3} \text{s}^{-1}$):

$$\mathcal{R}_{\pi^0} = \frac{n^2}{2} \langle \bar{\sigma} \bar{v} \rangle_{\pi^0} . \quad (\text{A.4})$$

Here, $\langle \bar{\sigma} \bar{v} \rangle_{\pi^0}$ (units of $\text{cm}^3 \text{s}^{-1}$) is the velocity weighted cross-section, which was evaluated for π^0 by Dahlbacka et al. in 1974, assuming experimental cross sections for pion production and a relativistic Maxwell-Boltzmann distribution for protons. This was further investigated by Weaver (1976) and Kolykhalov & Syunyaev (1979) who computed $\langle \bar{\sigma} \bar{v} \rangle$ for π^0 as well as for π^+ . This function is strongly dependent on the proton temperature. In 1986 Colpi et al. obtained a best fit to these curves, expression of which is given in Eq. 10 of their paper, and the same form was used to compute the emissivity of γ -rays. It is clear from Eq. A.2 that each π^0 decays into two photons, therefore the number of photons produced per unit time per unit volume is $n^2 \langle \bar{\sigma} \bar{v} \rangle_{\pi^0}$. We analysed a posteriori the total gamma-ray luminosity as measured by an observer at infinity using the methodology adopted in Colpi et al. (1984).

We checked the production of γ rays by varying the accretion rate of the system from $\dot{M} = 0.01$ (dotted, red) to 0.10 (dashed, green) and 1.0 (solid, blue) for a $10M_\odot$ BH (see Figs. A.3a1–a2). Since this emission is crucially dependent on the proton temperature we plot $\log T_p$ as a function of $\log r$ in Fig. A.3a1 for the different accretion rates. The set of disc parameters used are $\lambda = 2.61$ and $E = 1.0007$. For $\dot{M} = 0.01$, & 0.1, the accretion solution do not undergo shock transition and the T_p distribution of the global accretion solution are similar. But for the same set of E and λ and $\dot{M} = 1.0$, there is a stable accretion shock and the T_p jumps at the shock location. The corresponding spectra (Fig. A.3a2) for the three values of \dot{M} show marked difference, where the shocked accretion solution is more luminous and the spectrum is harder (solid, blue), and becomes less luminous and softer for lower \dot{M} . The gamma-ray emission (calculated a posteriori) is represented in grey colour. As a result of π^0 decay, the contribution in the high energy regime increases. Quantitatively, the gamma-ray luminosity for different accre-

A. TWO-TEMPERATURE ACCRETION DISCS AROUND BHS: IN HYDROSTATIC EQUILIBRIUM IN THE TRANSVERSE DIRECTION

tion rates are related by the following relation $L_{\gamma\text{ph}}(\dot{M} = 1.0) \simeq 200L_{\gamma\text{ph}}(\dot{M} = 0.1)$ and $L_{\gamma\text{ph}}(\dot{M} = 0.1) \simeq 100L_{\gamma\text{ph}}(\dot{M} = 0.01)$. Although $L_{\gamma\text{ph}}(\dot{M} = 1.0)$ is much higher than that compared to lower \dot{M} s but compared to the overall luminosity for each \dot{M} , $L_{\gamma\text{ph}}$ is pitifully low. We chose $\dot{M} = 0.1$ and the same values of E and λ and then studied the gamma-ray production for accretion discs onto different masses of central BH: $M_{\text{BH}} = 10^2$ (solid, blue), 10^4 (dashed, green) and 10^6 (dotted, red). We plot T_p vs r in log-log scale and the corresponding spectra in Figs. A.3b1, b2, respectively. M_{BH} affects the system quantitatively but not qualitatively. While the luminosity increases and spectra becomes more broad band with the increase in M_{BH} , but the efficiency of gamma-ray emission ($L_{\gamma\text{ph}}/(\dot{M}c^2)$) remains almost same $\sim 10^{-8}$. In both the cases we examined here (change in accretion rate and mass of BH), we found that the fractional change in luminosity is always $< 10^{-5}$. This analysis justifies our assumption of neglecting pion production leading to emission of γ -rays.

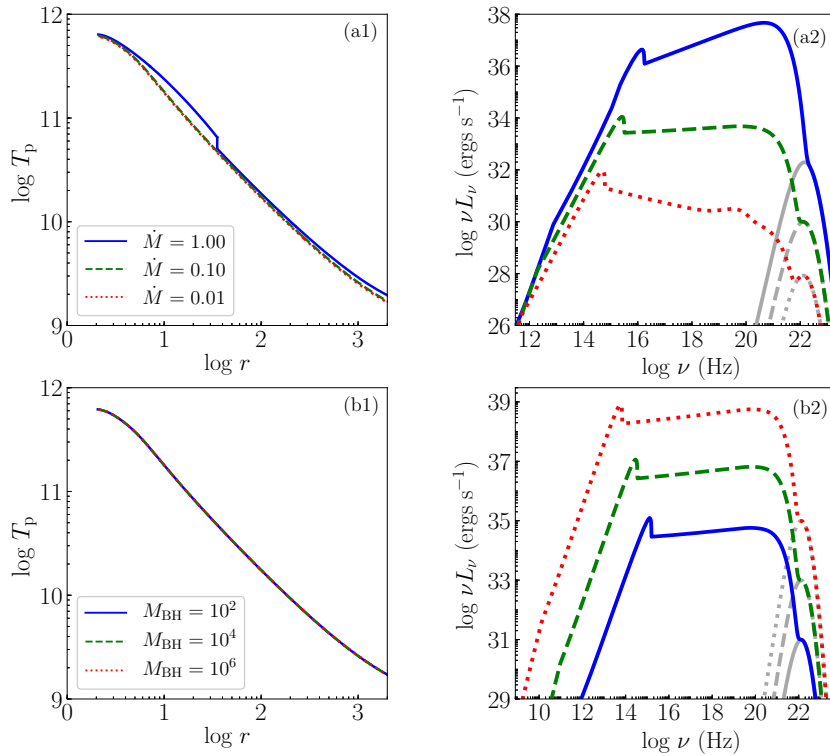


Figure A.3: Dependence of (1) $\log T_p$ as a function of $\log r$ and (2) $\log \nu L_\nu$ with $\log \nu$ for (a1, a2) different accretion rates: $\dot{M} = 0.01$ (dotted, red), 0.1 (dashed, green) and 1.0 (solid, blue) and (b1, b2) different BH masses: $M_{\text{BH}} = 10^2$ (solid, blue), 10^4 (dashed, green), 10^6 (dotted, red). The gamma ray emission is presented in grey in both the spectrums.

Appendix B

TWO-TEMPERATURE ACCRETION FLOWS AROUND NSs

B.1 REGENERATING ONE-TEMPERATURE ACCRETION SOLUTION AROUND NS USING THE NEW METHODOLOGY PROPOSED

In the one-temperature regime, for a given set of constants of motion E and \dot{M} , a transonic solution is unique. Therefore, one can solve it using different methodologies but every method will admit a unique solution. In this section, we show that our proposed ‘ghost solution’ method indeed regenerates the same accretion solution as was obtained by [Singh & Chattopadhyay \(2018b\)](#), who started the integration from the critical points.

In Fig. B.1a, a typical one-temperature transonic accretion solution onto an NS is presented, which has been obtained following the methodology of [Singh & Chattopadhyay \(2018b\)](#). Here, Mach number ($M = v/a_s$) is plotted against radial distance (r) from the center of the NS. The parameters used are, $E = 0.9977$, $P = 1.0s$, $\dot{M} = 2.957 \times 10^{15} \text{g/s}$, surface magnetic field $B_* = 10^{10} \text{G}$ and $M_* = 1.4M_\odot$. Radius of the NS, $r_* = 10^6 \text{cm} = 2.418r_g$, is marked in the figure and region below this is shaded in grey. The global transonic solution (satisfying NS boundary condition) is represented by dashed magenta curve with the sonic point r_c , marked using a black star. The star surface drives a primary shock (downward magenta arrow) at r_{ps} , located just near the surface (see, zoomed inset plot), after which matter becomes subsonic and then slowly settles down onto the star ($v \rightarrow 0$ at $r \rightarrow r_*$). If the matter would have directly hit the surface of the star without undergoing the primary shock transition, the supersonic branch in such a case would be the one which is marked using a thick dashed orange line. The cooling processes considered are same as those present in [Singh & Chattopadhyay \(2018b\)](#). The methodology adopted by these authors to obtain an accretion solution is the general ‘sonic point analysis’ method (Section 2.9). In this method, given a set of constants of motion, the location of r_c is found first. Then from r_c , the equations of motion are integrated inwards (till the star’s surface:

B. TWO-TEMPERATURE ACCRETION FLOWS AROUND NSS

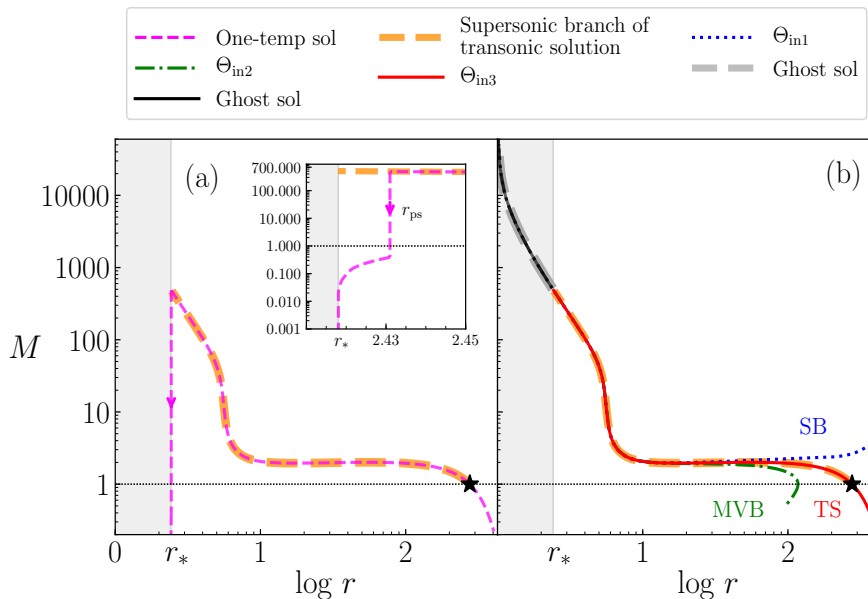


Figure B.1: (a) Transonic solution obtained by sonic point analysis of accretion flows around NS (Singh & Chattopadhyay, 2018b): Solution is represented by M vs $\log r$ plot (dashed, magenta) with sonic point marked with a black star, r_* represents the surface of the NS and the region below it, is shaded in grey. Thick dashed orange curve is the supersonic solution. A primary shock (r_{ps}) is formed near the surface of the NS (see zoomed inset). (b) Obtaining solutions with r_{in} as the inner boundary: Iterating on Θ_{in} until transonic solution TS (solid, red) is obtained, which completely coincides with dashed magenta/thick dashed orange curve. The solid black and thick dashed grey lines are the ghost solutions. The location of primary shock remains the same. The input parameters used are, $E = 0.9977$, $P = 1.0s$, $\dot{M} = 2.957 \times 10^{15}g/s$, $B_* = 10^{10}G$, $M_* = 1.4M_\odot$ and $r_* = 10^6cm = 2.418r_g$.

to obtain the supersonic branch; thick dashed orange curve) and outwards (till r_{corot} : to obtain the subsonic branch). Now, at every radius of the supersonic branch (especially in the region near the star’s surface), they check for the allowed shock transitions until the post-shock branch satisfies the NS boundary condition. In this way, the location of r_{ps} is found and a global transonic accretion solution is obtained.

In Fig. B.1b, we compare the transonic solution (dashed, magenta) obtained by standard sonic point analysis method (followed by Singh & Chattopadhyay (2018b)) with the ‘ghost solution method’ proposed in this chapter. We consider a point at $r_{in} \sim r_g$. Then, for the same set of constants of motion as in panel (a), we supply a guess value of $\Theta = \Theta_{in1}$ at r_{in} . We estimate $v_{in1} [\equiv v_{in}(E, \dot{M}, \Theta_{in1})]$ and integrate out from r_{in} , using the equations of motion. Chances are, we will find only a supersonic branch SB (dotted, blue). For a different guess value of $\Theta_{in} = \Theta_{in2}$ and correspondingly estimating the value of v_{in2} , we obtain a multi valued branch MVB (dashed dotted, green). We iterate in between these two Θ_{in} values until for Θ_{in3} we get a transonic solution (TS, solid red). This solution

completely masks the underlying dashed magenta curve, but the thick dashed orange supersonic branch bears the witness that the two transonic curves have coincided with each other. TS (solid, red) below the grey shaded region, represented using black curve, is the ‘ghost solution’ or the ‘projected transonic solution’. This is actually a continuation of the TS obtained by [Singh & Chattopadhyay \(2018b\)](#), i.e. when the supersonic branch obtained by sonic point analysis method (thick dashed orange) is integrated further inwards till r_{in} is reached and is not terminated at the NS surface (r_*), then the solution obtained below r_* (thick dashed grey) overlaps with the black curve. The location of primary shock remains the same for both these methods. Thus, using the ‘ghost solution’ method, we have regenerated the full transonic solution as was obtained by [Singh & Chattopadhyay \(2018b\)](#).

Hence we show that the new proposed method just uses the property of gravity, that is, it behaves as if the mass is concentrated at the centre and therefore the ‘ghost solution’ is actually a part of the full solution, only to be chopped off by the boundary condition. This method in brief, directs us to obtain the projected transonic accretion solution, which forms a shock near the star surface, but by starting the integration from a region smaller than the actual star surface.

References

- Abramowicz M. A., Calvani M., Nobili L., 1980, *ApJ*, 242, 772 [7](#)
- Abramowicz M. A., Chen X., Kato S., Lasota J.-P., Regev O., 1995, *ApJ*, 438, L37 [7](#)
- Abramowicz M. A., Czerny B., Lasota J. P., Szuszkiewicz E., 1988, *ApJ*, 332, 646 [7](#)
- Abramowicz M. A., Fragile P. C., 2013, *Living Reviews in Relativity*, 16, 1, 1 [13](#)
- Arons J., Klein R. I., Lea S. M., 1987, *ApJ*, 312, 666 [9](#)
- Artemova I. V., Bisnovatyi-Kogan G. S., Bjoernsson G., Novikov I. D., 1996, *ApJ*, 456, 119 [14](#)
- Becker P. A., 1998, *ApJ*, 498, 2, 790 [9](#)
- Becker P. A., Das S., Le T., 2008, *ApJ*, 677, 2, L93 [39](#), [74](#), [97](#)
- Becker P. A., Klochkov D., Schönherr G., et al., 2012, *A&A*, 544, A123 [9](#)
- Becker P. A., Le T., 2003, *ApJ*, 588, 1, 408 [39](#), [71](#), [74](#), [97](#)
- Becker P. A., Wolff M. T., 2005a, *ApJ*, 621, 1, L45 [9](#), [164](#)
- Becker P. A., Wolff M. T., 2005b, *ApJ*, 630, 1, 465 [9](#)
- Becker P. A., Wolff M. T., 2007, *ApJ*, 654, 1, 435 [9](#), [140](#), [164](#)
- Begelman M. C., Chiueh T., 1988, *ApJ*, 332, 872 [13](#)
- Beskin G. M., Karpov S. V., 2005, *A&A*, 440, 1, 223 [82](#), [97](#)
- Biretta J. A., Stern C. P., Harris D. E., 1991, *AJ*, 101, 1632 [130](#)
- Bisnovatyi-Kogan G. S., Lovelace R. V. E., 1997, *ApJ*, 486, 1, L43 [7](#)
- Bisnovatyi-Kogan G. S., Lovelace R. V. E., 2001, *New A Rev.*, 45, 11-12, 663 [7](#)
- Blaes O., 2014, *Space Sci. Rev.*, 183, 1-4, 21 [13](#)

REFERENCES

- Blandford R. D., Znajek R. L., 1977, MNRAS, 179, 433 [132](#)
- Blumenthal G. R., Mathews W. G., 1976, ApJ, 203, 714 [6](#)
- Boldt E., Serlemitsos P., 1969, ApJ, 157, 557 [26](#)
- Bondi H., 1952, MNRAS, 112, 195 [5](#), [74](#), [84](#), [97](#)
- Chakrabarti S., Titarchuk L. G., 1995, ApJ, 455, 623 [7](#), [12](#), [72](#)
- Chakrabarti S. K., 1989, ApJ, 347, 365 [8](#), [32](#), [104](#)
- Chakrabarti S. K., 1995, ApJ, 441, 576 [129](#)
- Chakrabarti S. K., 1996, ApJ, 464, 664 [8](#)
- Chakrabarti S. K., Khanna R., 1992, MNRAS, 256, 2, 300 [14](#)
- Chandrasekhar S., 1939, An introduction to the study of stellar structure [13](#), [14](#)
- Chandrasekhar S., 1956, ApJ, 124, 232 [23](#), [136](#)
- Chattopadhyay I., 2008, in American Institute of Physics Conference Series, edited by S. K. Chakrabarti, A. S. Majumdar, vol. 1053 of American Institute of Physics Conference Series, 353–356 [14](#), [20](#)
- Chattopadhyay I., Chakrabarti S. K., 2011, International Journal of Modern Physics D, 20, 9, 1597 [8](#), [13](#), [21](#), [22](#), [31](#), [35](#), [71](#), [84](#)
- Chattopadhyay I., Kumar R., 2016, MNRAS, 459, 4, 3792 [8](#), [13](#), [20](#), [21](#), [22](#), [25](#), [35](#), [73](#), [75](#), [82](#), [101](#), [172](#)
- Chattopadhyay I., Ryu D., 2009, ApJ, 694, 1, 492 [14](#), [20](#)
- Colpi M., Maraschi L., Treves A., 1984, ApJ, 280, 319 [10](#), [11](#), [72](#), [175](#)
- Colpi M., Maraschi L., Treves A., 1986, ApJ, 311, 150 [175](#)
- Contopoulos J., 1996, Astrophysical Letters and Communications, 34, 269 [23](#)
- Cox J. P., Giuli R. T., 1968, Principles of stellar structure [13](#)
- Dahlbacka G. H., Chapline G. F., Weaver T. A., 1974, Nature, 250, 5461, 36 [175](#)
- Davidson K., 1973, Nature Physical Science, 246, 149, 1 [9](#)
- Davidson K., Ostriker J. P., 1973, ApJ, 179, 585 [9](#), [135](#)
- Davies R. E., Pringle J. E., 1980, MNRAS, 191, 599 [82](#), [97](#)

- Di Matteo T., Allen S. W., Fabian A. C., Wilson A. S., Young A. J., 2003, *ApJ*, 582, 1, 133 [129](#), [130](#)
- Dihingia I. K., Das S., Mandal S., 2018, *MNRAS*, 475, 2, 2164 [12](#), [73](#)
- Dihingia I. K., Das S., Prabhakar G., Mandal S., 2020, *MNRAS*, 496, 3, 3043 [12](#), [73](#)
- Eilek J. A., 1980, *ApJ*, 236, 664 [174](#)
- Esin A. A., 1997, *ApJ*, 482, 1, 400 [28](#)
- Esin A. A., 1999, *ApJ*, 517, 1, 381 [8](#), [33](#), [38](#), [173](#)
- Event Horizon Telescope Collaboration, Akiyama K., Alberdi A., et al., 2019, *ApJ*, 875, 1, L1 [1](#), [129](#)
- Feng J., Wu Q., Lu R.-S., 2016, *ApJ*, 830, 1, 6 [129](#)
- Fukue J., 1986, *PASJ*, 38, 2, 167 [36](#)
- Fukue J., 1987, *PASJ*, 39, 2, 309 [8](#), [9](#), [13](#), [99](#), [104](#)
- Ghosh P., Lamb F. K., 1978, *ApJ*, 223, L83 [135](#)
- Ghosh P., Lamb F. K., 1979, *ApJ*, 232, 259 [9](#), [135](#)
- Ghosh P., Lamb F. K., Pethick C. J., 1977, *ApJ*, 217, 578 [135](#), [137](#)
- Giacconi R., Gursky H., Kellogg E., Schreier E., Tananbaum H., 1971, *ApJ*, 167, L67 [9](#), [135](#)
- Gould R. J., 1981, *Physics of Fluids*, 24, 1, 102 [10](#), [11](#)
- Gould R. J., Schröder G. P., 1967, *Physical Review*, 155, 5, 1404 [173](#)
- Gu W.-M., Lu J.-F., 2004, *Chinese Physics Letters*, 21, 12, 2551 [39](#)
- Heinemann M., Olbert S., 1978, *Journal of Geophysical Research: Space Physics*, 83, A6, 2457 [136](#)
- Hernández Melo C. A., 2014, *Applied Mathematics and Computation*, 232, 1025 [111](#)
- Herterich K., 1974, *Nature*, 250, 5464, 311 [8](#), [34](#)
- Ho L. C., 1999, *ApJ*, 516, 2, 672 [130](#)
- Holzer T. E., 1977, *J. Geophys. Res.*, 82, 1, 23 [6](#)
- Hoyle F., Lyttleton R. A., 1939, *Proceedings of the Cambridge Philosophical Society*, 35, 3, 405 [5](#)

REFERENCES

- Ichimaru S., 1977, *ApJ*, 214, 840 [7](#)
- Ipsier J. R., Price R. H., 1982, *ApJ*, 255, 654 [26](#), [82](#), [83](#), [95](#), [98](#)
- Junor W., Biretta J. A., Livio M., 1999, *Nature*, 401, 6756, 891 [129](#)
- Karino S., Kino M., Miller J. C., 2008, *Progress of Theoretical Physics*, 119, 5, 739 [9](#), [135](#), [141](#)
- Kazanas D., Hua X.-M., Titarchuk L., 1997, *ApJ*, 480, 2, 735 [8](#), [82](#), [97](#)
- Kennel C. F., Blandford R. D., Coppi P., 1989, *Journal of Plasma Physics*, 42, 2, 299 [32](#), [140](#)
- Kluźniak W., Lee W. H., 2002, *MNRAS*, 335, 1, L29 [14](#)
- Koldoba A. V., Lovelace R. V. E., Ustyugova G. V., Romanova M. M., 2002, *AJ*, 123, 4, 2019 [9](#), [78](#), [135](#), [137](#), [138](#), [141](#)
- Kolykhalov P. I., Syunyaev R. A., 1979, *Soviet Ast.*, 23, 189 [175](#)
- Kumar R., Chattopadhyay I., 2013, *MNRAS*, 430, 1, 386 [35](#), [73](#), [75](#)
- Kumar R., Chattopadhyay I., 2014, *MNRAS*, 443, 4, 3444 [13](#), [31](#), [35](#), [47](#), [71](#), [73](#), [75](#), [82](#)
- Kumar R., Chattopadhyay I., 2017, *MNRAS*, 469, 4, 4221 [22](#), [35](#), [75](#), [169](#)
- Kumar R., Singh C. B., Chattopadhyay I., Chakrabarti S. K., 2013, *MNRAS*, 436, 3, 2864 [8](#), [35](#), [75](#), [88](#)
- Kusunose M., Mineshige S., 1996, *ApJ*, 468, 330 [8](#)
- Kusunose M., Takahara F., 1988, *PASJ*, 40, 4, 435 [8](#), [15](#)
- Kusunose M., Takahara F., 1989, *PASJ*, 41, 263 [8](#), [15](#)
- Kusunose M., Takahara F., 1990, *PASJ*, 42, 347 [8](#), [15](#)
- Lamb F. K., Pethick C. J., Pines D., 1973, *ApJ*, 184, 271 [9](#), [135](#)
- Langer S. H., Rappaport S., 1982, *ApJ*, 257, 733 [12](#), [136](#)
- Lasota J. P., 1994, in *Theory of Accretion Disks — 2*, edited by W. J. Duschl, J. Frank, F. Meyer, E. Meyer-Hofmeister, W. M. Tscharnuter, 341–349, Springer Netherlands, Dordrecht [21](#)
- Laurent P., Titarchuk L., 1999, *ApJ*, 511, 1, 289 [72](#)
- Le T., Becker P. A., 2005, *ApJ*, 632, 1, 476 [71](#), [106](#)

- Le T., Wood K. S., Wolff M. T., Becker P. A., Putney J., 2016, *ApJ*, 819, 2, 112 [75](#), [97](#)
- Lee J. P., Becker P. A., 2017, *MNRAS*, 465, 2, 1409 [75](#), [97](#)
- Li J., Wickramasinghe D. T., Ruediger G., 1996, *ApJ*, 469, 765 [9](#), [135](#)
- Liang E. P. T., 1979, *ApJ*, 234, 1105 [8](#), [34](#)
- Liang E. P. T., Thompson K. A., 1980, *ApJ*, 240, 271 [8](#), [13](#), [72](#), [73](#), [99](#), [104](#)
- Lightman A. P., 1982, *ApJ*, 253, 842 [15](#), [34](#)
- Lightman A. P., Eardley D. M., 1974, *ApJ*, 187, L1 [7](#)
- Lightman A. P., Zdziarski A. A., 1987, *ApJ*, 319, 643 [8](#)
- Lightman A. P., Zdziarski A. A., Rees M. J., 1987, *ApJ*, 315, L113 [15](#)
- Lovell R. V. E., Mehanian C., Mobarry C. M., Sulkanen M. E., 1986, *ApJS*, 62, 1 [9](#), [23](#), [136](#)
- Lovell R. V. E., Romanova M. M., Bisnovatyi-Kogan G. S., 1995, *MNRAS*, 275, 2, 244 [9](#), [135](#)
- Macchetto F., Marconi A., Axon D. J., Capetti A., Sparks W., Crane P., 1997, *ApJ*, 489, 2, 579 [129](#)
- Mandal S., Chakrabarti S. K., 2005, *A&A*, 434, 3, 839 [12](#), [72](#), [73](#)
- Mandal S., Chakrabarti S. K., 2008, *ApJ*, 689, 1, L17 [xxxiv](#), [73](#), [129](#), [130](#), [133](#)
- Manmoto T., Mineshige S., Kusunose M., 1997, *ApJ*, 489, 2, 791 [72](#), [96](#), [98](#)
- Maoz D., Nagar N. M., Falcke H., Wilson A. S., 2005, *ApJ*, 625, 2, 699 [130](#)
- Mestel L., 1968, *MNRAS*, 138, 359 [137](#)
- Meszáros P., 1975, *A&A*, 44, 1, 59 [26](#)
- Michel F. C., 1972, *Ap&SS*, 15, 1, 153 [6](#)
- Mukhopadhyay B., Misra R., 2003, *ApJ*, 582, 1, 347 [14](#)
- Nakamura K. E., Kusunose M., Matsumoto R., Kato S., 1997, *PASJ*, 49, 503 [72](#)
- Nakamura K. E., Matsumoto R., Kusunose M., Kato S., 1996, *PASJ*, 48, 761 [12](#), [27](#), [72](#), [98](#)
- Narayan R., Yi I., 1994, *ApJ*, 428, L13 [7](#)

REFERENCES

- Narayan R., Yi I., 1995, *ApJ*, 452, 710 [7](#), [12](#), [27](#), [38](#), [72](#)
- Nowak M. A., Wagoner R. V., 1991, *ApJ*, 378, 656 [14](#)
- Paczynski B., Abramowicz M. A., 1982, *ApJ*, 253, 897 [7](#)
- Paczyński B., Wiita P. J., 1980, *A&A*, 500, 203 [14](#), [19](#), [23](#), [136](#)
- Park M.-G., 1990, *ApJ*, 354, 83 [8](#), [10](#), [34](#), [36](#)
- Park M.-G., Ostriker J. P., 1989, *ApJ*, 347, 679 [8](#), [34](#)
- Parker E. N., 1962, *Planet. Space Sci.*, 9, 8, 461 [6](#)
- Parker E. N., 1965, *Space Sci. Rev.*, 4, 5-6, 666 [6](#)
- Peitz J., Appl S., 1997, *Monthly Notices of the Royal Astronomical Society*, 286, 3, 681
[20](#), [21](#), [101](#), [172](#)
- Perlman E. S., Sparks W. B., Radomski J., et al., 2001, *ApJ*, 561, 1, L51 [130](#)
- Perlman E. S., Wilson A. S., 2005, *ApJ*, 627, 1, 140 [130](#)
- Phinney E. S., 1981, in *ESA Special Publication*, edited by S. A. Colgate, vol. 161 of
ESA Special Publication, 337 [13](#)
- Piran T., 1978, *ApJ*, 221, 652 [7](#)
- Pringle J. E., Rees M. J., 1972, *A&A*, 21, 1 [9](#), [135](#)
- Pringle J. E., Rees M. J., Pacholczyk A. G., 1973, *A&A*, 29, 179 [7](#)
- Rajesh S. R., Mukhopadhyay B., 2010, *MNRAS*, 402, 2, 961 [12](#), [13](#), [72](#)
- Rees M. J., Begelman M. C., Blandford R. D., Phinney E. S., 1982, *Nature*, 295, 5844, 17
[33](#)
- Reynolds C. S., Di Matteo T., Fabian A. C., Hwang U., Canizares C. R., 1996, *MNRAS*,
283, 4, L111 [130](#)
- Salpeter E. E., 1964, *ApJ*, 140, 796 [6](#)
- Sarkar S., Chattopadhyay I., 2019a, *International Journal of Modern Physics D*, 28, 2,
1950037 [76](#), [78](#), [99](#)
- Sarkar S., Chattopadhyay I., 2019b, in *Journal of Physics Conference Series*, vol. 1336 of
Journal of Physics Conference Series, 012019 [78](#), [112](#)

- Sarkar S., Chattopadhyay I., 2020, in *Journal of Physics Conference Series*, vol. 1640 of *Journal of Physics Conference Series*, 012022 [55](#), [68](#), [166](#)
- Sarkar S., Chattopadhyay I., Laurent P., 2020, *A&A*, 642, A209 [78](#), [115](#)
- Saxton C. J., Wu K., Cropper M., Ramsay G., 2005, *MNRAS*, 360, 3, 1091 [12](#)
- Schreier E., Giacconi R., Gursky H., Kellogg E., Tananbaum H., 1972, *ApJ*, 178, L71 [9](#)
- Semerák O., Karas V., 1999, *A&A*, 343, 325 [14](#)
- Shakura N. I., Sunyaev R. A., 1973, *A&A*, 500, 33 [6](#), [21](#), [52](#), [68](#), [99](#), [101](#)
- Shapiro S. L., 1973, *ApJ*, 180, 531 [29](#), [30](#), [95](#)
- Shapiro S. L., Lightman A. P., Eardley D. M., 1976, *ApJ*, 204, 187 [7](#), [12](#), [33](#), [71](#)
- Shapiro S. L., Teukolsky S. A., 1983, *Black holes, white dwarfs, and neutron stars : the physics of compact objects* [2](#), [29](#), [84](#)
- Sharma P., Quataert E., Hammett G. W., Stone J. M., 2007, *ApJ*, 667, 2, 714 [13](#)
- Shull J. M., 1979, *ApJ*, 229, 1092 [33](#)
- Shvartsman V. F., 1971, *Soviet Ast.*, 15, 377 [25](#)
- Singh K., Chattopadhyay I., 2018a, *Journal of Astrophysics and Astronomy*, 39, 1, 10 [10](#), [47](#), [76](#), [136](#), [141](#)
- Singh K., Chattopadhyay I., 2018b, *MNRAS*, 476, 3, 4123 [10](#), [47](#), [76](#), [135](#), [136](#), [141](#), [142](#), [177](#), [178](#), [179](#)
- Sparks W. B., Biretta J. A., Macchetto F., 1996, *ApJ*, 473, 254 [130](#)
- Spencer R. E., Junor W., 1986, *Nature*, 321, 6072, 753 [130](#)
- Spitzer L., 1962, *Physics of Fully Ionized Gases* [10](#)
- Stepney S., 1983, *Relativistic thermal plasmas*, Ph.D. thesis, Institute of Astronomy, University of Cambridge [26](#)
- Stepney S., 1983, *MNRAS*, 202, 467 [10](#), [11](#), [82](#)
- Stepney S., Guilbert P. W., 1983, *MNRAS*, 204, 1269 [26](#), [39](#)
- Stiavelli M., Peletier R. F., Carollo C. M., 1997, *MNRAS*, 285, 1, 181 [130](#)
- Svensson R., 1982a, *ApJ*, 258, 335 [15](#), [26](#), [27](#), [28](#), [38](#), [39](#), [173](#)
- Svensson R., 1982b, *ApJ*, 258, 321 [15](#), [28](#), [38](#), [39](#)

REFERENCES

- Svensson R., 1984, MNRAS, 209, 175 [15](#), [27](#), [173](#)
- Synge J. L., 1957, The relativistic gas., North-Holland Pub. Co.; Interscience Publishers, Amsterdam; New York [13](#)
- Tananbaum H., Gursky H., Kellogg E. M., Levinson R., Schreier E., Giacconi R., 1972, ApJ, 174, L143 [9](#)
- Taub A. H., 1948, Physical Review, 74, 3, 328 [31](#)
- Thorne K. S., Price R. H., 1975, ApJ, 195, L101 [7](#)
- Titarchuk L., Mastichiadis A., Kylafis N. D., 1997, ApJ, 487, 2, 834 [82](#), [97](#)
- Turolla R., Nobili L., Calvani M., 1986, ApJ, 303, 573 [27](#)
- Ustyugova G. V., Koldoba A. V., Romanova M. M., Chechetkin V. M., Lovelace R. V. E., 1999, ApJ, 516, 1, 221 [23](#), [137](#)
- Vincent F. H., Wielgus M., Abramowicz M. A., et al., 2021, A&A, 646, A37 [130](#)
- Vyas M. K., Kumar R., Mandal S., Chattopadhyay I., 2015, MNRAS, 453, 3, 2992 [14](#), [58](#)
- Wandel A., Yahil A., Milgrom M., 1984, ApJ, 282, 53 [33](#)
- Wardziński G., Zdziarski A. A., 2000, MNRAS, 314, 1, 183 [27](#), [28](#), [38](#)
- Weaver T. A., 1976, Phys. Rev. A, 13, 4, 1563 [175](#)
- Weber E. J., Davis Leverett J., 1967, ApJ, 148, 217 [137](#)
- White T. R., Lightman A. P., 1989, ApJ, 340, 1024 [8](#), [26](#), [27](#), [38](#)
- Wielgus M., Akiyama K., Blackburn L., et al., 2020, ApJ, 901, 1, 67 [130](#)
- Wolff M., Becker P. A., Coley J., et al., 2019, BAAS, 51, 3, 386 [9](#)
- Yahel R. Z., 1982, ApJ, 252, 356 [33](#)
- Yahel R. Z., Brinkmann W., 1981, ApJ, 244, L7 [15](#), [33](#), [36](#), [69](#), [166](#)
- Yuan F., Narayan R., 2014, ARA&A, 52, 529 [10](#), [25](#), [73](#)
- Yuan F., Quataert E., Narayan R., 2003, ApJ, 598, 1, 301 [10](#)
- Yuan F., Taam R. E., Xue Y., Cui W., 2006, ApJ, 636, 1, 46 [26](#), [73](#)
- Zdziarski A. A., 1985, ApJ, 289, 514 [38](#), [173](#)
- Zel'dovich Y. B., 1964, Soviet Physics Doklady, 9, 195 [6](#)
- Zeldovich Y. B., Novikov I. D., 1971, Relativistic astrophysics. Vol.1: Stars and relativity [29](#)

General relativistic two-temperature accretion solutions for spherical flows around black holes

Shilpa Sarkar* and Indranil Chattopadhyay†

*Aryabhata Research Institute of Observational Sciences,
Manora Peak, Nainital, Uttarakhand 263002, India*

**shilpa@aries.res.in*

†indra@aries.res.in

Received 18 August 2018

Revised 19 September 2018

Accepted 8 October 2018

Published 16 November 2018

Matter falling onto black holes is hot, fully ionized and has to be necessarily transonic. Since the electrons are responsible for radiative cooling via processes like synchrotron, bremsstrahlung and inverse-Compton, the electron gas and proton gas are supposed to settle into two separate temperature distribution. But the problem with two-temperature flow is that there is one more variable than the number of equations. Accretion flow in its simplest form is radial, which has two constants of motion, while the flow variables are the radial bulk three-velocity, electron and proton temperatures. Therefore, unlike single temperature flow, in the two-temperature regime, there are multiple transonic solutions, nonunique for any given set of constants of motion with a large variation in sonic points. We invoked the second law of thermodynamics to find a possible way to break the degeneracy, by showing only one of the solutions among all possible, has maximum entropy and therefore is the correct solution. By considering these correct solutions, we showed that the accretion efficiency increase with the increase in the mass accretion rate. We showed that radial flow onto super-massive black hole can radiate with efficiency more than 10%, if the accretion rate is more than 60% of the Eddington accretion rate, but accretion onto stellar-mass black hole achieve the same efficiency, when it is close to the Eddington limit. We also showed that dissipative heat quantitatively affects the two temperature solution. In the presence of explicit heat processes, the Coulomb coupling is weak.

Keywords: Accretion; black hole physics; hydrodynamics; radiative process.

PACS Number(s): 4.70.-s, 47.40.Hg, 51.30.+i, 95.30.Jx, 95.30.Lz, 97.10.Gz

1. Introduction

One of the most spectacular objects found in the Universe are black holes (BH). Although not directly observable, their presence is interpreted from the huge amount of energy they liberate through a process called accretion. BH is an extremely compact object found, with sizes of the order of $\sim 3 \text{ km}(M_{\text{BH}}/M_{\odot})$,

where M_{BH} is the mass of BH and M_{\odot} is the solar mass. Due to their compactness, the amount of energy released due to accretion might be of the order of rest mass energy of the matter falling onto it. In the Universe, there exist stellar-mass BHs which accrete matter from a companion star and are visible in the sky as X-ray binaries, or may exist as super-massive ($\sim 10^6 - 10^9 M_{\odot}$) BHs which can feed on a full galaxy. Centres of such active galaxies are famously known as the Active Galactic Nuclei (AGN) and are one of the brightest sources observed in the Universe.

The advent of the theory of accretion onto compact objects began with the seminal works done by Hoyle and Lyttleton^[1] and Bondi,^[2] where they studied radial flow onto a gravitating center. With the discovery of quasars^[3] and X-ray sources^[4] in 1960s, accretion of matter onto compact objects gained popularity. That is because, accretion onto a BH is the only plausible mechanism which could explain such high luminosities. In 1964, Salpeter^[5] computed the luminosity by using the Bondi accretion model, but failed to match it with observations. Matter radially falling in case of Bondi flows, do not get sufficient time to radiate. The general relativistic version of Bondi flow was presented by Michel^[6] and this version of Bondi flow was also found out to be “too fast” to produce significant radiation.^[7] At about the same time, the famous Shakura–Sunyaev disc (SSD) or the Keplerian disc (KD) model was proposed.^[8] Since Bondi flow could not explain the observed luminosity, therefore a rotation dominated disc model was envisaged in order to mitigate the effect of very fast infall velocity. KD or SSD model assumes that matter is rotating with Keplerian azimuthal velocity, with an anomalous viscosity removing angular momentum outward to accrete matter inward. The heat generated is radiated away efficiently and the spectra produced by the disc is a multicolored black body. Though this model could explain the thermal component of the spectrum, it was unable to explain the high energy, nonthermal part of the spectrum. It was also realized that the flow should not be Keplerian everywhere especially near the BH. Therefore the inner region of an accretion flow has to be sub-Keplerian and has to pass through the sonic point at least once before crossing the horizon as was shown by Liang and Thompson^[9] (hereafter, LT80). Subsequently, there was a significant body of work done by a number of workers on advective, transonic flows. Transonic flow has been studied for inviscid disc, viscous disc, around rotating BHs, discs harboring shocks and host of other circumstances.^[10, 23] While for inviscid, adiabatic flow the sonic point can be obtained by solving a polynomial equation for a given Bernoulli parameter and specific angular momentum, but obtaining sonic points for accretion flow in presence of heating and radiative cooling processes is not trivial. One can arbitrarily change the inner, or outer boundary conditions in order to obtain some solutions, but without a systematic approach it may lead to obtaining limited class of solutions or a few unphysical ones. In that context, Gu and Lu^[24] used the generalized Bernoulli parameter which is also a constant of motion to obtain transonic viscous accretion solutions for a particular viscosity prescription.^[25] The approach of Becker and Le^[26] and Becker *et al.*,^[27] of using the generalized Bernoulli parameter simultaneously

with the measure of entropy close to the horizon, to find the sonic point and therefore the transonic solution, is physically the most correct approach. Based on this approach, many papers were written to obtain solutions in single temperature accretion flows around BHs.^[19 21 22 28 29] Single temperature solutions are important to the extent that, it gives a general idea about the flow behavior, its dynamics as well as energetics. To study the luminosity and spectra of the accreting flow, one need to know electron temperature of the flow, which may or may not be same as the proton temperature.

Due to the extreme gravity, matter falling onto a BH is very hot and becomes fully ionized. A fully ionized astrophysical plasma would be mostly composed of electrons and protons because hydrogen is the most abundant element. Electrons radiate most of the energy and protons do not, in addition, the Coulomb coupling time scale is longer than the various cooling time scales, so in general, protons and electrons would relax into two separate temperature distributions. In 1976, Shapiro *et al.*^[30] (hereafter, SLE76) argued that the instability persisting at the inner region of the disk could swell this optically thick radiation pressure dominated region into an optically thin gas pressure dominated region and in this region, electrons and protons will maintain separate temperature distributions. Since flow near the BH is a two-temperature fluid, as a result research on two-temperature accretion flow started to gain prominence.^[30 31]

Two-temperature accretion solutions as presented by SLE76 incorporated inverse-Compton processes and could produce hard radiation. However, the hydrodynamics was significantly simplified, and the accretion solutions considered were not transonic. LT80 discussed primarily about single temperature transonic flow but also briefly discussed about two-temperature solutions by assuming the ratio of ion and electron temperature to be constant. Since then, many studies were undertaken using two-temperature model. Colpi *et al.*^[32] solved the two-temperature solution but by assuming freely falling matter. No transonic solutions were reported here. Similar work was done by Chakrabarti and Titarchuk^[33] where only inverse-Comptonization of soft photons from the SSD, by the inner post-shock region was considered. Mandal and Chakrabarti^[34] later extended this model for other cooling processes. In both these papers, the authors imposed a density enhancement in the flow to mimic the accretion shock. In these works, the assumption of free-fall implied that the radiative transfer was not self consistently coupled with the hydrodynamics of the system. Laurent and Titarchuk^[35] computed the spectra from the model of Chakrabarti and Titarchuk,^[33] by conducting a detailed Monte Carlo simulation of the interaction of electron gas with the soft photons from the underlying KD. In 1995, Narayan and Yi,^[36] studied self-similar class of advective solutions (termed as advection dominated accretion flow or ADAF) in the two-temperature regime. It was assumed that the amount of heat transferred from protons to electrons through Coulomb collisions is totally radiated away. This extra assumption helped them to deal away with any kind of parametrization, that was otherwise assumed by LT80. Needless to say self-similar class of solutions in conjunction with other assumptions

mentioned above, are not transonic. Nakamura *et al.*,^{[37][38]} was among the first, who actually solved transonic two-temperature solution. However, the solutions were only for a limited class, obtained by imposing at the outer boundary, the ion temperature to be a fraction of the virial temperature and that the heat transferred to the electrons is radiated away. Manmoto *et al.*^[39] followed similar outer boundary conditions, however, in the inner region they considered that the electron energy advection rate to be equivalent to the radiative cooling rate. Rajesh and Mukhopadhyay^[40] also obtained transonic solutions in the two-temperature regime, by choosing the viscosity prescription of Chakrabarti and Molteni,^[25] but only presented transonic solutions through a single sonic point. Dihingia *et al.* (2017)^[41] discussed the transonic global two-temperature solutions for smooth as well as shocked accretion solutions. All these works were in the pseudo-Newtonian regime (strong gravity is mimicked by modifying the Newtonian gravitational potential), and used two fixed adiabatic indices (Γ_e and Γ_p for electrons and protons, respectively) equation of state (EoS) of the gas. None of these works used the constants of motion (e.g. generalized Bernoulli constant) of the flow and the information of entropy close to the horizon to obtain the solutions. As discussed above, the hydrodynamics of single temperature regime is more complete and systematic. In two temperature regime, this approach is sadly lacking in the literature.

The problem with two-temperature solutions is that, without any increase in the number of governing equations, the number of flow variables increase, i.e. to say, now instead of a single temperature, one has to consider different temperatures for ion and electron. In addition, there is no known principle dictated by plasma physics which may constrain the relation between these two-temperatures in any of the boundaries. Some authors (cited above) assumed specific relations between electron heating and cooling, in order to obtain the solution. But those choices were arbitrary and cannot be considered a unique solution. Such arbitrary choices do not “haunt” single temperature solution, since a transonic single-temperature solution is unique for a given set of constants of motion. Still some other authors followed the methodology of specifying the electron or ion temperature in a chosen boundary and then iterate the other flow variables to obtain a transonic solution. However, a different combination of electron and ion temperature in that boundary can give rise to another transonic solution but for the same value of generalized Bernoulli parameter.^a This would give rise to degeneracy of solutions, i.e. multiple transonic solutions for the same set of constants of motion. But nature would prefer only one and the question is which one. Moreover, the electron and the ion temperature may vary by orders of magnitude from a large distance to the horizon, so a nonrelativistic EoS (i.e. EoS with fixed adiabatic indices) is untenable. However, it may also be remembered that use of relativistic EoS even in single temperature domain has been traditionally few and far between.^{[10][11][42]}

^aGeneralized Bernoulli parameter in steady state, is a constant of motion in presence of dissipation too.^{[19][21][22]}

In this paper, we address the basic problem of finding a unique two-temperature transonic solution around BHs, in the general relativistic regime, using the two-temperature version of the Chattopadhyay–Ryu (CR) EoS,^[43,44] and how to overcome the problem, by laying down a prescription to obtain the correct solution. As far as we know, such an attempt has not been undertaken before. Using the CR EoS removes the constraint of specifying the adiabatic indices for the electron and the ion gas. In this paper, we would confine our discussion for a fully ionized electron–proton gas.

The paper is organized in the following way. In Sec. 2 we present the assumptions and equations used in the paper which would cover the EoS used and the equations of motion. In Sec. 3, we will discuss the procedure to obtain unique transonic two-temperature solutions. In Sec. 4, we will present and discuss our results and finally conclude in Sec. 5.

2. Assumptions and Equations

In this paper, we focus on obtaining the unique two-temperature solution in steady state from all the degenerate solutions, which is actually difficult since plasma physics do not impose any constraint on the relation between electron and proton temperatures at any distance from the BH horizon. Therefore, we remove all frills that might complicate and obscure the question at hand. As a first simplification, we consider Schwarzschild metric i.e. the simplest BH. In order to further simplify the flow, we consider radial accretion i.e. rotation is neglected. Therefore the flow is spherical/conical. Although spherical accretion might look very simple, however, it is not entirely implausible as an accretion model. In the viscous, single temperature, rotating accretion flow regime, we have previously shown that the flow geometry in the inner region of the disc is close to conical flow with low angular momentum.^[21,22] Therefore, radial accretion might be used to mimic the inner region of AGNs and microquasars. This is to be expected too, since the BH gravity would start to dominate over other interactions in the inner accretion region around the BH, as a result a large number of papers do consider spherical flow to mimic the inner region of accretion flow.^[45,47] In addition, standard accretion model onto isolated BH from inter-stellar medium is indeed spherical.^[48,49] We consider all possible cooling mechanisms like bremsstrahlung, synchrotron and inverse-Compton processes, and it may be noted that the electron is the main agent of emission. Energy is exchanged between electrons and protons through the Coulomb interaction term given by Stepney.^[50] The effect of explicit heating is also discussed at the end.

It is to be noted that in the subsequent sections, all barred variables represent dimensional quantities and all nonbarred variables denote dimensionless quantities, until stated otherwise. Throughout this paper we have solved all the equations in the dimensionless domain. We have employed a unit system, where $G = M_{\text{BH}} = c = 1$, such that the unit of length is $r_g = GM_{\text{BH}}/c^2$ and time is in units of $t_g = GM_{\text{BH}}/c^3$. Here, G = Gravitational constant, M_{BH} = mass of the BH and c = speed of light.

2.1. Equations of motion

The background metric is that around a Schwarzschild BH. The nonzero components of the Schwarzschild metric are,

$$g_{tt} = -\left(1 - \frac{2}{r}\right); \quad g_{rr} = \left(1 - \frac{2}{r}\right)^{-1}; \quad g_{\theta\theta} = r^2; \quad g_{\phi\phi} = r^2 \sin^2\theta. \quad (1)$$

The energy-momentum tensor of accretion flow is $T^{\mu\nu} = (e + p)u^\mu u^\nu + pg^{\mu\nu}$, where e is the internal energy density of the fluid and p is the isotropic gas pressure, all measured in local fluid frame, μ and ν represent the spacetime coordinates and u^μ s are components of four velocities. The space component of the relativistic momentum balance equation is given by

$$[(e + p)u^\nu u_{;\nu}^i + (g^{i\nu} + u^i u^\nu)p_{;\nu}] = 0. \quad (2)$$

The radial component of the above equation is given by

$$u^r \frac{du^r}{dr} + \frac{1}{r^2} = -(g^{rr} + u^r u^r) \frac{1}{e + p} \frac{dp}{dr}. \quad (3)$$

The equation of conservation of particle density flux is

$$(nu^\nu)_{;\nu} = 0, \Rightarrow \frac{1}{\sqrt{-g}} \frac{\partial(\sqrt{-g}nu^\nu)}{\partial x^\nu} = 0, \quad (4)$$

where n is the number density of the particles in the flow and g is the determinant of the metric tensor. Integrating Eq. (4), we get the accretion rate which is a constant of motion throughout the flow, given by

$$\dot{M} = 4\pi\rho u^r r^2 \cos(\theta), \quad (5)$$

where θ is the co-latitude of the surface of the conical flow and is assumed to be $\theta = 60^\circ$ in this paper. The mass density is represented as ρ . The first law of thermodynamics is given by

$$u^\mu \left[\left(\frac{e + p}{\rho} \right) \rho_{;\mu} - e_{;\mu} \right] = \Delta Q, \quad (6)$$

where $\Delta Q = Q^+ - Q^-$, Q^+ being the heating term and Q^- the cooling term. The dimensional form of any quantity are written with a bar over it, \bar{Q} s are in units of $\text{ergs cm}^{-3} \text{ s}^{-1}$, until mentioned otherwise. The calculation of \bar{Q} s require the value of number density (in units of cm^{-3}). The number density is calculated from the dimensional form of the accretion rate equation (in the dimensional form, the accretion rate is expressed in terms of Eddington rate).

Since the flow contains electrons and protons equilibrating at two different temperatures we need to use the first law of thermodynamics separately for protons and electrons unlike in the case of one-temperature flows where the Coulomb coupling being extremely strong, allows protons and electrons to settle down to a single temperature.^{19, 23} These two energy equations are coupled by the Coulomb coupling term which allows protons and electrons to exchange energy. Therefore, ΔQ in the

proton energy equation can be written as, $\Delta Q_p = Q_p^+ - Q_p^-$ and in the electron energy equation as, $\Delta Q_e = Q_e^+ - Q_e^-$.

If we integrate the radial component of the relativistic Euler Equation (3) with the help of Eqs. (5) and (6), we obtain the generalized Bernoulli parameter which is a constant of motion and is given by

$$E = -hu_t \exp(X_f), \tag{7}$$

where $X_f = \int \frac{\Delta Q_p + \Delta Q_e}{\rho h u^r} dr$. This is conserved throughout the flow even in the presence of dissipation. In case of nondissipative flows, $X_f = 0$ and

$$E \rightarrow \mathcal{E} = -hu_t = h\gamma\sqrt{g_{tt}}, \tag{8}$$

where \mathcal{E} is the canonical form of relativistic Bernoulli parameter (8) for nondissipative relativistic flow. The exact form of specific enthalpy h will be presented in Sec. 2.2 and γ is the Lorentz factor.

2.2. EoS and the final form of equations of motion

To solve the equations of motion mentioned in Sec. 2.1, we need an EoS which relates temperature, pressure and internal energy of the system. As discussed before we would use CR EoS (4). Since the adiabatic index is actually a function of temperature and composition, so it does not appear explicitly in the EoS. The CR EoS is inspired by the exact calculations done earlier (51, 53). The advantage of using CR over the exact EoS is that, the form of CR is much simpler and has been shown to be equivalent (54). The explicit form of CR EoS for multispecies flow is given by

$$\bar{e} = \sum_i \bar{e}_i = \sum_i \left[\bar{n}_i m_i c^2 + \bar{p}_i \left(\frac{9\bar{p}_i + 3\bar{n}_i m_i c^2}{3\bar{p}_i + 2\bar{n}_i m_i c^2} \right) \right], \tag{9}$$

where $i =$ proton (p), electron (e^-), positron (e^+) and m_i is the mass of the corresponding i th species. In this paper, we consider the accretion flow to be electron-proton plasma ($e^- - p^+$). So, in the sections to follow, i would represent only protons and electrons.

We can define dimensional number density (\bar{n}), corresponding mass density ($\bar{\rho}$) and pressure (\bar{p}) present in Eq. (9) in the following way:

$$\bar{n} = \sum_i \bar{n}_i = \bar{n}_p + \bar{n}_e = 2\bar{n}_e, \tag{10}$$

where $\bar{n}_p =$ proton number density, and $\bar{n}_e =$ electron number density (in units of cm^{-3}).

$$\bar{\rho} = \sum_i \bar{n}_i m_i = \bar{n}_e m_e + \bar{n}_p m_p = \bar{n}_e m_e \left(1 + \frac{1}{\eta} \right) = \bar{n}_e m_e \tilde{K}, \tag{11}$$

$$\bar{p} = \sum_i \bar{p}_i = \sum_i \bar{n}_i k T_i = \bar{n}_e k (T_e + T_p) = \bar{n}_e m_e c^2 \left(\Theta_e + \frac{\Theta_p}{\eta} \right), \tag{12}$$

where $\eta = m_e/m_p$, $\tilde{K} = 1 + 1/\eta$, T_i is the temperature of the i th species (in units of Kelvin) and $k =$ Boltzmann constant. $\Theta_i = \frac{kT_i}{m_i c^2}$ is the nondimensional temperature which has been defined with respect to the rest-mass energy of the corresponding i th species.

Using Eqs. (10)–(12) we can simplify the EoS (9) to obtain,

$$\bar{e} = \bar{n}_e m_e c^2 \left(f_e + \frac{f_p}{\eta} \right) = \frac{\bar{\rho} c^2 f}{\tilde{K}}, \tag{13}$$

where f_i is defined as, $f_i = 1 + \Theta_i (\frac{9\Theta_i + 3}{3\Theta_i + 2})$ and $f = f_e + f_p/\eta$.

Enthalpy can be defined as

$$\bar{h} = \frac{\bar{e} + \bar{p}}{\bar{\rho}}. \tag{14}$$

Using Eqs. (11)–(13) we can reduce the above equation into a dimensionless form as

$$h = \frac{f + \left(\Theta_e + \frac{\Theta_p}{\eta} \right)}{\tilde{K}}. \tag{15}$$

The expression for polytropic index and adiabatic index for electrons and protons are given respectively as

$$N_p = \frac{df_p}{d\Theta_p}; \quad N_e = \frac{df_e}{d\Theta_e}; \quad \Gamma_p = 1 + \frac{1}{N_p}; \quad \text{and} \quad \Gamma_e = 1 + \frac{1}{N_e}. \tag{16}$$

The definition of the radial three-velocity is $v = [-(u_r u^r)/(u_t u^t)]^{1/2}$. Simplifying Eqs. (3)–(6), (9)–(16) we get the gradient of velocity,

$$\frac{dv}{dr} = \frac{\mathcal{N}}{\mathcal{D}}, \tag{17}$$

where $\mathcal{N} = -\frac{1}{r(r-2)} + a^2 \mathfrak{P} + (\Gamma_e - 1)\mathbb{E} + (\Gamma_p - 1)\mathbb{P}$ and $\mathcal{D} = \frac{v}{1-v^2}(1 - \frac{a^2}{v^2})$.

Here, we have defined the sound speed as, $a^2 = \mathcal{G}/h\tilde{K}$.

The expressions used in \mathcal{N} and \mathcal{D} are as follows:

$$\mathcal{G} = \Gamma_e \Theta_e + \frac{\Gamma_p \Theta_p}{\eta}; \quad \mathfrak{P} = \frac{2r - 3}{r(r - 2)}; \quad \mathbb{E} = \frac{\Delta Q_e}{\rho h u^r}; \quad \mathbb{P} = \frac{\Delta Q_p}{\rho h u^r}.$$

Substituting Eqs. (5), (10)–(13) in Eq. (6), we get the differential equation for both the proton and electron temperatures which is given by

$$\frac{d\Theta_p}{dr} = -\frac{\Theta_p}{N_p} \left(\mathfrak{P} + \frac{1}{v(1-v^2)} \frac{dv}{dr} \right) - \frac{\mathbb{P}\eta\tilde{K}h}{N_p}, \tag{18}$$

$$\frac{d\Theta_e}{dr} = -\frac{\Theta_e}{N_e} \left(\mathfrak{P} + \frac{1}{v(1-v^2)} \frac{dv}{dr} \right) - \frac{\mathbb{E}\tilde{K}h}{N_e}, \tag{19}$$

respectively.

2.2.1. Radiative processes considered

Cooling of protons can be caused due to Coulomb interactions (\bar{Q}_{ep}) with electrons if $T_p > T_e$, or due to inverse bremsstrahlung (\bar{Q}_{ib}). The expression for Coulomb interaction term in cgs unit is given by⁵⁵

$$\bar{Q}_{ep} = \frac{3}{2} \frac{m_e}{m_p} \bar{n}_e \bar{n}_p \sigma_T c k \frac{T_p - T_e}{K_2\left(\frac{1}{\Theta_e}\right) K_2\left(\frac{1}{\Theta_p}\right)} \ln \Lambda_c \times \left[\frac{2(\Theta_e + \Theta_p)^2 + 1}{\Theta_e + \Theta_p} K_1\left(\frac{\Theta_e + \Theta_p}{\Theta_e \Theta_p}\right) + 2K_0\left(\frac{\Theta_e + \Theta_p}{\Theta_e \Theta_p}\right) \right], \quad (20)$$

where σ_T is the Thomson scattering cross-section, $K_i(x)$'s are the modified Bessel functions of i th order and second kind, $\ln \Lambda_c$ is the Coulomb logarithm which we took to be equal to 20.

The expression for inverse bremsstrahlung is given by^{56,57}

$$\bar{Q}_{ib} = 1.4 \times 10^{-27} \bar{n}_e^2 \sqrt{\frac{m_e}{m_p} T_p}. \quad (21)$$

The cooling of electrons includes contributions from three radiative cooling mechanisms namely bremsstrahlung (\bar{Q}_{br}), synchrotron (\bar{Q}_{syn}) and inverse Compton scattering (\bar{Q}_{ic}). Therefore, $\bar{Q}_e^- = \bar{Q}_{br} + \bar{Q}_{syn} + \bar{Q}_{ic}$.

The expression for bremsstrahlung emissivity (in c.g.s units) is given by⁵⁸

$$\bar{Q}_{br} = 1.4 \times 10^{-27} \bar{n}_e^2 \sqrt{T_e} (1 + 4.4 \times 10^{-10} T_e). \quad (22)$$

The cooling per unit volume in case of synchrotron radiation is given as⁵⁶

$$\bar{Q}_{syn} = \frac{2\pi k T_e}{3c^2} \frac{\nu_c^3}{r r_g}, \quad (23)$$

where ν_c is the critical frequency below which the emission is self-absorbed. It can be defined as $\nu_c = \frac{3}{2} \nu_o \Theta_e^2 x_M$, where $\nu_o = 2.8 \times 10^6 B$. One has to solve a transcendental equation to obtain the value of x_M . Here, B is defined as the stochastic magnetic field present in the flow, whose value is obtained by assuming its pressure ($B^2/8\pi$) to be in partial or full equipartition with the gas pressure (\bar{p}). This ratio can be defined as β and is chosen as $\beta = 0.01$, unless otherwise mentioned.

The Comptonization of the soft photons generated through synchrotron process, is given as⁵⁹

$$\bar{Q}_{ic} = \zeta \bar{Q}_{syn}, \quad (24)$$

where ζ is the enhancement factor which is defined as the average change in energy of the photon at escape after all scatterings. It is expressed as $\zeta = P(A - 1)(1 - PA)^{-1} [1 - (x_c/(3\Theta_e))^{-(1+\ln P/\ln A)}]$. Here, $x_c = h\nu_c/m_e c^2$, $P = 1 - \exp(-\tau_{es})$ is the probability of a photon to be scattered in a medium with optical depth τ_{es} , and $A = 1 + 4\Theta_e + 16\Theta_e^2$, is the mean amplification factor in energy of the scattered

photon. The optical depth of a medium where electron-scattering is dominant is given by⁶⁰

$$\tau_{\text{es}} = 0.4[1 + (2.22T_e \times 10^{-9})^{0.86}]^{-1}.$$

The plasma is heated via magnetic dissipation and it primarily affects the proton distribution, and part of this heat is transmitted to the electrons through the Coulomb coupling term. The dissipative heating rate is given by^{47,49}

$$\bar{Q}_p^+ \approx \bar{Q}_B = \frac{3cu^r}{2rr_g} \frac{B^2}{8\pi} = \frac{3cu^r}{2rr_g} \beta \bar{n}_e k(T_e + T_p). \quad (25)$$

2.2.2. Entropy accretion rate expression

From single temperature solutions we know we can define an entropy-accretion rate by integrating Eqs. (18) and (19) by turning off the explicit heating and cooling terms.

$$\begin{aligned} \frac{d\Theta_p}{dr} &= \frac{\Theta_p}{N_p} \frac{1}{n_p} \frac{dn_p}{dr} + \frac{Q_{\text{ep}} \eta \tilde{K}}{\rho u^r N_p}, \\ \frac{d\Theta_e}{dr} &= \frac{\Theta_e}{N_e} \frac{1}{n_e} \frac{dn_e}{dr} - \frac{Q_{\text{ep}} \tilde{K}}{\rho u^r N_e}. \end{aligned} \quad (26)$$

In single temperature regime, it is very easy to integrate the above equation, but now, due to the presence of Coulomb interaction term, Eq. (26) is not generally integrable. And therefore, we cannot have an analytical expression for the measure of entropy at every r in two-temperature solutions.

However, in regions where Q_{ep} can be neglected, an analytical expression is admissible. Such a region is just outside the horizon, where gravity overwhelms any other interaction. So, near the horizon, where Q_{ep} is negligible, Eq. (26) can be integrated to obtain,

$$n_{\text{ein}} = \kappa_1 \exp\left(\frac{f_{\text{ein}} - 1}{\Theta_{\text{ein}}}\right) \Theta_{\text{ein}}^{\frac{3}{2}} (3\Theta_{\text{ein}} + 2)^{\frac{3}{2}}, \quad (27)$$

$$n_{\text{pin}} = \kappa_2 \exp\left(\frac{f_{\text{pin}} - 1}{\Theta_{\text{pin}}}\right) \Theta_{\text{pin}}^{\frac{3}{2}} (3\Theta_{\text{pin}} + 2)^{\frac{3}{2}}, \quad (28)$$

where κ_1 and κ_2 are the integration constants which are a measure of entropy. We know from charge neutrality condition that $n_{\text{ein}} = n_{\text{pin}} = n_{\text{in}}$. Subscript ‘‘in’’ indicates quantities measured just outside the horizon. Therefore we can write,

$$\begin{aligned} n_{\text{in}}^2 &= n_{\text{ein}} n_{\text{pin}} \Rightarrow n_{\text{in}} = \sqrt{n_{\text{ein}} n_{\text{pin}}} \\ &= \kappa \sqrt{\exp\left(\frac{f_{\text{ein}} - 1}{\Theta_{\text{ein}}}\right) \exp\left(\frac{f_{\text{pin}} - 1}{\Theta_{\text{pin}}}\right) \Theta_{\text{ein}}^{\frac{3}{2}} \Theta_{\text{pin}}^{\frac{3}{2}}} \\ &\quad \times \sqrt{(3\Theta_{\text{ein}} + 2)^{\frac{3}{2}} (3\Theta_{\text{pin}} + 2)^{\frac{3}{2}}}, \end{aligned} \quad (29)$$

where $\kappa = \sqrt{\kappa_1 \kappa_2}$.

Thus, the expression of entropy accretion rate can be written as

$$\begin{aligned} \mathcal{M}_{\text{in}} &= \frac{\dot{M}}{4\pi\kappa(m_e + m_p)\cos(\theta)} = \sqrt{\exp\left(\frac{f_{\text{ein}} - 1}{\Theta_{\text{ein}}}\right)\exp\left(\frac{f_{\text{pin}} - 1}{\Theta_{\text{pin}}}\right)\Theta_{\text{ein}}^{\frac{3}{2}}\Theta_{\text{pin}}^{\frac{3}{2}}} \\ &\times \sqrt{((3\Theta_{\text{ein}} + 2)^{\frac{3}{2}}(3\Theta_{\text{pin}} + 2)^{\frac{3}{2}})u^r r^2}. \end{aligned} \quad (30)$$

In Sec. 4.2, we will use Eq. (30) to obtain the correct accretion solution.

2.2.3. Sonic point conditions

As argued before, BH accretion is transonic in nature. So, at some $r = r_c$ the critical point, the flow $dv/dr \rightarrow 0/0$. This condition gives us the critical point conditions. Thus using Eq. (17) we get,

$$-\frac{1}{r_c(r_c - 2)} + a_c^2 \mathfrak{P}_c + (\Gamma_{ec} - 1)\mathbb{E}_c + (\Gamma_{pc} - 1)\mathbb{P}_c = 0, \quad (31)$$

and

$$\frac{v_c}{1 - v_c^2} \left(1 - \frac{a_c^2}{v_c^2}\right) = 0. \quad (32)$$

Here, “ c ” in the subscript resembles the values of the variables at the critical point. At r_c , the radial three-velocity is equal to the sound speed or $v_c = a_c$, i.e. the Mach number $M_c = v_c/a_c = 1$. Since the derivative of velocity at the critical point has a $0/0$ form, therefore it is calculated using l’Hospital rule.

3. Solution Procedure

It has already been established by Bondi,² that for a given boundary condition the entropy of the transonic global solution is maximum, and therefore, a transonic solution is the solution favored by nature. Therefore, we look for a transonic solution. The general procedure to find a solution in two-temperature is similar to the one in the single temperature regime, which is — for a given set of flow parameters (E, \dot{M}) , the sonic point is obtained first, and then integrate the gradient of velocity and temperature, that is Eqs. (17)–(19), from the sonic point inward and outward, in order to obtain self-consistent values of v , Θ_p and Θ_e , respectively throughout the flow. A spherical flow harbors only a single sonic point.

3.1. Method to find the sonic point: Single temperature versus two temperature

This is the first step in obtaining a general transonic solution. Finding a sonic point is not trivial in presence of heating and cooling. To find the sonic points, we need to first choose a boundary: horizon or infinity. The advantage of choosing the horizon as the boundary, is that atleast the inflow velocity on the horizon is known ($v_{\text{in}} = c$), while at the outer boundary its value is arbitrary. Unfortunately, there is

a coordinate singularity on the horizon, so one cannot start the integration from the horizon. Therefore, we chose a location asymptotically very close to the horizon, $r_{\text{in}} \rightarrow 2r_g$. Very close to the horizon gravity overwhelms all other interactions, therefore the flow becomes adiabatic, i.e. as $r_{\text{in}} \rightarrow 2r_g$, $E \rightarrow \mathcal{E}$. At r_{in} for single temperature flow, there are two unknowns v_{in} and the temperature. So for a given E , at r_{in} we supply a temperature in the expression of $E = \mathcal{E}$ to obtain a value of velocity, say v'_{in} . With these values of velocity and temperature we integrate the equations of gradient of velocity, and temperature to obtain a solution and check for sonic point conditions. If the solution does not pass through the sonic point, then we change the temperature supplied at r_{in} and repeat the process until and unless for a certain temperature at r_{in} we obtain a $v_{\text{in}} = v'_{\text{in}}$ which on integration satisfies the sonic point conditions at some $r = r_c$. Therefore, we obtain a transonic solution by iterating the temperature to give us the unique transonic solution. This is in essence a variation of the solution procedure of Becker and his collaborators.

For two-temperature flow however, we have three unknowns, v_{in} , Θ_{ein} and Θ_{pin} at r_{in} , and still two constants of motion E and \dot{M} . That is, the number of variables increases by one, while the number of equations, or equivalently the number of constants, remains the same as we had in the single temperature regime. So for a given E and \dot{M} , we supply Θ'_{pin} , Θ'_{ein} at r_{in} and compute v'_{in} from the expression of E . Considering Θ'_{pin} , Θ'_{ein} and v'_{in} as guess values of temperatures and flow velocity near the horizon, we integrate Eqs. (17)–(19) outward and check for sonic point conditions (Eqs. (31), (32)). If the sonic point condition is not satisfied, then we change the value of Θ'_{ein} , obtain another value of v'_{in} and again we integrate the same equations. Similarly we also change Θ'_{pin} and repeat the same procedure again, if no transonic solution is obtained. If the sonic point is found out, then the transonic solution with those values of $\Theta_{\text{pin}} = \Theta'_{\text{pin}}$, $\Theta_{\text{ein}} = \Theta'_{\text{ein}}$ and $v_{\text{in}} = v'_{\text{in}}$ for that particular set of E and \dot{M} , is the solution. We have chosen $r_{\text{in}} = 2.001 r_g$. One has to remember however, now the system is under determined, the consequence of which will be seen in Sec. 4. It may be further noted that, we mentioned Θ_{pin} is supplied to iterate Θ_{ein} and v_{in} from E , however while presenting results, we prefer to quote T_{pin} or T_{ein} instead. This will make it easier for the reader to relate to the problem.

4. Result

We initially assume $Q_{\text{p}}^+ = 0$ to discuss various features of two-temperature solution. The effect of $Q_{\text{p}}^+ \neq 0$ will be discussed later in Sec. 4.5.

4.1. Investigating degeneracy in two-temperature flows

In Figs. 1(a)-1(c), we present the accretion solutions of two-temperature Bondi flow for $M_{\text{BH}} = 10 M_{\odot}$, $\dot{M} = 0.01$ and $E = 1.0001$. Each panel shows the accretion Mach number or $M = v/a$ (solid, red) and corresponding wind M (dotted, red) as a function of r . The crossing points are the location of sonic/critical points. The three

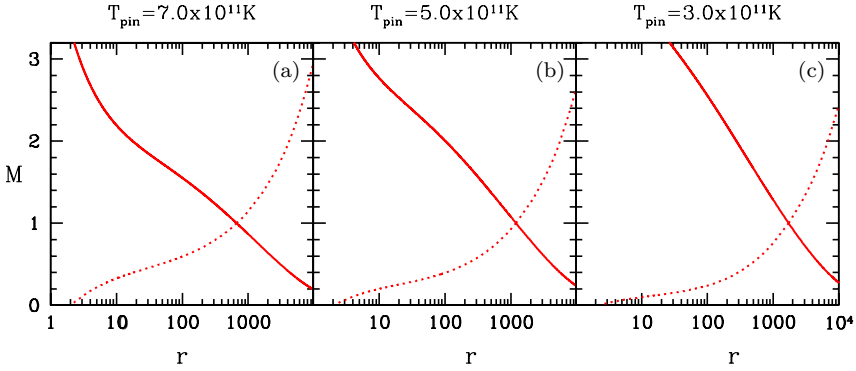


Fig. 1. (Color online) (a) Accretion M (solid, red) and wind M (dotted, red) as a function of r corresponding to $M_{\text{BH}} = 10 M_{\odot}$, $\dot{M} = 0.01$ and $E = 1.0001$. The different solutions are obtained changing T_{pin} (values are written on the top of each panel).

solutions plotted in the figure are obtained by changing the proton temperature T_{pin} ($T_{\text{pin}} = T_{\text{p}}|_{r \rightarrow r_{\text{in}}}$), but for the same E and \dot{M} for a given central BH. This implies that different values of T_{pin} would yield different solutions, each with a unique sonic point position and sonic point properties. In Sec. 3.1, we pointed out that the two-temperature regime is under determined, because we need to know three unknowns at r_{in} but there were only two constants of motion. The degeneracy in solution is the direct fall out of such a scenario. All transonic two-temperature solutions, whether in exact GR or in pseudo-Newtonian regime, suffers from this deficiency. In Sec. 4.2, we will discuss, the physical principle to be followed in order to obtain a unique two-temperature transonic solution.

4.2. Entropy measure as a tool to remove degeneracy in two-temperature flows

As has been shown in Figs. 1(a)–1(c), for a given set of constants of motion namely E and \dot{M} , there can be a plethora of transonic solutions, each differentiated by the T_{pin} at r_{in} . Now the only way this degeneracy can be removed is by invoking the second law of thermodynamics. It has also been shown in Sec. 2.2.2, that a general analytical expression of entropy measure is not possible, however, the entropy of the accreting matter very close to the BH can be calculated (Eq. (30)). So in Fig. 2 (top left panel) we plot the measure of entropy $\dot{\mathcal{M}}_{\text{in}}$ at $r = r_{\text{in}}$ as a function of T_{pin} , for an accretion flow characterized by constants of motion $\dot{M} = 0.1$ and $E = 1.001$ on to a BH of $M_{\text{BH}} = 10 M_{\odot}$. We have marked points “a” to “e” on the $\dot{\mathcal{M}}_{\text{in}}$ versus T_{pin} curve, and then have plotted the corresponding solutions (M versus r) in the adjacent panels also named as “a”–“e”. It is easy to note that the solutions are completely different since, the sonic points of the solutions vary by a few $\times 100 r_{\text{g}}$ for this particular E and \dot{M} . In particular, solution marked “a” and that marked “e” both have the same $\dot{\mathcal{M}}_{\text{in}}$ and E , but the sonic point of “a” is at $r_{\text{c}} = 75.008$ and

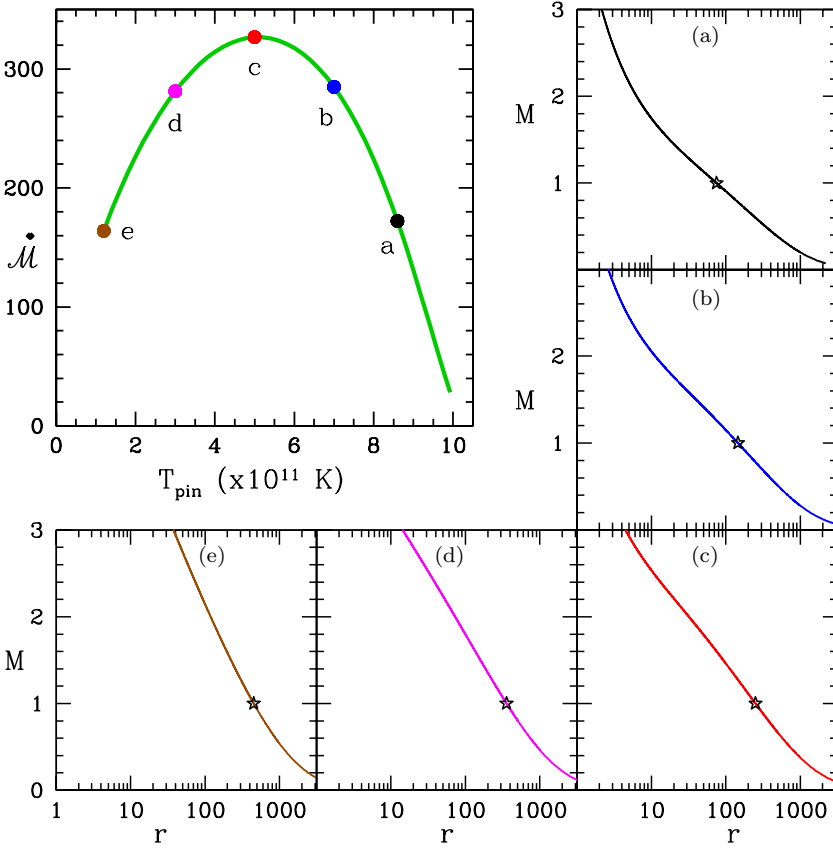


Fig. 2. Top left panel: Variation of \dot{M}_{in} as a function of T_{pin} for accretion flow of $\dot{M} = 0.1$ and $E = 1.001$ onto a $10 M_{\odot}$ BH. Panels “a” to “e” presents M of the accretion with r corresponding to each of the points “a”–“e” on the \dot{M}_{in} – T_{pin} curve. The stars show the location of sonic points. At $T_{pin} = 5.0 \times 10^{11}$ K (marked “c”) entropy maximizes, so panel “c” is the correct solution for the given E and \dot{M} .

that of “e” is at $r_c = 451.297$, respectively. Different proportions of T_e and T_p might give rise to the same \dot{M}_{in} and E ! This also implies a wrong choice of solution would lead us to wrong conclusions about the physical processes around BHs. *However, only one of them is correct.* It must be noted that, of all the solutions, the entropy distribution has single well behaved maxima at $T_{pin} = 5 \times 10^{11}$ K, and therefore, by the second law of thermodynamics, the accretion solution corresponding to this entropy at point “c” on the curve is the correct one.

4.3. Properties of unique two-temperature transonic solution

4.3.1. Critical point properties

For adiabatic flow, sonic points can be found directly from a given value of E , but in our case the sonic point can be obtained only after obtaining the solution. Since

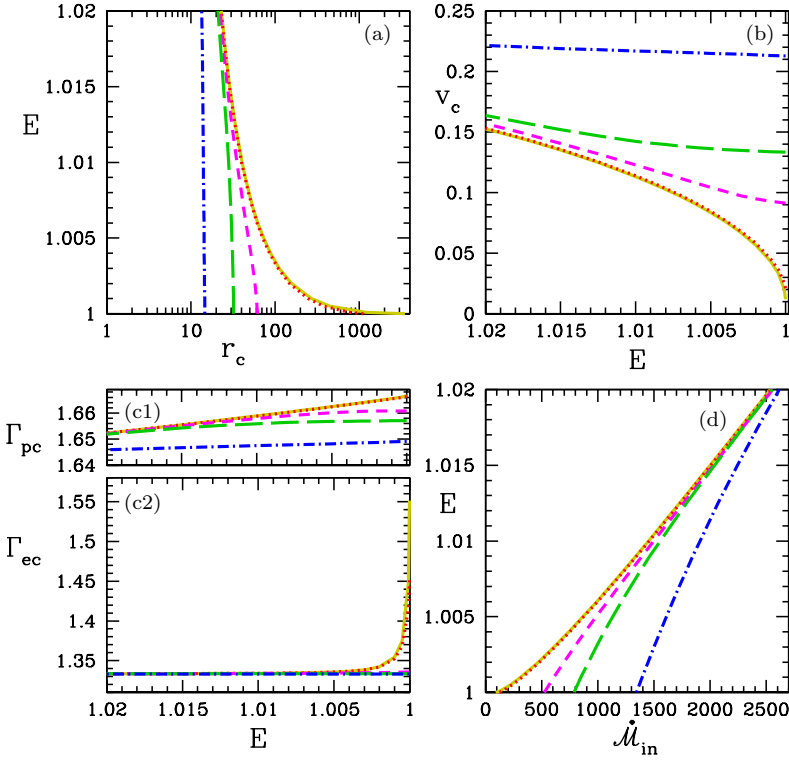


Fig. 3. (Color online) Variation of sonic points and its properties with the accretion rate (\dot{M}) of the BH. Here, we have assumed $M_{\text{BH}} = 10 M_{\odot}$. We have taken $\dot{M} = 0.01$ (yellow-solid), 0.10 (red-dotted), 0.50 (magenta-dashed), 1.00 (green-long-dashed) and 5.00 (blue-dot-dashed).

the system is under determined, unique r_c can only be obtained by invoking the second law of thermodynamics. Taking all these factors into consideration, we plot E as a function of r_c (Fig. 3(a)); while v_c (Fig. 3(b)); Γ_{pc} , Γ_{ec} (Fig. 3(c)) and \dot{M}_{in} (Fig. 3(d)) as functions of E . Each curves are for accretion rate $\dot{M} = 0.01$ (yellow-solid), 0.10 (red-dotted), 0.50 (magenta-dashed), 1.00 (green-long-dashed) and 5.00 (blue-dot-dashed). Here a BH of $10 M_{\odot}$ has been considered. For low accretion rates ($\dot{M} \leq 0.1$), the range of sonic points are $3 < r_c \rightarrow \infty$, however, for higher accretion rates, the sonic point range decreases significantly. In presence of significant cooling (i.e. higher \dot{M}), hot flows from large distance can be accreted, which otherwise could not be accreted. As a result v_c and the entropy both are higher for flows with higher \dot{M} . From all the plots it is clear that, for spherical accretion, there can be only one sonic point.

4.3.2. Flow variables and emissivity

In Figs. 4(a)–4(f), we present various flow variables of the correct Bondi accretion on to a BH $M_{\text{BH}} = 10 M_{\odot}$. The constants of motions are $E = 1.00001$ and $\dot{M} = 0.01$.

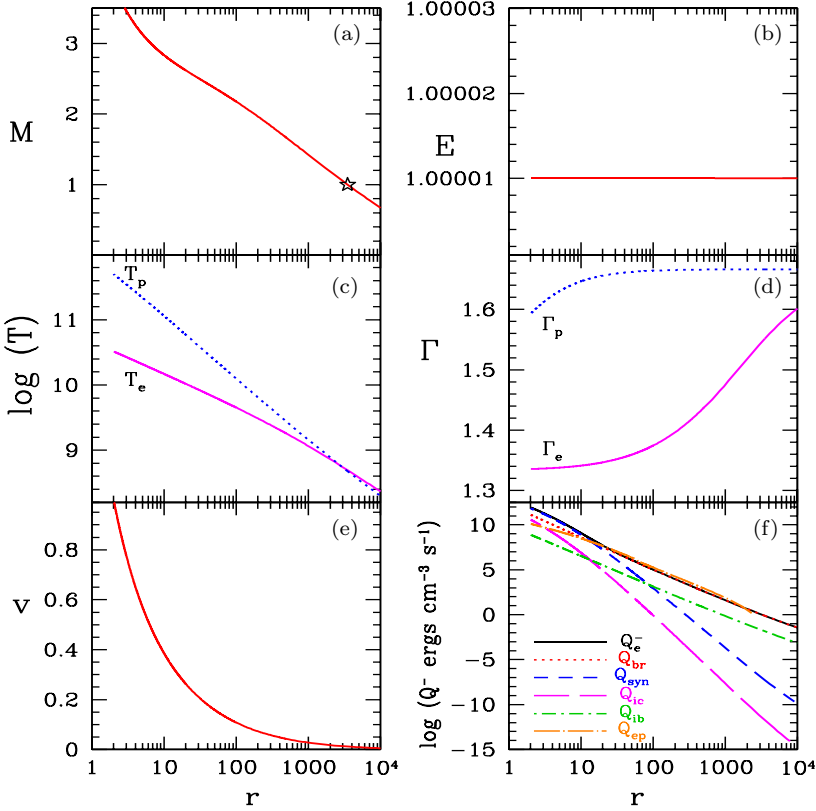


Fig. 4. Variation of (a) M ; (b) E ; (c) T_p and T_e ; (d) Γ_e and Γ_p ; (e) v ; and (f) total (Q_e^-), bremsstrahlung (Q_{br}), synchrotron (Q_{syn}), inverse-Compton (Q_{ic}), and inverse-bremsstrahlung (Q_{ib}) emissivities as a function of r . The Coulomb coupling Q_{ep} is over plotted. The star on the M distribution represent the location of the sonic point. The accretion disc parameters are $E = 1.00001$, $M_{\text{BH}} = 10 M_{\odot}$ and $\dot{M} = 0.01$. The Q s presented, are in physical units ($\text{ergs cm}^{-3} \text{ s}^{-1}$).

The flow variables plotted are M , E , T_p and T_e , Γ_e and Γ_p and v on the panels Figs. 4(a)–4(e), respectively. The star mark indicates the location of sonic point. Figure 4(b) shows that the generalized Bernoulli parameter E is indeed a constant of motion. It is also to be noted that, $T_e \approx T_p$ (solid, Fig. 4(c)) at large r and $T_e < T_p$ at $2 < r < 1000$. Moreover, the electron fluid while traveling a distance of about $10^4 r_g$ on the way to the BH, spans a temperature range of more than two orders of magnitude which means $1.6 > \Gamma_e \sim 4/3$ and do not have any constant value. In addition, $1.6 < \Gamma_p \sim 5/3$ and the temperature of the proton fluid spans more than three orders of magnitude. But the distribution of Γ_e and Γ_p would also change for a different set of constants of motion (E , \dot{M}). In other words, considering CR EoS is important. In Fig. 4(f), we plot the total electron emissivity or Q_e^- , bremsstrahlung (Q_{br}), synchrotron (Q_{syn}), inverse-Compton (Q_{ic}), inverse-bremsstrahlung (Q_{ib}) and Coulomb coupling term (Q_{ep}) as a function of distance.

All the Q s used are in physical units ($\text{ergs cm}^{-3} \text{s}^{-1}$), and for simplicity \bar{Q} are not used. Q_{br} dominates the radiative process for this particular set of E and \dot{M} , except near the horizon where the $Q_{\text{syn}} \gtrsim Q_{\text{br}}$. Q_{ic} is quite weak for low accretion rate. Q_{ib} may have larger contribution than Q_{syn} or Q_{ic} at larger distance, but $Q_{\text{ib}} \ll Q_{\text{e}}^-$. Since Q_{ep} is also comparable to Q_{e}^- except near the horizon, T_{p} and T_{e} is comparable in a large range of r . Close to the horizon, $Q_{\text{ep}} \ll Q_{\text{e}}^-$ as a result $T_{\text{p}} \gg T_{\text{e}}$. On careful inspection it is clear that at $r > 2000 r_{\text{g}}$, $Q_{\text{ep}} < 0$ and therefore $T_{\text{e}} > T_{\text{p}}$. So one can say, attainment of single temperature distribution or, two-temperature distribution depends on the relative strength of Coulomb interaction and various radiative processes.

4.3.3. Dependence of accretion flow on E and \dot{M}

In Figs. 5(a₁)–5(c₃) we show how the global transonic two-temperature solutions depend on constant of motion E (increases left to right) for a given \dot{M} on to a

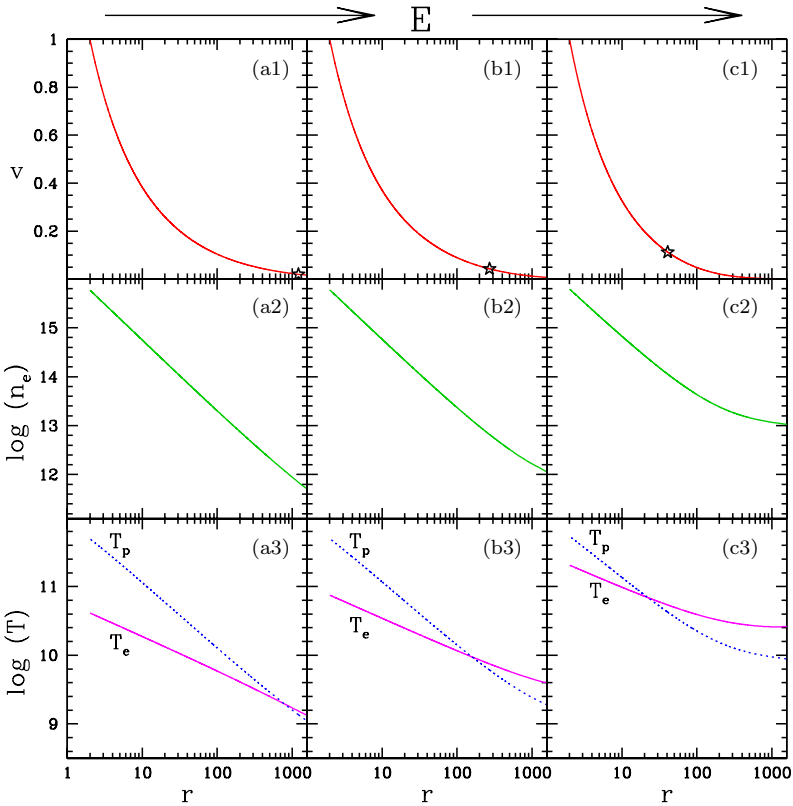


Fig. 5. Variation of v (a₁, b₁, c₁); electron number density n_{e} (a₂, b₂, c₂) and T_{p} and T_{e} in panels (a₃, b₃, c₃), as a function of r . The generalized Bernoulli parameter changes from the left panels $E = 1.0001$ (a₁, a₂, a₃), to the middle panels $E = 1.001$ (b₁, b₂, b₃) and then to the right panels $E = 1.01$ (c₁, c₂, c₃). Other parameters selected are $M_{\text{BH}} = 10 M_{\odot}$ and $\dot{M} = 0.01$.

stellar mass BH. We have plotted v (a_1, b_1, c_1); electron number density n_e (a_2, b_2, c_2) and T_p and T_e in panels (a_3, b_3, c_3), as a function of r . The star on the velocity curve shows the location of sonic point. For higher E , r_c is formed closer to the horizon. Increasing E , raises the temperature at the outer boundary and reduces v , thus the electron number density at the outer boundary is also higher for higher E .

Increasing \dot{M} has similar effect on the accretion solutions. We plot the velocity distribution (Figs. 6(a₁), 6(b₁) and 6(c₁)), n_e (Figs. 6(a₂), 6(b₂) and 6(c₂)), T_e

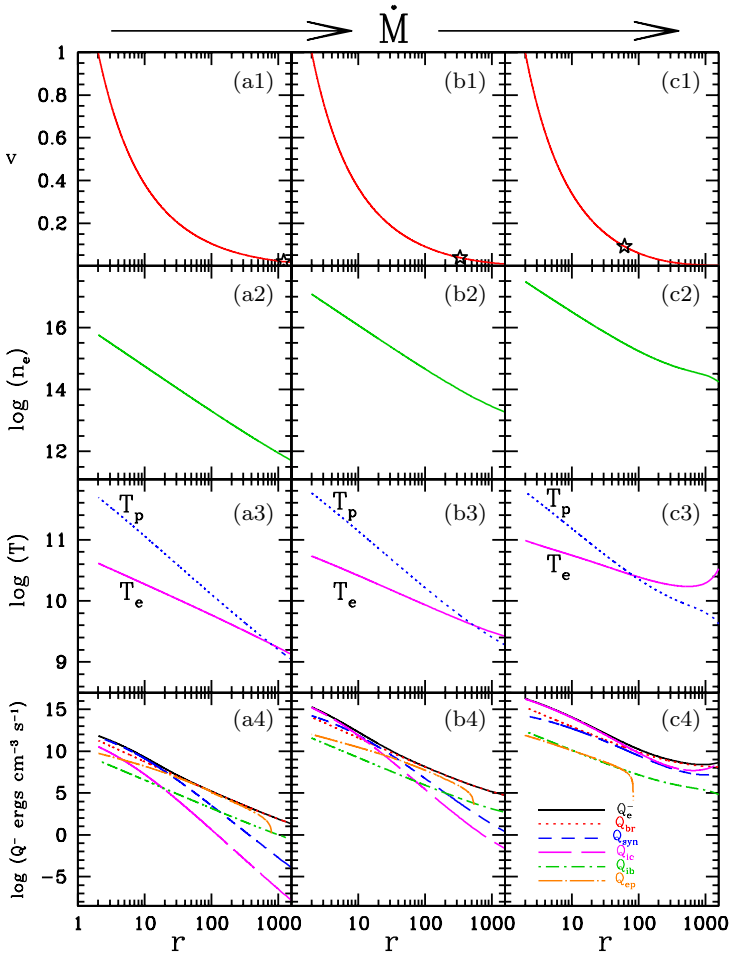


Fig. 6. Variation of v (a_1, b_1, c_1); electron number density n_e (a_2, b_2, c_2), T_p and T_e in panels (a_3, b_3, c_3) and various radiative emissivities and Q_{ep} (a_4, b_4, c_4) in panels (a_4, b_4, c_4) as a function of r . The accretion rate changes from the left panels $\dot{M} = 0.01$ (a_1, a_2, a_3, a_4), to the middle panels $\dot{M} = 0.2$ (b_1, b_2, b_3, b_4) and then to the right panels $\dot{M} = 0.5$ (c_1, c_2, c_3, c_4). Other parameters selected are $M_{BH} = 10 M_\odot$ and $E = 1.0001$. All Q s are presented in physical units ($\text{ergs cm}^{-3} \text{s}^{-1}$).

and T_p (Figs. 6(a₃), 6(b₃) and 6(c₃)) and different radiative emissivities and Q_{ep} (Figs. 6(a₄), 6(b₄) and 6(c₄)) as a function of r . Once again Q s presented in this figure are in physical units and we do not put ‘bar’ in order, not to make the figure clumsy. Keeping $E = 1.0001$ const. we change $\dot{M} = 0.01$ (a₁–a₄), to $\dot{M} = 0.2$ (b₁–b₄) and then to $\dot{M} = 0.5$ (c₁–c₄). Emission increases with the increase in \dot{M} , and therefore can accrete hotter flow at large distances. As a result the sonic points form closer to the horizon, even for same E . The sonic point in the figure can also be seen to move closer to the horizon (the star mark in the velocity distribution). For low \dot{M} , Q_{br} dominates (see also Fig. 4(f)). Interestingly, for a distance range of $20 < r < 1000$, $Q_{ep} \approx Q_e^-$ (long dashed-dot). Since Coulomb interaction is comparable to the bremsstrahlung emission, $T_e \approx T_p$ in the same range. As the accretion rate increases, inverse-Compton cooling becomes more efficient and dominates in the overall emissivity (Fig. 6(b₄)). The Q_{ep} term becomes less effective, as a result the difference between T_e and T_p increases. For even higher \dot{M} (Fig. 6(c₄)), inverse-Compton dominates the cooling and Coulomb term becomes even weaker and therefore T_e and T_p becomes significantly different from each other. In fact, Coulomb coupling is effective when emission process is not very strong.

4.3.4. Effect of the mass of the central BH

Since the mass supplied is described in the units of Eddington rate, so the net amount of mass flux increases with the central mass of the BH. The number density is proportional to the inverse of M_{BH} , but the volume would increase as M_{BH}^3 . Therefore, emissivity is proportional to M_{BH}^{-2} . As a result net radiative cooling increases with M_{BH} . This allows hotter matter to flow onto a more massive BH, which pushes the sonic point closer to horizon even for matter starting with same E and \dot{M} (in units of Eddington rate). We plot n_e (Figs. 7(a₁), 7(b₁) and 7(c₁)) and $Q_e^-, Q_{br}, Q_{syn}, Q_{ic}, Q_{ib}, Q_{ep}$ (Figs. 7(a₂), 7(b₂) and 7(c₂)) as a function of r , but for different $M_{BH} = 10 M_\odot$ (Figs. 7(a₁) and 7(a₂)), $M_{BH} = 10^3 M_\odot$ (Figs. 7(b₁) and 7(b₂)) and $M_{BH} = 10^6 M_\odot$ (Figs. 7(c₁) and 7(c₂)). The Q s are presented in physical units. The sonic point for $M_{BH} = 10 M_\odot$ is at $r_c = 61.535$, for $M_{BH} = 10^3 M_\odot$ the $r_c = 39.966$ and finally for $M_{BH} = 10^6 M_\odot$ the sonic point is at $r_c = 19.786$. So it is clear that radial accretion onto larger BH, is hotter and will be more luminous than the smaller ones. For low accretion rates where the number density is lower, Q_{ic} is generally lower than Q_{br} or Q_{syn} . But for higher \dot{M} accretion, Q_{ic} starts to dominate in the inner region. And since accreting larger BHs are more luminous, the total emissivity is dominated by Q_{ic} . These plots also shows that, for lower mass BH and higher \dot{M} , Q_{syn} is similar to Q_{br} , however, for higher M_{BH} , Q_{br} is much stronger than Q_{syn} . Whatever may be the mass of the central BH or accretion rate, Q_{ib} is significantly lower than the net emissivity. The Coulomb coupling term Q_{ep} is negligible for high \dot{M} and decreases even more for flow around massive BHs.

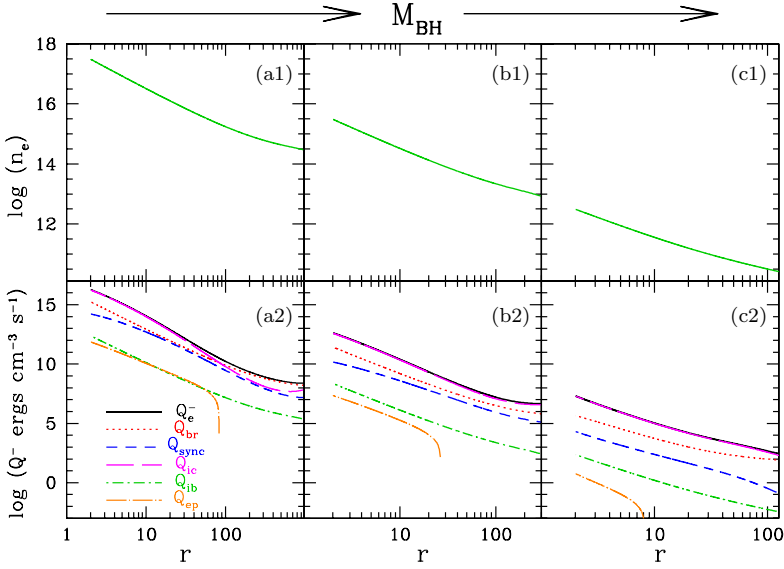


Fig. 7. Variation of n_e (a₁, b₁, c₁); emissivities and Coulomb coupling (a₂, b₂, c₂) as function of r . Left column panels (a₁ and a₂) are for $M_{\text{BH}} = 10 M_{\odot}$, the middle column are for $M_{\text{BH}} = 10^3 M_{\odot}$ (b₁, b₂) and for right column $M_{\text{BH}} = 10^6 M_{\odot}$ (c₁, c₂). Other parameters selected are $E = 1.0001$ and $\dot{M} = 0.5$. The Q s are in physical units ($\text{ergs cm}^{-3} \text{s}^{-1}$).

4.4. Luminosity and efficiency of the systems

Shapiro^[7] computed luminosity from Bondi flow via only the bremsstrahlung process, and concluded that radial flow is not efficient enough. However, that accretion model was not strictly two-temperature. Moreover, all classes of solutions were not investigated. From Figs. 4–6 of this paper, it is quite clear that the different cooling

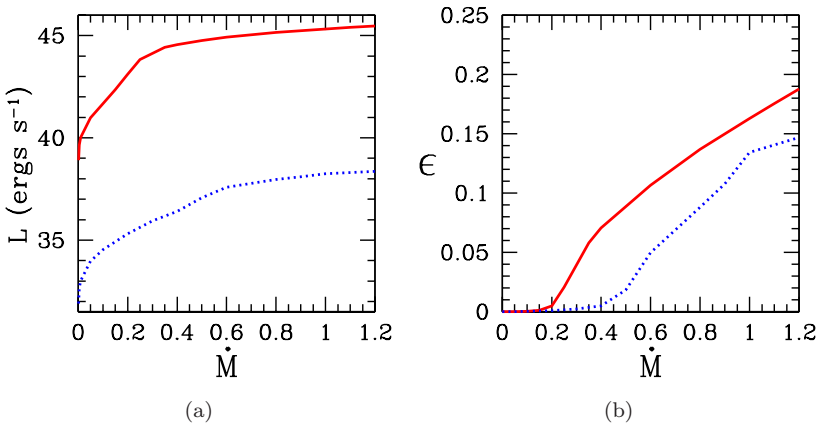


Fig. 8. (Color online) (a) Luminosity L , and (b) efficiency ϵ as a function of \dot{M} . Each curve corresponds to $M_{\text{BH}} = 10^8 M_{\odot}$ (solid, red) and $M_{\text{BH}} = 10 M_{\odot}$ (dotted, blue). Other parameter is $E = 1.001$.

processes start to dominate at different \dot{M} . For lower \dot{M} inverse-Compton is not a very dominant process, while for higher accretion rate, inverse-Compton becomes important. Therefore, it can be safely assumed that both luminosity and efficiency of the accretion flow would also depend on the accretion rates.

In Fig. 8(a), we plot the variation in luminosity (L) in units of ergs s^{-1} , with \dot{M} for accretion flow on to $M_{\text{BH}} = 10 M_{\odot}$ (dotted, blue), and $M_{\text{BH}} = 10^8 M_{\odot}$ (solid, red). Other parameter of the flow is $E = 1.001$. The efficiency of a BH system can be written as $\epsilon = L/(\dot{M}c^2)$. In Fig. 8(b), the corresponding ϵ is plotted as a function of \dot{M} . For low $\dot{M} \lesssim 0.2$, the efficiency of conversion of accretion energy to radiation is really low $\epsilon \lesssim 0.01$ for both kind of BHs. However, for $\dot{M} > 0.5$ the efficiency

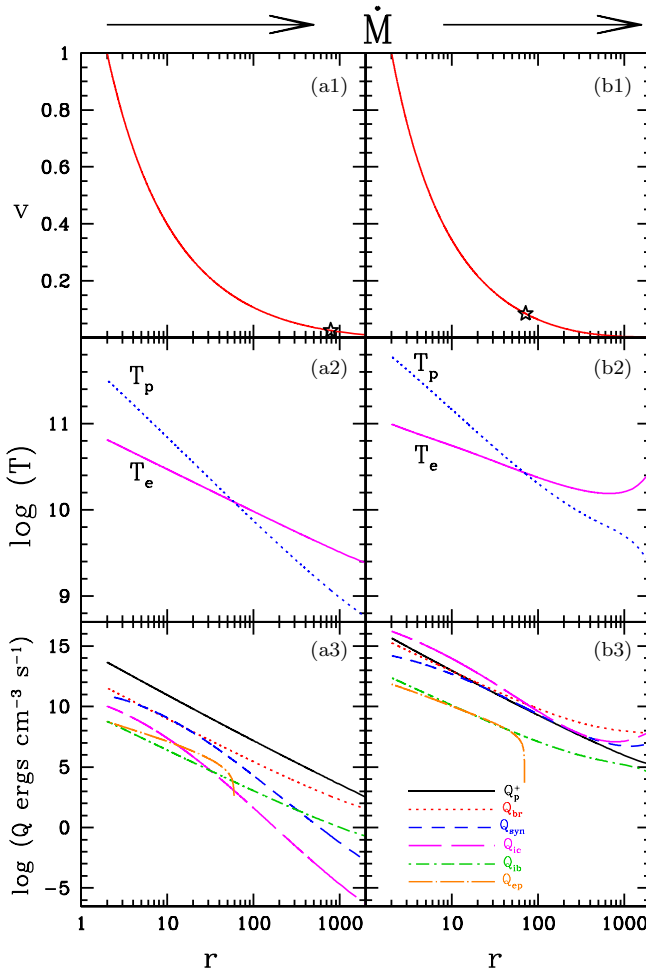


Fig. 9. Three-velocity v (a₁, b₁), temperatures (a₂, b₂) and emissivities, heating and Coulomb coupling (a₃, b₃) as a function of r . The solutions are for $\dot{M} = 0.01$ (a₁–a₃) and $\dot{M} = 0.5$ (b₁–b₃) Other parameters are for $E = 1.001$ and $M_{\text{BH}} = 10 M_{\odot}$.

$\gtrsim 0.1$ for accretion on to $10^8 M_\odot$ BH and comfortably produces $L \gtrsim 10^{44}$ ergs s^{-1} . At super Eddington accretion rates super massive BH produces luminosities above 10^{45} erg s^{-1} with efficiency $\epsilon \sim 0.2$. Accretion flow on to stellar mass BH can emit at $L \sim 10^{38}$ erg s^{-1} for $\dot{M} \gtrsim 0.8$. However, the efficiency of accretion flow around stellar mass BH is generally lower than the one around super-massive BH, however, for $\dot{M} > 0.8$ the efficiency $\epsilon > 0.1$. So not only the accretion flow onto massive BHs are brighter, even its radiative efficiency is more.

4.5. Effect of dissipative proton heating

So far in this paper, we considered no explicit heating. We now consider dissipative magnetic heating in the footsteps of Ipser and Price.⁴⁷ It mainly affects the protons, however, through Coulomb coupling the dissipated energy is also transmitted to the electrons. In Figs. 9(a₁)-9(a₃), we plot v (panel a₁), temperatures (panel a₂) and various emissivities, heating rate and the Coulomb coupling term (panel a₃). Comparing with Figs. 5(b₁)-5(b₃), which was for the same accretion parameters but without heating, the effect of heating is clearly seen. The sonic point in the present case is pushed back, i.e. BH is accreting matter with lower temperatures at the outer boundary. Since the \dot{M} is low, so the heating term Q_p^+ dominates. In Figs. 9(b₁)-9(b₃) the same variables are plotted but now for higher $\dot{M} = 0.5$. In this case the Q_e^- dominates over Q_p^+ . The Coulomb coupling on either case is negligible. Heating processes quantitatively affects the solutions, if the dissipative heat only directly affects the protons. This is because, in general Coulomb coupling is not very effective in energy exchange between electrons and protons and was also suggested by Mamamoto *et al.*³⁹

5. Discussions and Conclusions

A correct two-temperature solution is very important, because a proper electron temperature distribution for a given boundary condition, produces the correct spectrum and luminosity. Moreover, analytical solutions obtained in this paper is also important since, these solutions may act as tests, as well as, may be used as initial conditions for simulation codes.

Although there are few papers in the single temperature regime, which used constants of motion to obtain the solutions, but as far as we know, probably there are none in the two-temperature domain which even addresses the issue of constants of motion while obtaining the solutions. It may be remembered that, a fluid solution is not just characterized by its energy but also its entropy, and according to the second law of thermodynamics, any physical solution should correspond to the one with highest entropy. It was Bondi² who used this principle in order to stress that a transonic solution is the correct accretion solution under the influence of gravity. Later Becker and his collaborators^{26, 29} used the information of energy as well as the entropy to obtain transonic accretion solutions around a BH in presence

of dissipation. Since the set of equations in single temperature flow is complete, so finding a transonic solution suffices the criteria for second law of thermodynamics. However, as has been discussed extensively in the paper, the set of governing equations are less than the number of variables, second law of thermodynamics becomes essential even to find a proper solution. The novelty of this work is to identify this problem and laying down the procedure to overcome it, by actually following the footsteps of Bondi and Becker.

In this paper, we obtained the expression for the generalized Bernoulli parameter (E) for two temperature flow, by integrating the energy–momentum balance equation and showed that it is indeed a constant of motion. Moreover, integrating the continuity equation we obtained the expression for accretion rate (\dot{M}) which is the other constant of motion. In addition, we explicitly showed that degenerate transonic solutions exist for a given set of constants of motion. To remove the degeneracy we took the help of the second law of thermodynamics near the horizon, according to which the transonic solution which has maximum entropy should be the solution. The next hurdle was, that there was no analytical expression of entropy measure for two-temperature flow. We used the BH inner boundary condition (gravity overwhelms all other interactions), in order to obtain the analytical expression of entropy measure (\mathcal{M}_{in}) for a gas in two-temperature regime valid only near the horizon and that too, by using relativistic EoS.

To focus on the problem of degenerate two-temperature solutions and its possible remedy, we considered a simple accretion model of radial flow onto a BH. More complicated accretion model would have obscured the crux of the problem. Simple as it may be, but spherical accretion is preferred mode of accretion onto isolated BHs immersed in interstellar matter and has been shown by many authors.^[48 49] Moreover, the inner region of a BH accretion disc is also quasi spherical and many researchers have considered radial inflow to mimic inner accretion disc.^[45 46] Since radial flow has no angular momentum (quasi spherical flow may have minuscule amount), viscous transport should be negligible for accretion onto isolated BH or in the inner region of an accretion disc. Moreover, authors who have obtained transonic two-temperature solution before,^[39] are of the view that Coulomb coupling is not an efficient energy transfer process. Therefore any viscous heating will anyway not find its way into heating up the electrons. Looking into all these factors, we ignored viscous dissipation and concentrated two-temperature accretion flow by only considering cooling mechanisms in this paper. However, at the end we did consider dissipative proton heating.^[47] Heating has quantitative effect on the accretion solutions and confirmed that Coulomb coupling is weak as was mentioned by Manmoto *et al.*^[39]

Using the methodology explained above, we obtained all possible solutions for any given set of E and \dot{M} . For higher E and higher \dot{M} , sonic points were formed closer to the horizon, while for lower values of both the constants of motion, sonic points occurred at larger distances. We showed that for correct solutions the adiabatic index of electron and proton fluid varies from nonrelativistic to relativistic

values. We also showed that, different cooling processes become important for different values of \dot{M} . Therefore radiative efficiency depends on \dot{M} . For $\dot{M} < 0.1$, whether it is a super massive BH or a stellar one, the accretion flow is inefficient. However for super-massive BH, the accretion flow becomes radiatively efficient i.e. more than 10% for $\dot{M} \gtrsim 0.6$. For stellar mass BH, the accretion becomes radiatively efficient when the accretion rate is close to Eddington rate. It is observed that whenever local inverse-Compton processes dominate, the accretion flow becomes luminous. Therefore, it is not necessary that radial accretion is radiatively inefficient.

References

1. F. Hoyle and R. A. Lyttleton, *Proc. Camb. Philos. Soc.* **35** (1939) 405.
2. H. Bondi, *Mon. Not. R. Astron. Soc.* **112** (1952) 195.
3. M. Schmidt, *Nature* **197** (1963) 1040.
4. S. Bowyer, E. T. Byram, T. A. Chubb and H. Friedman, *Science* **147** (1965) 394.
5. E. E. Salpeter, *Astrophys. J.* **140** (1964) 796.
6. F. C. Michel, *Astrophys. Space Sci.* **15** (1972) 153.
7. S. L. Shapiro, *Astrophys. J.* **180** (1973) 531.
8. N. I. Shakura and R. A. Sunyaev, *Astron. Astrophys.* **24** (1973) 337.
9. E. P. T. Liang and K. A. Thompson, *Astrophys. J.* **240** (1980) L271.
10. J. Fukue, *Publ. Astron. Soc. Jpn.* **39** (1987) 309.
11. K. Nakayama and J. Fukue, *Publ. Astron. Soc. Jpn.* **41** (1989) 271.
12. S. K. Chakrabarti, *Astrophys. J.* **347** (1989) 365.
13. K. Nakayama, *Mon. Not. R. Astron. Soc.* **259** (1992) 259.
14. D. Molteni, G. Lanzafame and S. K. Chakrabarti, *Astrophys. J.* **425** (1994) 161.
15. G. Lanzafame, D. Molteni and D. Chakrabarti, *Mon. Not. R. Astron. Soc.* **299** (1998) 799.
16. K. Fukumura and S. Tsuruta, *Astrophys. J.* **611** (2004) 964.
17. K. Fukumura and D. Kazanas, *Astrophys. J.* **669** (2007) 85.
18. I. Chattopadhyay and S. K. Chakrabarti, *Int. J. Mod. Phys. D* **20** (2011) 1597.
19. R. Kumar and I. Chattopadhyay, *Mon. Not. R. Astron. Soc.* **430** (2013) 386.
20. R. Kumar, C. B. Singh, I. Chattopadhyay and S. K. Chakrabarti, *Mon. Not. R. Astron. Soc.* **436** (2013) 2864.
21. R. Kumar and I. Chattopadhyay, *Mon. Not. R. Astron. Soc.* **443** (2014) 3444.
22. I. Chattopadhyay and R. Kumar, *Mon. Not. R. Astron. Soc.* **459** (2016) 3792.
23. R. Kumar and I. Chattopadhyay, *Mon. Not. R. Astron. Soc.* **469** (2017) 4221.
24. W.-M. Gu and J.-F. Lu, *Chin. Phys. Lett.* **21** (2004) 2551.
25. S. K. Chakrabarti and D. Molteni, *Mon. Not. R. Astron. Soc.* **417** (1995) 672.
26. P. A. Becker and T. Le, *Astrophys. J.* **588** (2003) 408.
27. P. A. Becker, S. Das and T. Le, *Astrophys. J.* **677** (2008) L93.
28. T. Le *et al.*, *Astrophys. J.* **819** (2016) 112.
29. J. P. Lee and P. A. Becker, *Mon. Not. R. Astron. Soc.* **465** (2017) 1409.
30. S. L. Shapiro, A. P. Lightman and D. M. Eardley, *Astrophys. J.* **204** (1976) 187.
31. V. F. Shvratsman, *Soviet Astron.* **15** (1971) 377.
32. M. Colpi, L. Maraschi and A. Treves, *Astrophys. J.* **280** (1984) 319.
33. S. K. Chakrabarti and L. G. Titarchuk, *Astrophys. J.* **455** (1995) 623.
34. S. Mandal and S. K. Chakrabarti, *Astron. Astrophys.* **434** (2005) 839.
35. P. Laurent and L. Titarchuk, *Astrophys. J.* **511** (1999) 289.
36. R. Narayan and I. Yi, *Astrophys. J.* **452** (1995) 710.

37. K. E. Nakamura, M. Kusunose, R. Matsumoto and S. Kato, *Publ. Astron. Soc. Jpn.* **48** (1996) 761.
38. K. E. Nakamura, M. Kusunose, R. Matsumoto and S. Kato, *Publ. Astron. Soc. Jpn.* **49** (1997) 503.
39. T. Manmoto, S. Mineshige and M. Kusunose, *Astrophys. J.* **489** (1997) 791.
40. S. R. Rajesh and B. Mukhopadhyay, *Mon. Not. R. Astron. Soc.* **402** (2010) 961.
41. I. K. Dihingia, S. Das and S. Mandal, *Mon. Not. R. Astron. Soc.* **475** (2017) 2164.
42. G. R. Blumenthal and W. G. Mathews, *Astrophys. J.* **203** (1976) 714.
43. I. Chattopadhyay, *Proc. 2nd Kolkata Conf. on Observational Evidence of Black Holes in the Universe and the Satellite Meeting on Black Holes Neutron Stars and Gamma-Ray Bursts*, eds. S. K. Chakrabarti and A. S. Majumdar, AIP Conference Series, Vol. 1053 (American Institute of Physics, New York, 2008), p. 353.
44. I. Chattopadhyay and D. Ryu, *Astrophys. J.* **694** (2009) 492.
45. L. Titarchuk, A. Mastichiadis and N. D. Kulaifis, *Astrophys. J.* **487** (1997) 834.
46. D. Kazanas, X.-M. Hua and L. Titarchuk, *Astrophys. J.* **480** (1997) 735.
47. J. P. Ipser and R. H. Price, *Astrophys. J.* **255** (1982) 654.
48. R. E. Davies and J. E. Pringle, *Mon. Not. R. Astron. Soc.* **191** (1980) 599.
49. G. M. Beskin and S. V. Karpov, *Astron. Astrophys.* **440** (2005) 223.
50. S. Stepney, *Mon. Not. R. Astron. Soc.* **202** (1983) 467.
51. S. Chandrasekhar, *An Introduction to the Study of Stellar Structure* (Dover, New York, 1938).
52. J. L. Synge, *The Relativistic Gas* (North Holland, Amsterdam, 1957).
53. J. P. Cox and R. T. Giuli, *Principles of Stellar Structure*, Vol. 2 (Gordon and Breach Science Publishers, New York, 1968).
54. M. K. Vyas, R. Kumar, S. Mandal and I. Chattopadhyay, *Mon. Not. R. Astron. Soc.* **453** (2015) 2992.
55. S. Stepney and P. W. Guilbert, *Mon. Not. R. Astron. Soc.* **204** (1983) 1269.
56. E. Boldt and P. Serlemitsos, *Astrophys. J.* **157** (1969) 557.
57. F. C. Jones, *Astrophys. J.* **169** (1971) 503.
58. I. D. Novikov and K. S. Thorne, *Black Holes*, eds. B. S. Dewitt and C. Dewitt (Gordon and Breach, New York), p. 343.
59. C. D. Dermer, E. P. Liang and E. Canfield, *Astrophys. J.* **369** (1991) 410.
60. R. Turolla, L. Nobili and M. Calvani, *Astrophys. J.* **303** (1986) 573.

Two-temperature solutions and emergent spectra from relativistic accretion discs around black holes

Shilpa Sarkar^{1,2}, Indranil Chattopadhyay¹, and Philippe Laurent^{3,4}

¹ Aryabhata Research Institute of Observational Sciences (ARIES), Manora Peak, Nainital 263002, India
e-mail: shilpa@aries.res.in, indra@aries.res.in

² Pt. Ravishankar Shukla University, Great Eastern Rd, Amanaka, Raipur, Chhattisgarh 492010, India

³ IRFU/Service d'Astrophysique, Bat. 709 Orme des Merisiers, CEA Saclay, 91191 Gif-sur-Yvette Cedex, France
e-mail: philippe.laurent@cea.fr

⁴ Laboratoire Astroparticule et Cosmologie, Bâtiment Condorcet, 10 Rue Alice Domont et Léonie Duquet, 75205 Paris Cedex 13, France

Received 17 January 2020 / Accepted 27 June 2020

ABSTRACT

Aims. We investigate a two-temperature advective transonic accretion disc around a black hole and analyse its spectrum in the presence of radiative processes such as bremsstrahlung, synchrotron, and inverse-Comptonisation. The aim is to link the emergent spectra with constants of motion of the accretion disc fluid, however, the number of unknowns in two-temperature theory exceeds the number of equations for a given set of constants of motion. We intend to remove the degeneracy using a general methodology and obtain a unique solution, along with its spectrum.

Methods. We used hydrodynamic equations (continuity, momentum, and energy conservation equation) to obtain sonic points and solutions. To solve these equations of motion we used the 4th order Runge-Kutta method. For the spectral analysis, general and special relativistic effects were taken into consideration. The system is, nonetheless, degenerate and we remove the degeneracy by choosing the solution with maximum entropy, as dictated by the second law of thermodynamics.

Results. We obtained a unique transonic solution for a given set of constants of motion. The entropy expression is a tool used to make a selection between the degenerate solutions. We found that Coulomb coupling is a weak energy exchange term, which allows protons and electrons to settle down into two different temperatures, justifying, hence, our study of two-temperature flows. The information of the electron flow allows us to model the spectra. We show that the spectra of accretion solutions depend on the associated constants of motion. At low accretion rates, bremsstrahlung is important. A fraction of the bremsstrahlung photons may be of higher energy than the neighbouring electrons, energising them through the process of Compton scattering. Synchrotron emission, on the other hand, provides soft photons, which can be inverse-Comptonised to produce a hard power law part in the spectrum. Luminosity increases with the increase in the accretion rate of the system, as well as with the increase in BH mass. However, the radiative efficiency of the flow has almost no dependence on the BH mass, but it sharply rises with the increase in the accretion rate. The spectral index, however, hardens with the increase in the accretion rate, while it does not change much with the variation in BH mass. In addition to the constants of motion, the value of the plasma beta parameter and magnitude of magnetic dissipation in the system also helps in shaping the spectrum. A shocked solution exists in two-temperature accretion flows in a limited region of the parameter space. We find that a shocked solution is always brighter than a solution without a shock.

Conclusions. An accreting system in two-temperature regime admits multiple solutions for the same set of constants of motion, producing widely different spectra. Comparing the observed spectrum with that derived from a randomly chosen accretion solution would give us a wrong estimation of the accretion parameters of the system. The form of entropy measurement we obtained helped us to remove the degeneracy of the solutions and allowed us to understand the physics of the system, shorn of arbitrary assumptions. In this work, we show how the spectra and luminosities of an accreting system depend on the constants of motion, producing solutions ranging from radiatively inefficient flows to luminous flows. An increase in BH mass quantitatively changes the system, making the system more luminous, while the spectral bandwidth also increases. A higher BH mass system spans the range from radio to gamma-rays. However, increasing the accretion rate around a BH of certain mass has little influence on the frequency range of the spectra.

Key words. hydrodynamics – accretion, accretion disks – black hole physics – shock waves – radiation mechanisms: general

1. Introduction

Accretion is the primary mechanism that may explain the observation of radiation coming from microquasars and active galactic nuclei (AGN). Stellar mass black holes (BH) and neutron stars are thought to reside in microquasars, whereas super-massive BHs reside in AGNs. The energy released due to the accretion of matter onto relativistic compact objects, such as neutron stars and BHs, is a fraction of the rest mass energy of the matter

falling onto it. The study of the accretion process was initiated by [Hoyle & Lyttleton \(1939\)](#), where they studied accretion of matter onto a Newtonian star passing through the interstellar medium (ISM). In [Bondi \(1952\)](#) gave the first full analytical solution for spherical flows (also known as Bondi flows) around a static star. This theory is also relevant to the case of stellar winds. He showed that accretion and wind are characterised by a unique transonic solution having maximum entropy. But it took ten years, up until the discovery of quasars and X-ray sources

in the 1960s, that accretion phenomena gained in popularity. [Salpeter \(1964\)](#) and [Zel'dovich \(1964\)](#) extensively investigated accretion as a probable mechanism for driving and powering these luminous objects. It was concluded that the Bondi accretion model produced luminosities which are too low to explain the observations. As matter is radially falling and exhibiting short infall timescales compared to their cooling timescales, it leads to the low radiative efficiency of such flows. This finding led to the development of the famous [Shakura & Sunyaev \(1973\)](#) disc model (SSD) or the Keplerian disc model ([Pringle & Rees 1972](#); [Shakura & Sunyaev 1973](#); [Novikov et al. 1973](#)). In this model, it is assumed that matter is rotating in Keplerian orbits having negligible radial velocity and pressure gradient terms. The shear between differentially rotating matter gives rise to viscous stresses, which help in removing angular momentum outwards, allowing matter to spiral inwards and finally fall onto the central object. The time taken for inspiral allows for the matter to produce emission for a longer duration, unlike spherical flows. Since at every radius the angular momentum of the disc is Keplerian, the disc must therefore be geometrically thin. In other words, this implies that the heat generated due to viscous dissipation needs to be efficiently radiated away such that the angular momentum distribution remains close to the Keplerian one (hence the name “cool discs”, [King 2012](#)). In SSDs, matter and radiation are in thermal equilibrium, where each annulus of the disc emits a blackbody spectrum (or, depending on opacity, a modified version of it) that peaks at the temperature of the annulus of the disc. The composite spectrum is hence the sum of these blackbodies and is called the modified multicoloured blackbody spectrum. Although this model could successfully regenerate the thermal part of the spectrum from sources associated with BHs, it was unable to explain the non-thermal part. In addition, the assumption of Keplerian angular velocity at each annulus implied that the disc is arbitrarily terminated at the inner stable circular orbit (ISCO). Soon after, it was also concluded that these discs were thermally and secularly unstable ([Pringle et al. 1973](#); [Lightman & Eardley 1974](#); [Artemova et al. 1996](#)). In [Thorne & Price \(1975\)](#) argued that the instability present at the inner region of an SSD could expand into an optically thin gas-pressure dominated region. [Shapiro et al. \(1976, hereafter SLE76\)](#) considered this geometrically thick and optically thin, puffed-up region to be composed of protons and electrons described by two different temperature distributions. Using this model, they successfully reproduced the hard component part of Cygnus X-1 spectrum from 8–500 keV. Unfortunately, the SLE model was also found to be thermally unstable ([Piran 1978](#)). If the disc is heated, it expands, reducing its number density and thereby its cooling rate. This makes the system even hotter, leading to a runaway thermal instability. Although the system proved to be unstable, this study has served as one of the cornerstones in two-temperature accretion theory.

The models discussed above have suffered from simplifying assumptions, for example, the cooling rate at each radius of the disc was equated with the heating rate and the advection term was not properly dealt with. In general, the heating and cooling rates do not need to be equal and some part of the heat could be advected inwards, along with the bulk motion of the system. [Abramowicz et al. \(1988\)](#) extensively investigated advection, in their “slim” optically thick accretion disc model, and found that the solutions obtained were thermally and viscously stable. The importance of advection was further demonstrated, using self-similar solutions in the works of [Narayan & Yi \(1994\)](#), [Abramowicz et al. \(1995\)](#). Today, these discs are broadly classified as advection-dominated accretion flows (ADAFs) and

[Ichimaru \(1977\)](#) was the first to propose it (for review also see [Bisnovaty-Kogan & Lovelace 1997, 2001](#)).

A general conclusion can be drawn from the above models that an accretion flow does not need to be Keplerian throughout but it could also be sub-Keplerian or a combination of both. In addition, the flow must be transonic. Matter that is very far away from the horizon is subsonic, whereas the BH boundary condition insists that matter should cross the horizon at the speed of light. Thus, accreting matter has to pass through at least one sonic point, or in other words, the BH accretion solution is necessarily transonic. [Bondi \(1952\)](#) in his seminal paper already highlighted the importance of transonicity for spherical accretion flows. [Liang & Thompson \(1980; hereafter LT80\)](#) argued that similarly to spherical flows, which are characterised by a single sonic point, rotating flows around BHs are characterised by multiple sonic points. [Fukue \(1987\)](#) extended their work and presented in detail the nature of sonic points in transonic rotating accretion flows. He concluded that even though a BH does not possess any hard surface, it can undergo a shock transition in the presence of multiple sonic points (also see [Chakrabarti 1989](#)).

All the works mentioned above (except SLE76) assume one-temperature accretion flows. One-temperature flows are based on the fact that the timescale of the energy exchange process (like Coulomb coupling) between the ions and electrons is shorter or comparable to the dynamical time scale of the system, allowing the system to effectively settle down into a single temperature distribution ([Le & Becker 2005](#); [Chattopadhyay & Chakrabarti 2011](#); [Kumar & Chattopadhyay 2014](#)). Yet, in many astrophysical cases, infall timescales are generally much shorter than Coulomb collision timescales, that is, Coulomb coupling between the protons and electrons are not strong, allowing the two species to equilibrate to two different temperature distributions ([Rees et al. 1982](#); [Narayan & Yi 1995](#)). Therefore, in addition to the advective transonic nature of an accretion flow around a BH, the gas is likely to be in the two-temperature regime. Also, the electrons are more prone to radiative cooling, compared to ions. This makes the electron temperature deviate largely from the protons especially in the inner regions of the accretion disc.

After the seminal paper of SLE76, a two-temperature assumption was largely used to model accretion flows as it could successfully reproduce the observed spectrum, electrons being the main radiators. [Colpi et al. \(1984\)](#) included advection and solved the energy equation (or, first law of thermodynamics) for spherical accretion flows (i.e. with no angular momentum), and assumed a free-fall velocity field with radial dependence taking the form: $v \propto r^{-1/2}$. The transonic nature of the flow was not taken into account, but emission processes relative to protons and electrons were discussed briefly. [Narayan & Yi \(1995; hereafter NY95\)](#) incorporated angular momentum and extensively discussed the nature of two-temperature, optically thin accretion discs. The equations of motion were solved under the self-similar assumption. It is to be noted that self-similarity in accretion solution around BH is plausible only at a large distance from the horizon and not near it. Additionally, a self-similar solution is not transonic. NY95 neglected the electron advection term and assumed the heating and cooling rates of electrons to be equal. There have been other notable works done in a two-temperature regime, where the issue of transonicity was bypassed, but the radiative transfer part was properly treated nonetheless. One such work is by [Chakrabarti & Titarchuk \(1995\)](#), where the spectrum was computed assuming two-components in the accretion flow: a Keplerian and another sub-Keplerian. An exact Comptonisation model was incorporated, following a discussion of the variation in the spectrum with the change in mass of BH

and accretion rate. [Mandal & Chakrabarti \(2005\)](#) went a step further and included a non-thermal distribution of electrons along with the general thermal distribution inside the accretion flow. Similar to [Colpi et al. \(1984\)](#), in this paper the velocity field was assumed to be in free-fall, but the shocked solution and its signature in the observed spectrum were qualitatively studied.

[Nakamura et al. \(1996\)](#) obtained the first global transonic, two-temperature accretion solutions in which the advection terms were considered without any simplifying assumptions. However, at the outer boundary, the authors assumed the ion temperature to be a fraction of the virial temperature and Coulomb coupling was equated with bremsstrahlung. [Manmoto et al. \(1997\)](#) extended the work of [Nakamura et al. \(1996\)](#) to calculate the spectrum. In addition, they slightly modified the outer boundary conditions, where the total gas temperature (and not the ion temperature) was assumed to be a fraction of the virial temperature and equated Coulomb coupling with the total cooling of electrons (bremsstrahlung, synchrotron, and inverse-Comptonisation). Recently, a more general transonic advective two-temperature accretion solution was obtained by [Rajesh & Mukhopadhyay \(2010\)](#), where the viscous stress was assumed to be proportional to the sum of ram pressure and gas pressure (see [Chakrabarti 1996](#), for details on this particular viscosity prescription). In this work, a limited class of solutions were studied. This work was extended and a global class of transonic two-temperature solutions, including accretion-shock, were investigated by [Dihingia et al. \(2017\)](#). The most striking feature of the transonic two-temperature studies mentioned above is that the solutions depend on the choice of inner or outer boundary conditions, however, based on single-temperature hydrodynamics, we know that transonic solutions are unique for a given set of constants of motion. We highlight this issue in greater detail below.

Hydrodynamic equations, even in the single temperature regime, admit an infinite number of solutions, but a transonic solution is physically favoured because it has the highest entropy among all possible global solutions ([Bondi 1952](#)). In addition, the location of the sonic point corresponds to a unique boundary condition. The number of hydrodynamic equations for flows in one-temperature and two-temperature regimes are exactly the same, but there is one more variable in case of two-temperature flows (i.e. the existence of different ion and electron temperature distributions). Obtaining a self-consistent two-temperature flow would require solving basic hydrodynamic equations, but since there is one more flow variable in the two-temperature regime, the system is degenerate. We obtain a large number of transonic solutions for the same set of constants of motion, of the flow. A hint of the problem of degeneracy was reported briefly in [LT80](#), but it was skirted by parameterising the temperatures of protons and electrons to some constant value, arguing that the coupling between these species is unknown. As mentioned earlier in this paper, several authors also assumed an arbitrary proton or electron temperature at the boundary where they started integrating to find possible solutions. A global treatment of two-temperature problem would require all the equations to be solved self-consistently without taking recourse to any set of arbitrary assumptions on temperature values at any boundary. This problem of degeneracy was identified and a prescription for obtaining a unique transonic two-temperature solution was reported in [Sarkar & Chattopadhyay \(2019, hereafter SC19\)](#). However it was applied to flows having zero angular momentum. Spherical flows have single sonic points, which simplifies our problem, allowing us to focus only on the issue of degeneracy in a two-temperature regime. In [SC19](#), we reported that for a given set of constants of motion, infinite transonic solutions exist, each hav-

ing a sonic point property different from the rest. The question that arises is which solution should be chosen since nature generally disfavours degeneracy.

In a one-temperature regime, the transonic solution is unique ([Le & Becker 2005; Becker et al. 2008](#)) but for reasons cited above, a two-temperature solution is degenerate for the same set of constants of motion. Following [Bondi \(1952\)](#), we can look for the highest entropy solution to remove the degeneracy. However, the two-temperature energy equation within the adiabatic limit is not integrable (unlike in one-temperature regime, [Kumar et al. 2013; Kumar & Chattopadhyay 2013, 2014; Chattopadhyay & Kumar 2016](#)). This prevented us from obtaining an analytical expression for measuring entropy in the two-temperature regime. The integration of the energy equation is spoiled by the presence of the Coulomb coupling term. However keeping in mind the fact that near the horizon, gravity overpowers any other interaction or processes, we can neglect the Coulomb coupling term. Thus, as we reported in [SC19](#) for the first time, we can use a form of entropy measurement which would only be applied near the horizon. Using the formula, we measured the entropies at the horizon for the transonic spherical two-temperature solutions obtained for a given set of constants of motion. We saw that the entropy was maximum for a particular solution. Based on the second law of thermodynamics, we selected the solution with maximum entropy as the solution that nature would prefer. This solved the problem of degeneracy in a two-temperature model. It may, however be noted that spherical flows were simple to handle thanks to the presence of single sonic points.

It may be noted that much like the flow speed, the thermal state of the flow around a BH is also trans-relativistic in nature. This means that very far away from the horizon, matter is thermally non-relativistic and as it approaches the BH, it could be sub-relativistic or relativistic. Matter is referred as thermally relativistic when its thermal energy is comparable to or greater than its rest mass energy, $kT/mc^2 \gtrsim 1$ (where $k =$ Boltzmann constant, $T =$ temperature, $m =$ mass of the species), and its adiabatic index, $(\Gamma) \sim 4/3$; it is non-relativistic if its thermal energy is less than the rest mass energy ($kT/mc^2 < 1$) and $\Gamma \sim 5/3$. So, not only the temperature but also the mass of the constituent particles determine the relativistic nature of the flow. So, in two-temperature flows, where we consider two species with masses differing by $\gtrsim 1000$ times, an equation of state (EoS), with a fixed adiabatic index, is untenable. [Chattopadhyay \(2008\)](#) and [Chattopadhyay & Ryu \(2009\)](#), proposed an approximate EoS for multispecies flow (CR EoS, hereafter) that is analytical and computationally easy to handle. Although it is an approximation, it matches perfectly well ([Vyas et al. 2015](#)) with the relativistically perfect EoS obtained by [Chandrasekhar \(1939\)](#). In a later work, the authors extended the use of CR EoS for dissipative, relativistic accretion disc as well ([Chattopadhyay & Kumar 2016](#)). To incorporate the trans-relativistic nature of protons and electrons, it is necessary to utilise a variable adiabatic index EoS.

In this paper, we would like to extend our previous [Sarkar & Chattopadhyay \(2019\)](#) model to rotating flows and, thereby, to remove the degeneracy of accretion solutions around BHs. Needless to say, choosing any one of the degenerate solutions would give us an incorrect picture of the accretion parameters of the BH. To handle the trans-relativistic nature of these flows, we use the CR EoS, which freed us from having to specify the adiabatic indices of each species. Hydrostatic equilibrium along the disc thickness is maintained at each radius of the disc. The radiative processes with proper special and general

relativistic corrections have been incorporated to compute the spectrum.

In this paper, we aim to analyse how the correct unique accretion solution depends on the constants of motion of the flow, along with the mass of the BH, and to discuss how these properties play an active role in shaping the spectrum. Further, we intend to study the relative contribution of various radiative processes on the emitted spectrum and also investigate which part of the disc is likely to contribute the most in the emitted spectrum. In addition, we want to check whether an accretion shock imparts any special spectral signature. Apart from this, we would like to study the dependence of radiative efficiency and the spectral index with the variation in the accretion rate of the BH and its mass, in the presence of different radiative processes.

This paper is divided into the following sections. In Sect. 2, we give a brief overview of the basic equations and assumptions used to model the flow. In Sect. 3, we discuss the solution procedure for finding a unique transonic two-temperature solution. We present the results in Sect. 4 and our conclusions in Sect. 5.

2. Two-temperature advective disc model: assumptions and governing equations

In this paper, our main intention is to obtain all possible accretion solutions onto a BH and compute the typical spectrum corresponding to each mode of accretion. The solution involving a rotating accretion flow is much more complicated than spherical accretion due to the presence of multiple sonic points. Therefore, the spectra are different for different kinds of solutions. Furthermore, two-temperature flows are degenerate, which makes the method for obtaining a unique solution very important. In the next sub-sections, we discuss the equations we used to model the two-temperature accretion flow. We also give an overview of the radiative processes we incorporated and the methodology we used to implement these processes in curved space-time.

2.1. Equations of motion (EoM)

The space-time metric around a non-rotating BH is described using a Schwarzschild metric:

$$ds^2 = g_{tt}c^2 dt^2 + g_{rr}dr^2 + g_{\theta\theta}d\theta^2 + g_{\phi\phi}d\phi^2, \quad (1)$$

where the metric tensors are expressed as, $-g_{tt} = g_{rr}^{-1} = (1 - 2GM_{\text{BH}}/c^2 r)$ and $g_{\theta\theta} = g_{\phi\phi} = r^2$, since an accretion flow is described around the equatorial plane. Here, r , θ , and ϕ are the usual spherical coordinates and t is the time coordinate, G = Gravitational constant, and M_{BH} = mass of the BH. We note that throughout the paper, we employ a system of units where the unit of length, velocity, and time are defined as $r_g = GM_{\text{BH}}/c^2$, c and $r_g/c = GM_{\text{BH}}/c^3$, respectively. All the variables used in the rest of the paper are written in this unit system unless mentioned otherwise. The BH system that we model is in a steady state and axis-symmetric, therefore $\partial/\partial t = \partial/\partial\phi = 0$. Moreover, at any radius, we assume that only the radial gradient of any quantity is dominant, therefore, $\partial/\partial\theta = 0$.

The radial component of the momentum balance equation is:

$$u^r \frac{du^r}{dr} + \frac{1}{r^2} - (r-3)u^\phi u^\phi + (g^{rr} + u^r u^r) \frac{1}{e+p} \frac{dp}{dr} = 0, \quad (2)$$

where e and p are the internal energy density and isotropic gas pressure, respectively, measured in the local fluid frame, and u^μ s

are the components of four-velocity. The mass accretion rate is obtained by integrating the conservation of four mass-flux:

$$\dot{M} = 4\pi\rho H u^r r, \quad (3)$$

where $\rho = n(m_p + m_e)$ = local mass density of the flow, n is the particle number density, m_p and m_e are the mass of proton and electron, respectively, and H is the local half-height of the disc. Here, \dot{M} – the accretion rate, is a constant of motion throughout the flow. Half-height is calculated assuming hydrostatic equilibrium along the vertical direction of the disc (Lasota 1994; Chattopadhyay & Chakrabarti 2011) which can be written as

$$H = \sqrt{\frac{\rho r^3}{\rho \gamma_\phi^2}}. \quad (4)$$

Also, based on $u_\mu u^\mu = -1$, we obtain:

$$-u_t = \sqrt{\left(1 - \frac{2}{r}\right)} \gamma_v \gamma_\phi,$$

where, γ_v and γ_ϕ are the Lorentz factors in the radial and azimuthal directions, respectively and defined as $\gamma_v = \sqrt{1/(1-v^2)}$ and $\gamma_\phi = \sqrt{1/(1-v_\phi^2)}$, where $v_\phi = \sqrt{-u_\phi u^\phi / u_t u^t}$ and v is the velocity in the local co-rotating frame. It can be shown that $v^2 = \gamma_\phi^2 v_\phi^2$, where $v_\phi = \sqrt{-u_r u^r / u_t u^t}$. The total Lorentz factor, therefore is, $\gamma = \gamma_v \gamma_\phi$.

The first law of thermodynamics, or the energy balance equation, is $u_\mu T^{\mu\nu}_{;\nu} = \Delta Q$ and can be written as:

$$u^r \left[\left(\frac{e+p}{\rho} \right) \rho_{,r} - e_{,r} \right] = \Delta Q. \quad (5)$$

Here, $\Delta Q = Q^+ - Q^-$, where, Q^+ and Q^- represent the rate of heating and cooling present in the flow for all the species, respectively. These rates are in units of $\text{ergs cm}^{-3} \text{s}^{-1}$, which are converted into geometric units before being applied in the above equation.

Coulomb coupling serves as an energy exchange process, which transfers energy between protons and electrons. In the single-temperature case, with Coulomb coupling being infinitely strong, protons and electrons equilibrate locally into a single-temperature distribution (Lanzafame et al. 1998; Lee et al. 2011, 2016; Chattopadhyay & Kumar 2016). However for two-temperature flows, it is not strong enough, hence, protons and electrons are allowed to thermalise at two different temperatures. In other words, the timescale required for protons and electrons to attain a thermal equilibrium and settle down into a single temperature is more than the timescale in which each of the two populations thermalise separately. To describe such flows, we need to use two separate energy equations, one for protons and another for electrons. These two energy equations are not independent and, as discussed, are connected by the Coulomb coupling term which acts as a cooling term for protons and a heating term for electrons if the proton temperature is higher than electron temperature.

If we integrate the equation of motion (Eq. (2)) with the help of the energy equation (Eq. (5)), we obtain the generalised Bernoulli constant, given by

$$E = -hu_r \exp(X_f), \quad (6)$$

where, $h = (e+p)/\rho$ = specific enthalpy and $X_f = \int \frac{\Delta Q_p + \Delta Q_e}{\rho h u^r} dr$. Here, $\Delta Q_i = Q_i^+ - Q_i^-$ represents the difference in the heating

and cooling rates of the i th species. The generalised Bernoulli constant is conserved all throughout the flow, even in the presence of heating and cooling. The X_f term mainly comes up due to the presence of dissipation. In case of adiabatic flows, with no dissipation, $X_f = 0$ and $E \rightarrow \mathcal{E} = -hu_r$, which is the canonical form of relativistic Bernoulli constant (Lightman et al. 1975; Chattopadhyay & Chakrabarti 2011).

2.2. EoS and the final form of the EoS

We ought to note that in this sub-section, barred variables have been used to denote dimensional quantities and unbarred variables are, as before, non-dimensional. In order to solve the above equations of motion, we need to supply an equation of state (EoS). In this paper, we use the Chattopadhyay-Ryu (CR) EoS given by Chattopadhyay (2008), Chattopadhyay & Ryu (2009). The form of CR EoS for multispecies flow is:

$$\bar{e} = \sum_i \bar{e}_i = \sum_i \left[\bar{n}_i m_i c^2 + \bar{p}_i \left(\frac{9\bar{p}_i + 3\bar{n}_i m_i c^2}{3\bar{p}_i + 2\bar{n}_i m_i c^2} \right) \right], \quad (7)$$

where, the summation is over i th species. Since, in this paper, we consider the accretion flow to be composed of protons and electrons ($e^- - p^+$) only, thus i represents these two species. Number density (n), mass density (ρ), and isotropic gas pressure (p), present in Eq. (7), can be represented in dimensional form in the following way:

$$\bar{n} = \sum_i \bar{n}_i = \bar{n}_p + \bar{n}_e = 2\bar{n}_e, \quad (8)$$

$$\bar{\rho} = \sum_i \bar{n}_i m_i = \bar{n}_e m_e + \bar{n}_p m_p = \bar{n}_e m_e \left(1 + \frac{1}{\eta} \right) = \bar{n}_e m_e \tilde{K}, \quad (9)$$

$$\bar{p} = \sum_i \bar{p}_i = \sum_i \bar{n}_i k T_i = \bar{n}_e k (T_e + T_p) = \bar{n}_e m_e c^2 \left(\Theta_e + \frac{\Theta_p}{\eta} \right), \quad (10)$$

where, $\eta = m_e/m_p$ and $\tilde{K} = 1 + 1/\eta$. T_i is the temperature in units

of kelvin, while $\Theta_i = \frac{kT_i}{m_i c^2}$ is the non-dimensional temperature

defined with respect to the rest-mass energy of the respective i th species. The EoS, Eq. (7), can be simplified using Eqs. (8)–(10) to

$$\bar{e} = \bar{n}_e m_e c^2 \left(f_e + \frac{f_p}{\eta} \right) = \frac{\bar{\rho} c^2 f}{\tilde{K}}, \quad (11)$$

where, $f_i = 1 + \Theta_i \left(\frac{9\Theta_i + 3}{3\Theta_i + 2} \right)$ and $f = f_e + \frac{f_p}{\eta}$.

Polytropic index and adiabatic index can be written as

$$N_i = \frac{df_i}{d\Theta_i} \quad \text{and} \quad \Gamma_i = 1 + \frac{1}{N_i}. \quad (12)$$

The equation for half-height (Eq. (4)), can be simplified to:

$$H = \sqrt{\frac{[r^3 - \lambda^2(r-2)]}{\tilde{K}}} \left(\Theta_e + \frac{\Theta_p}{\eta} \right). \quad (13)$$

Here, $\lambda = -u_\phi/u_t$ is the specific angular momentum of the flow. Angular momentum plays a very important role in accretion disc physics because it can significantly modify the infall time scale. Using Eqs. (8)–(13), we can simplify the energy equation

(Eq. (5)) and obtain two differential equations for temperature, one for protons and another for electrons. They are as follows:

$$\frac{d\Theta_p}{dr} = -\frac{2\Theta_p}{2N_p + 1} \left(\mathcal{A} + \frac{1}{v(1-v^2)} \frac{dv}{dr} \right) - \mathbb{P}\eta, \quad (14)$$

$$\frac{d\Theta_e}{dr} = -\frac{2\Theta_e}{2N_e + 1} \left(\mathcal{A} + \frac{1}{v(1-v^2)} \frac{dv}{dr} \right) - \mathbb{E}, \quad (15)$$

respectively, where,

$$\mathcal{A} = -\frac{r}{r(r-2)} - \frac{3r^2 - \lambda^2}{2[r^3 - \lambda^2(r-2)]}, \quad \mathbb{P} = \frac{2\Delta Q_p \tilde{K}}{\rho u^r (2N_p + 1)}, \quad \text{and}$$

$$\mathbb{E} = \frac{2\Delta Q_e \tilde{K}}{\rho u^r (2N_e + 1)}.$$

If we simplify the radial component of the relativistic momentum balance equation (Eq. (2)) using Eqs. (8)–(15), we get the expression of gradient of three-velocity, which has the form:

$$\frac{dv}{dr} = \frac{\mathcal{N}}{\mathcal{D}}, \quad (16)$$

where,

$$\mathcal{N} = -\frac{1}{r(r-2)} + \frac{\lambda^2 \gamma_\phi^2 (r-3)}{r^4} + a^2 \mathcal{A} + \frac{\Gamma_p N_p \mathbb{P} + \Gamma_e N_e \mathbb{E}}{h\tilde{K}} - \frac{\Delta Q}{\rho h u^r},$$

$$\text{and } \mathcal{D} = \frac{v}{1-v^2} \left(1 - \frac{a^2}{v^2} \right).$$

The effective sound speed (a) has been defined as

$$a^2 = \frac{\mathcal{G}}{h\tilde{K}}, \quad (17)$$

$$\text{where, } \mathcal{G} = \frac{2\Gamma_p N_p \Theta_p}{\eta(2N_p + 1)} + \frac{2\Gamma_e N_e \Theta_e}{(2N_e + 1)}.$$

2.3. Heating and cooling processes included in the flow

In the following sub-sections, we briefly discuss the processes that lead to the heating and cooling of plasma in the accretion flow.

2.3.1. Heating due to magnetic dissipation

The magnetic field in the medium surrounding the BH would be frozen into the highly conductive infalling plasma. As the matter falls inwards, its magnetic field strength would increase by $1/r^2$ and magnetic energy density ($B^2/8\pi$) by $1/r^4$. Schwartzman (1971) argued that before the magnetic energy density exceeds the thermal energy density, turbulence and hydromagnetic instabilities would lead to reconnection of magnetic field lines. In other words, it means that the magnetic energy density is limited by equipartition with thermal energy density. This magnetic energy dissipated would heat up the matter, either protons or electrons or both, ensuring relativistic temperatures even far away from the BH. The expression for the dissipative heating rate, as given by Ipsier & Price (1982) is

$$\dot{Q}_B = \frac{3u^r c B^2}{2rr_g 8\pi} = \frac{3u^r c}{2rr_g} \beta_a \bar{p} = \frac{3u^r c}{2rr_g} \beta_a \bar{n}_e k (T_p + T_e) \quad \text{ergs cm}^{-3} \text{ s}^{-1}. \quad (18)$$

The above equation is a measure of the heating due to magnetic dissipation. However, there are uncertainties in the estimates of

heating processes that are controlled by β_d . We used $\beta_d = 0.001$, unless stated otherwise, as a representative case. In Sect. 4.6, we varied the value of β_d and studied how the solutions depend on it. In this work, we assume that both protons and electrons can absorb the magnetic energy dissipated. Hence, we can write

$$Q_p^+ = \delta Q_B \quad \text{and} \quad Q_e^+ = (1 - \delta) Q_B, \quad (19)$$

where δ is the uncertainty parameter, which dictates the amount of heat absorbed by protons, the rest being absorbed by electrons. There is insufficient knowledge available in the literature relating to this issue. Thus, throughout our work, for simplicity, we consider $\delta = 0.5$, which means that 50% of this heat would go to protons and the remaining 50% into electrons, unless otherwise specified.

In our present study, we investigate inviscid flows since the proper handling of the general relativistic (GR) form of viscosity in transonic flows is not trivial. The shear tensor in GR contains a derivative of u_ϕ , v and other terms (Peitz & Appl 1997, hereafter PA97). It is impossible to obtain a solution if all the terms of the shear tensor is considered. In PA97, the authors proposed an approximate form of shear tensor by neglecting all derivatives of v and then presented a limited class of solutions. Chattopadhyay & Kumar (2016) used the same form of viscosity but obtained the full range of solutions. They also computed the mass-loss from such advective accretion solutions. We envisage that the method to obtain viscous solution is not easy since the Bernoulli parameter of viscous flow has no analytical form. In addition, the sonic point is not known a priori and it needs to be obtained as a part of the eigenvalue of the solution. Moreover, the angular momentum on the horizon needs to be computed. And yet the solutions obtained are limited because the viscosity is still phenomenological and various terms of the relativistic version of the shear tensor has to be neglected in order to obtain a solution. The two-temperature regime further complicates the problem as pointed out above. Most of the works from the literature assume a Newtonian form of viscosity or the Shakura & Sunyaev (1973) α -viscosity prescription (hereafter SS), which would not be appropriate for our GR model. So we avoided the use of any form of viscosity since the prime focus of this paper is to present a novel methodology for obtaining unique transonic two-temperature solutions for accretion discs around BHs. In addition, it is extensively shown in Figs. 2h–i; 3h–i of Chattopadhyay & Kumar (2016) that the specific angular momentum ($\lambda = -u_\phi/u_r$) and bulk angular momentum ($L = hu_\phi$) in the last few $100r_g$ is almost constant and sub-Keplerian. This is to be expected as gravity supersedes all other interactions near the BH horizon. In order to exhibit the qualitative effect of viscosity as a representative case, the one-temperature, viscous accretion disc solutions are presented in Appendix A, following the methodology of Chattopadhyay & Kumar (2016). We use two forms of viscosity, where the viscous stress tensor is given by (i) $t_{r\phi} = -2\eta_{\text{vis}}\sigma_{r\phi}$, (abbreviated as PA) and (ii) $t_{r\phi} = -\alpha_{\text{vis}}p$ (SS form of viscosity). The form of $\sigma_{r\phi}$ of PA is adopted from Peitz & Appl (1997), Chattopadhyay & Kumar (2016), but presently, we assume the dynamical viscosity coefficient $\eta_{\text{vis}} = \rho h\nu_{\text{vis}}$, instead of $\eta_{\text{vis}} = \rho\nu_{\text{vis}}$, where ν_{vis} is the kinematic viscosity. In Fig. 14a, we show that for both the form of viscosities (PA and SS), $\lambda \approx \text{constant}$ for $r \lesssim 1000r_g$. In Fig. 14b, we plot the heat dissipated by various processes. The PA form of viscosity is stronger than the SS type of viscosity, but it is generally much weaker than Q_B . It is comparable to Q_B only in a very narrow region. Close to the horizon, the angular momentum variation of the flow is quite small and the viscous heat dissipated is less than the magnetic heating; as a result, for simplicity, in

this paper we study accretion in the weak viscosity limit. We concentrate on obtaining self-consistent two-temperature, transonic, rotating accretion solutions by considering low-angular-momentum flows at the outer boundary and compute the spectra for such flows. We study how the accretion rate, angular momentum, and mass of the central black hole might affect the solution, as well as the emergent spectra that come from such solutions.

2.3.2. Coulomb coupling

As discussed above, Coulomb coupling (Q_{ep}) serves as an energy exchange process between protons and electrons. Therefore,

$$Q_p^- = Q_e^+ = Q_{\text{ep}}. \quad (20)$$

The expression for Coulomb coupling in cgs units ($\text{ergs cm}^{-3}\text{s}^{-1}$) is given by Stepney & Guilbert (1983),

$$\begin{aligned} \bar{Q}_{\text{ep}} = & \frac{3}{2} \frac{m_e}{m_p} \bar{n}_e \bar{n}_p \sigma_T c k \frac{T_p - T_e}{K_2(1/\Theta_e) K_2(1/\Theta_p)} \ln \Lambda_c \\ & \times \left[\frac{2(\Theta_e + \Theta_p)^2 + 1}{\Theta_e + \Theta_p} K_1 \left(\frac{\Theta_e + \Theta_p}{\Theta_e \Theta_p} \right) + 2K_0 \left(\frac{\Theta_e + \Theta_p}{\Theta_e \Theta_p} \right) \right], \end{aligned} \quad (21)$$

where σ_T is the Thomson scattering cross-section, $K_i(x)$'s are the modified Bessel functions of second kind and i th order and $\ln \Lambda_c$ is the Coulomb logarithm which is set to be equal to 20.

Apprehensions have been expressed about the possibility that more efficient energy exchange processes might exist between ions and electrons, in addition to Coulomb coupling. In that case, the accretion flow may settle down into a single temperature distribution (Phinney 1981). Begelman & Chiueh (1988) used plasma waves and Sharma et al. (2007) used magneto-rotational instability to increase the energy exchange between the two species inside the flow. However, some authors have raised doubts about the effectiveness of these processes (Blaes 2014; Abramowicz & Fragile 2013). In this paper, we ignore any type of collective effects and consider only Coulomb coupling as the main energy exchange process between the protons and electrons.

2.3.3. Inverse bremsstrahlung

Inverse bremsstrahlung (\bar{Q}_{ib}) is a radiative loss term for the protons, the expression of which is given as (Boldt & Serlemitsos 1969),

$$\bar{Q}_{\text{ib}} = 1.4 \times 10^{-27} \bar{n}_e^2 \sqrt{\frac{m_e}{m_p}} T_p. \quad \text{ergs cm}^{-3} \text{s}^{-1}. \quad (22)$$

2.3.4. Radiative mechanisms leading to cooling of electrons

The cooling of electrons could be caused by three basic cooling mechanisms (1) bremsstrahlung (Q_{br}), (2) synchrotron (Q_{syn}), and (3) inverse-Comptonisation (Q_{ic}). Emissivity due to bremsstrahlung (in $\text{ergs cm}^{-3} \text{s}^{-1}$) is given by Novikov et al. (1973),

$$\bar{Q}_{\text{br}} = 1.4 \times 10^{-27} \bar{n}_e^2 \sqrt{T_e} \left(1 + 4.4 \times 10^{-10} T_e \right). \quad (23)$$

We used thermal synchrotron radiation in our model, following the prescription of [Wardziński & Zdziarski \(2000\)](#). The emissivity is given by:

$$\bar{Q}_{\text{syn}} = \frac{2\pi}{3} \frac{\nu_t^3}{rr_g} m_e \Theta_e, \quad (24)$$

where, ν_t is the turnover frequency, above which the plasma is optically thin to synchrotron radiation and below which it is highly self-absorbed by the electrons itself. For the calculation of ν_t , we need the information of magnetic field in the flow. For this purpose, we consider a stochastic magnetic field which is in partial or total equipartition with the gas pressure, as mentioned in Sect. 2.3.1. Thus, $B = \sqrt{8\pi\beta\bar{p}}$. We set $\beta = 0.01$ throughout this paper unless otherwise specified. In Sect. 4.5, we vary the value of β and discuss how the spectrum depends on it.

The soft photons generated through thermal synchrotron process could be inverse-Comptonised by the electrons present in the plasma. This is given by ([Wardziński & Zdziarski 2000](#)),

$$\bar{Q}_{\text{ic}} = \zeta \bar{Q}_{\text{syn}}, \quad (25)$$

where, ζ is the enhancement factor. It is expressed as

$$\zeta = 3\varphi \left(\frac{x_t}{\Theta_e} \right)^{\alpha_0 - 1} \left[\Gamma_{\text{inc}} \left(1 - \alpha_0, \frac{x_t}{\Theta_e} \right) + \frac{6\Gamma_{\text{inc}}(\alpha_0)P_{\text{sc}}}{\Gamma_{\text{inc}}(2\alpha_0 + 3)} \right].$$

Here, Γ_{inc} is the incomplete gamma function, $x_t = \frac{h\nu_t}{m_e c^2}$,

$$\varphi = \frac{[1 + (2\Theta_e)^2]}{[1 + 10(2\Theta_e)^2]}, \quad \alpha_0 \text{ is the spectral index which can be}$$

defined as:

$$\alpha_0 = -\frac{\ln P_{\text{sc}}}{\ln A}. \quad (26)$$

It is the slope of the power-law photons that are generated due to inverse-Comptonisation at each radius. Therefore, the net spectral index (α) of the final inverse-Compton spectrum is obtained from the contributions of all the values of α_0 from each radius of the disc. In Eq. (26), $A = 1 + 4\Theta_e + 16\Theta_e^2$, is the average amplification factor in energy of photon per scattering and $P_{\text{sc}} = 1 - \exp(-\tau_{\text{es}})$ is the probability that a photon is scattered. Here, τ_{es} is defined as the optical depth of the medium where electron scattering is important, the expression of which is given by ([Turolla et al. 1986](#)),

$$\tau_{\text{es}} = 0.4 \left[1 + \left(2.22T_e \times 10^{-9} \right)^{0.86} \right]^{-1} \bar{\rho} H r_g. \quad (27)$$

2.3.5. Compton heating

As discussed above, less energetic photons would cool the flow through the process of inverse-Comptonisation. However if the temperature of the electrons is less than the temperature of the photons present in the flow, then the electrons will gain energy via Compton scattering. This would lead to the Compton heating of the electrons. We assume that this has the same expression as that of inverse-Comptonisation, but the sign changes ([Esin 1997](#)), causing heating rather than cooling. Therefore,

$$\bar{Q}_{\text{e}}^+ = \bar{Q}_{\text{comp}}. \quad (28)$$

2.3.6. Final expressions for ΔQ_p and ΔQ_e

So, to conclude, we have taken for heating and cooling of protons:

$$Q_p^+ = \delta Q_B, \quad \text{and} \quad Q_p^- = Q_{\text{ep}} + Q_{\text{ib}}, \quad (29)$$

respectively. And for heating and cooling of electrons:

$$Q_e^+ = (1 - \delta)Q_B + Q_{\text{ep}} + Q_{\text{comp}}, \quad \text{and} \quad Q_e^- = Q_{\text{br}} + Q_{\text{syn}} + Q_{\text{ic}} \quad (30)$$

respectively.

Therefore, $\Delta Q_p = \delta Q_B - Q_{\text{ep}} - Q_{\text{ib}}$, and $\Delta Q_e = (1 - \delta)Q_B + Q_{\text{ep}} + Q_{\text{comp}} - Q_{\text{br}} - Q_{\text{syn}} - Q_{\text{ic}}$.

In this paper, we ignore pion production and its contribution to the observed spectra, in addition to ignoring pair production arising from the interactions of high energy photons present inside the disc. Further on, in Sect. 4, based on posteriori calculations, we show that the contribution of both processes is not significant.

2.4. Entropy accretion rate expression

If we switch off the explicit heating and cooling of protons and electrons, the gradient of proton and electron temperatures becomes (using Eq. (5)):

$$\frac{d\Theta_p}{dr} = \frac{\Theta_p}{N_p} \frac{1}{n_p} \frac{dn_p}{dr} + \frac{Q_{\text{ep}} \eta \tilde{K}}{\rho u^r N_p} \quad \text{and} \quad (31)$$

$$\frac{d\Theta_e}{dr} = \frac{\Theta_e}{N_e} \frac{1}{n_e} \frac{dn_e}{dr} - \frac{Q_{\text{ep}} \tilde{K}}{\rho u^r N_e}. \quad (32)$$

Due to the presence of the Coulomb interaction term, we cannot integrate the above equation and obtain an analytical form¹. Hence, we cannot have a measure of entropy at every point of the flow.

However, an analytical expression is admissible only in regions where Q_{ep} is negligible. Such a region is near the horizon (r_{in}), where gravity overpowers any other interaction. The integrated form of Eqs. (31) and (32) are:

$$n_{\text{ein}} = \kappa_1 \exp\left(\frac{f_{\text{ein}}}{\Theta_{\text{ein}}}\right) \Theta_{\text{ein}}^{\frac{3}{2}} (3\Theta_{\text{ein}} + 2)^{\frac{3}{2}} \quad (33)$$

$$n_{\text{pin}} = \kappa_2 \exp\left(\frac{f_{\text{pin}}}{\Theta_{\text{pin}}}\right) \Theta_{\text{pin}}^{\frac{3}{2}} (3\Theta_{\text{pin}} + 2)^{\frac{3}{2}}, \quad (34)$$

where κ_1 and κ_2 are the integration constants which are measures of entropy. The neutrality of the plasma implies $n_{\text{ein}} = n_{\text{pin}} = n_{\text{in}}$. The subscript ‘‘in’’ indicates quantities measured just outside the horizon. Therefore,

$$n_{\text{in}}^2 = n_{\text{ein}} n_{\text{pin}} \Rightarrow n_{\text{in}} = \sqrt{n_{\text{ein}} n_{\text{pin}}}. \quad (35)$$

Thus, we can write

$$n_{\text{in}} = \kappa \sqrt{\exp\left(\frac{f_{\text{ein}}}{\Theta_{\text{ein}}}\right) \exp\left(\frac{f_{\text{pin}}}{\Theta_{\text{pin}}}\right) \Theta_{\text{ein}}^{\frac{3}{2}} \Theta_{\text{pin}}^{\frac{3}{2}} (3\Theta_{\text{ein}} + 2)^{\frac{3}{2}} (3\Theta_{\text{pin}} + 2)^{\frac{3}{2}}}, \quad (36)$$

¹ In a single-temperature regime, the absence of Coulomb coupling makes it easier to integrate the corresponding equation and obtain an analytical measure of entropy for all r ([Kumar et al. 2013](#)).

where, $\kappa = \sqrt{\kappa_1 \kappa_2}$.

The expression of the entropy accretion rate, using Eq. (3), can be written as

$$\begin{aligned} \dot{M}_{\text{in}} &= \frac{\dot{M}}{4\pi\kappa(m_e + m_p)} \\ &= \frac{4\pi n_{\text{in}}(m_e + m_p)H_{\text{in}}u_{\text{in}}^r r_{\text{in}}}{4\pi\kappa(m_e + m_p)} \\ &= \left[\sqrt{\exp\left(\frac{f_{\text{ein}}}{\Theta_{\text{ein}}}\right) \exp\left(\frac{f_{\text{pin}}}{\Theta_{\text{pin}}}\right) \Theta_{\text{ein}}^{\frac{3}{2}} \Theta_{\text{pin}}^{\frac{3}{2}} (3\Theta_{\text{ein}} + 2)^{\frac{3}{2}} (3\Theta_{\text{pin}} + 2)^{\frac{3}{2}}} \right] \\ &\quad \times H_{\text{in}}u_{\text{in}}^r r_{\text{in}}. \end{aligned} \quad (37)$$

2.5. Sonic point conditions

The mathematical form of Eq. (16) suggests that at some point of the flow, where $a = v$, the denominator (\mathcal{D}) goes to 0. Then, for the flow to be continuous, the numerator (\mathcal{N}) also has to go to 0. This is called the sonic point of the flow. Sonic points exist whenever $dv/dr = \mathcal{N}/\mathcal{D} = 0/0$. Thus, the sonic point conditions are:

$$\begin{aligned} -\frac{1}{r_c(r_c - 2)} + \frac{\lambda_c^2 \gamma_{\phi_c}^2 (r_c - 3)}{r_c^4} + a_c^2 \mathcal{A}_c + \frac{\Gamma_{\text{pc}} N_{\text{pc}} \mathbb{P}_c + \Gamma_{\text{ec}} N_{\text{ec}} \mathbb{E}_c}{h_c \tilde{K}} \\ - \frac{\Delta Q_c}{\rho_c h_c u_c^r} = 0 \end{aligned} \quad (38)$$

and

$$\frac{v_c}{1 - v_c^2} \left(1 - \frac{a_c^2}{v_c^2}\right) = 0 \Rightarrow v_c = a_c. \quad (39)$$

Here, the subscript ‘‘c’’ corresponds to the value of flow variables at the sonic point. The derivative at the sonic point $dv/dr|_c$, is computed using the L’Hospital rule.

2.6. Shock conditions

The relativistic shock conditions or the Rankine-Hugoniot conditions (Taub 1948) are:

Conservation of mass flux across the shock: $[\dot{M}] = 0$

Conservation of energy flux: $[\dot{E}] = 0$

Conservation of momentum flux: $[\Sigma h \gamma_v^2 v^2 + W] = 0$,

where, $\Sigma = 2\rho H$ and $W = 2pH$ are the vertically averaged density and pressure, respectively. The square brackets denote the difference of the quantities across the shock.

2.7. Observed spectrum

In this model, we include radiative processes such as bremsstrahlung, synchrotron, and inverse-Comptonisation, which give rise to emissions spanning the whole electromagnetic spectrum. This emission (measured in units of $\text{ergs s}^{-1} \text{Hz}^{-1}$) when plotted as a function of frequency (in units of Hz) gives us the spectrum. The spectrum is an observational tool that helps us in determining the intrinsic properties of any object (distant or nearby). Thus, the calculation of the correct spectrum is important. While obtaining a solution for a given set of flow parameters, that is, the mass of the BH, accretion rate etc, we have information on the emission coming from each radius; or, in other words, the spectrum at each radius is known and is computed as a function of the local v , ρ , and T . When the contribution from each radius is added, we get the total observed spectrum. The model presented in this paper

is in the pure GR regime, so we take into account all the general and special relativistic effects in the observed spectrum. Below, we explain the methodology used to compute the spectrum.

Let us assume that the isotropic emissivity per frequency interval per unit solid angle in the fluid rest frame is j_ν . If we transform this emissivity to a local flat frame, then by using special-relativistic transformations this becomes:

$$j'_{\nu'} = j_\nu \frac{1 - v^2}{(1 - v \cos \theta')^2} \quad \text{and} \quad \nu' = \nu \frac{\sqrt{1 - v^2}}{(1 - v \cos \theta')}. \quad (40)$$

Here, θ' is the angle which the velocity of the fluid element directed inwards makes with the line of sight.

We note that all the photons emerging from the disc do not need to reach the observer. Some would be captured by the BH due to its extreme gravity. The amount of emission captured by the BH, depends on its distance from the BH. The expression to calculate this was given by Zel’dovich & Novikov (1971):

$$|\cos \theta^*| = \sqrt{\frac{27}{4} \left(\frac{2}{r}\right)^2 \left(\frac{2}{r}\right) + 1}, \quad (41)$$

where θ^* is the angle within which photons will be captured by the BH and hence lost.

Now if we integrate the emissivity expression over the whole volume of the disc and on all solid angles, taking into account θ^* , we get the luminosity of the system as a function of frequency and, hence, the spectrum. We also account for the gravitational redshift, which introduces a factor of $\sqrt{1 - 2/r}$ into the observed frequency. Furthermore, if we want to calculate the bolometric luminosity of the system, we need to integrate the frequency-dependent luminosity over all the frequencies. For more details on calculating the spectrum, see Shapiro (1973). In the total spectrum, there are signatures of all the emission processes; this is discussed extensively in the results section. Bremsstrahlung emission always comes in the high-frequency part of the spectrum. When the accretion rate of the system is low, the contribution from bremsstrahlung emission is visible in the spectrum. Synchrotron emission is characterised by the turnover/absorption frequency (ν_t). Inverse-Comptonisation, on the other hand, is identified as a power-law part in the spectrum, following the relation $F_\nu \propto \nu^\alpha$, α as the spectral index.

3. Solution procedure

Accretion discs around BHs are transonic in nature and may possess multiple sonic points (LT80; Fukue 1987; Chakrabarti 1989). The nature of the sonic point is also dictated by the slope of the solution at the sonic point. If the slope (i.e. $dM/dr|_c$, here $M = v/a$ is the Mach number) admits two real roots at the sonic point, then a solution can actually pass through it. These types of sonic points are termed X-type or saddle-type. The accretion solution corresponds to the negative slope, while the excretion solution corresponds to the positive slope. However, if both the roots of the slope are imaginary or complex, then matter cannot pass through them. These sonic points are called O-type (imaginary slope) and spiral-type (complex), respectively. The combined effect of the flow parameters like E , λ , & \dot{M} , determines the number of sonic points formed inside an accretion flow, as well as the topology of the solution. An accretion flow with low values of λ admits only one outer sonic point (r_{co} ; located at larger distance from the BH), while those with higher values of λ admit only inner sonic points (r_{ci} ; closer to the BH). In

the intermediate λ range, the accretion disc may admit a maximum of three sonic points : inner (r_{ci}), middle (r_{cm}), and outer (r_{co}), where r_{ci} and r_{co} are X-type, while the middle sonic may be spiral or O-type depending on whether the system is dissipative or non-dissipative, respectively (for further information on sonic points see, [Holzer 1977](#); [LT80](#); [Ferrari et al. 1985](#); [Fukue 1987](#); [Chakrabarti 1989](#)). Flows with high value of E , generally admit only one r_{ci} . On the other hand, \dot{M} controls radiative cooling and modifies the thermal state of the flow. This, in turn, modifies the range of E and λ , which allows for the formation of multiple sonic points.

In Sect. 3.1, we describe the method for finding sonic points. In Sect. 3.2, we show that the transonic solutions are degenerate and we present an extensive discussion of how to remove the degeneracy.

3.1. Method for obtaining sonic points in two-temperature flows

In a single temperature regime, the location of the sonic point and its property is unique for a given set of constants of motion. In dissipative systems, sonic points are not known a priori and they are obtained self-consistently by integrating the equations of motion. So, presently, in the two temperature regime, we follow exactly the same procedure to solve the equations, as done in the single temperature realm. We need to select some fixed boundary from where we can start integrating dv/dr , $d\Theta_p/dr$ and $d\Theta_e/dr$ to find the sonic point. As $r \rightarrow 2r_g$: $v \rightarrow c$ and E is defined at the horizon, the latter being a constant of motion. However, we cannot start integration from $r = 2r_g$ because of coordinate singularity on the horizon. Therefore, we select a point asymptotically close to the horizon ($r_{in} = 2.001r_g$). It is here, where gravity overpowers any other processes or interactions, therefore, infall timescales are much smaller than any other timescales. In other words, at $r = r_{in}$, $X_f \rightarrow 0$ and $E \rightarrow \mathcal{E} = -hu_t$ (from Eq. (6)). Simplifying this, we obtain an expression of v_{in} in terms of E , λ , r_{in} , Θ_{pin} , and Θ_{ein} . We list the procedure for obtaining a transonic solution below:

1. For a given set of values of E , λ & \dot{M} , we start integration from a point asymptotically close to the horizon at $r_{in} = 2.001$ (in units of r_g).
2. As $r_{in} \rightarrow 2$, $E \rightarrow \mathcal{E} = -h_{in}u_t = h_{in}(1 - 2/r_{in})^{1/2}\gamma_v\gamma_\phi$. Here $h_{in} = h_{in}(\Theta_{pin}, \Theta_{ein})$ is the specific enthalpy at r_{in} .
3. We supply Θ_{pin} .
4. We also supply Θ_{ein} . Then v_{in} is obtained as a function of the flow parameters and can be expressed as

$$v_{in} = \left[1 - \frac{(1 - 2/r_{in})}{\mathcal{E}^2} \frac{r_{in}^3}{\{r_{in}^3 - \lambda^2(r_{in} - 2)\}} h_{in}^2 \right]^{1/2}.$$

5. Using the values of Θ_{pin} , Θ_{ein} , and v_{in} we integrate Eqs. (14)–(16), from $r = r_{in}$ to outwards. As we integrate, we simultaneously check the sonic point conditions (Eqs. (38) and (39)).
6. If a sonic point is not found, we supply another value of Θ_{ein} and repeat steps 4 and 5 until the sonic point conditions are satisfied.
7. Once a sonic point is found, we integrate the equations of motion from sonic point to larger distances and obtain the full, global, transonic two-temperature accretion solution.
8. After we locate one sonic point, we change Θ_{ein} again and repeat steps 4–7 to check if any other sonic point exists. If it is found, we obtain its corresponding transonic solution.

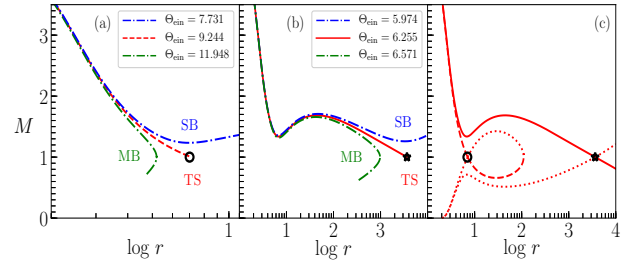


Fig. 1. Method for finding sonic points. Solutions are presented in terms of Mach number $M (= v/a)$ vs $\log r$ plot. $\Theta_{pin} = 7.162 \times 10^{-2}$ for all iterations. *Panel a*: iterations to obtain inner sonic point r_{ci} (black circle) and *panel b*: iterations to obtain outer sonic point r_{co} (black star). Various branches plotted are multivalued branches (MB; green dashed-dot), transonic (TS; red dashed), and supersonic (SB; blue dashed-dot). Respective Θ_{ein} s are mentioned inside the panels. *Panel c*: full set of transonic solutions. Global accretion solution (red solid) through r_{co} and accretion solution through r_{ci} (red, dashed) is plotted. Equatorial global wind (through r_{co}) and non-global wind (through r_{ci}) are represented using red dotted curve. The accretion disc flow parameters used are $\lambda = 2.5$, $E = 1.000045$, $\dot{M} = 0.001\dot{M}_{Edd}$, and $m_{BH} = 10 M_\odot$.

We note that if our supplied guess value of Θ_{pin} is unphysical, then even by iterating with all possible values of Θ_{ein} , the sonic point conditions can never be satisfied. This is basically the modified version of the methodology adopted by [Le & Becker \(2005\)](#), who obtained accretion solutions for a dissipative flow in the single temperature regime.

We illustrate the procedure to find transonic solutions, enlisted above, in Figs. 1a–c. All three panels in this figure plots Mach number ($M = v/a$) vs $\log r$. The accretion disc parameters are $\lambda = 2.5$, $E = 1.000045$, and $\dot{M} = 0.001\dot{M}_{Edd}$ around a BH of $10 M_\odot$. We would like to point out that all these accretion disc parameters and the BH mass chosen are for representative purposes only. These have been varied and their effect on the solution were studied later.

In Fig. 1a, we present the method to obtain inner sonic point or r_{ci} and the transonic solution through it. Following steps 1, 2, and 3, we supply $\Theta_{pin} = 7.162 \times 10^{-2}$ for the aforementioned values of E , λ , and \dot{M} . Following step 4, we start by supplying a high value of Θ_{ein} and obtain v_{in} . Then we integrate the equations of motion (step 5). For higher values of Θ_{ein} , we obtain a multi-valued branch (MB) of solutions. We plot one such MB solution (green dashed-dot) corresponding to $\Theta_{ein} = 11.948$. Clearly, the MB solutions are not correct. We reduce the value of Θ_{ein} (step 6) and repeat the whole procedure up to step 5. We observe that as we reduce Θ_{ein} , the MB solutions approach the transonic solution, that is, they would shift rightward, but in all probability, we would overshoot the transonic solution and end up with a purely supersonic branch (SB) solution (i.e. when $v > a$ or $M > 1$ at all r). We plot a representative case of a purely SB solution (blue dashed-dot) corresponding to $\Theta_{ein} = 7.731$. When the solutions corresponding to various Θ_{ein} suddenly shift from an MB solution to SB, then we know that the Θ_{ein} corresponding to a transonic solution (TS) lies in between these two values of Θ_{ein} . We iterate using the electron temperature at r_{in} within the range $7.731 < \Theta_{ein} < 11.948$ and obtain the transonic solution (TS) (red dashed) and the sonic point is at $r_{ci} = 5.186$ (black circle). Then, by following step 7, we obtain the complete transonic solution from r_{in} to a large distance through r_{ci} . In Fig. 1b, we present the procedure for finding the existence of the outer sonic point for the same set of flow parameters. Following step 8, we reduce Θ_{ein} by a comparatively large value, such that we start obtaining MB type solutions similar to the

ones we obtained while trying to locate r_{ci} . In this panel, we present an example of an MB solution (green dashed-dot) for $\Theta_{ein} = 6.571$. We repeat steps 4–6 and check when the solution jumps from MB to SB. In this instance, it corresponds to $\Theta_{ein} = 7.106$ (blue dashed-dot). We iterate on Θ_{ein} between the two limits, $6.571 < \Theta_{ein} < 7.106$, until we obtain a transonic solution through $r_{co} = 3644.9$ (black star). No other sonic point exists for these flow parameters (E , λ , \dot{M}). In Fig. 1c, we plot the complete set of transonic solutions, accretion (red dashed and red solid) as well as equatorial wind solutions (red dotted) for the disc parameters $\lambda = 2.5$, $E = 1.000045$ and $\dot{M} = 0.001\dot{M}_{Edd}$ around a BH of $10 M_{\odot}$. The global accretion solution connecting infinity to the horizon is represented by a red solid line, while a red dashed line represents an accretion solution which is not global. We should remember that not all set of disc parameters produce multiple sonic points and this point is discussed in detail in the following sections.

3.2. Presence of degeneracy in two-temperature transonic solutions : Method for removing it to obtain unique transonic solutions, invoking the second law of thermodynamics

In the last section, we laid down the procedure to obtain transonic solution by supplying a guess value of Θ_{pin} and iterating with various values of Θ_{ein} , until we get the sonic point. This has been elaborately discussed in steps 1–8 in Sect. 3.1. Now, if we choose a different value of Θ_{pin} and again follow the steps 1–8 of Sect. 3.1 for the same set of disc parameters (E , λ & \dot{M}), we obtain a different transonic solution with distinctly different sonic point properties. This means that for a given set of constants of motion, two-temperature EoMs admit multiple transonic solutions. Since the number of EoMs (accretion rate, momentum, and energy equation) are less than the number of flow variables (density, velocity components, and two temperatures), even the transonic solutions become degenerate as a result. From the second law of thermodynamics, it is clear that out of all the possible solutions, only the solution with the highest entropy (\dot{M}) would be expected to be favoured by nature (Sarkar & Chattopadhyay 2019). In dissipative systems, entropy is not conserved, so we measure entropy in the region near the event horizon (see, Eq. (37) of Sect. 2.4). For each transonic solution corresponding to a given Θ_{pin} , we compute \dot{M}_{in} . If the computed \dot{M}_{in} is plotted with respect to Θ_{pin} , then there is a clear maxima in \dot{M}_{in} . Following the second law of thermodynamics, the solution (corresponding to a Θ_{pin}) with maximum entropy (\dot{M}_{in}) is the physically plausible solution. Hence, we are able to constrain the degeneracy and obtain a unique transonic two-temperature solution for a given set of constants of motion.

In Figs. 2a–g, we illustrate the methodology for obtaining a unique two-temperature transonic solution. We choose the accretion disc flow parameters: $E = 1.0015$, $\lambda = 2.6$, $\dot{M} = 0.02\dot{M}_{Edd}$, and $M_{BH} = 10 M_{\odot}$. As described above, we supply a Θ_{pin} or equivalently T_{pin} and then we iterate on Θ_{ein} (or T_{ein}) to obtain a transonic solution. The entropy accretion rate \dot{M}_{in} , corresponding to the transonic solution for the particular T_{pin} , is plotted in Fig. 2g. The black solid line is for those T_{pin} whose solution passes through outer sonic point (r_{co}) and black dotted line is for those passing through inner sonic point (r_{ci}). From this figure, we select few T_{pin} s (points marked “a”–“f”) which are (a) 3.1×10^{11} K, (b) 5.605×10^{11} K, (c) 6.04×10^{11} K, (d) 6.460×10^{11} K, (e) 6.554×10^{11} K and (f) 7.0×10^{11} K and plot

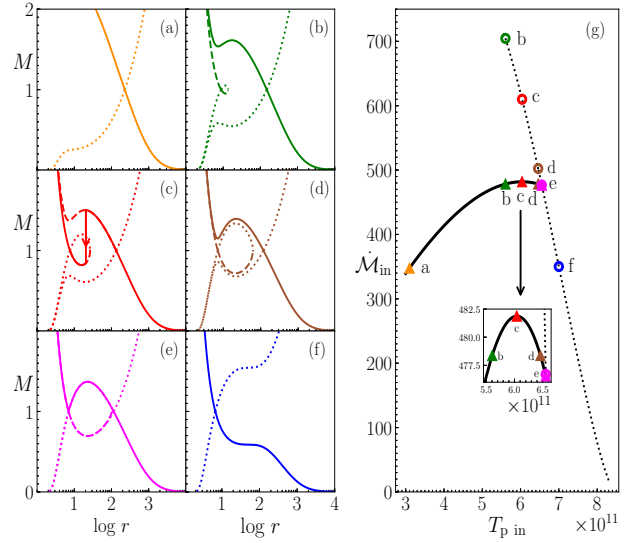


Fig. 2. Left: \dot{M} vs $\log r$ plot for various values of T_{pin} . (a) $T_{pin} = 3.1 \times 10^{11}$ K, (b) $T_{pin} = 5.605 \times 10^{11}$ K, (c) $T_{pin} = 6.04 \times 10^{11}$ K, (d) $T_{pin} = 6.460 \times 10^{11}$ K, (e) $T_{pin} = 6.554 \times 10^{11}$ K and (f) $T_{pin} = 7.0 \times 10^{11}$ K. Global solutions are represented by solid lines. Panel g: \dot{M}_{in} vs T_{pin} . Solid black curve is for the solutions passing through outer sonic point, while dotted black curve is for solutions passing through inner sonic point. Panels a–f: solutions corresponding to the points marked in right panel g. The disc flow parameters are $E = 1.0015$, $\lambda = 2.6$ and $\dot{M} = 0.02\dot{M}_{Edd}$. The space-time is described by a BH of mass $10 M_{\odot}$.

their solutions in terms of \dot{M} vs $\log r$, presented in Figs. 2a–f, respectively. The global accretion solutions are represented by solid curves, dotted are the wind types, while the dashed curves are accretion solutions which are not global. There is a range of T_{pin} where both inner and outer sonic points are present and is the multiple sonic point regime. For example, “b”, “c” and “d” has both inner (marked circle) and outer sonic points (marked triangle). For point “e”, the solutions passing through inner and outer sonic points (magenta triangle and magenta circle), have almost the same value of \dot{M}_{in} (see inset). A corresponding solution is plotted in Fig. 2e, which shows that the global solution (connecting horizon to large distances) passes through r_{co} . Now, corresponding to point “a” (orange triangle, in panel g), the solution passes only through r_{co} (Fig. 2a), while for point “f” (blue circle), the solution passes through r_{ci} (Fig. 2f). However, the entropy is exactly same for both these points. This means that the solution character can be completely different even if \dot{M}_{in} has the same value. Similarly another pair, “b” and “d”, also has the same entropy but different T_{pin} . Also, their corresponding solutions are significantly different, although both solutions lie in the multiple sonic point regime. This shows that not only all solutions presented in the figure have the same E , \dot{M} , λ , but they may even have the same \dot{M}_{in} and yet, the solutions are completely different.

In order to drive the point all the way home, we present T_{pin} , \dot{M}_{in} , r_c , v_c , & L (luminosity) for all degenerate solutions in Table 1. Some solutions can be about four times more luminous than other solutions. It is evident from the figure and table that degeneracy in two-temperature model is a serious problem. An observational parameter such as L is quite different for different degenerate solutions. Any random choice from the pool of degenerate solutions would provide us with completely wrong information about the system as well as an erroneous spectrum.

Table 1. Various flow properties of the solutions plotted in Figs. 2a–f.

	T_{pin} ($\times 10^{11}$ K)	\dot{M}_{in}		r_c (sonic point)		v_c (v at r_c)		L ($\times 10^{33}$ ergs s^{-1})
		Inner	Outer	Inner	Outer	Inner	Outer	
a	3.100	–	350.132	–	227.514	–	0.041	1.092
b	5.605	704.505	478.373	8.826	149.380	0.177	0.051	1.763
c	6.040	609.971	481.873	7.651	134.135	0.191	0.054	4.467
d	6.460	502.357	478.377	7.118	118.565	0.199	0.057	2.457
e	6.554	476.702	476.552	7.027	11.946	0.200	0.058	2.722
f	7.000	350.168	–	6.672	–	0.207	–	3.020

Notes. The disc parameters used are $E = 1.0015$, $\lambda = 2.6$, $\dot{M} = 0.02\dot{M}_{\text{Edd}}$ around $M_{\text{BH}} = 10 M_{\odot}$.

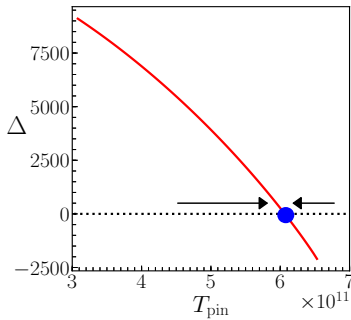


Fig. 3. Stability analysis of the unique transonic two-temperature solution with maximum entropy. The flow parameters used are same as Fig. 2. $\Delta = (d\dot{M}_{\text{in}}/dT_{\text{pin}})$ is plotted against variation of T_{pin} . The arrows indicate that Δ converge at $T_{\text{pin}} = T_{\text{pin|max}}$ (blue dot) and is the stable equilibrium solution. This T_{pin} is the solution with maximum entropy marked “c” in Fig. 2g.

Hence, the removal of degeneracy is important. Although all the solutions presented above have the same energy, angular momentum, and accretion rate, only one of them possesses the highest entropy (highest \dot{M}_{in}). In this particular case, the highest entropy solution is the one corresponding to point “c” (red triangle) in $\dot{M}_{\text{in}}-T_{\text{pin}}$ curve (Fig. 2g), and the correct, unique two-temperature accretion solution is represented in Fig. 2c (red solid).

3.3. The stability of the highest entropy transonic solutions

In this section, we investigate the stability of the unique transonic two-temperature solution selected from the available set of degenerate solutions. We note that the proposed unique solution is that of the highest entropy and, based on the second law of thermodynamics, nature should prefer it. Therefore, the solution should be stable. However, because there is a degeneracy of solutions, we need to study the stability of the proposed unique solution as well. We provide a qualitative analysis for the stability of the unique two-temperature solution.

Let us assign $\dot{M}_{\text{in|max}} = \max(\dot{M}_{\text{in}})$ and $T_{\text{pin|max}} = T_{\text{pin}}$ for which \dot{M}_{in} is maximum. Let us further define δT_{pin} which is the difference between adjacent higher and lower T_{pin} and $\Delta = (d\dot{M}_{\text{in}}/dT_{\text{pin}})$ as the gradient of \dot{M}_{in} . Now the change in \dot{M}_{in} is given by

$$\delta\dot{M}_{\text{in}} = \left(\frac{d\dot{M}_{\text{in}}}{dT_{\text{pin}}} \right) \delta T_{\text{pin}} = \Delta \delta T_{\text{pin}}. \quad (42)$$

It is clear that $\Delta = 0$ for any extrema of $\dot{M}_{\text{in}} - T_{\text{pin}}$ curve, but the solution is said to be stable if T_{pin} moves away from the value $T_{\text{pin|max}}$ and the system adjusts automatically to regain its old value. We prefer the graphical method to investigate the stability and the technique is similar to the first derivative test for obtaining local extrema (Melo 2014). We plot Δ vs T_{pin} in Fig. 3. At $T_{\text{pin}} < T_{\text{pin|max}}$, the figure shows that $\Delta > 0$. Then from Eq. (42), $\delta\dot{M}_{\text{in}} > 0$. So the system tends to go to higher \dot{M}_{in} , which we denote using a rightward arrow. Similarly, for $T_{\text{pin}} > T_{\text{pin|max}}$, $\Delta < 0$ which implies $\delta\dot{M}_{\text{in}} < 0$. Since, based on the second law of thermodynamics, a physical system is not amenable to decreasing its entropy, therefore for $T_{\text{pin}} > T_{\text{pin|max}}$, the system would tend to come back to $T_{\text{pin|max}}$. We represent this in the figure by using a leftward arrow. In other words, entropy can only increase ($\delta\dot{M}_{\text{in}} > 0$), if $T_{\text{pin}} \rightarrow T_{\text{pin|max}}$ from either side of $T_{\text{pin|max}}$. Hence, a solution corresponding to $T_{\text{pin}} = T_{\text{pin|max}}$ must be stable. Therefore, in addition to the fact that $T_{\text{pin|max}}$ corresponds to a solution with maximum entropy, we can conclude that the solution is also stable.

4. Results

Two-temperature accretion solutions are parameterised by E , λ , \dot{M} . In addition, β_d and β controls heating and cooling. Since we quote accretion rates in terms of the Eddington rate, therefore, the information on M_{BH} also enters the solution. In this section, we study in detail the two-temperature accretion solutions and discuss their spectral properties. We only analyse solutions with maximum entropy, selected from the available degenerate group of solutions.

4.1. General two-temperature solutions

In Fig. 4, we study a typical two-temperature transonic advective accretion disc solution. The parameters used are, $E = 1.000045$, $\lambda = 2.5$, $\dot{M} = 0.001\dot{M}_{\text{Edd}}$, and $M_{\text{BH}} = 10 M_{\odot}$. In Fig. 4a, we plot \dot{M}_{in} vs T_{pin} . The solution with $T_{\text{pin}} = 6.0 \times 10^{11}$ K has the maximum entropy (marked with green triangle) and the corresponding M vs $\log r$ (green solid line) is plotted in Fig. 4b. The global solution passes through an outer sonic point whose position is $r_{\text{co}} = 3040.182$ (black star). The radial three-velocity (v ; cyan solid) in co-rotating frame and flow velocity in the azimuthal direction (v_{ϕ} ; blue dotted) is plotted in Fig. 4c. Matter far away from the horizon has negligible velocity in the radial as well as in the azimuthal directions. As it approaches the BH ($r \rightarrow r_g$), $v \rightarrow c$, thus satisfying the BH boundary condition. On the other hand, v_{ϕ} increases with the decrease of r , but is maximised at $r \sim 3r_g$ and finally goes to zero on the horizon.

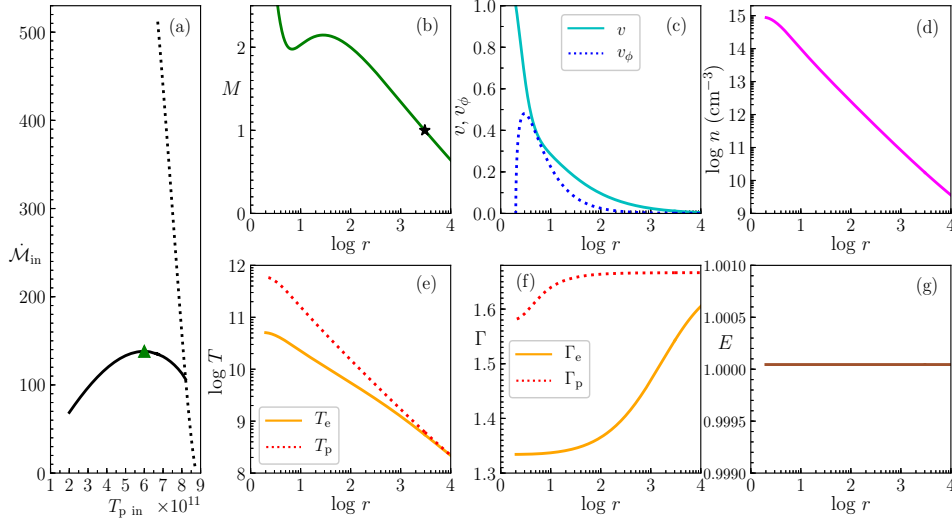


Fig. 4. (a) \dot{M}_{in} plotted against T_{pin} . The entropy for inner sonic point solutions (black, dotted) and outer sonic points (black, solid) are presented. T_{pin} marked with green triangle corresponds to maximum entropy solution. Flow variables plotted are (b) M (green, solid), (c) v (cyan, solid) and v_{ϕ} (blue, dotted), (d) $\log n$ (magenta, solid), (e) T_p (red, dotted), T_e (orange, solid), (f) Γ_p (red, dotted), Γ_e (orange, solid), (g) E (brown, solid) as functions of $\log r$. The flow parameters are $E = 1.000045$, $\lambda = 2.5$, $\dot{M} = 0.001\dot{M}_{\text{Edd}}$ and $M_{\text{BH}} = 10 M_{\odot}$. Panel b: the sonic point is marked with a black star.

This is mainly because near the horizon infall timescale is much shorter than any other timescales. The strong gravity does not allow the matter enough time to rotate in the azimuthal direction. In Fig. 4d, we plot the number density (in units of cm^{-3}) as a function of radius. The number density increases with the decrease in radius, as it should be for a convergent flow. Values for T_p (red dotted) and T_e (orange solid) are plotted in Fig. 4e. The cooling processes are dominated by electrons compared to protons. They are, however, coupled by a Coulomb coupling term which acts as an energy exchange term between the protons and electrons, as previously discussed. This term is weak, which allows protons and electrons to equilibrate into two different temperatures (T_p and T_e), unlike in the case of single-temperature flows where Coulomb coupling term is assumed to be very efficient, allowing protons and electrons to attain a single temperature. Figure 4f shows that adiabatic indices of both protons (red dotted) and electrons (orange solid) vary with the flow. This justifies our use of CR EoS. $\Gamma_p \sim 1.66$ and $\Gamma_e \sim 1.60$ at large distances away from the BH, hence, both the species are thermally non-relativistic. When the flow approaches the BH, Γ_e becomes relativistic i.e. $\Gamma_e \sim 1.33$ near the horizon. We can see that Γ_p does not vary much but it becomes mildly-relativistic near the horizon owing to the higher mass of protons. In Fig. 4g, we prove that the generalised Bernoulli constant is a constant of motion throughout the flow, even in the presence of dissipation.

Emissivities and spectral properties

In Fig. 5, we present the heating and cooling rates for the solution plotted in Fig. 4. In Fig. 5a, we plot the heating terms. The red solid line represents the heating due to magnetic dissipation. This amount of heat is assumed to be equally distributed among protons and electrons. Blue dotted line represents the Compton heating of electrons. It is mainly the hard bremsstrahlung photons present inside the flow which leads to the heating of the electrons, which is due to their higher energy as compared to protons. In Fig. 5b, we plot Coulomb Coupling term (yellow

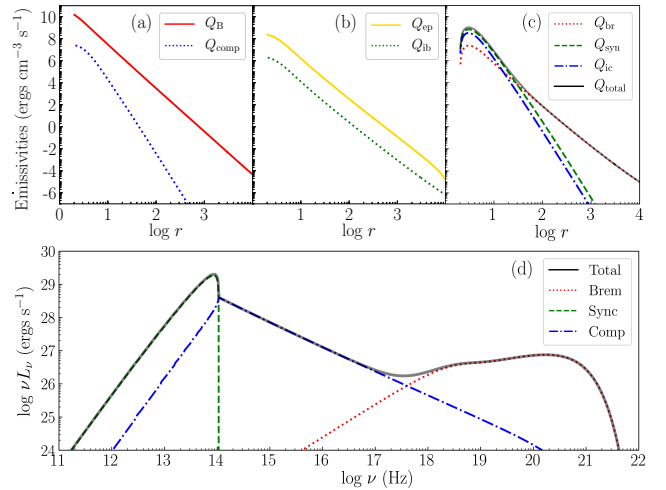


Fig. 5. Emissivity vs $\log r$ plot for the flow presented in Fig. 4, shown here in the *top three panels*. *Bottom panel*: spectrum of the accretion flow.

solid line) and inverse bremsstrahlung (green dotted line). The strongest heating term is represented by Q_B .

In Fig. 5c, we plot the emissivities of all the cooling processes for electrons: bremsstrahlung (red dotted line), synchrotron (green dashed line), and inverse-Comptonisation (blue dashed-dotted line). For the present set of disc parameters, at the outer boundary of the disc, the temperatures are non-relativistic and, therefore, bremsstrahlung emission dominates over all other processes. In the inner regions of the accretion disc, that is, close to the BH horizon, synchrotron and inverse-Comptonisation becomes important and exceeds bremsstrahlung. However, inverse-Comptonisation is less than synchrotron emission, mainly due to the low accretion rate of the flow. The total cooling of electrons is represented by a black solid line. In Fig. 5d, we plot the spectrum for the accretion flow (black solid line). It is plotted by summing up the contributions of all emission processes at each radius. General and special

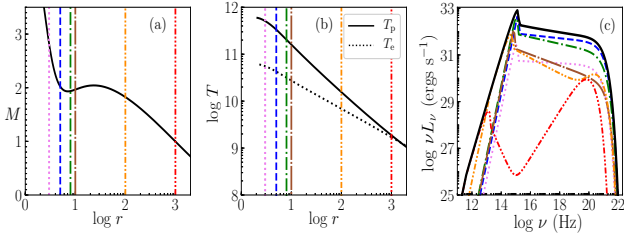


Fig. 6. (a) M and (b) $\log T$ vs $\log r$, and (c) total spectrum (black solid) plus contribution from various length scales of the accretion disc, $2-3r_g$ (magenta, dotted), $3-5r_g$ (blue, dashed), $5-8r_g$ (green, short-dashed-dotted), $8-10r_g$ (brown, long-dashed-dotted), $10-100r_g$ (orange, dashed-double-dotted) and $100-1000r_g$ (red, dashed-triple-dotted). Flow parameters are $E = 1.0002$, $\lambda = 2.48$, $\dot{M} = 0.05\dot{M}_{\text{Edd}}$, and $M_{\text{BH}} = 10 M_\odot$.

relativistic frame transformations from the fluid rest frame to the observer frame are taken into account while computing the spectra, including photon capture and photon bending effect due to the presence of strong gravity. This is widely discussed in Sect. 2.7. Spectrum of each emission process is also plotted. Bremsstrahlung is shown as a red dotted line, synchrotron by a green dashed line, and inverse-Comptonisation by a blue dashed-dotted line. The overall luminosity of the system is low, namely, $L = 2.536 \times 10^{29}$ ergs s^{-1} , with a radiative efficiency of $\eta_r = 1.957 \times 10^{-5}$. It may be noted that efficiency is defined as $\eta_r = L/(\dot{M}c^2)$. The spectral index is $\alpha = 1.744$.

4.2. Contributions of different regions of the accretion disc to the overall spectrum

In Fig. 5d, we show the contribution of all the emission processes in the total broad band continuum spectrum. However, in the following, we aim to investigate the contribution of various regions of an accretion disc in the overall spectrum. We chose a set of flow parameters: $E = 1.0002$, $\lambda = 2.48$, $\dot{M} = 0.05\dot{M}_{\text{Edd}}$, and $M_{\text{BH}} = 10 M_\odot$. In Fig. 6a, we plot the Mach number M of the accretion flow and in Fig. 6b, we plot T_p (black solid) and T_e (black dotted) as a function of $\log r$. In panels a and b, we indicate various regions with vertical lines which represents accretion disc section from $2-3r_g$ (magenta, dotted), $3-5r_g$ (blue, dashed), $5-8r_g$ (green, short-dashed-dotted), $8-10r_g$ (brown, long-dashed-dotted), $10-100r_g$ (orange, dashed-double-dotted) and $100-1000r_g$ (red, dashed-triple-dotted). The spectra from all these regions are separately over plotted in Fig. 6c, the colour-coding of the spectra matches the region from which they are computed. The black curve represents the overall spectrum for the disc parameters stated above. The contribution from the region $r = 10^3-10^4 r_g$ is too low in the overall spectrum and is not plotted, therefore, in order to avoid cluttering the figure. The spectrum computed from the region $2-3r_g$ is low in spite of the high values of n and T_e since a significant number of photons emitted from that region are captured by the BH. Most of the high energy emission is contributed by accreting matter from the region between $3-5r_g$ and $5-8r_g$ and the low-energy end of the spectra from this region is always around and above 10^{12} Hz. We tabulated these details and other spectral properties in Table 2. We can conclude from the table that $\sim 90\%$ of the emission comes from a region $<10r_g$ of the accretion disc. The lower energy part of the spectrum is mostly contributed by the outer part of the disc. Since we only considered the advective disc, the spectrum is hard and the radiative efficiency for this particular set of disc parameters is less than 1%.

Table 2. Spectral properties of the regions marked in Fig. 5.

Colour	Region (in r_g)	% of L_{tot}	α
Magenta	2–3	3.597	1.044
Blue	3–5	45.810	1.072
Green	5–8	35.250	1.141
Brown	8–10	6.965	1.236
Orange	10–100	7.845	1.323
Red	100–1000	0.286	2.392
–	1000–10000	0.247	2.233×10^{-5}

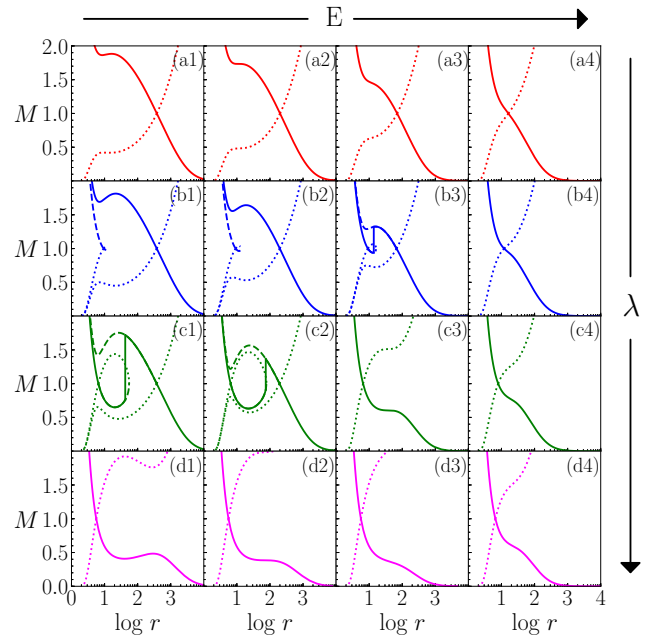


Fig. 7. Variation of solutions, M as a function of $\log r$ with variation of E and λ . From left to right: the specific energy increases as $E = 1.0005$, 1.001, 1.003, and 1.01. From top to bottom: the angular momentum increases as $\lambda = 2.40$, 2.55, 2.70, and 2.85. The other parameters are $\dot{M} = 0.01\dot{M}_{\text{Edd}}$ and $M_{\text{BH}} = 10 M_\odot$.

4.3. Dependence of accretion solutions and corresponding spectra on energy and angular momentum

In Figs. 7 and 8, we investigate the dependence of accretion solutions and the corresponding spectra on E and λ for a $10 M_\odot$ BH with $\dot{M} = 0.01\dot{M}_{\text{Edd}}$. In these figures, E increases from left to right and the values are $E = 1.0005$, 1.001, 1.003, and 1.01; whereas, as we go from top to bottom, λ increases as $\lambda = 2.40$, 2.55, 2.70, and 2.85. In short, E changes along the row while λ changes along the column. Low-angular-momentum flows ($\lambda = 2.40$) behave as Bondi flow, possessing a single sonic point, through which the global solution passes (see Figs. 7a1–a4), irrespective of the value of E . As angular momentum increases, the rotation head of the specific energy (E) of the flow plays a significant role inside the system and multiple sonic points form in an appreciable section of the parameter space. For $\lambda = 2.55$ (Figs. 7b1–b3), multiple sonic point exists in a large range of E . In Figs. 7b1–b2, the global solution (blue, solid) passes through the outer sonic point; whereas in Fig. 7b3, the solution (blue, solid) harbours a shock and passes through both inner and outer sonic points. In Fig. 7b4, only a single sonic point exists. This is mainly due to the fact that for flows with higher energy, the

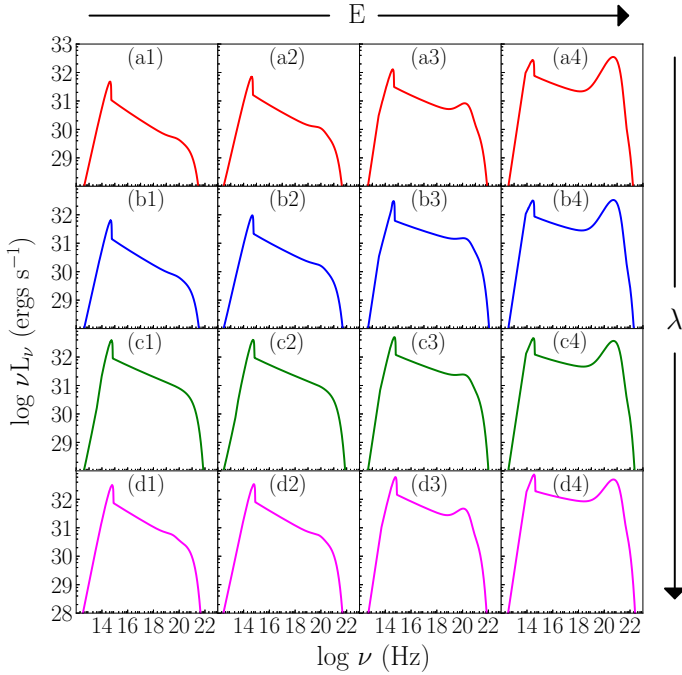


Fig. 8. Variation of the spectrum with E and λ . The set of values for E and λ and other parameters are same as in Fig. 7.

distribution of sound speed a is generally higher compared to flows with lower E . Therefore, the flow can only become transonic when v increases significantly, which can happen only very close to the BH. For low values of E , the sound speed distribution $a(r)$ is comparatively low. Therefore the sonic points form further out because the flow becomes transonic whenever the infall velocity $v(r)$ attains moderately high values.

Angular momentum has a different effect on the flow structure. If we increase λ , then the distribution of $v_\phi(r)$ increases. Higher values of v_ϕ restrict the increase of v to moderate values, except near the horizon. So for flows with higher λ , the sonic points shift towards the BH. For even higher $\lambda \geq 2.85$, only inner sonic point exists irrespective of the value of E (see Figs. 7d1–d4). In Figs. 7c1–c2 which are for $\lambda = 2.70$, shocks form even at low energies. If one compares with single temperature accretion discs (Chattopadhyay & Chakrabarti 2011; Kumar & Chattopadhyay 2014, 2017; Chattopadhyay & Kumar 2016), it is clear that multiple sonic points form in a much smaller range of the energy-angular momentum parameter space of a two-temperature accretion disc, as is shown in Figs. 7a1–d4.

Figure 8 shows the corresponding spectra, which span from 10^{12} – 10^{22} Hz. As a general trend, with the increase in λ of the system, luminosity increases since matter gets enough time to radiate. However the spectral shape and slope (arising because of inverse-Comptonisation) remains roughly the same, except for the solutions which harbours shock. The spectral slope is flatter in case of shocked solutions. With the increase in E , thermal energy of the system increases, emission is hence higher. The spectral shape and slope is visibly changed. Bremsstrahlung emission, the broad peak in the higher frequency range, is increased with the increase in E (left to right), while angular momentum seems to have little effect on this particular radiative process. Since, in this case, we are dealing with a flow with a low accretion rate, the spectrum is relatively soft as inverse-Comptonisation is not significant.

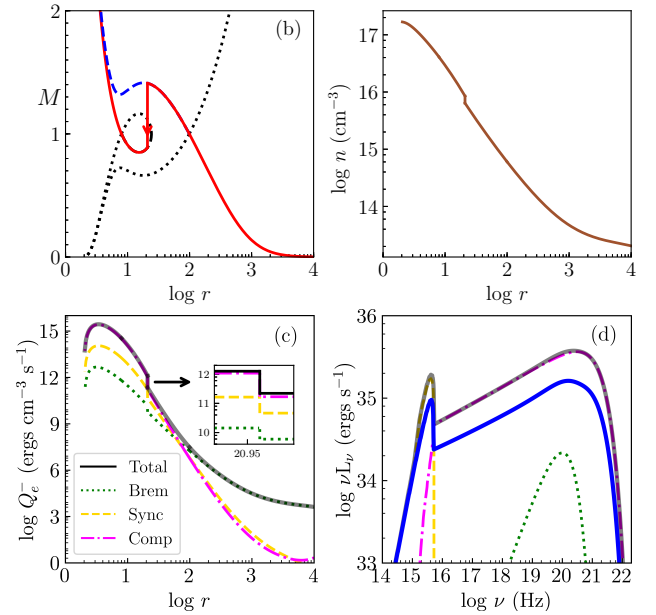


Fig. 9. Typical shocked solution (a), with its corresponding number density (b), emissivities, (c) and spectrum (d), is presented. The parameters taken are $E = 1.002$, $\lambda = 2.58$, $\dot{M} = 0.2\dot{M}_{\text{Edd}}$, and $M_{\text{BH}} = 10 M_\odot$.

4.4. Shocked solution, spectra and the parameter space

In Figs. 7b3,c1,c2, the accretion solutions admit stable shocks. As previously discussed, for low λ , a flow admits only one sonic point (Figs. 7a1–a4). As λ increases, the flow possess multiple sonic points. A flow can pass through both the sonic points only when the shock conditions are satisfied (see, Sect. 2.6). With the increase in λ , the centrifugal term increases and the twin effect of the centrifugal and the thermal term can restrict the infalling matter, leading to a centrifugal pressure mediated shock transition. In the following section, we analyse the shocks present in two-temperature accretion flows.

In Fig. 9a, we present a typical shock solution for the parameters $E = 1.002$, $\lambda = 2.58$, $\dot{M} = 0.2\dot{M}_{\text{Edd}}$, and $M_{\text{BH}} = 10 M_\odot$. For these parameters, the flow possess multiple sonic points. The blue dashed line is for the accretion solution passing through the outer sonic point r_{co} . When this solution becomes supersonic, it encounters a shock at $r_{\text{sh}} = 20.952$. Then it jumps to the subsonic branch and enters the BH supersonically after crossing through the inner sonic point r_{ci} . The global solution is represented with a red solid line. The compression ratio ($R = u'_-/u'_+$, \pm implies post and pre-shock quantities, respectively) is 1.459 in this case. In Fig. 9b, we plot the number density as a function of r . At the shock, there is an increase in number density of both protons and electrons equally. This leads to increased cooling in the system which is evident from Fig. 9c, where we plot emissivities of various cooling processes related to electrons. The corresponding spectrum is plotted in Fig. 9d. In Figs. 9c–d, bremsstrahlung is represented using dotted green line, synchrotron in dashed yellow, and inverse-Comptonisation in dashed-dotted magenta, while the total cooling is represented by solid black line. The accretion rate of the system is high, so the spectrum is mainly dominated by inverse-Comptonisation, especially in the post-shock region.

In Fig. 9d, the total spectrum of the system is plotted in black, while superimposed upon it is the spectrum (blue solid) of the shock-free solution (blue dashed of panel a). The luminosity of the system is 2.831×10^{36} ergs s^{-1} , which corresponds

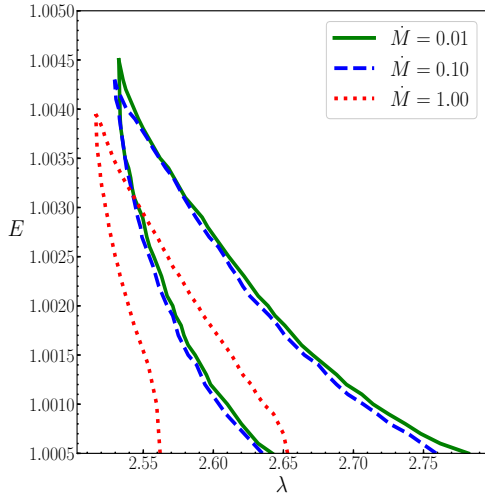


Fig. 10. Shock parameter space for $\dot{M} = 0.01\dot{M}_{\text{Edd}}$ (green, solid), $0.10\dot{M}_{\text{Edd}}$ (blue, dashed), and $1.00\dot{M}_{\text{Edd}}$ (red, dotted) around a $10 M_{\odot}$ BH.

to an efficiency (η_r) of 1.09%, while for a shock-free branch (blue dashed), the luminosity would be 1.293×10^{36} ergs s^{-1} and $\eta_r = 0.50\%$. Because of the shock, the luminosity and, hence, the efficiency of the system doubles. However, it seems that there is no special spectral signature of shock in accretion flow, except that the luminosity of the power-law part of the spectrum increases. This is also evident in Figs. 8b3, c1, and c2.

The bounded region in E - λ space in Fig. 10, represents the shock parameter space, i.e. a flow with E , λ values from the bounded region for the given \dot{M} that is to undergo a stable shock transition. Each bounded region or shock-parameter space is characterised by different accretion rates: $\dot{M} = 0.01$ (green, solid), $\dot{M} = 0.1$ (blue, dashed), and $\dot{M} = 1.0$ (red, dotted) around a $10 M_{\odot}$ BH. We can see that as \dot{M} increases, the parameter space decreases and shifts to the lower angular momentum side. High values of \dot{M} imply higher rates of cooling and, therefore, much hotter flow at the outer boundary, which can accrete and form the disc. Hence, even for lower λ , the centrifugal term in conjunction with the thermal term can resist the infall to produce an accretion shock. That is why for higher \dot{M} , the shock parameter space shifts to the lower λ values. For low \dot{M} , the shock parameter space is almost similar, it significantly changes only in the presence of high accretion rates. More interestingly, it is clear that an accretion flow with high accretion rate may also harbour accretion shocks.

4.5. Dependence of spectrum on β

The magnitude of stochastic magnetic field inside the flow is controlled by β . Any change to it would lead to a change in synchrotron emission from electrons and, eventually, a change in the radiation due to inverse-Comptonisation. Hence, the spectra that an observer would see significantly depends on the value of β . In Fig. 11, we plot the change in spectra with change in β for the flow parameters $E = 1.003$, $\lambda = 2.54$, $\dot{M} = 0.1\dot{M}_{\text{Edd}}$, and $M_{\text{BH}} = 10 M_{\odot}$. We varied β : 0.002 (blue, solid), 0.01 (green, dashed), and 0.02 (red, dotted). The present flow has high accretion rate where cooling is more pronounced. Even for low β , the power law signature in the spectrum arising due to inverse-Comptonisation, is hard. However, the dominant emission comes from bremsstrahlung, as can be inferred from its bump at higher frequency regime. As we increase β , the bump feature vanishes.

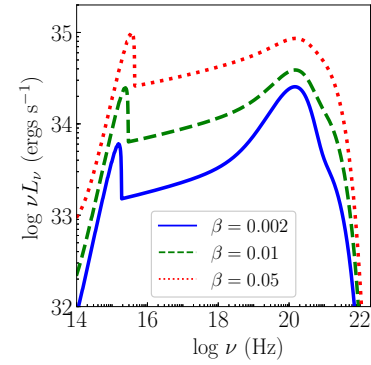


Fig. 11. Change in spectra with increase in $\beta = 0.002$ (blue, solid), 0.01 (green, dashed), and 0.02 (red, dotted). Other parameters used are $E = 1.003$, $\lambda = 2.54$, and $\dot{M} = 0.1\dot{M}_{\text{Edd}}$ in an accretion disc around $M_{\text{BH}} = 10 M_{\odot}$.

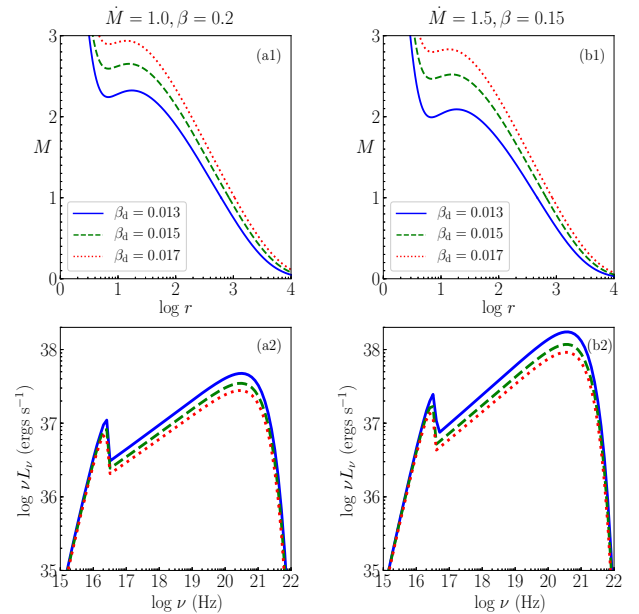


Fig. 12. Accretion solutions (a1, b1) and their corresponding spectra (a2, b2) plotted for a flow with $E = 1.001$, $\lambda = 2.61$ around $M_{\text{BH}} = 10 M_{\odot}$. Various curves are for $\beta_d = 0.013$ (blue, solid), $\beta_d = 0.015$ (green, dashed) and $\beta_d = 0.017$ (red, dotted). The accretion rates and ratio of magnetic to gas pressure are chosen as $\dot{M} = 1.0\dot{M}_{\text{Edd}}$, $\beta = 0.2$ (a1, a2), and $\dot{M} = 1.5\dot{M}_{\text{Edd}}$, $\beta = 0.15$ (b1, b2).

This is mainly due to the fact that with the increase in β , synchrotron emission and, hence, inverse-Comptonisation increases more as compared to bremsstrahlung, which is independent of the magnitude of the magnetic field in the flow. The synchrotron turnover frequency also shifts to higher frequencies with the increase in β .

4.6. Dependence of solutions and spectra on β_d

Figure 5a shows that magnetic dissipation is a more efficient heating mechanism compared to Compton heating and to the Coulomb heating of electrons. In Figs. 12a1–b2, we vary β_d , which controls magnetic dissipation. We compare the solutions and resultant spectra for $\beta_d = 0.013$ (blue, solid), 0.015 (green, dashed), and 0.017 (red, dotted). For Figs. 12a1,a2, we chose a higher ratio between magnetic and gas pressure, $\beta = 0.2$, and accretion rate $\dot{M} = 1.0\dot{M}_{\text{Edd}}$. For Figs. 12b1,b2, we selected

$\dot{M} = 1.5\dot{M}_{\text{Edd}}$ and $\beta = 0.15$. For both the cases, we have $E = 1.001$, $\lambda = 2.61$ and $M_{\text{BH}} = 10 M_{\odot}$. The sonic point, luminosities, and spectral index of the accretion flows are given in Table 3. Evidently, luminosity and, hence, efficiency, decreases with increasing β_d , but increases with increasing \dot{M} . If the dissipative heating is higher (i.e. higher β_d), then matter with lower temperature at large r may achieve the same E . Therefore, the accretion flow would have an overall lower temperature and would emit less. That is exactly, what is observed in Figs. 12a2,b2, where the luminosity goes down with the increase in β_d . The spectrum is decisively hard for super-Eddington accretion rates. It means that no single flow parameter can dictate whether the spectrum is hard or soft; instead all the flow parameters together contribute for the final outcome. However, it is clear that β_d does influence the emitted spectra and luminosity significantly.

4.7. Possibility of pair production and pion production

Up to this point, we have investigated how various factors can affect the two-temperature solutions and resulting spectra. However, it may be noted that we have ignored pair production from particle-particle interactions in the accretion disc or from accretion disc radiations. We have also ignored the production of gamma-rays due to high energy interactions like pion decay. We assumed that these processes will not significantly affect the solutions. In Appendix B, we investigate the pair production processes a posteriori. We compare the number densities of protons n_p with positrons n_{e^+} (Figs. B.1a1, b1) generated through photon interactions produced in accretion discs as well as compare the total emissivity Q_{total} with pair annihilation emissivity Q_{ann} (Figs. B.1a2, b2). We consider two sets of accretion disc parameters (1) $\dot{M} = 1.0$, $\beta = 0.2$ (Figs. B.1a1, a2) and (2) $\dot{M} = 1.5$, $\beta = 0.15$ (Figs. B.1b1, b2). The rest of the parameters are common for both the cases, namely, $\beta_d = 0.013$, $E = 1.001$, and $\lambda = 2.61$. These two accretion disc cases are described around a BH of $10 M_{\odot}$. After the a posteriori calculations, elaborately discussed in Appendix B, we can conclude that, $n_{e^+} \ll n_p$ and $Q_{\text{ann}} \ll Q_{\text{total}}$.

In Appendix C, we compute the production of pions (π^0) a posteriori and the gamma rays emitted due to its decay. We plot $\log T_p$ vs $\log r$ in Figs. C.1a1, b1 and the corresponding spectra in Figs. C.1a2, b2. We study the generation of pions and gamma ray photons for two cases (1) by varying accretion rate ($\dot{M} = 0.01$: red, dotted, 0.1 : green, dashed, and 1.0 : blue, solid) around a BH of $M_{\text{BH}} = 10 M_{\odot}$ (Figs. C.1a1, b1) and (2) by varying mass of the BH ($M_{\text{BH}} = 10^2$: blue, solid, 10^4 : green, dashed, and 10^6 : red, dotted), keeping the accretion rate $\dot{M} = 0.1$ constant. The other disc parameters are $E = 1.0007$, $\lambda = 2.61$, $\beta = 0.01$, & $\beta_d = 0.001$. Luminosity for higher \dot{M} is higher and so is the gamma-ray produced by decay of pions. The same trend is observed when we increase the BH mass. However, the gamma ray luminosity is always $<10^{-5}$ times that of the total luminosity. An elaborate discussion on these two cases is presented in Appendix C. We can conclude that the consideration of pair production or pion decay does not affect the accretion solutions or the spectra significantly.

4.8. Dependence on \dot{M} and M_{BH}

In Fig. 13a, we plot the continuum spectra for $\dot{M} = 0.1\dot{M}_{\text{Edd}}$ (blue, solid), $\dot{M} = 0.6\dot{M}_{\text{Edd}}$ (green, dashed), and $\dot{M} = 1.2\dot{M}_{\text{Edd}}$ (red, dotted) from a disc around a BH of $10 M_{\odot}$. The disc becomes brighter as \dot{M} increases and even the efficiency also

increases. The spectra also becomes harder, mainly because the inverse-Compton output increases with the increase in number density of hot electrons inside the flow. However, the range of frequency ν on which the spectrum is distributed do not increase appreciably with the increase in accretion rate. The corresponding spectral properties are presented in Table 4.

In Fig. 13b, we plot spectra from discs with the same accretion rate $\dot{M} = 0.1\dot{M}_{\text{Edd}}$, but around different M_{BH} which are: $10 M_{\odot}$ (blue, solid), $10^3 M_{\odot}$ (magenta, dashed), and $10^6 M_{\odot}$ (brown, dotted). The more massive the black hole, the brighter the disc since absolute accretion rate increases. In addition, the spectrum spans a larger range of ν , with significant emission from radio to γ rays. It may be noted that higher M_{BH} results in a more broadband spectra, therefore, the disc becomes more luminous but the spectral index does not change much. The spectral properties are presented in Table 5.

4.9. Luminosity, efficiency, and spectral index of two-temperature flows

In Fig. 14a, we calculate the luminosities and in Fig. 14b, we plot the efficiency of the accretion of matter onto BHs of different masses ($10 M_{\odot}$, $10^3 M_{\odot}$ and $10^6 M_{\odot}$) as a function of the accretion rate (\dot{M}). The sizes of the circles are in order of increasing value of the BH mass. The parameters used are $E = 1.001$ and $\lambda = 2.4$. We note that luminosity rises steeply with the increase in accretion rate of the system for all BH masses. The more matter is supplied, the greater the conversion of it into energy. However, at higher accretions rates, luminosities approach asymptotic values. Radiation emitted by the accretion disc is the effect of conversion of gravitational energy released in the act of accretion into electro-magnetic radiation. So as \dot{M} increases, emission increases due to an increased supply of matter. However, it cannot emit more than the energy obtained from the accretion process and, therefore, it reaches a ceiling around $\eta \sim 10\%$. It is apparent from Fig. 14b, that the efficiency is slightly affected by the BH mass. The spectral index (α) is represented as colour bar over both Figs. 14a,b. It changes visibly with the increase in accretion rate of the system (also, see Fig. 13a and Table 4) but does not change much with the change in BH mass (also, see Fig. 13b and Table 5).

5. Discussion and conclusions

In this paper, we study solutions for two-temperature accretion discs around non-rotating BHs. We note that the spin of the BH may play an important role in jet generation via a process called Blandford-Znajek mechanism (Blandford & Znajek 1977), however, accretion is still the primary mechanism for explaining the observed luminosities. A proper two-temperature accretion solution is the best way to obtain the spectra from such systems. Two-temperature equations produce a degenerate set of solutions even when they have the same set of disc parameters such as the generalised Bernoulli parameter (E), accretion rate (\dot{M}) and angular momentum (λ). For the given set of disc parameters, a choice of proton temperature may produce a transonic solution through the outer sonic point, while some other choice of the temperature would produce a solution through inner sonic point and yet another would produce solutions which undergo shock transition. The resulting radiation also varies accordingly. In fact some solutions may exhibit four times more luminosity compared to some other solutions (see Fig. 2 and Table 1). Therefore, this degeneracy issue is serious and calls for urgent attention.

Table 3. Various flow properties of the solutions plotted in Fig. 12.

Parameters	β_d	r_c	L $\times 10^{38}$ (ergs s^{-1})	α
$\dot{M} = 1.0\dot{M}_{\text{Edd}}$ and $\beta = 0.20$	0.013	613.365	2.523	0.672
	0.015	838.022	1.877	0.680
	0.017	1053.310	1.514	0.683
$\dot{M} = 1.5\dot{M}_{\text{Edd}}$ and $\beta = 0.15$	0.013	466.718	8.31	0.606
	0.015	669.746	5.726	0.619
	0.017	849.084	4.518	0.625

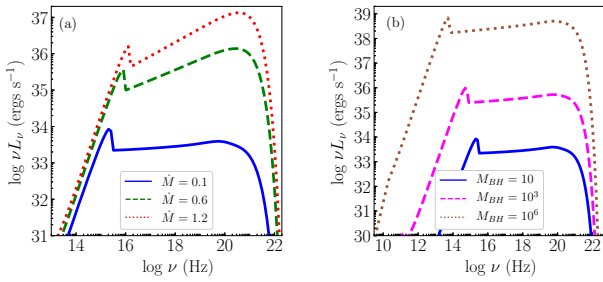

Fig. 13. Spectra from (a) $M_{\text{BH}} = 10 M_\odot$ for different accretion rates $\dot{M} = 0.1\dot{M}_{\text{Edd}}$ (blue, solid), $\dot{M} = 0.6\dot{M}_{\text{Edd}}$ (green, dashed), and $\dot{M} = 1.2\dot{M}_{\text{Edd}}$ (red, dotted); (b) $\dot{M} = 0.1\dot{M}_{\text{Edd}}$ but around $M_{\text{BH}} = 10 M_\odot$ (blue, solid), $M_{\text{BH}} = 10^3 M_\odot$ (magenta, dashed), and $M_{\text{BH}} = 10^6 M_\odot$ (brown, dotted). Other disc parameters are $E = 1.001$ and $\lambda = 2.4$.

Table 4. Various properties of the spectra plotted in Fig. 13a.

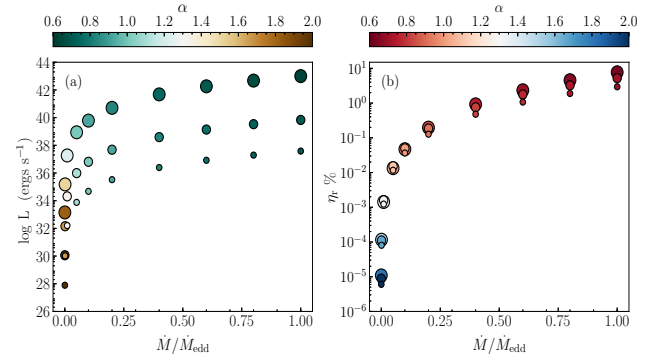
\dot{M} (\dot{M}_{Edd})	L (ergs s^{-1})	η_r (%)	α
0.1	4.731×10^{34}	0.037	0.939
0.6	8.301×10^{36}	1.068	0.720
1.2	6.684×10^{37}	4.298	0.627

In this work, we lay down the methodology to obtain a unique two-temperature solution using the principles of the second law of thermodynamics. We stated that the solution with the highest entropy near the horizon is the correct solution. Since the proposed correct transonic solution is the one with the highest entropy, therefore it is warranted that these solutions should be stable for the relevant boundary conditions. In fact, the collective wisdom of the community on accretion solutions has led to an expectation that close to the horizon, accretion should be transonic. However, for a given set of accretion disc parameters such as \dot{M} , E , and λ , we do have a large number of transonic two-temperature solutions and the question of stability of the solutions arises. In Sect. 3.3, we show that the gradient of entropy of the flow with the proton temperature, that is, $d\dot{M}_{\text{in}}/dT_{\text{pin}}$, is such that it tends to push the solution towards the temperature corresponding to the highest entropy solution. In other words, if our proposed solution is perturbed, then $d\dot{M}_{\text{in}}/dT_{\text{pin}}$ would automatically try to restore the solution to the one corresponding to the highest entropy.

Once we have established the method for obtaining the unique two-temperature solution in a rotating disc, we investigate the effects of various disc parameters on two-temperature accretion solutions. We obtained all possible solutions depending on E and λ for a given \dot{M} and M_{BH} (Fig. 7) and, in addition,

Table 5. Various properties of the spectra plotted in Fig. 13b.

M_{BH} (M_\odot)	L (ergs s^{-1})	η_r (%)	α
10	4.731×10^{34}	0.037	0.939
10^3	6.426×10^{36}	0.049	0.936
10^6	6.106×10^{39}	0.047	0.915


Fig. 14. (a) Variation of bolometric luminosity (in ergs s^{-1}) and (b) efficiency (in %) as a function of \dot{M} (in units of Eddington rate, \dot{M}_{Edd}). Colour bar indicates the spectral index (α). The BHs of different masses: $10 M_\odot$ (small circle), $10^3 M_\odot$ (medium circle), and $10^6 M_\odot$ (largest circle) are represented with increasing sizes of the circles. The parameters used here are $E = 1.001$ and $\lambda = 2.4$.

we also plot the emitted spectrum (Fig. 8). This also shows \dot{M} or M_{BH} do not alone determine the emitted spectrum or even the luminosity. Depending on E and λ , the solution changes and, thus, so do the spectrum and luminosity. The constants of motion are uniquely linked to the obtained spectrum.

There are indeed shocked accretion solutions even in the two-temperature regime. The shocked solutions are more luminous because in the post-shock region, inverse-Comptonisation becomes effective, the intensity of the power-law photons increases, as compared to a shock-free solution (Fig. 9). We also show that accretion flow can harbour steady shocks in a small but significant patch of the energy angular momentum parameter space (see Fig. 10). However, in general, the shock strength in the two-temperature flow is less than that in a one-temperature flow. Moreover, we did not find any particular spectral signature for the presence of shock, only that the shocked solution is more luminous than shock-free ones. However, it has been found in cases where the accretion rate of the flow is low, and where a weak bremsstrahlung feature is visible (in the high frequency end of the spectrum) in a shock-free

solution, that this feature disappears in a shocked solution (see Figs. 8c1,c2).

The radiative properties of a BH system depend on β and β_d , along with E , λ , M , and M_{BH} . For low values of β and β_d , the radiative efficiency is around a few percent, but for higher values, the efficiency can easily surpass ten percent, even for the same accretion rate and mass of the BH. We also showed that the spectra becomes broad-band if the mass of the central BH considered is higher, it also becomes more luminous but the spectral index remains roughly the same. Whereas, with the increase in accretion rate of the BH, the bandwidth of spectra remains the same, while the luminosity and the spectral index change significantly.

We did not consider pair production from the radiation of the accretion disc, nor did we consider particle production due to high energy interaction of the protons. We show, based on a posteriori calculations, that pair production is negligible and, therefore, the contribution of the pair annihilation emission in the total spectrum of the disc is also negligible. Similarly, we showed, with the help of a posteriori estimate, that the gamma-ray production from pion decay is also negligible.

In this work, we do not consider the viscosity of the flow, but invoking our results from our previous works on viscous accretion solutions in the single temperature regime (and also Appendix A), we argue that since the angular momentum is almost constant in the inner part of the disc and the viscous heating is much weaker than the magnetic dissipation, we neglect viscosity to ease our computation. Considering the single-temperature viscous flow as the representative case, we may conclude that there would not be any qualitative change resulting from a consideration of viscosity, although a possible quantitative effect cannot be ruled out. In fact, since we show magnetic dissipation to be a very efficient heating process, we could incorporate most heating processes by tuning the parameter β_d .

In conclusion, it is absolutely necessary to obtain a unique transonic two-temperature solution. To interpret the relevant observations, the hydrodynamics of the system must be properly handled. Selecting an arbitrary solution would mislead us. We allowed the second law of thermodynamics to dictate and select the solution, without taking recourse to any assumption, so that consistency is maintained. In addition to spherical flow (Sarkar & Chattopadhyay 2019), the accretion disc solution also corresponds to the highest entropy solution.

Acknowledgements. The authors acknowledge the anonymous referee for helpful suggestions which improved the quality of the paper. SS acknowledges Mr. Kuldeep Singh for help in python plotting.

References

- Abramowicz, M. A., & Fragile, P. C. 2013, *LRR*, 16, 1
- Abramowicz, M. A., Czerny, B., Lasota, J. P., & Szuszkiewicz, E. 1988, *ApJ*, 332, 646
- Abramowicz, M. A., Chen, X., Kato, S., Lasota, J. P., & Regev, O. 1995, *ApJ*, 438, L37
- Artemova, I. V., Bisnovatyi-Kogan, G. S., Bjoernsson, G., & Novikov, I. D. 1996, *ApJ*, 456, 119
- Becker, P. A., Das, S., & Le, T. 2008, *ApJ*, 677, L93
- Begelman, M. C., & Chiueh, T. 1988, *ApJ*, 332, 872
- Bisnovatyi-Kogan, G. S., & Lovelace, R. V. E. 1997, *ApJ*, 486, L43
- Bisnovatyi-Kogan, G. S., & Lovelace, R. V. E. 2001, *New Astron. Rev.*, 45, 663
- Blaes, O. 2014, *SSRv*, 183, 21
- Blandford, R. D., & Znajek, R. L. 1977, *MNRAS*, 179, 433
- Bondi, H. 1952, *MNRAS*, 112, 195
- Boldt, E., & Serlemitsos, P. 1969, *ApJ*, 157, 557
- Chakrabarti, S. K. 1989, *ApJ*, 347, 365
- Chakrabarti, S. K. 1996, *ApJ*, 464, 664
- Chakrabarti, S. K., & Titarchuk, L. G. 1995, *ApJ*, 455, 623
- Chandrasekhar, S. 1939, *An Introduction to the Study of Stellar Structure* (Chicago: Univ. of Chicago Press)
- Chattopadhyay, I. 2008, *AIP Conf. Ser.*, 1053, 353
- Chattopadhyay, I., & Chakrabarti, S. K. 2011, *Int. Journ. Mod. Phys. D*, 20, 1597
- Chattopadhyay, I., & Kumar, R. 2016, *MNRAS*, 459, 3792 (CK16)
- Chattopadhyay, I., & Ryu, D. 2009, *ApJ*, 694, 492
- Colpi, M., Maraschi, L., & Treves, A. 1984, *ApJ*, 280, 319
- Colpi, M., Maraschi, L., & Treves, A. 1986, *ApJ*, 311, 150
- Dahlbacka, G. H., Chapline, G. F., & Weaver, T. A. 1974, *Nature*, 250, 37
- Dihingia, I. K., Das, S., & Mandal, S. 2017, *MNRAS*, 475, 2164
- Eilek, J. A. 1980, *ApJ*, 236, 664
- Esin, A. A. 1997, *ApJ*, 482, 400
- Esin, A. A. 1999, *ApJ*, 517, 381
- Ferrari, A., Trussoni, E., Rosner, R., & Tsinganos, K. 1985, *ApJ*, 294, 397
- Fukue, J. 1987, *PASJ*, 39, 309
- Gould, R. J., & Schröder, G. P. 1967, *PhRv*, 155, 1404
- Holzer, T. E. 1977, *JGr*, 82, 23
- Hoyle, F., & Lyttleton, R. A. 1939, *Proc. Cam. Phil. Soc.*, 35, 405
- Ichimaru, S. 1977, *ApJ*, 214, 840
- Ipser, J. P., & Price, R. H. 1982, *ApJ*, 255, 654
- King, A. 2012, *MmSAI*, 83, 466
- Kolykhalov, P. I., & Syunyaev, R. A. 1979, *SvA*, 23, 189
- Kumar, R., & Chattopadhyay, I. 2013, *MNRAS*, 430, 386
- Kumar, R., & Chattopadhyay, I. 2014, *MNRAS*, 443, 3444
- Kumar, R., & Chattopadhyay, I. 2017, *MNRAS*, 469, 4221
- Kumar, R., Singh, C. B., Chattopadhyay, I., & Chakrabarti, S. K. 2013, *MNRAS*, 436, 2864
- Lanzafame, G., Molteni, D., & Chakrabarti, S. K. 1998, *MNRAS*, 299, 799
- Lasota, J. P. 1994, *Theory of Accretion Discs*, eds. W. J. Duschl, J. Frank, F. Meyer-Hofmeister, & W. M. Tscharnuter (Dordrecht: Kluwer), 2, 341
- Le, T., & Becker, P. A. 2005, *ApJ*, 632, 476
- Lee, S.-J., Ryu, D., & Chattopadhyay, I. 2011, *ApJ*, 728, 142
- Lee, S.-J., Chattopadhyay, I., Kumar, R., Hyung, S., & Ryu, D. 2016, *ApJ*, 831, 33
- Liang, E. P. T., & Thompson, K. A. 1980, *ApJ*, 240, L271
- Lightman, A. P., & Eardley, D. M. 1974, *ApJ*, 187, L1
- Lightman, A. P., Press, W. H., Price, R. H., & Teukolsky, S. 1975, *Problem Book in Relativity and Gravitation* (New Jersey: Princeton University Press)
- Mandal, S., & Chakrabarti, S. K. 2005, *A&A*, 434, 839
- Manmoto, T., Mineshige, S., & Kusunose, M. 1997, *ApJ*, 489, 791
- Melo, C. A. H. 2014, *Appl. Math. Comput.*, 232, 1025
- Nakamura, K. E., Kusunose, M., Matsumoto, R., & Kato, S. 1996, *PASJ*, 48, 761
- Narayan, R., & Yi, I. 1994, *ApJ*, 428, L13
- Narayan, R., & Yi, I. 1995, *ApJ*, 452, 710
- Novikov, I. D., & Thorne, K. S. 1973, *Black Holes*, eds. B. S. Dewitt, & C. Dewitt (New York: Gordon and Breach), 343
- Pringle, J. E., & Rees, M. J. 1972, *A&A*, 21, 1
- Pringle, J. E., Rees, M. J., & Pacholczyk, A. G. 1973, *A&A*, 29, 179
- Peitz, J., & Appl, S. 1997, *MNRAS*, 286, 681 (PA97)
- Phinney, E. S. 1981, *ESASP*, 161, 337
- Piran, T. 1978, *ApJ*, 221, 652
- Rees, M. J., Begelman, M. C., Blandford, R. D., & Phinney, E. S. 1982, *Nature*, 295, 17
- Rajesh, S. R., & Mukhopadhyay, B. 2010, *MNRAS*, 402, 961
- Salpeter, E. E. 1964, *ApJ*, 140, 796
- Sarkar, S., & Chattopadhyay, I. 2019, *Int. J. Mod. Phys. D*, 28, 1950037 (SC19)
- Schwartzman, V. F. 1971, *Sov. Astr.-AJ*, 15, 377
- Shakura, N. I., & Sunyaev, R. A. 1973, *A&A*, 24, 337
- Shapiro, S. L. 1973, *ApJ*, 180, 531
- Shapiro, S. L., Lightman, A. P., & Eardley, D. M. 1976, *ApJ*, 204, 187 (SLE76)
- Sharma, P., Quataert, E., Hammett, G. W., & Stone, J. M. 2007, *ApJ*, 667, 714
- Stepney, S., & Guilbert, P. W. 1983, *MNRAS*, 204, 1269
- Taub, A. H. 1948, *Phys. Rev.*, 74, 328
- Svensson, R. 1982a, *ApJ*, 258, 321
- Svensson, R. 1982b, *ApJ*, 258, 335
- Svensson, R. 1984, *MNRAS*, 209, 175
- Thorne, K. S., & Price, R. H. 1975, *ApJ*, 195, L101
- Turolla, R., Nobili, L., & Calvani, M. 1986, *ApJ*, 303, 573
- Vyas, M. K., Kumar, R., Mandal, S., & Chattopadhyay, I. 2015, *MNRAS*, 453, 2992 (VKMC15)
- Wardziński, G., & Zdziarski, A. 2000, *MNRAS*, 314, 183
- Weaver, T. A. 1976, *Phys. Rev. A*, 13, 1563
- Zel'dovich, Y. B. 1964, *Sov. Phys. Dok.*, 9, 195
- Zel'dovich, Y. B., & Novikov, I. D. 1971, *Relativistic Astrophysics Stars and Relativity* (Chicago: University of Chicago Press), 1
- Zdziarski, A. A. 1985, *ApJ*, 289, 514

Appendix A: Effects of viscosity in the system

Here, we discuss the effect of viscosity as (1) a mechanism to remove angular momentum outwards and (2) a source of heating in the system. The handling of viscosity is not trivial and applying it to two-temperature flows might further complicate the scenario and divert us from the question at hand, which is to find the unique transonic two-temperature accretion solutions for rotating flows. Presently, we recall the physics of viscosity in a relativistic but a single-temperature disc like [Chattopadhyay & Kumar \(2016\)](#) and show that near the horizon viscosity would have marginal effect. And in the outer region it would have a more significant effect, but since that region contributes less in the spectrum, so for our purpose, we can neglect it without compromising on the qualitative aspect of the present work. In viscous one-temperature flows we have azimuthal component of radial-momentum equation, the integrated form of which is:

$$-\rho u^r (L - L_0) = 2\eta\sigma_{\phi}^r, \quad (\text{A.1})$$

where, L_0 is the bulk angular momentum at the horizon. L is the local bulk angular momentum expressed as $L = hu_{\phi} = hl$. The specific angular momentum is defined as $\lambda = -u_{\phi}/u_t = -l/u_t$. The dynamical viscosity coefficient is $\eta_{\text{vis}} = \rho h\nu_{\text{vis}}$. Here, $\nu_{\text{vis}} = \alpha_{\text{vis}}ar(1 - v^2)^2$, is the kinematic viscosity, α_{vis} being the [Shakura & Sunyaev](#) viscosity parameter. σ_{ϕ}^r is the $r - \phi$ component of the shear tensor which has been evaluated using the expression given in [Peitz & Appl \(1997\)](#), [Chattopadhyay & Kumar \(2016\)](#). We abbreviate this form of viscosity as PA. Using the same procedure followed in [Chattopadhyay & Kumar \(2016\)](#), we find solutions for $E = 1.0005$, $\alpha_{\text{vis}} = 0.01$, $\lambda_0 = 2.60$, $\dot{M} = 0.01\dot{M}_{\text{Edd}}$ and $M_{\text{BH}} = 10 M_{\odot}$. Also, we investigate another case of one-temperature flows using the same set of parameters but assuming a form of viscosity which is generally followed in non-relativistic accretion disc equations and is given by $t_{r\phi} = -2\eta_{\text{vis}}\sigma_{r\phi} = -\alpha P$. We abbreviate it as the SS form of viscosity.

We plot in [Fig. A.1a](#) the angular momentum distribution of the system as a function of radius where each curve represent PA form of viscosity (green, solid) and SS viscosity (magenta, dotted). It is evident from the figure that angular momentum has been transported outwards (for both the cases) due to the presence of viscosity. Within a distance $r \sim 1000r_g$, angular momentum is almost constant, similar to the case of inviscid flows. The SS form of viscosity is weaker so it is less efficient in removing angular momentum and hence angular momentum remains almost constant $\lesssim 3 \times 10^4 r_g$. So, neglecting viscosity within these regions does not affect the system qualitatively. Viscosity in addition to removing angular momentum, also heats up the system. We plot in [Fig. A.1b](#) the heat that is dissipated due to the presence of the PA form of viscosity (green, solid) and SS form of viscosity (magenta, dotted). We see that using SS viscosity is inefficient with regard to heating up the system and it is always 3 orders of magnitude less than PA viscosity. Very far away from the BH, it is 9 orders of magnitude less than the former. We also compare the heating due to magnetic dissipation (Q_B , blue, dashed), which is the source of heating in this work of two-temperature inviscid flows. In [Fig. A.1b](#), Q_B has been calculated using the velocity, temperature, and pressure of the corresponding one-temperature flow and using $\beta_d = 0.02$. We see that Q_B is an efficient source of heating in the system. It always supercedes the heating due to the presence of GR viscosity, except in a very small region near the BH, where it becomes comparable. Thus, our assumption of taking Q_B as a source of heating in the

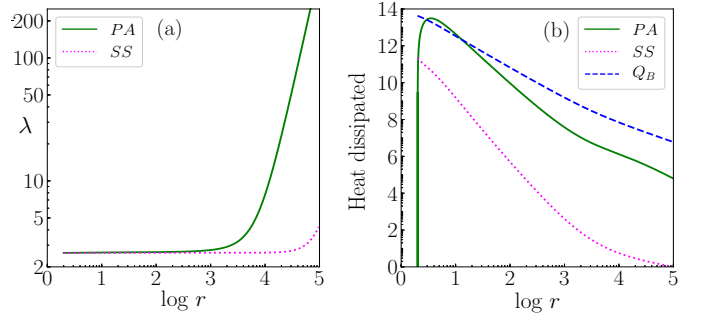


Fig. A.1. (a) Distribution of specific angular momentum (λ) and (b) heating in the system as a function of radius ($\log r$), when viscosity assumed is relativistic (green, solid) and Newtonian (magenta, dotted). Panel b: we also compare the heating due to magnetic dissipation, Q_B (blue, dashed), assuming $\beta_d = 0.02$. The flow parameters are $E = 1.0005$, $\alpha_{\text{vis}} = 0.01$, $\lambda_0 = 2.60$, $\dot{M} = 0.01\dot{M}_{\text{Edd}}$, and $M_{\text{BH}} = 10 M_{\odot}$.

absence of viscosity suffices for our problem. If viscosity was present, then the total heating would not have changed much, except in a very narrow region.

Appendix B: Estimation of electron-positron pair production in an advective two-temperature accretion disc

In this section, we estimate how many pairs can be produced using the two-temperature accretion solution as the background solution. There are three processes which could lead to pair (electron and positron) production in accretion discs, namely: photon-particle (electron, positron, or proton) interaction, particle-particle interaction, and photon-photon interaction. [Svensson \(1982a,b, 1984\)](#) gave a detailed analysis of the effect of electron-positron pairs present in relativistic and mildly relativistic plasmas. From these papers, it is apparent that photon-photon interaction is the dominant process responsible for the generation of pairs in accretion discs around BH. The reason behind particle-particle interactions and photon-particle interactions to be of less importance is their excessively small reaction cross-sections, which are of the order of $1/137$ (value of fine structure constant) and $(1/137)^2$, respectively. The photon-photon pair production process has a threshold condition, which is $E_1 E_2 (1 - \cos \theta_{pp}) \geq 2(m_e c^2)^2$, where E_1 and E_2 are the energies of the photons and θ_{pp} is the angle between these two photons. The advective two-temperature accretion disc solution take into account synchrotron emission which can produce ample amount of soft photons.

These photons are too soft to satisfy the criterion for pair production ([Esin 1999](#)). However, these photons, after interacting with high-energy electrons, can get upscattered to high energies, contributing to pair production. Also, the bremsstrahlung emission process produce ample amount of hard photons. Thus, at any particular radius, we can assume the radiation field to be made of a flat bremsstrahlung spectrum which is flat with a high energy cut-off and a Comptonisation spectrum, which is the sum of cut-off power law and the Wien tail ([Gould & Schröder 1967](#); [Zdziarski 1985](#); [Esin 1999](#)). We used the formula given by (see Eq. (B1) of the paper [Svensson 1984](#)) to compute the rate of photon photon pair production from two power law (PL) photon distribution with an exponentially cut-off, Wien photon interaction (W-W) and power law photons with Wien photons (PL-W). The pair density is estimated a posteriori, by using the temperature profile and velocity profile of the two-temperature solution

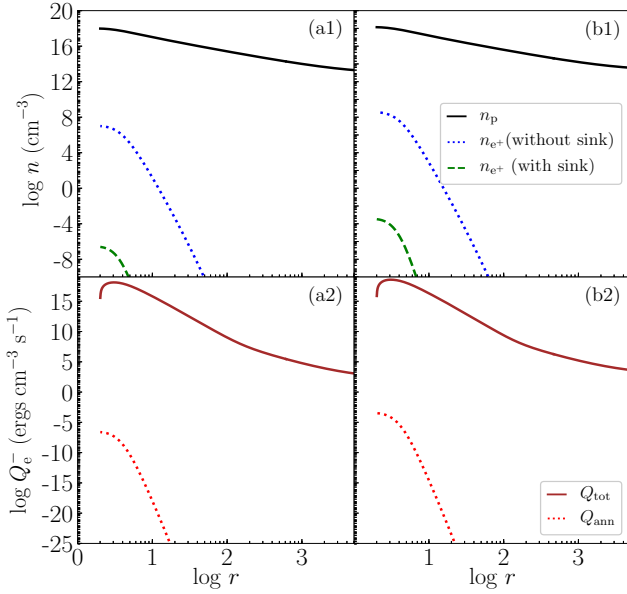


Fig. B.1. *a1, b1*: comparison of number density of protons n_p (black, solid), positron number densities n_{e^+} (without annihilation, blue, dotted), and with both production and annihilation rates (green, dashed). *a2, b2*: comparison of emissivities of the total radiative cooling Q_{tot} and emissivities due to annihilation of pairs Q_{ann} . For two sets of accretion disc parameters, (*a1, a2*) $\dot{M} = 1.0$, $\beta = 0.2$ and (*b1, b2*) $\dot{M} = 1.5$, $\beta = 0.15$. The other parameters are $\beta_d = 0.013$, $E = 1.001$, $\lambda = 2.61$ and $M_{\text{BH}} = 10 M_{\odot}$.

of this paper. The positron number density is computed from

$$n_{e^+} = \frac{1}{rH} \int (S^+ - S^-) r H dr. \quad (\text{B.1})$$

Here, n_{e^+} is the positron number density, S^{\pm} are the source and the sink terms or pair production and annihilation rate, respectively. S^{\pm} rates are adopted from Svensson (1984, 1982a, respectively). Since the accretion disc studied in this paper is composed of $e^- - p^+$ fluid, we first integrate Eq. (B.1) with only the S^+ term to compute the maximum possible n_{e^+} produced. With this distribution of n_{e^+} , we compute annihilation rate. We iterate few times till the solution converges. To estimate the production of electron-positron pairs (i.e. $e^- - e^+$), we chose two sets of accretion disc parameters presented in the manuscript since the spectrum for this disc parameters is hard and it is possible to obtain significant hard photons which satisfy pair-production threshold condition mentioned above. We compute pair production for the case of $\beta_d = 0.013$ of Fig. 12, and present in Figs. B.1a1, a2 the same two cases $\dot{M} = 1.0$, $\beta = 0.2$ and (b1, b2) $\dot{M} = 1.5$, $\beta = 0.15$. In the upper panels (a1, b1), we compare the proton number density n_p (black, solid), estimated positron number density n_{e^+} when annihilation rate is ignored (blue, dotted) and the ones for which both production and annihilation rates are considered (green, dashed). The blue curve is the maximum possible number of positrons that can be produced in the disc and $n_{e^+} \ll n_p$. In the bottom panels (a2, b2), we plot the corresponding emissivity Q_{ann} obtained due to the annihilation of pairs (red, dotted) and compared that with the total emissivity Q_{tot} (brown, solid). The estimated number density of positrons is negligible and the contribution to the total emissivity is negligibly small compared to the total emissivity obtained from radiative processes like, synchrotron, bremsstrahlung, and Comptonisation. This a posteriori estimation justifies our assumption of not considering pair production in the present work.

Appendix C: Estimation of the gamma-ray emission by pion interaction

In this section, we discuss whether pion production leads to a viable amount of cooling in the disc and whether it exhibits any observational signature. The reactions leading to pion (π^{\pm} , π^0) production by proton-proton interactions are as given below (Eilek 1980):



The threshold temperature for these reactions is 290 MeV. For negative pions temperatures of >2 GeV are required. Thus, it is assumed that negligible π^- will be present in the disc. The π^0 further decay into gamma-ray photons (Kolykhalov & Syunyaev 1979):



and π^+ decays into muon and muon neutrinos, which further decays into electron neutrinos, muon anti-neutrinos and positrons, respectively.



We restrict our study to neutral pions π^0 since we are interested to study the gamma ray emissivities obtained from an accreting Schwarzschild BH. The rate of π^0 production is given by (in units of $\text{cm}^{-3} \text{s}^{-1}$):

$$\mathcal{R}_{\pi^0} = \frac{n^2}{2} \langle \bar{\sigma} \bar{v} \rangle_{\pi^0}. \quad (\text{C.4})$$

Here, $\langle \bar{\sigma} \bar{v} \rangle_{\pi^0}$ (units of $\text{cm}^3 \text{s}^{-1}$) is the velocity-weighted cross-section, which was evaluated for π^0 by Dahlbacka et al. (1974), assuming experimental cross sections for pion production and a relativistic Maxwell-Boltzmann distribution for protons. This was further investigated by Weaver (1976) and Kolykhalov & Syunyaev (1979), who computed $\langle \bar{\sigma} \bar{v} \rangle$ for π^0 as well as for π^+ . This function is strongly dependent on the proton temperature. In Colpi et al. (1986) obtained a best-fit to these curves, the expression of which is given in Eqs. (10) of their paper and the same form is used to compute the emissivity of γ -rays. It is clear from Eq. (C.2) that each π^0 decays into two photons, therefore, the number of photons produced per unit time per unit volume is $n^2 \langle \bar{\sigma} \bar{v} \rangle_{\pi^0}$. We analysed a posteriori the total gamma-ray luminosity as measured by an observer at infinity using the methodology adopted in Colpi et al. (1984).

We checked the production of γ rays by varying the accretion rate of the system from $\dot{M} = 0.01$ (red, dotted) to 0.10 (green, dashed) and 1.0 (blue, solid) for a $10 M_{\odot}$ BH (see Figs. C.1a1, a2). Since this emission is crucially dependent on the proton temperature, we plot $\log T_p$ as a function of $\log r$ in Fig. C.1a1 for the different accretion rates. The set of disc parameters used are $\lambda = 2.61$ and $E = 1.0007$. For $\dot{M} = 0.01$, & 0.1, the accretion solution does not undergo shock transition (see, Fig. 9) and the T_p distribution of the global accretion solution is similar. However, for the same set of E , λ but $\dot{M} = 1.0$, there is a stable accretion shock and the T_p jumps at the shock location. The corresponding spectra (Fig. C.1a2) for the three values of \dot{M} show a marked difference where the shocked accretion solution is more luminous and the spectrum is harder (solid, blue), and becomes

less luminous and softer for lower \dot{M} . The gamma-ray emission (calculated a posteriori) is represented in grey colour. As a result of π^0 decay, the contribution in the high energy regime increases. Quantitatively, the gamma-ray luminosity for different accretion rates are related by the following relation $L_{\gamma\text{ph}}(\dot{M} = 1.0) \simeq 200L_{\gamma\text{ph}}(\dot{M} = 0.1)$ and $L_{\gamma\text{ph}}(\dot{M} = 0.1) \simeq 100L_{\gamma\text{ph}}(\dot{M} = 0.01)$. Although $L_{\gamma\text{ph}}(\dot{M} = 1.0)$ is much higher than that compared to lower \dot{M} s but compared to the overall luminosity for each \dot{M} , $L_{\gamma\text{ph}}$ is pitifully low. We chose $\dot{M} = 0.1$ and the same values of E and λ and then studied the gamma-ray production for accretion discs onto different masses of central BH. We plot the proton temperature distribution T_p vs r in log-log scale and the corresponding spectra in Figs. C.1b1, b2, for central BH masses $M_{\text{BH}} = 10^2$ (blue, solid), 10^4 (green, dashed) and 10^6 (red, dotted). The M_{BH} affects the system quantitatively but not qualitatively. While the luminosity increases and spectra become more broad band with the increase in M_{BH} , but the efficiency of gamma-ray emission ($L_{\gamma\text{ph}}/(\dot{M}c^2)$) remains almost same $\sim 10^{-8}$. In both cases (change in accretion rate and mass of BH), the fractional change in luminosity is always $< 10^{-5}$. This analysis justifies our assumption of neglecting pion production leading to emission of γ -rays.

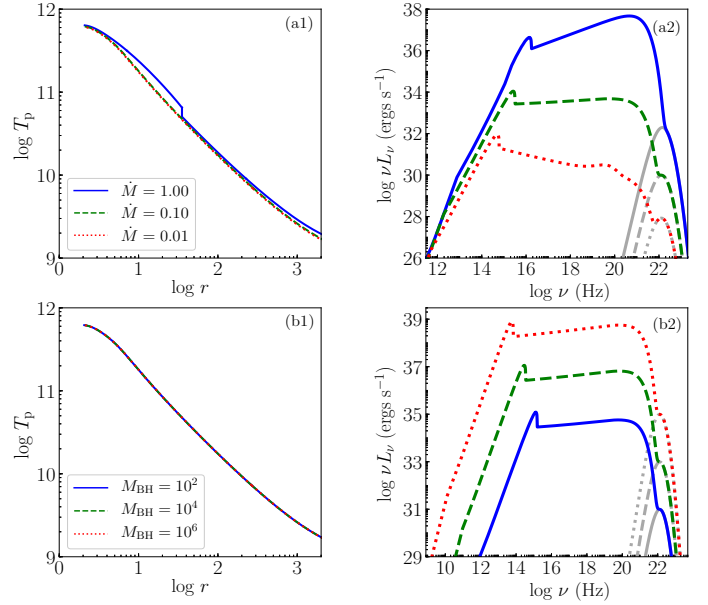


Fig. C.1. *a1, a2:* dependence on the accretion rate, $\dot{M} = 0.01$ (red, dotted), 0.1 (green, dashed), and 1.0 (blue, solid). *(a1)* $\log T_p$ as a function of $\log r$ and *(a2)* $\log \nu L_\nu$, with $\log \nu$. *(b1, b2)* Dependence on mass of BH, $M_{\text{BH}} = 10^2$ (blue, solid), 10^4 (green, dashed), 10^6 (red, dotted) in the production of γ rays. *(b1)* $\log T_p$ as a function of $\log r$ and in *(b2)* the corresponding spectra are plotted. The gamma ray emission is presented in grey.

**Institute of Computational Mathematics and Mathematical Geophysics
of Siberian Branch of Russian Academy of Sciences**

CERTIFICATE of PARTICIPATION

This is to certify that

Shilpa Sarkar

has participated to Second Workshop on Numerical Modeling
in MHD and Plasma Physics: methods, tools, and outcomes

Vice-chair of Program committee



Dr. Igor Kulikov

October 10-11, 2019, Moscow, Russia

Two-temperature advective transonic accretion flows around black holes

Shilpa Sarkar^{1,2*}, Indranil Chattopadhyay^{1**}

¹Aryabhata Research Institute of Observational Sciences (ARIES), Manora Peak, Nainital-263002, India

²Pt. Ravishankar Shukla University, Great Eastern Road, Amanaka, Raipur, Chhattisgarh 492010, India

E-mail: *shilpa@aries.res.in, **indra@aries.res.in

Abstract. We present here unique transonic two-temperature accretion solutions in presence of radiation processes. Unlike one-temperature flow, the set of equations governing two-temperature flow is not complete, since for the latter, the number of equations is less than the number of flow variables. Consequently, a large number of transonic solutions of the equations of motion exist, for a given set of constants of motion. We invoke the second law of thermodynamics and identified the solution with the maximum entropy as the physically possible solution. In this paper, we compare spherical and rotating accretion two-temperature flows. We also show that the luminosity, as well as radiative efficiency of rotating flows, is higher by an order of magnitude, as compared to spherical flows.

1. Introduction

Accretion is a process by which the gravity of a compact object like white dwarf, neutron star or a black hole (BH), accumulates matter onto it, from the surrounding environment. This mechanism powers the brightest sources in the Universe, which are Active Galactic Nuclei (AGN). Accretion model started with the seminal papers of Hoyle & Lyttleton[1] (1939) and Bondi (1952)[2] who gave the first accretion solutions around a Sun-like star and a compact object respectively. But it was until a decade later, with the discovery of quasars and X-ray binaries, that accretion as a mechanism to explain the huge amount of emission coming from these objects, was realised. In 1964, Salpeter[3], used the Bondi accretion model (available at that time) to explain the luminosities of quasars ($L \sim 10^{12}L_{\odot}$). But, he reported that this flow is too fast to explain it. Shakura & Sunyaev (1973)[4], on the other hand, considered a rotation dominated flow to allow maximum time before the flow enters into the BH. Such a flow has Keplerian azimuthal velocity and negligible radial velocity. The flow is cold with negligible pressure gradient force, geometrically thin and optically thick. These disks were famously known as Shakura-Sunyaev disks (SSD) or Keplerian Disks (KD). The overall spectral profile of a SSD is a modified multi-coloured blackbody. Although this model was successful in explaining the thermal component of X-ray binaries and AGNs, but it could not explain the non-thermal part present in the spectra of these objects. Thorne & Price in 1975[7] argued that the instability present at the inner portion of the accretion disk could puff up the optically thick, radiation pressure dominated region into an optically thin, gas pressure dominated region. Using this assumption, Shapiro, Lightman & Eardley in 1976[6], put forward the first model of



two-temperature theory. They assumed that the inner puffed up region consisted of protons and electrons described by two-different temperature distributions and explained the hard X-rays coming from Cygnus X-1. From the above papers, a general conclusion can be drawn that accretion flow should be a combination of Keplerian and sub-Keplerian matter. It has to be transonic, since the matter crosses the horizon at the speed of light, while at the outer boundary it should be subsonic. In 1980, Liang & Thompson (LT80)[8] pointed out this fact and reported that rotating sub-Keplerian flows around BH possess multiple sonic points, due to the presence of gravity and angular momentum. Presence of relativistic effects induces the formation of another sonic point. It was later showed that rotating sub-Keplerian flows passing through the outer sonic point, may undergo shock transition and enter the BH through the inner sonic point (Fukue 1987[9], Chakrabarti 1989[10]). Sub-Keplerian flows also have significant advection and the flow is also hotter than SSD (Abramowicz *et al.* 1988[11], for a brief review see, Bisnovatyi-Kogan & Lovelace 2001[12]). Few works were also focussed to study radiative properties of these systems. Colpi, Marashi & Treves (1984)[13] studied two-temperature version of spherical flows around BHs, where they elaborately discussed the radiative mechanisms while Narayan & Yi (1995) (NY95)[14] considered rotating advection-dominated two-temperature flows in order to obtain the spectra of low accreting BH systems. But in NY95, self-similarity was assumed while obtaining solutions, which is valid only far away from the BH and cannot be assumed throughout the flow. Also electron energy equation was dealt locally, neglecting its advection. In 1996, Nakamura *et al.* [15], were the first to obtain global transonic two-temperature advection dominated accretion solutions. Manmoto *et al.* [16] in 1997, computed the spectra of such flows. Since then, works have been done in two-temperature advection dominated branch of solutions, notable being by Chakrabarti & Titarchuk (1995) [17], Bisnovatyi-Kogan & Lovelace (1997)[18] and Mandal & Chakrabarti (2005)[19]. Few works considered transonicity like Rajesh & Mukhopadhyay (2010)[20] and Dihingia *et al.* (2017)[21].

Flows around BH are trans-relativistic in nature varying from thermally non-relativistic, adiabatic index (Γ) $\sim 5/3$, very far away from the central object to mildly-relativistic/relativistic, $\Gamma \rightarrow 4/3$, near the horizon, therefore a fixed Γ equation of state (EoS) is untenable. However, most of the previous works in two-temperature model assumed so. In 2009, Chattopadhyay & Ryu[22], gave an approximate analytical form of EoS for multispecies flow, which is easy to handle and it matches perfectly well[23] with the relativistically perfect EoS[24].

It is worth noting that the number of hydrodynamic equations in one-temperature and two-temperature is same, but there is one more variable in the latter (T_e =electron and T_p =ion temperature). Number of unknowns is hence more than the number of equations. Or in other words the *two-temperature model is degenerate*. If we scan the parameter space of two-temperature transonic solutions we can obtain infinite solutions for the same constants of motion. This problem was never been reported and solved for, in literature known so far, although hint of this was given in LT80, where they parametrized T_e and T_p by a constant ratio. The standard Coulomb interaction between electrons and ions is weak, therefore the energy exchange is not substantial to establish a stronger correlation between T_e and T_p . In absence of any other physical processes dictated by plasma physics, all other parametrization employed by various authors are arbitrary. In Sarkar & Chattopadhyay (2019) (SC19)[25], we gave a detailed methodology to obtain a unique transonic two-temperature accretion solution around BHs, albeit for spherical accretion. In SC19, we derived for the first time, an entropy measure form, close to the horizon. Second law of thermodynamics dictates that nature prefers a solution with maximum entropy. Hence, we select the maximum entropy solution as the unique transonic two-temperature solution for a given set of constants of motion. In this paper, we extend SC19 to rotating, conical accretion flow around BHs. Since, rotating flows possess multiple sonic points, complexity of the problem is increased further. In the methodology section, we will discuss in detail how SC19 is modified

in the present paper. We have also used the variable Γ index CR EoS which removed the problem of specifying the adiabatic indices of the species.

The paper is divided into the following sections. In section (2), we will give a brief overview of the basic equations and assumptions used to model the flow. In section (3), we will discuss the methodology to find unique transonic two-temperature solutions, showing some important results in section (4) and would finally conclude in section (5).

2. Basic Equations and Assumptions

We consider here inviscid conical rotating axis-symmetric two-temperature accretion flows around BHs described by Schwarzschild metric. It is to be noted that qualitative feature of the flow is not hampered while neglecting viscosity. It has been observed in viscous, single temperature, rotating accretion flow that angular momentum remains almost constant till \sim few $\times 100$ Schwarzschild radius (r_g) [26, 27, 28]. Spherical coordinate system has been employed where, r , θ , ϕ have their usual meaning and t is the time coordinate. It is to be noted that throughout the paper, we have used a system of units where, $G = M = c = 1$, such that the unit of length, time and velocity are given as $r_g = GM/c^2$, $r_g/c = GM/c^3$ and c , respectively, where $G =$ Gravitational constant, $M =$ mass of BH, $c =$ speed of light. In the subsequent sections all the variables are in this unit system unless otherwise mentioned. The system is in steady state and is axis-symmetric. Additionally, all the quantities are averaged in the vertical direction. Therefore, $\partial/\partial t = \partial/\partial \phi = \partial/\partial \theta = 0$.

The energy momentum tensor of the accreting matter is $T^{\mu\nu} = (e + p)u^\mu u^\nu + pg^{\mu\nu} + t_{rad}$, where, e and p are the internal energy density and isotropic gas pressure, all measured in local fluid frame, u^μ s are the components of four-velocity and t_{rad} is the radiation tensor. $g^{\mu\nu}$ s are the inverse of metric tensor components, non-zero components of which are :

$$g_{tt} = -\left(1 - \frac{2}{r}\right); g_{rr} = \left(1 - \frac{2}{r}\right)^{-1}; g_{\theta\theta} = r^2; g_{\phi\phi} = r^2 \sin^2 \theta \quad (1)$$

Conservation law for : (1) Energy : $T^{\mu\nu}_{;\nu} = 0$, (2) particle density flux : $(nu^\nu)_{;\nu} = 0$ where, $n =$ particle number density. If we project the four-divergence of the energy-momentum tensor along the space direction, *i.e.* $h^i_\mu T^{\mu\nu}_{;\nu} = 0$, we get the Euler equation, radial component of which is :

$$u^r \frac{du^r}{dr} + \frac{1}{r^2} - (r - 3)u^\phi u^\phi + (g^{rr} + u^r u^r) \frac{1}{e + p} \frac{dp}{dr} = 0. \quad (2)$$

The azimuthal component is absent, since the angular momentum is a constant of motion in the absence of viscosity.

On integrating the equation for conservation of particle density flux, we get the form of mass accretion rate, which is another constant of motion :

$$\dot{M} = 4\pi \rho u^r r^2 \cos \theta, \quad (3)$$

where, $\rho = n(m_p + m_e) =$ mass density, m_p and m_e being the mass of proton and electron respectively, θ is the angle which the surface of the flow makes with the normal.

The first law of thermodynamics is $u_\mu T^{\mu\nu}_{;\nu} = 0$ and can be simplified to :

$$u^r \left[\left(\frac{e + p}{\rho} \right) \rho_{,r} - e_{,r} \right] = \Delta Q, \quad (4)$$

where, $\Delta Q = Q^+ - Q^-$. Q^+ is the rate of heating present in the flow and Q^- gives the cooling rate. Generalised Bernoulli constant, a constant of motion, is obtained by integrating Eq.(2) with the help of Eq.(4) and is given by,

$$E = -hu_t \exp(X_f), \quad (5)$$

where, $h = (e + p)/\rho$, is the specific enthalpy and $X_f = \int \frac{\Delta Q_p + \Delta Q_e}{\rho h u^r} dr$. E is constant even in the presence of dissipation. In case of no dissipation, $X_f = 0$ and $E \rightarrow \mathcal{E} = -h u_t$, which is the canonical form of relativistic Bernoulli constant [26].

To close the equations of motion, we use CR EoS [22], which for electron-proton plasma, in geometric units, is given by,

$$e = n_e m_e \left(f_e + \frac{f_p}{\eta} \right) = \frac{\rho f}{\tilde{K}}, \quad (6)$$

where, $\tilde{K} = 1 + 1/\eta$ and $\eta = m_e/m_p$. Here, $f_i = 1 + \Theta_i \left(\frac{9\Theta_i + 3}{3\Theta_i + 2} \right)$ and $\Theta_i = \frac{kT_i}{m_i c^2}$ is the non-dimensional conjugate of the dimensional temperature (T_i), where $k =$ Boltzmann constant and $i \equiv$ electron or proton. Polytropic index and adiabatic index are defined as, $N_i = \frac{df_i}{d\Theta_i}$ and $\Gamma_i = 1 + \frac{1}{N_i}$. If we rewrite the first law of thermodynamics Eq.(4), separately for protons and electrons using Eq.(6), we get the differential equation for their temperatures :

$$\frac{d\Theta_p}{dr} = -\frac{\Theta_p}{N_p} \left(\mathcal{A} + \frac{1}{v(1-v^2)} \frac{dv}{dr} \right) - \mathbb{P}\eta \quad \text{and} \quad \frac{d\Theta_e}{dr} = -\frac{\Theta_e}{N_e} \left(\mathcal{A} + \frac{1}{v(1-v^2)} \frac{dv}{dr} \right) - \mathbb{E}, \quad (7)$$

where, $\mathcal{A} = -\frac{2r-3}{r(r-2)}$, $\mathbb{P} = \frac{\Delta Q_p \tilde{K}}{\rho u^r N_p}$, $\mathbb{E} = \frac{\Delta Q_e \tilde{K}}{\rho u^r N_e}$, These equations are not independent, but are coupled by a Coulomb coupling term. If we simplify Eq.(2), using Eqs.(3),(6-7), we obtain:

$$\frac{dv}{dr} = \frac{\mathcal{N}}{\mathcal{D}}, \quad (8)$$

where, $v = \sqrt{u_r u^r / (1 + u_r u^r)}$, $\mathcal{N} = -\frac{1}{r(r-2)} + \frac{\lambda^2 \gamma_\phi^2 (r-3)}{r^4} + a^2 \mathcal{A} + \frac{\Gamma_p N_p \mathbb{P} + \Gamma_e N_e \mathbb{E}}{h \tilde{K}} - \frac{\Delta Q}{\rho h u^r}$ and $\mathcal{D} = \frac{v}{1-v^2} \left(1 - \frac{a^2}{v^2} \right)$. The sound speed is defined as, $a = \sqrt{\mathcal{G}/h \tilde{K}}$, where $\mathcal{G} = \frac{\Gamma_p \Theta_p}{\eta} + \Gamma_e \Theta_e$.

2.1. Sonic point conditions and shock conditions :

The mathematical form of Eq.(8) suggests that there exists a point where the numerator vanishes. For smooth continuous flow, the denominator also has to vanish. Thus, dv/dr has a 0/0 form and this point is called the sonic point of the flow. The sonic point conditions are : $\mathcal{N} = 0$ and $\mathcal{D} = 0$. At the sonic point we need to employ L'Hospital rule in order to find $(dv/dr)_c$.

The relativistic shock conditions or the Rankine-Hugoniot conditions [29] are : (1) Conservation of mass flux : $[M] = 0$, (2) energy flux : $[E] = 0$ and (3) momentum flux : $[(e+p)u^r u^r + pg^{rr}] = 0$, where, the square brackets denote the difference of the quantities across the shock.

2.2. Radiative processes :

- Equipartition of magnetic energy density demands that magnetic field lines reconnect such that magnetic field is not frozen into the plasma [30, 31]. The heat dissipated [32] in such a way (Q_B) is assumed to be absorbed by protons and electrons in equal portions ($\delta = 0.5$).
- Coulomb coupling (Q_{ep}) cause energy exchange between electrons and protons [33].
- Inverse bremsstrahlung (Q_{ib}) acts as a cooling mechanism for protons [34, 35].
- Electron is cooled via three processes : bremsstrahlung (Q_{br}) [36], synchrotron (Q_{syn}) [37] and inverse-Comptonization (Q_{ic}) [37].
- If the temperature of the electrons is less than the energy of the interacting photons, then electrons can gain heat via Compton heating (Q_{comp}).

Thus to conclude we have, for protons : $Q_p^+ = \delta Q_B$ and $Q_p^- = Q_{ep} + Q_{ib}$, and for electrons : $Q_e^+ = (1 - \delta)Q_B + Q_{ep} + Q_{comp}$ and $Q_e^- = Q_{br} + Q_{syn} + Q_{ic}$. In addition, all the relativistic transformations have been considered to compute the actual energy loss.

2.3. Entropy accretion rate expression :

To obtain the expression for entropy, one needs to integrate the first law of thermodynamics by switching off explicit heating and cooling terms . Due to the presence of Coulomb interaction term, Eq.(4) is not analytically integrable. However, close to the BH horizon, gravity overpowers all other interactions. Therefore, at $r = r_{\text{in}}$ (asymptotically close to the horizon), Q_{ep} can be neglected. Thus we obtain,

$$\frac{d\Theta_p}{dr} = \frac{\Theta_p}{N_p} \frac{1}{n_p} \frac{dn_p}{dr} \quad \text{and} \quad \frac{d\Theta_e}{dr} = \frac{\Theta_e}{N_e} \frac{1}{n_e} \frac{dn_e}{dr} \quad (9)$$

Hence, we can integrate equation (9) at r_{in} to obtain :

$$n_{\text{ein}} = \kappa_1 \exp\left(\frac{f_{\text{ein}} - 1}{\Theta_{\text{ein}}}\right) \Theta_{\text{ein}}^{\frac{3}{2}} (3\Theta_{\text{ein}} + 2)^{\frac{3}{2}} \quad \text{and} \quad n_{\text{pin}} = \kappa_2 \exp\left(\frac{f_{\text{pin}} - 1}{\Theta_{\text{pin}}}\right) \Theta_{\text{pin}}^{\frac{3}{2}} (3\Theta_{\text{pin}} + 2)^{\frac{3}{2}} \quad (10)$$

where, κ_1 and κ_2 are the integration constants which are measure of entropy. Subscript ‘in’ indicates quantities measured just outside the horizon. Due to charge neutrality in the flow $n_{\text{ein}} = n_{\text{pin}} = n_{\text{in}}$. Therefore we can write,

$$n_{\text{in}} = \sqrt{n_{\text{ein}} n_{\text{pin}}} = \kappa \sqrt{\exp\left(\frac{f_{\text{ein}} - 1}{\Theta_{\text{ein}}}\right) \exp\left(\frac{f_{\text{pin}} - 1}{\Theta_{\text{pin}}}\right) \Theta_{\text{ein}}^{\frac{3}{2}} \Theta_{\text{pin}}^{\frac{3}{2}} (3\Theta_{\text{ein}} + 2)^{\frac{3}{2}} (3\Theta_{\text{pin}} + 2)^{\frac{3}{2}}}, \quad (11)$$

where, $\kappa = \sqrt{\kappa_1 \kappa_2}$. Thus, the expression of entropy accretion rate can be written as,

$$\begin{aligned} \dot{\mathcal{M}}_{\text{in}} &= \frac{\dot{M}}{4\pi\kappa(m_e + m_p)} \\ &= \sqrt{\exp\left(\frac{f_{\text{ein}} - 1}{\Theta_{\text{ein}}}\right) \exp\left(\frac{f_{\text{pin}} - 1}{\Theta_{\text{pin}}}\right) \Theta_{\text{ein}}^{\frac{3}{2}} \Theta_{\text{pin}}^{\frac{3}{2}} (3\Theta_{\text{ein}} + 2)^{\frac{3}{2}} (3\Theta_{\text{pin}} + 2)^{\frac{3}{2}} u^r r^2 \cos(\theta)} \quad (12) \end{aligned}$$

In the next section we will briefly discuss the significance of this formula and its use as a tool to remove degeneracy in two-temperature problem.

3. Methodology for obtaining unique transonic solutions

3.1. Finding of sonic points and obtaining a transonic solution :

This is the first step to find a general two-temperature accretion solution. Since the system is dissipative, sonic points are not known a priori. In order to compute the location of the sonic point/points, for a given set of constants of motion (E , \dot{M} and λ), we start, with integration from $r_{\text{in}} = 2.001$. At r_{in} , $X_f = 0$ and from Eq.(5), $E \simeq \mathcal{E}$. Simplifying this, we obtain an analytical form for v_{in} (which is a function of $T_{\text{p in}}$, $T_{\text{e in}}$). We assume a value of $T_{\text{p in}}$ and iterate $T_{\text{e in}}$, while simultaneously calculating v_{in} , until both the sonic point conditions (see, section 2.1) are satisfied. But as discussed before, rotating flows can possess multiple sonic points. So we keep $T_{\text{p in}}$ same and reduce/increase $T_{\text{e in}}$ by a large factor, and iterate it again until the sonic point conditions are satisfied. However, multiple sonic points form only for a limited range of constants of motion. Once we get the sonic point, we integrate Eqs.(7) and (8) inwards and outwards from the sonic point, using 4th order Runge-Kutta method to obtain transonic solutions. At the sonic point, $dv/dr = (dv/dr)_c$ (see section 2.1).

Fig.1(a1-a4), shows the Mach number ($M = v/a$) plot vs $\log r$ plot for ‘spherical’ flows ($\lambda = 0$) and in panel (b1-b6) solutions are for ‘rotating’ conical flows ($\lambda = 2.5$) around BH. Parameters used are $E = 1.002$, $\dot{M} = 0.05\dot{M}_{\text{edd}}$, $M_{\text{BH}} = 10M_{\odot}$, $\theta = 60^\circ$. Thus, the constants of motion are same in all the cases, but $T_{\text{p in}}$ is varied to get different solutions. The dotted solutions in every

case are mathematical transonic outflows. Solid lines denote the global accretion solutions since it connects BH horizon from infinity.

We can see that in case of spherical flows the global solution always passes through a single sonic point (a1-a4), while in case of rotating flows, the flow might pass through one or more sonic points (b1-b6). In (b1-b2), global solution passes through the outer sonic point only, while in (b6) it passes through the inner sonic point. In both the cases only one physical sonic point is present. In (b3-b6) solutions possess multiple sonic points, out of which in (b4), we see that the flow harbours shock. So the global solution first passes through the outer sonic point, becomes supersonic and then after going through a shock transition, jumps to the subsonic branch and enter the BH supersonically after passing through the inner sonic point.

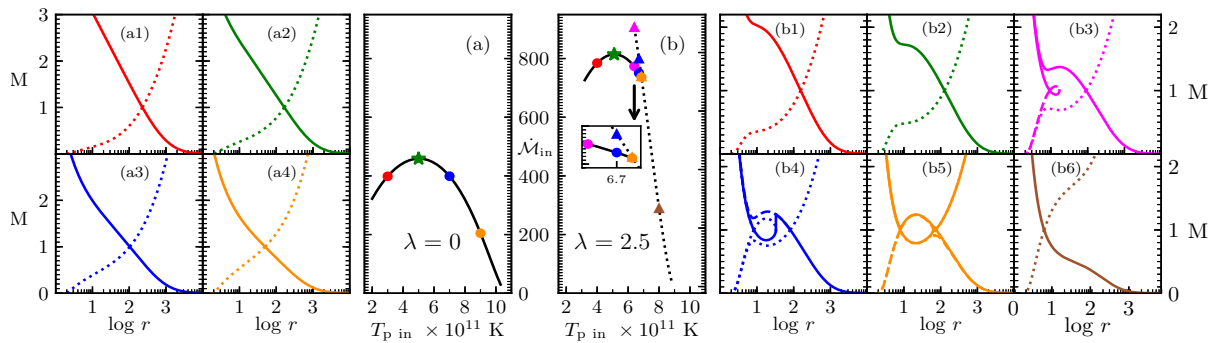


Figure 1: Left : (a) \dot{M}_{in} vs $T_{p in}$ plot for spherical flows. Single sonic point exist for every $T_{p in}$. Panels (a1-a4) M vs $\log r$ plot for various $T'_{p in}$ s marked with solid coloured dots in panel (a). The values of $T_{p in}$ are : (a1) $3.0 \times 10^{11} K$, (a2) $4.0 \times 10^{11} K$, (a3) $5.0 \times 10^{11} K$, (a4) $6.0 \times 10^{11} K$. Right : (b) Shows \dot{M}_{in} vs $T_{p in}$ plot for rotating conical flows ($\lambda = 2.5$). Solid black curve is for the solutions passing through outer sonic point, while dotted black curve is for solutions passing through inner sonic points. Panels (b1-b4): Shows solutions for various $T'_{p in}$ s marked in panel (b), value of which are: (b1) $4.0 \times 10^{11} K$, (b2) $5.1 \times 10^{11} K$, (b3) $6.4 \times 10^{11} K$, (b4) $6.7 \times 10^{11} K$, (b5) $6.86 \times 10^{11} K$, (b6) $8.0 \times 10^{11} K$. Entropy maximises at a certain $T_{p in}$ in both the cases (green star). Parameters used are $E = 1.002$, $\dot{M} = 0.05\dot{M}_{edd}$, $M_{BH} = 10M_{\odot}$, $\theta = 60^{\circ}$.

3.2. Selection of a unique solution :

A solution should be unique for a given set of constants of motion, but in Fig.1(a1-a4) and (b1-b6), it was noticed that a change in $T_{p in}$ gave solutions with completely new topology and sonic point properties. In Fig.1, we plotted the case of spherical flows, in order to contrast for the complexity that arises due to the presence of angular momentum. Any wrong choice of solution would give us a completely different information and hence a wrong spectrum. So it is necessary to select the correct solution. The only way to deal with this degeneracy is to have a *measure of entropy* of the system. This measure of entropy is plotted in panel (a) and (b) against the corresponding $T'_{p in}$ s, using the entropy form given by Eq.(12).

In case of spherical flows, which possess single sonic points, there is a clear entropy maxima at $T_{p in} = 5 \times 10^{11} K$ (green star). By employing the second law of thermodynamics, we select this solution (panel a2). Thus, we are able to obtain a unique transonic two-temperature solution for the given set of constants of motion [25].

In case of rotating flows, global solutions may pass through one or more sonic points. So the system is complicated unlike spherical flows. Dotted black curve in panel (b) is for solutions passing through inner sonic points while solid black curve is for solutions passing through outer sonic points. In a certain range of $T_{p in}$ both inner and outer sonic points exist (solution b3-b5).

We can see that the entropy maximises in the outer sonic point branch of solutions (green star). Since flow starts from infinity, it would select the maximum entropy solution. Then, it could pass through an inner sonic point only if the shock conditions are satisfied (see section 2.1). For the present case, $T_{p\text{ in}} = 5.1 \times 10^{11} K$ possess maximum entropy and the global solution passes through outer sonic point (solution b2). In the sections to follow, we use this method of maximising entropy to obtain global advective transonic two-temperature accretion solutions.

4. Results

4.1. General transonic two-temperature solution :

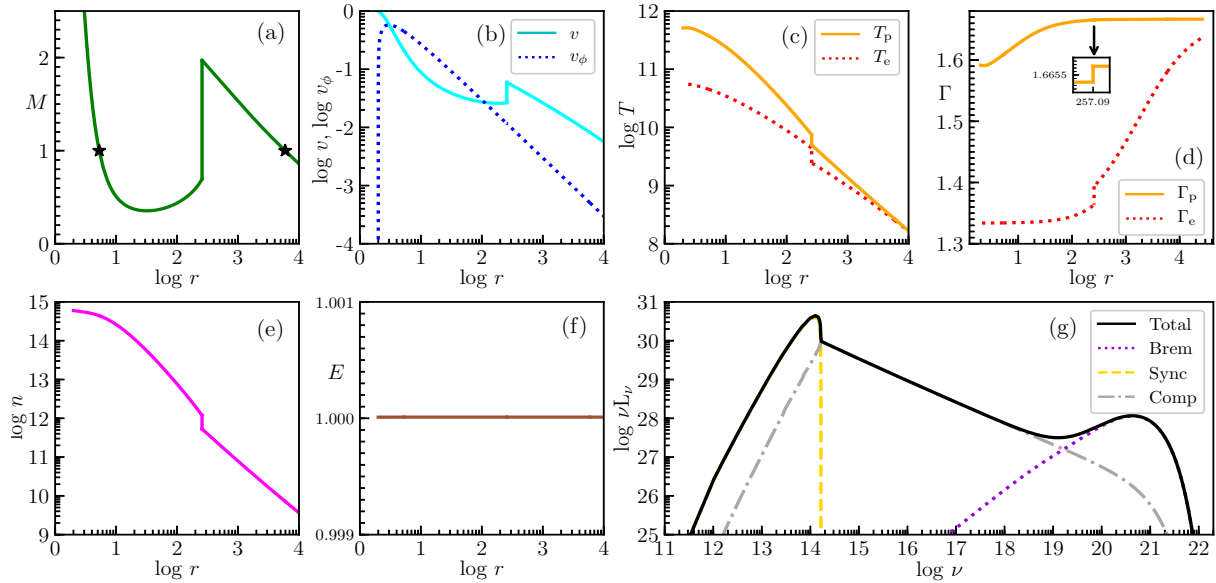


Figure 2: We plot (a) Mach number (M), (b) v (solid, cyan) and v_ϕ (dotted, blue), (c) T_p (solid, orange), T_e (dotted, red), (d) Γ_p (solid, orange), Γ_e (dotted, red), (e) $\log(n)$ (solid, magenta), (f) E (solid, brown), with respect to $\log r$. In panel (g) we plot the total spectrum (solid black) along with contributions coming from bremsstrahlung emission (dotted violet), synchrotron (dashed yellow) and inverse Comptonization (dotted-dashed grey). The set of flow parameters used are $E = 1.00001$, $\lambda = 3.0$, $\dot{M} = 0.001\dot{M}_{\text{edd}}$, $M_{\text{BH}} = 10M_\odot$ and $\theta = 60^\circ$

In Fig.(2), we plot a typical two-temperature transonic advective accretion disk solution with its corresponding flow variables. The parameters used are, $E = 1.00001$, $\lambda = 3.0$, $\dot{M} = 0.001\dot{M}_{\text{edd}}$, $M_{\text{BH}} = 10M_\odot$ and $\theta = 60^\circ$. In panel (a) we plot the global solution, which passes through multiple sonic points (green solid line). First the solution passes through an outer sonic point $r_{\text{co}} = 5935.59r_g$ and then through an inner sonic point $r_{\text{ci}} = 6.29r_g$ (denoted by black stars) through a shock transition at $r_{\text{shock}} = 257.09r_g$. The infall speed of the supersonic matter after passing through the outer sonic point, is slowed down, due to the twin effect of centrifugal force and thermal pressure. This slowed down matter acts as a barrier to the matter coming from behind. This causes the formation of a shock. After the shock, matter becomes subsonic but it ultimately falls into the BH supersonically after passing through the inner sonic point. The radial three-velocity (v) in co-rotating frame and flow velocity in the azimuthal direction (v_ϕ) is plotted in panel (b) (solid cyan and dotted blue respectively). The fate of v and v_ϕ near the horizon is quite different, one approaching c while the other going to 0, since near the BH, gravity is so strong that matter only has a radial velocity component and negligible azimuthal

component. T_p (solid, orange) and T_e (dotted, red) as a function of r is plotted in panel (c). At very large r , $T_p \simeq T_e$. But as the matter flows inwards, cooling processes in electrons starts to dominate. Thus, protons and electrons settle down into two-different temperatures. They are however, coupled by a Coulomb coupling term which acts as an energy exchange term between the protons and electrons. But the term is weak, unlike in one-temperature case, where it is infinite. Panel (d), shows that gamma index of both protons (solid, orange) and electrons (dotted, red) varies with the flow. This justifies our use of CR EoS. Γ_p and $\Gamma_e \sim 1.66$ at very large distances, suggesting that both of them are thermally non-relativistic. When the flow nears the BH, Γ_e becomes mildly-relativistic and then relativistic with $\Gamma_e \sim 1.33$ near the horizon, though Γ_p never becomes truly relativistic. In (e), we have plotted number density (in units of cm^{-3}) vs $\log r$. Since accretion is an example of convergent flow, the number density increases with decrease in radius. In panel (f), we prove that the generalised Bernoulli constant is a constant of motion throughout the flow, even in the presence of dissipation. In panel (g), we plot the spectrum for the accretion flow. It is plotted by summing up all the emissions coming from each radius. Spectrum of each emission process is also plotted separately. Bremsstrahlung is shown in dotted violet line, synchrotron by dashed yellow line and inverse-Comptonization by dotted-dashed grey line.

4.2. Luminosity and Efficiency of Bondi flows as compared to rotating flows :

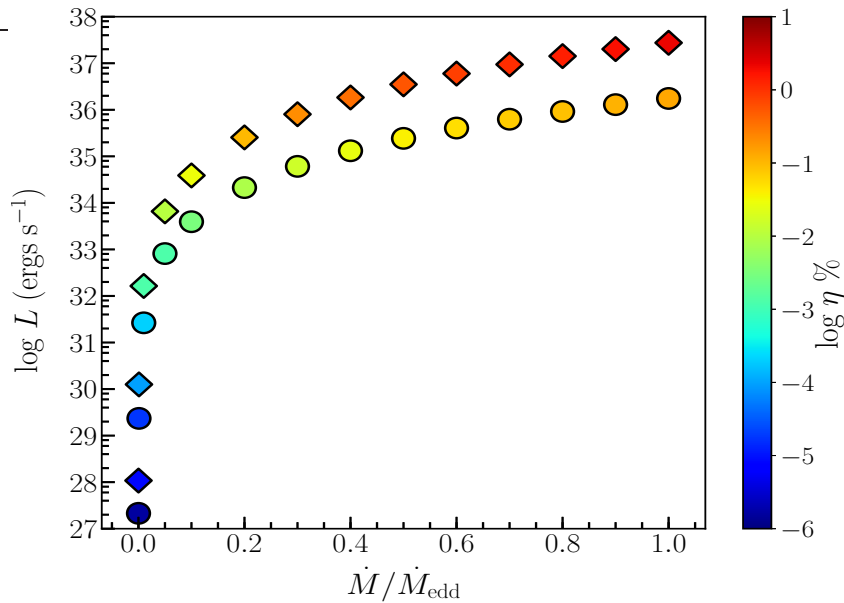


Figure 3: Plot shows the variation of luminosity with \dot{M} which is normalised with respect to Eddington rate (\dot{M}_{edd}). The color bar shows the change in efficiency (in logarithmic scale). The circled points are for spherical flows while diamond shaped points are for flows having angular momentum $\lambda = 2.4$. The other parameters used here are, $E = 1.001$, $M_{\text{BH}} = 10M_{\odot}$ and $\theta = 60^{\circ}$

In Fig.3, we have compared the change in luminosity with increase in accretion rate (\dot{M}), which is in terms of Eddington rate (\dot{M}_{edd}). Circled points are for spherically symmetric flows whereas diamond shaped points are for flows having angular momentum $\lambda = 2.4$. For both the flows parameters used are $E = 1.001$, $M_{\text{BH}} = 10M_{\odot}$ and $\theta = 60^{\circ}$. We can see that as the supplied matter is increased the luminosity increases, irrespective of the type of flow. It is apparent from the plot that Bondi flows are less luminous flows, about an order of magnitude lower than rotating flows. The presence of angular momentum slows down the matter giving it more time to radiate. The color bar plots the efficiency of the system, which is given by the formula, $\tilde{\eta} = L/(\dot{M}c^2)$. The efficiency also have a similar trend, with the increase in accretion rate efficiency increases but flows with angular momentum have a higher efficiency than spherical flows, at a given an accretion rate.

5. Conclusions

In this paper we present our results in case of two-temperature rotating flows, that is flows having some angular momentum. Pure GR treatment was made, which helped us, model the strong gravity of BHs. In these flows, Coulomb coupling is never too strong, to make the flow attain a single temperature. We have also presented results of spherical flows in few cases in order to contrast the differences of these flows with flows having angular momentum.

Our focus in this paper is to obtain unique transonic solutions in two-temperature model. We, in SC19, have reported that two-temperature solutions are degenerate in nature. Infinite transonic solutions exist for the same constants of motion. We solved the problem with the help of the entropy measure (Eq.12) which was obtained from the first principles. In this paper we first demonstrated the use of this entropy form in case of spherical flows, since spherical flows are simple and possess single sonic points. We could see a clear maxima at a certain solution. We applied the same methodology in case of rotating flows as well. But these systems are complex. Still the entropy measure form of ours worked and we again selected the solution with maximum entropy. This helped us in selecting a unique solution from the infinite solutions obtained, for a given set of constants of motion, in case of rotating conical flows. This is the first time, to the best of our knowledge, that such work has been done. This methodology to remove the degeneracy in two-temperature flows is required since any wrong choice of solution would give us a wrong solution and hence an overall wrong information of the system.

In our previous paper SC19, although we have worked on spherical transonic two-temperature flows but we did not consider any GR and doppler effects. We also ignored any photon trapping effects by BH. This led us to high luminosity values in case of spherical flows. In this paper we took these corrections into account and compared the luminosities of these flows with rotating flows. We saw that at $1M_{\text{edd}}$, Bondi flows have efficiencies $\simeq 0.14\%$, while rotating flows have efficiencies $\simeq 2.12\%$. Rotating flows were always an order of magnitude more luminous than spherical flows. Similar trend was also observed in efficiency.

References

- [1] Hoyle, F., and Lyttleton, R. A. 1939, *Proc. Cam. Phil. Soc.*, **35**, 405
- [2] Bondi, H. 1952, *MNRAS*, **112**, 195.
- [3] Salpeter, E. E., 1964, *ApJ*, **140**, 796.
- [4] Shakura N. I., Sunyaev R. A., 1973, *A&A*, **24**, 337.
- [5] Thorne K. S., Price R. H., 1975, *ApJ*, **195**, L101
- [6] Shapiro, S. L., Lightman, A. P., & Eardley, D. M., 1976, *ApJ*, **204**, 187
- [7] Thorne K. S., Price R. H., 1975, *ApJ*, **195**, L101
- [8] Liang E. P. T., Thompson K. A., 1980, *ApJ*, **240**, L271
- [9] Fukue J., 1987, *PASJ*, **39**, 309
- [10] Chakrabarti S. K., 1989, *ApJ*, **347**, 365
- [11] Abramowicz, M. A., Czerny, B., Lasota, J. P., & Szuszkiewicz, E. 1988, *ApJ*, **332**, 646
- [12] Bisnovaty-Kogan, G. S., Lovelace, R.V.E., 2001, *New Astron. Rev.*, **45**, 663
- [13] Colpi M., Maraschi L., Treves A., 1984, *ApJ*, **280**, 319
- [14] Narayan R., Yi I., 1995, *ApJ*, **452**, 710
- [15] Nakamura K. E., Kusunose M., Matsumoto R., Kato S., 1996, *PASJ*, **48**, 761
- [16] Manmoto T., Mineshige S., Kusunose M., 1997, *ApJ*, **489**, 791
- [17] Chakrabarti, S. K., Titarchuk, L. G., 1995, *ApJ*, **455**, 623
- [18] Bisnovaty-Kogan, G. S., Lovelace, R.V.E., 1997, *ApJ*, **486**, L43
- [19] Mandal S., Chakrabarti S. K., 2005, *A&A*, **434**, 839
- [20] Rajesh S. R., Mukhopadhyay B., 2010, *MNRAS*, **402**, 961
- [21] Dihingia I. K., Das S., Mandal S., 2017, *MNRAS*, **475**, 2164
- [22] Chattopadhyay I., Ryu D., 2009, *ApJ*, **694**, 492
- [23] Vyas, M. K., Kumar, R., Mandal, S., Chattopadhyay, I., 2015, *MNRAS*, **453**, 2992
- [24] Chandrasekhar, S., 1938, *An Introduction to the Study of Stellar Structure*, Dover, New York
- [25] Sarkar, S., Chattopadhyay, I., 2019, *Int. J. Mod. Phys. D*, **28**, 1950037
- [26] Chattopadhyay I., Chakrabarti S. K., 2011, *Int. J. Mod. Phys. D*, **20**, 1597

- [27] Kumar R., Chattopadhyay I., 2014, *MNRAS*, **443**, 3444
- [28] Chattopadhyay I., Kumar R., 2016, *MNRAS*, **459**, 3792
- [29] Taub, A. H., 1948, *Phys. Rev.*, **74**, 328
- [30] Schwartzman, V. F., 1971, *Soviet Astr. AJ*, **15**, 377.
- [31] Bisnovatyi-Kogan, G. S., & Ruzmaikin, A. A., 1974, *Ap&SS*, **28**, 45
- [32] Ipser J. P., Price R. H., 1982, *ApJ*, **255**, 654.
- [33] Stepney, S., & Guilbert, P. W. 1983, *MNRAS*, **204**, 1269
- [34] Boldt E., Serlemitsos P., 1969, *ApJ*, **157**, 557.
- [35] Jones, F. C., 1971, *ApJ*, **169**, 503.
- [36] Novikov I. D., Thorne, K. S., 1973, in Dewitt B. S., Dewitt C., eds, *Black Holes*. Gordon and Breach, New York, p. 343.
- [37] Wardziński G., Zdziarski A., 2000, *MNRAS*, **314**, 183

**Institute of Computational Mathematics and Mathematical Geophysics
of Siberian Branch of Russian Academy of Sciences**

CERTIFICATE of PARTICIPATION

This is to certify that

Shilpa Sarkar

has participated to Third Virtual Workshop on Numerical Modeling
in MHD and Plasma Physics: Methods, Tools, and Outcomes.

Honor of Academician Guri I. Marchuk 95th Birthday

Vice-chair of Program committee



Dr. Igor Kulikov

October 12-16, 2020

Pair production and annihilation in advective accretion disks around black holes

Shilpa Sarkar^{1*}, Indranil Chattopadhyay^{1**}

¹Aryabhata Research Institute of Observational Sciences (ARIES), Manora Peak, Nainital-263002, India

E-mail: *shilpa@aries.res.in, **indra@aries.res.in

Abstract. We investigate the role of pair production and annihilation in the presence of radiation processes like bremsstrahlung and inverse-Comptonization, assuming no magnetic fields present in the system. The disk is assumed to be viscous, advective and in hydrostatic equilibrium. Photon-photon interactions leading to pair production is the most dominant process. Threshold for this process is, $h\nu_1 h\nu_2 \gtrsim (m_e c^2)^2$. We find that, for accretion rates lower than $0.8\dot{M}_{\text{edd}}$, we can neglect the presence of any pairs. Maximum number of pair production occurs in a region $< 50r_g$. When the number density of pairs is optimal, a bump is observed near $m_e c^2$ in the spectrum, which is a signature of the annihilated photons.

1. Introduction

Accretion is the best possible mechanism to explain the most luminous objects in the Universe, the Active Galactic Nuclei (AGN). Works by Hoyle & Littleton (1939) [1] and Bondi (1952) [2] laid the foundation for the theory of accretion. These theories shot into prominence when the enormous luminosities emitted from AGNs and X-ray binaries could only be explained with the help of accretion theory. Since then, accretion models have been improvised to match the observational evidences obtained from the new generation of telescopes. One such model was given by Shapiro, Lightman & Eardley [3]. This was the first accretion model which was composed of hot flows and could match the hard power law part of Cygnus X-1 (the first object to be realised as a black hole candidate). They predicted that the electron temperature in accretion disks to be approximately equal to or greater than the electron rest mass energy, $kT_e \gtrsim m_e c^2 = 511 \text{ keV}$ (where, k is the Boltzmann constant, T_e is the electron temperature, m_e is the mass of the electron and c is the speed of light). It was soon realised that the production of $e^+ - e^-$ pairs as well as its annihilation, is an important process and may play a significant role in accretion disc dynamics as well as in shaping the output spectrum.

In 1966, Jelley [4] pointed out that high energy gamma ray photons generated by luminous astrophysical sources on interaction with low-energy photons present in intergalactic and interstellar medium, could lead to the creation of electron-positron pairs. The reaction reads as: $\gamma + \gamma \rightarrow e^+ + e^-$. Herterich (1974) [5] showed that photon-photon pair production process has a threshold condition: $E_1 E_2 (1 - \cos \theta_{\text{pp}}) \geq 2(m_e c^2)^2$, where $E_1 = h\nu_1$ and $E_2 = h\nu_2$ are the energies of the interacting photons and θ_{pp} is the angle between them. He concluded that this process could significantly change the radiative output of the system as well as composition of the flow.



In 1979, Liang [6] proposed one of the first models of an optically thin accretion disk solution including pair production. In this work he assumed the generation of $e^+ - e^-$ pairs through interaction of photons produced by unsaturated Comptonization and found an order of magnitude reduction in electron temperature because of enhanced cooling by these pairs. Unfortunately, detailed analysis was not presented. Also, the treatment was made for sub-relativistic and trans-relativistic electron temperatures, assuming large optical depths, which allowed the photons to scatter efficiently. This scenario is not true in all astrophysical cases. Lightman & Zdziarski (1987) [7] studied the importance of pairs in AGNs and concluded that luminosities are reduced when there is sufficient pair production. Kusunose & Takahara (1988, 1989, 1990) [8, 9, 10] in a series of papers extensively discussed the effect of pairs in two-temperature accretion disks assuming pair equilibrium. These papers covered almost all the photon generation processes leading to the production of pairs : bremsstrahlung, synchrotron, inverse-Comptonization of bremsstrahlung and synchrotron photons (also see White & Lightman (1989) [11]) and external soft photons. But, the ion and electron energy advection term was neglected. Main conclusion of these papers were, for any given accretion rate, there existed two branches of solutions, one with a high pair to ion density ratio (defined as z) and one with a low z . The solution with a high z would generate unphysically high proton temperatures, half-heights and even long relaxation times. These were also unstable against thermal, secular and pair density perturbations. On the contrary, the solution with a low z was stable with negligible effect on the electron temperature or spectra. The authors also showed that a forbidden region will be formed when accretion rates exceed a certain critical value. In this region no steady-state solutions are possible. The reason for formation of this region is the enforcement of pair equilibrium, even in situations where pair production rate exceed the pair annihilation rate. This value of critical accretion rate is characteristic of the type of photon distribution.

Most of the initial works dealing with pair production either assumed a static plasma flow with the assumption of pair equilibrium [12, 13, 14] or a fixed efficiency of the system was considered [15]. Although these studies showed the importance of pair production in different accreting systems, they were not self-consistent. Shull (1979) [16] and Wandel, Yahil, and Milgrom (1984) [17] obtained self-consistent solutions but detailed work on the dynamics of the flow was not done and the radiative transfer part was not properly dealt with. They did not consider the effect of produced pairs back onto the system. Lightman (1982) [18] correctly quoted, that the problem of pair-production is highly non-linear; “pairs produce photons and photons produce more pairs”. Yahel & Brinkman (1981) [19] and Yahel (1982) [20] investigated pair production in the most self-consistent way. But their methodology to obtain solutions were too sensitive, which inhibited them from getting a larger picture of the parameter space. Yahel & Brinkman (1981) concluded that there will be a characteristic spectral signature, a bump like feature near $m_e c^2$, due to $e^+ - e^-$ pairs, unless the number density of pairs is very low. Following them, more realistic self-consistent two-temperature work including pairs was done by Park & Ostriker (1989) [21] and Park (1990) [22] where they assumed spherical flows and implemented radiation hydrodynamic equations. Radiative processes considered were : line cooling, photoionizational heating, bremsstrahlung, Comptonization, pair creation and annihilation. They also considered the effects of generated radiation on the dynamics of the gas flow. The authors concluded that including pair processes in two-temperature solutions does not affect the accretion systems significantly. Advection-dominated disks soon came into existence and Kusunose & Mineshige (1996) [23] investigated the effect of pairs in these disks [24]. They concluded that pairs have negligible effect in these systems.

The discrepancies cited above were due to the fact that different works assumed different radiative processes and hence different radiation field producing pairs. In order to obtain a larger picture, we investigated this matter in greater details in the general-relativistic regime for one-temperature flows. There are three processes which could lead to pair production : photon-

particle (electron, positron or proton), particle-particle and photon-photon interaction. Out of them photon-photon interaction is the most dominant process responsible for the production of $e^+ - e^-$ pairs [25]. Particle-particle interactions and photon-particle interactions are of less importance because their reaction cross-section decreases in the order of $(1/137)$ (value of fine structure constant) and $(1/137)^2$ respectively. Hence, we can safely ignore them. In this work we assume that there are no magnetic fields present in the system. Thus, as a preliminary step, we include only bremsstrahlung and its inverse-Comptonization. The photons generated due to bremsstrahlung are in general, hard (of higher energy). If a photon's energy is lower than the energy of the ambient electrons, they can get upscattered to higher energies through the process of inverse-Comptonization. The probability for a photon to get scattered depends on the optical depth of the system. Thus, in the present work, the radiation field is made of a flat unscattered bremsstrahlung spectrum and a Wien tail. If these photons satisfy the criterion for pair production, $e^+ - e^-$ pairs would be produced [24]. Depending on the number density of the pairs produced, simultaneous annihilation will occur. After the annihilation process the radiation field will also contain these photons apart from the usual bremsstrahlung and inverse-Compton photon distribution.

Flows around BHs are trans-relativistic in nature. They are non-relativistic ($kT < m_e c^2$, adiabatic index= $\Gamma \sim 5/3$) very far away from the horizon. As matter approaches the BH, it is compressed to smaller and smaller regions, with radiative processes playing significant role, the flow becomes mildly relativistic or relativistic ($kT \gtrsim m_e c^2$, $\Gamma \sim 4/3$). The exact equation of state (EoS) for such a flow was given by Chandrasekhar in 1939 [26]. This equation is computationally difficult to implement. Thus, we have used the Chattopadhyay & Ryu (2009) [27] EoS (CR EoS hereafter) for multispecies flow with variable adiabatic index. This EoS is analytical and exact which helped us to deal away with specifying any value of adiabatic index for each species at each point of the flow.

The paper is divided into the following sections. In section (2), we will cover the basic equations and assumptions used to model the flow. In section (3), we will discuss the methodology to find a self-consistent one-temperature transonic solution, including pair processes. We will show some important results in section (4) and finally conclude in section (5).

2. Assumptions and equations used to model the flow

We assume an advective viscous transonic accretion disk in hydrostatic equilibrium around a Schwarzschild BH. The treatment is in the pure general-relativistic regime where the line element in terms of spherical coordinate system is given by [28, 29]:

$$ds^2 = g_{tt}dt^2 + g_{rr}dr^2 + g_{\phi\phi}d\phi^2 + g_{\theta\theta}d\theta^2, \quad (1)$$

where, $g_{\mu\nu}$ s are the metric tensor components. The non-zero components are $g_{tt} = -(1 - \frac{2}{r})$; $g_{rr} = (1 - \frac{2}{r})^{-1}$; $g_{\theta\theta} = r^2$; $g_{\phi\phi} = r^2 \sin^2 \theta$. We have employed a system of units where, $G = M = c = 1$, such that the unit of length is in $r_g = GM_{\text{BH}}/c^2$ (where G = Gravitational constant, M_{BH} = mass of BH) and the unit of velocity is in terms of light speed c . This unit system has been used throughout the paper unless mentioned otherwise. We assume the flow to be in steady state and around the equatorial plane, hence $\partial/\partial t = 0$ and $\theta = 90^\circ$, respectively. In addition, we assume fully ionized plasma and charge neutrality in the system. Accretion flows are governed by the following equations :

$$(1) \text{ Continuity equation: } (nu^\nu)_{;\nu} = S_i - S_o,$$

where, n = number density of the particles and u^μ s are the four-velocity components, and S_i and S_o are source and sink terms of pair production. In presence of pair production, the particle four-flux are not conserved. So, we define separately, the continuity equation for each particle

(proton: n_p , electron: n_{e^-} and positron: n_{e^+}).

(a) Proton: In the process of pair production, proton number density is not affected and hence the continuity equation can be integrated to obtain a form of conservation of proton mass flux or the proton-accretion rate of the system.

$$\dot{M} = 2\pi\rho_p u^r r H, \quad (2)$$

where, ρ_p is the proton mass density and H is the half-height at each radius of the disk, the disk being in hydrostatic equilibrium. The form of half-height is obtained using the prescription given by Lasota (1994) [30, 31].

(b) Positron: The continuity equation for positron can be written as [32] :

$$\frac{dn_{e^+}}{dr} = \frac{(\dot{n}_C - \dot{n}_A)}{u^r} - \frac{n_{e^+}}{rHu^r} \frac{d(rHu^r)}{dr} \quad (3)$$

where, \dot{n}_C and \dot{n}_A are the creation and annihilation rates per unit volume, expressions of which will be discussed later.

(c) Electron : Charge neutrality demands that the number of positive charges equal the number of negative charges. This gives us the electron number where :

$$n_{e^-} = n_{e^+} + n_p \quad (4)$$

(2) Conservation of energy-momentum : $T^{\mu\nu}_{;\nu} = 0$,

where $T^{\mu\nu}$ is the energy-momentum tensor of a fully ionized viscous fluid and is given by :

$$T^{\mu\nu} = (e + p)u^\mu u^\nu + pg^{\mu\nu} + t^{\mu\nu}, \quad (5)$$

where, e , p and $t^{\mu\nu}$ are the local internal energy density, local isotropic gas pressure and viscous stress tensor, respectively. Projecting the four-divergence of $T^{\mu\nu}$ along the space direction, gives the relativistic Navier-Stokes equation, radial component of which is:

$$u^r \frac{du^r}{dr} + \frac{1}{r^2} - (r - 3)u^\phi u^\phi + (g^{rr} + u^r u^r) \frac{1}{e + p} \frac{dp}{dr} = 0. \quad (6)$$

and the integrated form of the azimuthal component gives :

$$\rho u^r (L - L_0) = t^{\mu\nu} \quad (7)$$

Here, $L = hu_\phi$ and L_0 is the local bulk angular momentum defined at each radius and that defined at the horizon, respectively [33]. The specific angular momentum of the fluid is defined as $\lambda = -u_\phi/u_t$. Assuming shear to be the only factor giving rise to viscosity, we have $t^{\mu\nu} = -2\eta\sigma^{\mu\nu}$, where, η is the viscosity coefficient, defined as $\eta = \rho h\bar{\nu}$. Here, $\bar{\nu} = \alpha_\nu ar(1 - v^2)$ is defined as the kinematic viscosity, with α_ν being the usual Shakura & Sunyaev viscosity parameter [34] and $v = \sqrt{u_r u^r}/(1 + u_r u^r)$ is the radial three-velocity defined in the local co-rotating frame. Enthalpy and speed of sound in the medium is defined using h and a , respectively.

(3) First law of thermodynamics : $u_\mu T^{\mu\nu}_{;\nu} = 0$,

which can be simplified using Eq.(5) to :

$$u^r \left[\left(\frac{e + p}{\rho} \right) \rho_{,r} - e_{,r} \right] = \Delta Q, \quad (8)$$

where, $\Delta Q = Q^+ - Q^-$ is the difference in the heating and cooling rate of the system.

2.1. Equation of state and the simplified equations of motion

As discussed before, we use the CR EoS which is given by,

$$e = \frac{\rho}{\tilde{K}} f = \frac{\rho}{\tilde{K}} (2 - \xi) \left[1 + \Theta \left(\frac{9\Theta + 3}{3\Theta + 2} \right) \right] + \xi \left[1 + \Theta \left(\frac{9\Theta + 3/\chi}{3\Theta + 2/\chi} \right) \right] \quad (9)$$

where, $\tilde{K} = 1 + 1/\chi$, $\xi = n_p/n_{e^-}$, $\chi = m_e/m_p$ and $\Theta = \frac{kT}{m_e c^2}$ is the non-dimensional form of temperature defined w.r.t the rest mass energy of the electron. Polytropic and adiabatic indices are defined as, $N = \frac{1}{2} \frac{df}{d\Theta}$ and $\Gamma = 1 + \frac{1}{N}$ respectively.

Using EoS, Eq.(9), we can simplify the first law of thermodynamics Eq.(8), to obtain :

$$\frac{d\Theta}{dr} = -\frac{\Theta}{\Theta H_\Theta + N} \left(\mathcal{A} + \mathcal{B} \frac{dl}{dr} + \mathcal{C} \frac{dv}{dr} - \frac{\mathbb{Q} - \mathbb{P}}{2\Theta} \right) \quad (10)$$

where, $H_x = \frac{1}{H} \frac{\partial H}{\partial x}$, $\mathcal{A} = H_r + \frac{r-1}{r(r-2)}$, $\mathcal{B} = H_l$, $\mathcal{C} = H_v + \frac{1}{v(1-v^2)}$ and $\mathbb{Q} = \frac{\Delta Q \tilde{K}}{\rho u^r}$. The term \mathbb{P} is used to calculate the leptons internal energy consumed in producing pairs. If we simplify the azimuthal component of Navier-Stokes equation Eq.(7), we have :

$$\frac{dl}{dr} = \left[-\frac{\rho u^r (L - L_0)}{\eta \left(1 - \frac{2}{r}\right)} + \frac{2l}{r} \right] (1 - v^2), \quad (11)$$

here, $l = u_\phi$. Now, we can obtain the differential equation for velocity from Eq.(6), using Eqs.(2-4) and (9-11), to obtain:

$$\frac{dv}{dr} = \frac{\mathcal{N}}{\mathcal{D}}, \quad (12)$$

where, $\mathcal{N} = -\frac{1}{r(r-2)} + \frac{(r-3)l^2}{(r-2)r^3\gamma_v^2} + \frac{Na^2}{\Theta H_\Theta + N} \left(\mathcal{A} + \mathcal{C} \frac{dl}{dr} + \frac{(1-\Theta H_\Theta)(\mathbb{Q}-\mathbb{P})}{hKNa^2} \right)$ and $\mathcal{D} = \frac{v}{1-v^2} - \frac{Na^2\mathcal{B}}{\Theta H_\Theta + N}$.

The sound speed is defined as, $a = \sqrt{\frac{\Gamma p}{e+p}}$. If we integrate Eq.(6) using Eq.(8) we obtain the generalised Bernoulli constant :

$$E = -h\gamma_v \sqrt{1 - \frac{2}{r}} \exp(-X_f), \quad (13)$$

which is a constant of motion even in the presence of dissipation. When the system is adiabatic and there is no dissipation $E \rightarrow \mathcal{E} = -h u_t$, which is the canonical form of relativistic Bernoulli constant [31].

2.2. Pair production and annihilation processes

We assume pair production only through photon-photon interactions as mentioned before : $\gamma + \gamma \rightarrow e^+ + e^-$. The threshold condition is $E_1 E_2 (1 - \cos \theta_{pp}) \geq 2(m_e c^2)^2$, suggesting that photons of energy $> m_e c^2$ can only contribute to this process. Photon production mechanisms considered in this work are bremsstrahlung, inverse-Comptonization and the pair-annihilation photons.

Bremsstrahlung photons (\dot{n}_{br}) can be produced by $e^\pm - p$, $e^\pm - e^\pm$ and $e^+ - e^-$ interactions. Their expressions are given in Svensson (1984) [14] and White & Lightman (1989) [11]. The photons generated through inverse-Comptonization (\dot{n}_{ic}) can be calculated using the form $\dot{n}_{ic} = f_b \dot{n}_{br}$, where f_b is the fraction of emitted bremsstrahlung photons that are scattered upto the Wien peak before escaping the disk. Thus, it depends on the optical depth of the system as well as the temperature of the ambient electrons. It is calculated using the prescription given by Nakamura *et. al.* (1996) [35]. For computing the photons produced due to annihilation (\dot{n}_{ann})

we use the expression given by White & Lightman (1989) [11]. Thus, to calculate the total number of photons contributing to pair-production (n_γ), we solve the photon balance equation, which reads:

$$n_\gamma = [(1 + f_B)\dot{n}_{br} + \dot{n}_{ann}]t_{esc} \quad (14)$$

where, $t_{esc} = H/c(1 + \tau_{es})$, is the photon escape time and τ_{es} is the optical depth of the system. After we have information of the radiation fields present in the system, we identify all the possible combinations, which can lead to pair production. They are as follows : collisions between (1) photons of the same Wien peak (\dot{n}_{WW}), (2) between Wien and flat unscattered bremsstrahlung photons (\dot{n}_{WF}), (3) between the photons belonging to the same unscattered flat part (\dot{n}_{FF}), (4) Wien photon and the annihilation photons (\dot{n}_{WA}), (5) flat part of bremsstrahlung photons with annihilation photons (\dot{n}_{FA}) and (6) between the same distribution of annihilation photons (\dot{n}_{AA}). Thus the creation rate can be written as :

$$\dot{n}_C = \dot{n}_{WW} + \dot{n}_{WF} + \dot{n}_{FF} + \dot{n}_{WA} + \dot{n}_{FA} + \dot{n}_{AA} \quad (15)$$

All these 6 scenarios have been included in this work, expressions of which are taken from White & Lightman (1989) [11] and Esin (1999) [24]. The annihilation rate can be written as [13] :

$$\dot{n}_A = n_{e^+}n_{e^-}cr_e^2 \frac{\pi}{1 + \frac{2\Theta^2}{\ln(1.12\Theta+1.3)}} \quad (16)$$

where, r_e is the electron radius.

2.3. Radiative processes

The radiative processes considered are as follows :

- Electron is cooled via three processes : (1) bremsstrahlung (Q_{br}) radiation (through $e^\pm - p$, $e^\pm - e^\pm$ and $e^+ - e^-$ collisions [11]) (2) inverse-Comptonization of bremsstrahlung photons (Q_{ic}) [11] and (3) annihilation (Q_{ann}) [12]
- Viscous dissipation of energy leads to heating in the system. Shakura & Sunyaev α_v parameter [34] controls the amount of this dissipation.
- The pairs produced, have same thermal energies as the other particles present in the system, thus contributing to an overall heating term : $Q_{pair-heat} = \langle h\nu_1 + h\nu_2 \rangle \dot{n}_C$.
- If the temperature of the electrons are less than the energy of the ambient photons, then electrons can heat up via Compton heating (Q_{comp}) mechanism [29].

Thus to summarize : $Q^+ = Q_B + Q_{pair-heat} + Q_{comp}$ and $Q^- = Q_{br} - Q_{ic} - Q_{ann}$. In addition, we have implemented all the special and general relativistic transformations while computing the actual energy loss as well as while plotting the spectrum.

2.4. Sonic point conditions and shock conditions

Mathematically a sonic point is defined as the point where dv/dr has a 0/0 form. Hence, from Eq.(12), the sonic point conditions are: $\mathcal{N} = 0$ and $\mathcal{D} = 0$. To find the derivative of the velocity at the sonic point ($dv/dr|_c$) we need to use the L'Hospital rule. Presence of angular momentum and relativistic effects causes the multiplicity of sonic points. Depending on the flow parameters, an accretion solution may harbour one or more sonic points [29]. The sonic points are named according to its distance from the BH : inner (r_{ci}), middle (r_{cm}) and outer (r_{co}). Inner and outer sonic points are X-type sonic points and are physical in nature, *i.e.* flows pass through them, while O-type sonic points are unphysical in nature. Due to the multiplicity of sonic points, shocks can also be formed. Supersonic matter (after it has passed through r_{co}), due to the

twin effect of centrifugal and thermal pressure could act as a barrier to the matter following it, inducing the formation of a centrifugal-force mediated shock transition. After the shock jump, matter becomes subsonic, but crosses the horizon supersonically after passing through r_{ci} . The relativistic shock conditions [38] are: (1) Conservation of mass flux: $[M] = 0$, (2) Conservation of energy flux: $[\dot{E}] = 0$, (3) Conservation of azimuthal momentum flux : $[\dot{M}L_0] = 0$ and (4) Conservation of radial momentum flux: $[\rho H h \gamma_v^2 v^2 + p H] = 0$, where, the square brackets denotes the difference of the quantities across the shock.

3. Methodology to obtain a solution

3.1. Finding a general transonic solution without pairs

Here, we discuss the method to find a general one-temperature advective transonic solution without any pair processes. The system we are dealing with, is still dissipative (viscous dissipation as well as radiative processes are included), hence sonic points are not known a priori. For a given a set of flow parameters (E , λ_{in} , α_v , β_d , \dot{M} and M_{BH}), a solution may harbour one or more sonic points (see Section 2.4). Finding of sonic points is not trivial. The first step is to specify the boundary conditions. For this, we select a point asymptotically close to the horizon, say, $r_{in} = 2.001$ (in terms of r_g), horizon being a co-ordinate singularity. The reason for this choice is that, near the horizon, the value of the variables are known, $r \rightarrow 2r_g$ and $v \rightarrow c$. Also, $E \rightarrow \mathcal{E} = -hu_t$, because very near the horizon, gravity overpowers any process or interaction, preventing the matter to either interact with itself or its environment, making the region adiabatic in nature. We now give a step-by-step procedure for finding solutions:

(1) Obtaining boundary conditions (v_{in} , l_{in} and L_0): We first assume any arbitrary value of Θ_{in} . We evaluate the value of l_{in} from the definition of specific angular momentum, $\lambda_{in} = -u_\phi/u_t = -l_{in}/(E/h_{in})$, h_{in} being a function of only Θ_{in} . Simplifying $E = -h_{in}u_t$ near the horizon, gives us an analytical expression for velocity near the horizon (v_{in}). Hence, supplying the value of E , $h_{in}(\Theta_{in})$ and l_{in} (as obtained before), would give us the value of v_{in} . The adiabaticity condition near the horizon reads $E \simeq \mathcal{E}$, which implies $\gamma_\phi \exp(X_f) = 1$, from Eq. (13). Calculating its derivative w.r.t r and then simplifying it, would give us a quadratic equation in $(L_{in} - L_0)$, (where, $L_{in} = l_{in}h_{in}$) from which we can find the value of L_0 .

(2) Finding sonic point (obtaining Θ_{in}): After finding v_{in} , l_{in} and L_0 for a given set of flow parameters and a given arbitrary Θ_{in} , we integrate the equations of motion Eq.(3) and Eq.(10-12) from r_{in} outwards, towards infinity using 4th order Runge-Kutta integration technique. We check whether the solution obtained passes through the sonic point or not. If it does not, then we change Θ_{in} , until the sonic point conditions are satisfied. We note that, although it is a pair-free iteration, we calculate the maximum positron density that could be obtained with the current radiative processes.

(3) Obtaining the transonic solution : As soon as we get the sonic point, we find the derivative $dv/dr|_c$ using L' Hospital rule and integrate further outwards until we reach infinity (around $r \rightarrow 10^4 r_g$) or the velocity of the solution becomes too low.

(4) Checking for other sonic points : Since angular momentum and relativistic effects induces the formation of multiple sonic points, we need to check whether any other sonic point exists for the same L_0 . For this we change Θ_{in} by a larger value and repeat the steps described from 1-2. If there is another sonic point present then we follow step 3 to obtain a transonic solution.

(5) Checking of shock transitions : When a certain set of flow parameters harbour multiple sonic points, we need to check whether the solutions passing through them satisfy the shock conditions (see, Section 2.4 for shock conditions). If, satisfied, the solution first passes through the outer sonic point (r_{co}) encounters a shock (r_s) and then passes through the inner sonic point (r_{ci}), entering the horizon supersonically. At the shock location, the velocity of the flow becomes subsonic while temperature and density jumps to higher values.

3.2. Including of pair processes and using an iteration technique to obtain a solution

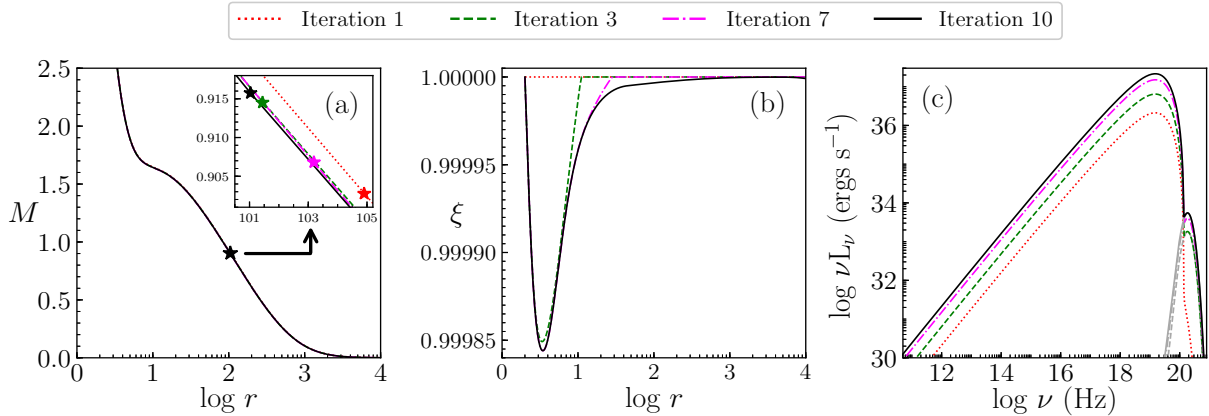


Figure 1: Finding of transonic solution with pairs, using iteration technique. Iteration 1 is pair-free. From iteration 2 onwards, pair-production and annihilation processes are included. Iteration process continues until the solutions converge. The corresponding change in Mach number, $M = v/a$ (panel a), composition of the flow, $\xi = n_p/n_{e^-}$ (panel b) and spectrum (panel c), with the change in iteration is plotted. Grey curves are the emission from annihilation photons, corresponding to each iteration. The flow parameters used are, $E = 1.001$, $\lambda_{\text{in}} = 2.5$, $\dot{M} = 0.6\dot{M}_{\text{edd}}$, $\alpha_v = 0.05$ and $M_{\text{BH}} = 10M_{\odot}$.

The methodology described above is for a pair-free model. We name it as iteration 1. In iteration 2, we repeat steps 1-5, mentioned in the above section, using the positron number density calculated in iteration 1. But now, we include the pair creation and annihilation processes along with the processes included before in iteration 1. We continue this process of iterating, until the solutions converge.

To explain it further, we plot in Fig.(1a), Mach number, defined as, $M = v/a$ and in Fig.(1b) the composition of the flow, defined using $\xi = n_p/n_{e^-}$. The flow parameters used are, $E = 1.001$, $\lambda_{\text{in}} = 2.5$, $\dot{M} = 0.6\dot{M}_{\text{edd}}$, $\alpha_v = 0.05$ and $M_{\text{BH}} = 10M_{\odot}$. Iteration 1 is denoted using red, dotted line. We can see that, the solution passes through a single sonic point (marked with a red star, in panel a, clearly visible in inset) and $\xi = 1$ for the first iteration (panel b), *i.e.* pair-free. As we perform iterations, there is a play between pair production and annihilation processes. The annihilation photons introduces an additional radiation field into the system, hence, there will be an increase in pair production and the interplay between these processes will go on. Coloured stars in panel (a) depicts the sonic point, which shifts to different locations with each iteration. We select the solution after 10 iterations or until the solutions converge, whichever is earlier. This is clearly visible from panels (a) and (b), where, we have performed 10 iterations and during the last iterations the solutions are almost converged (only intermediate iterations are plotted). The final transonic solution (panel a) and composition of the flow (panel b), in the presence of pair production and annihilation, for the given set of flow parameters, is shown in black, solid line. In panel (c), we plot the change in spectrum with iterations. Grey curves depict the emission due to annihilation, corresponding to each iteration, while the rest of the spectral emission comes from bremsstrahlung and its inverse-Comptonization. We see that, in iteration 1, there is no emission from annihilation, because of the absence of positrons. While, as we increase the number of iterations, the spectral shape changes depending on the pair processes and annihilation, ultimately converging to the spectrum shown in black, solid line.

4. Results

4.1. General one-temperature transonic solutions including pair production and annihilation

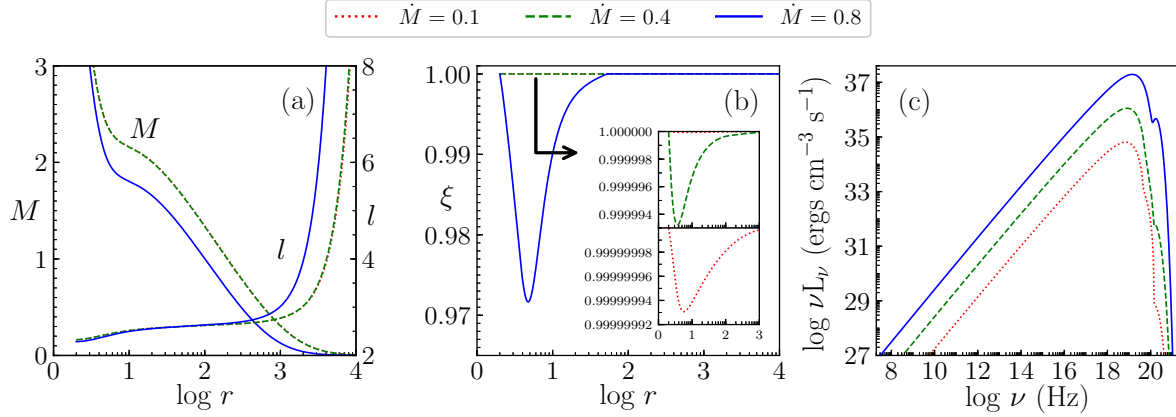


Figure 2: (a) M , l and (b) ξ vs $\log r$ plotted for different accretion rates of the system. Their corresponding spectrum is plotted in panel (c). The accretion rates used are: $\dot{M} = 0.1\dot{M}_{\text{edd}}$ (red, dotted), $\dot{M} = 0.4\dot{M}_{\text{edd}}$ (green, dashed) and $\dot{M} = 0.8\dot{M}_{\text{edd}}$ (blue, solid). Rest of the flow parameters are $E = 1.001$, $\lambda_{\text{in}} = 2.60$, $\alpha_v = 0.01$ and $M_{\text{BH}} = 10M_\odot$.

We investigate a general transonic one-temperature solution, including pair processes. The solution is obtained using the methodology elaborately described before. A typical solution is represented using Mach number (M) and the covariant azimuthal component of four-velocity l or u_ϕ plotted in Fig.(2a), while the composition of the flow $\xi = n_p/n_{e^-} = n_p/(n_p + n_{e^+})$ is plotted in Fig.(2b). Both of these have been plotted against $\log r$. The different curves represent the different accretion rates of the system: $\dot{M} = 0.1\dot{M}_{\text{edd}}$ (red, dotted), $\dot{M} = 0.4\dot{M}_{\text{edd}}$ (green, dashed) and $\dot{M} = 0.8\dot{M}_{\text{edd}}$ (blue, solid). Other flow parameters are, $E = 1.001$, $\lambda_{\text{in}} = 2.60$, $\alpha_v = 0.01$ and $M_{\text{BH}} = 10M_\odot$. From the plot it is apparent that for these set of flow parameters only an outer sonic point exists. As we increase the accretion rate of the system the sonic point shifts inwards, towards the BH (clearly visible for $\dot{M} = 0.8\dot{M}_{\text{edd}}$ solution). This is mainly because of the increase in cooling of the system with the increase in accretion rate. We note that there is a minor decrease in the location of the sonic point for the solution represented by accretion rate $0.8\dot{M}_{\text{edd}}$ as compared to $0.4\dot{M}_{\text{edd}}$. The solutions represented in panel (a) for these accretion rates is hence seen to be overlapped. Panel (b) interprets the presence of positrons in the flow. A decrease in ξ , suggests an increase in the number of positrons in the flow. We see that, at infinity and just near the horizon, $\xi = 1$, meaning that there are no positrons present in these regions. At infinity, radiative mechanisms are less effective due to low temperatures and low number densities. Thus, the radiation field giving rise to pair production is weak, leading to negligible production of positrons. While, near the horizon, photon trapping effects of the BH dominate, thereby reducing the number density of photons and hence, lowering of pair production rates occur. But, there could be ample amount of advected positrons and electrons. The annihilation rate is found to be higher in these regions reducing the number of positrons to ~ 0 . Now, as we increase the accretion rate of the system, matter supply becomes more, hence, there is more cooling in the system. Thus, the solution will take a higher temperature branch, to sustain the excessive cooling. This will, in turn, increase the pair production rate, contributing to the rise in positron number density in the flow and hence decreasing ξ (panel b). In panel (c), spectrums are plotted, where, with the increase in accretion rate, the system becomes more luminous. There is a bump in all the spectrums near $\sim m_e c^2$, whose magnitude increases with the increase in accretion rate of the system. This bump is a signature of the amount of annihilation photons. More the accretion rate more would be the pairs produced and

hence more will be the photons generated through pair annihilation.

5. Conclusions

In this paper, we present one-temperature advective, viscous, transonic solutions, in the presence of cooling processes like bremsstrahlung, inverse-Comptonization as well as incorporating pair production and annihilation mechanisms. There was no fixed adiabatic index for the flow. CR EoS helped us in dealing with it. Pair production was assumed to be from the interactions between the photons generated through the above mentioned processes. We find that the number of pairs produced by bremsstrahlung, inverse-Compton and annihilation photons are not significant, since the minimum ξ is > 0.97 for an accretion rate of $\dot{M} = 0.8\dot{M}_{\text{edd}}$. For accretion rates lower than this, we can neglect the presence of any pairs. Also, the maximum number of pairs are produced in a region $< 50r_g$. When the number density of pairs is not very low, like for accretion rates $> 0.8\dot{M}_{\text{edd}}$, there is a bump near $m_e c^2$ in the spectrum. This is a spectral signature of the annihilated photons. We plan to carry out detailed analysis of this work in future.

References

- [1] Hoyle, F., and Lyttleton, R. A. 1939, *Proc. Cam. Phil. Soc.*, **35**, 405.
- [2] Bondi, H. 1952, *MNRAS*, **112**, 195.
- [3] Shapiro, S. L., Lightman, A. P., & Eardley, D. M., 1976, *ApJ*, **204**, 187.
- [4] Jelley, J.V., 1966, *Nature*, **211**, 472.
- [5] Herterich, K., 1974, *Nature*, **250**, 311.
- [6] Liang E. P. T., 1979, *ApJ*, **234**, 1105.
- [7] Lightman, A.P. and Zdziarski, A.A., 1987, *ApJ* **319**, 643.
- [8] Kusunose M., Takahara F., 1988, *PASJ*, **40**, 435.
- [9] Kusunose M., Takahara F., 1989, *PASJ*, **41**, 263.
- [10] Kusunose M., Takahara F., 1990, *PASJ*, **42**, 347.
- [11] White T. R., Lightman A. P., 1989, *ApJ*, **340**, 1024.
- [12] Svensson R., 1982, *ApJ*, **258**, 321.
- [13] Svensson R., 1982, *ApJ*, **258**, 335.
- [14] Svensson R., 1984, *MNRAS*, **209**, 175.
- [15] Lightman, A.P., Zdziarski, A.A., and Rees, M.J., 1987, *ApJ*, **315**, L113.
- [16] Shull, J.M., 1979, *ApJ*, **229**, 1092.
- [17] Wandel, A., Yahil, A., and Milgrom, M., 1984, *ApJ*, **282**, 53.
- [18] Lightman, A.P., 1982, *ApJ*, **253**, 842.
- [19] Yahel, R.Z. and Brinkmann, W., 1981, *ApJ*, **244**, L7.
- [20] Yahel, R.Z., 1982, *ApJ*, **252**, 356.
- [21] Park, M.-G. and Ostriker, J.P., 1989, *ApJ*, **347**, 679.
- [22] Park M.-G., 1990, *ApJ*, **354**, 83.
- [23] Kusunose M., Mineshige S., 1996, *ApJ*, **468**, 330.
- [24] Esin A. A., 1999, *ApJ*, **517**, 381.
- [25] Colpi M., Maraschi L., Treves A., 1984, *ApJ*, **280**, 319.
- [26] Chandrasekhar, S., 1939, *An Introduction to the Study of Stellar Structure*, Univ. of Chicago Press, 1939.
- [27] Chattopadhyay I., Ryu D., 2009, *ApJ*, **694**, 492.
- [28] Sarkar, S., Chattopadhyay, I., 2019, *Int. J. Mod. Phys. D*, **28**, 1950037.
- [29] Sarkar, S., Chattopadhyay, I., Laurent, P., 2020, *A&A*, DOI : 10.1051/0004-6361/202037520.
- [30] Lasota, J. P. 1994, in *Theory of Accretion Discs*, Vol. 2, ed., 341.
- [31] Chattopadhyay I., Chakrabarti S. K., 2011, *Int. J. Mod. Phys. D*, **20**, 1597.
- [32] Fukue, J., 1986, *PASJ*, **38**, 167.
- [33] Chattopadhyay I., Kumar R., 2016, *MNRAS*, **459**, 3792.
- [34] Shakura N. I., & Sunyaev R. A., 1973, *A&A*, **24**, 337.
- [35] Nakamura K. E., Kusunose M., Matsumoto R., Kato S., 1996, *PASJ*, **48**, 761.
- [36] Schwartzman, V. F., 1971, *Soviet Astr. AJ*, **15**, 377.
- [37] Ipser J. P., Price R. H., 1982, *ApJ*, **255**, 654.
- [38] Taub, A. H., 1948, *Phys. Rev.*, **74**, 328.